AFRL-OSR-VA-TR-2013-0616

Exploring Electrical and Magnetic Resonances from Coherently Correlated Long-Lived Radical Pairs towards Development of Negative Refractive-Index Materials

PI: Bin Hu

04/29/2015
Final Report

DISTRIBUTION A: Distribution approved for public release.

Air Force Research Laboratory
AF Office Of Scientific Research (AFOSR)/ RTD
Arlington, Virginia 22203
Air Force Materiel Command

REPORT DOCUMENTATION PAGE

Form Approved
OMB No. 0704-0188

The public reporting burden for this collection of information is estimated to average 1 hour per response, including the time for reviewing instructions, searching existing data sources, gathering and maintaining the data needed, and completing and reviewing the collection of information. Send comments regarding this burden estimate or any other aspect of this collection of information, including suggestions for reducing the burden, to the Department of Defense, Executive Service Directorate (0704-0188). Respondents should be aware that notwithstanding any other provision of law, no person shall be subject to any penalty for failing to comply with a collection of information if it does not display a currently valid OMB control number.

PLEASE DO NOT RETURN YOUR FORM TO THE ABOVE ORGANIZATION.

1. REPORT DATE *(DD-MM-YYYY)*	2. REPORT TYPE	3. DATES COVERED *(From - To)*
01/03/2015	Final report	July 01 2011 - December 31 2014

4. TITLE AND SUBTITLE

Project title: Exploring Electrical and Magnetic Resonances from Coherently Correlated Long-Lived Radical Pairs towards Development of Negative Refractive-Index Materials

Subtitle:

Task 1: Radicals Based Molecular Metamaterials

Task 2: Thin-Film Based Polymer Thermoelectric Devices

5a. CONTRACT NUMBER

5b. GRANT NUMBER

FA9550-11-0082

5c. PROGRAM ELEMENT NUMBER

6. AUTHOR(S)

PI: Bin Hu

Participants: Dr. Lei He, Dr. Dehua Hu, PhD student: Liang Yan, PhD student: Mingxing Li, Ph.D student: Huidong Zang, Ph.D student: Qing Liu

5d. PROJECT NUMBER

5e. TASK NUMBER

5f. WORK UNIT NUMBER

7. PERFORMING ORGANIZATION NAME(S) AND ADDRESS(ES)

University of Tennessee
Department of Materials Science and Engineering
1508 Middle Drive
Knoxville, TN 37996

8. PERFORMING ORGANIZATION REPORT NUMBER

9. SPONSORING/MONITORING AGENCY NAME(S) AND ADDRESS(ES)

Air Force Office of Scientific Research
875 N. Randolph Street, room 3112
Arlington, VA 22203

10. SPONSOR/MONITOR'S ACRONYM(S)

11. SPONSOR/MONITOR'S REPORT NUMBER(S)

12. DISTRIBUTION/AVAILABILITY STATEMENT

DISTRIBUTION A

13. SUPPLEMENTARY NOTES

14. ABSTRACT

The research efforts have made following major breakthroughs:

1. Developed new strategy to couple pi-d electrons for the development of molecular metamaterials [J. Am. Chem. Soc. 134, 3549, 2012]
2. Explored new mechanism to utilize intermolecular excited states for realizing electric-magnetic coupling towards developing molecular metamaterials [Adv. Mater. 23, 2216, 2011]
3. Developed new method to use radicals for electric-magnetic coupling towards radicals-based metamaterials [Adv. Mater 26, 3956, 2014]
4. Discovered a novel mechanism to generate magneto-optic properties by establishing spin-exchange interaction in electron-hole pairs in ferroelectrically semiconducting materials [Advanced Materials, DOI: 10.1002/adma.201405946, 2015]
5. Developing new strategy to separately control electrical and thermal conductivities by using interfacial polarization [Adv. Mater. 23, 4120, 2011]

15. SUBJECT TERMS

16. SECURITY CLASSIFICATION OF:			17. LIMITATION OF ABSTRACT	18. NUMBER OF PAGES	19a. NAME OF RESPONSIBLE PERSON
a. REPORT	b. ABSTRACT	c. THIS PAGE			19b. TELEPHONE NUMBER *(Include area code)*

Reset

INSTRUCTIONS FOR COMPLETING SF 298

1. REPORT DATE. Full publication date, including day, month, if available. Must cite at least the year and be Year 2000 compliant, e.g. 30-06-1998; xx-06-1998; xx-xx-1998.

2. REPORT TYPE. State the type of report, such as final, technical, interim, memorandum, master's thesis, progress, quarterly, research, special, group study, etc.

3. DATES COVERED. Indicate the time during which the work was performed and the report was written, e.g., Jun 1997 - Jun 1998; 1-10 Jun 1996; May - Nov 1998; Nov 1998.

4. TITLE. Enter title and subtitle with volume number and part number, if applicable. On classified documents, enter the title classification in parentheses.

5a. CONTRACT NUMBER. Enter all contract numbers as they appear in the report, e.g. F33615-86-C-5169.

5b. GRANT NUMBER. Enter all grant numbers as they appear in the report, e.g. AFOSR-82-1234.

5c. PROGRAM ELEMENT NUMBER. Enter all program element numbers as they appear in the report, e.g. 61101A.

5d. PROJECT NUMBER. Enter all project numbers as they appear in the report, e.g. 1F665702D1257; ILIR.

5e. TASK NUMBER. Enter all task numbers as they appear in the report, e.g. 05; RF0330201; T4112.

5f. WORK UNIT NUMBER. Enter all work unit numbers as they appear in the report, e.g. 001; AFAPL30480105.

6. AUTHOR(S). Enter name(s) of person(s) responsible for writing the report, performing the research, or credited with the content of the report. The form of entry is the last name, first name, middle initial, and additional qualifiers separated by commas, e.g. Smith, Richard, J, Jr.

7. PERFORMING ORGANIZATION NAME(S) AND ADDRESS(ES). Self-explanatory.

8. PERFORMING ORGANIZATION REPORT NUMBER. Enter all unique alphanumeric report numbers assigned by the performing organization, e.g. BRL-1234; AFWL-TR-85-4017-Vol-21-PT-2.

9. SPONSORING/MONITORING AGENCY NAME(S) AND ADDRESS(ES). Enter the name and address of the organization(s) financially responsible for and monitoring the work.

10. SPONSOR/MONITOR'S ACRONYM(S). Enter, if available, e.g. BRL, ARDEC, NADC.

11. SPONSOR/MONITOR'S REPORT NUMBER(S). Enter report number as assigned by the sponsoring/ monitoring agency, if available, e.g. BRL-TR-829; -215.

12. DISTRIBUTION/AVAILABILITY STATEMENT. Use agency-mandated availability statements to indicate the public availability or distribution limitations of the report. If additional limitations/ restrictions or special markings are indicated, follow agency authorization procedures, e.g. RD/FRD, PROPIN, ITAR, etc. Include copyright information.

13. SUPPLEMENTARY NOTES. Enter information not included elsewhere such as: prepared in cooperation with; translation of; report supersedes; old edition number, etc.

14. ABSTRACT. A brief (approximately 200 words) factual summary of the most significant information.

15. SUBJECT TERMS. Key words or phrases identifying major concepts in the report.

16. SECURITY CLASSIFICATION. Enter security classification in accordance with security classification regulations, e.g. U, C, S, etc. If this form contains classified information, stamp classification level on the top and bottom of this page.

17. LIMITATION OF ABSTRACT. This block must be completed to assign a distribution limitation to the abstract. Enter UU (Unclassified Unlimited) or SAR (Same as Report). An entry in this block is necessary if the abstract is to be limited.

Final Report

July 01, 2011 – December 31, 2014

Project title:

Exploring Electric and Magnetic Resonances from Coherently Correlated Long-Lived Radical Pairs towards Development of Negative-Index Materials

Principle Investigator:

Bin Hu

Institution:

University of Tennessee

Address:

Department of Materials Science and Engineering
University of Tennessee
Knoxville, TN 37996
1508 Middle Drive
Email: bhu@utk.edu
Phone: 865-974-3946
Fax: 865-974-4115

Agreement Number:

FA9550-11-1-0082

DISTRIBUTION A: Distribution approved for public release.

Objectives:

This project has two objectives: (i) exploring electric and magnetic responses from spin radical pairs to develop molecular metamaterials and (ii) investigating new mechanisms to control the co-operative relationships between key thermoelectric parameters for developing high thermoelectric effects based on hybrid metal/polymer/metal thin-film devices.

Status of Effort:

The research efforts have made following major breakthroughs on molecular metamaterials by using spin radicals and on thermoelectric effects by using polymer/metal interface-controllable thermal and electric conductions.

1. Developed new strategy to couple semiconducting π electrons and magnetic *d* electrons for the development of molecular metamaterials [*J. Am. Chem. Soc.* 134, 3549-3554, 2012]

   The project has developed a new strategy for coupling semiconducting π electrons and magnetic d electrons by combining optically-generated intermolecular excited states with surface-modified magnetic nanoparticles. This new strategy can lead to optically-controllable composite metamaterials.

2. Explored new mechanism to utilize intermolecular excited states for realizing electric-magnetic coupling towards developing molecular metamaterials [*Adv. Mater*. **23**, 2216-2220, 2011]

   The project has developed a new mechanism for realizing electric-magnetic coupling by using optically-generated intermolecular excited states in organic semiconducting materials. This new mechanism can generate optically-controllable molecular metamaterials.

3. Developed new method to use spin radicals for realizing electric-magnetic coupling towards radicals-based metamaterials [*Adv. Mater* **26**, 3956-3961, 2014]

   The project has introduced spin radicals into organic semiconducting materials for the development of radicals-based metamaterials. This new method can develop spin-tunable electric-magnetic coupling for development of radicals-based metamaterials.

4. Discovered a novel mechanism to generate magneto-optic properties by establishing spin-exchange interaction in electron-hole pairs in ferroelectrically semiconducting materials [*Advanced Materials*, DOI: 10.1002/adma.201405946, 2015]

   The project has discovered a novel mechanism to generate magneto-optic properties by establishing spin-exchange interaction in ferroelectrically semiconducting perovskites. This new mechanism leads to a breakthrough to create magneto-optic functions in all functional materials.

DISTRIBUTION A: Distribution approved for public release.

5. Developing new strategy to separately control electrical and thermal conductivities by using interfacial polarization [*Adv. Mater.* 23, 4120-4124, 2011]

   The project explored a new strategy by using interfacial polarization to address the challenging issue: separate controlling on electric and thermal conductions. This new strategy can lead to a significant enhancement on Seebeck effect.

DISTRIBUTION A: Distribution approved for public release.

Accomplishments/New Findings:

I. Radicals-based molecular metamaterials

This research task has made the following five accomplishments including:

1. Discovery: new mechanism to realize electric-magnetic coupling by using π-d electron coupling for the development of molecular metamaterials

◆ **Electric-magnetic coupling from organic-magnetic nano-composite in ground state** [*J. Am. Chem. Soc.* 134, 3549-3554, 2012]

We found that a significant electric-magnetic coupling between charge-transfer states, and spin dipoles in ground state can be realized when intermolecular charge-transfer complexes are combined with soluble surface-modified magnetic nanoparticales through nano-composite design. Fig. 1 shows a very interesting magnetocurrent phenomenon that consists three components related to organic semiconducting molecules, magnetic nanoparticles, and a coupling between semiconducting molecules and magnetic nanoparticles. Clearly, this interesting magnetocurrent phenomenon implies that combining intermolecular charge-transfer complexes with magnetic d electrons leads to a new strategy to generate an electric-magnetic coupling in ground state.

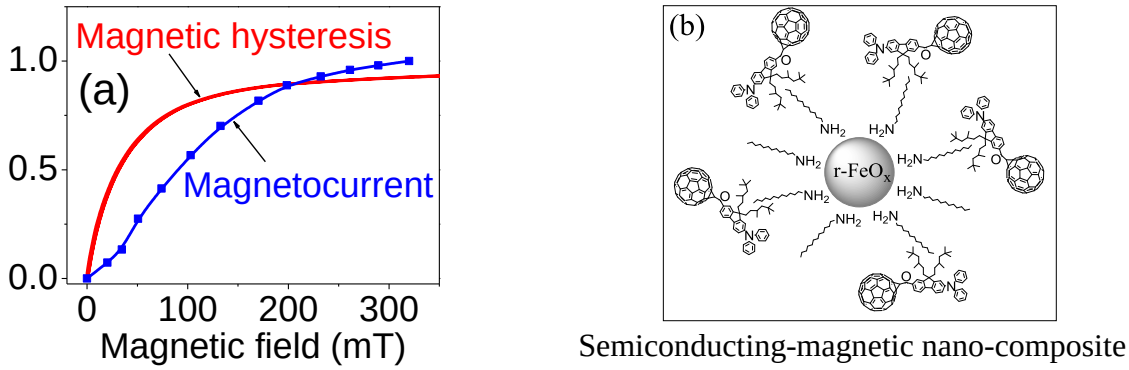

Fig. 1 (a) Magnetocurrent to show semiconducting, magnetic, and semiconducting-magnetic components. (b) Chemical structure of semiconducting-magnetic nano-composite to show π-d electron coupling.

◆ **Enhanced electric-magnetic coupling from organic-magnetic nano-composite in excited state metamaterials** [Submitted to *Advanced Electronic Materials*]**.**

We found that a stronger electric-magnetic coupling between charge-transfer states and spin dipoles in electric-magnetic nano-composite can be realized when exciting the nano-composite into excited state. Fig. 2 shows an obvious enhanced amplitude and a line-shape change of

DISTRIBUTION A: Distribution approved for public release.

magnetocapacitance in excited state from electric-magnetic nano-composite. Apparently, this striking mangetocapacitance change suggests that photoexcitation provide a new method to enlarge the electric-magnetic coupling between charge-transfer states and spin dipoles in the electric-magnetic nano-composite in excited state.

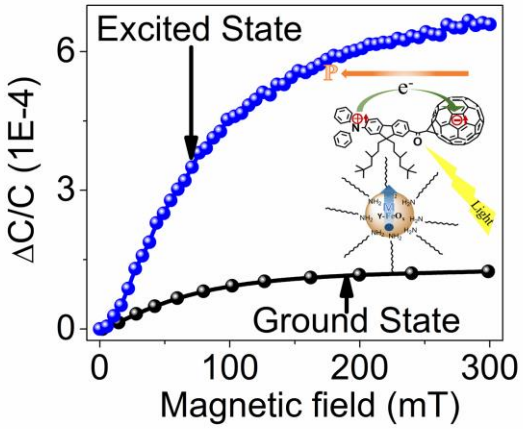

Fig. 2 Magnetocapacitance to show the larger electric-magnetic coupling in excited state.

◆ **Electric-magnetic coupling from radical pairs in organic molecules** [*Adv. Mater* **26**, 3956-3961, 2014].

We have discovered a new mechanism to generate electric-magnetic coupling by using radical pairs in organic semiconducting donor:acceptor systems. We can see in Fig. 3 that a pure semiconducting donor:acceptor (BBOT:TPD) demonstrates a significant magneto-dielectric function under photoexcitation: a magnetic field can change capacitance in organic semiconducting materials under photoexcitation. This magneto-dielectric function indicates a significant electric-magnetic coupling. Therefore, radical pairs present a new mechanism to generate electric-magnetic coupling towards the development of molecular metamaterials.

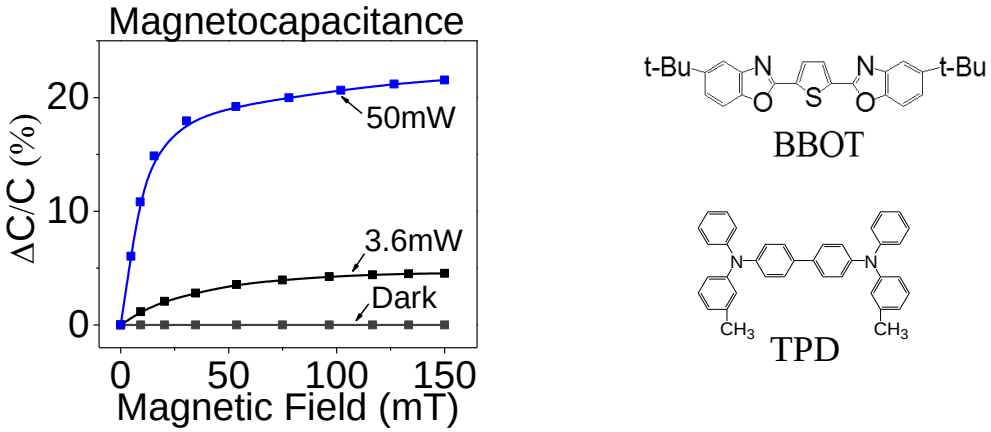

Fig. 3 Magnetocapacitance from optically-generated intermolecular excited states in semiconducting donor:acceptor (BBOT:TPD) composite.

DISTRIBUTION A: Distribution approved for public release.

2. New approach: Optically controlling magnetic properties by using charge-transfer states

◆ **Optically tunable magnetic properties through the interaction between intermolecular charge-transfer states** [*Adv. Mater* **26**, 3956-3961, 2014; *Physical Review B* 89, 155304 (2014)].

We have found that the spin-exchange energy in intermolecular charge-transfer states can be manipulated by the photoexcitation through changing the Coulomb interaction spin interaction among the intermolecular charge-transfer states. Fig. 4 indicates that the magnitude and line-shape of magnetocapacitance and magnetophotoluminescence can be changed by increasing the photoexcitation. Consequently, the line-shape narrowing of magnetocapacitance and magnetophotoluminescence illustrates a new way to tune the magnetic properties by photoexcitation through the interaction between intermolecular charge-transfer states, leading a new method to realize the molecular metamaterials.

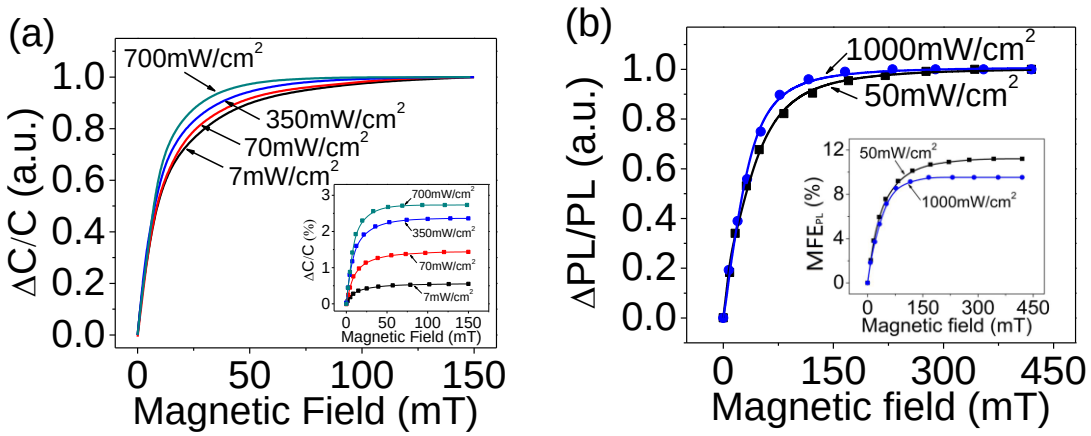

Fig. 4 (a) Magnetocapacitance in semiconducting donor:acceptor (BBOT:TPD) composite under different photoexcitation intensities. (b) Magnetophotoluminescence in semiconducting donor:acceptor (Pyrene:DMA) in DMF under different photoexcitation intensities.

◆ **Optically tunable magnetic properties through the interaction between intermolecular charge-transfer states and spin dipoles** [Submitted to *Advanced Electronic Materials*].

We have discovered that the magnetic properties of intermolecular charge-transfer states in electric-magnetic nano-composite can be adjusted by photoexcitation though varying the Coulomb interaction between intermolecular charge-transfer states and magnetic spin dipoles. Fig. 5 depicts an interesting phenomenon of narrowing line-shape and increasing amplitude of magnetocapacitance with increasing photoexcitation intensities. As a consequence, this straightforward phenomenon clarify a unique way to tune the magnetic properties through

DISTRIBUTION A: Distribution approved for public release.

changing the interaction between intermolecular charge-transfer states and magnetic spin dipoles with varied photoexcitation intensities.

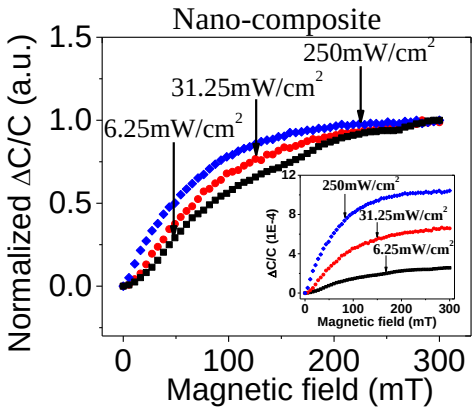

Fig. 5 Magnetocapacitance in electric-magnetic nano-composite under different photoexcitation intensities.

3. Discovery: New approach to realize optically tunable plasmonics [to be publsiehd]

We have discovered a new mechanism to separately control the magnetized charge-transfer states and photo-induced charge-transfer states through the coupling interaction between them. Fig. 6 shows the coupling interaction between magnetized charge-transfer states and photo-induced charge transfer states becomes stronger with the decreasing distance. This new phenomenon on one hand provides a unique way to magnetically control the photo-induced charge-transfer states. On the other hand, it predicts a method to optically tune the magnetic plasmonic response. Consequently, this new finding affords a new approach to coupling the electric, optic and magnetic properties for developing new metamaterials.

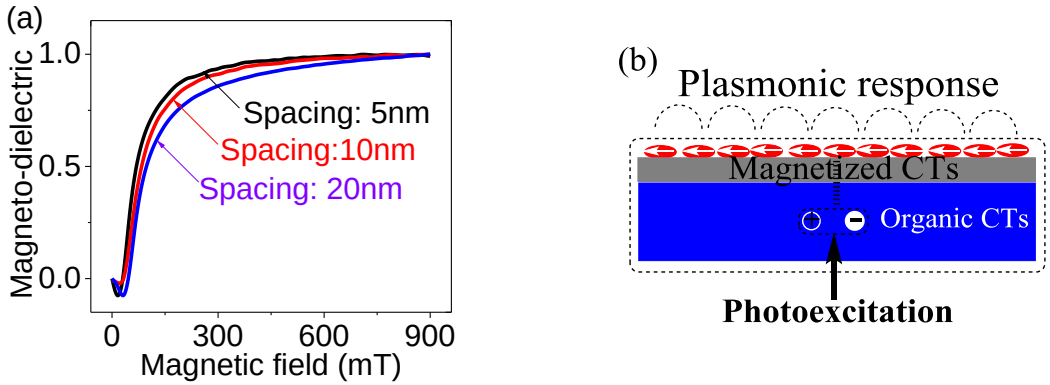

Fig. 6 (a) Magneto-dielectric property to show the coupling interaction between magnetized charge-transfer states and photo-induced charge transfer states. (b) Schematic for illustrating excitons-based plasmonics with optical tuning.

DISTRIBUTION A: Distribution approved for public release.

4. **New mechanism to develop magneto-optic properties by combining Hall effects with spin radicals** [*Adv. Mater*. 23, 2216-2220, 2011]

We have found a new mechanism to develop magneto-optic properties by combining Hall effects with spin radicals. This new mechanism has led to huge magneto-optic function based on organic spin radicals. Fig. 7 presents that the electroluminescence can be significantly changed up to > 400 % by a magnetic field at room temperature and low field (< 700 mT). This experimental discovery indicates a new mechanism to develop magneto-optic properties in liquid states.

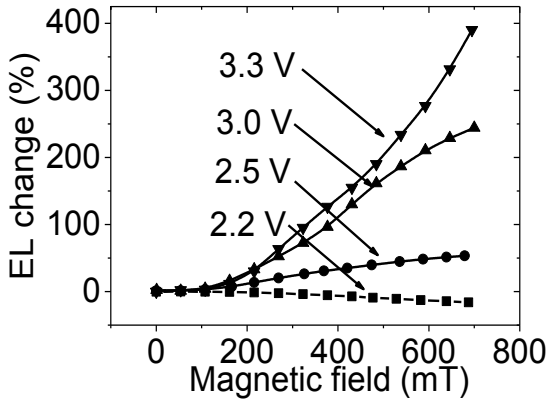

Fig.7 Electroluminescence from radical pairs as a function of magnetic field in triplet tris(2, 2'-bipyridyl) ruthenium(II)–tripropylamine.

5. **Discovery: Optically induced ferromagnetic properties from radical pairs** [*Scientific report*s 5, 2015]

We have discovered a new phenomenon that electrogenerated chemiluminescence can produce a magnetic property after removing the applied magnetic field. Fig. 8 shows an abnormal magnetic field effect on electrogenerated chemiluminescence: the electrogenerated chemiluminescence can still present a change even without a magnetic field. This unexpected phenomenon suggests that the activated charge-transfer [Ru(bpy)33+…TPrA•] complexes may become magnetized in magnetic field and experience a long magnetic relaxation after removing magnetic field. Therefore, this new discovery presents a new way to manipulate the magnetic property for developing new metamaterials.

DISTRIBUTION A: Distribution approved for public release.

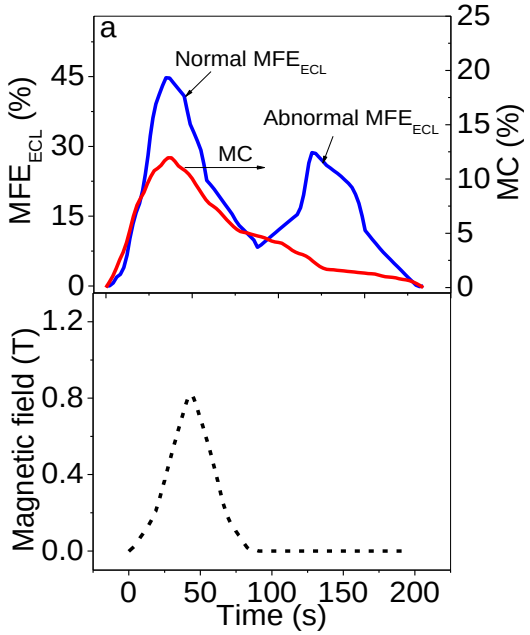

Fig. 8 (a) Magnetic field effect on electrogenerated chemiluminescence and magnetocurrent showing the magnetized charge-transfer states.

DISTRIBUTION A: Distribution approved for public release.

II. Thin-film based polymer thermoelectric devices

This research task has made the following five accomplishments including:

1. Rational design on polymer/conductor interface to develop high Seebeck effect based on vertical conductor/polymer/conductor thin-film devices [*Adv. Mater.* 23, 4120-4124, 2011]

We have discovered a new strategy to separately control electrical and thermal conductions by combining low thermal-conducting polymer and high electric-conducting metal in hybrid metal/polymer/polymer thin-film design. We can see in Fig. 9 that the hybrid Al/doped polypyrrole/Al thin-film device can exhibit a high Seebeck coefficient (100 ~ 200 μV/K). This high Seebeck coefficient implies a high-electric conduction and a low-thermal conduction existed in the Al/doped polypyrrole/Al thin-film device. In particular, this discovery presents a new design to separately control electric and thermal conductions by polymer/metal interface.

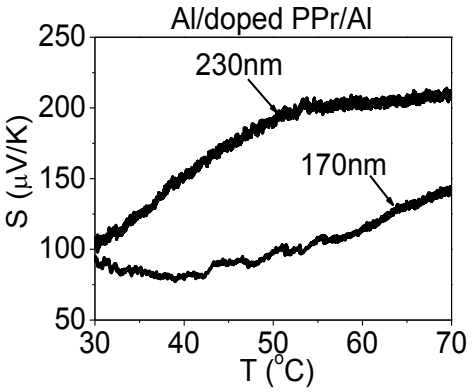

Fig. 9 Seebeck coefficients

2. New driving force of temperature-dependent surface polarization to cooperatively enhance Seebeck effect and electrical conductivity in vertical multilayer organic thin-film devices [*Phys. Chem. Chem. Phys.* 16, 22201-22206, 2014]

We have explored a new mechanism to develop Seebeck effects by using temperature-dependent surface polarization based on vertical multi-layer thin-film devices (Al/P3HT:PCBM/Al, & Al/MoO_3/P3HT:PCBM/Al). Here, the temperature-dependent surface polarization functions as an additional driving force, as compared with the traditional driving force from entropy difference, to diffuse the charge carriers under temperature difference towards the development of Seebeck effects. We have demonstrate simultaneously enhanced Seebeck coefficient and electrical conductivity by using dielectric interface through the temperature-dependent surface polarization to diffuse charge carriers in the Al/MoO_3/P3HT:PCBM/Al thin-film device (Fig. 10). This temperature-dependent surface polarization provides a new mechanism allowing a co-operative relationship between Seebeck coefficient and electrical conductivity.

DISTRIBUTION A: Distribution approved for public release.

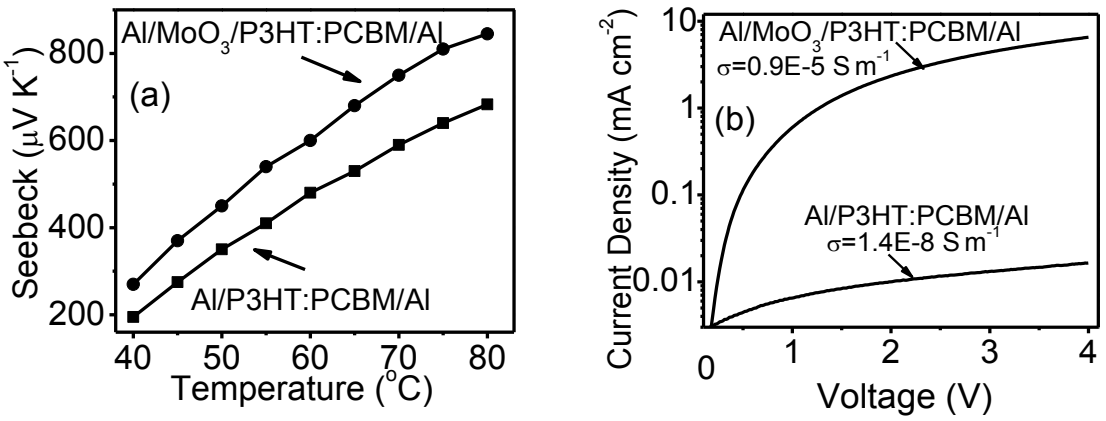

Fig. 10 (a) Seebeck coefficients in dark condition. (b) Electric conduction in dark condition.

3. Dual functions of Seebeck and cooling effects in organic thin-film devices [Submitted]

Here we have explored the possibilities of using temperature-dependent surface polarization as a new thermoelectric driving force to solve the conflicting requirement between electrical and thermal conductions in developing dual Seebeck and cooling effects based on the hybrid organic/inorganic Au/P(VDF-TrFE)/MoO_3/ITO thin-film device (Fig. 11). On one hand, the temperature-dependent surface polarization can lead to a temperature-dependent electrical field to drift charge carriers from high to low-temperature surface, generating a large Seebeck effect. On the other hand, the temperature-dependent surface polarization can absorb heat at the Au/organic interface through charge-phonon coupling by thermionic injection mechanisms when the charge carriers are injected upon applying an electrical bias, leading to a cooling effect. Essentially, the temperature-dependent surface polarization provides a mechanism to develop dual Seebeck and cooling effects through charge-phonon coupling based on thin-film electrode/organic/electrode devices.

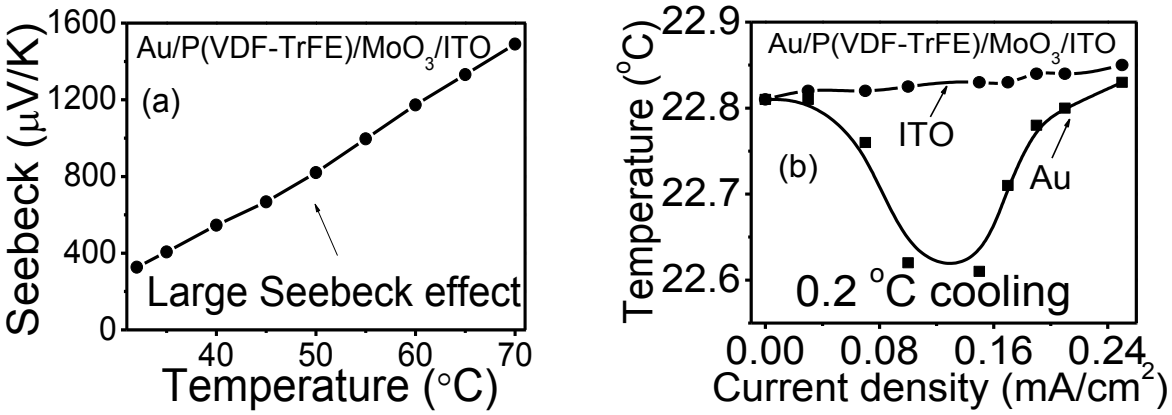

Fig. 11 (a) Seebeck coefficients. (b) Cooling effects with small injection currents.

DISTRIBUTION A: Distribution approved for public release.

4. Excited-states based Seebeck effect with decoupled three key parameters of Seebeck coefficient, electrical conductivity, and thermal conductivity [*J. Phys. Chem. C*, 117, 10264-10269, 2013]

Recently, we have discovered a new mechanism to further separately control electrical and thermal conductions by using photoexcitation. *Traditionally*, doping has been largely used to control thermoelectric functions. But, doping can cause conflicting phenomena: increasing electrical conductivity but decreasing Seebeck effect. This leads to a big challenge for simultaneously increasing electrical conductivity and Seebeck coefficient to enhance thermoelectric functions. Now, we have discovered that photoexcitation can lead to an increased Seebeck effect in the organic semiconducting system (MEHPPV) (Fig. 12). The observed increased Seebeck effect implies that using photoexcited states can develop a separate control on electrical and thermal conductions towards the development of high-efficiency thermoelectric devices. Essentially, excited states can provide three unique properties to develop Seebeck effect. First, the excited-states can generate high electrical conductivity; second, the excited-states can lead to tunable electron-phonon coupling; third, the excited states can provide a mechanism of phonon-trapping to trap thermal transport in bulk polymer films during charge transport.

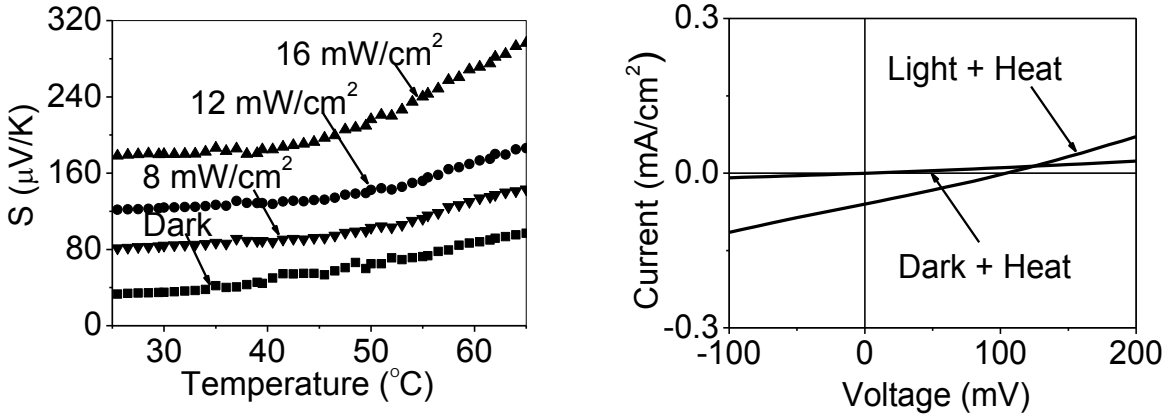

Fig. 12 (a) Seebeck coefficients for photoexcitation and dark conditions. (b) Electric conductions for photoexcitation (16mW/cm^2) and dark conditions. The system is based on ITO/MEH-PPV/Au devices.

5. New mechanism to generate magneto-Seebeck effect by applying Hall effect on organic thin-film devices [Submitted]

Hall effect can generate magneto-transport phenomenon in organic thin-film devices, and vertical organic thin-film devices can lead to large Seebeck effect. Therefore, combination of Hall effect and vertical organic thin-film devices can lead to a new mechanism to generate magneto-Seebeck effect. Here we have discovered giant magnetic field effects on Seebeck coefficients by applying Hall effect on vertical multi-layer ITO/PEDOT:PSS/Au thin-film

DISTRIBUTION A: Distribution approved for public release.

devices (Fig. 13). This discovery demonstrates a magnetic approach to control the thermoelectric properties in organic thin-film devices.

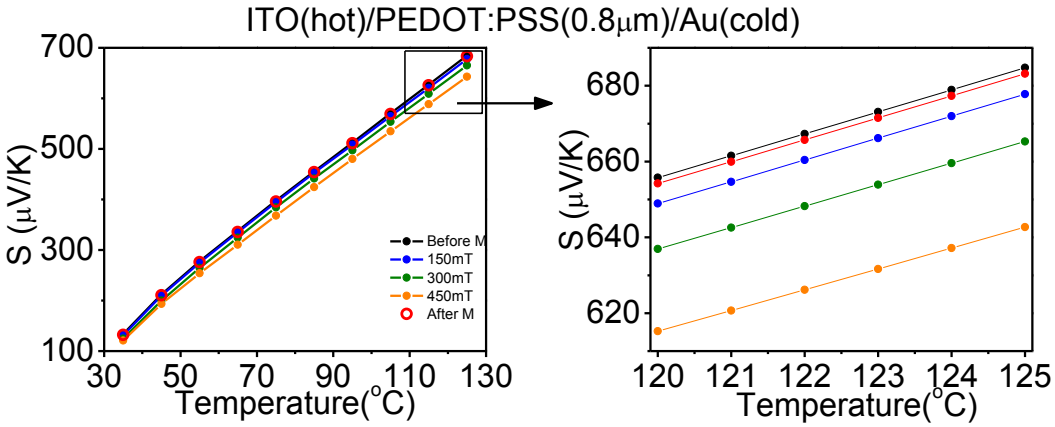

Fig. 13 Seebeck coefficient as a function of temperature under different magnetic field when magnetic field is perpendicular to temperature gradient.

DISTRIBUTION A: Distribution approved for public release.

Personnel Supported:

1. Dr. Lei He with full support
2. Dr. Dehua Hu with full support
3. Ph.D student Liang Yan with full support
4. Ph.D student Huidong Zang with full support
5. Ph.D student Mingxing Li with full support
6. Ph.D student Qing Liu with full support

Publication preparation from July 01 2011 to December 31 2014

1. Magneto-Optical Studies on Spin-Dependent Charge Recombination and Dissociation in Perovskite Solar Cells
   Yu-Che Hsiao, Ting Wu, Mingxing Li, and Bin Hu
   Advanced Materials, DOI: 10.1002/adma.201405946, 2015
2. Abnormal Magnetic Field Effects on Electrogenerated Chemiluminescence
   Haiping Pan, Yan Shen, Hongfeng Wang, Lei He, Bin Hu*
   Scientific Reports, DOI: 10.1038/srep09105, 2015
3. Changing the sign of exchange interaction in radical pairs to tune magnetic field effect on electrogenerated chemiluminescence
   Haiping Pan, Yan Shen, Lin Luan, Kai Lu, Jiashun Duan, and Bin Hu
   J. Phys. Chem. DOI: 10.1021/acs.jpcc.5b01541, 2015
4. Dynamic Coupling between Electrode Interface and Donor/Acceptor Interface via Charge Dissociation in Organic Solar Cells at Device-Operating Condition
   Ting Wu, Yu-Che Hsiao, Mingxing Li, Nam-Goo Kang, Jimmy W. Mays, Bin Hu*
   J. Phys. Chem. C, DOI: 10.1021/acs.jpcc.5b00082, 2015
5. Optically-Tunable Magneto-Capacitance Phenomenon in Organic Semiconducting Materials Developed by Electrical Polarization of Intermolecular Charge-Transfer States
   Lei He, Mingxing Li, Augustine Urbas, and Bin Hu*
   Advanced Materials, **26**, 3956, 2014
6. Changing Line-Shape in Magnetic Field Effects through Interactions between Excited States in Organic Semiconducting Materials
   Lei He, Mingxing Li, Augustine Urbas, and Bin Hu*
   Phys. Rev. B **89**, 155304, 2014
7. Optically tunable spin-exchange energy at donor:acceptor interfaces in organic solar cells
   Mingxing Li, Hongfeng Wang, Lei He, Huidong Zang, Hengxing Xu, and Bin Hu
   Appl. Phys. Lett. **105**, 023302, 2014
8. Inter-triplet spin-spin interaction effects on inter-conversion between different spin states in intermediate triplet-triplet pairs towards singlet fission
   Xianfeng Qiao, Lin Luan, Yuchun Liu, Zhigang Yu, and Bin Hu

DISTRIBUTION A: Distribution approved for public release.

Organic Electronics, **15**, 2168, 2014

9. Light induced structural change in Iridium complexes studied by electron spin resonance
   A. Batagin-Netol, A.P. Assis, J.F. Lima , C.J. Magon , L. Yan , M. Shao, B. Hu, and C.F.O. Graeff
   Journal of Physical Chemistry-A, **118**, 3717, 2014
10. Magneto-Dielectric Effects Induced by Optically-Generated Intermolecular Charge-Transfer States in Organic Semiconducting Materials
    Huidong Zang, Liang Yan, Mingxing Li, Lei He, Zheng Gai, Ilia Ivanov, Min Wang, Long Chiang, Augustine Urbas, and Bin Hu*,
    Scientific Reports, DOI: 10.1038， 2013
11. Precise Structural Development and Its Correlation to Function in Conjugated Polymer: Fullerene Thin Films by Solvent Annealing
    Huipeng Chen, Shen Hu, Huidong Zang, Bin Hu, and Mark Dadmun
    Advanced Functional Materials, **23**, 1701-1710, 2013
12. Spin Radicals Enhanced Magnetocapacitance Effect in Intermolecular Excited States
    Huidong Zang, Jianguo Wang, Mingxing Li, Lei He, Zitong Liu, Deqing Zhang, and Bin Hu
    J. Phys. Chem. C, **117**，14136-14140， 2013
13. Effects of Purity on the Electro-Optical Properties of Single Wall Nanotube-Based Transparent Conductive Electrodes
    Matthew Garret, Ilia N. Ivanov, David Geohegan, Bin Hu
    Carbon, **64**, 1-5, 2013
14. Enhancing Seebeck Effects by Using Excited States in Organic Semiconducting Polymer MEH-PPV Based on Multi-layer Electrode/Polymer/Electrode Thin-Film Structure
    Ling Xu, Yuchun Liu, Matthew P.Garrett, Bingbing Chen, and Bin Hu
    Journal of Physics Chemistry C, **117**, 10264, 2013
15. Triplet-Charge Annihilation versus Triplet-Triplet Annihilation in Organic Semiconductors
    Ming Shao, Liang Yan, Li Mingxing, Ivanov Ilia, and Bin Hu*
    Journal of Materials Chemistry C, **1**, 1330-1336, 2013
16. High Seebeck Effects from Conducting Polymer: Poly(3,4-ethylenedioxythiophene): Poly(styrenesulfonate) Based Thin-Film Device with Hybrid Metal/Polymer/Metal Architecture
    Michael Stanford, Hsin Wang, Ilia Ivanov, and Bin Hu*
    Applied Physics Letters **101**, 173304, 2012
17. Doping Effects on Internally Coupled Seebeck Coefficient, Electrical and Thermal Conductivities in Aluminum-Doped TiO_2
    Ling Xu, Matthew P.Garrett, and Bin Hu
    Journal of Physical Chemistry C, **116**, 13020-13025, 2012
18. "Magnetocurrent of Charge-Polarizable C_{60}-Diphenylaminofluorene Monoadduct-Derived Magnetic Nanocomposites"

DISTRIBUTION A: Distribution approved for public release.

Liang Yan, Min Wang, N.P. Raju, Arthur Epstein, Loon-Seng Tan, Augustine Urbas, Long Y. Chiang, Bin Hu*
J. Am. Chem. Soc. **134**, 3549-3554, 2012

19. "Changing Inter-molecular Spin-Orbital Coupling for Generating Magnetic Field Effects in Phosphorescent Organic Semiconductors"
Liang Yan, Ming Shao, Carlos F. O. Graeff, Ivo Hummelgen, Dongge Ma, Bin Hu
Appl. Phys. Lett. **100**, 013301, 2012
20. The impact of controlled solvent exposure on the morphology, structure and function of bulk heterojunction solar cells
Raghavendra Hegde, Nathan Henry, Ben Whittle, Huidong Zang, Bin Hu, Jihua Chen, Kai Xiao, Mark Dadmun
Solar Energy Materials and Solar Cells, **107**, 112-124, 2012
21. "High Seebeck Effects from Hybrid Metal/Polymer/Metal Thin-Film Devices"
Liang Yan, Ming Shao, Hsin Wang, Doug Dudis, Augustine Urbas, and Bin Hu*
Adv. Mater. **23**, 4120-4124, 2011
22. "Intra-Molecular "Donor-Acceptor" Interaction Effects on Charge Dissociation, Charge Transport, and Charge Collection in Bulk-Heterojunction Organic Solar Cells"
Huidong Zang, Yongye Liang, Luping Yu,* and Bin Hu*
Adv. Energ. Mater. **1**, 923, 2011
23. "Giant Magnetic Field Effects on Electroluminescence in Electrochemical Cells",
Ming Shao, Liang Yan, Ilia Ivanov, Bin Hu*,
Adv. Mater. **23**, 2216-2220, 2011.
24. "Effects of single walled carbon nanotubes on the electroluminescent performance of organic light-emitting diodes", Ming Shao, Matthew Garrett, Xinjun Xu, Ilia Ivanov, Stanislaus Wong, and Bin Hu*,
Organic Electronics, **12**, 1098-1102, 2011.
25. "Electrical dipole-dipole interaction effects on magnetocurret in organic phosphorescent materials",
Ming Shao, Yanfeng Dai, Dongge Ma, and Bin Hu
Appl. Phys. Lett. **99**, 073302, 2011
26. "Magnetoconductance responses in organic charge-transfer-complex molecules"
Tsung-Hsun Lee, Jhen-Hao Li, Wei-Shun Huang, Bin Hu, J. C. A. Huang, Tzung-Fang Guo, and Ten-Chin Wen
Appl. Phys. Lett. **99**, 0733097, 2011

Interactions and Transitions:

a. Presentations at Conferences

Invited Presentation from July 01 2011 to December 31 2014

(1) Magneto-Optical Studies on Organic and Perovskite Solar Cells
Bin Hu

DISTRIBUTION A: Distribution approved for public release.

Asian Conference on Organic Electronics, National Cheng Kung University, Tainan, Taiwan, November 12-15, 2014

(2) Magneto-Dielectric Effects Generated by Charge-Transfer States in Organic Semiconductors
Bin Hu
5th Topical Meeting on Spins in Organic Semiconductors, Himeji, Japan, October 14-17, 2014

(3) New Magnetic Field Effects in Organic Semiconductors
Bin Hu
2014 International Symposium on Materials for Enabling Nanodevices, National Cheng Kung University, Tainan, Taiwan, September 03-06, 2014

(4) Magneto-optic properties in organic materials
Bin Hu
AOARD conference on magnetic nanomaterials, University of Maryland, June 16-17, 2014

(5) Organic spintronics, organic solar cells, and organic thermoelectrics
Bin Hu
E-MRS, Lille, France, May 26-30, 2014

(6) Magneto-optic properties in organic materials
Bin Hu
US-Taiwan Air Force Conference, Hualien, Taiwan, May 13-15, 2014

(7) Magneto-optic studies of photovoltaic processes at D:A interface and electrode interface in organic solar cells
Bin Hu
Indo-US Joint Workshop on Organic Solar Cells, Kanpur, India, March 20-22, 2014

(8) Interface enhanced photovoltaic and Seebeck effects in organic solar cells and thermoelectric devices
Bin Hu
ACS Annual Meeting, Dallas, TX, March 16, 2014

(9) Multiferroic Effects from Intermolecular Excited States in Organic Semiconductors
Bin Hu
Brazil-MRS meeting, Campos do Jordao, September 30 – October 04, 2013

(10) Magneto-Optic, Magneto-Electric, and Magneto-Thermoelectric Effects in Organic Semiconductors
Bin Hu
BES Program Review for the CNMS at Oak Ridge National Laboratory, September 24-26, 2013

(11) Organic Thin-Film Thermoelectric Devices
Bin Hu
Flexible Thermoelectric Workshop organized by AFOSR, Arlington, VA, July 09-10, 2013

(12) Effects of Intermolecular and Dielectric-layer Interfaces on Internal Photovoltaic Processes in Organic Solar Cells
Bin Hu

DISTRIBUTION A: Distribution approved for public release.

Indo-US Joint Workshop on Organic Solar Cells, National Reviewable Energy Laboratory, Golden, Co, June 24-25, 2013

(13) Magneto-optical Studies on Internal Photovoltaic Processes in Organic Solar Cells
Bin Hu
2013 TechConnect World, National Innovation Summit and National SBIR Conference, Gaylord Hotel, National Harbor, Maryland, May 13-16, 2013

(14) Magneto-Dielectric Functions Developed by Intermolecular Excited States
Bin Hu
MRS Meetings, San Francisco, CA, April 01-05, 2013

(15) Departmental Seminar: Organic Spintronics
Bin Hu
National Taiwan University, Taipei, Taiwan, December 11, 2012

(16) Workshop on Organic Spintronics
Bin Hu
Intermolecular Excited States-Based Organic Spintronics
National Cheng Kung University, Tainan, Taiwan, December 06-07, 2012

(17) Effects of Intermolecular and Dielectric-layer Interfaces on Internal Photovoltaic Processes in Organic Solar Cells
Bin Hu
International Symposium on Organic and Dye-Sensitized Solar Cells 2012 (IS-OPVDSC 2012), Taipei, Taiwan, November 24-29, 2012

(18) Electric-Magnetic Coupling in Organic Sintronics
Bin Hu
9th National Conference on Organic Solids Electronics, Yangzhou, China, November 10-12, 2012

(19) Magneto-optical studies on internal photovoltaic processes in organic solar cells
Bin Hu
Workshop on key scientific and technological issues for development of next-generation organic solar cells
Arlington, VA, September 20 – 21, 2012

(20) Multi-Ferroic Functions Developed by Inter-molecular Excited States
Bin Hu
4th Topical Meeting on Spintronics in Organic Semiconductors, London, UK, September 10 – 14, 2012

(21) Excited States-Based Organic Spintronics
Bin Hu
International Workshop on Novel Nano-Magnetic and Multifunctional Materials 2012
Seoul, Korea, June 11-14, 2012

(22) Magneto-Optical Studies of Internal Photovoltaic Processes in Organic Solar Cells
Bin Hu
Departmental seminar at Department of Materials Science and Engineering, University of Florida, Gainesville, FL, April 04, 2012

(23) Organic Molecular Metamaterials
Bin Hu
Organic Metamaterials Workshop, Army Research Laboratory, March 02, 2012

DISTRIBUTION A: Distribution approved for public release.

(24) Characterization and Understanding on Internal Photovoltaic Processes in Organic Solar Cells
Bin Hu
International Photonics Conference – 2011, Tainan, Taiwan, December 07-08, 2011

(25) Organic Spintronics: Magnetic Field Effects
Bin Hu
International Symposium on Organic Dye Sensitized Solar Cells, Tainan, Taiwan, December 08-10, 2011

(26) The Role of Inter-molecular Electron-Hole Pairs in Magnetic Field Effects in Organic Materials,
Bin Hu
61st Annual Meeting of Japan Coordination Chemistry Society, Okayama, Japan, September 17-19, 2011

(27) Characterization and Understanding on Charge Dissociation, Transport, Collection in Organic Solar Cells
Bin Hu
Workshop on Sustainable Energy Future: Focus on Organic Photovoltaics, Oak Ridge National Laboratory, September 21 – 23, 2011

(28) Electromagnetic and Thermoelectric Responses from Inter-molecular Excited States: Radicals Pairs
Bin Hu
8th US-Taiwan NanoScience Workshop, Seattle, Washington, April 05-06, 2011

b. Consultative and advisory functions

None.

c. Transitions

None.

New Discoveries

Four experimental discoveries have been made. They include:

(1) New strategy to couple semiconducting π electrons and magnetic d electrons for development of molecular metamaterials
(2) New mechanism to use intermolecular excited states for realizing electric-magnetic coupling towards development of molecular metamaterials
(3) New method to use spin radicals for realizing electric-magnetic coupling towards radicals-based metamaterials
(4) New mechanism to develop significant magneto-optic properties by combining Hall effect with spin nradicals
(5) New strategy to separately control electrical and thermal conductivities by using interfacial polarization

DISTRIBUTION A: Distribution approved for public release.

Honors/Awards:

Research Achievement Award – April 2014
College of Engineering
University of Tennessee

Research Fellow Award – April 2012
College of Engineering
University of Tennessee

DISTRIBUTION A: Distribution approved for public release.

1.

1. Report Type

Final Report

Primary Contact E-mail

Contact email if there is a problem with the report.

bhu@utk.edu

Primary Contact Phone Number

Contact phone number if there is a problem with the report

865-974-3946

Organization / Institution name

The University of Tennessee

Grant/Contract Title

The full title of the funded effort.

Exploring Electrical and Magnetic Resonances from Coherently Correlated Long-Lived Radical Pairs towards Development of Negative Refractive-Index materials

Grant/Contract Number

AFOSR assigned control number. It must begin with "FA9550" or "F49620" or "FA2386".

FA9550-11-1-0082

Principal Investigator Name

The full name of the principal investigator on the grant or contract.

Dr. Bin Hu

Program Manager

The AFOSR Program Manager currently assigned to the award

Dr. Charles Lee

Reporting Period Start Date

06/01/2011

Reporting Period End Date

12/31/2014

Abstract

The research efforts have made following major breakthroughs:
1. Developed new strategy to couple pi-d electrons for the development of molecular metamaterials [J. Am. Chem. Soc. 134, 3549, 2012]
2. Explored new mechanism to utilize intermolecular excited states for realizing electric-magnetic coupling towards developing molecular metamaterials [Adv. Mater. 23, 2216, 2011]
3. Developed new method to use radicals for electric-magnetic coupling towards radicals-based metamaterials [Adv. Mater 26, 3956, 2014]
4. Discovered a novel mechanism to generate magneto-optic properties by establishing spin-exchange interaction in electron-hole pairs in ferroelectrically semiconducting materials [Advanced Materials, DOI: 10.1002/adma.201405946, 2015]
5. Developing new strategy to separately control electrical and thermal conductivities by using interfacial polarization [Adv. Mater. 23, 4120, 2011]

Distribution Statement

DISTRIBUTION A: Distribution approved for public release.

This is block 12 on the SF298 form.

Distribution A - Approved for Public Release

Explanation for Distribution Statement

If this is not approved for public release, please provide a short explanation. E.g., contains proprietary information.

SF298 Form

Please attach your SF298 form. A blank SF298 can be found here. Please do not password protect or secure the PDF The maximum file size for an SF298 is 50MB.

Final report-298-Bin Hu.pdf

Upload the Report Document. File must be a PDF. Please do not password protect or secure the PDF . The maximum file size for the Report Document is 50MB.

Final Performance Report-04-12-2015-Bin Hu-submitted.pdf

Upload a Report Document, if any. The maximum file size for the Report Document is 50MB.

Archival Publications (published) during reporting period:

Changes in research objectives (if any):

Change in AFOSR Program Manager, if any:

Extensions granted or milestones slipped, if any:

AFOSR LRIR Number

LRIR Title

Reporting Period

Laboratory Task Manager

Program Officer

Research Objectives

Technical Summary

Funding Summary by Cost Category (by FY, $K)

	Starting FY	FY+1	FY+2
Salary			
Equipment/Facilities			
Supplies			
Total			

Report Document

Report Document - Text Analysis

Report Document - Text Analysis

Appendix Documents

2. Thank You

E-mail user

Apr 16, 2015 14:26:17 Success: Email Sent to: bhu@utk.edu

REPORT DOCUMENTATION PAGE

Form Approved
OMB No. 0704-0188

The public reporting burden for this collection of information is estimated to average 1 hour per response, including the time for reviewing instructions, searching existing data sources, gathering and maintaining the data needed, and completing and reviewing the collection of information. Send comments regarding this burden estimate or any other aspect of this collection of information, including suggestions for reducing the burden, to the Department of Defense, Executive Service Directorate (0704-0188). Respondents should be aware that notwithstanding any other provision of law, no person shall be subject to any penalty for failing to comply with a collection of information if it does not display a currently valid OMB control number.

PLEASE DO NOT RETURN YOUR FORM TO THE ABOVE ORGANIZATION.

1. REPORT DATE *(DD-MM-YYYY)*	2. REPORT TYPE	3. DATES COVERED *(From - To)*
11/14/2013	Final	8/15/2008-8/14/2013

4. TITLE AND SUBTITLE
TOWARDS COMBINED ACTIVE CONTROL OF FILM COOLING AND TURBINE BLADE AERODYNAMICS

5a. CONTRACT NUMBER
FA9550-08-1-0440

5b. GRANT NUMBER
N/A

5c. PROGRAM ELEMENT NUMBER
N/A

6. AUTHOR(S)
Dimitris E. Nikitopoulos,
Guoxiang Gu,
Shengmin Guo,
Guillaume Bidan

5d. PROJECT NUMBER
N/A

5e. TASK NUMBER
N/A

5f. WORK UNIT NUMBER
N/A

7. PERFORMING ORGANIZATION NAME(S) AND ADDRESS(ES)
Louisiana State University System,
3810 W Lakeshore Drive, Room 107, System Bldg,
Baton Rouge, LA 70808

8. PERFORMING ORGANIZATION REPORT NUMBER
N/A

9. SPONSORING/MONITORING AGENCY NAME(S) AND ADDRESS(ES)
Air Force Office of Science and Research / JA
875 Randolph Street
Suite 325 Room 3112
Arlington, VA 22203

10. SPONSOR/MONITOR'S ACRONYM(S)
AFOSR / JA

11. SPONSOR/MONITOR'S REPORT NUMBER(S)

12. DISTRIBUTION/AVAILABILITY STATEMENT
Please withhold the distribution of this Final Report for 1 year, to allow for complete publication of the discussed results in peer-reviewed journal publications. After this period of time, Distribution A.

13. SUPPLEMENTARY NOTES

14. ABSTRACT
In this study, actively controlled film cooling flows were investigated in view of improved film cooling metrics and increased adaptability. In the first place a mechanistic analysis was carried out on unforced and forced film cooling geometries of a vertical and an inclined jet in cross-flow, evidencing characteristic vortical systems and scaling parameters for those systems. A cutting edge linear cascade facility including a realistic wake generator was designed, fabricated and validated. PIV measurements and Mie scattering visualizations evidenced the effect of the wake on film cooling jets as it impinged the blade. The first Reduced Order Models (ROMs) of unforced and forced film cooling jets velocity and temperature fields were derived using the POD-Galerkin projection method. ROM stabilization techniques were developed and implemented to improve the models stability and accuracy. An optimization method using Direct Numerical Simulations was developed to identify optimum forcing parameters for improved film cooling metrics. Finally, a linear state feedback controller for stabilization of a POD-based ROM of film cooling system was developed and implemented. The designed controller was able to stabilize the flow to the selected operating point in DNS for a short time period.

15. SUBJECT TERMS

16. SECURITY CLASSIFICATION OF:			17. LIMITATION OF ABSTRACT	18. NUMBER OF PAGES	19a. NAME OF RESPONSIBLE PERSON
a. REPORT	b. ABSTRACT	c. THIS PAGE			19b. TELEPHONE NUMBER *(Include area code)*

Standard Form 298 (Rev. 8/98)
Prescribed by ANSI Std. Z39.18
Adobe Professional 7.0

DISTRIBUTION A: Distribution approved for public release.

INSTRUCTIONS FOR COMPLETING SF 298

1. REPORT DATE. Full publication date, including day, month, if available. Must cite at least the year and be Year 2000 compliant, e.g. 30-06-1998; xx-06-1998; xx-xx-1998.

2. REPORT TYPE. State the type of report, such as final, technical, interim, memorandum, master's thesis, progress, quarterly, research, special, group study, etc.

3. DATES COVERED. Indicate the time during which the work was performed and the report was written, e.g., Jun 1997 - Jun 1998; 1-10 Jun 1996; May - Nov 1998; Nov 1998.

4. TITLE. Enter title and subtitle with volume number and part number, if applicable. On classified documents, enter the title classification in parentheses.

5a. CONTRACT NUMBER. Enter all contract numbers as they appear in the report, e.g. F33615-86-C-5169.

5b. GRANT NUMBER. Enter all grant numbers as they appear in the report, e.g. AFOSR-82-1234.

5c. PROGRAM ELEMENT NUMBER. Enter all program element numbers as they appear in the report, e.g. 61101A.

5d. PROJECT NUMBER. Enter all project numbers as they appear in the report, e.g. 1F665702D1257; ILIR.

5e. TASK NUMBER. Enter all task numbers as they appear in the report, e.g. 05; RF0330201; T4112.

5f. WORK UNIT NUMBER. Enter all work unit numbers as they appear in the report, e.g. 001; AFAPL30480105.

6. AUTHOR(S). Enter name(s) of person(s) responsible for writing the report, performing the research, or credited with the content of the report. The form of entry is the last name, first name, middle initial, and additional qualifiers separated by commas, e.g. Smith, Richard, J, Jr.

7. PERFORMING ORGANIZATION NAME(S) AND ADDRESS(ES). Self-explanatory.

8. PERFORMING ORGANIZATION REPORT NUMBER. Enter all unique alphanumeric report numbers assigned by the performing organization, e.g. BRL-1234; AFWL-TR-85-4017-Vol-21-PT-2.

9. SPONSORING/MONITORING AGENCY NAME(S) AND ADDRESS(ES). Enter the name and address of the organization(s) financially responsible for and monitoring the work.

10. SPONSOR/MONITOR'S ACRONYM(S). Enter, if available, e.g. BRL, ARDEC, NADC.

11. SPONSOR/MONITOR'S REPORT NUMBER(S). Enter report number as assigned by the sponsoring/ monitoring agency, if available, e.g. BRL-TR-829; -215.

12. DISTRIBUTION/AVAILABILITY STATEMENT. Use agency-mandated availability statements to indicate the public availability or distribution limitations of the report. If additional limitations/ restrictions or special markings are indicated, follow agency authorization procedures, e.g. RD/FRD, PROPIN, ITAR, etc. Include copyright information.

13. SUPPLEMENTARY NOTES. Enter information not included elsewhere such as: prepared in cooperation with; translation of; report supersedes; old edition number, etc.

14. ABSTRACT. A brief (approximately 200 words) factual summary of the most significant information.

15. SUBJECT TERMS. Key words or phrases identifying major concepts in the report.

16. SECURITY CLASSIFICATION. Enter security classification in accordance with security classification regulations, e.g. U, C, S, etc. If this form contains classified information, stamp classification level on the top and bottom of this page.

17. LIMITATION OF ABSTRACT. This block must be completed to assign a distribution limitation to the abstract. Enter UU (Unclassified Unlimited) or SAR (Same as Report). An entry in this block is necessary if the abstract is to be limited.

AFOSR Final Performance Report

DISTRIBUTION A: Distribution approved for public release.

Project Title:	Towards Combined Active Control of Film Cooling and Turbine Blade Aerodynamics.
Award Number:	FA9550-08-1-0440
Dates Covered:	8/15/2008 - 8/14/2013
Program Manager:	Dr. Douglas Smith
Principal Investigator:	Dimitris E. Nikitopoulos Mechanical Engineering Department Louisiana State University Baton Rouge, Louisiana 70803 Tel: (225)-578-5903, email : medimi@lsu.edu
Co-Investigators:	Shengmin Guo, Guoxiang Gu, and Sumanta Acharya Mechanical Engineering Department Louisiana State University Baton Rouge, Louisiana 70803

Abstract:

In this study, actively controlled film cooling flows were investigated in view of improved film cooling metrics and increased adaptability. In the first place a mechanistic analysis was carried out on unforced and forced film cooling geometries of a vertical and an inclined jet in cross-flow, evidencing characteristic vortical systems and scaling parameters for those systems. A cutting edge linear cascade facility including a realistic wake generator was designed, fabricated and validated. PIV measurements and Mie scattering visualizations evidenced the effect of the wake on film cooling jets as it impinged the blade. The first Reduced Order Models (ROMs) of unforced and forced film cooling jets velocity and temperature fields were derived using the POD-Galerkin projection method. ROM stabilization techniques were developed and implemented to improve the models stability and accuracy. An optimization method using Direct Numerical Simulations was developed to identify optimum forcing parameters for improved film cooling metrics. Finally, a linear state feedback controller for stabilization of a POD-based ROM of film cooling system was developed and implemented. The designed controller was able to stabilize the flow to the selected operating point in DNS for a short time period until the DNS solution diverged to another operating condition.

DISTRIBUTION A: Distribution approved for public release.

DISTRIBUTION A: Distribution approved for public release.

REPORT DOCUMENTATION PAGE

Form Approved
OMB No. 0704-0188

The public reporting burden for this collection of information is estimated to average 1 hour per response, including the time for reviewing instructions, searching existing data sources, gathering and maintaining the data needed, and completing and reviewing the collection of information. Send comments regarding this burden estimate or any other aspect of this collection of information, including suggestions for reducing the burden, to the Department of Defense, Executive Service Directorate (0704-0188). Respondents should be aware that notwithstanding any other provision of law, no person shall be subject to any penalty for failing to comply with a collection of information if it does not display a currently valid OMB control number.

PLEASE DO NOT RETURN YOUR FORM TO THE ABOVE ORGANIZATION.

1. REPORT DATE *(DD-MM-YYYY)*	2. REPORT TYPE	3. DATES COVERED *(From - To)*
11/14/2013	Final	8/15/2008-8/14/2013

4. TITLE AND SUBTITLE
TOWARDS COMBINED ACTIVE CONTROL OF FILM COOLING AND TURBINE BLADE AERODYNAMICS

5a. CONTRACT NUMBER
FA9550-08-1-0440

5b. GRANT NUMBER
N/A

5c. PROGRAM ELEMENT NUMBER
N/A

6. AUTHOR(S)
Dimitris E. Nikitopoulos,
Guoxiang Gu,
Shengmin Guo,
Guillaume Bidan

5d. PROJECT NUMBER
N/A

5e. TASK NUMBER
N/A

5f. WORK UNIT NUMBER
N/A

7. PERFORMING ORGANIZATION NAME(S) AND ADDRESS(ES)
Louisiana State University System,
3810 W Lakeshore Drive, Room 107, System Bldg,
Baton Rouge, LA 70808

8. PERFORMING ORGANIZATION REPORT NUMBER
N/A

9. SPONSORING/MONITORING AGENCY NAME(S) AND ADDRESS(ES)
Air Force Office of Science and Research / JA
875 Randolph Street
Suite 325 Room 3112
Arlington, VA 22203

10. SPONSOR/MONITOR'S ACRONYM(S)
AFOSR / JA

11. SPONSOR/MONITOR'S REPORT NUMBER(S)

12. DISTRIBUTION/AVAILABILITY STATEMENT
Please withhold the distribution of this Final Report for 1 year, to allow for complete publication of the discussed results in peer-reviewed journal publications. After this period of time, Distribution A.

13. SUPPLEMENTARY NOTES

14. ABSTRACT
In this study, actively controlled film cooling flows were investigated in view of improved film cooling metrics and increased adaptability. In the first place a mechanistic analysis was carried out on unforced and forced film cooling geometries of a vertical and an inclined jet in cross-flow, evidencing characteristic vortical systems and scaling parameters for those systems. A cutting edge linear cascade facility including a realistic wake generator was designed, fabricated and validated. PIV measurements and Mie scattering visualizations evidenced the effect of the wake on film cooling jets as it impinged the blade. The first Reduced Order Models (ROMs) of unforced and forced film cooling jets velocity and temperature fields were derived using the POD-Galerkin projection method. ROM stabilization techniques were developed and implemented to improve the models stability and accuracy. An optimization method using Direct Numerical Simulations was developed to identify optimum forcing parameters for improved film cooling metrics. Finally, a linear state feedback controller for stabilization of a POD-based ROM of film cooling system was developed and implemented. The designed controller was able to stabilize the flow to the selected operating point in DNS for a short time period.

15. SUBJECT TERMS

16. SECURITY CLASSIFICATION OF:			17. LIMITATION OF ABSTRACT	18. NUMBER OF PAGES	19a. NAME OF RESPONSIBLE PERSON
a. REPORT	b. ABSTRACT	c. THIS PAGE			19b. TELEPHONE NUMBER *(Include area code)*

DISTRIBUTION A: Distribution approved for public release.

Contents

I Project Description **8**

1 Personnel **9**

2 Publications **9**
2.1 Theses and Dissertations 9
2.2 Archival Publications 10
2.2.1 Peer Reviewed Journal Publications: 10
2.2.2 Conference Proceedings 10

3 Motivations **11**

4 Initial Objectives **15**

5 Changes in research objectives **17**

6 Accomplishments/Findings **18**

II Mechanistic Analysis **21**

1 Vertical Jet in Cross-flow **22**
1.1 Experimental and Numerical Setup 22
1.1.1 Wind Tunnel Experiments 22
1.1.2 Numerical Simulations 23
1.2 Results 25
1.2.1 Unforced Jet 25
1.2.2 Forced Jet 33

2 Inclined Jet in Cross-flow **44**
2.1 Experimental and Numerical Setup 44
2.1.1 Wind Tunnel Experiments 44
2.1.2 Numerical Simulations 45
2.1.2.1 Mechanistic Analysis Grid 45
2.1.2.2 Reduced Order Modeling Grid 47
2.1.2.3 Inlet Conditions Grid 49
2.2 Unforced Jet 50
2.3 Forced Jet 55
2.3.1 Low-to-High Blowing Ratio Transition: Starting Vortices 57

DISTRIBUTION A: Distribution approved for public release.

3 Cascade Wind Tunnel **68**
3.1 Experimental Setup Design . . . 68
3.1.1 Wind tunnel design . . . 68
3.1.2 Test section design . . . 70
3.1.3 Wake generator design . . . 73
3.1.4 Additional equipment . . . 74
3.2 Linear Cascade Characterization without Wake Generator . . . 76
3.2.1 Pressure Distribution along the Wind Tunnel . . . 77
3.2.2 Test Section Velocity Distribution . . . 77
3.2.3 Test Section Spectral Content . . . 80
3.2.4 Pressure Profiles . . . 81
3.3 Linear Cascade Characterization with Wake Generator . . . 83
3.3.1 Test Section Velocity Distribution . . . 83
3.3.2 Test Section Spectral Content . . . 87
3.3.3 Pressure Measurements . . . 89
3.4 Particle Image Velocimetry and Mie scattering visualizations . . . 92

III Optimization, Reduced Order Modeling and Flow Control 99

1 Optimization of Forced Film Cooling Jets **100**
1.1 Methodology . . . 100
1.1.1 Optimization Problem . . . 101
1.2 Simulation details . . . 102
1.2.1 Computational Mesh . . . 102
1.3 Results and Discussion . . . 104
1.3.1 Effect of pulsation on film cooling performance . . . 104
1.3.2 Optimal and sub-optimal behavior . . . 106
1.3.3 Film cooling response surface . . . 113
1.4 Conclusions . . . 113

2 Canonical Systems Reduced Order Models **116**
2.1 POD-Galerkin Method . . . 116
2.2 Two-dimensional Two-sided Lid Driven Cavity . . . 117
2.2.1 Numerical Setup . . . 118
2.2.2 Base Flow . . . 118
2.2.3 Proper Orthogonal Decomposition . . . 120
2.2.4 Reduced Order Model . . . 122
2.3 Two-dimensional Cylinder in a Cross-flow . . . 124
2.3.1 Numerical Setup . . . 124
2.3.2 Base Flow . . . 125
2.3.3 Proper Orthogonal Decomposition . . . 126
2.3.4 Reduced Order Model . . . 129

DISTRIBUTION A: Distribution approved for public release.

3 Film Cooling Jets Reduced Order Models **132**
3.1 Preliminary Statistical POD Analysis of Film Cooling Jets 132
3.1.1 Unforced Jets 132
3.1.2 Forced Jets 139
3.2 Reduced Order Models 153
3.2.1 Stabilization Methods 153
3.2.2 Unforced Jets 155
3.2.2.1 Attached Regime 155
3.2.2.2 Transitional Regime 162
3.2.3 Forced Jets 170
3.2.3.1 Instantaneous Flow 170
3.2.3.1.1 Reduced Order Models 172
3.2.3.2 Phase Averaged Flow 179
3.2.3.2.1 Reduced Order Models 179
3.3 Conclusion 185

4 Flow Control **189**
4.1 Jet in Cross-flow Modeling 189
4.1.1 Numerical Method 190
4.1.2 Reduced Order Model Based on POD/Galerkin Projection 190
4.2 Feedback Control 193
4.2.1 Problem Statement 193
4.2.2 Controller Design 193
4.3 Results 196
4.3.1 Open Loop Dynamics 196
4.3.2 Closed Loop Dynamics 200
4.4 Conclusion 204

References **206**

DISTRIBUTION A: Distribution approved for public release.

Part I
Project Description

DISTRIBUTION A: Distribution approved for public release.

1 Personnel

Professors

- Dimitris, E., Nikitopoulos
- Guoxiang Guo
- Sumanta Acharya
- Guoxiang Gu

Graduate Students

- Clementine Vezier - M.Sc. (2009)
- Lemuel, A., Wells - M.Sc. (left before completing degree)
- Jean Philippe Junca-Laplace - M.Sc. (2011)
- Jason, W., Bitting - Ph.D. (expected 2015)
- Christopher, Foreman - M.Sc. (2012)
- Shiloh, M., Meyers - M.Sc. (expected 2014)
- Luis, D., Alvergue PhD (2012)
- Guillaume, F., Bidan - Ph.D. (2013)
- Hessam, Babbae - Ph.D. (2013)

2 Publications

2.1 Theses and Dissertations

All thesis and dissertations are available online at *etd.lsu.edu*

- C. Vezier, "Dynamics of Vortical Structures in a Low-Blowing-Ratio Pulsed Transverse Jet", M.Sc. Thesis, Louisiana State University, 2009.
- J.-P. Junca-Laplace, Design, Fabrication, and Characterization of a New Wind Tunnel Facility - Linear Cascade with a Wake Simulator", M.Sc. Thesis, Louisiana State University, 2011.
- L., D., Alvergue, "Feedback Control of Sector-Bound Nonlinear Systems with Applications to Aeroengine Control", Ph.D. Dissertation, 2012.
- C. Foreman, "Characterization and Verification of a Closed Loop Wind Tunnel with a Linear Cascade and Upstream Wake Generator", M.Sc. Thesis, Louisiana State University, 2013.

DISTRIBUTION A: Distribution approved for public release.

- G., F., Bidan, "Mechanistic Analysis and Reduced Order Modeling of Forced Film Cooling Jets", Ph.D. Dissertation, Louisiana State University, 2013.

- H. Babaee, "Analysis and Optimization of Film Cooling Effectiveness ", Ph.D. Dissertation, Louisiana State University, 2013.

2.2 Archival Publications

2.2.1 Peer Reviewed Journal Publications:

- Guillaume Bidan and Dimitris E. Nikitopoulos, "Fundamental Study of Modulated Transverse Jets from a Film-Cooling Perspective", AIAA Journal, Vol. 49, No. 7 (2011), pp. 1498-1510, doi: 10.2514/1.J050903.

- Alvergue, Luis, Guoxiang Gu, and Sumanta Acharya, "A generalized sector-bound approach to feedback stabilization of nonlinear control systems", International Journal of Robust and Nonlinear Control (2012), Vol. 23, No. 14, pp.1563-1580, doi: 10.1002/rnc.2843.

- Guillaume Bidan, Clémentine Vézier and Dimitris E. Nikitopoulos, "Study of unforced and modulated film-cooling jets using proper orthogonal decomposition–part I: unforced jets", Journal of Turbomachinery, Vol. 135, No. 2 (2013), pp. 021037, doi: 10.1115/1.4006599.

- Guillaume Bidan, Clémentine Vézier and Dimitris E. Nikitopoulos, "Study of unforced and modulated film-cooling jets using proper orthogonal decomposition–part II: forced jets", Journal of Turbomachinery, Vol. 135, No. 2 (2013), pp. 021038, doi: 10.1115/1.4006600.

- Guillaume Bidan and Dimitris E. Nikitopoulos, "On steady and pulsed low-blowing ratio transverse jets", Journal of Fluid Mechanics, Vol. 714 (2013), pp. 393-433, doi: i:10.1017/jfm.2012.482.

- Luis Alvergue, Guoxiang Gu, and Sumanta Acharya, "A Generalized Sector Bound Approach to Feedback Stabilization of Nonlinear Control Systems", International Journal of Robust and Nonlinear Control, Vol. 23, No. 14 (2013), pp. 1563-1580.

2.2.2 Conference Proceedings

- Guillaume Bidan, Pierre-Emmanuel Bouladoux, Jeremiah E. Oertling, Dimitris E. Nikitopoulos, "Experimental and Numerical Study of Steady and Modulated Transverse Jets at Low Blowing Ratios", ASME Turbo Expo 2010, June 14th–18th 2010, Glasgow, UK, GT2010-23013, pp. 2525-2535, doi: 10.1115/GT2010-23013.

- Luis Alvergue, Guoxiang Gu, and Sumanta Acharya, "A Novel Feedback Controller for Reduced Order Fluid Flow Models", 30th Chinese Control Conference (CCC), July 22nd-24th 2011, Yantai, China, pages 711-716. 2

DISTRIBUTION A: Distribution approved for public release.

- Hessam Babaee and Sumanta Acharya, "A semi-staggered numerical procedure for the incompressible Navier-Stokes equations on curvilinear grids", ASME 2011 International Mechanical Engineering Congress and Exposition (IMECE2011), pp. 927-936.

- Guillaume Bidan, Clémentine Vézier and Dimitris E. Nikitopoulos, "Study of Unforced and Modulated Inclined Film-Cooling Jets Using Proper Orthogonal Decomposition: Part I-Unforced Jets", ASME Turbo Expo 2011, June 6th-10th 2011, Vancouver, British Columbia, Canada, GT2011-45400, pp. 1517-1528, doi: 10.1115/GT2011-45400.

- Guillaume Bidan, Clémentine Vézier and Dimitris E. Nikitopoulos, "Study of Unforced and Modulated Inclined Film-Cooling Jets Using Proper Orthogonal Decomposition: Part II-Forced Jets", ASME Turbo Expo 2011, June 6th-10th 2011, Vancouver, British Columbia, Canada, GT2011-46901, pp. 1809-1822, doi: 10.1115/GT2011-46901.

- Alvergue, Luis, and Guoxiang Gu., "Feedback Control for Quadratic Nonlinear Systems", 24th Chinese Control and Decision Conference (CCDC), May 23rd-25th 2012, Taiyuan, China, pp. 2566- 2571.

- Hessam Babaee and Sumanta Acharya, "A Symmetric Finite Difference Discretization of Pressure-Poisson Equation on Curvilinear Grids", 42nd AIAA Fluid Dynamics Conference and Exhibit, June 25th-28th 2012, New Orleans, Louisiana.

- Luis D. Alvergue, Guoxiang Gu, and Sumanta Acharya, "A Generalized Sector Bound Approach to Feedback Stabilization of Nonlinear Control Systems", 2012 American Control Conference, June 27th-29th 2012, Montreal, Canada, pp. 2583-2588.

- Guillaume Bidan, Dimitris E. Nikitopoulos, "Film-Cooling Jets Analyzed with Proper Orthogonal Decomposition and Dynamic Mode Decomposition", AIAA 43rd Fluid Dynamics Conference and Exhibits, June 24th-27th 2013, San Diego, California, doi: 10.2514/6.2013-2970.

3 Motivations

Film cooling systems remain a critical component in jet engines both in terms of reliability and performance. The considerable and diverse benefits of an actively controlled film-cooling system on an intelligent power producing engine are summarized in the chart below (figure 1 - modified from (55)).

Apart from the obvious benefits from increases in Turbine Inlet Temperature (T41) and possible reduction of net coolant flow rates, an actively controlled thermal management system can lead to power producers that are more flexible in accommodating a broader range of fuels (with varying heating values and properties) without adverse effects on performance, serviceability and lifetime. This is becoming of increased importance as various fuels are entering the mainstream in power production; e.g. shale gas, LNG and synthetic gases from gasification of coal and a variety of bio-fuels such as bagasse and other biomasses. Controlling the temperature of gas-turbine components to within limits acceptable for their health, irrespectively of the fuel feed-stock, is feasible though an actively controlled cooling

DISTRIBUTION A: Distribution approved for public release.

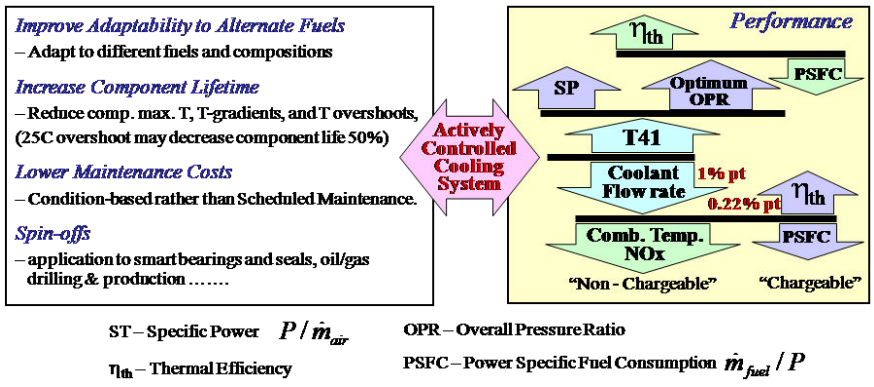

Figure 1: Benefits summary of Actively Controlled Cooling System.

system and very important (an overshoot of as little as 2% of blade critical temperature can lead to a decrease in the part lifetime of as much as 50%).

Film cooling systems involve arrays of continuously blowing jets located on the surface of the part to be cooled and supplied with cooler air diverted from the compressor through internal cooling channels. More 'intelligent' and adaptable systems could lead to a decrease in the overall amount of coolant necessary to operate and yield overall lower emissions and/or higher performance while maintaining system reliability. Although methods to improve film cooling systems through jet hole geometry optimization have been implemented (13), those systems remain passive in nature and lack adaptability to local or global changes in operating conditions. Investigations of the effects of cross-flow unsteadiness, for instance encountered by systems located beyond the turbine first stage, showed that bulk cross-flow pulsations can have a catastrophic effect on cooling performance due to passive jet pulsation (8, 48, 49, 77). Actively controlled film cooling systems using pulsed jets for instance, could provide adaptable jet exit conditions while mitigating the detrimental effects of cross-flow unsteadiness.

The four fundamental vortical structures involved in unforced jet cross-flow configuration have been previously established by (26, 41): the shear layer vortices (Slv), counter rotating vortex pair ($CRVP$), horseshoe vortex (Hv) and wake vortices (Wv) (figure 2). The shear layer vortices are near-field structures, generally considered to be the result of Kelvin-Helmholtz type instability of the jet cylindrical shear layer. The CRVP is the dominant mixing structure in transverse jets and has been the topic of many studies concerned with mixing enhancement or prevention. Formed downstream of the jet exit and dominating the far field, the CRVP consists of a pair of quasi-streamwise counter-rotating vortices. The horseshoe vortex constitutes the third characteristic vortical structure of transverse jets and is the result of cross-flow boundary layer separation upstream of the jet exit previously studied by (42, 44). Finally, the wake vortices are, according to (26), tornado like quasi-vertical vortices, located below the jet core and originating from cross-flow boundary layer separation due to the adverse pressure gradient past the jet column. Numerous studies have dealt with the characterizations of general quantities such as jet penetration, spread, mixing rate, and have identified the jet-to-cross-flow mass-flux ratio (blowing ratio BR) and the jet-to-cross-flow momentum ratio as two of the principal scaled parameters for transverse jets. Since mixing enhancement and VSTOL propulsion have been the main concern in the

DISTRIBUTION A: Distribution approved for public release.

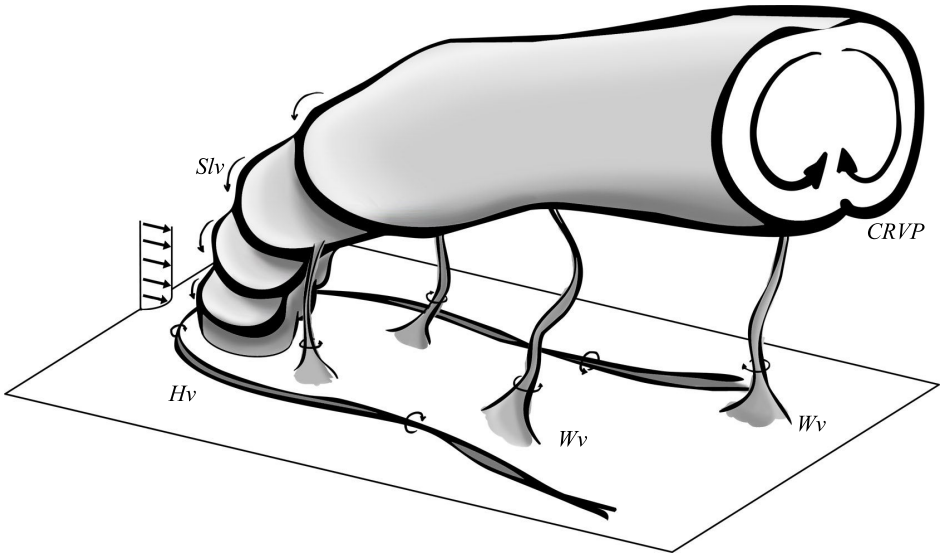

Figure 2: Jet in cross-flow dominant vortical structures

past, most of the studies have been focusing on rather high blowing ratio, vertical jets while only few studies have considered blowing ratios less than 1.0, or inclined jets.

A substantial amount of research has been devoted so far to the control and suppression of boundary-layer separation under conditions prevailing in low-pressure turbine (LPT) airfoils. Vortex generator jets (VGJ) were initially demonstrated to have a significant effect on reducing separation by (50) and have configurations very similar to those used for film-cooling jets according to (3). Both experimental and computational studies from (18) and (33) indicate that this single vortex is very effective in bringing higher-momentum free-stream fluid close to the wall. This adds the kinetic energy necessary for the flow to overcome friction and the adverse pressure gradient near the wall, and thus delay or suppress separation. This mechanism has also been demonstrated computationally with large vortices generated by pulsed normal jets as agents of the momentum transfer from the free stream to the wall region in (78). Jet injection combined with pulsing has been used to suppress separation of wall-bounded flows for several applications. Separation control through the use of pulsed injection through non-zero compound angled VGJs has been successfully realized by several studies (see (54)) including applications to diffusers in (62) and to LPT blade separation control in (12, 32). For the latter case of the LPT application detailed investigations have been conducted on the effect of jet pulsing frequency by (3) indicating that the highest effectiveness in separation control was achieved at low frequencies (relative to the characteristic separated flow frequencies) because of the relatively long relaxation time of the boundary layer as it resumes its separated state. This low-frequency effectiveness together with observations from (47), and analysis of (55), pointing towards a low-frequency envelope for improved film-cooling, provide substantial motivation to investigate the possibility of combined film-cooling and separation control. It also indicates that should the film-cooling system be used for separation control on the HPT airfoils it is likely that the control action is not going to compromise the film-cooling performance. Both of these issues are subjects of the proposed investigation.

DISTRIBUTION A: Distribution approved for public release.

Previous studies by (25, 21) on forced film cooling jets in steady cross-flow environment gave mixed results with both improved and degraded performance over comparable steady state jets. Comparable systems coupled with a spoked wheel wake generator were also studied by (76), in an attempt at counter-balancing large scale cross-flow perturbations and lead to the conclusion that forced jets did not provide amelioration of the film cooling performance. Given the overwhelming number of actuation parameters available (high blowing ratio - BR_h, low blowing ratio - BR_l, forcing frequency - f_f, duty cycle - DC, phase difference - φ ... to name a few) and the highly non-linear character of forced film cooling flows, it appears almost impossible to identify optimum forcing conditions through linear test matrices. This suggests that improved film cooling metrics can only be achieved through 'smarter', self-tuning systems with closed loop control.

Such systems necessitate flow governing equations and/or models in order to operate. Although advances in computational fluid dynamics have led to significant improvement in the results accuracy through large eddy simulations (LES) and direct numerical simulations (DNS), such models require considerable computing power to simulate only a small fraction of time. More reasonable reduced order models (ROM) of the flow are therefore preferable in order to be implemented in closed loop, time-resolved actuation systems. Such ROM-based controlled systems have been successfully implemented for flow systems in (63, 66, 9, 29, 30), to name a few, leading to improved desired metrics. Reduced order modeling is generally achieved in two steps, consisting of first extracting a spatially dependent orthogonal set from experimental data, and then using a subset in a Galerkin projection method onto the Navier-Stokes and energy equations to obtain a set of governing non-linear first order differential equations, providing approximations of the flow and temperature fields.Although the method is well established and successful in two-dimensional low Reynolds number flows, it has been found to often lead to models with low accuracy or even fail in complex three-dimensional systems (22, 65). Indeed, such systems often involve multiple length and energy scales which can create some difficulties when the turbulent interactions are not always captured by the POD-Galerkin method. In the literature there are many works concerned with stabilizing a perturbation of a flow to an equilibrium point using the ROM methodology. For example, (1) studies the linearized dynamics of flow past a flat plate and the stabilization of unstable steady states via balanced Proper Orthogonal Decomposition (POD) ROMs. The application is to regulate vortices in separated flows behind low aspect-ratio wings. Investigating the growth of Tollmien-Schlichting waves in the linearized Navier-Stokes equation, and their attenuation to a steady state using feedback control is considered in (68). In (6), a feedback controller is designed to stabilize a linearized open cavity flow to a steady flow. Global modes, POD, and balanced POD modes are used as expansion bases for the ROM and their performance is compared. The article (64) considers feedback stabilization of flow past an airfoil by a POD/Galerkin ROM. The feedback controller stabilizes the ROM solution but it stops short of implementing the controller in the full order model. With respect to the jet in cross-flow, in (37) the transition from steady to unsteady flow of a jet in cross-flow is analyzed. It applies the tools of linear stability analysis to characterize the critical value of blowing ratio that destabilizes the flow from an equilibrium point.

A common practice for controller design is to linearize the dynamics about a steady state solution (also called an operating point) and apply linear controller design methods. There are many investigations which follow this line of research and they have shown to be effective (39, 1, 64, 40), however the resultant feedback stability is only a local property that may not be applicable to solving practical flow control problems. The main limitation is the lack

DISTRIBUTION A: Distribution approved for public release.

of a characterization of the region of attraction (RoA), which roughly speaking is the set of initial conditions for which the closed loop system is stable. The RoA is an invariant set that is typically difficult to represent and much effort has been devoted to methods for estimating the RoA (11, 27).

In view of the past studies on forced film cooling systems, the identification of ideal forcing parameters to obtain increased film cooling performance using results from a predetermined test matrix appears as a challenging if not impossible task, particularly when considering the rather poor knowledge of the fluidics associated with forced film cooling flows. Active control of the film cooling jets subjected to a closed loop controller appears as a viable solution to converge towards optimum forcing conditions in steady but particularly unsteady cross-flow environment. It was established previously that integration of the complete Navier-Stokes equations is neither desirable, nor feasible, when considering the design of a controller-based system. Thus, one of the key steps in the implementation of a close-loop controlled system resides in the derivation of low order equations representative of the flow of interest, here in particular film cooling flows. The final step is the design of a close loop feedback control strategy, adapted to film cooling metrics.

4 Initial Objectives

The general objectives of the proposed research were to: (A) investigate the physics of the interaction between pulsed film-cooling flow and the downstream separation-prone flow-field on the suction side of gas-turbine blades, (B) examine the possibility of achieving combined improvement of film-cooling and separation suppression, under unsteady upstream conditions (e.g. caused by rotor wake passage), (C) develop and implement an active feedback-control system and algorithm(s) to this effect and assess their performance, (D) lay the foundations for future implementation of active control of the flows of interest using distributed sensing and actuation. These objectives were to be achieved through the combination of an experimental investigation, numerical simulations, and a parallel theoretical effort geared towards development of reduced-order models (ROMs) of the physical processes and appropriate feedback-control algorithms. The experimental effort was to consist of cold-flow studies performed on a scaled-up cascade with realistic vanes and film-cooling geometry, including a wake-passage unsteadiness simulator device and a film-cooling-flow pulsing system. The tasks of this phase were to:

1. Address general objectives A and B above, using an array of pulsed film-cooling jets located on the vane suction surface near the shower-head region. The pulsing control parameters (frequency, amplitude, duty cycle, phase) were to be selected considering the characteristics of the wake-passage unsteadiness characteristics and on the basis of current and past research on the independent improvement of film-cooling and separation suppression.

2. Address general objective B above in determining the existence of pulsing control parameters for which the film-cooling flow (e.g. in terms of limiting lift-off and maintaining film coverage) and separation prevention are optimized. This task of the experimental investigation was to be closely tied to the simulation and feedback controller development tasks.

DISTRIBUTION A: Distribution approved for public release.

3. Contribute to the development of ROMs for the relevant flow-field from velocity-field data in support of general objective C. This task was also to be intimately tied to the feedback controller task, because control actions in general influence the ROM, necessitating the understanding of this interaction

4. Provide experimental data needed to set realistic boundary conditions for the numerical simulations and the validation of simulation results.

5. Implement, validate and assess the feedback control scheme/algorithm on the physical experiment in support of general objectives B and C.

The theoretical control work had the following tasks:

1. Develop a feedback flow-control algorithm utilizing ROMs emanating from corresponding tasks of the experimental and numerical efforts. Part of this task was also to be directed to the development of the ROMs themselves.

2. Support the implementation of this algorithm on the physical as well as on the numerical experiments and assess its performance.

The numerical effort was to employ DNS and/or LES of the flow of interest including heat transfer and will be tightly integrated with the experimental and theoretical ones. Its tasks were to:

1. Address general objectives A and B above, by conducting numerical simulations of flow and heat-transfer for the geometry and conditions of the physical experiments. This task was also to contribute to the understanding of the coupling between flow and heat transfer in the film-cooling region.

2. Implement and assess the feedback control scheme/algorithm through numerical simulation experiments and provide guidance for the physical experiments and the theoretical control effort, in support of general objectives B and C.

3. Address general objective B in searching for the existence of pulsing control parameters for which film-cooling performance and separation prevention are mutually optimized.

4. Investigate in detail the influence of control actions on the ROMs and contribute to their development from simulation data in support of general objective C.

The experimental and numerical efforts were to be conducted in a mutually complementary fashion, as reflected by the commonality of scope in their respective tasks. The technical results obtained though the proposed combined effort were to provide the knowledge and experience base for future implementation of control of these flows in the hot gas path employing local rather than global actuation coupled with local sensing, as per the longest term general objective D.

DISTRIBUTION A: Distribution approved for public release.

5 Changes in research objectives

The experimental work has been delayed by a period of approximately 20 months starting shortly after the beginning of the grant. There are two major reasons for the delay. First, a leak on the roof of the wind-tunnel laboratory building caused by a tree fall during hurricane Gustav (9/2008) destroyed the pulsed laser used for visualizations and PIV and caused the warping of the wind-tunnel screen and contraction sections, which resulted in unacceptably poor flow quality for experiments. The second cause for this delay was the subsequent renovation of the building in which the Wind-Tunnel is located, and in which the cascade facility for this project would be located. The construction shut down operations from 1/2009-7/2010. These problems and delays were documented in the annual reports for the project as they occurred. During this period no experiments could be conducted, and indeed they did not start in earnest until 9/2010 after the laboratory was cleaned and the equipment reconnected and tested.

1. Heat transfer measurements on the cascade facility were not possible and were not carried out;

2. A new cascade facility was designed and built in view of an existing one not being adequate for the purpose and not being serviceable. The latter was dismantled and rendered not operational because of it being transferred to another building. Furthermore, the wake generator of this facility did not meet the desired requirements. This in addition to the aforementioned delays resulting from the damages caused by hurricane Gustav and construction work, significantly affected the progress of experimental measurements on realistic film cooling systems. For these reasons, investigations on interactions between film cooling jets and flow separation region were not possible, and focus was kept on investigation of forced film cooling physics, their optimization and reduced order modeling.

3. The fundamental scope of work was substantially expanded in order to meet the challenges of developing 3D reduced order models for the complex film-cooling flows addressed by the project. This was deemed necessary in order to lay the groundwork towards the combined active control of film cooling flows and turbine blade aerodynamics.

Based on these considerations, the initial objectives were changed to:

- Experimental investigations:

    1. To perform a fundamental mechanistic analysis of unforced and forced low blowing ratio jets in cross-flow. To this end, both vertical and inclined low blowing ratios forced and unforced jets in cross-flow will be investigated in an effort to extend the otherwise extensive literature concerning those flows at high blowing ratios.
    2. To develop, build and characterize a realistic film cooling linear cascade type capable of producing engine like Reynolds numbers ($Re \simeq 500,000$) with realistic incoming wake signatures. This facility would be capable of reproducing engine conditions in the turbine stages beyond the first nozzle guide vanes. This facility will be designed around an AFRL L1-A profile, equipped with film cooling holes.

DISTRIBUTION A: Distribution approved for public release.

3. To provide support in developing a reduced order model of unforced and forced film cooling velocity and temperature fields.

- Numerical effort:

1. To identify optimum forcing conditions for forced film cooling systems. To this end, Direct Numerical Simulations of film cooling systems will be carried out and a methodology for the identification of optimum forcing parameters will be developed.
2. Investigate in detail the influence of control actions on the ROMs and contribute to their development from simulation data.
3. Implement and assess the feedback control scheme/algorithm through numerical simulation experiments.
4. To develop a reduced order model of unforced and forced film cooling velocity and temperature fields.

- Theoretical control:

1. Develop a feedback flow-control algorithm utilizing ROMs emanating from corresponding tasks of the experimental and numerical efforts. Part of this task was also to be directed to the development of the ROMs themselves.
2. Support the implementation of this algorithm on the physical as well as on the numerical experiments and assess its performance.

6 Accomplishments/Findings

- Investigation of the fundamental forced film cooling systems using experimental and numerical (LES) methods:

  – Identification and detailed description of the vortical system developing in unforced low blowing ratio transverse jets (90 degrees injection angle). In particular, description of a stable inner vortex vortex inside the jet pipe for blowing ratios below 0.275 interacting with the well-known horseshoe vortex system. The destabilization of this structure is responsible for transition of the jet from attached to detached configuration and clear film cooling performance degradation.

  – Experimental verification of the vortical system formed in forced transverse jets with non-zero low blowing ratio, and definition of the proper scaling parameters for such jets. Experiments allowed to confirm the existence of four starting vortex regimes in agreement with previous numerical studies. Additional investigations revealed the proper scaling parameters to be used in forced transverse jets with residual low flow-rate were (BR_h, SR_h). Experiments showed that previous numerical studies over predicted the threshold values between different starting vortex regimes by as much as a factor 3.

DISTRIBUTION A: Distribution approved for public release.

- Experimental and numerical investigations and detailed description of the vortical system developing in low blowing ratio film cooling geometries and their impact on adiabatic effectiveness.
- First time description of the vortical system born from jet forcing in forced film cooling setups. Identification of 6 vortical regimes, and derivation of the proper scaling parameters (BR_h, SR_h) based on PIV measurements. Forced film cooling systems were found to have lower performances compared to unforced systems when actuated in "open loop" fashion.Investigation of realistic film cooling systems using cascade wind tunnel experiments and realistic wake generator:
- Complete design, fabrication and validation of a linear cascade setup with realistic flow conditions ($Re \simeq 500,000$) and realistic incoming wake profiles, equipped with L1-A two dimensional profiles.
- Characterization of the L1-A wake profile and characteristic frequency under unsteady cross-flow conditions.
- Mie scattering visualizations and PIV measurements evidencing the impact of the wake on film cooling jet behavior.

- Numerical simulations and forced film cooling optimization:
  - An optimization strategy combining high-fidelity simulations with response surface construction, was applied to pulsed film cooling for turbine blades. The response surface was constructed for the film cooling effectiveness as a function of duty cycle, in the range of DC between 0.05 and 1, and pulsation frequency St in the range of 0.2-2, using a pseudo-spectral projection method. 73 direct numerical simulations (DNS) using spectral element method were performed to sample the film cooling effectiveness on a Clenshaw-Curtis grid in the design space and evidenced a global optimum at DC = 0.14 and St = 1.03.
  - Extraction of the first known reduced order models of unforced film cooling systems velocity and temperature fields at $BR = 0.15$ and $BR = 0.5$, using the POD-Galerkin projection modeling method. Implementation of known and new stabilization techniques for improved model reliability.
  - Extraction of the first known reduced order models of forced film cooling systems instantaneous and phase averaged velocity and temperature fields, using the POD-Galerkin projection modeling method. Implementation of known and new stabilization techniques for improved model reliability.
  - Description of the impact of forcing frequency on film cooling reduced order models through mode segregation mechanism at low forcing frequencies.
  - Description of the impact of blowing ratio on unforced film cooling reduced order models and emphasis of the necessity to implement efficient stabilization methods at high blowing ratios.

- Feedback flow control of film cooling systems:
  - Development of a generalized sector bound approach to feedback stabilization of nonlinear control systems described by state-space models. Regional stabilization

DISTRIBUTION A: Distribution approved for public release.

of the nonlinear dynamics and maximization of the estimated region of quadratic attraction.

– Development of a sequence of linear controllers regionally stabilizing the desired equilibrium using a a switching strategy based on the assumption of a centered-epsilon-cover equilibria path. The controller was used to successfully stabilize a reduced order model (ROM) of a jet in cross-flow to a steady low kinetic energy flow.

DISTRIBUTION A: Distribution approved for public release.

Part II
Mechanistic Analysis

DISTRIBUTION A: Distribution approved for public release.

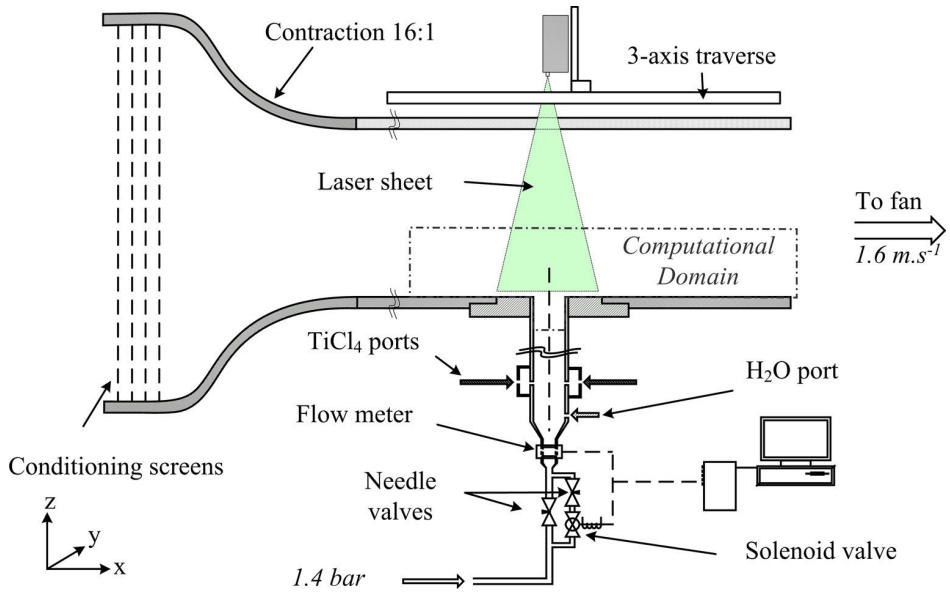

Figure 3: Vertical jet experimental apparatus.

1 Vertical Jet in Cross-flow

In order to gain physical insight on forced film cooling jets, the vortical structures generated in low blowing ratio partly modulated vertical jets in cross-flow are investigated first. Though not strictly application-relevant when it comes to film cooling, these jets offer the advantage of having been well documented in the past, though at blowing ratio values usually relatively high, and constitute a good starting point for a mechanistic analysis and understanding of forced film cooling flows.

First, a detailed unforced survey was conducted to provide a description of the vortical structures found in low blowing ratio transverse jets as well as their evolution as the blowing ratio was increased to reach a more commonly studied detached configuration. Then, partially modulated transverse jets were investigated with a particular focus on the transient regimes introduced by jet forcing. These results were based on experimental results using hot wire anemometry and Mie scattering visualizations while monitoring the jet flow rate in a time-resolved manner. Large Eddy Simulation (LES) as implemented in Ansys Fluent™ was also used to provide additional insights on the behavior of the vortical structures. Film cooling performance was evaluated from the numerical simulations for the forced jets and compared to the unforced results.

1.1 Experimental and Numerical Setup

1.1.1 Wind Tunnel Experiments

Experiments were conducted in an open loop aerodynamic wind tunnel with a $9m$ long test section and a $0.9 \times 0.6m$ cross-section, schematically presented in figure 3. A set of four conditioning screens followed by a contraction with an area ratio of $16:1$ were located directly upstream of the test section to provide stable inlet conditions during the experiments.

DISTRIBUTION A: Distribution approved for public release.

Optical access was available through a set of transparent acrylic walls constituting the top and one of the side walls of the test section, respectively allowing visualizations in planes parallel to the bottom wall (X-Y) and parallel to the jet symmetry plane (X-Z). The coordinates x, y, and z are respectively associated with the stream-wise, span-wise and vertical directions of the flow as shown in figure 3, the origin is taken at the center of the jet exit and the quantities X_j, Y_j, and Z_j correspond to the normalized coordinates with respect to the jet diameter D_j (resp. x/D_j, y/D_j and z/D_j). The free stream flow in the test section had turbulence intensity levels of less than 0.5%, with a boundary layer Reynolds number at the jet level of $Re_\infty = U_\infty \delta/\nu = 1,700$ (with δ the 99% boundary layer thickness and ν the air kinematic viscosity). The jet exited from a $25.4mm$ (D_j) round exit located $762mm$ downstream of the test section inlet and was mounted flush to the bottom wall. At the jet inlet, the setup was composed of two branches, a principal and a bypass, each comporting a metering needle valve to control the flow in the branch. The bypass also comported a computer-controlled solenoid valve which is used to pulse the flow during forced flow experiments (see figure 3). This system provided the ability to independently and accurately set the low (BR_l) and high (BR_h) jet blowing ratios in forced experiments, recorded in a time resolved manner by an inline flow-meter. The jet and cross-flow were at ambient temperature therefore the density ratio was approximately one. The experimental setup is studied using laser sheet Mie scattering visualizations, hot wire anemometry and time resolved flow rate records.

1.1.2 Numerical Simulations

Numerical simulations were carried out in parallel to the experiments in order to provide more detailed information on the vortical structures and their formation mechanisms under forced and unforced conditions. A commercial solver (Ansys Fluent™) was used to simulate the unsteady, turbulent flow through incompressible Large Eddy Simulation (LES) using a dynamic Smagorinsky sub-grid scale model with second order accuracy for both spatial and temporal discretizations. Figure 4 shows the simulated domain consisting of a rectangular box representing a part of the wind-tunnel test section and of the jet pipe as well as the applied boundary conditions. The main computational domain was $18D_j$ long (stream-wise x-direction), $8D_j$ wide (span-wise y-direction) and $6D_j$ tall (vertical z-direction) and accounts for $174 \times 92 \times 76$ cells along the respective dimensions. The jet exit center was located $6D_j$ downstream from the domain inlet and the jet pipe domain is $8D_j$ long to allow development of the artificial inlet boundary conditions, the parameters of which are adjusted to approximate the natural flow induced during experiments. The jet tube mesh consisted of an O-grid type mesh with 3060 cells in the cross-section and 150 cells along the pipe axis. The full mesh was structured and contained overall 1.8 million cells. The first cells in contact with solid walls were on average $0.03D_j$ tall in the normal direction for y^+ values below or close to unity. To obtain statistically significant data, the flow was integrated over several thousands iterations for each case on high performance computing platforms at Louisiana State University (IBM Power5+ at $1.9GHz$), using an average of 24 processors per run. Velocity characteristics and boundary layer profiles for the inlet of the computational domain were obtained from hot wire measurements performed in the wind tunnel as summarized in table 1, where δ^*, θ and H correspond respectively to the boundary layer displacement, momentum thickness and shape factor.

DISTRIBUTION A: Distribution approved for public release.

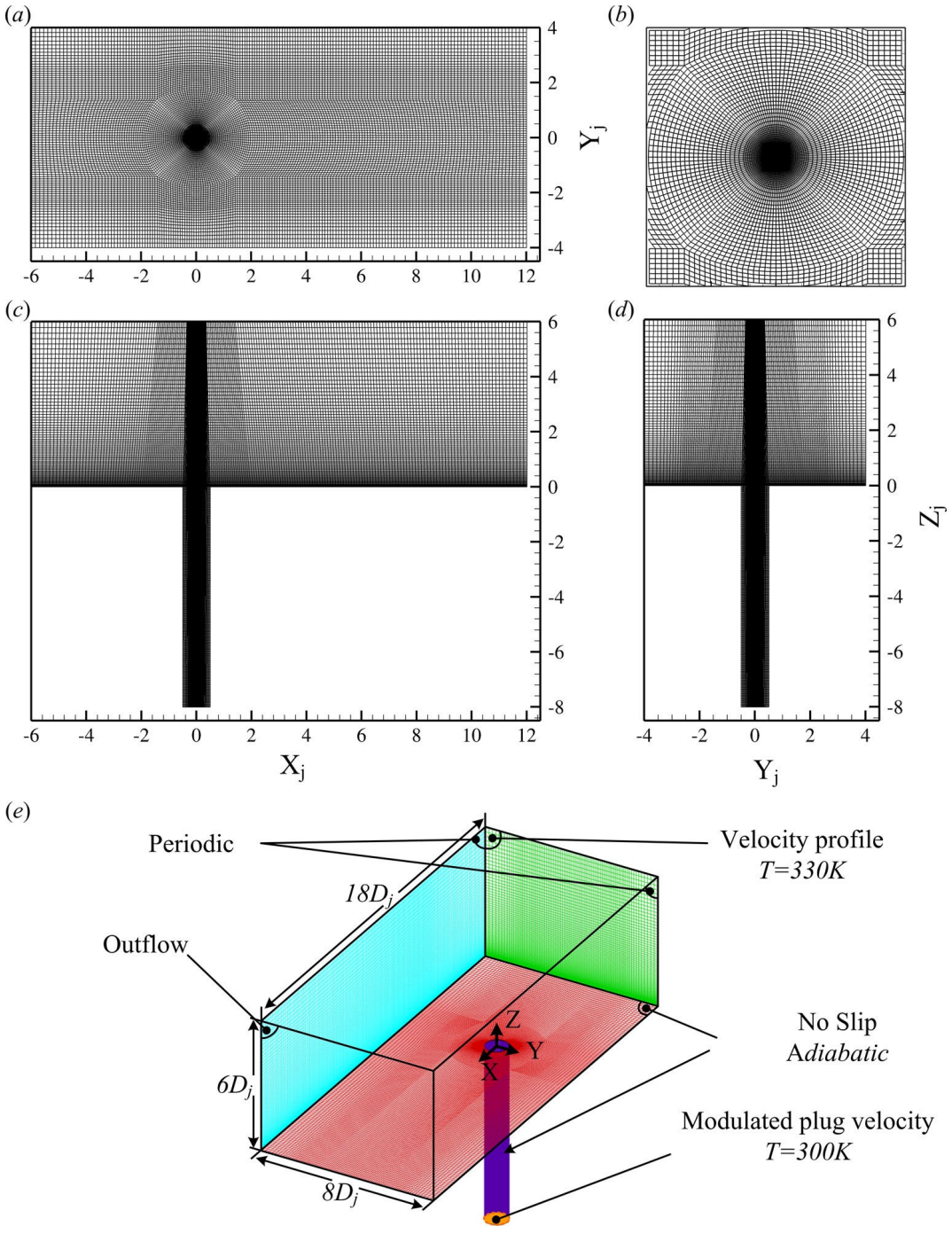

Figure 4: Vertical jet numerical grid details and boundary conditions. (a) X-Y view, (b) X-Y view detail, (c) X-Z view, (d) Y-Z view, (e) global view and imposed boundary conditions.

DISTRIBUTION A: Distribution approved for public release.

Table 1: Inlet boundary layer characteristics at $X_j = -6$, $Y_j = 0$.

U_∞	Ti	δ/D_j	δ^*/D_j	θ/D_j	H
$1.6ms^{-1}$	$< 0.5\%$	0.630	0.172	0.077	2.23

At the inlet of the jet pipe, uniform velocity was set so as to equal the volumetric flow rate of the experiment. In the pulsed jet simulations, the velocity was modulated by using the signal of the unsteady volumetric flow rate measurement from the flow-meters during experiments. Spatial profile perturbations were provided using the spectral synthesizer method implemented in Fluent with a characteristic length scale equal to D_j and a cross-flow characteristic boundary layer length scale equal to 0.4δ. Based on the experimental measurements presented in table 1, a 0.5% perturbation level was imposed at the cross-flow inlet. Because the experimental setup does not allow measurements $8D_j$ inside the jet pipe, the perturbation levels at the jet inlet were adjusted so that simulated and experimental perturbation levels at the jet exit would match. The jet and test section walls were set as adiabatic. Periodic boundary conditions were applied to the side boundaries of the test section box and a standard convective outflow boundary condition was used on the outlet plane. Finally, conversely to the experiment, the jet and cross flow fluids were maintained at constant temperatures of respectively 300 and $330K$ similarly to what was done in the experiments of (25). The density difference associated with those temperature gradients was sufficiently low as to not affect the velocity field.

Figure 5 shows a comparison between experimentally measured and predicted velocity magnitude profiles at two stream-wise locations, $X_j = 1.0$ and $X_j = 3.5$ in the symmetry plane $Y_j = 0$ for three values of the blowing ratio. Because experimental profiles were obtained using single component hot wire anemometry, no distinction could be made between stream-wise and vertical velocity components, thus velocity magnitudes were chosen as a comparison basis. In addition, recirculatory flow present near the wall at $X_j = 1.0$ could be measured accurately because of hot wire signal rectification, thus no experimental data is reported in this region. The velocity profiles in figure 5 compare reasonably well at $BR = 0.15$ and $BR = 0.465$ for both stream-wise locations, while at $BR = 0.25$, the simulations appear to under predict the velocity magnitude in the jet wake. This result is consistent with a mismatch in the transition behavior between experimental and numerical data which will be described later. Overall, the agreement of the rudimentary mean flow comparisons between simulation and experimental results is quite good and re-enforces the qualitative and mechanistic comparisons between the simulation results and the visualizations presented in the following sections. Thus, both physical and simulated flows are deemed comparable enough to be used concurrently in interpreting and understanding fundamental processes.

1.2 Results

1.2.1 Unforced Jet

A rather extensive study of the unforced jet over a wide range of blowing ratios from $BR = 0.150$ to $BR = 4.3$ was conducted as a baseline for the subsequent pulsed jet study. Based on the characteristic vortical structures of the jet at various blowing ratios, attached and detached jet regimes were identified at blowing ratios below 0.275 and above 0.6 respectively.

DISTRIBUTION A: Distribution approved for public release.

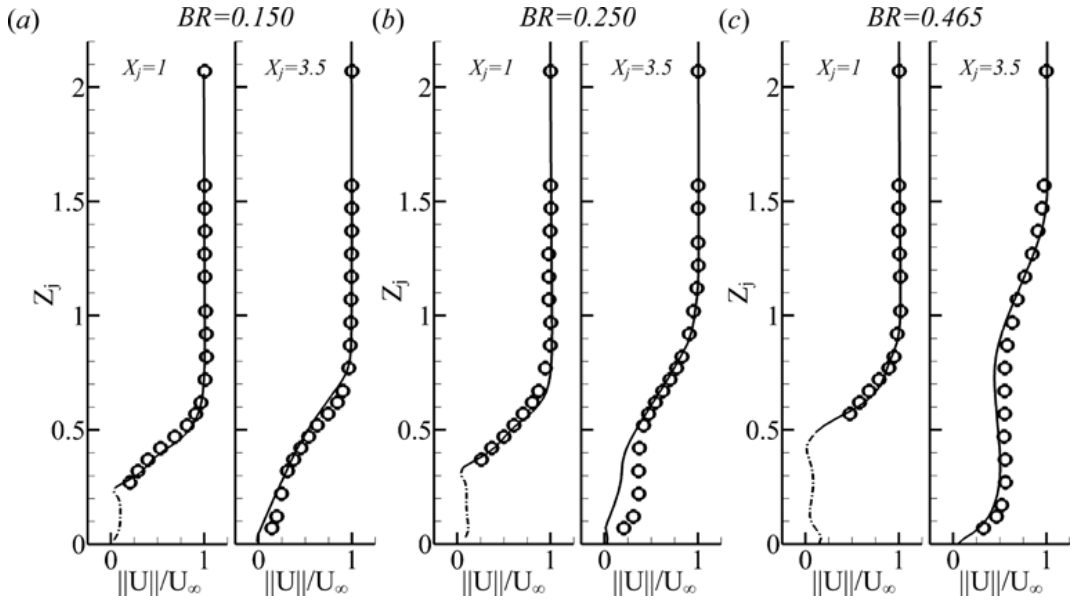

Figure 5: Experimental (*symbols*) and simulated (*solid line*) velocity magnitude profiles in the symmetry plane at $X_j = 1$ and $X_j = 3.5$ for (a) $BR = 0.15$, (b) $BR = 0.25$, (c) $BR = 0.465$.

The latter exhibited classic transverse jet vortical structures (horseshoe vortex, ring shear layer vortices, wake vortices). At intermediate values of the blowing ratio ($0.275 \leq BR < 0.600$) the transition cases exhibited features from both types of flows.

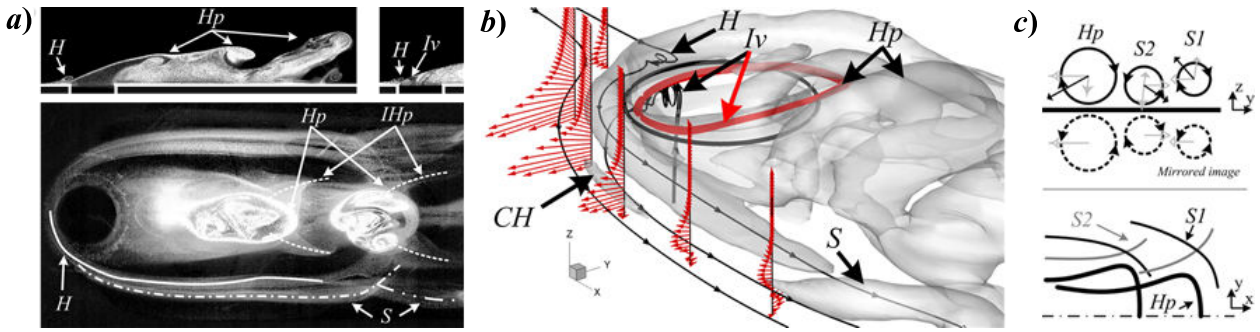

Figure 6: (a) Reactive Mie scattering visualization in the plane $Y_j = 0$ (top) and $Z_j = 0.5$ (bottom) at $BR = 0.188$; (b) Laplacian of the pressure iso-surface at $\Delta P = 1kPa.m^{-2}$ and local velocity profiles with spanwise and vertical component only, in the vicinity of the jet exit from LES at $BR = 0.188$; (c) Induction effects between hairpin (*Hp*) and side vortices (*S1* and *S2*) and their respective mirrored images. *H* - Horseshoe vortex, *CH* - Counter-horseshoe vortex, *Iv* - Inner vortex, *Hp* - Hairpin vortices, *S* - Side vortices (*dash-dot line*), *IHp* - Inverted hairpin vortices (*dashed line*).

DISTRIBUTION A: Distribution approved for public release.

The regime most relevant to film cooling application, the attached jet, was investigated in great details for the first time in this study, and a set of characteristic vortical structures were identified:

- *Recirculation region* - A recirculation region was identified directly downstream of the jet exit in both experimental visualizations and numerical results (figure 6*a*). Time-averaged streamlines from LES, showed that the recirculation region was mainly supplied by jet fluid issuing from the sides of the jet tube, although a certain amount of cross-flow fluid (moist air in the experiment) was entrained and reacted to generate the seed particles in the visualizations as well.

- *Shear layer hairpin vortices* - The dominant shear layer structures were found to be of the interlocked hairpin type (*Hp* in figure 6). These vortices were formed periodically in the lower shear layer with increasing formation frequency as the blowing ratio was increased. Multiple self-induction and mirrored induction effects dictated the behavior of the hairpin vortices as they were convected downstream by the cross-flow momentum.

- *Horseshoe vortex* - A stable horseshoe vortex was located above and on the leading edge of the jet exit (*H* in figure 6). Relatively small at the lowest blowing ratios, (approximately $0.19D_j$ in radius at $BR = 0.15$), the primary vortex became larger in diameter with increasing values of the blowing ratio (up to $0.26D_j$ at $BR = 0.275$), while being pushed further upstream from the leading edge of the jet. Seeding particles entrained from the upper lip of the jet into the horseshoe vortex system in experimental visualizations, evidenced transport of jet fluid by the structure. Cases with blowing ratios in the range $0.225 \leq BR \leq 0.275$, exhibited irregular transport of the horseshoe vortex, which was convected downstream on top of the jet upper shear layer. This destabilization was likely provoked by an interaction between the horseshoe vortex and the inner vortex. Although not immediately seeded and entirely visible, a second horseshoe vortex very quickly replaced the convected one in the cross-flow boundary layer upstream of the jet.

- *Side vortices* - Additional stream-wise wall vortices were found in both Mie scattering visualizations and numerical simulations (*S* in figure 6). In the near field, these side vortices, were located on the outside of the horseshoe vortex. The origins of these secondary vortices were explained by a strong positive spanwise (or locally radial outwards) velocity gradient in the vertical (wall-normal) direction due to jet fluid injected around the jet hole, as well as cross-flow deflection imposed by the jet blockage (figure 6*b*). Further downstream, both horseshoe and counter-horseshoe vortices interacted with the shear layer structures, to respectively form positive and negative side-vortices *S1* and *S2*. Due to their closeness to the wall and their opposite vorticity, both types of side-vortices behave differently as they are convected. Figure 6 (*c*) illustrates first order mutual induction effects as well as mirrored induction effects. As they were convected downstream, the negative side-vortices had a tendency to ride on top of the positive ones while converging toward the symmetry plane, whereas the latter diverged from the symmetry plane. The different relative motions of the side vortices resulted in "X-patterned" structures lying on each side of the jet core, which can be observed both in the Mie scattering visualizations and LES results.

DISTRIBUTION A: Distribution approved for public release.

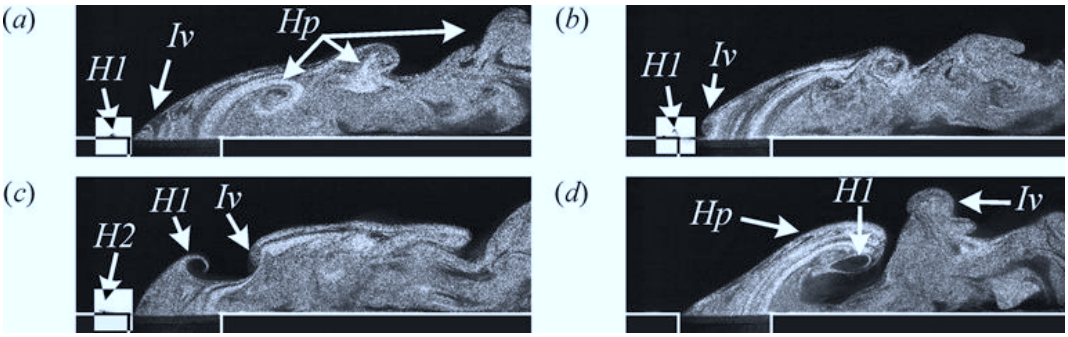

Figure 7: Fully Reacted Mie scattering visualizations at $Y_j = 0$ and $BR = 0.365$ (a) $t_c = t_0$; (b) $t_c = t_0 + 6$ $(95ms)$; (c) $t_c = t_0 + 7.9$ $(125ms)$; (d) $t_c = t_0 + 9.8$ $(155ms)$. Hn - Horseshoe vortex #n, *Iv* - Inner vortex, *Hp* - Hairpin vortices.

- *Inner vortex* - Amongst the few low-blowing-ratio studies of the past, (28) suggested that at low blowing ratios, the span-wise vorticity from the boundary layer, resulting in the formation of the horseshoe vortex, interacted with the jet upper shear layer vorticity and ultimately canceled it so that, conversely to the higher blowing ratio cases, the upstream shear layer was not rolling and no vortical structure was formed at the leading edge of the jet. The current study showed the presence of a stable rollup of reacted seed, or inner vortex (*Iv* in figure 6), resulting from jet flow separation inside the pipe and located at the leading edge. The shedding of this vortex was prevented by the blockage exerted by the cross-flow on the jet as suggested by the relatively advanced position of the horseshoe vortex. Accordingly, LES showed a high pressure region located upstream and above the jet exit, creating an adverse pressure gradient for part of the jet fluid exiting from the pipe, thus forcing it to roll up at the jet leading edge. Jet fluid from the upstream region of the jet was found to exit on the sides of the jet pipe as well as upstream, underneath the primary horseshoe vortex. The inner vortex and the consecutive hairpin vortices formed a series of interlocked rings, sharing the upstream part. For blowing ratios between 0.275 and 0.6, inner vortex started to shed, as the jet entered the the transitional regime. A typical convection sequence of this vortical structure is presented in figure 7. The inner vortex (Iv), still partly inside the jet tube in figure 7(a), is convected in figure 7(b), which is followed by an ingestion of cross-flow fluid inside the jet pipe at the leading edge. The perturbation of the jet/cross-flow interface also triggered the transport of the horseshoe vortex (*H1*) in figure 7(c), followed by the formation of a large hairpin vortex (Hp) in figure 7(d). At values of the blowing ratio approaching 0.6, the size of the transported inner vortex became comparable to the downstream shear layer vortices and the ingestion of cross-flow fluid that followed the inner vortex transport, was gradually decreased, until it completely disappeared beyond $BR = 0.6$.

- *Counter Rotating Vortex Pair (CRVP)* - In time averaged stream-wise vorticity field, a pair of stream-wise counter-rotating vortices was located on each side of the symmetry plane (*filled arrows*). This result is a common feature in transverse jets and is usually identified as the CRVP. According to the instantaneous observations, the vorticity of this vortex pair was generated by the hairpin vortices. Although close from the usual

DISTRIBUTION A: Distribution approved for public release.

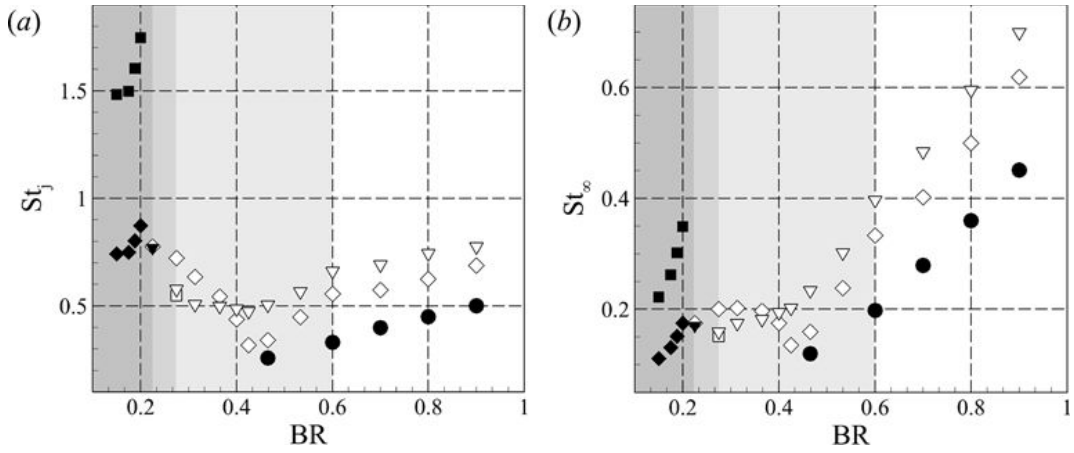

Figure 8: Fundamental frequencies scaled using (a) time averaged jet velocity; (b) cross-flow velocity. In the experiment these were identified from hot wire records using wavelet analysis. The symbol $\diamond$ corresponds to the jet exit ($X_j = 0$, $Z_j = 0$); $\triangledown$ is from location ($X_j = 0$, $Z_j = 0.25$) and $\blacktriangledown$ from location ($X_j = 0$, $Z_j = 0.5$), both inside the upper shear layer; $\blacksquare$ corresponds to the fundamental and $\blacklozenge$ to its subharmonic from downstream location ($X_j = 3.5$, $Z_j = 0.75$); $\square$ is from location ($X_j = 3.5$, $Z_j = 1.25$). The symbol $\bullet$ indicates characteristic frequencies from the LES at the center of the jet exit ($X_j = 0$, $Z_j = 0$).

CRVP structure described in most high blowing ratio jets in cross-flow studies, the attached jet CRVP was found to be instantaneously discontinuous since induced by hairpin vortices, and was not the dominant feature of the far field, where the vorticity in the CRVP was twice as low as the one in the average side vortices found near the wall.

- *Characteristic frequency modes* - Single component hot wire measurements were performed at select locations, chosen based on the visualizations in order to identify frequency modes associated with the previously described structures. The velocity signals were subjected to both Fourier and wavelet spectral analysis, the latter between 0 and $50Hz$ (corresponding to Strouhal numbers St_∞ between 0 and 0.794), guided by the results from the former. The results presented in figure 8, summarize the fundamental frequencies found at each location scaled by jet diameter and mean jet velocity ($St_j = f.D_j/U_j$) in figure 8(a) and scaled by jet diameter and cross-flow velocity ($St_\infty = f.D_j/U_\infty$) in figure 8($b$). Results from the attached jet regime showed an increase in Strouhal number with increasing blowing ratio, corresponding to the rate of formation of hairpin vortices. Similarly, results from the detached jet at $BR = 0.6$ showed a nearly linear rate of increase in Strouhal number with blowing ratio at both locations, corresponding to the formation rate of ring vortices. The simulation results showed an identical trend but with overall lower frequencies and a slightly lower rate of increase. Overall, the value of St_∞ appeared relatively constant around 0.2 over the range $0.225 < BR < 0.425$, while St_j decreased continuously from 0.780 to 0.32 at the jet exit. This indicates that the dominant feature, in this case the transport of the horseshoe vortex and the inner vortex, were better scaled by the cross-flow velocity and

DISTRIBUTION A: Distribution approved for public release.

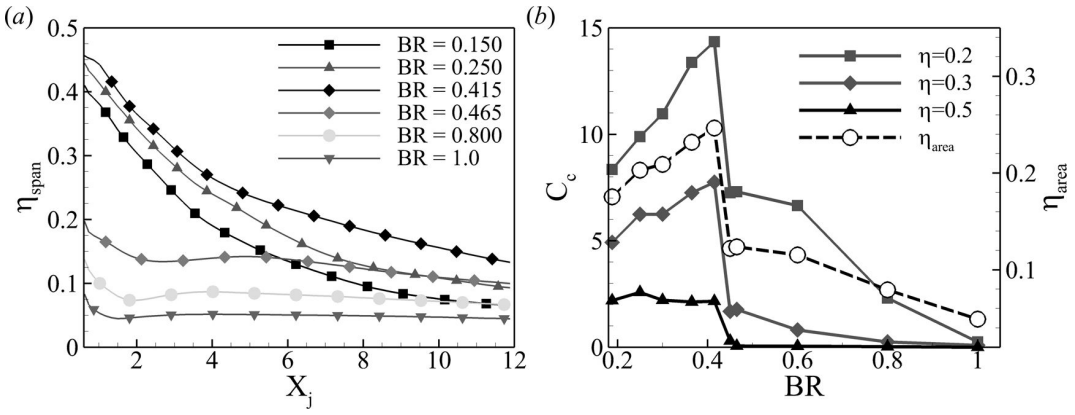

Figure 9: Film cooling performance: (a) Spanwise averaged adiabatic effectiveness; (b) Area averaged adiabatic effectiveness and coverage coefficient for thresholds $\eta = 0.2$, 0.3, 0.5 as a function of BR after LES.

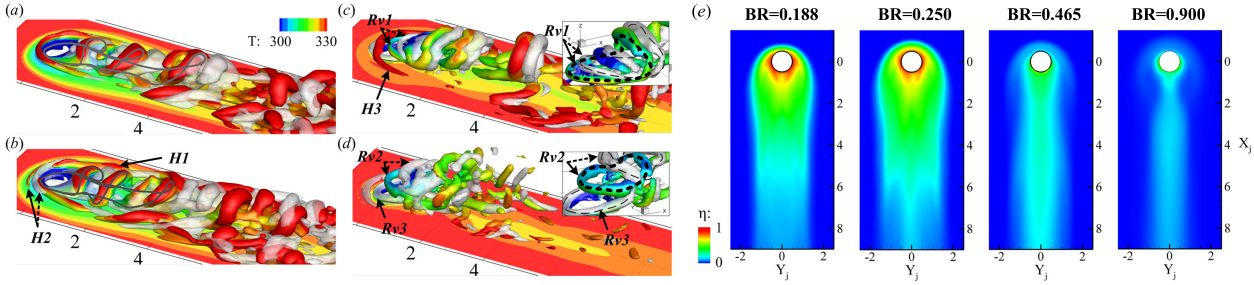

Figure 10: (a-d)ΔP iso-surfaces at two superposed time instants separated by Δt_c, first iso-surface colored by temperature: (a) $BR = 0.188$, $\Delta P = 1500$, $\Delta t_c = 1.25$; (b) $BR = 0.25$, $\Delta P = 2000$, $\Delta t_c = 2.2$; (c) $BR = 0.465$, $\Delta P = 5000$, $\Delta t_c = 0.6$; (d) $BR = 0.9$, $\Delta P = 1500$, $\Delta t_c = 0.6$. (e) Time averaged wall adiabatic effectiveness at: (a) $BR = 0.188$; (b) $BR = 0.25$; (c) $BR = 0.465$; (d) $BR = 0.9$.

thus suggested that the transport mechanism was initiated by the horseshoe vortex. On the other hand, for $0.425 \leq BR < 0.6$, St_j values tended to reach saturation, while St_∞ was clearly increasing, indicating a shift in the transport initiating structure from the horseshoe vortex to the inner vortex.

- *Film Cooling Performance* - Vortical structures influencing the wall temperature field were identified. The area of highest adiabatic effectiveness in the attached configuration was located in the recirculation region, which was essentially seeded by jet fluid (figure 10). The fluid forced to exit on the sides of the jet pipe by the high pressure region also provided additional coverage. The horseshoe vortex was found to entrain significant amounts of coolant upstream of the jet due to its position above the jet exit and have a positive effect on film cooling adiabatic effectiveness in this region. The counter-horseshoe and horseshoe vortices had an opposite impact on the jet spread at the wall

DISTRIBUTION A: Distribution approved for public release.

because of their respective velocity fields. Near the wall the horseshoe vortex had a velocity field pointing away from the symmetry plane and tend to entrain cooler fluid from the jet core region toward the wall, whereas the counter-horseshoe vortices had an associated opposite velocity field carrying free stream fluid near the bottom surface. Consequently, the formation of the X-patterned structures directly downstream of the hairpin vortices resulted in dramatic decrease in local wall adiabatic effectiveness. Along the symmetry plane, the legs of the hairpin vortices were responsible for the transport of most of the coolant. These results show the significant role of the horseshoe vortex and the inner vortex in the jet coverage near the wall. As the horseshoe vortex started to be convected beyond $BR = 0.25$, the coolant supply upstream of the jet exit was never interrupted and coverage was continuously provided to this area. As BR increases, the horseshoe vortex was strengthened and pushed further upstream from the jet exit, thus augmenting the jet coverage at the wall. Finally, the hairpin vortices at $BR = 0.25$ were stronger when compared to the lower blowing ratio cases, and stayed coherent further downstream, carrying more coolant along the symmetry plane. The transitional regime marked the beginning of coverage degradation. At $BR = 0.465$, the hairpin vortices' legs immediately lifted off of the wall after the jet exit because of increased mutual induction, as well as the shedding of the inner vortex. The consequent drop in coverage observed in the contours of adiabatic effectiveness (figure 10) was explained by the consecutive transports of the inner and horseshoe vortices, interrupting the coolant flow upstream and on the sides of the jet exit. In the detached configuration, at $BR = 0.9$, the shear layer ring vortices (R2) were formed on a periodic basis and were directly convected away from the wall, therefore not providing coverage. Conversely to the transitional regime, the horseshoe vortex formed ahead of the jet was not convected, though it oscillated as the shear layer ring vortices shed, and its impact on the wall temperature was only minor. Marginal amounts of coolant reached the jet wake region transported by the wake vortices as evidenced by the η contours as well as the presence of seed particles in experimental Mie scattering visualizations. An increase in spanwise averaged adiabatic effectiveness was found (figure $9a$) for increasing values of the blowing ratio until the transitional threshold was reached ($BR = 0.415$) and then dropped precipitously. As BR continued to increase, the effectiveness decreased asymptotically toward zero. A local minimum in η_{span} profiles for the transitional jet was observed downstream of the jet exit, corresponding to the location where the cross-flow recovered behind the jet and moved upstream toward the jet exit as BR increased. Maximum coverage was reached at $BR = 0.415$. The area averaged adiabatic effectiveness,η_{area}, (figure $9b$) was computed from the simulations, assessing the overall film cooling performance at a given blowing ratio. Accordingly to η_{span} trends, film cooling was improved for increasing values of BR below the transitional threshold, and decreased dramatically beyond this point.

Investigations of the unforced jet showed that the transitional threshold constitutes a limitation to the improvement of film cooling performance because of the transport of the inner vortex and the associated interruption of coolant supply to the upstream region. Based on the evolution of the film cooling metrics in the attached jet regime, delaying the transport of the inner vortex to higher values of BR could lead to improved overall coverage.

DISTRIBUTION A: Distribution approved for public release.

Table 2: Forced cases parameters †: No flow-meter record available, ‡: No experiments at these conditions, *: Simulations carried at these conditions.

$Case\#$	BR_m	BR_l	BR_h	BR_{pp}	$DC(\%)$
1^{*}	0.250	0.188	0.438	0.250	25
2	0.250	0.075	0.325	0.250	70
3^{*}	0.350	0.188	0.836	0.648	25
4^{*}	0.350	0.188	0.513	0.325	50
5	0.350	0.225	0.475	0.250	50
6	0.350	0.175	0.425	0.250	70
$7^{\dagger}$	0.750	0.200	2.20	2.00	25
$8^{\dagger}$	1.25	0.200	4.20	4.00	25
$9^{\ddagger *}$	1.25	0.200	2.20	2.00	50
$10^{\ddagger *}$	0.365	0.200	2.20	2.00	8
$11^{\ddagger *}$	1.28	0.700	3.00	2.30	25
12^{*}	0.465	0.188	0.712	0.524	50

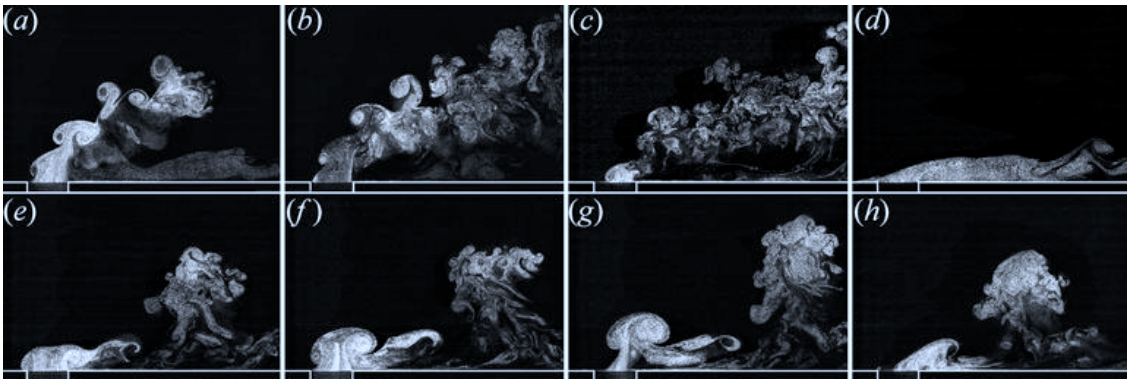

Figure 11: Mie scattering visualizations in the plane $Y_j = 0$ for *Case 3*, (a) $t^* = 0.1$; (b) $t^* = 0.2$; (c) $t^* = DC + 0.025$; (d) $t^* = DC + 0.63$ at $St_\infty = 0.016$ and (e) $t^* = 0.1$; (f) $t^* = 0.2$; (g) $t^* = DC + 0.025$; (h) $t^* = DC + 0.63$ at $St_\infty = 0.159$.

DISTRIBUTION A: Distribution approved for public release.

1.2.2 Forced Jet

Forced jet experiments were performed using a nominal square wave actuation signal for the solenoid valve shown in figure 3. A wide range of forcing parameters' values for BR_m, BR_l, BR_h, BR_{pp}, (respectively mean, low, high, peak to peak blowing ratios over a cycle) and DC (duty cycle) was covered and are summarized in table 2. Each individual case was observed at 4 distinct forcing frequencies (f_f) of 0.5, 1.0, 5.0 and $10.0Hz$, respectively corresponding to Strouhal numbers of $St_\infty = 0.008$, 0.016, 0.079 and 0.159. These were selected to stay below the shear layer natural frequencies of the unforced jet so as to minimize the potential of direct resonant amplification (see 55), although resonance with sub-harmonic and other lower harmonics giving rise to stronger non-linear effects (see 56 and (57)) cannot be ruled out. Phase locked Mie scattering visualizations, supplemented by hot wire anemometry and Large Eddy Simulations, were used to document the forced cases. Because of the large number of parameters attached to partly modulated transverse jets, the use of the cross-flow Strouhal number St_∞, defined in the previous sections, was preferred over the parameter St_j, necessitating the identification of characteristic velocity scales for each forced case. The dimensionless time $t^* = t \times f_f$ was used to report instants inside a cycle. Using this parameter, the transition from low to high blowing ratio occurred at $t^* = 0$, while the transition from high to low blowing ratio occurred at $t^* = DC$.

The typical forced jet in cross-flow cycle could be composed of up to four distinct phases.

- *Generation of a starting vortex system* at the transition from low to high blowing ratio with starting vortices (figure 11*a*), due to increased shear and mass surplus in the jet pipe.
- *Quasi-unforced plateau* in the high blowing ratio part of the cycle with typical structures encountered in the unforced jet at $BR = BR_h$ (figure 11*b*),
- *Cross-flow ingestion* inside the jet pipe at the transition from high to low blowing ratio with (figure 11*c*) due to mass deficit at the jet shutdown
- *Quasi-unforced plateau* in the low part of the cycle with typical structures encountered in the unforced jet at $BR = BR_l$ (figure 11*d*).

At higher forcing frequencies, only two overlapping phases were found: a transition from low to high blowing ratio with the formation of a starting structure (figure *11e, f*) and a transition from high to low blowing ratio with cross-flow ingestion inside the jet pipe (figure 11*g, h*).

- Starting vortices - At the high blowing ratio onset, a starting vortex was formed at the edge of the jet exit due to the higher shear generated across the jet/cross-flow interface by the bulk flow rate increase. These starting structures were observed and described in many pulsed jets in cross-flow experiments and simulations for their potential in mixing and penetration improvement, though generally at higher average blowing ratios and forcing frequencies than in this work. Over the range of forcing parameters covered in this study, four regimes of starting vortices could be observed:
  - *Single starting hairpin vortex* - formed at rather low BR_h values for short injection times. They were very similar to the one observed under unforced conditions, yet

DISTRIBUTION A: Distribution approved for public release.

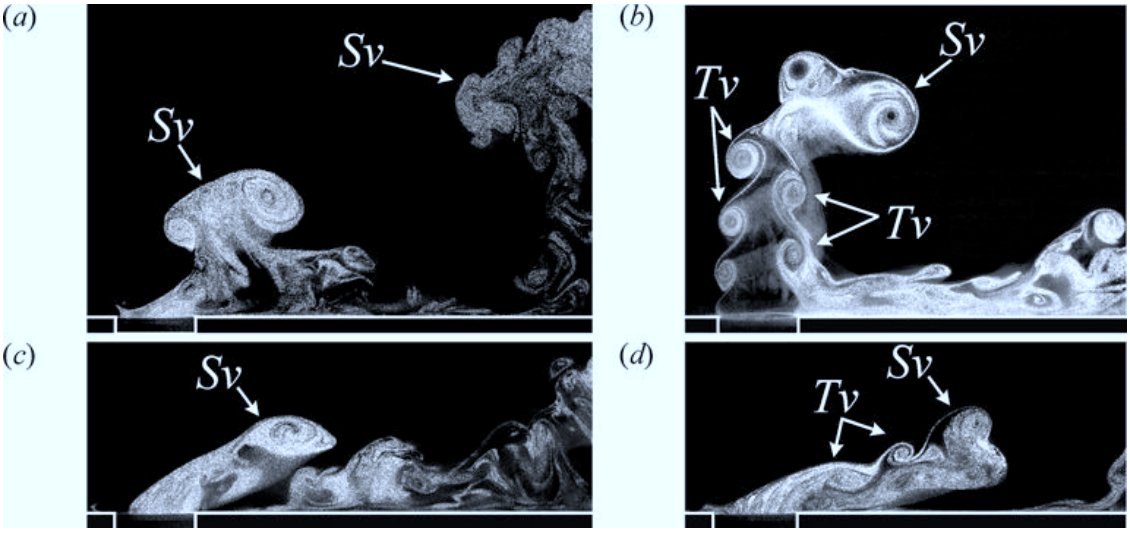

Figure 12: Mie scattering visualizations in the plane $Y_j = 0$ for (a) *Case 3* at $St_\infty = 0.159$ – Single starting vortex ring; (b) *Case 3* at $St_\infty = 0.016$ – Leading starting vortex ring and trailing vortices; (c) *Case 1* at $St_\infty = 0.159$ – Single starting hairpin vortex; (d) *Case 2* at $St_\infty = 0.079$ – Leading starting hairpin vortex and trailing hairpin vortices. (Sv) Starting vortex, (Tv) Trailing vortices.

considerably larger as shown in (figure 12c). Interestingly, these hairpin vortices were found to be formed even though the BR_h value ($BR_h = 0.438$ in *Case 1*) was significantly higher than the unforced jet transitional blowing ratio threshold ($BR_{tr} = 0.275$). This mechanism was attributed to transient dynamics of the horseshoe and inner vortices at the jet onset.

– *Starting hairpin vortex and trailing vortices* - formed at rather low BR_h values for long injection times (figure 12d). Their dynamics were found to be essentially identical to the ones in unforced conditions.

– *Single starting vortex ring* - formed at rather high values of BR_h and for short injection times (figure 12a). The starting vortex tilted towards the upstream direction as it was convected downstream and away from the wall. To observe the dynamics of single starting vortex rings, a forcing signal using an idealized square wave at $St_\infty = 0.159$ was used such that $BR_l = 0.200$, $BR_h = 2.20$, $DC = 8\%$ (identified as *Case 10* in table 2 figure 13). As the starting vortex departed from the bottom wall (figure 13b), the structure acquired an initial tilt angle toward the upstream direction which increased progressively. Under the action of the cross-flow, the vortex ring was deformed and progressively folded, the upstream and downstream parts approaching each other, while the side arms relatively dropped. The jet exit velocity profiles showed a continuous momentum and vorticity deficit at the leading edge, compared to the trailing edge, throughout the starting vortex formation process. This suggested that the circulation and initial convection velocity imbalances responsible for the tilting also originated from the characteristic skewness of the jet in cross-flow velocity profiles.

DISTRIBUTION A: Distribution approved for public release.

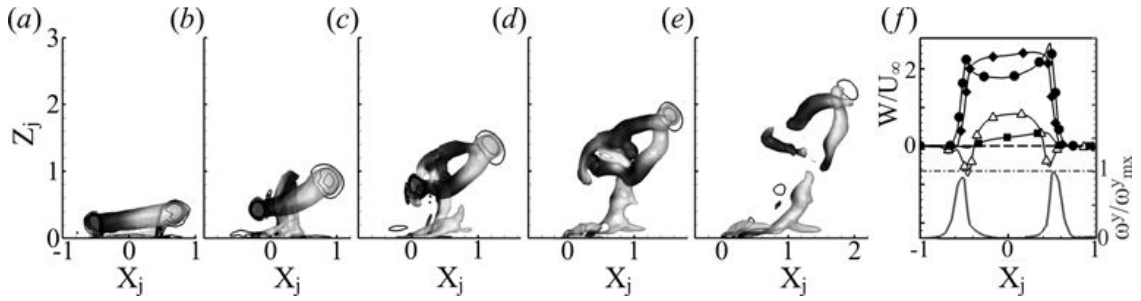

Figure 13: X-Z view of Laplacian of the pressure iso-surfaces at $\Delta P = 80kPa.m^{-2}$ for *Case 10* at $St_\infty = 0.159$ for time instants (a) $t^* = 0.085$; (b) $t^* = 0.19$; (c) $t^* = 0.29$; (d) $t^* = 0.39$; (e) $t^* = 0.49$, colored by spanwise vorticity from *black* (negative) to *white* (positive). (f) Jet exit velocity profiles at ($\blacksquare$) $t^* = 0^-$,($\diamond$) $t^* = 0.005$, ($\bullet$) $t^* = 0.075$, ($\triangle$) $t^* = DC + 0.005$ and spanwise vorticity profile (*gray*) at $t^* = 0.005$.

- *Starting vortex ring and trailing column* - formed at rather high values of BR_h and for long injection times (figure $12a$). In this configuration, the leading ring vortex was followed by a series of smaller vortex rings constituting a trailing column (figure $14a$). The leading vortex ring initially tilted in the upstream direction due to interaction with the cross-flow boundary layer and velocity distribution skewness. As it departed from the wall and the first trailing vortex ring was formed and the leading vortex ring tilting was reversed towards the downstream direction, "swallowing" the downstream part of the first trailing vortex. This "partial leapfrogging" of the first trailing vortex as well as the downstream tilting of the leading vortex ring could easily be explained by 2D inviscid considerations. The reorientation of the trailing vortices was found to be an important feature since it generated vertical vorticity from the side-arms of the trailing column ring vortices and therefore provided a source for the initialization of the CRVP. The simulated dynamics of the leading vortex ring and the trailing vortices for *Case 9* (figure 15), confirmed the partial leapfrogging of the trailing vortices as well as the tilting dynamics. Additional insight was gained on the behavior of the side arms of the trailing vortices as they were convected in the free stream and away from the wall. The first trailing vortex was distorted due to the rapid ingestion of its downstream rollup by the starting vortex ring. The trailing vortices (*Tv2*, *Tv3*, *Tv4* ...) followed similar dynamics so that the overall reorientation of the trailing vortices generated coherent vertical vorticity and resulted in the formation of a quasi-vertical vortex pair on the lee-side of the jet. This pair of vortices was consistent with the CRVP of the unforced jet observed in the experimental visualizations. Both experimental and numerical observations indicated a CRVP initiation mechanism based on trailing vortices partial leapfrogging combining tilting, stretching, and deforming in agreement with the mechanism described by (41), (20) or (52).

- Starting Vortices Classification - The different types of starting structures were sorted against two sets of parameters : (SR_h, BR_h) and (SR_{pp}, BR_{pp}) such as $SR_x = U_x\tau/D_j = BR_xU_\infty DC/(f_fD_j) = BR_xDC/St_\infty$with $x = pp$ or $x = h$. Overall, both

DISTRIBUTION A: Distribution approved for public release.

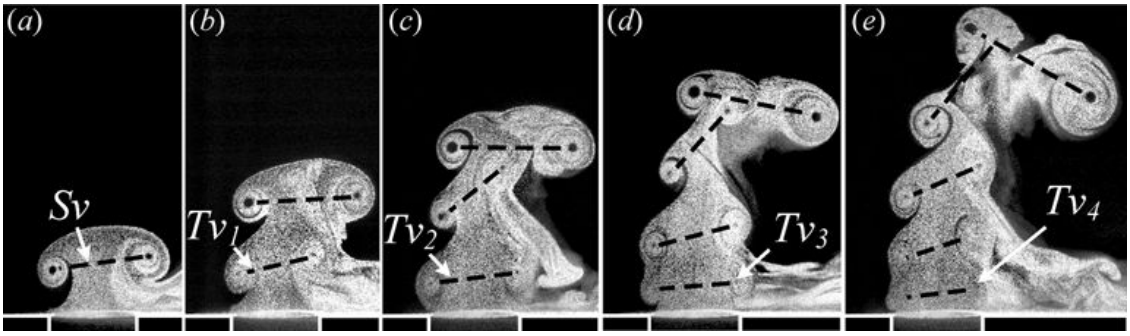

Figure 14: Mie scattering visualizations in the plane $Y_j = 0$ for *Case 8* at $St_\infty = 0.079$ showing leading vortex ring and trailing column formed at the jet transition from BR_l to BR_h. The first ring of the trailing column ($Tv1$) is ingested by the leading vortex ring (Sv).

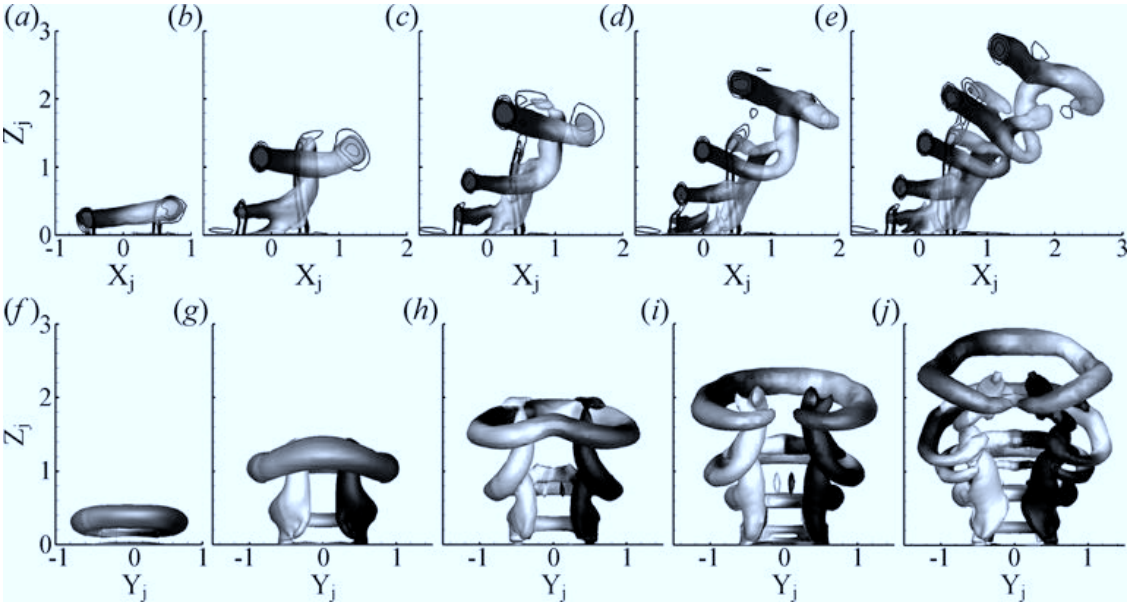

Figure 15: *Top*: *X-Z* view, *Bottom*: *Y-Z* view of Laplacian of the pressure iso-surfaces at $\Delta P = 100kPa.m^{-2}$ for *Case 9* at $St_\infty = 0.159$ for time instants (*a, f*) $t^* = 0.085$; (*b, g*) $t^* = 0.25$; (*c, h*) $t^* = 0.33$; (*d, i*) $t^* = 0.39$; (*e, j*) $t^* = 0.49$, colored by spanwise (*Top*) and vertical (*Bottom*) vorticity ranging from *black* (negative) to *white* (positive).

DISTRIBUTION A: Distribution approved for public release.

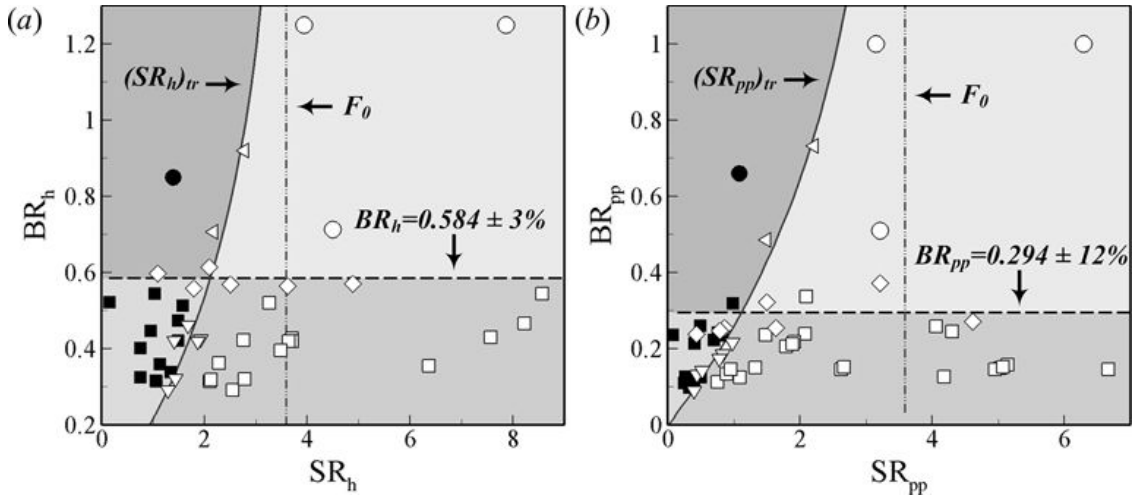

Figure 16: Classification of the starting vortices observed in forced experiments with respect to characteristic stroke ratios and blowing ratios (a) SR_h, BR_h; (b) SR_{pp}, BR_{pp}. ○ Leading vortex ring and trailing column; ● Single vortex ring; ▷ Limiting case vortex ring with/without trailing column; □ Leading hairpin vortex and trailing hairpins; ■ Single hairpin vortex; ◇ Limiting case hairpin/ring vortex; ▽ Limiting case hairpin vortex with/without trailing vortices. $F_0 = 3.6$ - Asymptotic formation number from (67). Transition stroke number fit $(SR_x)_{tr} = F_0 - A_1.exp(-A_2.BR_x)$ (a) $(SR_h)_{tr}$: $A_1 = 3.6$, $A_2 = 1.51$; (b) $(SR_{pp})_{tr}$: $A_1 = 3.6$, $A_2 = 1.26$.

sets of parameters exhibited a similar distribution to the one provided by (67), with a differentiation of the four different starting vortices. A better separation between the regimes was achieved when using the set (SR_h, BR_h) with less overlapping of the zones compared to the one obtained with (SR_{pp}, BR_{pp}). The distinction between the two principal starting structures regimes observed in figure 16(a) shows that hairpin vortices were formed in cases with $BR_h < 0.584 \pm 3\%$, while this separation occurred for cases with $BR_{pp} < 0.294 \pm 12\%$ in figure 16(b). Based on these observations, the set (SR_h, BR_h) appeared to provide a more precise classification map of the starting vortices. A better separation between the regimes is achieved when using the set (SR_h, BR_h) with less overlapping of the zones compared to the one obtained with (SR_{pp}, BR_{pp}). This was confirmed using with idealized square wave models of different amplitudes and pulse widths, simulated using LES. Based on a two dimensional assumption, the total circulation was computed at the jet exit by integrating the spanwise vorticity on the domains $\{\Omega_1 : -2 \leq X_j < 0, Y_j = 0, 0 < Z_j \leq 2.5\}$ and $\{\Omega_2 : 0 < X_j \leq 2, Y_j = 0, 0 < Z_j \leq 2.5\}$, respectively at the leading and trailing edges of the jet exit. Figure 17 shows that the high blowing ratio velocity U_h clearly provided a fixed proportional relationship between the scaled total circulation at the jet exit ($\Gamma^* = \Gamma/(U_c D_j)$ and the formation time ($t^* = tU_c/D_j$) for all forcing conditions, conversely to U_h, and was therefore the proper scaling parameter.

This study exhibited qualitatively good agreement with the observations from (67) in terms of the type of starting vortices generated and their dynamics, although a discrepancy

DISTRIBUTION A: Distribution approved for public release.

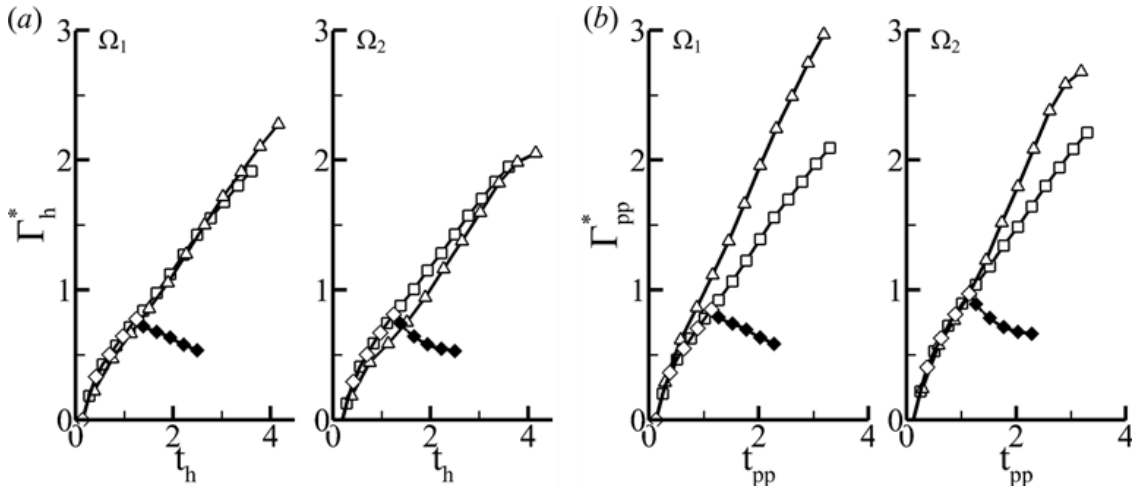

Figure 17: Total 2D circulation from LES scaled using (a) U_h and (b) U_{pp} for *Case 9* ($\square$), *Case 10* ($\diamond$ - high flow on; $\blacklozenge$ - low flow on), *Case 11* ($\triangle$) in domains Ω_1 and Ω_2.

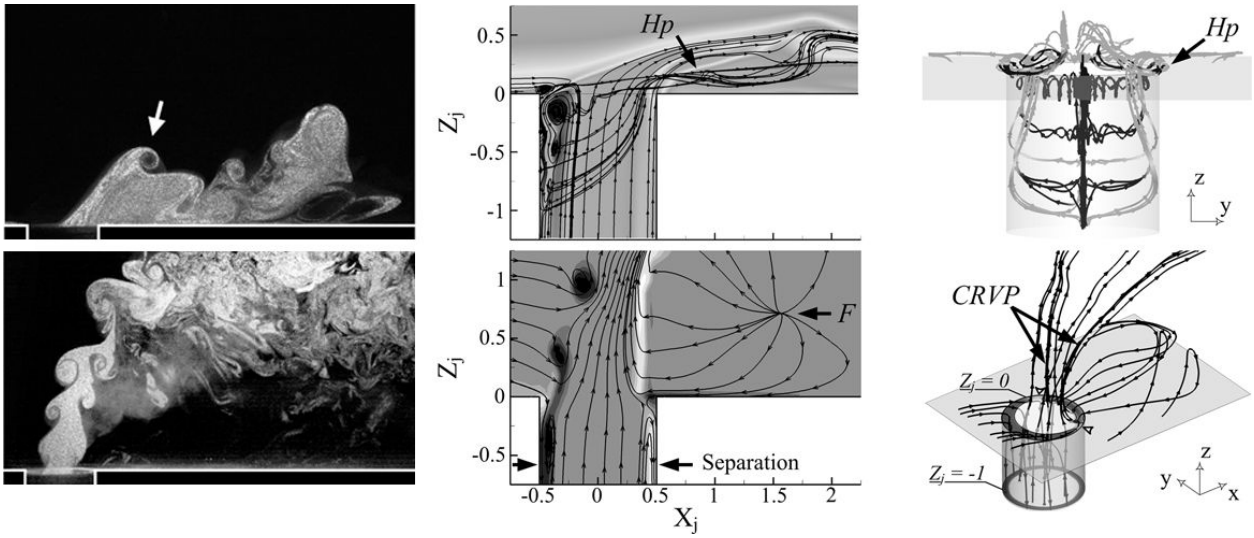

Figure 18: Top: leading edge ingestion; Bottom: Peripheral ingestion.

was found in the threshold value of BR_h between the formation of starting hairpin vortices and starting ring vortices. Indeed in (67) a threshold value of $BR_h = 2.0$ was established, whereas a value of $BR_h = 0.584$ was found in this study's experimental results.

- Cross-flow ingestion - At the jet shutdown, most of the cases with $BR_{pp} > 0.150$ exhibited clear ingestion of cross-flow fluid inside the jet feeding tube. As shown in figure 18, two types of ingestion could be observed.

  - *Leading edge ingestion* - At low BR_h values, the ingestion principally occurred at the leading edge of the jet exit and triggered the convection of the horseshoe vortex in the downstream direction. At the jet shutdown, the horseshoe vortex was

DISTRIBUTION A: Distribution approved for public release.

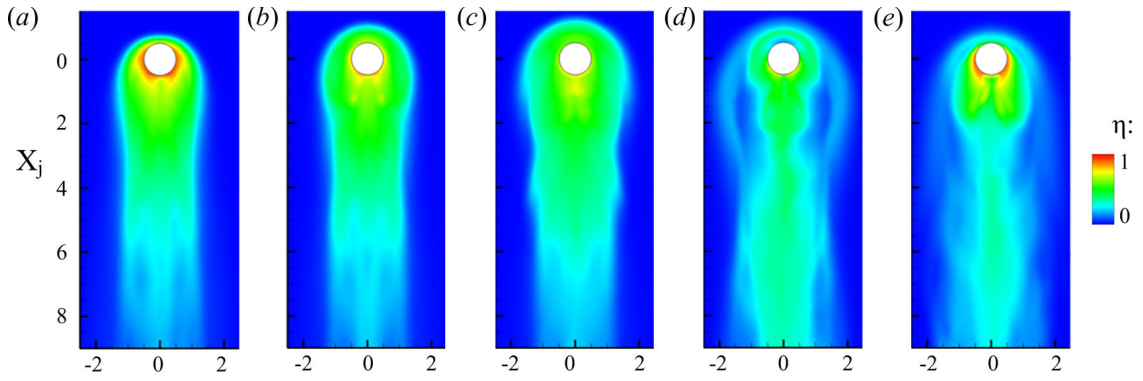

Figure 19: Instantaneous wall adiabatic effectiveness contours from LES. Top: $BR_m = 0.35$, $DC = 50\%$ (*Case 4*) at $St_\infty = 0.016$, time stamps: (a) $t^* = -0.03$; (b) $t^* = 0.08$; (c) $t^* = 0.20$; (d) $t^* = 0.43$; (e) $t^* = DC + 0.10$.

partially ingested inside the jet pipe, while the inner vortex was pulled further inside. Flow separation occurred at the jet leading and trailing edges and the higher shear introduced by the backward flow entrained the rollup of the jet shear layer, forming a complex vortical system, composed of three vortices of negative spanwise vorticity and two of opposite vorticity near the wall. Over time, the multiple inner vortices eventually paired, so that only one stable rollup persisted in the jet pipe, in the same fashion as the corresponding unforced regime. The BR_{pp} parameter, directly related to the mass deficit between high and low parts of the cycle, was found to play a significant role in the scaling of the ingestion extent. This is also supported by the experimental observations that no ingestion was observed for $BR_{pp} < 0.15$.

- *Peripheral ingestion* - For higher values of BR_h, the cross-flow ingestion occurred on the whole circumference of the jet exit. The lack of seed in the cross-flow and the absence of visibility in the jet pipe prevented a more detailed characterization of this transition using Mie scattering visualizations. Numerical simulations were then used to gain additional physical insight on these transient regimes. The flow inside the jet pipe separated over the total circumference of the jet, therefore reducing the effective flow area and increasing the effective blowing ratio. The jet shear layer was clearly disrupted with the formation of regions of vorticity opposite to the natural shear layer vorticity at the jet exit. Only two regions at the jet exit, maintained positive velocity values throughout this transient and corresponded to the location of the roots of the CRVP.

The extent of the separation regions in both cases and the evacuation of transient structures inside the feeding pipe explained the rather "chaotic" character of the flow during the early moments of the low part of the cycle.

- *Film cooling performance* - In the starting hairpin vortex regime, during the early stages of the BR_l to BR_h transient regime, jet fluid continuously flowed from the upstream

DISTRIBUTION A: Distribution approved for public release.

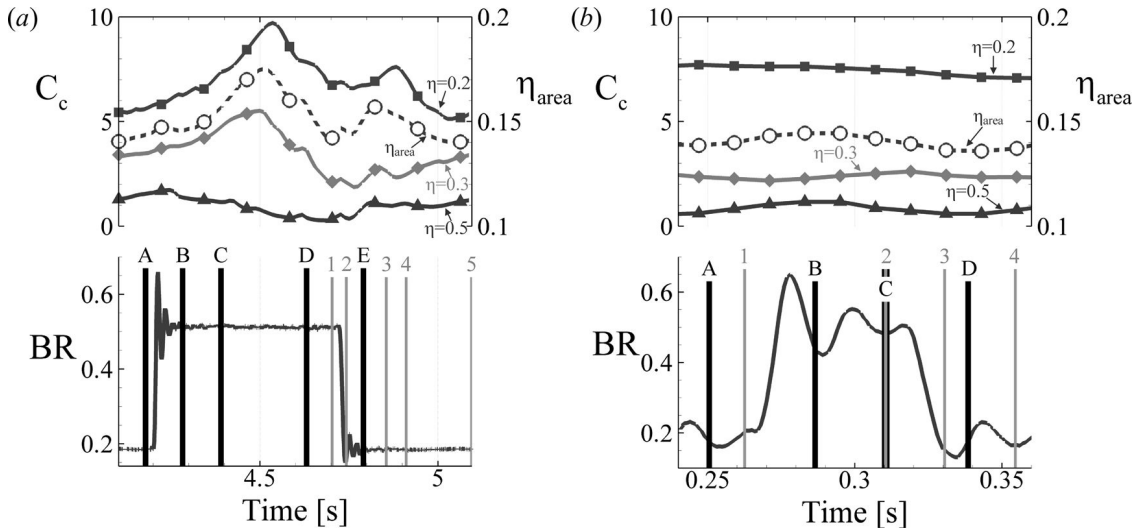

Figure 20: *Top*: Instantaneous coverage coefficient (*solid*) and area averaged adiabatic effectiveness (*dashed*); Bottom: Typical blowing ratio profile over a cycle for: (a) $BR_m = 0.35$, $DC = 50\%$ $(Case\ 4)$ at $St_\infty = 0.016$ vertical bars represent snapshot instants for figure 19; (b) $BR_m = 0.35$, $DC = 50\%$ $(Case\ 4)$ at $St_\infty = 0.0159$ vertical bars represent snapshot instants for figure 21.

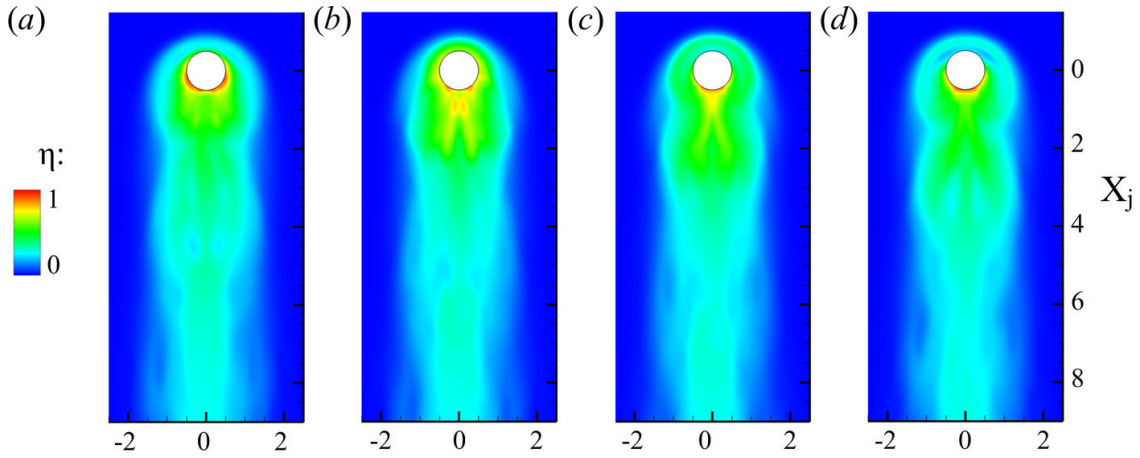

Figure 21: Instantaneous wall adiabatic effectiveness contours from LES. Top: $BR_m = 0.35$, $DC = 50\%$ $(Case\ 4)$ at $St_\infty = 0.159$, time stamps: (a) $t^* = -0.16$; (b) $t^* = 0.20$; (c) $t^* = 0.44$; (d) $t^* = DC + 0.22$.

DISTRIBUTION A: Distribution approved for public release.

edge of the jet, weakening the inner vortex while slightly elevating and enhancing the principal horseshoe vortex, therefore temporarily preventing shedding of the inner vortex. An increase of the cooled area around the jet during the low-to-high transient part of the cycle was observed (figure 21*a-c*), relative to the previous low blowing ratio part. This was confirmed by the trends of the time dependent η_{area} and C_c values over a cycle (figure 20*a*). An increase in η_{area} and $C_c(\eta < 0.5)$ was observed immediately after the transition from low to high blowing ratio over one quarter of the cycle period ($t^* < 0.25$), compared to the values during the low part of the cycle. The supply of jet fluid to the upstream region was slowly disrupted as the pressure overshoot from the low-to-high blowing ratio transition settled and the difference in pressure increased across the jet/cross-flow interface. As the inner vortex was freed, the jet behaved in a quasi-unforced manner at $BR = 0.512$ and the coverage was dramatically decreased when the jet became transitional, and the values of η_{area} and C_c decreased continuously during the remaining high part of the cycle. These trends provide some guidance towards tailoring the forcing signal in order to improve film-cooling metrics. Truncating the high part of the cycle, before the quasi-unforced high blowing ratio state settles, could prevent the performance degradation after the transient associated with the arrival of the pulse has washed out, while retaining the initial improvement associated with the arrival of the pulse. At the high-to-low blowing ratio transition, ingestion of cross-flow fluid at the jet upstream lip occurred, and hot cross-flow fluid was entrained inside the jet pipe by the inner vortex and an instantaneous decrease in film coverage around the jet exit could be observed (figure 21*e*). As the jet settled in the low blowing ratio quasi-unforced regime, this pocket of hot fluid was slowly evacuated. This explained in part the lowest performance of the pulsed jet during the BR_h to BR_l transient part of the cycle relative to the unforced jet. This indicates that a smoother transition from BR_h to BR_l, for instance via a ramp signal, could suppress part of the ingestion by decreasing the mass deficit induced by the rapid jet draw down. At higher forcing frequency, injection of jet fluid in the upstream region occurred briefly at the jet onset but was not as prominent as the one observed at lower forcing frequency and was rapidly stopped as the jet shuts down. Instantaneous estimates of η_{area} and C_c (20*b*) showed almost no fluctuations throughout the cycle. Time averaged values for η_{span}, η_{area} and C_c extracted from simulated adiabatic effectiveness and presented in figure 22 and table 3 show that forced jets at $St_\infty = 0.016$ and $St_\infty = 0.159$ had very comparable performances in terms of spanwise averaged effectiveness and coverage, despite the significant fluctuations of instantaneous values of η_{span} and C_c observed in instantaneous trends at $St_\infty = 0.016$, compared to quasi-unforced values at $St_\infty = 0.159$. Overall, these two cases had spanwise averaged adiabatic effectiveness values approximately 30% lower than the corresponding unforced jet at equivalent mean blowing ratio ($BR = BR_m$). Accordingly, the coverage coefficients were on average 50% to 70% lower than corresponding unforced jet values at constant mass flow. The area averaged adiabatic effectiveness painted a similar picture. Simulations for *Case 3* showed significantly deteriorated performance compared to equivalent unforced results with 90% and 65% decrease in C_c and η_{area} respectively, attributed to the high value of BR_{pp}, yielding strong starting vortices and carrying coolant away from the wall, while generating large mass deficit at the jet shutdown and considerable cross-flow ingestion. The last two simulations at $BR_m = 0.45$, corresponding to *Case 12*, showed some improvement over the corresponding unforced jet results directly downstream of

DISTRIBUTION A: Distribution approved for public release.

Table 3: Coverage coefficient and area averaged adiabatic effectiveness from LES under forced conditions compared to equivalent mass flow rate unforced cases.

Conditions	C_c			η_{area}
	$\eta = 0.2$	$\eta = 0.3$	$\eta = 0.5$	
$BR = BR_m = 0.350 - St_\infty = 0$	12.82	7.02	2.15	0.226
$BR = BR_h = 0.513 - St_\infty = 0$	7.05	1.47	0.21	0.123
$Case\,4 - St_\infty = 0.016$	**7.22**	**3.23**	**0.81**	**0.162**
$Case\,4 - St_\infty = 0.159$	**7.26**	**2.63**	**0.66**	**0.145**
$BR = BR_h = 0.836 - St_\infty = 0$	1.91	0.21	0.05	0.071
$Case\,3 - St_\infty = 0.159$	**1.99**	**0.75**	**0.30**	**0.079**
$BR = BR_m = 0.450 - St_\infty = 0$	7.25	1.68	0.30	0.122
$BR = BR_h = 0.720 - St_\infty = 0$	3.96	0.47	0.08	0.093
$Case\,12 - St_\infty = 0.016$	**5.62**	**1.91**	**0.20**	**0.121**
$Case\,12 - St_\infty = 0.159$	**4.29**	**1.39**	**0.34**	**0.113**
$BR = 0.415 - St_\infty = 0$	14.42	7.87	2.17	0.247

the jet exit for $X_j < 4$. The coverage coefficients of the forced cases (table 3) matched or exceed the values of the unforced jet when $St_\infty = 0.159$, while the values of η_{area} were comparable to the unforced one. Overall, the forcing frequency appeared to have only a limited influence on film cooling performance of the jet for *Case 4* and *Case 12*. However, flow visualizations clearly showed that the degradation of the film cooling performance at $St_\infty = 0.016$ could be attributed to the settling of the jet in the high part of the cycle with transitional features such as the transport of the inner vortex, while at $St_\infty = 0.159$ the high entrainment of cross-flow fluid generated by the starting vortex was responsible for such performance decrease. Effectively the same outcome in terms of thermal performance was perpetrated by different flow dynamic mechanisms. Overall, jet forcing around an average value below the unforced transitional threshold had a greater influence (yet detrimental) on the film cooling metrics, than forcing around an average value beyond the transitional threshold. This shows that the beneficial effect of decreasing the blowing ratio below the transitional value during the low part of the cycle was less significant than the detrimental action of increasing it above this threshold.

DISTRIBUTION A: Distribution approved for public release.

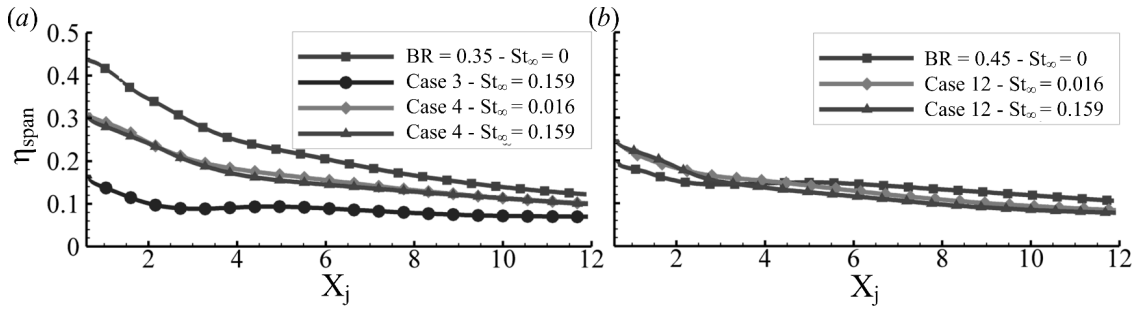

Figure 22: Spanwise averaged adiabatic effectiveness for forced jet in cross-flow and associated constant mass flow rate unforced jet results after LES.

DISTRIBUTION A: Distribution approved for public release.

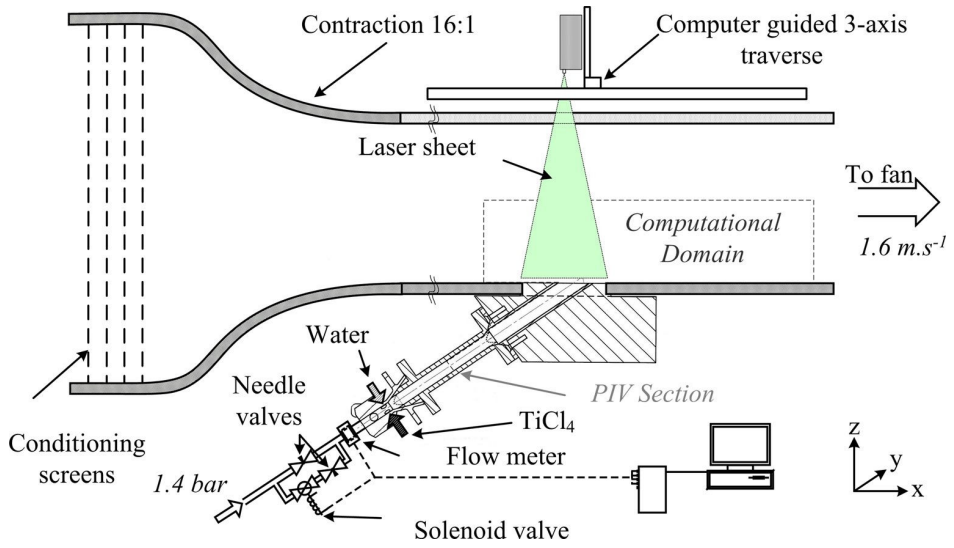

Figure 23: Inclined jet experimental apparatus.

2 Inclined Jet in Cross-flow

A more application-relevant geometry of a 35° inclined modulated jet over a flat plate is investigated using reactive Mie scattering visualizations, hot wire anemometry and PIV measurements, complemented by Large Eddy Simulations (LES) to provide details on the flow and temperature fields in the near-field of the jet exit. As for the vertical jet, the first part focuses on the characterization of the unforced jet baseline, while the second section investigates the specifics of modulated inclined jets.

2.1 Experimental and Numerical Setup

2.1.1 Wind Tunnel Experiments

The experiments for the 35° jet were carried out in the same wind tunnel as the one used in the 90° jet study. Notations and coordinate systems for the inclined jet were also identical to the previous chapter, taking the origin at the jet exit center. The only major difference between both configurations was the implementation of a PIV (Particle Image Velocimetry) section in the jet pipe consisting in a square acrylic tube of $6D_j$ long presented in figure 23. This section will be used in a close future for PIV (Particle Image Velocimetry) measurements in view of obtaining realistic inlet conditions for LES. The cross-flow conditions were identical to the 90° jet study and are provided in table 1. The jet exited from a $25.4mm$ round tube mounted flush to the bottom wall at an angle of 35° with respect to the cross-flow direction and zero compound angle. The tube length, including the PIV section was approximately $12D_j$. A seeding system injecting $TiCl_4$ and water inside the jet was also used during reactive and fully reacted Mie scattering visualizations. The jet supply system was identical to the one of the vertical jet with two branches one of which includes a computer-controlled solenoid valve used to pulse the flow (figure 23). The experiment was designed so that the jet natural frequencies would be relatively low ($< 100Hz \sim St_\infty = 1.5$) and forcing is applied at

DISTRIBUTION A: Distribution approved for public release.

Table 4: Simulation parameters for the ROM grid.

	$BR = 0.15$	$BR = 0.5$	$BR = 1.0$	*Case IV*
Fluctuation levels	30%	50%	60%	50%
Number of vortices	150	190	210	190
Time step	1×10^{-4}	5×10^{-5}	1×10^{-5}	1×10^{-5}

frequencies lower than these natural frequencies consistently with the scaled-down (relative to this work) experiments of (25) and theoretical assessments of (55).

In the forced jet experiment, an additional visualization plane (Y-Z) was acquired at four distinct streamwise locations of $X_j = 0$, 0.5, 1 and 1.5. For those visualizations, the camera was set downstream of the visualization plane at an angle of approximately 30° with the streamwise direction and the focus plane was adjusted using a Scheimpflug mount offsetting the lens axis from the camera sensor axis to satisfy the Scheimpflug condition (see (61)). The obtained images were then dewarped based on a linear transformation algorithm, using a previously acquired calibration image. These images (and the one in the $Y_j = 0$ plane for the forced jet) were obtained in a time resolved manner at 1000 frames per second (fps) using a Dantec Dynamics Nanosense MkIII camera with a 1280×1024 sensor. Finally, the forced jet was also documented using 2D-PIV measurements in the $Y_j = 0$ plane. These measurements were obtained using the same camera operated at $500fps$ with an average time delay between both laser shots of $\Delta t = 250ms$. An adaptive correlation algorithm was used with an initial interrogation window of 64 pixels, a final interrogation window of 16 pixels and a 50% overlap. At least 30 cycles were acquired for each forcing conditions to obtain accurate phase averages. Seeding for PIV measurements was achieved using $2\mu m$ porous silica particles with extremely low specific gravity and high reflectivity, following the flow very accurately.

2.1.2 Numerical Simulations

As for the previous configuration, numerical simulations were carried out in parallel to the experiments using Ansys Fluent$^{\text{TM}}$. Large Eddy Simulations (LES) with dynamic Smagorinsky sub-grid scale models were used. A set of three simulation grids was used in this part of the study. All three of them were built on the same principles as the vertical jet grid, representing a part of the jet pipe and of the wind-tunnel test section.

2.1.2.1 Mechanistic Analysis Grid The first grid corresponded to the one used in (74). This grid was primarily used for flow understanding and a preliminary statistical POD analysis. The domain consisted of a rectangular box representing a part of the wind-tunnel test section and part of the jet feeding tube. The computational domain was $18D_j$ long (x-direction), $8D_j$ wide (y-direction) and $8D_j$ tall (z-direction), respectively discretized into $160 \times 100 \times 90$ hexahedral cells, while the jet pipe feeding was $8D_j$ long, discretized by 2000 nodes in the cross-section and 120 nodes in the axial direction. The grid was structured and counted approximately 1.6 million hexahedral cells. The jet exit center was located $6D_j$ downstream from the domain inlet. The first cells in contact with the walls were approximately $0.03D_j$ tall, providing average y^+ values of the order of 1, thus reaching the

DISTRIBUTION A: Distribution approved for public release.

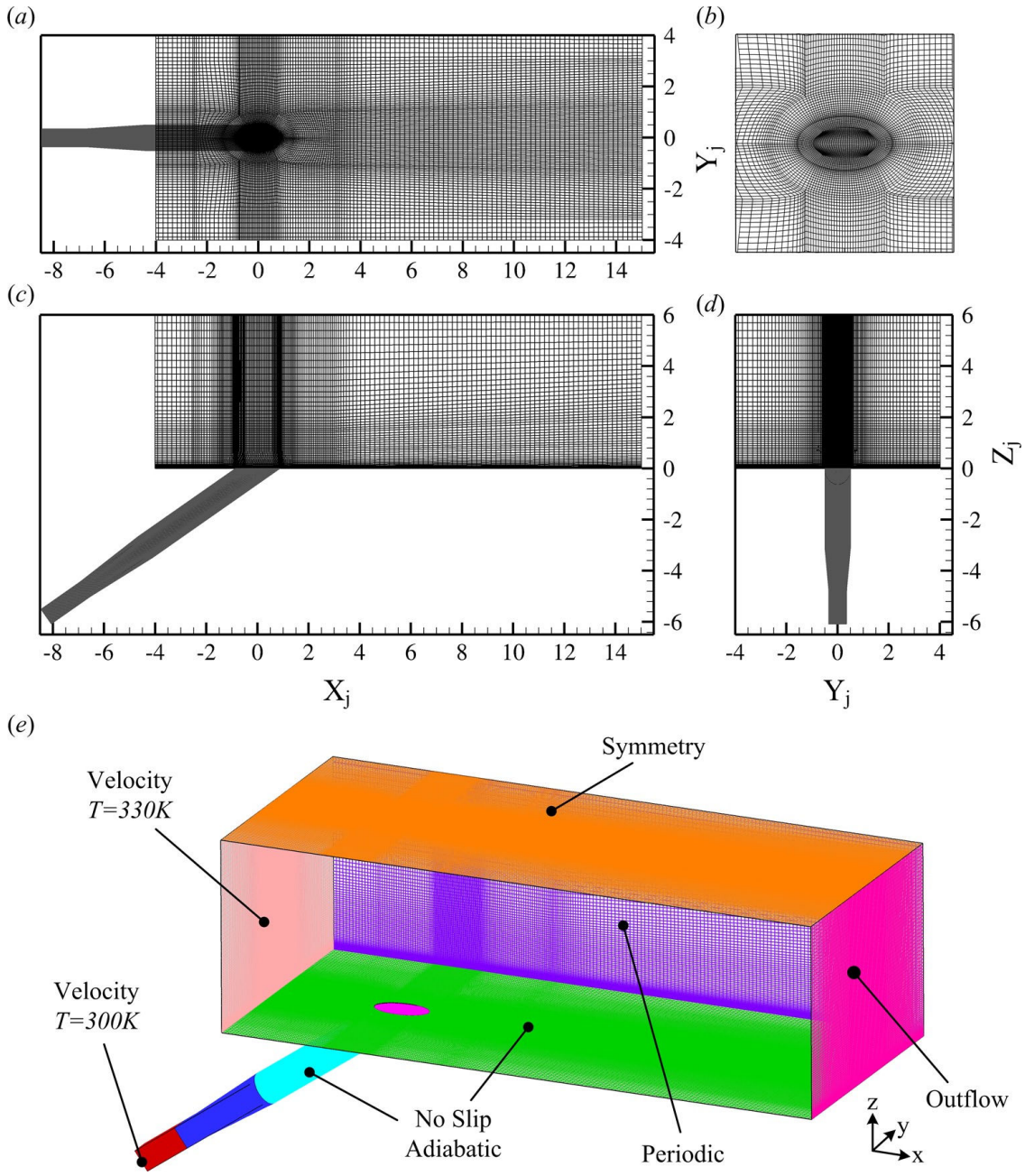

Figure 24: Inclined jet numerical grid details and boundary conditions. (a) X-Y view, (b) X-Y view detail, (c) X-Z view, (d) Y-Z view, (e) global view and boundary conditions.

DISTRIBUTION A: Distribution approved for public release.

viscous sub-layer and allowing direct solving of the wall shear stress from laminar stress-strain relationship, without using wall functions.

Velocity characteristics and boundary layer profiles for the inlet of the computational domain were obtained from hot wire measurements performed in the wind tunnel as summarized in table 1. The numerical solver used was pressure based with second order accuracy in time and space. The integration time steps used ranged from $5.10^{-5}s$ at $BR = 1.2$ to $5.10^{-4}s$ at $BR = 0.15$ so as to remain below the minimum Kolmogorov time scale in the domain. At the inlet of the jet pipe, uniform velocity profile was set so as to equal the volumetric flow rate of the experiment. The jet and cross flow fluids were maintained at constant temperature of respectively 300 and $330K$, not affecting the velocity field. A grid independence study was carried out using this particular grid and is available in (74).

2.1.2.2 Reduced Order Modeling Grid The second grid is presented in figure 24 and corresponded to a refined and extended version of the first grid. It was primarily used to obtain flow and temperature fields snapshots for reduced order modeling purposes. The domain was extended of $3D_j$ in the downstream direction and the jet exit relocated $4D_j$ downstream of the domain inlet to give a $19D_j$ long grid. The spanwise dimension was left unchanged while the height is brought down to $6D_j$. The pipe geometry was slightly modified to account for an updated, longer jet pipe PIV section. The main domain comported $240\times148\times75$ hexahedral cells in respectively the streamwise, spanwise and vertical directions. The jet pipe was meshed using an O-grid of 6500 cells in the cross-section and 175 cells in the pipe axis direction. This accounted for a total of over 4 million cells. The first cell in contact with the wall was on average $0.005D_j$ tall resulting in much less than unity y^+ values. The main domain inlet velocity profile was obtained from experimental measurements as summarized in table 1. The pipe inlet velocity profile was obtained from $k-\omega$ simulations in Fluent using the inlet condition grid described below. Perturbations to the velocity field were added at the pipe inlet using Fluent vortex method with a length scale of D_j. The perturbation levels and number of vortices were adjusted on a case-to-case basis so as to match point-wise hot wire measurements at the jet exit and are summarized in table 4. High perturbation levels had to be implemented to recreate the fluctuation levels introduced by the injection jets of the seeding system (see inlet condition grid below). The integration time step for each individual blowing ratio case was evaluated based on the Kolmogorov time-scale determined from initial $k-\epsilon$ RANS simulations. The corresponding time steps are summarized in table 4.

A series of constant temperature anemometry measurements were performed at blowing ratios of $BR = 0.15$, $BR = 0.5$ and $BR = 1.0$, at 4 different streamwise locations ($X_j = 0$, 2.5, 5, 10) and are presented in figure 25 along with extracted corresponding simulation results. Overall the LES results compared extremely well with the experimental measurements at all streamwise locations and at all three blowing ratio. Only a minor discrepancy was found directly at the jet exit at $BR = 0.15$ which could be attributed to rectification of the hot wire probe signal. Indeed, at such low blowing ratio, the seeding flow rate accounted for a large amount of the overall jet flow rate (more than 60%) and the fluctuation levels introduced by the seeding jets along the hot wire direction were likely non-negligible and could locally increase the sensed velocity magnitude. These validation measurements provided good confidence in the obtained numerical results.

DISTRIBUTION A: Distribution approved for public release.

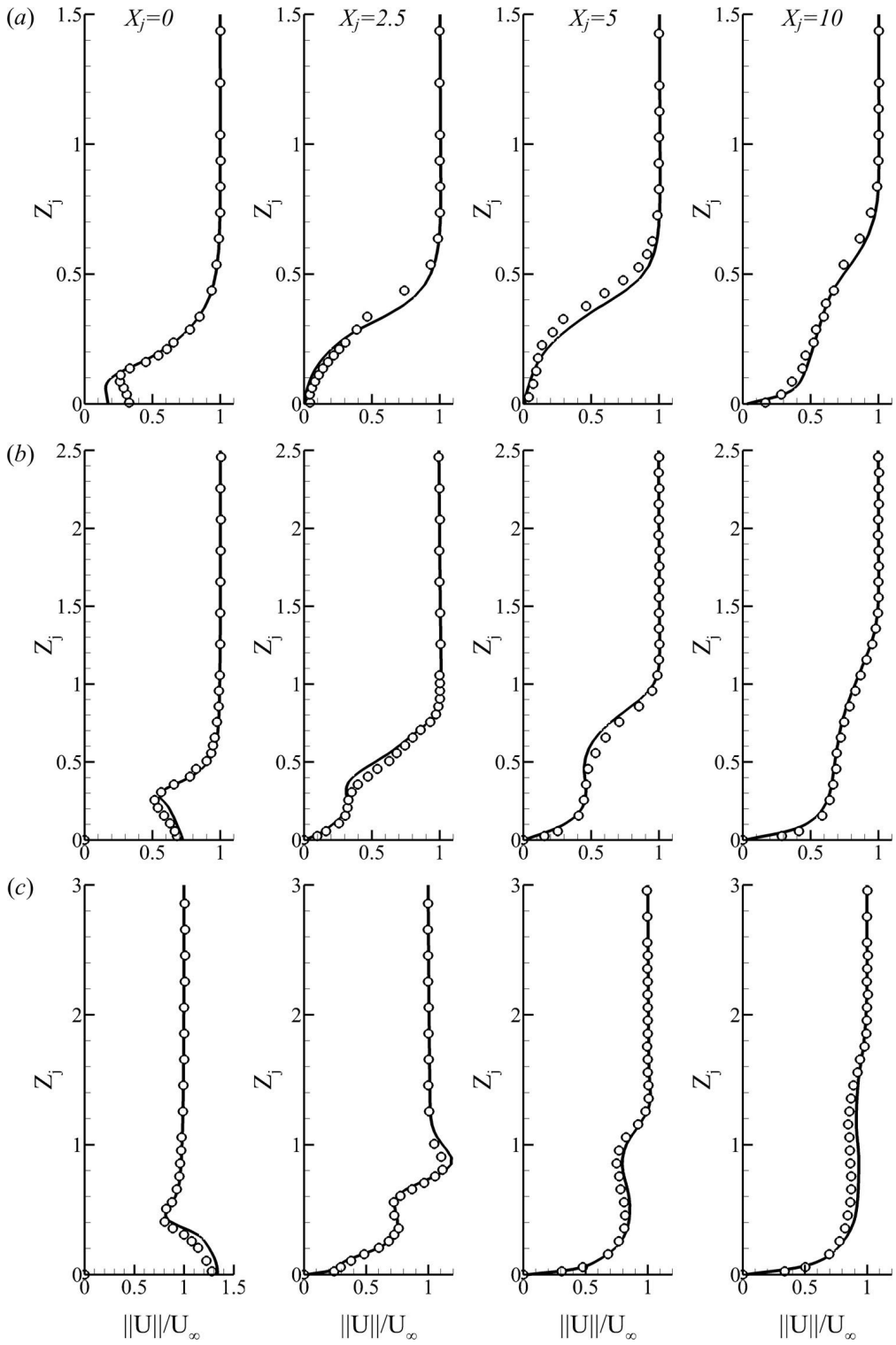

Figure 25: Experimental (*symbols*) and LES (*solid line*) time averaged velocity magnitude profiles at (*a*) $BR = 0.15$; (*b*) $BR = 0.5$; (*c*) $BR = 1.0$ at $X_j = 0$, 2.5, 5 and 10.

DISTRIBUTION A: Distribution approved for public release.

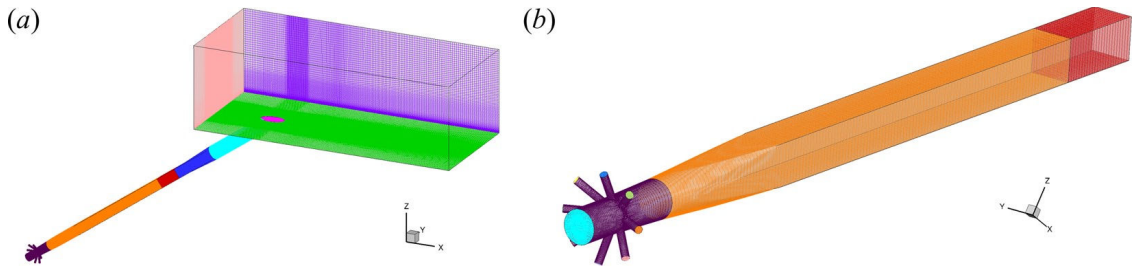

Figure 26: Extended inlet conditions grid.

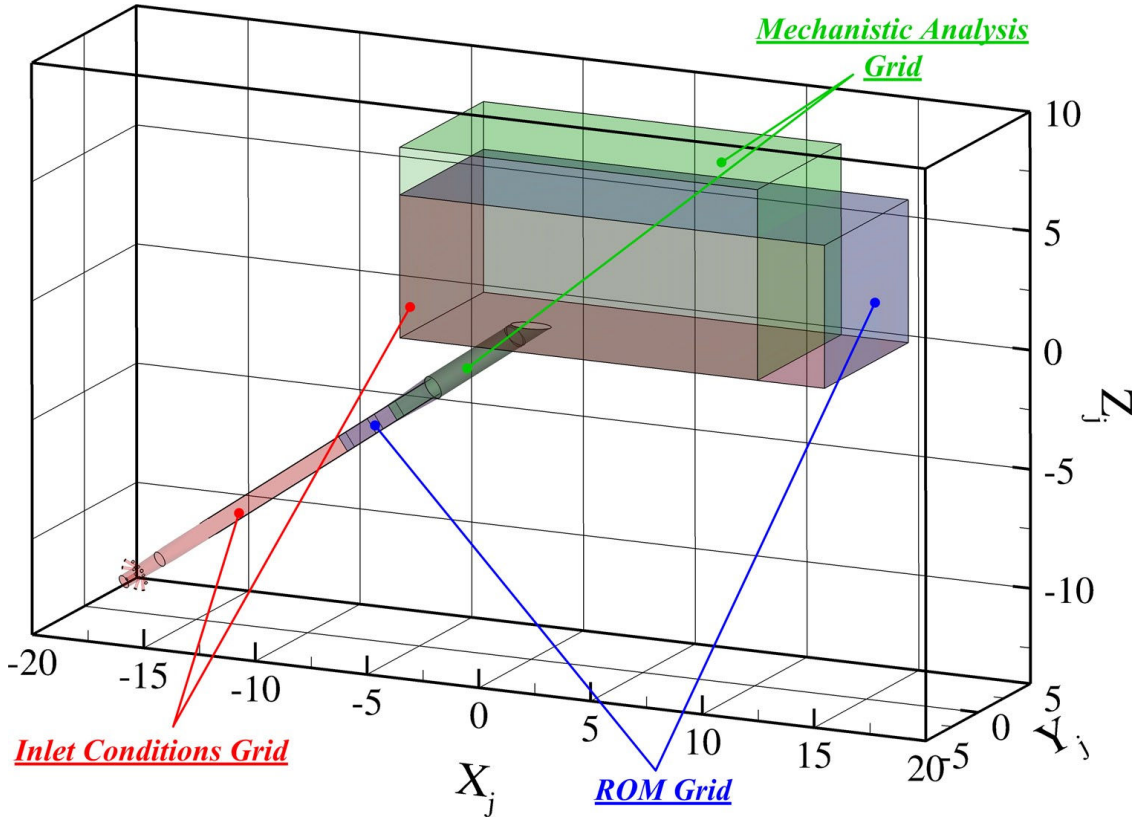

Figure 27: Geometries of the different grids.

2.1.2.3 Inlet Conditions Grid A third and last grid was used to obtain the jet inlet velocity profile. This grid was based on the previous one, with an extended pipe geometry, including the complete jet PIV section, seeding injection block and jets and an approximation of the flow-meter geometry. Figure 26 shows the extended pipe geometry. The complete mesh comported 5.7 million cells. The simulations were ran with a $k-\omega$ model with fully developed inlet velocity profiles for the main pipe inlet as well as the seed injection jets. Average velocity magnitude profiles were extracted at the location of the ROM grid inlet plane and used as inlet conditions for these simulations.

Finally, figure 27 shows the geometries of all the different grids for comparison purposes.

DISTRIBUTION A: Distribution approved for public release.

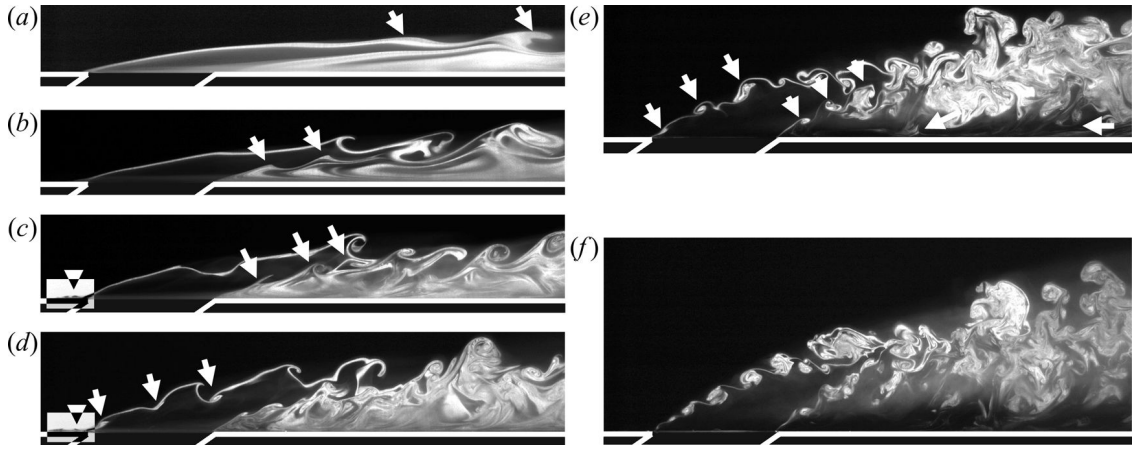

Figure 28: Experimental Mie scattering visualizations in the plane $Y_j = 0$ at (a) $BR = 0.15$; (b) $BR = 0.3$; (c) $BR = 0.4$; (d) $BR = 0.75$; (e) $BR = 1.1$; (f) $BR = 1.2$.

2.2 Unforced Jet

In unforced conditions, the jet was studied using reactive and fully reacted Mie scattering visualizations. Selected cases at $BR = 0.15$, 0.3, 0.4, 0.75, 1.0 and 1.2 were simulated with LES using the mechanistic analysis grid. Similarly to the vertical jet in cross-flow described in the previous section, several unforced jet regimes were observed. At low blowing ratios under $BR = 0.4$, the jet was fully attached to the wall while at blowing ratios above $BR = 1.0$, the jet was found to be completely detached from it. At intermediate blowing ratios, the jet exhibited vortical structures from both regimes.

The attached jet was the most relevant configuration to film cooling and shows strong similarities with the vertical jet configuration. A series of characteristic vortical structures were also identified:

- *Recirculation region* - Directly downstream of the jet exit, an area of reacted seed evidenced the characteristic recirculation region present in the attached jet configuration (figure 28a). This region, mainly supplied by jet fluid, was also observed in the LES results and corresponded to an area of lower temperatures encompassed by the hairpin vortices legs (in figure 29a, c). This region was found to be much smaller than the one found in the vertical jet configuration at comparable blowing ratio values.

- *Shear layer interlocked hairpin vortices* - The dominant shear layer vortical structures consisted in interlocked hairpin vortices observed in the experimental side-views as well as the LES renderings at $BR = 0.15$ (figures 28a 29a-b), developing as a result from Helmholtz or Landman-Saffman type of instability in the jet shear layers. At low blowing ratio ($BR = 0.15$), the instability developed sooner in the upper shear layer where the initial rollup occurred first, and eventually both upper and lower shear layers merged a few diameters downstream of the jet exit and the hairpin vortex fully formed. The dynamics of the hairpin vortices were comparable to those observed for the vertical jet and dictated by cross-flow convection as well as mutual, self, and mirrored inductions with respect to the bottom wall. At $BR = 0.3$ (figure 28b), instability in the lower shear layer started to develop and eventually at $BR = 0.4$ (figure 28c) both

DISTRIBUTION A: Distribution approved for public release.

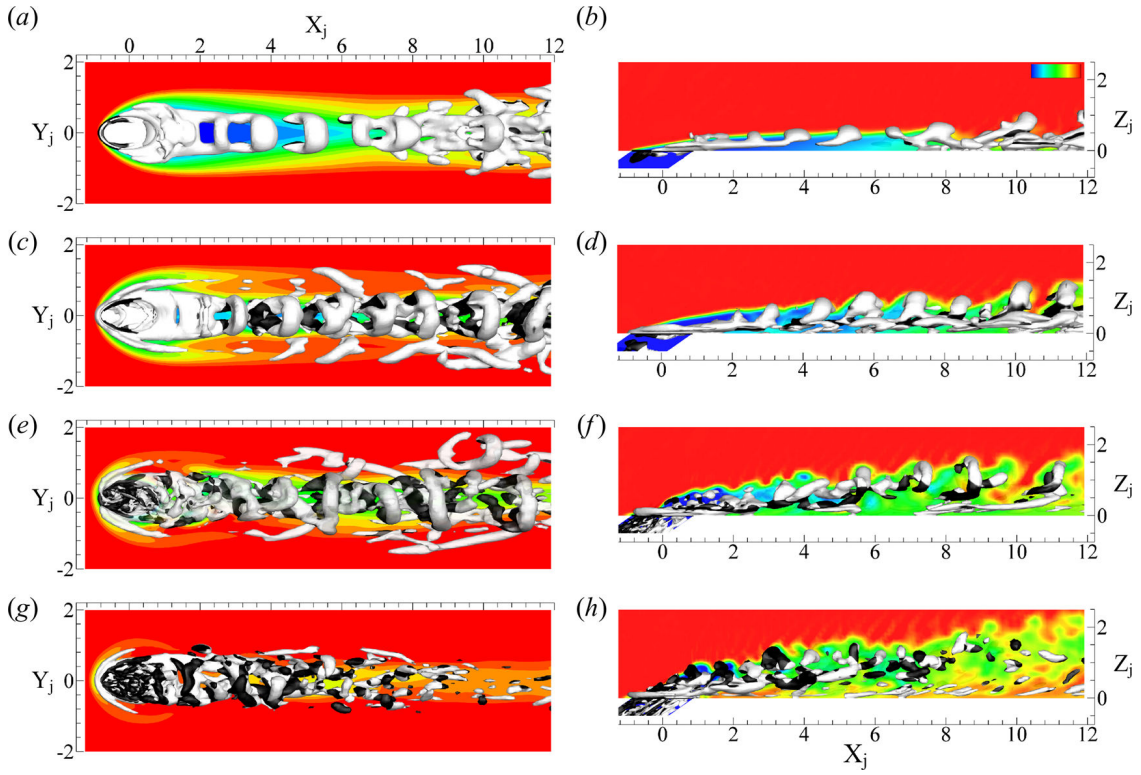

Figure 29: Laplacian of the pressure iso-surfaces from LES colored with spanwise vorticity contours from negative (*black*) to positive (*white*) at (*a*-*b*) $BR = 0.15$, $\Delta P = 0.4kPa.m^{-2}$; (*c*-*d*) $BR = 0.4$, $\Delta P = 0.7kPa.m^{-2}$; (*e*-*f*) $BR = 0.75$,$\Delta P = 2.5kPa.m^{-2}$; (*g*-*h*) $BR = 1.2$, $\Delta P = 5kPa.m^{-2}$ and instantaneous temperature contours in the planes $Z_j = 0$ (*left*) and $Y_j = 0$ (*right*).

DISTRIBUTION A: Distribution approved for public release.

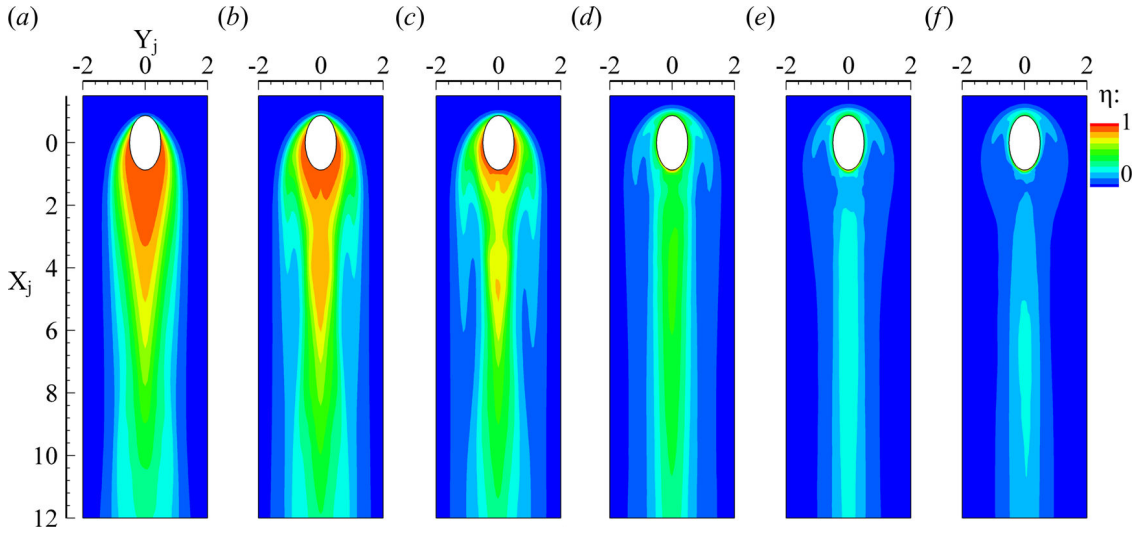

Figure 30: Wall adiabatic effectiveness contours from LES at (a) $BR = 0.15$; (b) $BR = 0.3$; (c) $BR = 0.4$; (d) $BR = 0.75$; (e) $BR = 1.0$; (f) $BR = 1.2$.

shear layers exhibited distinct rollups, each corresponding to a hairpin vortex, merging as they were convected downstream.

- *Horseshoe vortex* - Upstream of the jet exit, the horseshoe vortex system was absent from the experimental side visualizations at the lowest blowing ratios of $BR = 0.15$ and $BR = 0.3$, as well as from the LES results (figure $29a$). However, a pair of streamwise vortices containing vorticity coherent with the horseshoe vortex developed on the sides of the jet without connecting upstream in the usual U-shape as evidenced. This is identical to the mechanism responsible for the formation of the counter-horseshoe vortex and the side vortices in the 90° jet configuration. The absence of a full horseshoe vortex has been documented in previous studies such as (72) or (31) in cases where the cross-flow blockage due to the presence of the jet was weak. At $BR = 0.4$, the jet blockage was important enough to cause the cross-flow boundary layer to fully separate upstream of the jet exit and form a complete horseshoe vortex (figure $28c$ and $29c$). Conversely to the vertical jet, the horseshoe vortex was never found to be transported over the jet due to the absence of destabilizing interaction with the inner vortex in this setup.

- *Wall side vortices* - At $BR = 0.15$, in the far-field of figure $29(a)$ X-patterned structures were formed around $X_j = 10$, identical to the ones observed in the attached vertical jet setup. These became stronger and started forming earlier as the jet blowing ratio and the associated cross-flow deflection increased.

The inner vortex was found to be absent to the inclined jet configuration due to lower adverse pressure gradient for the flow exiting the jet pipe. It should be noted that conversely to the vertical jet, the horseshoe vortex was never found to be transported over the jet. This is also explained by the absence of destabilizing interaction with the inner vortex in this setup.

DISTRIBUTION A: Distribution approved for public release.

- *Film cooling performance* - The impact of the different vortical structures on the wall temperature and the film cooling performance were investigated using the results from the simulations. In the attached jet configuration, the shear layer vortical structures had a strong influence on the wall temperature field since they carried most of the coolant fluid from the jet while generating a velocity field responsible for entraining cross-flow fluid into the wall region (figure 29*c*-*d*). Jet fluid exited from the sides of the jet exit, very close to the wall to provide significant wall coverage as evidenced by the temperature contours of figure 29(*a*) and 29(*c*). Quantitative information was extracted from the numerical simulations to provide a performance benchmark to the forced results and was also compared to the vertical jet results. At $BR = 0.15$, (figure 30*a*), the area of high adiabatic effectiveness directly downstream of the jet exit corresponded to the recirculation region enclosed by the legs of the successive hairpin vortices. As the blowing ratio was increased up to $BR = 0.4$, the hairpin vortices legs with higher circulation lifted off the wall sooner due to self induction and therefore carried coolant away from the wall, resulting in film coverage breakup and entrainment of hot cross-flow fluid near the wall (figure 29*a*-*d*). On the other hand, from $BR = 0.15$ to $BR = 0.4$, a relative increase in spread was observed further away from the jet exit ($X_j \geq 7$) due to the beneficial effect of the side vortices and their favorable velocity field, as well as near the jet exit due to the strengthening and formation of the horseshoe vortex. However, due to the absence of inner vortex in the inclined jet configuration, the upstream region was almost not cooled at all. As the jet entered the transitional regime ($0.4 < BR \leq 0.9$), the wall coverage downstream of the hole was degraded due to lift off of the shear layer structures. The coverage finally became marginal in the detached configurations where the jet wake was the only region showing some form of cooling effect. Spanwise averaged adiabatic effectiveness η_{span} as well as center-line adiabatic effectiveness $\eta_{centerline}$ and comparable results from the vertical jet (figure 31*a*), showed that directly downstream of the jet exit ($X_j < 6$), the case at $BR = 0.15$ demonstrated best performance due to the presence of the steady recirculation region fed by jet fluid. However further downstream ($X_j > 6$) the case at $BR = 0.3$ provided best adiabatic effectiveness due to the increased coolant flow rate and spread over the case at $BR = 0.15$. As the blowing ratio was increased beyond 0.3, the spanwise averaged performance of the inclined jet decreased consistently. The center-line results for the inclined jet (figure 31*b*) showed similar trends. The local decrease in $\eta_{centerline}$ observed for $BR \geq 0.3$ directly downstream of the jet exit was attributed to early lift-off of the shear layer vortices. For $BR \leq 0.3$, the inclined jet showed greater spanwise averaged and center line adiabatic effectiveness, compared to the vertical jet. However, the inclined jet performance was degraded beyond $BR = 0.3$, which was not the case for the vertical jet where performance continued to increase up to $BR = 0.415$. Consequently, at $BR = 0.4$, the vertical jet exhibited greater η_{span} values than those of the inclined configuration. At higher blowing ratios ($BR \geq 0.75$), the inclined jet performed better than the vertical jet. The $\eta_{centerline}$ trends showed that the inclined jet always provided greater center-line effectiveness over the vertical jet. This confirmed that the overall better performance of the vertical jet at $BR = 0.4$ was essentially provided by a greater spanwise spread of the film. Area-averaged adiabatic effectiveness and coverage coefficient estimates for both inclined and vertical jets (figure 32), provided a global performance index at every blowing ratio. The η_{area} trends for the inclined jet exhibited a constant decrease in performance past

DISTRIBUTION A: Distribution approved for public release.

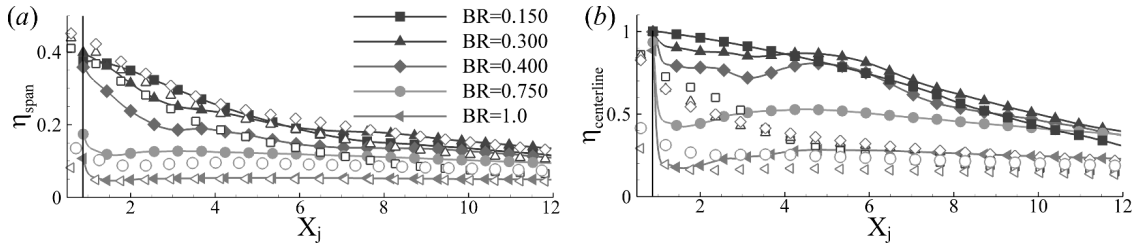

Figure 31: Film cooling performance: (a) Spanwise averaged adiabatic effectiveness η_{span}; (b) center-line adiabatic effectiveness $\eta_{centerline}$ after LES for the inclined jet (*solid line*, *filled symbols*) and the vertical jet (*open symbols*).

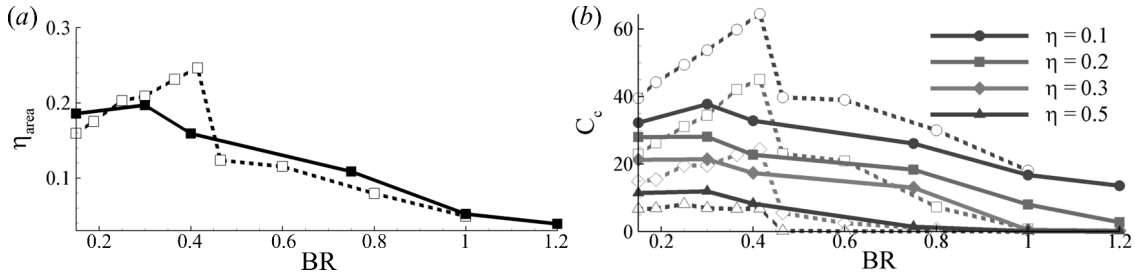

Figure 32: Unforced film cooling performance (a) Area averaged adiabatic effectiveness η_{area} for the inclined jet (*solid line*) and the vertical jet (*dashed line*); (b) coverage coefficient C_c for thresholds $\eta = 0.1, 0.2, 0.3, 0.5$.

$BR = 0.3$ with a slight improvement from $BR = 0.15$ to $BR = 0.3$. This result was consistent with observations based on η_{span} values. The improvement from $BR = 0.15$ to $BR = 0.3$ was attributed to an increase in η values beyond $X_j = 5$. A local maximum was found between $BR = 0.15$ and $BR = 0.3$ which was rather low for an inclined jet configuration and could be justified by the use of single jet in laminar cross-flow conditions. The comparisons with the vertical jet results showed that the expected performance degradation as the blowing ratio increased was less abrupt in the inclined configuration than in the vertical setup. Interestingly, the vertical jet performed better at $BR = 0.415$ with an area averaged adiabatic effectiveness of 0.225 within the considered field of view ($-1.2 < X_j < 12$). The coverage coefficient trends confirmed the above mentioned results with a consistent decrease in performance beyond $BR = 0.3$ for the inclined jet. Once again when compared to the vertical jet, the inclined jet provided more coverage at high effectiveness ($\eta \geq 0.5$) values. The vertical jet though provided significantly greater coverage at lower effectiveness levels (almost double in some cases), sign of increased spread at higher injection angles. Higher spread and performance in the neighborhood of the jet exit ($X_j < 12$) for high injection angles were previously reported in studies such as (79).

The overall greater performance of the vertical jet in this study should be put in perspective with respect of two considerations. First, the domain of the current study was limited to the near field ($X_j < 12$), which in (79) was the approximate streamwise location beyond which the inclined jet started to evidence better performance than the vertical one.

DISTRIBUTION A: Distribution approved for public release.

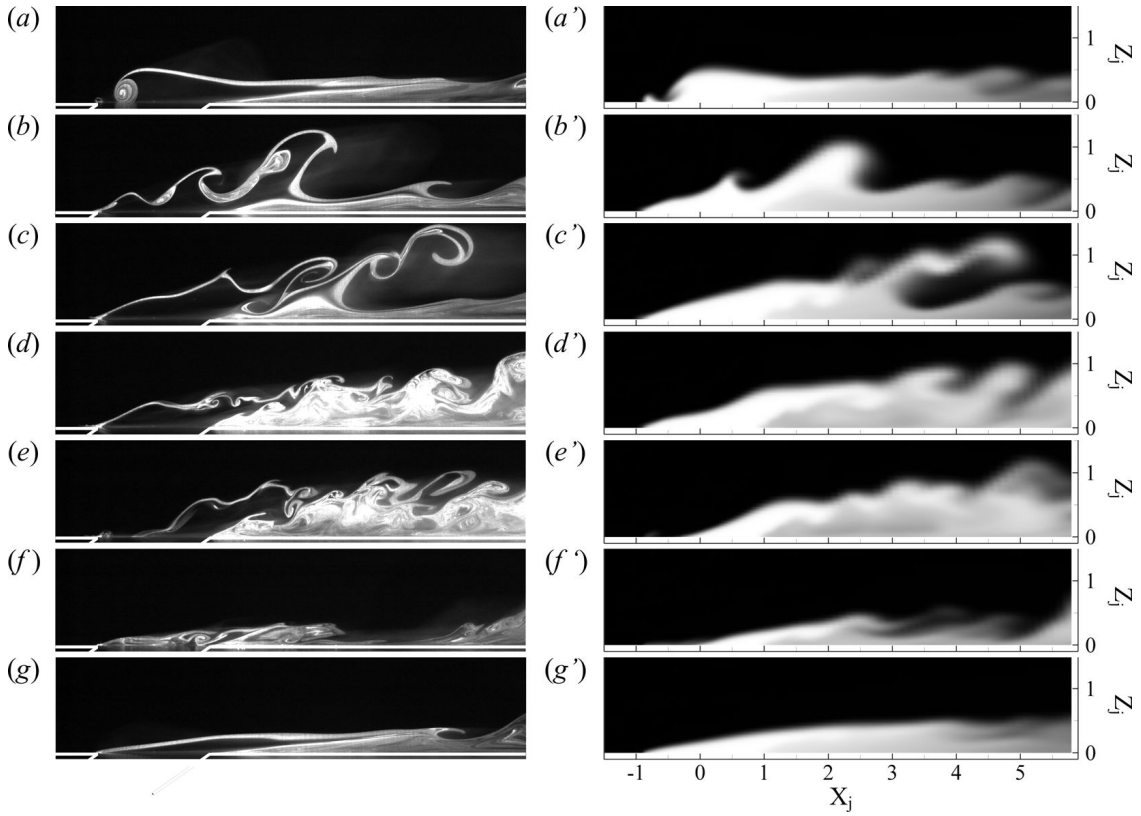

Figure 33: Instantaneous reactive Mie scattering visualizations in the plane $Y_j = 0$ (*left*) and temperature field from LES (*right*) at: (a) $t^* = 0.04$; (b) $t^* = 0.09$; (c) $t^* = 0.13$; (d) $t^* = 0.49$; (e) $t^* = DC + 0.07$; (f) $t^* = DC + 0.19$; (g) $t^* = DC + 0.47$ for *Case X* at $St_\infty = 0.016$.

Also, it was demonstrated in the vertical jet study that the sudden decrease in performance in the 90° injection configuration was due to a destabilization of the inner vortex formed inside the jet tube, extremely sensitive to both cross-flow and jet inlet conditions. Hence, it is expected that outside the laminar cross-flow boundary layer conditions used in this study, the transition for the vertical jet could happen significantly sooner, therefore leading to better performance for the inclined configuration.

2.3 Forced Jet

Forced jet experiments were carried out using a nominal square wave excitation according to the forcing parameters summarized in Table 5. Most of those cases were observed at 4 forcing frequencies of 0.5, 1.0, 5.0 and $10.0Hz$, respectively corresponding to Strouhal numbers of $St_\infty = 0.008$, 0.016, 0.079 and 0.159.

As for the the forced vertical jet configuration, a total of four phases can be identified during forced cycles.

DISTRIBUTION A: Distribution approved for public release.

Table 5: Forced inclined jet cases. *: Simulations carried at these conditions using mechanistic analysis grid, †: Simulations carried out at these conditions using ROM grid.

Case#	BR_m	BR_l	BR_h	BR_{pp}	$DC(\%)$
I	0.151	0.150	0.250	0.100	0.7
II	0.200	0.150	0.250	0.100	50
III	0.153	0.150	0.500	0.350	0.7
IV†	0.325	0.150	0.500	0.350	50
V	0.156	0.150	1.00	0.850	0.7
VI	0.575	0.150	1.00	0.850	50
VII	0.164	0.150	2.00	1.85	0.7
VIII	1.08	0.150	2.00	1.85	50
IX	0.171	0.150	3.00	1.85	0.6
X*	0.300	0.150	0.450	0.300	50
XI*	0.450	0.150	0.750	0.600	50
XII	0.875	0.750	1.00	0.250	50
XIII	1.08	0.650	1.50	0.850	50
XIV	1.58	1.15	2.00	0.850	50
XV	1.88	1.75	2.00	0.250	50

- *Starting vortices* - transient introduced at the transition from BR_l to BR_h consisting in the formation of a single or series of vortical structures (figure 33*a-c*).
- *Quasi-unforced regime established at high blowing ratio* - settled as the transient associated with the starting vortices was washed away and while the jet remained at high flow rate. In this phase, the jet behaves identically to an unforced jet at equivalent blowing ratio of BR_h (figure 33*d*).
- *Cross-flow ingestion* - transient triggered by the sudden decrease in mass-flow at the moment the solenoid valve is closed and the blowing ratio transitions from BR_h to BR_l. During this phase (figure 33*e*, *f*), cross-flow fluid is ingested inside the jet pipe and the jet flow is disrupted.
- *Quasi-unforced regime at low blowing ratio* - established as the transient dynamics from the ingestion are washed away while the jet remains in low flow rate. In this part of the cycle, the jet behaves similarly to an unforced jet at equivalent blowing ratio of BR_l (figure 33*g*).

As for the vertical jet, the two quasi-unforced regimes were not always observed depending on the duty cycle and forcing frequency which determine the duration of the low and high parts of the cycle and therefore the available time for the transients to be evacuated before the next transient is introduced. In the current study, a majority of the cases at $St_\infty = 0.008$ and $St_\infty = 0.016$ (respectively corresponding to 0.5 and $1Hz$) exhibits all four regimes while cases at $St_\infty = 0.08$ and $St_\infty = 0.159$ (respectively 5 and $10Hz$) only exhibits the transients.

DISTRIBUTION A: Distribution approved for public release.

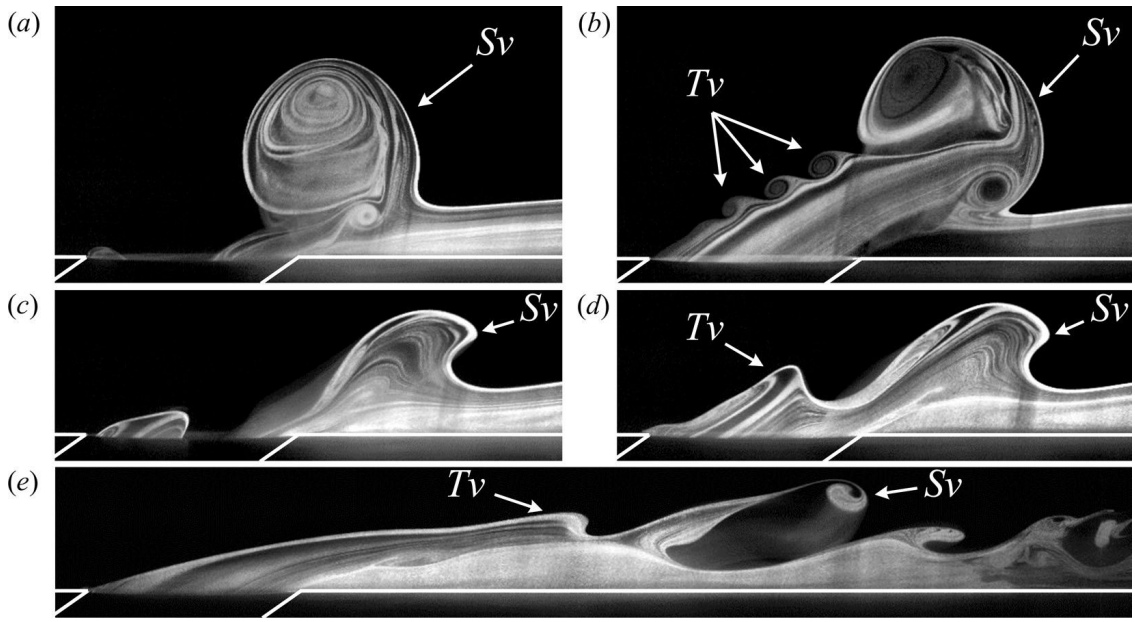

Figure 34: Mie scattering visualizations in the plane $Y_j = 0$ for (a) *Case V* at $St_\infty = 0.008$ – Single starting vortex ring; (b) *Case VIII* at $St_\infty = 0.008$ – Leading starting vortex ring and trailing vortices; (c) *Case III* at $St_\infty = 0.008$ – Single compound starting vortex; (d) *Case IV* at $St_\infty = 0.008$ – Compound starting vortex and trailing vortices; (e) *Case II* at $St_\infty = 0.008$ - Starting hairpin vortex and trailing vortex. (Sv) Starting vortex, (Tv) Trailing vortices.

2.3.1 Low-to-High Blowing Ratio Transition: Starting Vortices

- Starting vortices - In the forced inclined jet configuration, starting vortices were also observed as the blowing ratio transitioned from BR_l to BR_h due to the associated sudden increase in shear at the jet/cross-flow. While for the vertical jet only two principal regimes of starting structures/systems were identified, the inclined jet exhibited six dominant types of starting vortices presented in figure 34.

  - *Single starting hairpin vortex* - At the lower end of the investigated BR_h range, and for short injection times, the starting vortices consisted of a rather large hairpin vortex with dynamics were overall identical to the ones of the unforced jet. Because of the inclined geometry of the jet, the expansion wave generated at the valve opening reached the leading edge of the jet exit first and triggered the formation of a shear layer rollup with negative vorticity at the leading edge. However, due to the relatively low magnitude of the pulse, the vorticity generated at the leading edge remained low and the rollup was rapidly dissipated by the incoming boundary layer with opposite vorticity before it could accumulate enough circulation to be transported. The transition from low to high blowing ratio in those cases did not carry enough energy to force the jet shear layer to roll into a coherent starting vortex. However, the propagation of the expansion wave into the free stream acted as a perturbation for the natural jet shear layer

DISTRIBUTION A: Distribution approved for public release.

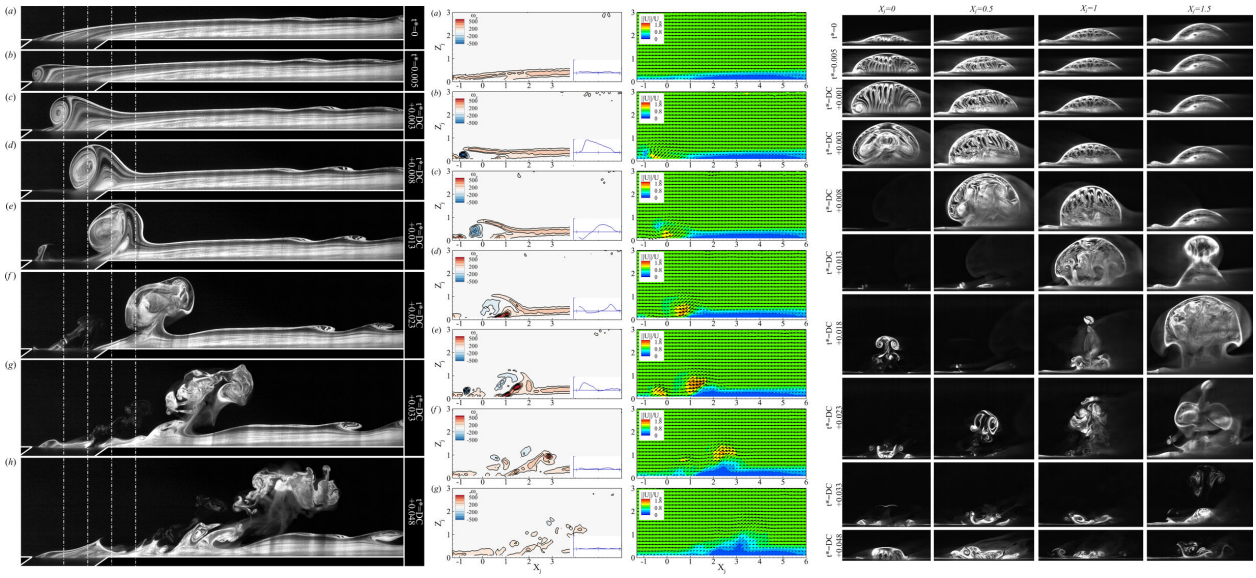

Figure 35: Single starting vortex ring (a) X-Z Mie scattering visualizations; (b) X-Z PIV; (c) Y-Z Mie scattering visualizations.

instability and triggered the formation of a large hairpin vortex. A similar regime was observed in the vertical jet study.

– *Starting hairpin vortex and trailing vortices* - For low BR_h values but with longer injection times, the leading starting hairpin vortex was followed by series of smaller hairpin vortices (figure 34*e*). A similar regime was observed in the vertical jet study.

– *Single starting vortex ring* - At high values of BR_h but for short injection times, only a single starting ring vortex was generated (figure 35). The upper shear layer started rolling up first due to the slanted nature of the jet geometry and the way the pressure wave traveled down the jet pipe, therefore creating a local increase in velocity at the jet leading edge. The upper rollup of the starting vortex departed the wall first while the lower shear layer rollup was just starting to form. However, as the upstream part of the starting vortex was convected above the jet exit, the pulse was interrupted and the actuation valve is closed leading to cross-flow ingestion and affecting the upstream part of the starting vortex ring, still located above the jet exit. The backward flow had strong impact on the starting vortex, interrupting its initial positive rotation and even reverting it. While convected, the weakened starting vortex started to dissipate and lose its coherence rapidly. A similar regime was observed in the vertical jet study, with yet different vortex dynamics.

– *Starting vortex ring and trailing column* - At high values of BR_h, for long injection times, the starting vortices were of the ring kind, followed by a series of smaller trailing ring vortices (figure 36). The leading starting vortex started to roll at

DISTRIBUTION A: Distribution approved for public release.

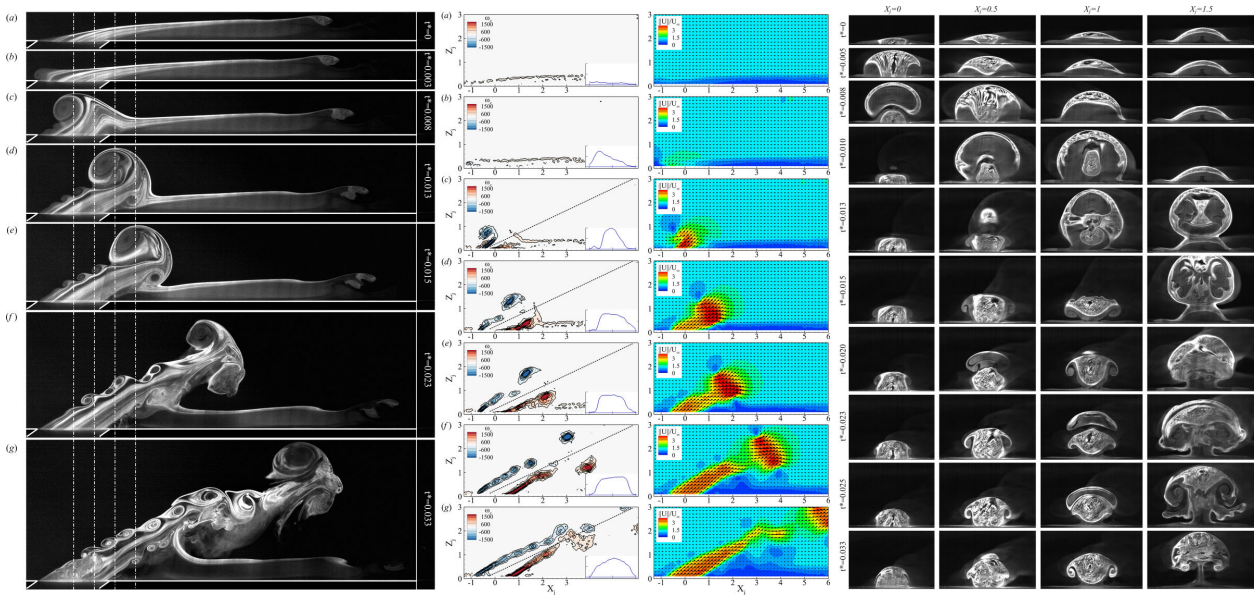

Figure 36: Leading vortex ring and trailing vortices (a) X-Z Mie scattering visualizations; (b) X-Z PIV; (c) Y-Z Mie scattering visualizations.

the leading edge due to the slanted geometry of the jet, and the shear layer progressively rolled up towards the downstream edge. Because of this delay, the formation process time-lines for the upstream and downstream part of the starting vortex ring were offset in time and the upstream part of the starting vortex departed the leading edge first after having accumulated sufficient amount of circulation, while the downstream part departed the wall later. Consequently, the starting vortex axis rotated continuously in the positive direction from 0° to approximately 50° at the moment of the departure of the downstream rollup and reached an equilibrium at approximately 60° while convected in the free stream. After the departure of the leading vortex ring, the jet shear layer rolled up into additional trailing vortices, smaller in size, yet in nature very similar to the starting vortex ring and following comparable trajectories. Conversely to the vertical jet, pairing of consecutive trailing vortices was clearly observed on both the upper and lower shear layers. The vortical system developing in the wake of the starting vortex took the form of a mushroom-like shape and a pair of strong counter-rotating vortices developed on the lower part of the jet body, coherent with the CRVP structure of high blowing ratio unforced detached jets. A similar regime was observed in the vertical jet study, with yet different vortex dynamics.

– *Compound starting vortex system and trailing vortices* - At intermediate values of BR_h, for long injection times the forced inclined jet could generate starting structures of a third, hybrid type. At the transition from BR_l to BR_h, the increased shear at the jet/cross-flow upstream interface triggered the rolling of the upper shear layer to form a starting vortex ring with relatively low vertical momentum. After shedding of the leading vortex, a region of positive velocity redeveloped

DISTRIBUTION A: Distribution approved for public release.

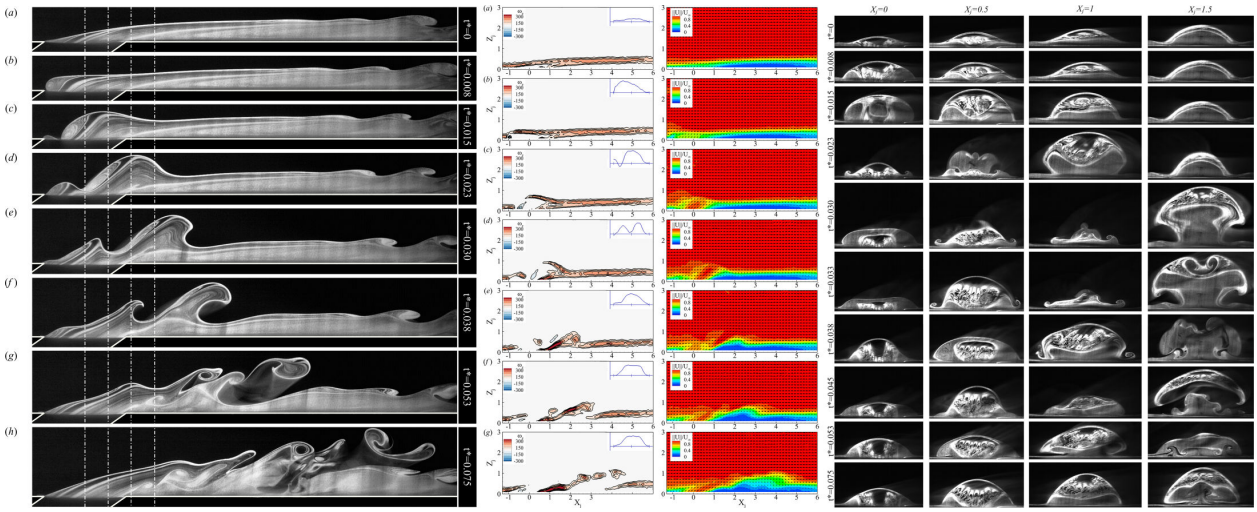

Figure 37: Compound starting vortex system and trailing vortices (a) X-Z Mie scattering visualizations; (b) X-Z PIV; (c) Y-Z Mie scattering visualizations.

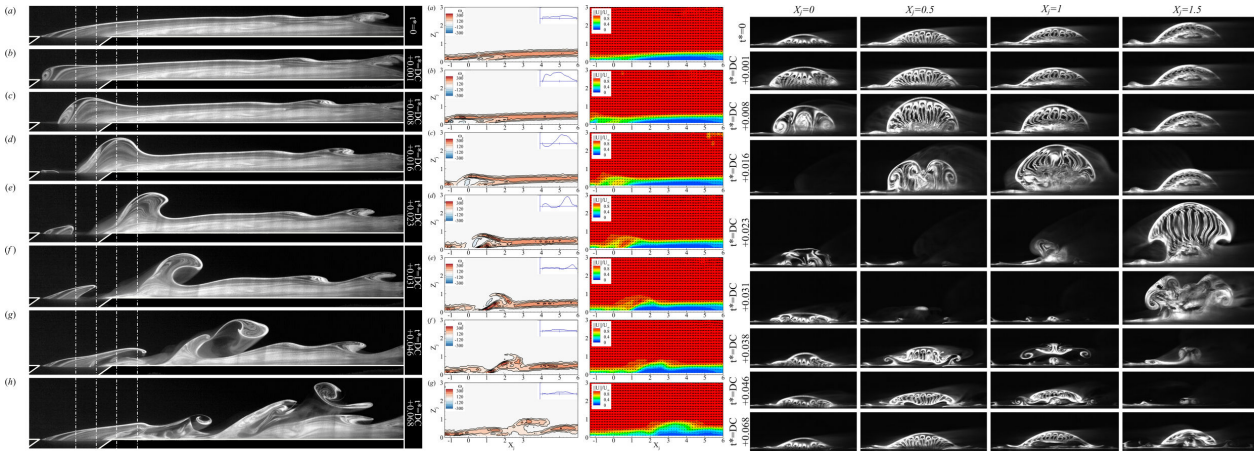

Figure 38: Single compound starting vortex system (a) X-Z Mie scattering visualizations; (b) X-Z PIV; (c) Y-Z Mie scattering visualizations.

at the leading edge and triggered the formation of a trailing structure. This pattern was repeated, though with less amplitude, until two trailing structures were formed in the wake of the leading starting vortex ring. As the starting vortex and its trailing vortices penetrated the free stream, secondary positive rollups originating from the jet upper shear layer natural vorticity, developed downstream of the convected upper shear layer rollups. These secondary structures eventually evolved into large hairpin vortices, subsisting while the primary starting vortex ring and trailing vortices were diffused by the overall positive vorticity.

– *Single compound starting vortex system* - This type of complex starting vortex was formed at intermediate values of BR_h and for short injection times (38). In this

DISTRIBUTION A: Distribution approved for public release.

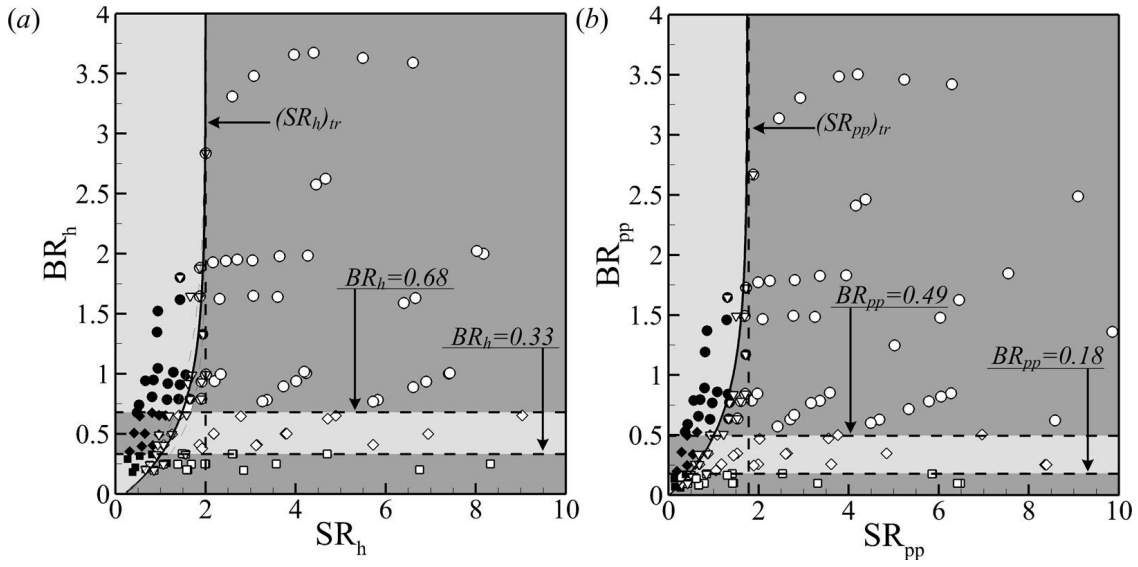

Figure 39: Classification of the starting vortices observed in forced experiments against characteristic stroke and blowing ratios (a) SR_h, BR_h; (b) SR_{pp}, BR_{pp}. ○ Starting vortex ring and trailing column; ● Single vortex ring; ▽ Limiting case single/multiple starting structures; □ Leading hairpin vortex and trailing hairpins; ■ Single hairpin vortex; ; Limiting case hairpin vortex with/without trailing vortices. Transition stroke number fit $(SR_x)_{tr} = F_0 - A_1.exp(-A_2.BR_x)$ (a) $(SR_h)_{tr}$: $F_0 = 2.0$, $A_1 = 1.8$, $A_2 = 1.82$; (b) $(SR_{pp})_{tr}$: $F_0 = 1.75$, $A_1 = 1.75$, $A_2 = 1.7$.

case, only the leading structures (primary ring and secondary hairpin) developed albeit with slightly modified dynamics compared to the previous regime. In this regime, as the upstream rollup of the primary starting vortex departed the jet exit leading edge, the actuation valve was closed, leading to cross-flow ingestion inside the jet pipe and affecting the trajectory of the primary the vortex ring, partly ingested in the jet pipe, and decreasing its circulation. A secondary hairpin vortex eventually developed downstream of the primary ring vortex which was later on dissipated by the overall positive cross-flow vorticity.

- Starting vortices classification - A classification similar to the one of the vertical jet was made, against scaling parameters (SR_h, BR_h) and (SR_{pp}, BR_{pp}) (figure 39). Both sets of parameters provided comparable and satisfactory maps. Using the (SR_h, BR_h) scaling, starting hairpin vortices were formed for BR_h values below 0.33, starting ring vortices formed for $BR_h > 0.68$ and compound vortices generated at intermediate values. The transition stroke ratio $(SR_h)_{tr}$ was found to decrease consistently with decreasing values of BR_h. A formation number (asymptotic value of $(SR_h)_{tr}$) of $F_0 = 2.0$ was identified, which was significantly lower than for the vertical jet (close to 3.6). The (SR_{pp}, BR_{pp}) classification showed identically shaped regions for the different starting structures. Overall the threshold values were so that starting hairpin vortices were formed for $BR_{pp} < 0.18$, starting ring vortices for $BR_{pp} > 0.49$, and compound

DISTRIBUTION A: Distribution approved for public release.

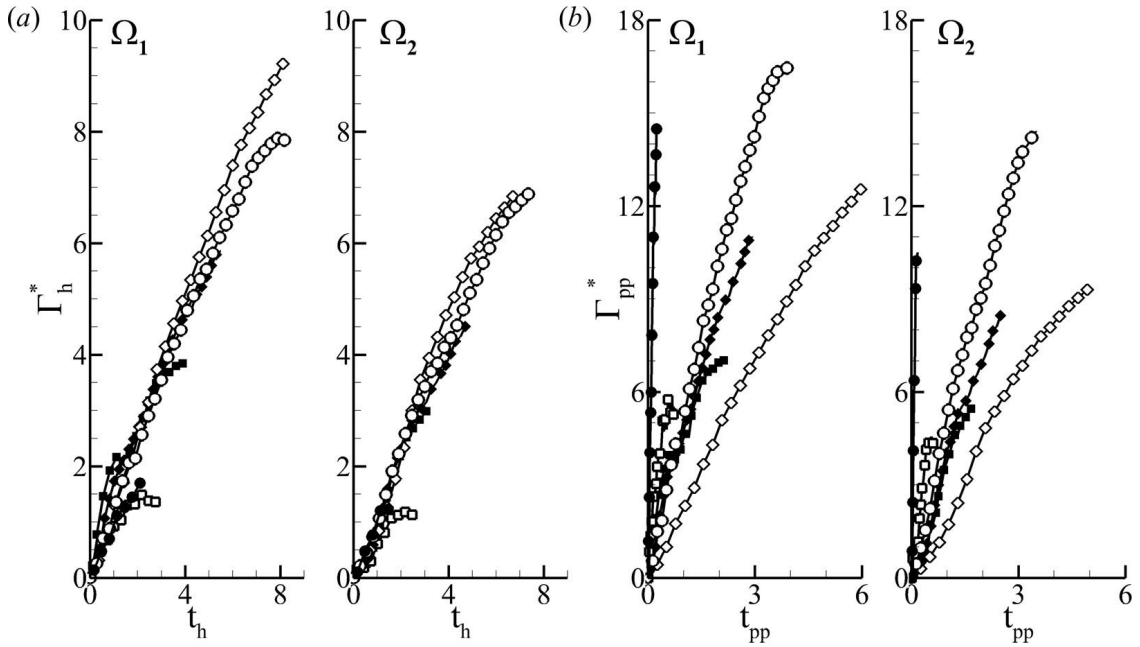

Figure 40: Total 2D circulation from PIV measurements, scaled using (*a*) U_h and (*b*) U_{pp} for *Case VI* (■), *Case VIII* (◊), *Case XII* (□), *Case XIII* (♦), *Case XIV* (○), *Case XV* (●).

starting vortices were formed at intermediate values. The transition stroke number $(SR_{pp})_{tr}$, was also found to decrease with decreasing values of BR_{pp} and the formation number was found at approximately $F_0 = 1.75$, also lower than the vertical jet value. Such decrease in the formation number was explained by the geometrical configuration of the inclined jet which led to higher co-flowing components of the velocity between the jet and the cross-flow compared to the vertical jet, in agreement with findings from (46) for co-flowing flows. As for the vertical jet, rates of generation of the circulation at both the leading and trailing edges were evaluated, this time based on PIV measurements, to identify the correct scaling parameter. The leading edge and trailing edge domains were taken to be the areas of the PIV domain, respectively Ω_1 above and Ω_2 below the line $Y_j = \frac{2.9}{6}X_j + 0.2$ which was found to accommodate all the considered cases. The results were scaled using experimentally determined values of BR_h and BR_{pp} and clearly showed that the scaled results using U_h caused the circulation trends on both domains to collapse nicely onto a single line, making (SR_h, BR_h) the proper scaling parameters for inclined partly modulated jets in cross-flow.

- Cross-flow Ingestion - At the transition from BR_h to BR_l, the rapid decrease in flow rate was accompanied by an ingestion of cross-flow fluid at the jet inlet leading edge, observed in both experiments and simulations (figure 41). The flow separated inside the jet pipe and cross-flow fluid was ingested at the upstream edge of the jet while the horseshoe vortex was convected downstream as the adverse pressure gradient caused by the presence of the jet vanished. The ingestion was more consequent in *Case XI* with a greater BR_h/BR_{pp} value since the mass deficit at the closing of the solenoid valve was more significant. Conversely to the vertical jet, no particular quasi-stationary

DISTRIBUTION A: Distribution approved for public release.

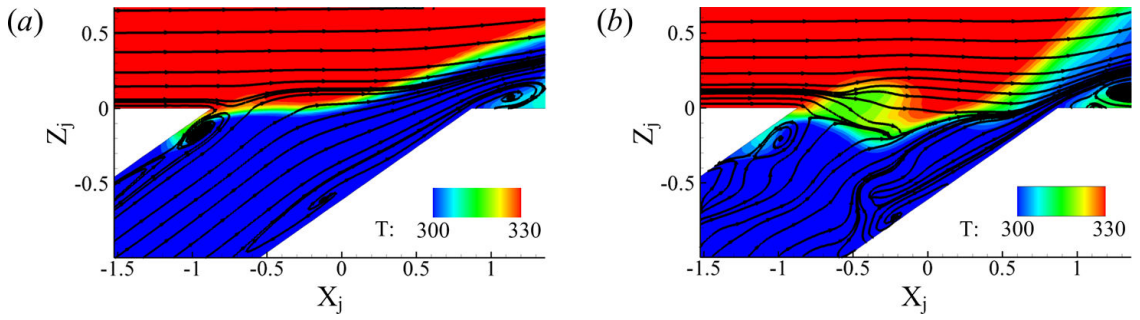

Figure 41: Temperature field and 2D U-W streamlines for (*a*) *Case X*; (*b*) *Case XI* at $t^* = DC + 0.03$.

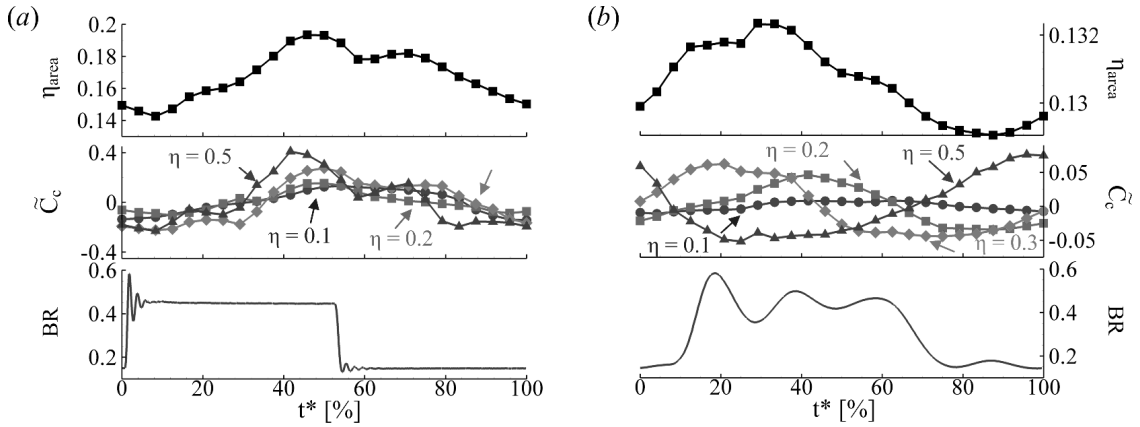

Figure 42: Phase Averaged η_{area} (*top*), relative coverage coefficient fluctuation for $\eta = 0.1$, 0.2, 0.3 and 0.5 (*center*), blowing ratio (*bottom*) for *Case X* at (*a*) $St_\infty = 0.016$; (*b*) $St_\infty = 0.159$.

vortical structures developed after the flow separation and all transients were directly evacuated. This was explained by the difference in pressure gradient across the jet exit between both configurations. Only a single ingestion mode corresponding to the leading edge ingestion was observed in the inclined jet configuration, even in high BR_h cases.

- Film Cooling Performance - The impact of the starting structures on the temperature field was investigated using LES results. Instantaneous wall adiabatic effectiveness and Laplacian of the pressure iso-surfaces for *Case X* (figure 33*b-d*), showed an increase in spread around the jet exit observed at the onset of the high blowing ratio, due to jet fluid exiting on the side of the jet exit. The coverage was also affected by draft induced by the secondary starting vortices and the associated cross-flow fluid entrainment. A 'pinch' in the coverage developed near the secondary starting structures legs as they were convected downstream. For *Case XI* (figure 33*j-l*) corresponding to a higher value of BR_h, although a relatively low increase in the spread could be observed, the cooling performance of the jet was significantly degraded as the jet lifted

DISTRIBUTION A: Distribution approved for public release.

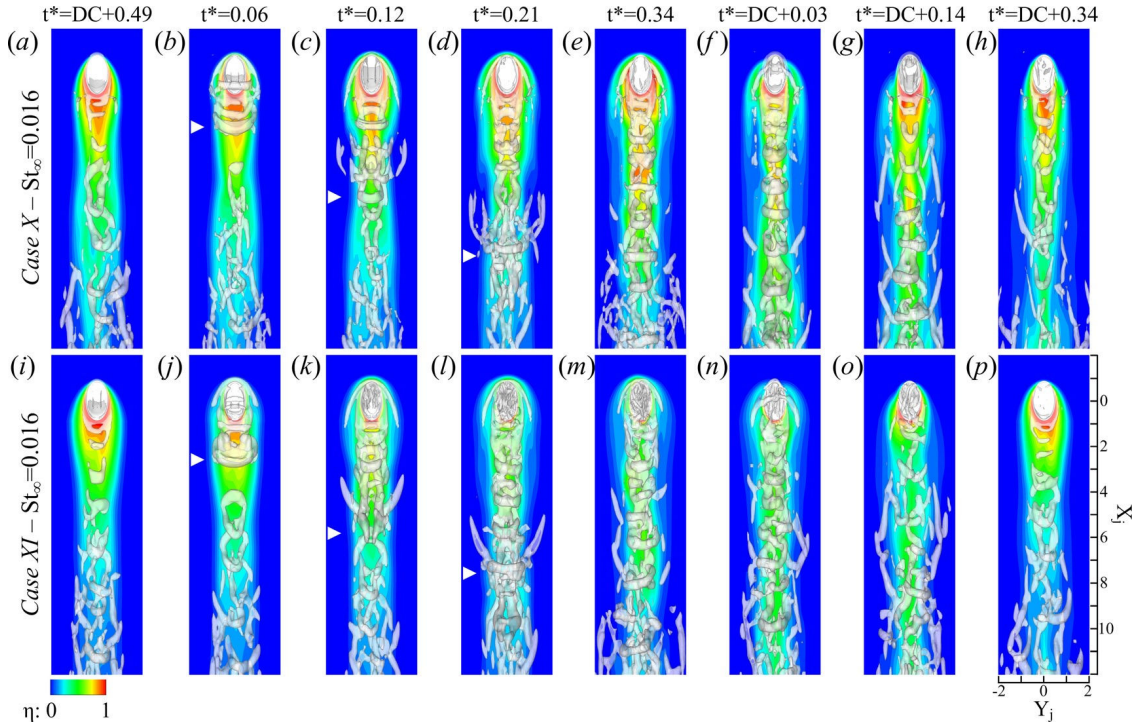

Figure 43: Instantaneous wall adiabatic effectiveness and Laplacian of the pressure iso-surfaces from LES for (*a-h*) *Case X*; (*i-p*) *Case XI* (bottom) at $St_\infty = 0.016$ at $t^* = DC + 0.49$, 0.06, 0.12, 0.21, 0.34, $DC + 0.03$, $DC + 0.014$ and $DC + 0.34$.

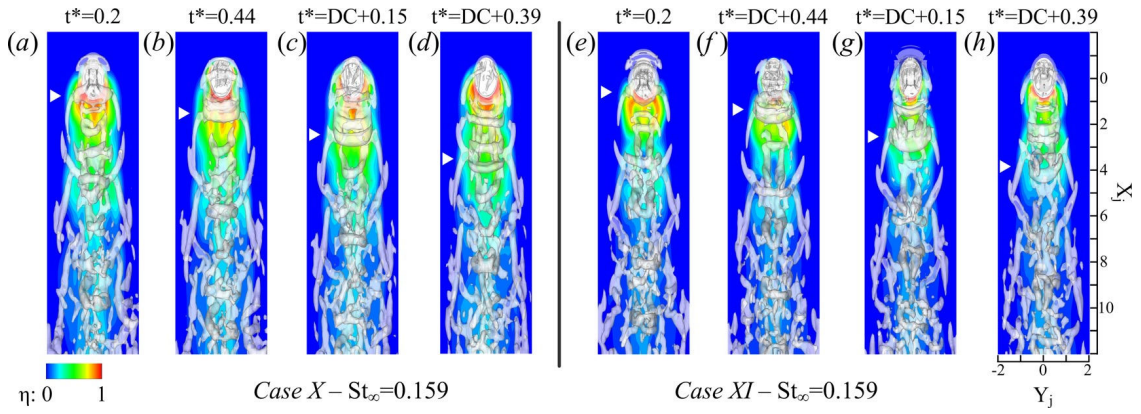

Figure 44: Instantaneous wall adiabatic effectiveness and Laplacian of the pressure iso-surfaces from LES for (*a-d*) *Case X* and (*e-h*) *Case XI* at $St_\infty = 0.159$ during a forcing cycle.

DISTRIBUTION A: Distribution approved for public release.

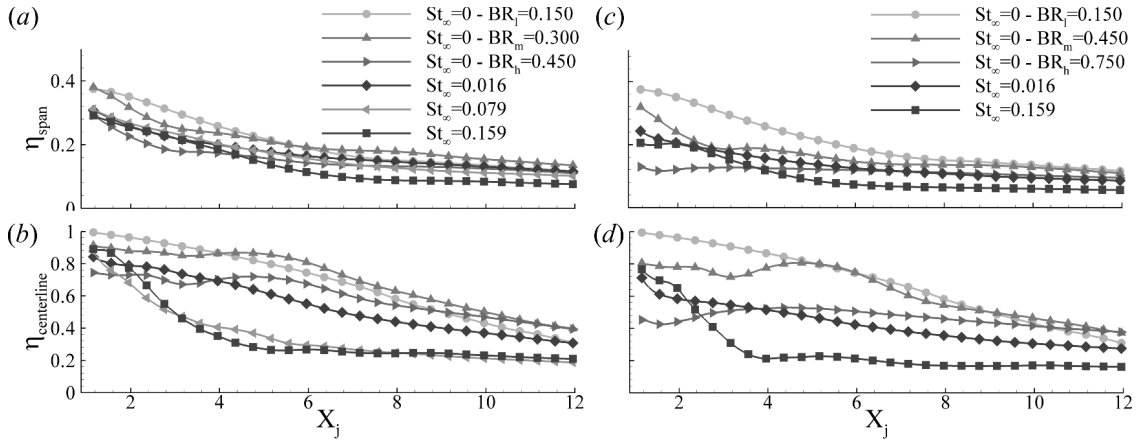

Figure 45: Film cooling performance: Spanwise averaged (*top*) and Center line (*bottom*) adiabatic effectiveness from LES for the forced inclined jet for (*a*, *b*) *Case X*; (*c*, *d*) *Case XI*.

partially off the wall shortly after the transition to BR_h. Simulations at a higher forcing frequency showed that coverage was brought to the wall essentially by the secondary starting vortices (figure 44) as they were convected downstream. In *Case X* ($BR_h = 0.45$), the coverage beyond $X_j = 6$ was marginal as the starting structures consistently lifted off the wall at this point. For *Case XI* ($BR_h = 0.75$), the average coverage breakup point was even closer to the jet exit, about $X_j = 4$, as the starting structures possessed more strength and vertical momentum compared to the lower blowing ratio case, thus lifting off the wall earlier. In both cases, large X-patterned structures from the combination of side vortices and wake vortices associated with the leading starting vortex velocity field, were formed downstream of the starting structures, and while the upper legs of the 'X' affected coverage negatively, the lower legs of the 'X' with opposite vorticity favored the spread, hence the "rosary-like" pattern observed at the wall from the succession of pinch/spread. Although the disruption of coolant at the jet shut down due to ingestion significantly affected the coverage during most of the low part of the cycle. The perturbation was even greater for larger values of the BR_{pp} parameter. Time averaged η_{span} and $\eta_{centerline}$ values for *Case X* and *XI*, were compared to relevant unforced jet trends at constant low, high and average blowing ratios. For forced jets at $BR_h = 0.45$, the span-wise average effectiveness trends showed that forced cases at $St_\infty = 0.016$ and $St_\infty = 0.079$ had performances comparable to the unforced case at $BR = BR_h = 0.45$ with yet center-line adiabatic effectiveness lower and decreasing consistently with increasing forcing frequency. Overall η_{span} and $\eta_{centerline}$ values decreased with increasing frequency, but suggested an increase in spread for the forced cases with overall more homogeneous wall adiabatic effectiveness values over the unforced jet. *At* $BR_h = 0.75$, although no improvement in η_{span} were found in forced cases over the $BR = BR_l$ and $BR = BR_m$ unforced jets, forcing the jet at $St_\infty = 0.016$ provided overall higher η_{span} values than the one of the unforced jet at$BR = BR_h$ particularly for $X_j < 6$. At $St_\infty = 0.159$ higher η_{span} values were achieved for $X_j < 4$ over the case at $BR = BR_h$ with lower values downstream of this point. Once again, forced jet center-line adiabatic

DISTRIBUTION A: Distribution approved for public release.

Table 6: Coverage coefficient and area averaged adiabatic effectiveness from LES under forced conditions compared to equivalent mass flow rate unforced cases. Values for the unforced jet are interpolated from figure 32.

Conditions	C_c			η_{area}
	$\eta = 0.2$	$\eta = 0.3$	$\eta = 0.5$	
$BR = BR_m = 0.3 - St_\infty = 0$	28.0	21.4	11.9	0.197
$BR = BR_h = 0.45 - St_\infty = 0$	22.2	16.8	7.29	0.152
$Case\,X - St_\infty = 0.016$	**25.5**	**17.9**	**8.96**	**0.168**
$Case\,X - St_\infty = 0.159$	**19.9**	**10.9**	**5.31**	**0.131**
$BR = BR_h = 0.75 - St_\infty = 0$	18.3	13.0	1.43	0.109
$Case\,XI - St_\infty = 0.016$	**20.3**	**13.0**	**4.42**	**0.129**
$Case\,XI - St_\infty = 0.159$	**10.4**	**6.47**	**3.07**	**0.091**

effectiveness were lower than those of unforced cases at $BR = BR_l$ and $BR = BR_m$ but higher $\eta_{centerline}$ values were achieved over the case $BR = BR_h$ for $St_\infty = 0.016$ and $St_\infty = 0.159$ for respectively $X_j < 4$ and $X_j < 2.5$. The phase averaged temporal evolutions of forced cases at $BR_h = 0.45$ showed high fluctuations of η_{area} at low forcing frequencies and in particular the the negative impacts of the ingestion transient and of the quasi-unforced high blowing ratio regime on film cooling performance. Fluctuations (and averages) were found to be much lower in the higher forcing frequency case and overall the coverage appeared relatively constant. Global performance for the forced jet summarized in table 6 along with relevant unforced jet performance. In all cases, forcing led to decreased performance over the equivalent unforced jet at constant mean blowing ratio ($BR = BR_m$). However, the forced cases at $St_\infty = 0.016$ performed systematically better than the equivalent unforced jets at fixed high blowing ratio ($BR = BR_h$). At fixed BR_h, BR_l and DC, the jets forced at the highest forcing frequency ($St_\infty = 0.159$) had systematically the lowest performance.

- Other studies put in perspective of the current findings - Studies from (25) and (21) (or 76 which has operating conditions identical to those of 21) were put in perspective of the current findings in terms of forced jet in cross-flow scaling parameters in a an attempt at explaining how they could have provided such disparities in their results. First of all, while they were carried out at comparable blowing ratios and forcing frequencies, the corresponding scaled parameters, using the scaling defined in the current study, show that both studies actually did not investigate the jet in the same conditions. When using the current study delimitation of the (SR_h, BR_h) map (figure 46), it appears rather clearly that some flow regimes have been sampled more extensively than others, in particular the starting ring vortex and trailing column regime, which, according to figure 36 appears poorly suited for film cooling purposes. On the other hand, only one data set was investigated in the hairpin vortex regime, and only one value of BR_h in the compound starting vortex regime. The current study also evidenced the differences in vortex dynamics between a vertical and inclined jet and suggest a great disparity between the physics of the jets involved in (25) (inclined jet

DISTRIBUTION A: Distribution approved for public release.

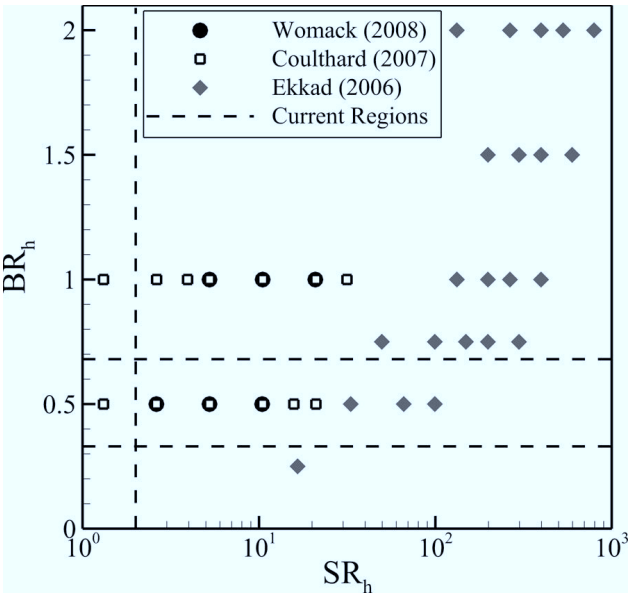

Figure 46: Scaled operating points for previous forced inclined jet studies from (25), (21), and (76) based on the scaling parameters identified in the current work.

with injection angle of 20° with respect to the streamwise direction, and a compound angle of 90°over a leading edge model) and (21) (row of inclined jets at 35° over a flat plate, similar to the one of the current study). Given the considerable impact the introduction of compound angles can have on unforced jets (see 53), it is strongly believed it will also affect the formation mechanisms and dynamics of the starting structures.

DISTRIBUTION A: Distribution approved for public release.

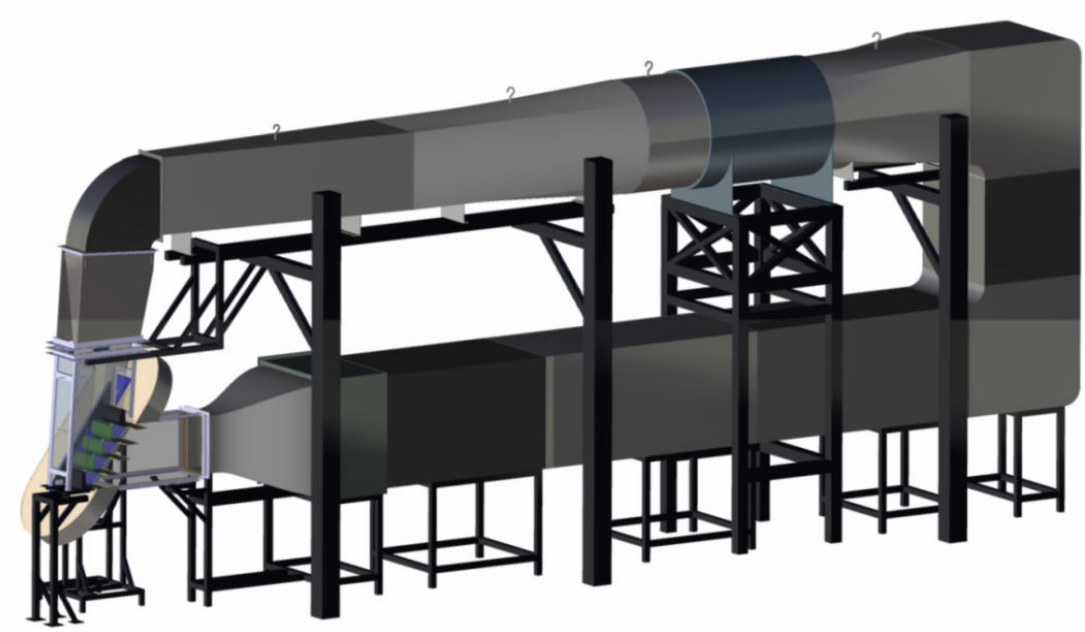

Figure 47: Global view of the wind tunnel

3 Cascade Wind Tunnel

3.1 Experimental Setup Design

3.1.1 Wind tunnel design

A new wind tunnel has been designed and constructed at the LSU Mechanical Engineering Laboratories. The objective was to design a test facility adapted to a wide range of experimental measurements on turbine blades. The test section consists of a 4 passage linear cascade composed of 3 full blades and 2 shaped wall blades (inner and outer blades). A conveyor setup was designed and fabricated to simulate passing wakes upstream of the cascade. Aerodynamic and heat transfer experimental tests were conducted in a relative frame with fixed rotor turbine blades while the nozzle guide vanes are rotating. This facility was designed to enable easy interchanges of different experimental setups. All the parts, as well as the complete assembly, have been fully designed using a Computer Aided Design (CAD) software. Figure 47 shows a general view of the 3D design.

The new test facility was chosen to be a closed-circuit wind tunnel to ensure a controlled return flow and to reach low levels of turbulence and unsteadiness in the test section. The whole wind tunnel is 33 feet long and 11 feet high. The fan diameter is 38 inches. After the test section, the flow is expanding through a first diverging duct and reaches the first corner vanes. Then 2 consecutive diffusers with equivalent cone angles of 5° expand the flow without separation before passing through the fan. The fan is surrounded by 2 flexible ducts to prevent excessive vibration propagation within the wind tunnel. After the fan, the flow passes through a last diffuser and expands into a 38 inches side square section duct. Then the flow goes through 2 more corners with 13 corner vanes in each. A heat exchanger with circulating chilled water is located in between the two bends to regulate the temperature

DISTRIBUTION A: Distribution approved for public release.

Table 7: Pressure losses estimation

Part	K_0	Total Losses (%)
Test section inlet	0.021	6.9
Cascade	0.0384	12.6
Test section outlet	0.0348	11.4
Divergent 1	0.0886	29.0
Corner 1	0.0377	12.3
Divergent 2 & 3	0.0187	6.1
Main duct	0.0017	0.6
Corner 2	0.0015	0.5
Corner 3	0.0015	0.5
Settling chamber	0.0615	20.0
Contraction cone	0.0005	0.2
TOTAL	0.3059	100

inside the wind tunnel during operation. A 19 feet long duct with constant section follows before the flow goes into the settling chamber. The settling chamber consists of a 2 inches thick honeycomb to straighten the flow and 5 screens to reduce turbulence levels. Then, the well-conditioned and uniformed flow enters the contraction cone and is accelerated to the test section inlet. The contraction cone consists of 2 matched cubic polynomial curves to guide the flow from a 38 in square duct to a $19.5in \times 12in$ rectangle duct, equivalent to a contraction ratio of 6.16.

Pressure Loss Estimation in the Wind Tunnel - In this closed-loop wind tunnel, the axial fan produces a rise in static pressure, which compensate for the total pressure losses in the rest of the tunnel. To estimate pressure losses through the different parts of the wind tunnel, the pressure loss coefficient K is used. This coefficient is defined as the ratio of pressure drop in static pressure ΔP over the mean flow dynamic pressure q.

Wattendorf (1938) developed a logical approach to calculate the different pressure losses in a closed circuit wind tunnel. This approach was to divide the wind tunnel into four different kinds of parts: (1) straight, constant area sections, (2) corners, (3) divergent sections, (4) contracting sections. Then, he referred all local losses to the "jet" dynamic pressure q0, greatest dynamic pressure in the wind tunnel. In our wind tunnel, this dynamic pressure q_0 occurs at the exit of the cascade. Then the coefficient of loss becomes:

$$K_0 = \frac{\Delta P}{q}\frac{q}{q_0} = K\frac{q}{q_0} = K\frac{D_0^4}{D^4}$$

Where: D_0 is the jet equivalent diameter, D is the local tunnel equivalent diameter.

Then, the wind tunnel energy ratio ER_t can be defined as:

$$ER_t = \frac{\text{Jet energy}}{\sum\text{Circuit losses}} = \frac{1}{\sum K_0}$$

Below is an estimation of the loss coefficients K_0 for each wind tunnel components, as suggested by Wattendorf:

DISTRIBUTION A: Distribution approved for public release.

The corresponding wind tunnel energy ratio was evaluated at $ER_t = 3.27$. An energy ratio of 3.27 is within the range of most closed circuit wind tunnels. Thus, this design can be seen as a good balance between flow quality, cost, and complexity of fabrication.

3.1.2 Test section design

The 2D blade shape profile of the cascade was provided by the Air Force Research Laboratories (AFRL). It is a High Lift Low Pressure Turbine (LPT) blade 'L1A' profile with a 1.34 incompressible Zweifel coefficient (figure 48). A 6-inch axial chord and 1 foot span were chosen. The span is chosen to be two times the axial chord to make sure we have a nominally 2D flow at the mid span. The solidity of the cascade, ratio of the axial chord to the spacing, is 1. The blade inlet air angle is 35 degrees from axial, and the exit angle is -60 degrees from axial, resulting in a 95 degrees total turning. The linear cascade inlet plane is 1 ft high and 2 ft wide. The nominal inlet velocity is $50m/s$ and was chosen as a reference, with the axial chord to determine the Reynolds number. Two inlet bleeds and two tailboards are placed upstream and downstream of the cascade to adjust the flow and obtain periodic cascade performances as specified by Eldrege and Bons (2004). The cascade inlet plane angle was adjusted from 35°, flow inlet angle of the cascade test blade to 36° to take into consideration the deviation of the mainstream airflow due to the wake simulator. The tangential velocity component induced by the wake generator can be estimated at $1m/s$, which is the nominal operating translation velocity of the moving plates. Considering a $50m/s$ nominal freestream velocity, a simple vector decomposition gives a velocity triangle with about 1° angle of deviation of the mainstream flow (figure 51). The designation used is the same as turbomachinery theory, the absolute velocity is C, the relative velocity is $W = 50m/s$ and U is the rotor blade speed $1m/s$. Then, the total turning angle of the cascade with wake simulator is 96°, which is 1° more than the deviation angle of the test blades.

- *Pressure Measurement Blade* - A pressure tap blade was constructed to measure the pressure profile on the central test blade and compare it to known results. The blade is an assembly of nine parts spanning 12 inches. The pressure tap sections are located at 3 inches, 6 inches, and 9 inches along the blade height. Each pressure tap section has forty-one pressure taps built into it totaling one hundred twenty three pressure taps. The large number of pressure taps enabled a high resolution capture of the pressure profile along the length of the blade. Having the taps spaced every three inches allowed the straightness of the blade to be validated by comparing the pressure acquired by each section. Because of its complexity, the pressure tap sections had to be manufactured using rapid prototyping process called stereolithography (SLA). This process uses an acrylonitrile butadiene styrene (ABS) like material called Accura 55 (details in Appendix II Data Sheets). GPI Prototype and Manufacturing Services, Inc. located in Lake Bluff, IL made the pressure tap sections. Two Scanivalve DSA3217 differential pressure scanners were used to measure the pressure profiles.

- *Film Cooling Blade* - The film cooling blade is shown in Figure 49. The film cooling blade was designed to accommodate measurements using PIV and IRT techniques. The blade has thirty 1/8" diameter film cooling holes connected to an internal plenum. The holes are angled 35° to the local tangent of the surface and are spaced 3/8"

DISTRIBUTION A: Distribution approved for public release.

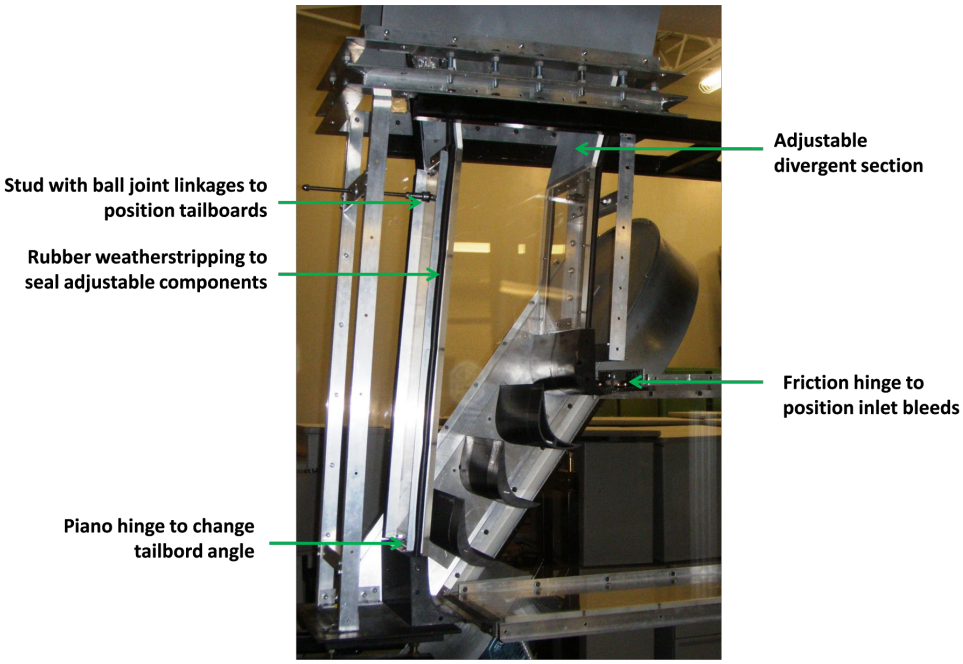

Figure 48: Cascade image

Table 8: Location of Pressure Taps as Percent of Axial Chord (X/C_x)

Suction Side						**Pressure Side**			
Tap #	% of C_x	**Tap #**	% of C_x	**Tap #**	% of C_x	**Tap #**	% of C_x	**Tap #**	% of C_x
1	1	**10**	35	**19**	65	**1**	1	**10**	71
2	3	**11**	40	**20**	67.5	**2**	3	**11**	76
3	5	**12**	45	**21**	70	**3**	5	**12**	81
4	7.5	**13**	50	**22**	72.5	**4**	11	**13**	86
5	10	**14**	52.5	**23**	77.5	**5**	21	**14**	91
6	15	**15**	55	**24**	82.5	**6**	31		
7	20	**16**	57.5	**25**	87.5	**7**	41		
8	25	**17**	60	**26**	92.5	**8**	51		
9	30	**18**	62.5	**27**	97.5	**9**	61		

DISTRIBUTION A: Distribution approved for public release.

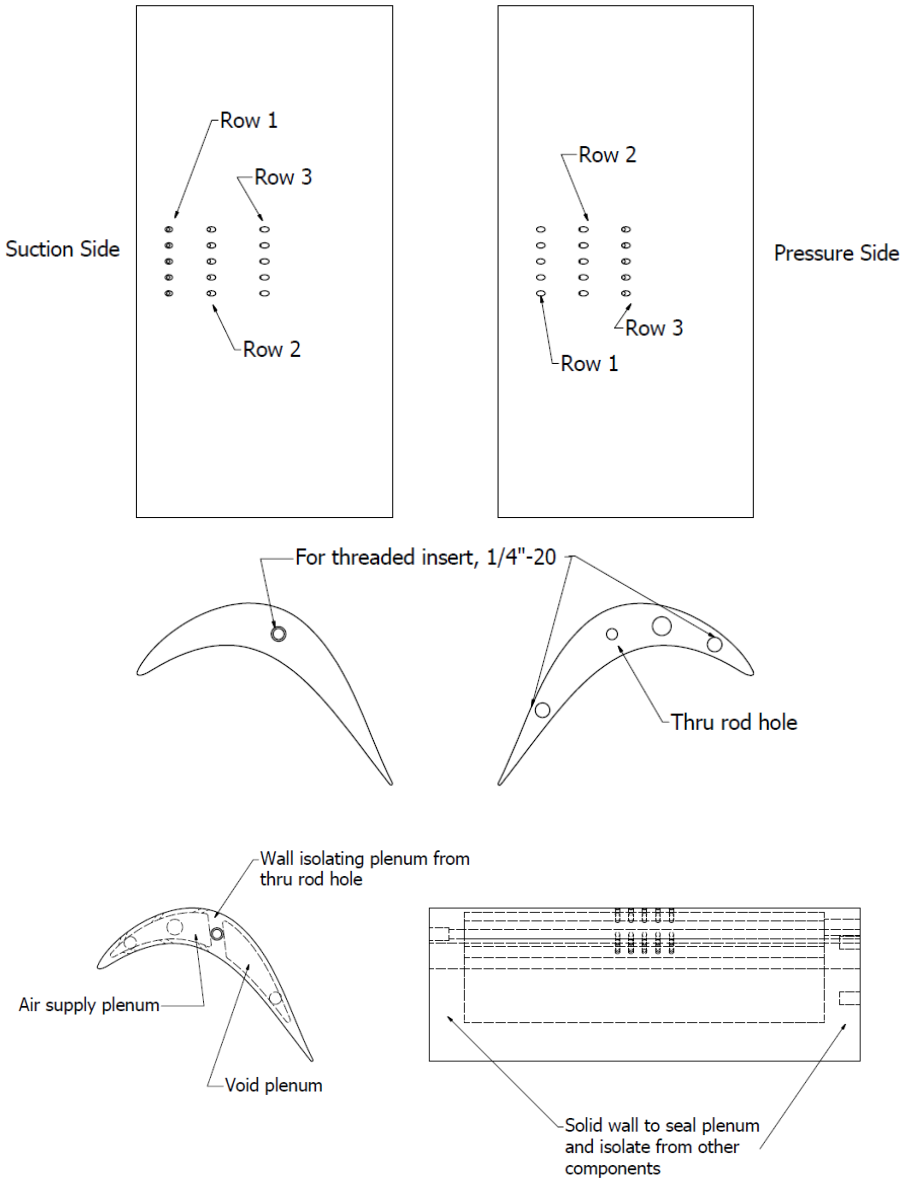

Figure 49: (Top) Suction/Pressure Side Views, (Middle) Left/Right Side Views, (Bottom) Left/Back View w/ Hidden Lines Shown of the Film Cooling Blade

laterally. The length to depth ratios of the holes are listed in Table 9 assuming a 1/8" diameter. The internal plenum is connected to an air supply via a $\frac{1}{4}$" NPT fitting and is completely isolated from the other components of the blade such as the thru-rod hole and the threaded insert holes as shown in Figure 49. The blade was manufactured using the same process, material and company as the pressure tap sections.

DISTRIBUTION A: Distribution approved for public release.

Table 9: Locations and L/D Ratio of Film Cooling Holes

Row/Side		% Chord Location (X/C_x)	Length to Diameter Ratio, L/D
Suction	1	12.5	1.816
	2	29.167	1.824
	3	50	1.880
Pressure	1	16.667	1.694
	2	33.333	1.664
	3	50	1.664

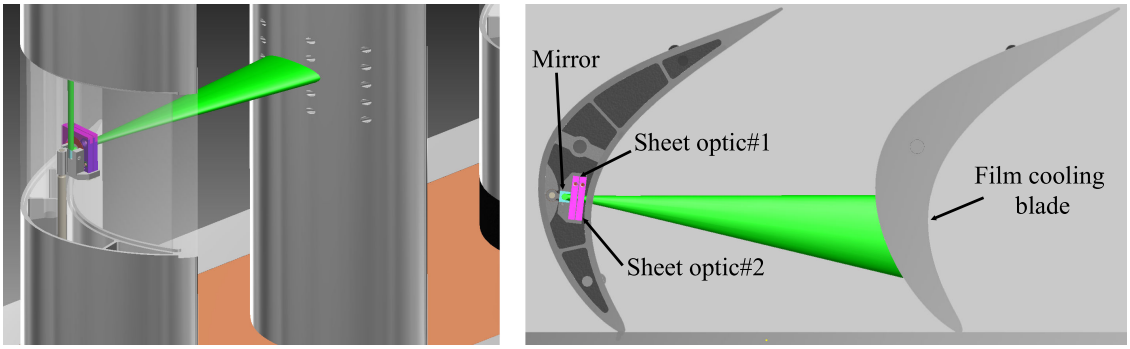

Figure 50: Assembled PIV Side Blade with optical setup for PIV measurements / Mie scattering visualizations

- *PIV Side Blades* - The PIV side blades were built to accommodate PIV measurements in the test section using the film cooling blade. There are two of them, one on either side of the central test blade in the cascade, and they are manufactured in five separate parts as shown in Figure 50 below. The plastic base spacer and acrylic sections are optically transparent to allow a laser sheet to pass through them. The blade was designed to allow the laser beam to enter from the left of the plastic base spacer, travel through the blade to mid-height of the blade. The beam is then redirected at 90° through a prism, and epxanded in one (2D-PIV)or two dimensions (3D-PIV) through cylindrical optics to generate a laser sheet or volume for PIV measurements. Finally, the sheet (or volume) illuminates the film cooling holes on the film cooling blade (figure 50). The entire mirror/optics ensemble can be traversed up and down the side blades using an in-house designed traverse system to illuminate different spanwise locations of the film cooling blade.

3.1.3 Wake generator design

Wakes are generated with aluminum plates in translation on a conveyor setup parallel to the mainstream airflow (figure 52 and 53). Those plates are 3/8 inch thick and are designed to be in size similar to the cascade test blades. The conveyor with the 17 moving plates is enclosed in an airtight shell. The design speed is 1 m/s but can be adjusted to study its influence. The plate length and pitch were chosen to be equal to the axial chord of

DISTRIBUTION A: Distribution approved for public release.

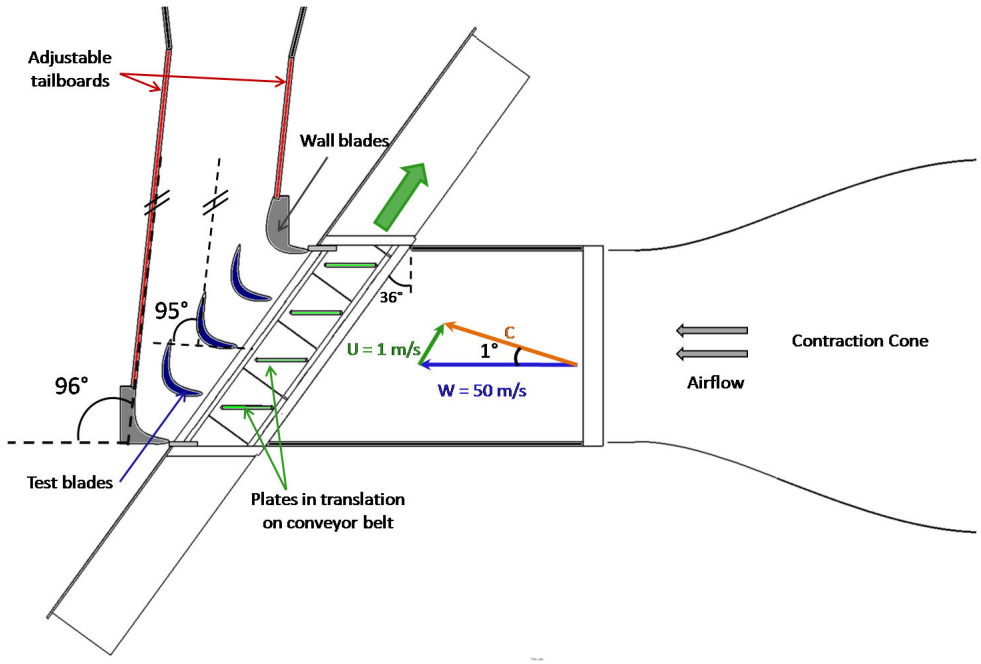

Figure 51: Cascade angles and velocity triangle.

the cascade blade (6 inches). The distance between the trailing edges of the plate and the cascade inlet plane is 2.4 inches, which is 40 % of their chord, and similar to engine stator-rotor stage spacing. Trailing and leading edges of the plates are interchangeable to study different configurations. In addition, plates are removable and can be substituted with more realistic airfoil profiles if required in the future.

The conveyor mechanism was specificaly designed and fabricated for this application. The conveyor belt and standard conveyor components such that spockets, wearstrips or shafts have been purchased from a company specialized in modular plastic conveyor belts, Intralox L.L.C. The frames, stand, cover and plate assemblies have been designed using a CAD software and built in house at the LSU Mechanical and Chemical Engineering machine shops with exception of the conveyor shell which was built by an external contractor, specialized in sheet metal work (BMR Metal Works LLC, Watson. LA).

The conveyor gearmotor is a combination of an AC electric motor, a gear unit to reduce the rotational speed and a Variable Frequency Drive (VFD) to control the output speed of the motor. This is a SEW-EURODRIVE gearmotor, model # KAF37DRE80M4 / MM11. The AC electric motor is a DRE80M4 model, 3-phase with a $1.5HP$ power. Coupled to a MM11 VFD, the output speed range of this gearmotor can vary from 19 to $189rpm$, with a $486in-lb$ nominal torque at $189rpm$. This RPM range corresponds to a belt velocity range from $0.28m/s$ to $2.76m/s$.

3.1.4 Additional equipment

Three axis linear traverse - A three axis linear traverse was designed and assembled to accommodate constant temperature anemometry (CTA) measurements. The possibility

DISTRIBUTION A: Distribution approved for public release.

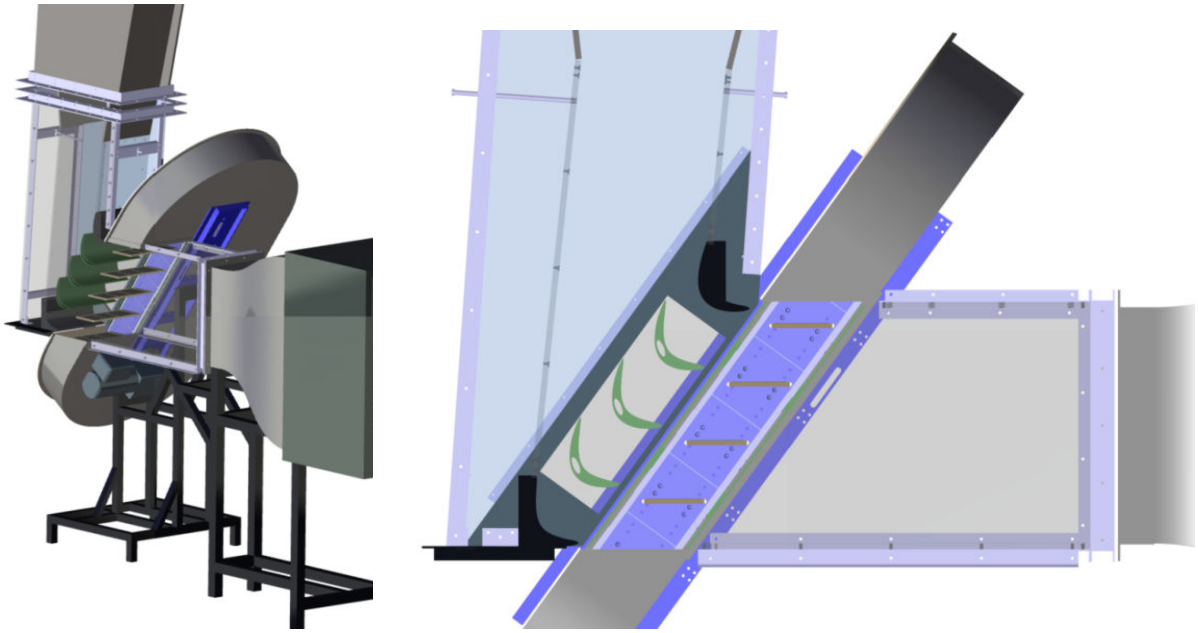

(a) (b)

Figure 52: Views of the wake simulator mechanism integrated to the test section.

(a) (b)

Figure 53: CAD view and picture of the wake simulator.

DISTRIBUTION A: Distribution approved for public release.

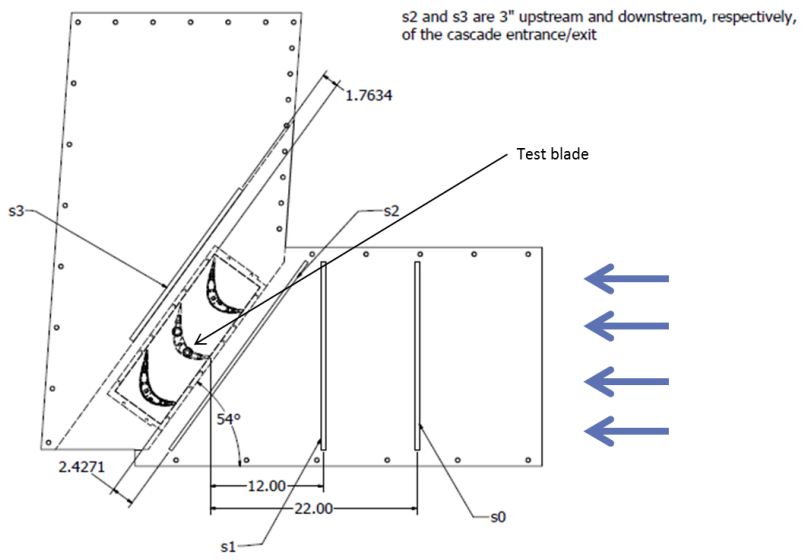

Figure 54: 2D Schematic of Test Section w/o Wake Generator w/ Labeled CTA Slots.

of other uses such as particle image velocimetry (PIV) and infrared thermography (IRT) measurement techniques was taken into account in its design as well. The traverse has two vertical axes coupled with a timing belt. A counter-weight system (not shown) was also implemented to increase the payload of the traverse by supporting the 60*lbs*. weight of the X and Y axes. (two 15*lbs* steel cylinders suspended on the far side of the traverse using a pulley). The linear stages that make up the individual axes are Velmex Bislides lead screw and ball design with 2 mm/rev leads. Stepper motors equipped with encoders (no encoder on Z axis) are used to power the axes of the traverse. NEMA 23 Danaher Motion stepper motors (Model # T22NRLG-LDN-NS-00) are used on the X and Y axes. A NEMA 34 Oriental Motors stepper motor (Model # PK296-03BA) is used on the Z axis. National Instruments quadrature encoders (Model # 15T-01SA-1000-N5RHV-F00-CE) are used on the X and Y axis, only.

3.2 Linear Cascade Characterization without Wake Generator

Experimental studies in wind tunnels generally aim at measuring various parameters of the airflow around aerodynamic bodies. In general, three main parameters are measured: velocity, pressure and temperature. These data measured over an area and through time can yield to more practical characteristics such as heat transfer or aerodynamic measurements, turbulence level or boundary layer profiles. In order to perform reliable measurements on different quantities in a wind tunnel, several steps are necessary: 1- Selection of equipment, 2- Experiment planning, 3- System configuration and installation, 4- Calibration, 5- Data acquisition, 6- Data reduction. Finally, data can be analyzed and some corrections can be applied if necessary. All these steps will be detailed in the following chapter.

DISTRIBUTION A: Distribution approved for public release.

3.2.1 Pressure Distribution along the Wind Tunnel

Static and dynamic pressures were measured with a Pitot tube linked to a handheld digital manometer at different locations along the flow path in the closed circuit wind tunnel. Figure $55a$) represents the variation of static, dynamic and total pressure along the wind tunnel for a mean velocity in the test section inlet of $53m/s$. The graph starts at the test section inlet (x=0 foot) and ends at the contraction cone outlet (x= 70 feet) to close the loop.

As expected, a permanent total pressure decrease along the wind tunnel occurs due to pressure losses. Static and dynamic pressures vary symmetrically, in function of the section areas. As predicted Part 2.3, most pressure losses occur around the cascade, where the dynamic pressure is the highest. Static pressure rises across the fan by 7 inches H_2O at this particular wind tunnel working point with a calculated flow rate of around 17,000 CFM.

3.2.2 Test Section Velocity Distribution

- *Test section inlet* - CTA measurements were used to characterize the contraction outlet plane 's0' and cascade inlet plane 's2' (figure 54).

  - *Contraction outlet* (s0) - The velocity variation in the core of the section was approximately $1m/s \pm 0.02m/s$ with a 95% confidence interval. Refined measurement in a corner of the same plane 's0' showed fluctuations of $\pm 1.5m/s$ in the corner flow for a 95% confidence interval. The turbulence intensity reached levels as low as 0.12% in the center of the cross-sectionand 7% in the corners. The incoming boundary layer profile was acquired for a mainstream flow velocity at $50m/s$ (figure 55). The boundary layer characteristics are summarized in table 10. Full velocity profiles were acquired at slot s0 in both the vertical (Z) and horizontal (Y) directions; s2 in the direction along the slot and in the horizontal direction. The velocity was uniform at $50m/s$ across about 95% of the cross-section in the vertical direction. The horizontal direction showed much of the same except with a slight drop of about $1m/s$ in the horizontal direction from $Y/H = 0.8$ to 0.95. The turbulence intensity in the freestream was about 0.20% for both cases.
  - *Cascade inlet* (s2) - The incoming air flow at slot s2 was beginning "feel" the effects of the leading edge of the cascade blades. The velocity varied from $50m/s$ upstream of the leading edge to $53m/s$ between the leading edges of the cascade blades. The variance between the velocities at the leading edge, $s/S = 0.25, 0.50, 0.75$, of the blades was approximately 1% of the freestream velocity. In the horizontal direction, the velocity was uniform from $Y/H = 0.05$ to 0.65. Beginning at $Y/H = 0.65$, the velocity dropped to about $49m/s$ and stayed there until $Y/H = 0.95$. The turbulence intensity was about 0.20% in the freestream again for both cases. The temperature (figure 56c) stayed at around $24°C$ from $Z/L = 0.20$ to 0.95. Starting at $Z/L = 0.05$ and extending to $Z/L = 0.20$, the temperature rose from $23°C$ to $24°C$. This temperature rise is most likely due to an increase in the overall, bulk temperature of the air flow in the wind tunnel.

- *Test section outlet* (s3)- The mean velocity values were measured at mid-span, 50% of the axial chord downstream of the cascade outlet plane at the slot 's3' . The inlet

DISTRIBUTION A: Distribution approved for public release.

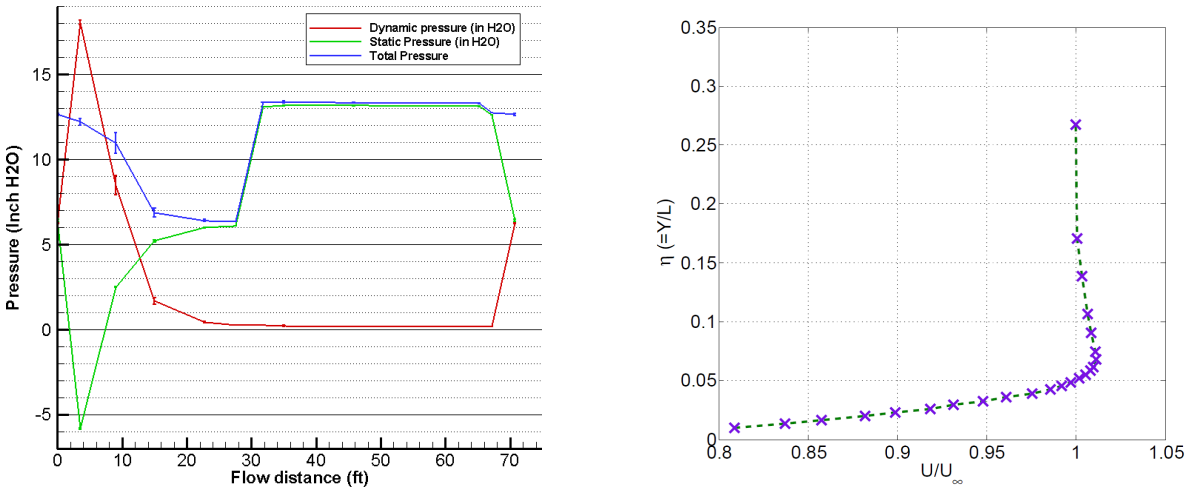

(a) (b)

Figure 55: a) Variation of static dynamic and total pressure along the wind tunnel; b) Boundary Layer Profile.

Table 10: Inlet boundary layer characteristics at $X_j = -6$, $Y_j = 0$.

U_∞	Ti	$\delta_{99\%}/L$	δ^*/L	θ/L	H	Re_θ
$50ms^{-1}$	$< 0.12\%$	0.04	0.077	0.058	1.33	4,334

mean velocity U_∞ was $50m/s$, which gives a Reynolds number based on the blade axial chord of 450,000. The wake profile of the center blade of the cascade is shown Figure 57. The pressure side is on the right side of the graph and the suction side on the left. The wake profile in Figure 58a) had a periodic shape as hoped. The minimum velocity in the wake of each blade varied from $62m/s$ $(1.24U_\infty)$ to $59m/s$ $(1.18U_\infty)$, from $s/S = 0.25, 0.50, 0.75$. In between the blades, the velocity started at about $73m/s$ $(1.46U_\infty)$ then decreased in a curved, concave fashion to about $70m/s$ $(1.4U_\infty)$ on the edge of the blades wake. The turbulence intensity downstream of the cascade was approximately 0.25% in between the blades and peaked at about 2% downstream of the central test blade. The turbulence intensity downstream of the two side blades was about 1.5% each. The maximum turbulence intensity at the pressure side and suction side walls was about 10% and 2%, respectively The effect of altering the angle of attack on the central test blade was also investigated. Figure 58b showed decreasing the angle of attack from 0° to −2.5° decreased the velocity downstream of the trailing edge by about $1m/s$ and, in general, decreased the suction side wake velocity by about 2 m/s; the pressure side wake was reduced by $1m/s$. It also shifted the position of minimum velocity slightly to the left. When the angle of attack was increased from 0° to +2.5°, the minimum velocity in the wake was decreased by approximately $25m/s$ $(0.5U_\infty)$. This increase in angle of attack also created a wake about 350% larger than the 0° wake. A second measurement of the wake at a later time, shown in purple, produced a different result. In this case, the wake minimum velocity was about $15m/s$ $(0.3U_\infty)$ lower than the 0° angle of attack case. This result most likely occurred because the

DISTRIBUTION A: Distribution approved for public release.

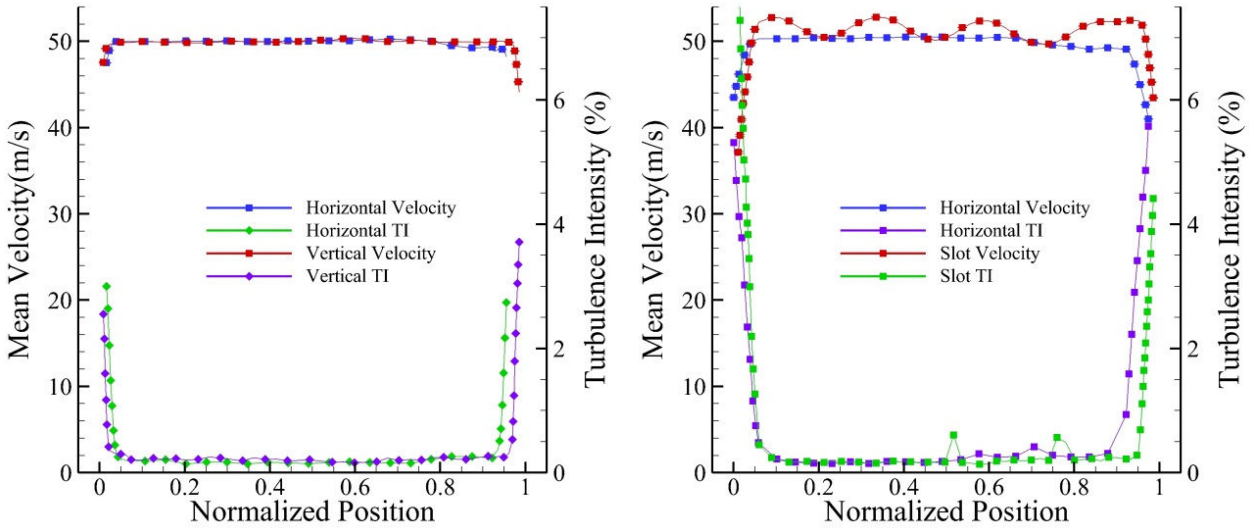

(a) Mean Velocity and Turbulence Intensity at Slot s0 (b) Mean Velocity and Turbulence Intensity at Slot s2

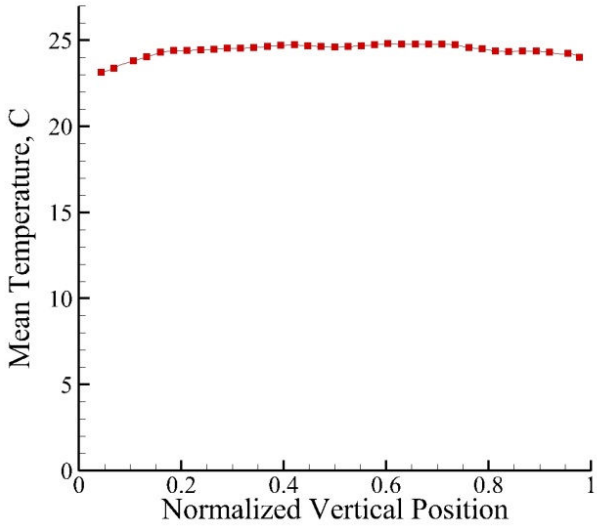

(c) Mean Temperature vs. Vertical Direction at Slot s0

Figure 56: Velocity, turbulence intensity and temperature profiles for slot s0 and s2.

DISTRIBUTION A: Distribution approved for public release.

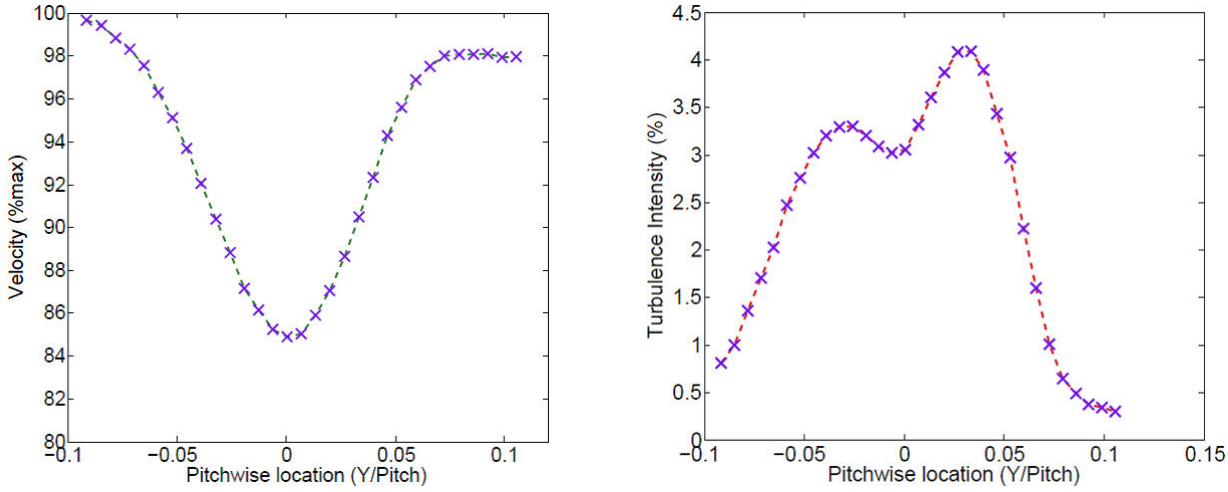

(a) (b)

Figure 57: a) Wake velocity profile on a L1A blade at $Re = 450,000$; b) Turbulence intensity profile on a L1A blade at $Re = 450,000$.

Table 11: Results of Frequency Analysis on Wind Tunnel Ducting and Test Section Walls

Location	Characteristic Length, $L_c(m)$	Natural Frequency, $\omega_n(Hz)$	Characteristic Frequency, $f(Hz)$
Upstream Duct	0.9652	180	10
Bottom & Top Wall	0.3048	570	164
Left & Right Wall	0.4953	350	100

blade was not at a $+2.5°$ angle of attack when the measurement took place, but instead was at an angle of attack slightly lower ($2.0°$). However, this is still useful because it shows the blade is very sensitive to an increasing angle of attack.

3.2.3 Test Section Spectral Content

- *Test section inlet* (s0) - The energy spectrum at all four walls and the center of the test section was measured in slot s0 (figure 59). In all cases, a peak occurred at $15Hz$. At the center of the test section, a peak occurred at $470Hz$ as well. A more distributed set of peaks also occurred from $200 - 300Hz$ in the center of the test section. The peaks in energy were compared to the natural frequency of the wind tunnel ducts, and test section walls (table 11). Based on those estimates, the $15Hz$ peak is consistent with the tunnel ducting and the $470Hz$ peak with the test section walls natural frequencies. The "hump" from $200 - 300Hz$ could arise from a combination of the natural frequency and the characteristic frequency of the test section walls.

DISTRIBUTION A: Distribution approved for public release.

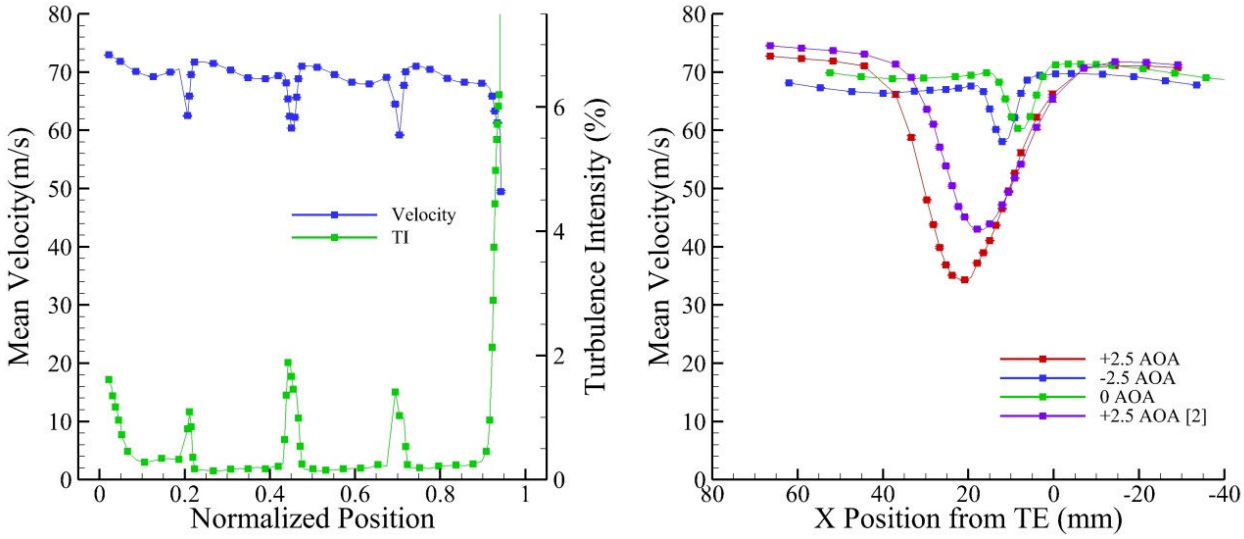

(a) Mean Velocity and Turbulence Intensity at Slot s3 (b) Comparison of Blade Wake Profiles at Different Angle of Attack

Figure 58: Wake velocity profiles at slot s3.

- *Test section outlet* (s3) - The energy spectrum of the central test blade wake was also investigated at different angles of angles of attack from $+2.5°$ to $-2.5°$ (figure 60). A small peak occurred at about $15Hz$ for the $0°$ and $-2.5°$ angle of attack cases, consistent with the one found at the test section inlet. For the $+2.5°$ case, a hump occurred from $200Hz$ to $500Hz$. This hump or peak in the energy spectrum is possibly the wake shedding frequency of an unstable or separated boundary layer. The supposed reason for the $+2.5°$ wake to produce two different energy spectra is an error in the blade position. It is believe the case labeled "+2.5 AOA" was actually at an angle of attack $+2°$. However, the fact that the hump disappeared when the angle of attack was slightly decreased shows the blade becomes very sensitive when the angle of attack is increased to $+2°$.

3.2.4 Pressure Profiles

Pressure profiles were acquired using the in-house designed pressure tap blade and two Scanivalve DSA 3217 Pressure Scanners. The pressure coefficient results were also put in perspective of provided AFOSR reference pressure profiles, and $k-\epsilon$ simulations using Ansys Fluent (figure 61). The experimental coefficient of pressure (C_P) shown has decent agreement with the AFOSR results but better agreement with the CFD results. The largest deviations occur on the suction side of the blade where the blade has high curvature, and at the trailing edge of the blade. The most likely cause of the discrepancies is the test section pressure bleeds which were opened to balance the flow at slot s2 and slot s3. The C_P trends were measured at three different incoming velocities (figure 61b), chosen because within 5% of the nominal incoming Reynolds number, and collapsed on top of each other as expected.

DISTRIBUTION A: Distribution approved for public release.

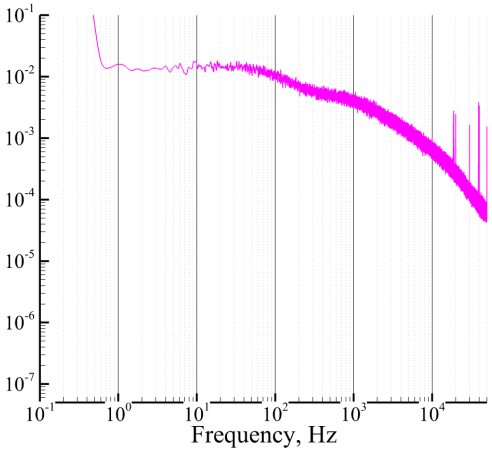

(a) -Z Wall

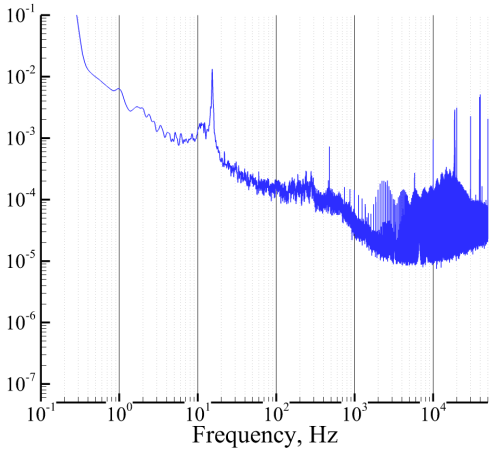

(b) Middle

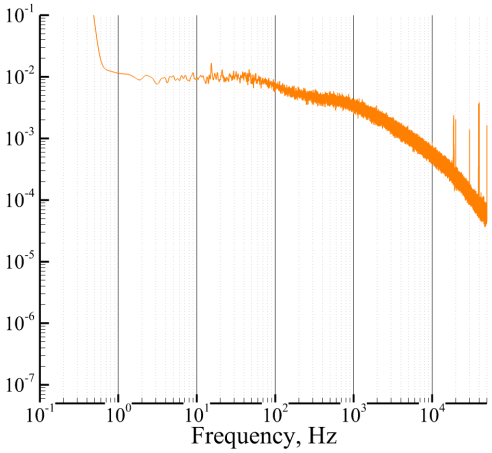

(c) +Z Wall

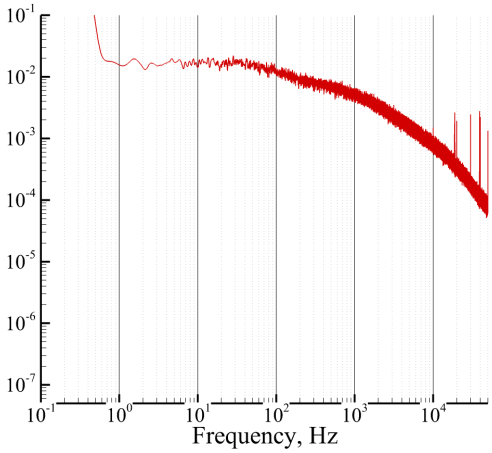

(d) -Y Wall

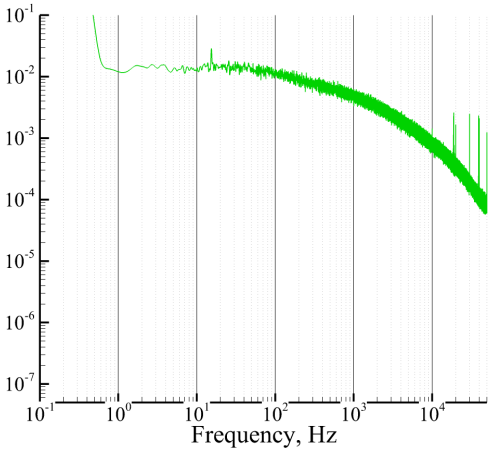

(e) +Y Wall

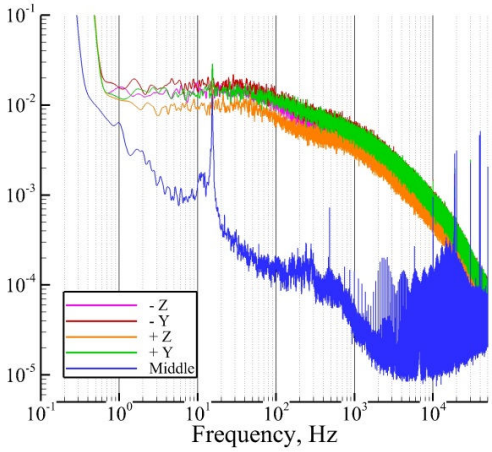

(f) Comparison of a-e

Figure 59: Energy Spectra at Slot s0

DISTRIBUTION A: Distribution approved for public release.

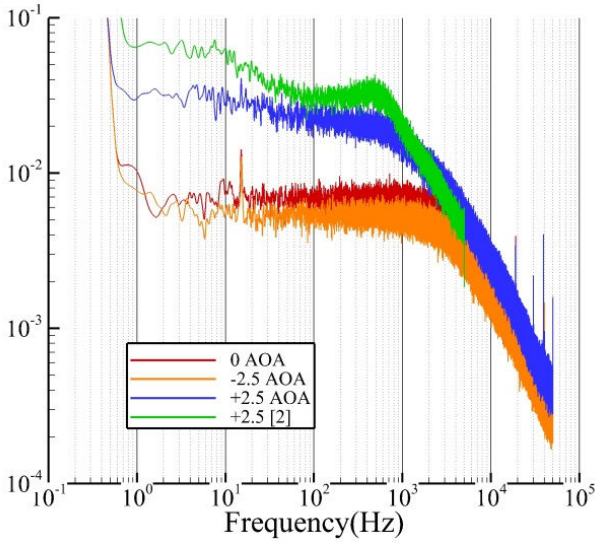

Figure 60: Central Test Blade Wake Spectra at +2.5°, 0°, and -2.5° Angle of Attack.

Similarly, C_P trends were measured at three different angles of attack and decreased on the suction side as the angle of attack was increased, and remained essentially constant on the pressure side (except near the leading and trailing edges). The C_P trends evidenced a boundary layer separation (figure 61c) when at +2.5°, consistent with the findings in the spectral measurements.

3.3 Linear Cascade Characterization with Wake Generator

Incoming velocity profiles were acquired at slot s0 (figure 62), Cascade wake measurements were acquired at the downstream slot located $3in$ from the cascade trailing edge plane. The slot was located $3in$ downstream of the cascade blade leading edges in the Z direction not the direction depicted in Figure 62.

All "running" results were acquired when the wake generator was running at a translation velocity of $1m/s$. This corresponds to a wake passing frequency of $6.5Hz$ based on a blade spacing of $6in$. Other results were acquired with the wake generator at a fixed position to compare with the running results. These results are labeled "aligned" and "misaligned" and the positions are depicted below in Figure 63.

The spacing between the leading edge of the cascade blades and the trailing edge of the wake generator blades was designed to be 40% of the axial chord or 2.4 inches.

3.3.1 Test Section Velocity Distribution

- *Test section inlet* (s0) - The velocity profiles and turbulence intensities at slot s0 (figure 64). Velocity profile and turbulence intensity were evaluated with the wake generator blades in the aligned, misaligned, and running positions. Velocity profiles are uniform across vertical and horizontal direction of the test section. A single point measurement of the velocity was acquired at slot s0 for fluctuation purposes. The mean velocity when

DISTRIBUTION A: Distribution approved for public release.

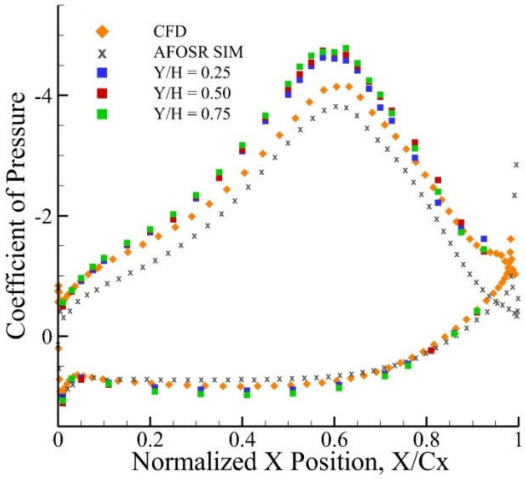

(a) $C_P$with AOA $= 0°$ and $U_\infty = 49.04 \pm 0.11 m/s$ on the Cascade Blade Compared to an AFOSR Simulation at $Re_{Cx} = 500,000$ and a k-ε 3D Simulation at $Re_{Cx} = 500,000$.

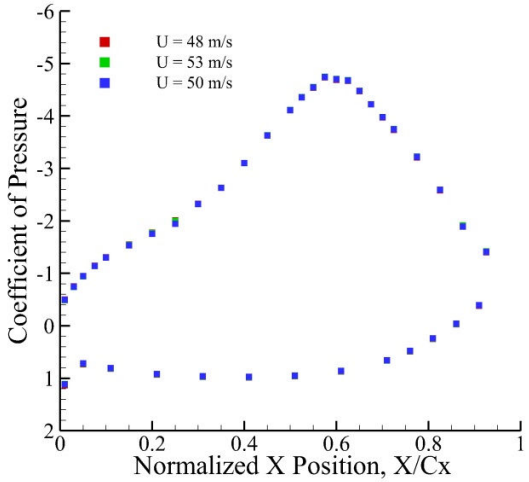

(b) Comparison of $Y/H = 0.50$ C_P at Different Incoming Velocities and 0° AOA

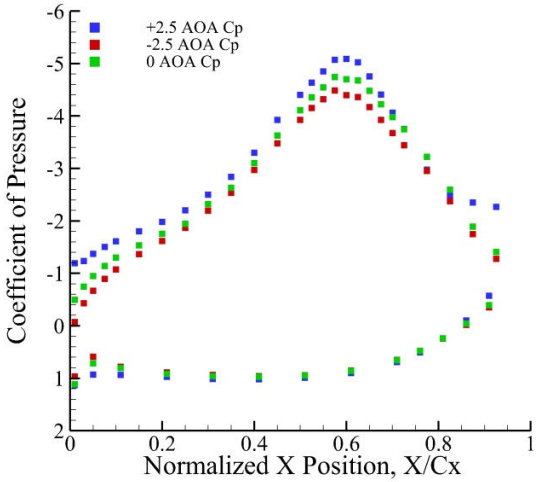

(c) Comparison of $Y/H = 0.50$ C_P at different Angle of Attack and $U_\infty = 48.71 \pm 0.33 m/s$.

Figure 61: Experimental, AFOSR and CFD pressure profiles.

DISTRIBUTION A: Distribution approved for public release.

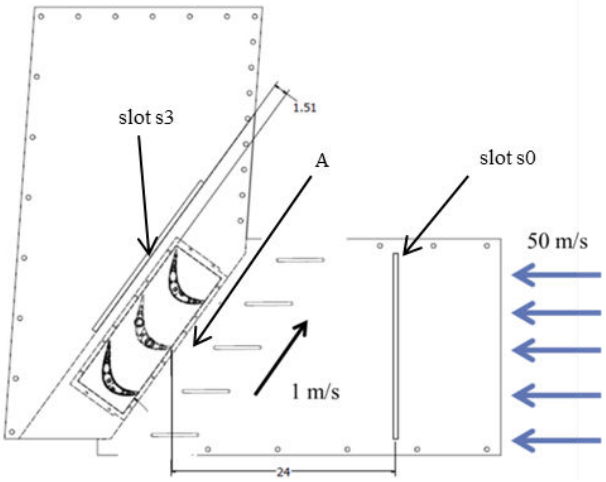

Figure 62: Illustration of Test Section with Wake Generator Installed and CTA Slots Labeled.

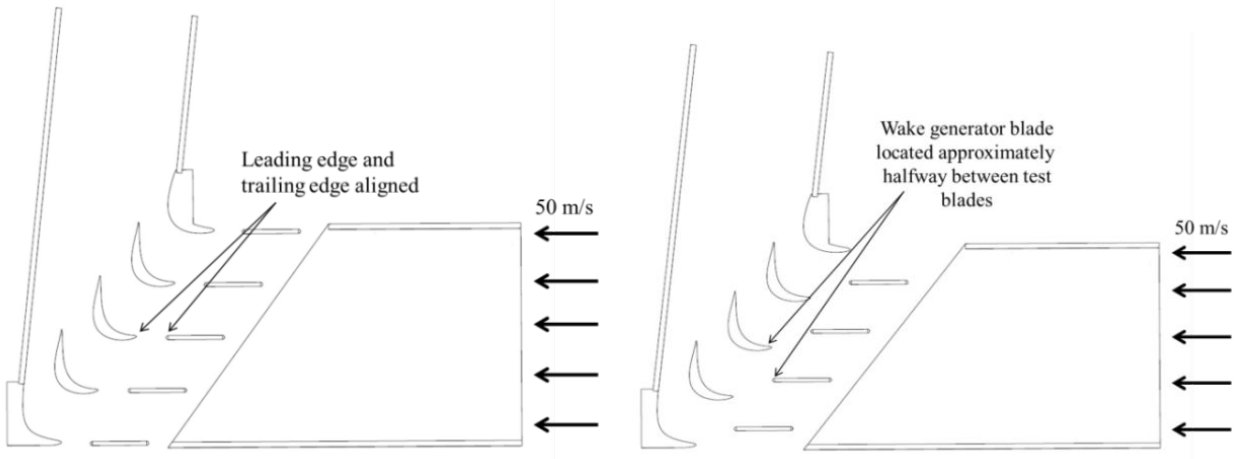

(a) (b)

Figure 63: Illustration of "Aligned" (left) and "Misaligned" (right) Configurations

DISTRIBUTION A: Distribution approved for public release.

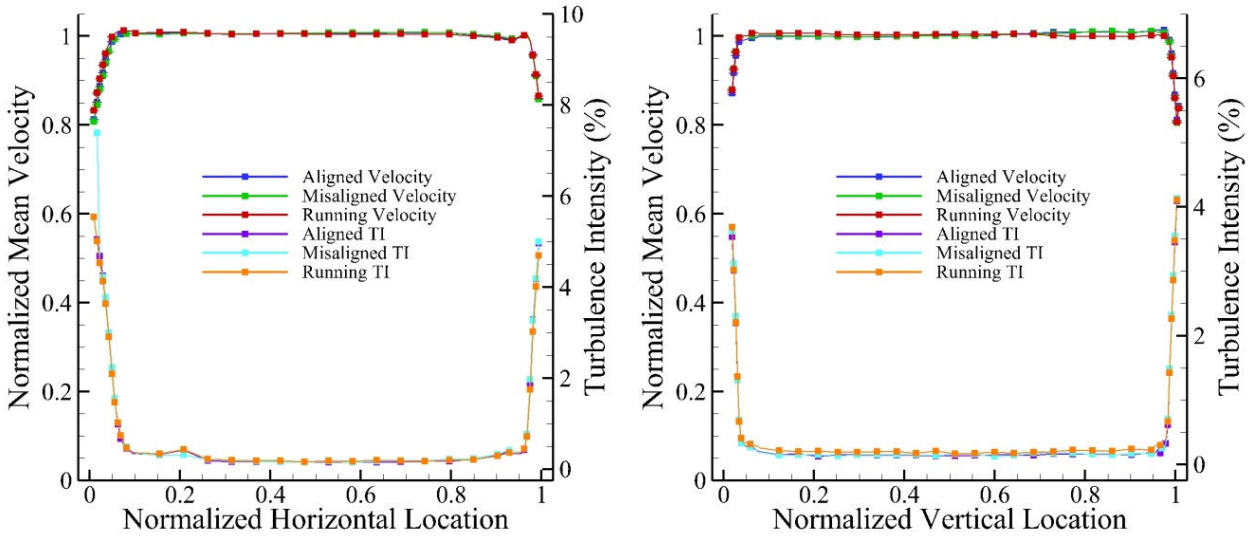

(a) Horizontal (b) Vertical

Figure 64: Velocity Profiles and Turbulence Intensities in Slot s0 for Different Cases.

the wake generator was aligned was $50.029 \pm 0.035 m/s$ and $49.972 \pm 0.037 m/s$ when it was misaligned. When the wake generator was running, the velocity varied from $49.991 m/s$ to $49.840 m/s$. However, phase averaged results acquired over 104 cycles at the same positions showed no cyclic pattern occurring with the wake generator running. The turbulence intensity in the freestream was about 0.20% with the wake generator running and about 0.15% with it off for the horizontal and vertical profiles. It increases, as expected, near the walls and in the boundary layer.

- *Test section outlet* (s3) - The wake of the cascade blades was acquired with the wake generator blades in the aligned and misaligned positions, and compared to the case without the wake generator installed. The velocity in the wake was slightly higher with the wake generator installed than without it (not shown in Figure 65). The test section bleeds changed the mass flow rate exiting the cascade and thus, caused a decrease in the overall velocity downstream of the cascade. With the wake generator installed, the bleeds were not used producing a higher mass flow rate; therefore, the velocity was also higher. The central test blade minimum velocity was about $5 m/s$ lower than the top and bottom test blades for the aligned case (figure 65). In this same case, the velocity between the blades started at about $80 m/s$ ($1.6 U_\infty$) on the pressure side and slowly decreased to about $78 m/s$ ($1.56 U_\infty$) on the suction side before the wake of the blades begins. The aligned profile was also shifted to the left by $l/L = 0.02$ and had a lower minimum velocity for each blade than the misaligned profile. The values there are from 0.50 compared to 0.25% in the "Velocity w/o Wake Generator" case. The overall velocity profile, in the misaligned case, decreased slightly with increasing position (from left to right) possibly due to flow restrictions caused by the wake generator blade locations. The aligned case turbulence intensity was larger

DISTRIBUTION A: Distribution approved for public release.

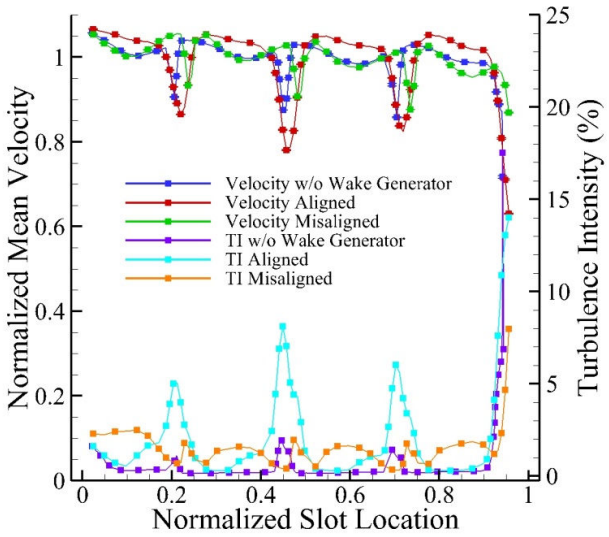

Figure 65: Comparison of the Velocity and Turbulence Intensity in the Wake of the Cascade Blades with the Wake Generator in Different Positions and without the Wake Generator Installed.

than the misaligned case with values of 5%, 9%, and 7% from bottom to top in the cascade (figure 65).

- *Phase averaged results in the wakes* - The results were phase averaged over 208 cycles for the central test blade and 104 cycles for the wake generator blade. The period of one cycle was calculated to be $T = 0.15385s$ based on the $6.5Hz$ wake passing frequency. The wake generator profile (figure 66a) was measured at the leading edge of the central test blade and shows an initial incoming velocity of $50m/s$ at $t0$ then a decrease starting at $t/T = 0.50$. The minimum velocity, $U = 38m/s$, occurred at $t/T = 0.7175$. After this time, the velocity increased back to $50m/s$ at $t/T = 1.0$. The effect of the passing wake on the central test blade wake (figure 66b) show that the wake profile initially looks very similar to the one of the misaligned case, then started to shift towards the suction side at $t/T = 0.50$ and grow wider, moving closer to the profile observed in the aligned case. The wake was about $l/L = 0.25$ wide at $t/T = 0$, and grew to $l/L = 0.41$ at $t/T = 0.75$. The minimum velocity was approximately $60m/s$ $(1.2U_\infty)$ and the wake very wide. After time $t/T = 0.75$, the wake shifts back towards the pressure side and eventually goes back to the same shape as at $t0$.

3.3.2 Test Section Spectral Content

- *Test section inlet* (s0) - The energy spectrums computed at the walls and center of slot s0 were acquired with the wake generator running and in the aligned position. The spectra at the test section walls (figure 67a) have the same very high frequency peaks observed without the wake generator at $1kHz$. The center of the test section

DISTRIBUTION A: Distribution approved for public release.

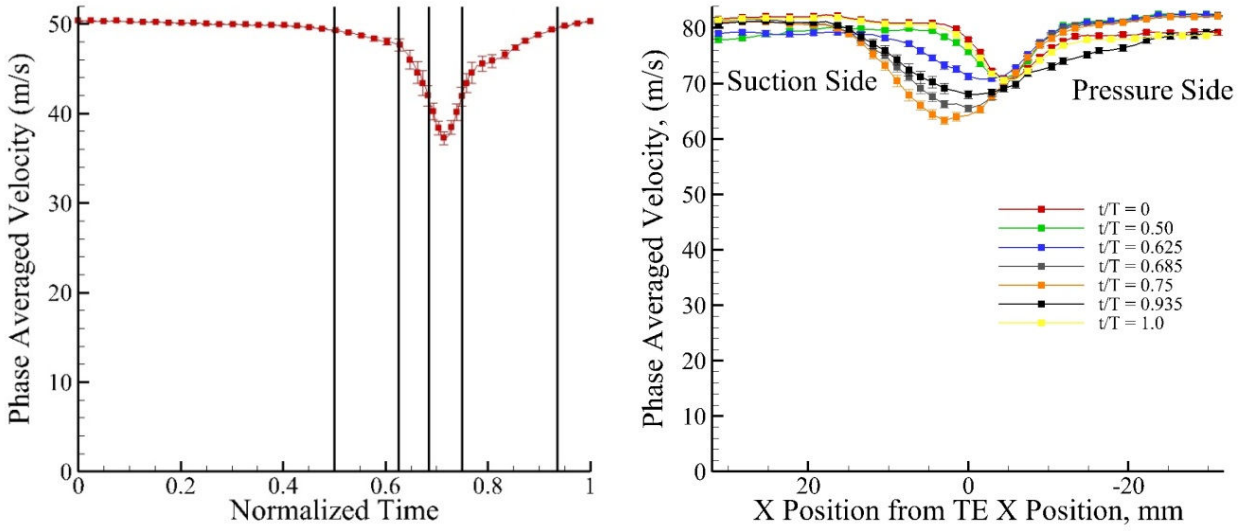

(a) (b)

Figure 66: (a) Phase Averaged Time Record of the Wake Generator Blade; (b) Phase Averaged Velocity Profile of the Central Test Blade Wake at Different Times

exhibited those same peaks, although at lower amplitude, and peaks at $11Hz$, $30Hz$ and $90Hz$ and lower overall energy levels due to lower turbulence level. While the $11Hz$ peak was consistent with the tunnel ducting, the 90 and $1000Hz$ peaks were associated with the insertion of the wake generator. In particular, the $1kHz$ peak was found to be close to a characteristic frequency based on the freestream velocity and the blade spacing, $2.5C_x$. This peak disappeared from the boundary layer spectrum as soon as the wake generator was immobilized in a steady position, while the rest of the spectra remained identical. The wake generator blade passing frequency ($6.5Hz$) was also clearly captured in the test section center rotating sprectra.

- *Test section outlet* (s3) - The wake of the central test blade (figure 68) was acquired with the wake generator blades aligned, misaligned and running; the wake of the wake generator blade was acquired in the aligned and running positions. The central test blade measurement was acquired at the location of the minimum velocity in the wake. The wake generator measurement was at $Y/H = 0.5$ and about $1in$ upstream of the leading edge of the central test blade ("A" in figure 62). The aligned case (figure 68a) has higher energy content compared to the misaligned case indicating a more turbulent wake. Peaks occured at about $30Hz$ and $900Hz$ in that case. Both of these peaks are most likely the same ones observed in the center of the test section. The $900Hz$ peak occured in the misaligned case as well, although shifted to slightly higher values since the distance from blade to vane was increased. The wake passing frequency was picked up along with the resulting harmonics in the running case. In Figure 68b, the expected $6.5Hz$ peak and its harmonics are present along with the same $900Hz$ peak observed upstream of the wake generator for the running case, yet with overall lower energy

DISTRIBUTION A: Distribution approved for public release.

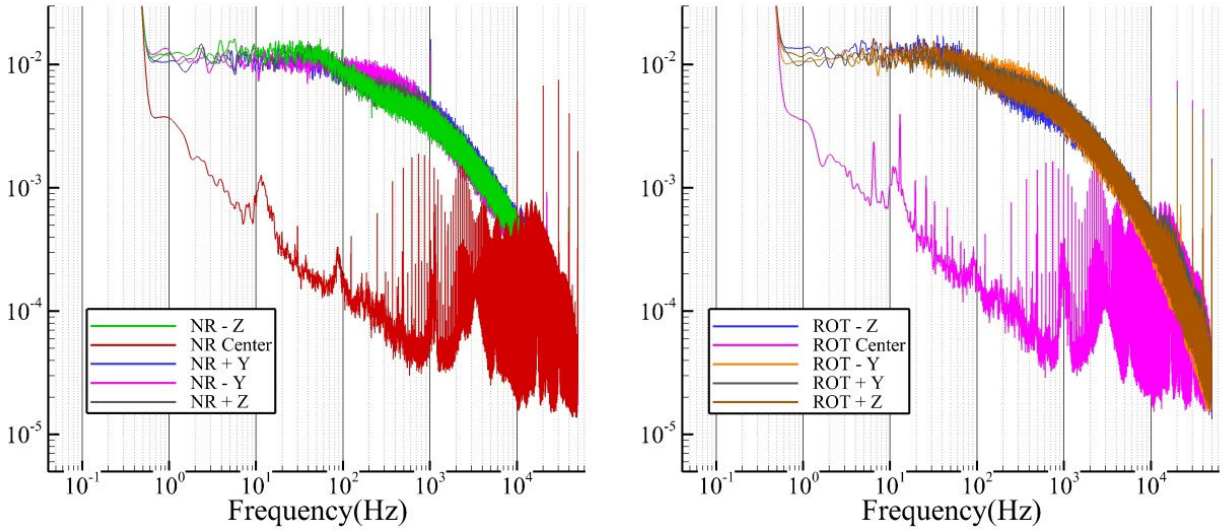

(a) Not Rotating (NR)

(b) Rotating (ROT)

Figure 67: Slot s0 Energy Spectrum at Different Positions.

content. The peak at $1000Hz$ in the aligned case was also a full order of magnitude larger than in figure 67 and 68a. For the running case, the peak at about $900Hz$ was actually wider and had lower peak energy because of the fluctuating blade spacing due to the blade motion.

3.3.3 Pressure Measurements

- *Time Independent Measurements* - Pressure measurements were acquired with the wake generator blades in the aligned and misaligned positions to compare with the phase averaged profiles acquired with the wake generator running. The coefficient of pressure distribution on the pressure tap blade at three locations along the blade height: $Y/H = 0.25, 0.50$ and 0.75 were acquired in the aligned and misaligned positions (figure 69). Overall the agreement was very good and the results were well within 10% of one another. Static comparisons (aligned and misaligned - figure 70) with AFOSR and CFD C_P values at $Y/H = 0.5$ show that the current experimental results agree very well with the CFD results and slightly less with the AFOSR results, in particular at the trailing edge. C_P on the suction side when the wake generator was not installed was the lowest compared to the aligned and misaligned cases, most likely due to the test section bleeds. As expected, the aligned case resulted in the highest coefficient of pressure on the suction side compared to the other two cases. The experimental results for the misaligned case followed the CFD curve almost exactly and wer only slightly shifted compared to the AFOSR results. In Figure 69, the coefficient of pressure distribution on the pressure tap blade is presented for three locations along the blade height: $Y/H = 0.25, 0.50$, and 0.75. The results are shown for the aligned and misaligned cases. In both cases, there is some slight disagreement between the spanwise sections on the

DISTRIBUTION A: Distribution approved for public release.

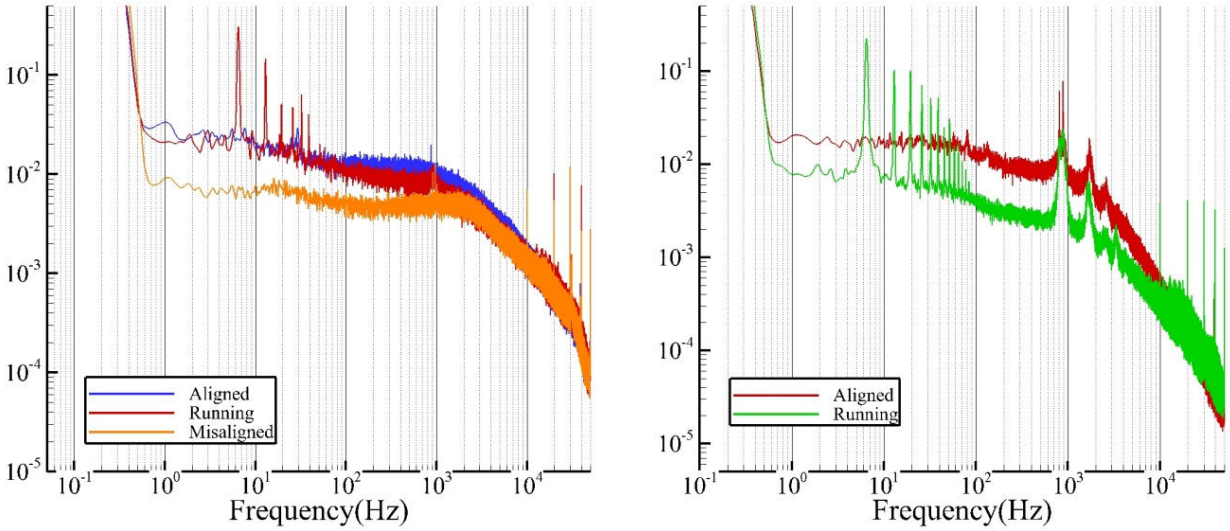

(a) Central Test Blade

(b) Wake Generator Blades

Figure 68: Energy Spectrum in the Wake of the Blades.

pressure side and on the suction side near the trailing edge. However, the overall agreement is very good and the results are well within 10% of one another. Figure 70 compares the experimental results with the previously presented computational and experimental results. Only the experimental results for the section at $Y/H = 0.50$ are presented to unclutter the graph. C_P on the pressure side appears to be the same for all cases, even at the leading edge. On the pressure side, the experimental results agree very well with the CFD results and slightly less with the AFOSR results. Again, the results at the trailing edge do not agree with the AFOSR data. C_P on the suction side when the wake generator is not installed is the lowest compared to the aligned and misaligned cases, most likely due to the test section bleeds. As expected, the aligned case resulted in the highest coefficient of pressure on the suction side compared to the other two cases; therefore, it the blade produced the least amount of lift in that case. The experimental results for the misaligned case follow the CFD curve almost exactly and are only slightly shifted compared to the AFOSR results.

- *Phase Averaged Results* - The pressure distribution on the blade profile was captured when the wake generator was running with a wake passing frequency of $6.5Hz$ over a total of 104 cycles (figure 71). The stagnation point at the leading edge of the blade fluctuated as the wake passed, varrying from 0.9, initially, to 1.0 then down to 0.8 at $t/T = 0.90$ and indicating that the freestream flow lost energy due to losses occurring in the wake of the wake generator blade. Overall, the C_P value increased homogeneously until about $t/T = 0.60$ as a result of the flow accelerating and recovering after a wake passage, and decreased as the wake passed. The suction side was first impacted by the wake and therefore C_P values decreased there first. The pressure side was impacted $t/T = 0.10$ later, with a decrease in C_P. Overall, the fluctuations were very small and did not affect the airfoil lift by much.

DISTRIBUTION A: Distribution approved for public release.

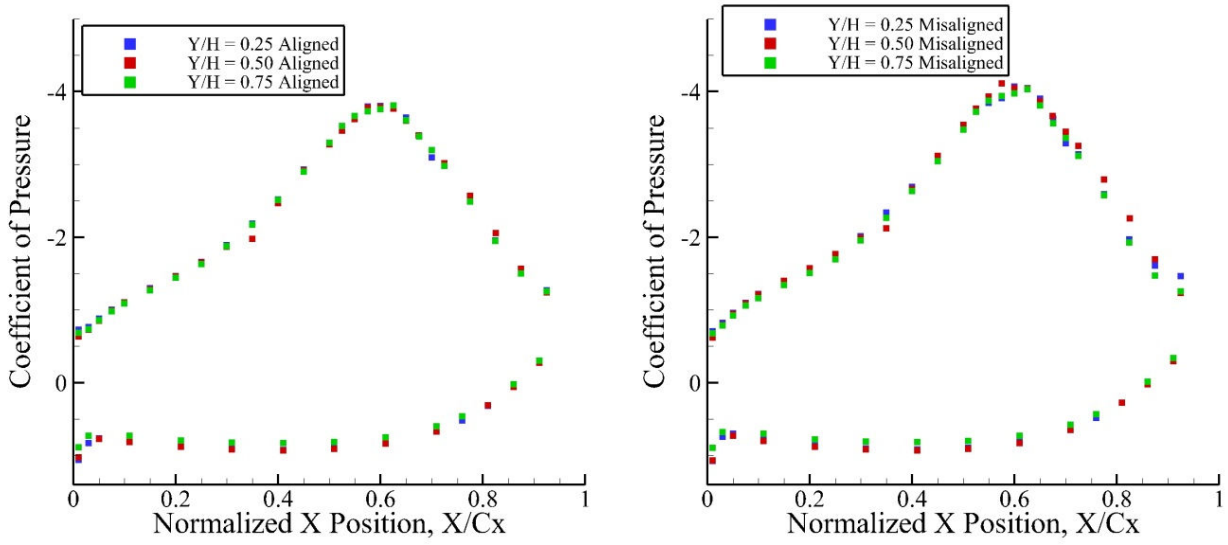

(a) Aligned (b) Misaligned

Figure 69: Coefficient of Pressure Distribution on the Pressure Tap Blade with the Wake Generator Blades in Different Positions.

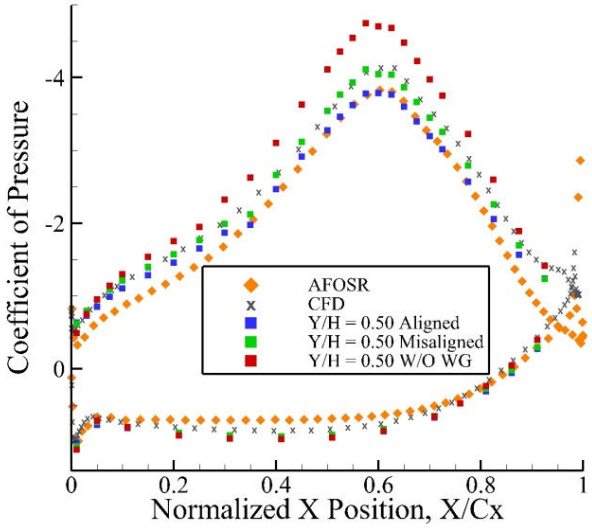

Figure 70: Comparison of the Coefficient of Pressure Distribution with the AFOSR and CFD Results.

DISTRIBUTION A: Distribution approved for public release.

3.4 Particle Image Velocimetry and Mie scattering visualizations

PIV measurements and Mie scattering visualizations were realized using the optical setup described previously. The reference field U_0 is shown in figure 72 with the conveyor off, and the wind tunnel operating at $Re = 450,000$. It shows the flow acceleration over the suction side of the blade, up to twice the incoming free-stream velocity. In figure 73, the normalized phase averaged velocity field for the cascade running at $Re = 450,000$, compared to the velocity field without the conveyor running. The phase location is so that the wake impinges on the blade at the phase locked position $\phi = 0$ (or $\phi = 1$). The absolute velocity field fluctuates very little throughout the conveyor cycle when compared to the field without the conveyor running. The velocity difference between the field at phase locked position ϕ and the field without the conveyor running ($\|U - U_0\| / U_\infty$) is provided in figure 74. The wake is clearly evidenced impacting the blade with a momentum deficit of approximately 10% with respect to the undisturbed field. The corresponding vorticity field is shown in figure 75 evidences the phase averaged vorticity field associated with the wake as it approaches the blade.

Finally, figure 76 shows Mie scattering visualizations of the blade with a film cooling jet located at the $x/C_x = 33\%$ location, operating at a blowing ratio of $BR_\infty = 0.5$, based on the free stream velocity such that $BR_\infty = U_j/U_\infty$. While the image at the top shows an undisturbed film cooling jet when the wake is away from the blade, the following images show the impact of the wake impinging on the blade and the disruptions of the film it creates.

DISTRIBUTION A: Distribution approved for public release.

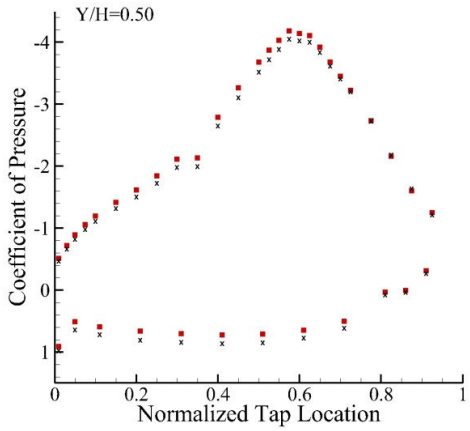

(a) $t/T = 0.0$

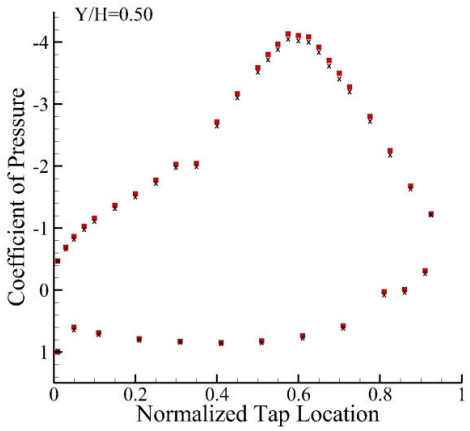

(b) $t/T = 0.2$

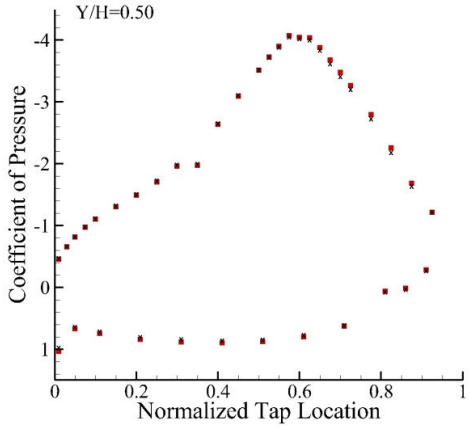

(c) $t/T = 0.4$

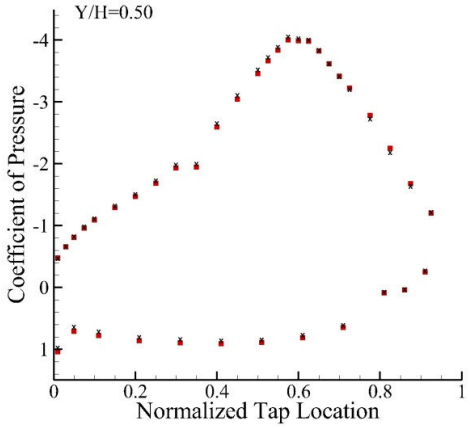

(d) $t/T = 0.6$

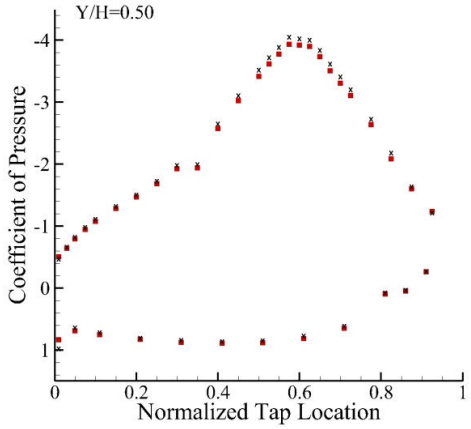

(e) $t/T = 0.8$

Figure 71: Phase Averaged Coefficient of Pressure Profile ($Y/H = 0.5$) at Different Times during a Cycle (*red symbols*) and time averaged coefficients of pressure profile (black symbols).

DISTRIBUTION A: Distribution approved for public release.

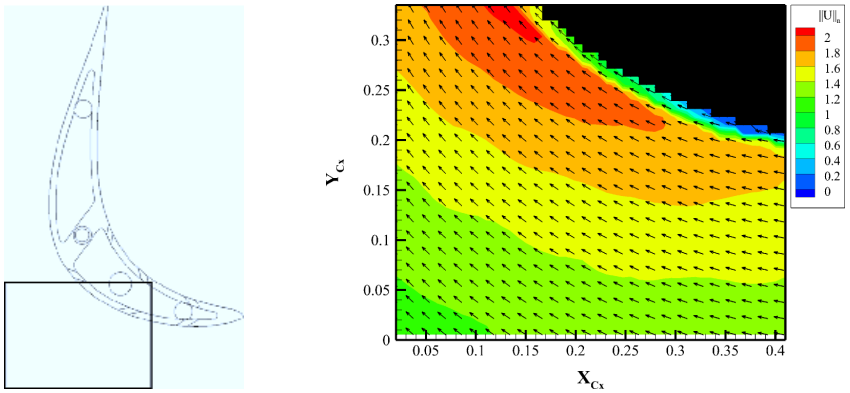

(a) (b)

Figure 72: a) Field of view; b) Normalized velocity magnitude with conveyor off - $\|U_0\|/U_\infty$, for $Re = 450,000$

DISTRIBUTION A: Distribution approved for public release.

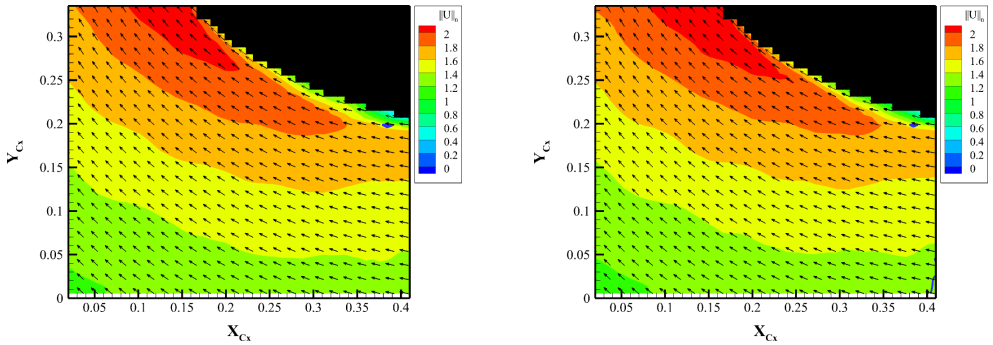

(a) $\phi = 0.13$ (b) $\phi = 0.26$

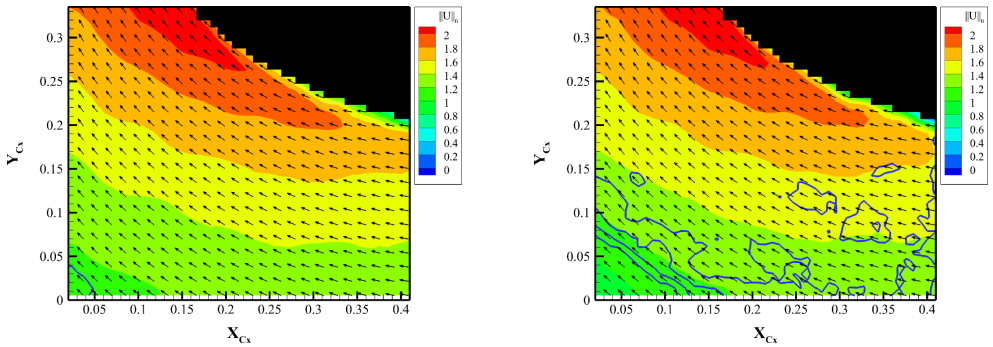

(c) $\phi = 0.40$ (d) $\phi = 0.53$

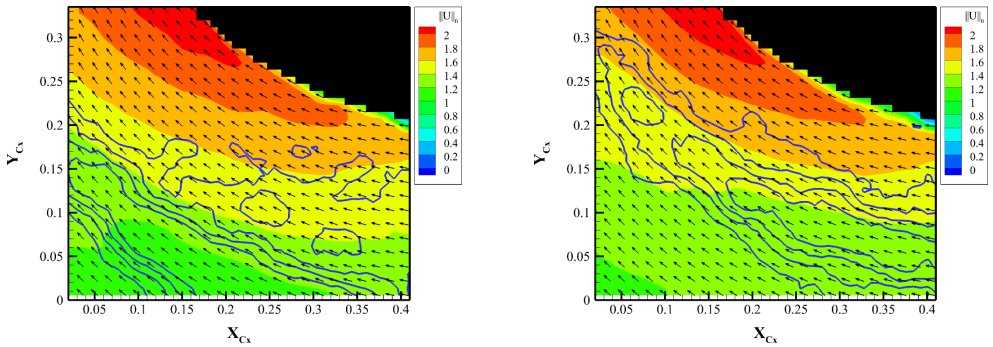

(e) $\phi = 0.66$ (f) $\phi = 0.80$

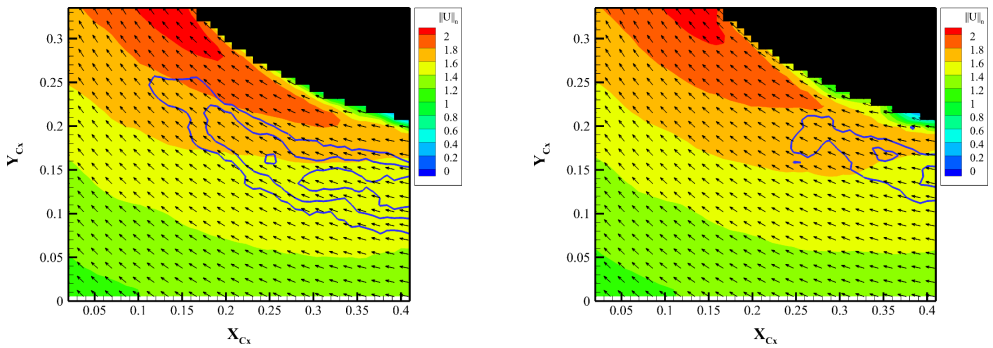

(g) $\phi = 0.93$ (h) $\phi = 1$

Figure 73: Phase Averaged Velocity magnitude $\|U\|/U_\infty$ with conveyor running, and $Re = 450,000$

DISTRIBUTION A: Distribution approved for public release.

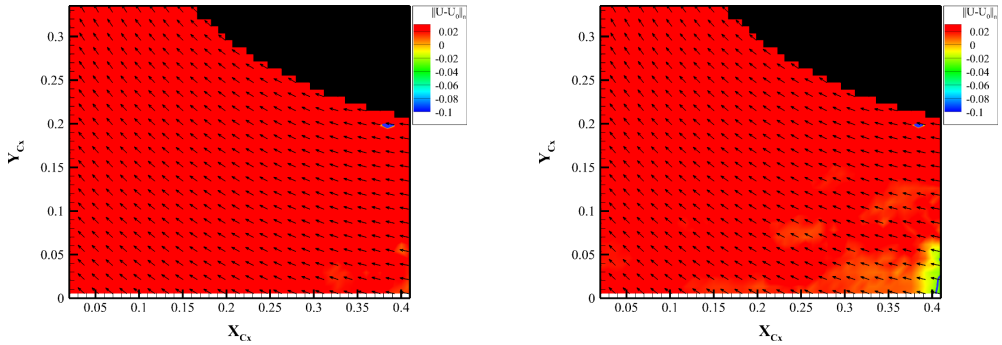

(a) $\phi = 0.13$ (b) $\phi = 0.26$

(c) $\phi = 0.40$ (d) $\phi = 0.53$

(e) $\phi = 0.66$ (f) $\phi = 0.80$

(g) $\phi = 0.93$ (h) $\phi = 1$

Figure 74: Phase Averaged Velocity magnitude difference $\|U - U_0\| / U_\infty$ with conveyor running, and $Re = 450,000$

DISTRIBUTION A: Distribution approved for public release.

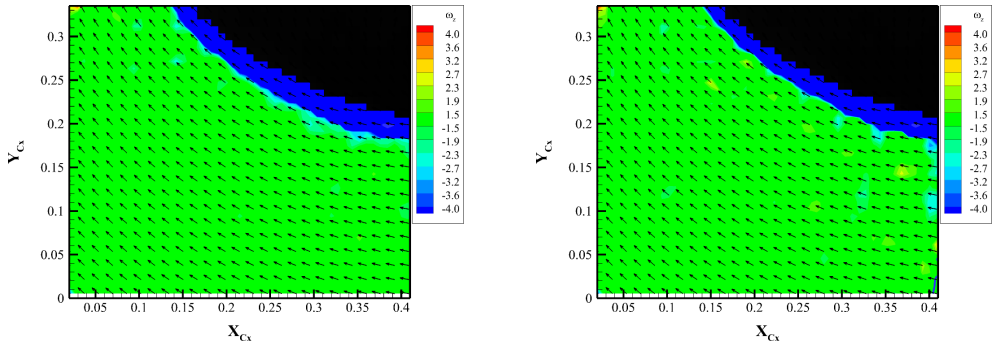

(a) $\phi = 0.13$

(b) $\phi = 0.26$

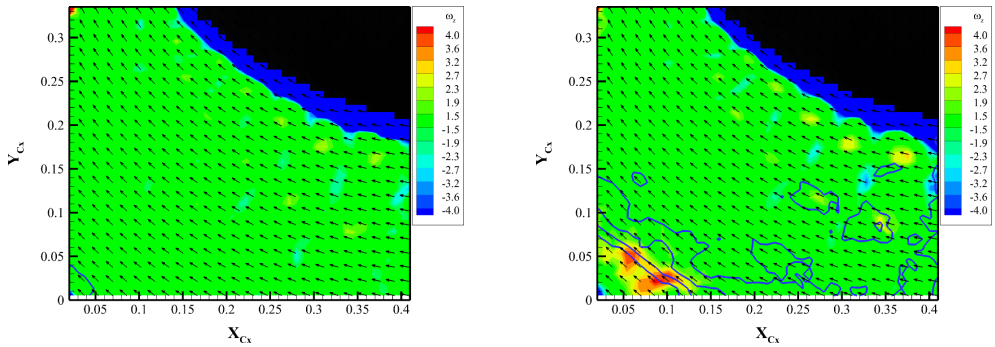

(c) $\phi = 0.40$

(d) $\phi = 0.53$

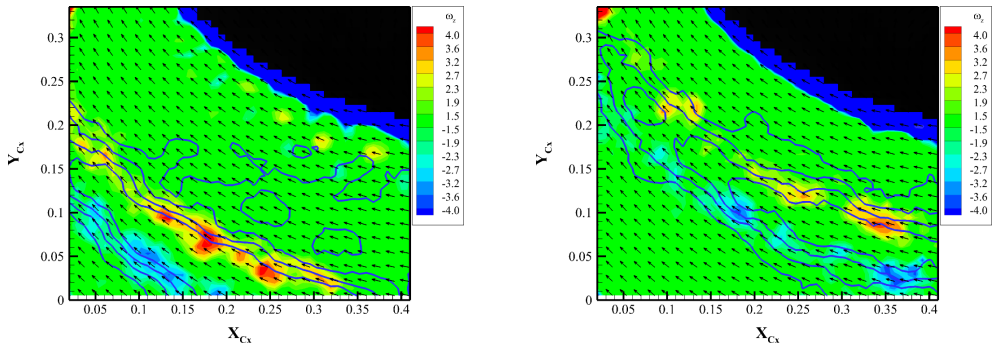

(e) $\phi = 0.66$

(f) $\phi = 0.80$

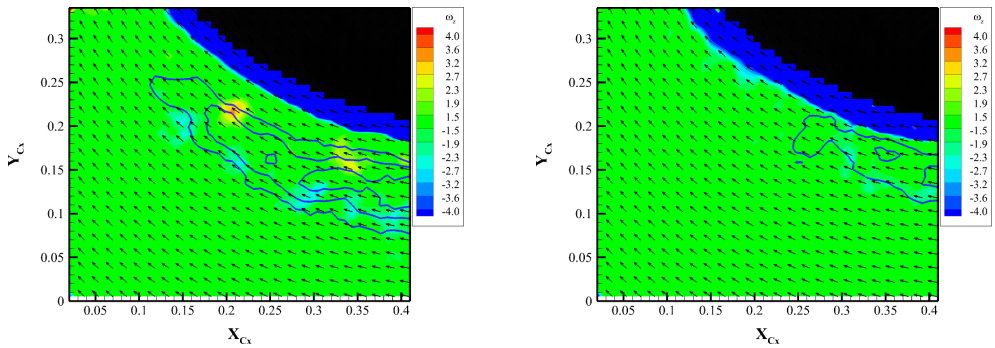

(g) $\phi = 0.93$

(h) $\phi = 1$

Figure 75: Phase Averaged Vorticity field of the normalized velocity field

DISTRIBUTION A: Distribution approved for public release.

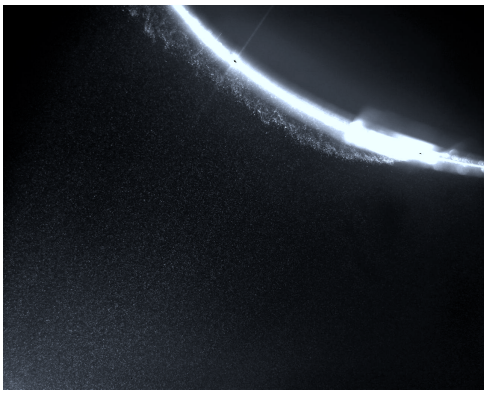

(a) Undisturbed film cooling jet

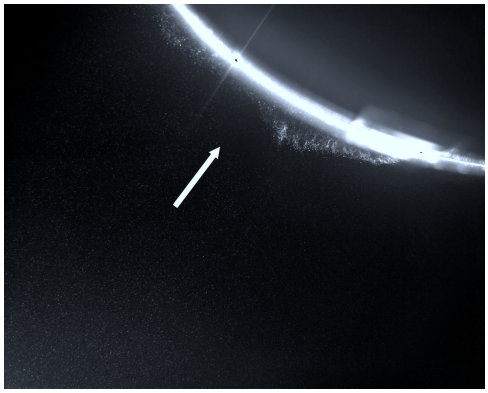

(b)

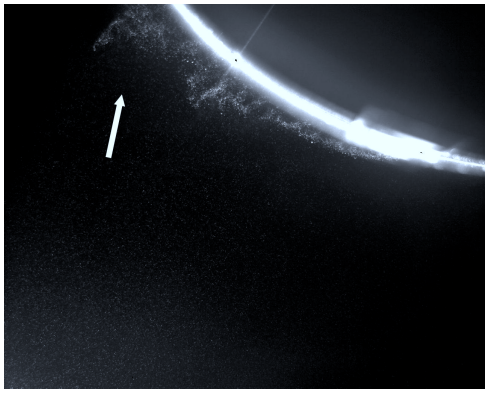

(c)

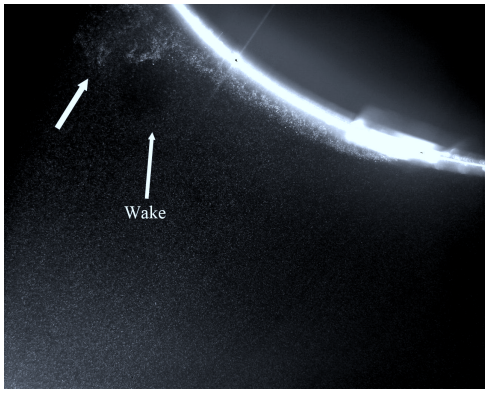

(d)

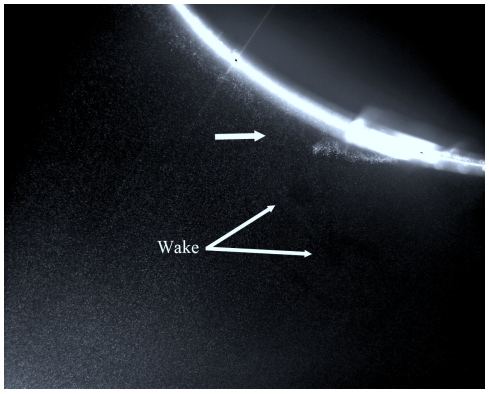

(e)

Figure 76: Undisturbed and disturbed ($\phi = 1$) film cooling jets at $BR = 0.5$, with conveyor running, and $Re = 450,000$.

DISTRIBUTION A: Distribution approved for public release.

Part III

Optimization, Reduced Order Modeling and Flow Control

DISTRIBUTION A: Distribution approved for public release.

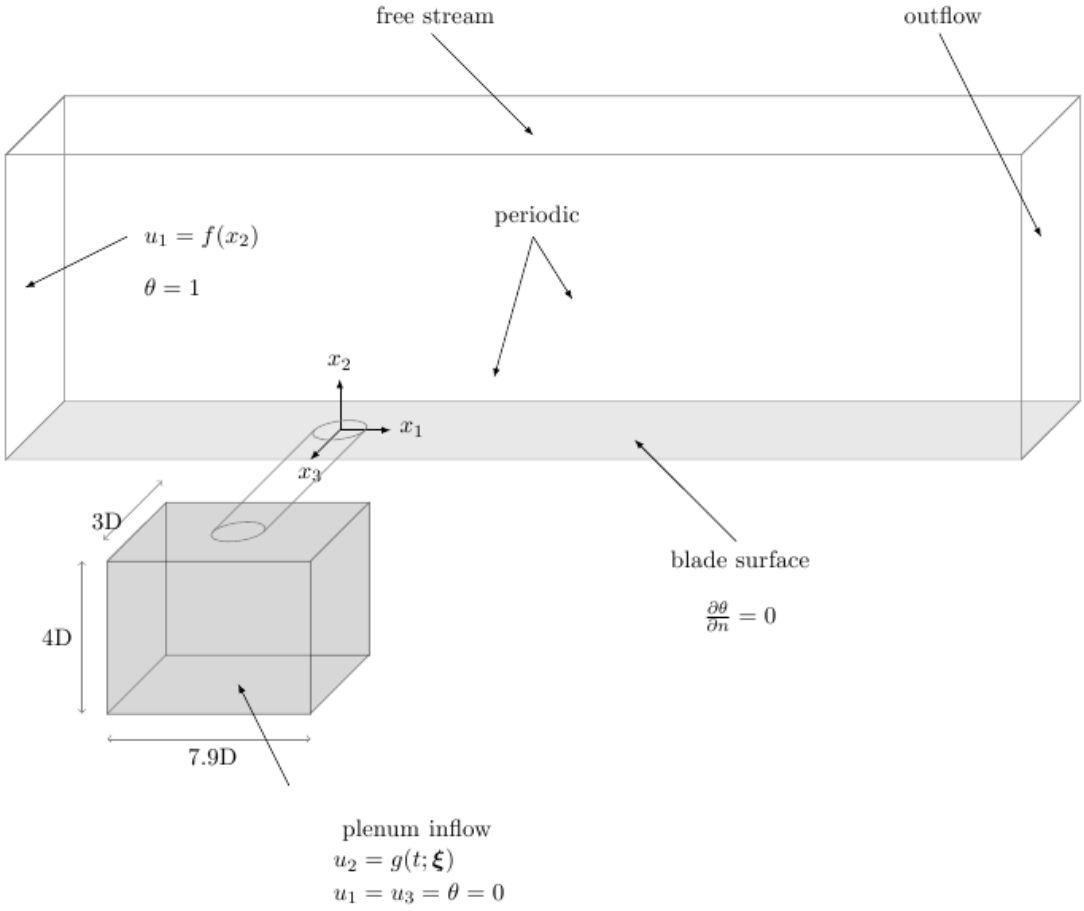

Figure 77: Schematic of the jet in cross-flow

1 Optimization of Forced Film Cooling Jets

1.1 Methodology

The incompressible Navier-Stokes/energy equations are solved without any use of a turbulence model by resolving all time and space scales. We consider $u = u(x,t;\xi)$, $p = p(x,t;\xi)$ and $\vartheta = \vartheta(x,t;\xi)$ where $\xi = (\xi_1, \xi_2)$ is a two- dimensional vector of design or control parameters. In the current study, design parameters are the duty cycle DC, and the non-dimensional pulsation period $Tp = U_\infty / Df$, where U_∞ is the cross-flow velocity, D is the jet diameter and f is the dimensional pulsation frequency.

As it will be explained later in this section DC and Tp are related to ξ_1 and ξ_2 through a linear mapping. The Reynolds number is defined as $Re = U_\infty D/\nu$, where ν is the kinematic viscosity. Figure 77 shows the schematic of the problem. The velocity signal at the bottom of the plenum, $g(t;\xi)$ is fixed by specifying the design parameters (DC, Tp) and the maximum and minimum plenum-inflow velocity. In figure 78, the generic form of the signal $g(t;\xi)$ is

DISTRIBUTION A: Distribution approved for public release.

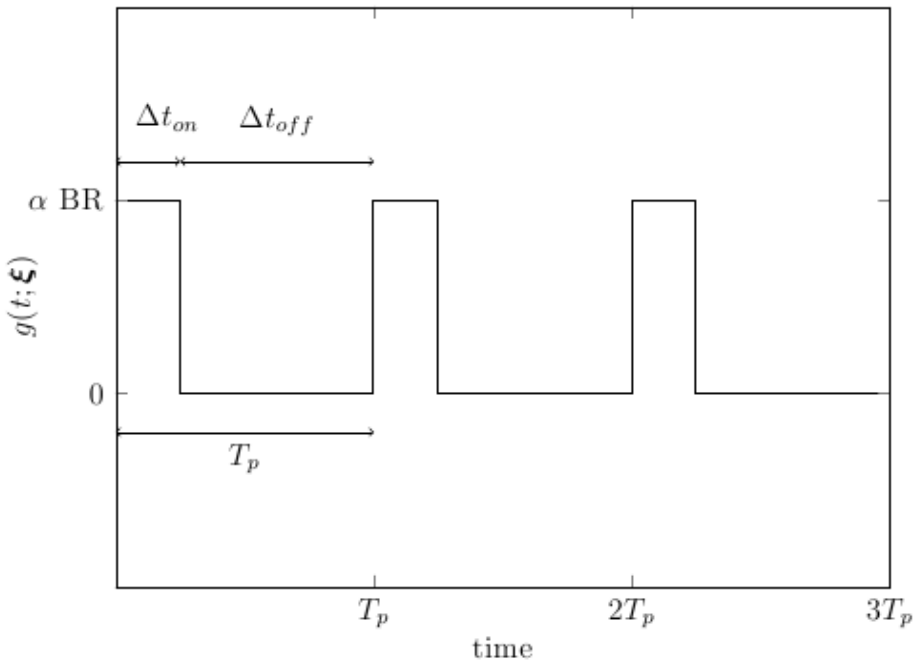

Figure 78: Blowing ration signal $g(t;\xi)$

shown. The amount of the time that the jet is on within each full period is denoted by Δt_{on} and therefore $DC = \Delta t_{on}/Tp$. We also introduce τ that shows the time percentage during a cycle. Therefore $\tau < DC$ represents the period that the jet is on and $\tau > DC$ when the jet is off. When the jet is on, the vertical velocity at the bottom of the plenum is equal to αBR. Here $\alpha = \pi D^2/4A_p$, with A_p being the area of the bottom of the plenum, accounts for the ratio of the area of the delivery tube to that of the plenum. When the jet is off, it is turned completely off and during this time the net mass flow rate through any x_2-section at the plenum or delivery tube is zero.

1.1.1 Optimization Problem

Our objective is to maximize the film cooling effectiveness as a function of duty cycle and pulsation period. To measure the effectiveness of film cooling we first define the spanwise-averaged film cooling effectiveness which is given by:

$$\eta(x_1,\xi) = \frac{1}{w\,(t_f - t_i)} \int_{t_i}^{t_f} \int_{-w/2}^{w/2} (1 - \theta\,(\mathbf{x}, t; \xi))\,|_{x_2=0} dx_3 dt$$

with w being the width of the cooled surface, t_i and t_f are the beginning and the end of the period over which the time-averaged quantities are calculated. In order to obtain an overall measure of the film cooling effectiveness, we further calculate the streamwise average of $\eta(x_1;\xi)$. This results:

$$\tilde{\eta}(\xi) = \frac{1}{x_{1_e} - x_{1_s}} \int_{x_{1_s}}^{x_{1_e}} \eta(x_1;\xi) dx_1$$

DISTRIBUTION A: Distribution approved for public release.

where x_{1_s} and x_{1_e} are the two ends of the interval in the streamwise direction within which the average film cooling effectiveness is calculated. The overall film cooling effectiveness, $\tilde{\eta}(\xi)$, is a function of two independent variables DC and Tp, with BR and geometry fixed. The goal is to find the DC and Tp at which the average film cooling effectiveness, $\tilde{\eta}(\xi)$, is globally maximum, and to understand the reasons that lead to this condition.

1.2 Simulation details

In all the cases in this study we perform direct numerical simulation on the jet in cross-flow with the schematic of the problem shown in figure 77. The origin of the coordinate system is at the center of the jet exit and x_1 is aligned with the streamwise direction, x_2 with the direction normal to the cooled surface and x_3 with the spanwise direction. The plenum has the length, height and width of $7.9D$, $4D$ and $3D$ respectively. The length of the delivery tube is $3.5D$ and the inclination angle is 35 degree. The mainstream domain, where the cross-flow and the coolant interact, spans the volume with the size of $22D \times 10D \times 3D$.

The center of the jet exit is located $7D$ downstream from the cross-flow inlet. The cross-flow boundary condition is assumed to be a laminar boundary layer flow with boundary layer thickness of $\delta_{99\%}/D = 0.5$ where $\delta_{99\%}$ is the thickness that the streamwise velocity in the boundary layer reaches 99% of the free-stream velocity. On the top boundary plane, free-stream flow is assumed with $u(x_1, 10, x_3) = (U_\infty, 0, 0)$ and $\vartheta(x_1, 10, x_3) = 1$, and on the spanwise direction periodic boundary condition is enforced. The periodic boundary condition mimics the situation where a row of holes are arranged in the spanwise direction. In the current case, the center-to-center distance between two consecutive holes is $3D$. A zero normal derivative boundary condition is assumed at the outflow. The uniform boundary condition $g(t;\xi)$ (see figure 78) is used for the vertical velocity component u_2 at the bottom of the plenum with $u_1 = u_3 = 0$ and $\vartheta = 0$. The area scaling factor is $\alpha = 0.0331$. As noted earlier, each pair of the design variables (DC, Tp), and the peak blowing ratio (the blowing ratio when the jet in on and is set to 1.5) specifies the signal $g(t;\xi)$. The Reynolds number, $Re_j = U_j D/\nu$, based on the jet space-averaged velocity (when the jet is on) is 1500 throughout and Prandtl number is $Pr = 1$. For all the wall boundaries, adiabatic condition is assumed for temperature. The computational time step was roughly 0.001. All simulations were advanced at least $40D/U_\infty$ before the statistics are collected. The statistics are then collected for approximately another $40D/U_\infty$. Care was taken to ensure that the calculation of the statistics starts at the beginning of a pulsation cycle and finishes at the end of another pulsation cycle. Additional sampling did not change the result.

1.2.1 Computational Mesh

We use hexahedral elements of spectral order of three and four in the current simulations. Figure 79(a) shows the three-dimensional view of the grid. To generate the grid, quadrilateral meshes were first generated in the x_1–x_3 planes in the main-stream domain, the delivery tube and the plenum. The quadrilateral elements exactly match across the common faces in between the volume parts. The two-dimensional mesh was then swept along the x_2 direction in the mainstream domain and plenum and along the axis of the cylinder in the delivery tube. The height of the first element in the cross-flow boundary layer is $0.06D$. The height of the elements increases (with 16 elements) using hyperbolic distribution to $0.3D$ at $x_2 = 4$. Two elements were used from $x_2 = 4$ to the top boundary at $x_2 = 10$. Note that flow in this region

DISTRIBUTION A: Distribution approved for public release.

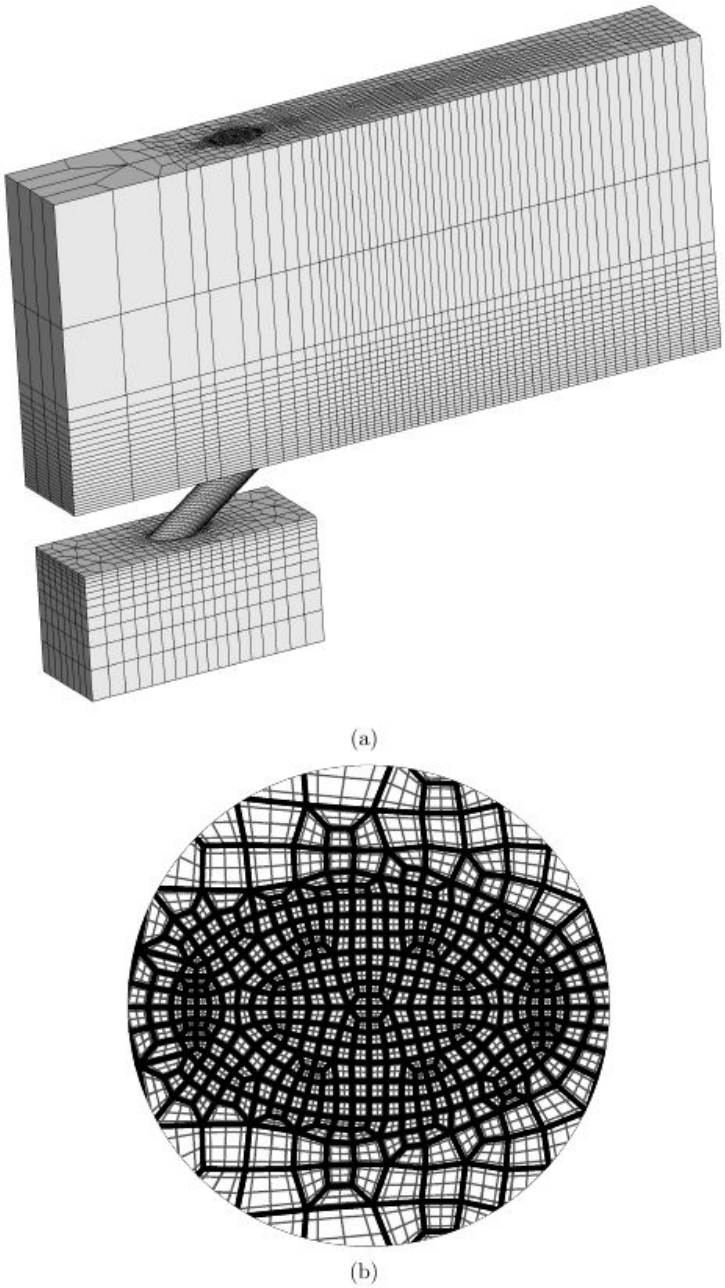

Figure 79: Unstructured hexahedral grid; (a) three-dimensional view; (b) x_1–x_3 view of the grid in the vicinity of the jet exit with spectral order $m = 4$.

DISTRIBUTION A: Distribution approved for public release.

remains steady with small gradients which justifies using large elements. Along the delivery tube, 16 elements with uniform distribution were used. The finest elements are found in the delivery tube, especially in the boundary layer region where flow is highly unsteady with steep gradients. A close x_1–x_3 view of the mesh in the vicinity of the jet exit is shown in figure 79(b). In the plenum, 11 elements were used in the x_2 direction with $\Delta x_2 = 0.06D$ for the topmost elements and $\Delta x_2 = 0.12D$ for the first element in the bottom. The elements in between were distributed using hyperbolic distribution. In total, 48162 hexahedral elements were created. In each element spectral polynomials with order three or four were used. This amounts to a total degree of freedom of 3.1 millions for spectral order three, and 6.0 millions for spectral order of four.

1.3 Results and Discussion

1.3.1 Effect of pulsation on film cooling performance

In examining these results, it is important to remember that the blowing ratio fluctuates between 1.5, when the valve is open, and 0, when the valve is closed, and any comparisons with the steady $BR = 1.5$ case is therefore not at a constant coolant mass injection rate when integrated over a time duration. For the pulsed cases, the integrated coolant injection rates are lower, and an equal or greater cooling effectiveness than the baseline steady jet of $BR = 1.5$ represents an improvement in the cooling strategy. We choose the pulsation period to be in the range of $Tp \in [0.5, 5]$, which corresponds to Strouhal number in the range of $St \in [0.2, 2]$, and duty cycle in the range of $DC \in [0.05, 1]$. All the sampling points with $DC = 1$ correspond to a steady jet and therefore only one simulation was performed for these points. Figure 80 shows the non-dimensional temperature at the x_2-plane which represents the cooling effectiveness on the surface and the flow temperature at the exit of the coolant hole. As noted earlier, the two control parameters being varied include the duty cycle (DC) and the time period of pulsation (Tp) which is inversely proportional to frequency or Strouhal number. The rightmost column represents the steady blowing condition at a BR of 1.5. The signature of the near-hole jet blow off and the downstream spread of the coolant jet on the surface can be seen. Both duty cycle and time period have important and significant influence on the cooling effectiveness. In figure 80, it is observed that the cooling effectiveness generally improves at a lower duty cycle (which represents a lower amount of integrated coolant injection) and higher frequencies, and that optimal conditions exist with global maxima in the lower left quadrant of the DC–Tp design space within the range of design parameters considered. However, the integrated values of the cooling effectiveness do not show any distinct linear or monotonic behavior in the design space, and local maxima or peaks are obtained at other points as shown later in figure 87. More discussions on the mechanisms leading to the global maxima are discussed in the next section for the case with $DC = 0.09$ and $Tp = 1.16$, which is a point close to the global-maxima condition. In figure 81 the temperature distributions at $Tp = 1.16$ for increasing DC from 0.09 to 1 (steady injection) are shown. One can see that in the baseline condition ($DC = 1$), the coolant jet is characterized by unsteady vortical structures that entrain and mix out the cross-flow. The cross-flow penetration to the surface is clearly evident in the longitudinal structures at elevated temperatures near the surface. As DC is reduced from 1, the turbulent structures and the near-wall thermal field are clearly influenced, with the lower duty cycles showing better organized structures and lower temperatures (presence of

DISTRIBUTION A: Distribution approved for public release.

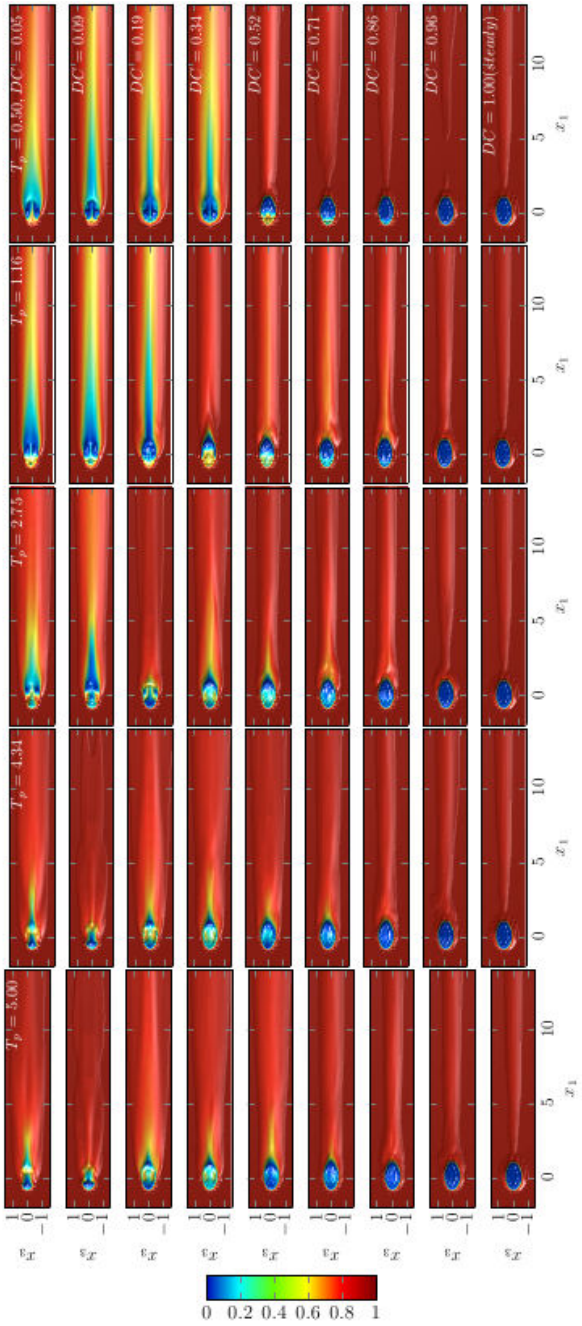

Figure 80: Time-averaged temperature contours for quadrature points on cooled surface ($x_2 = 0$). Each row: constant Tp; Each column: constant DC.

DISTRIBUTION A: Distribution approved for public release.

more coolant) near the wall. For DC larger than 0.34, the jet lift-off is observed immediately after entering the main domain resulting in poor coverage of the surface; this can also be seen in figure 80 where both the lateral and streamwise coverage of the coolant is poor. As DC is further decreased the coolant remains close to the surface and the cross-flow entrainment under the coolant jet and close to the surface is reduced, and therefore lower coolant temperatures near the surfaces are observed. Thus the film cooling provides an effective coverage. These observations translate to higher cooling effectiveness as it is also observed in figure 80. Further discussions on why the lower DC's (where the integrated coolant mass flowrate is lower) leads to improved cooling effectiveness is provided later, and is related to the interaction between the mainstream and the coolant flow leaving the delivery tube. Figure 82 shows the instantaneous temperature distribution in the vertical mid-plane ($x_3 = 0$) at $DC = 0.52$ with increasing time periods from 0.67 to 5. At higher time periods of $Tp \geq 1.89$, the coolant jet exhibits discrete vortex rings that are formed during the on-protion of the pulsation cycle. The same vortex structures were also recognized by (67) for a pulsed vertical jet. These vortex rings are responsible for carrying the coolant flow downstream of the jet hole. The distance between successive vortex rings increases as the pulsation frequency decreases or the time period increases. Note that the instantaneous blowing ratio during the on-portion of the cycle is $BR = 1.5$ which roughly becomes the velocity at which the vortex rings are convected along the axis of the delivery tube (35 degree with x_1). As a result, in figure 82, a distance of $d = 1.5Tp$ can be observed between two successive vortex rings. Since BR and DC remain unchanged for all the cases shown in figure 82, the higher pulsation period translates to more amount of the injected coolant, leading to the formation of larger and stronger vortex rings and greater instantaneous vertical-penetration. A visible trailing column can be seen for $Tp \geq 3.61$. For the case with $Tp = 4.34$ the upper shear layer shows strong oscillations, caused by the traveling vortices created when the flow leaves the plenum and enters the delivery tube and undergoes a sharp turn. As a result an unsteady separation bubble forms in the upstream side of the tube, generating vortical structures that for a large enough pulsation period, such as $Tp = 4.34$, can travel the pipe length of $3.5D$ and affect the upper shear layer; a phenomena that is absent in smaller pulsation periods.

1.3.2 Optimal and sub-optimal behavior

In this section we investigate three cases in more details. In the previous section it was clear that lower duty cycle and high pulsation frequency (lower Tp) leads to higher film cooling effectiveness. The first case that we consider has $DC = 0.09$ and $Tp = 1.16$ which lies in the high film-cooling-effectiveness region in the design space and shows near-optimal film cooling performance (see figure 87). Temperature contours at four time instants of one pulsation cycle for this case are shown in figure 83. Note that τ represents the percentage of time during each cycle with $\tau = 0\%$ being the beginning and $\tau = 100\%$ the end of the cycle, and thus for $\tau < DC$ the jet is on and for $\tau > DC$ the jet is completely off. At $\tau = 4\%$ the jet is on and the injected coolant initiates hairpin vortices (shown by arrows in figure 83) in the shear layer. The hairpin vortices are periodically generated and convected downstream. As the valve closes at $\tau = 9\%$, the cross-flow enters the delivery tube from the leading edge of the hole, pushing the coolant in the delivery tube towards the downstream side of the hole and the coolant leaves the tube from the downstream edge of the hole (this adjustment in the exit flow is driven by mass conservation since the plenum-inflow was abruptly shut off). The ingestion of the cross-flow into the delivery tube continues by forming a vortex ring that

DISTRIBUTION A: Distribution approved for public release.

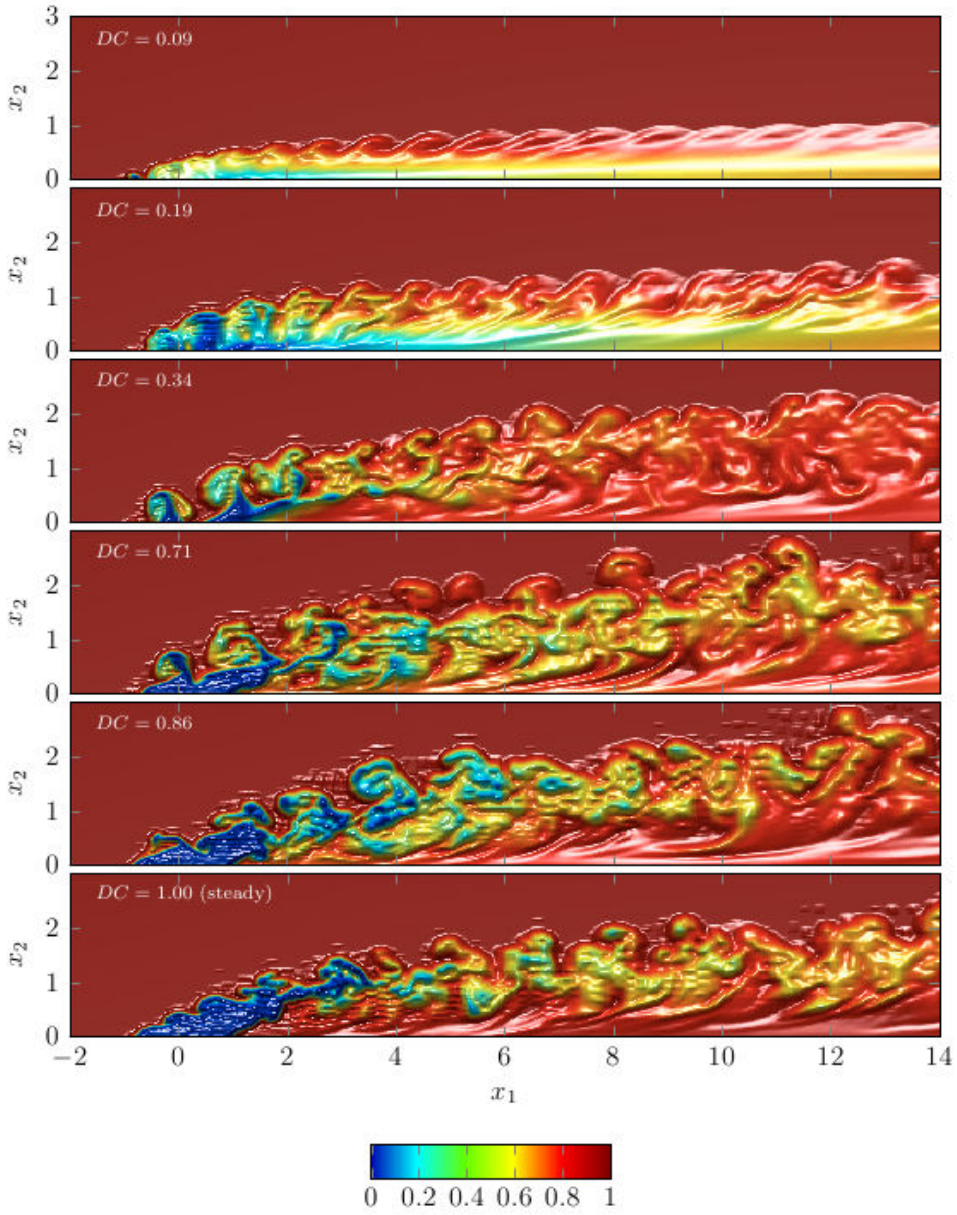

Figure 81: Instantaneous temperature surface in the mid-plane ($x_3 = 0$) with constant pulsation period of $Tp = 1.16$.

DISTRIBUTION A: Distribution approved for public release.

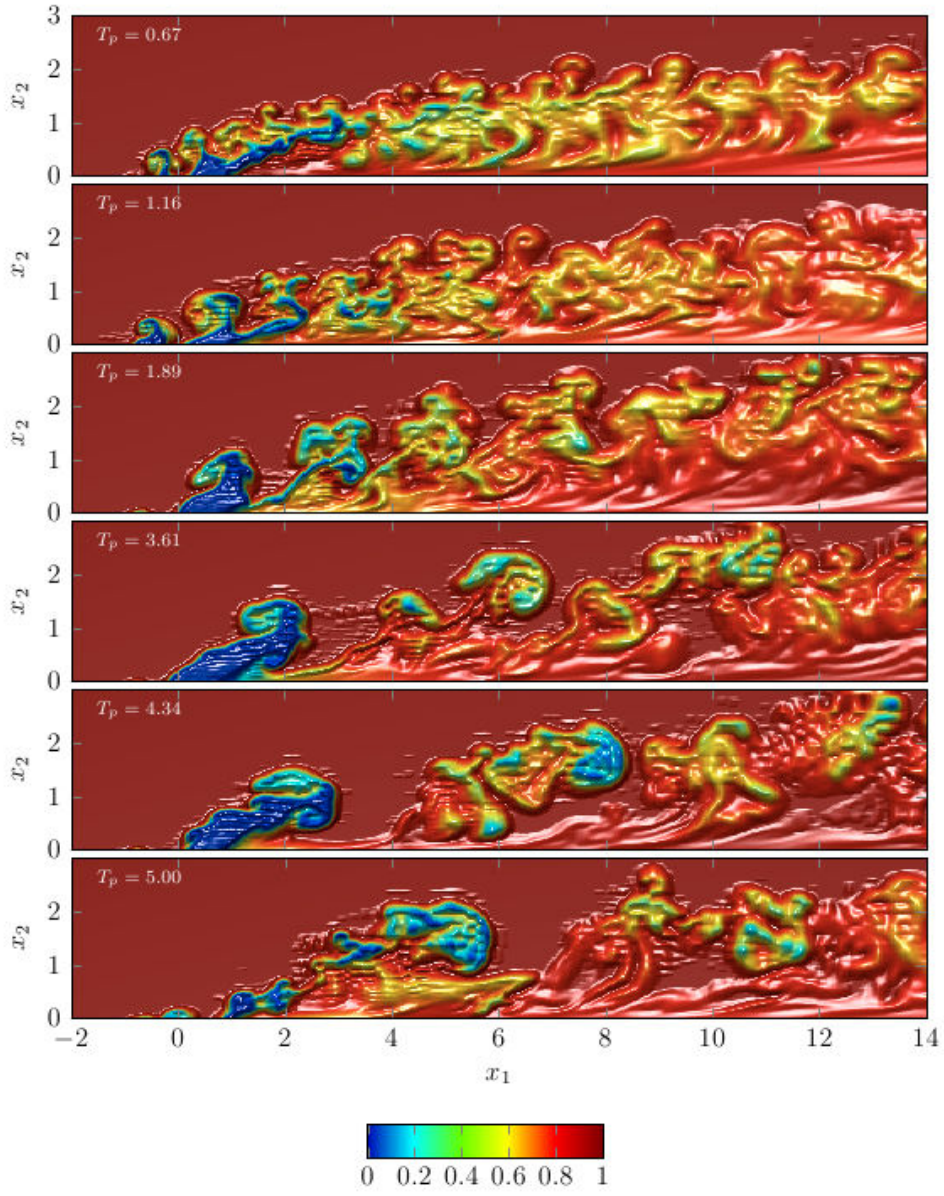

Figure 82: Instantaneous temperature surface in the mid-plane ($x_3 = 0$) with constant duty cycle of $DC = 0.52$.

DISTRIBUTION A: Distribution approved for public release.

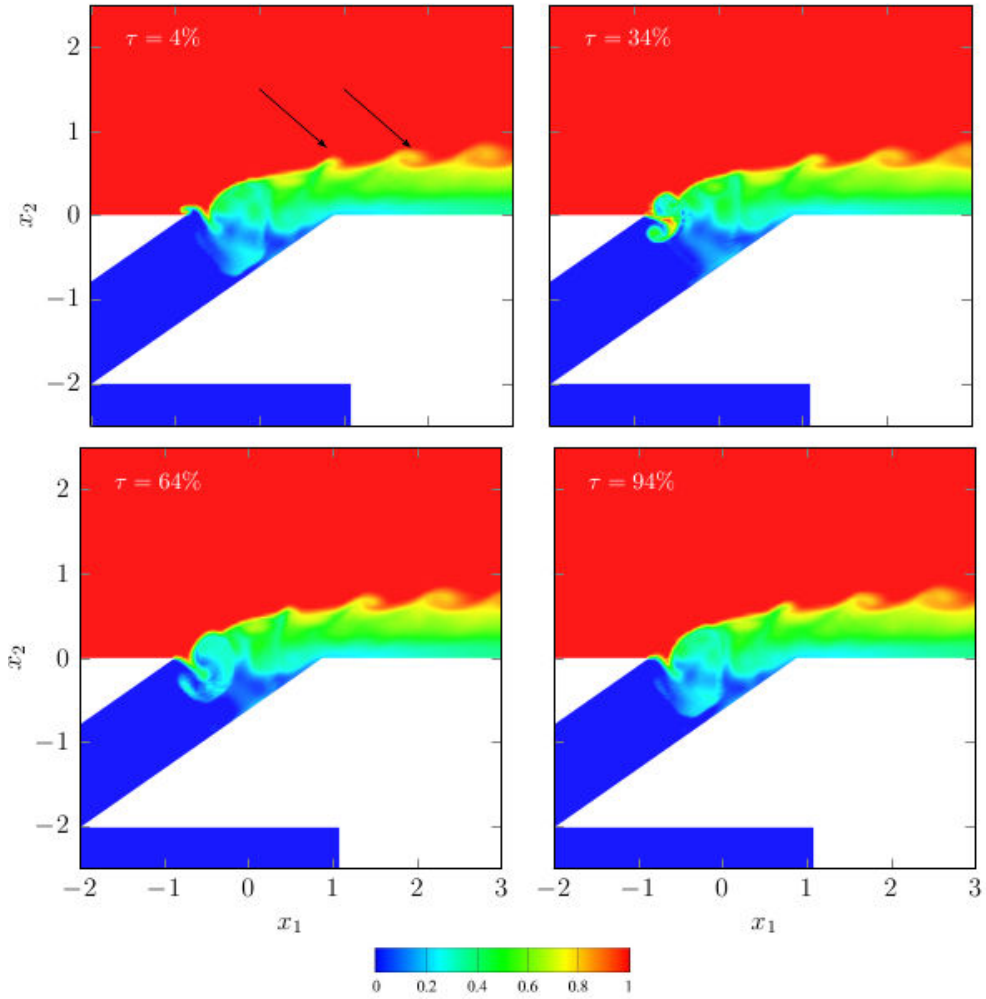

Figure 83: Snapshots of instantaneous temperature at $x_3 = 0$ during one pulsation cycle with $DC = 0.09$, $Tp = 1.16$, $\Delta t_{on} = 0.10$ and $\Delta t_{off} = 1.06$.

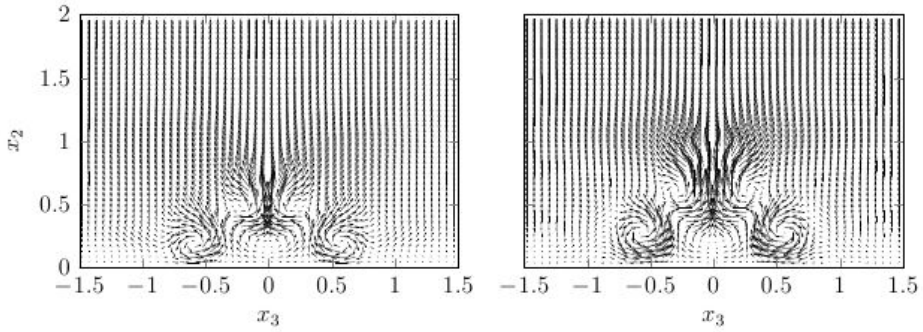

Figure 84: Instantaneousu_2−u_3 velocity vector field at: left $x_1 = 2$; right $x_1 = 4$, at $DC = 0.09$ and $Tp = 1.16$.

DISTRIBUTION A: Distribution approved for public release.

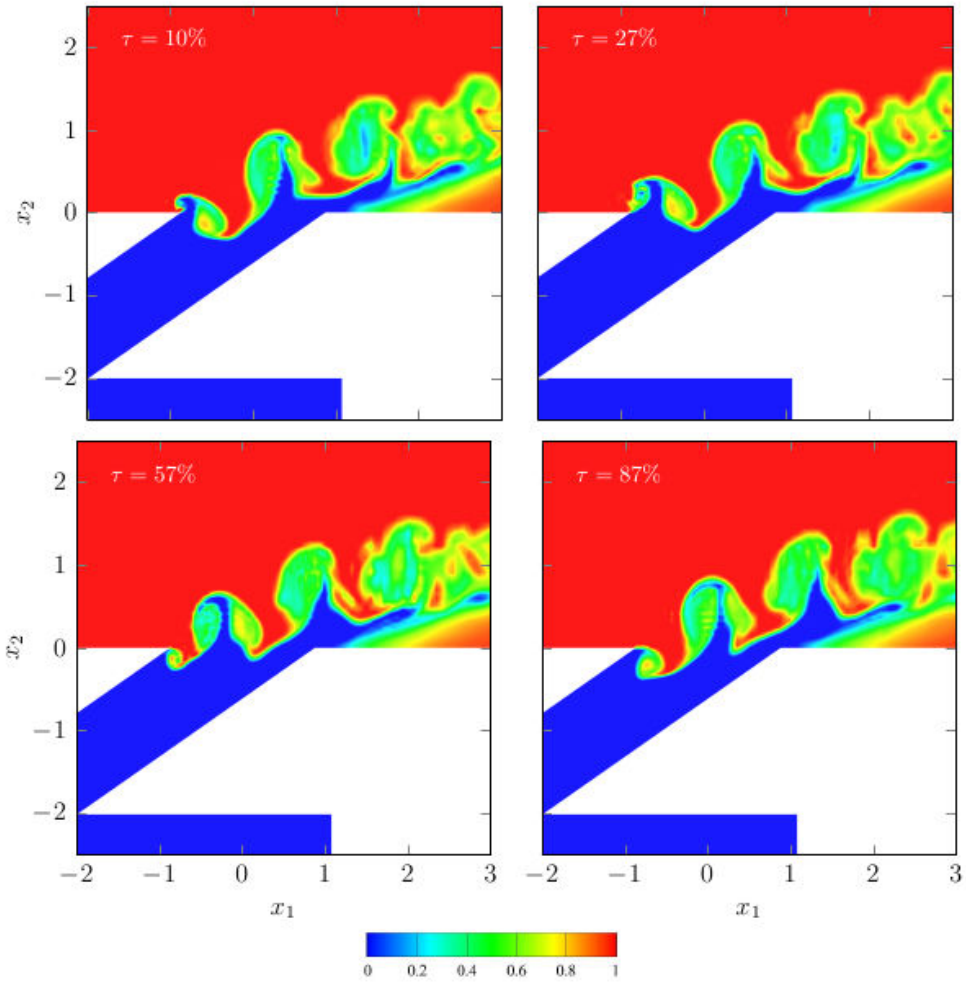

Figure 85: Snapshots of instantaneous temperature at $x_3 = 0$ during one pulsation cycle with $DC = 0.34$, $Tp = 1.16$, $\Delta t_{on} = 0.39$ and $\Delta t_{off} = 0.77$.

DISTRIBUTION A: Distribution approved for public release.

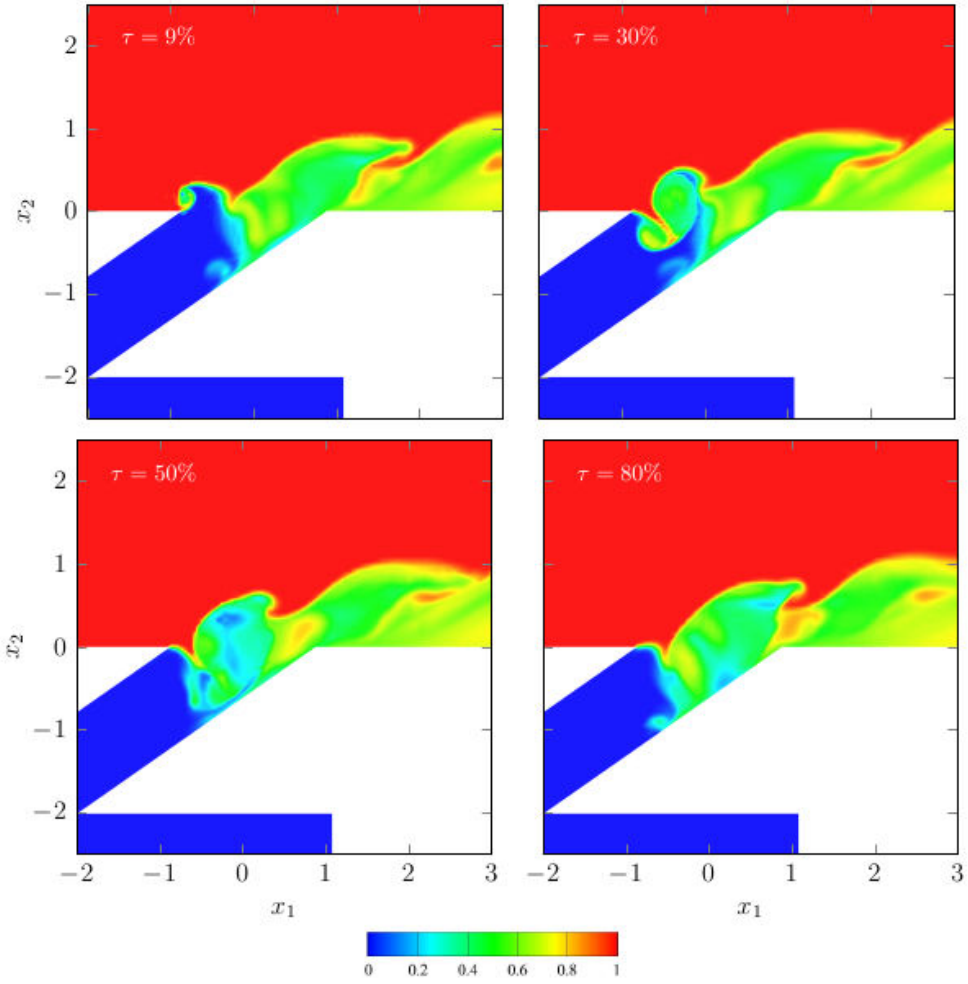

Figure 86: Snapshots of instantaneous temperature at $x_3 = 0$ during one pulsation cycle with $DC = 0.09$, $Tp = 2.75$, $\Delta t_{on} = 0.25$ and $\Delta t_{off} = 2.5$

DISTRIBUTION A: Distribution approved for public release.

is clearly visible in the tube and near the exit at $\tau = 34\%$ and $\tau = 64\%$. The ingested gas reaches very close to the opposite wall of the delivery tube at $\tau = 94\%$. Note that the speed of the propagation of the vortex ring inside the delivery tube is slightly less than the non-dimensional cross-flow velocity of one (due to entrainment), and during the off-portion of the cycle with non-dimensional $\Delta t_{off} = 1.06$ (corresponding to DC of 0.09), the vortex ring has long enough time to travel one non-dimensional unit of length (tube diameter) across the delivery tube and nearly reaches the opposite wall ($\tau = 94\%$). However, due to the short pulsation period, the plenum inflow is re-initiated before the ingested flow penetrates fully to the downstream-edge of the delivery tube, and before the ingested cross-flow gas can cause a significant temperature rise in the interior wall of the delivery tube; this can be seen at the beginning of the new cycle at time $\tau = 4\%$ in figure 83. Other than the hairpin vortices, the steady presence of a counter rotating vortex pair (CRVP) is observed. Figure 84 shows the lateral-vertical velocity vectors at two streamwise sections. A double-deck vortex pair is observed with the lower deck showing the CRVP and the upper deck is resulted by crossing the hairpin vortex legs. The velocity field that is induced by each pair of these vortex structures tend to lift the jet off the surface and unfavorably affects the cooling performance. The amount of the induced vertical velocity, however, is directly proportional to the strength of the vortex pair which is supplied by the amount of the coolant injection. Due to both short duty cycle ($DC = 0.09$) and pulsation period ($Tp = 1.16$), the induced vertical velocity for this case is small (0.01 of the cross-flow velocity) resulting in slow rise of the coolant from the surface (see the first image in figure 81) and thus providing an effective coverage of the surface. The second case we discuss here is the pulsed film cooling with higher duty cycle of $DC = 0.34$ compared to the first case and with the same pulsation period of $Tp = 1.16$. Four snapshots during one pulsation period are shown in figure 85. The top images show the injection of the coolant into the cross-flow. The coolant forms a vortex ring that gains more strength as the time progresses during the on-portion of the cycle and the size of the vortex ring increases from $\tau = 10\%$ to $\tau = 27\%$. In this case larger duty cycle injects more mass flow rate during the on-period and allows the complete formation of a vortex ring, an observation in contrast with the case at $DC = 0.09$ where the smaller duty cycle is not long enough to allow the formation of vortex rings during the injection time. The vortex rings, which carry significant amount of the coolant, penetrate the mainstream flow and are separated from the surface, thus allowing the entrainment of the cross-flow to the surface below the jet. This leads to poor coverage of the surface as it can be seen in figure 80. During the off-portion of the cycle the initial stages of the cross-flow ingestion into the delivery tube can be observed in figure 85 at $\tau = 57\%$ and $\tau = 87\%$ by the rolling up inside the hole. However, due to the low pulsation period ($Tp = 1.16$) and small non-dimensional time length in the off-portion of the cycle ($\Delta t_{off} = 0.77$), the hot gas cannot reach the tube walls before the next cycle begins. This shows that despite the ingestion of the hot gas into delivery tube, the wall temperature does not increase.

The third case investigated in this work is at $DC = 0.09$ and $Tp = 2.75$, which has the same duty cycle as that of the first case but higher pulsation time period. Four instants of temperature contours during one cycle are shown in figure 86. During the on-portion of the cycle ($\tau = 9\%$), a starting vortex forms which gains more strength compared to that of the first case (due to the longer Δt_{on} for this case) and grows larger in size, entraining more amount the hot mainstream flow, leading to increased mixing. During the off-portion of the cycle, a vortex ring similar to the first case forms, causing the ingestion of the cross-flow into the delivery tube. The longer amount of the pulsation period ($\Delta t_{off} = 2.50$) compared

DISTRIBUTION A: Distribution approved for public release.

to the first case ($\Delta t_{off} = 1.06$) gives the ingested gas enough time to impinge to the tube wall, causing significant increase in the wall temperature. Between two successive pulses, the cross-flow penetrates to the delivery tube surface due to larger lapses between the coolant pulses and thus adversely affecting the cooling coverage. The last two cases demonstrate the mechanisms that are responsible for the deterioration of the film cooling effectiveness when either duty cycle or pulsation period increases with respect to the near-optimal case ($DC = 0.09$ and $Tp = 1.16$). We also note that for pulsed cases with very small duty cycle ($DC < 0.05$), the film cooling coverage is severely affected by the overwhelming amount of the cross-flow compared to the coolant. Also for lower pulsation periods than $Tp = 1.16$ the overall film cooling effectiveness slightly decreases, but the physical mechanisms in the flow remain similar to the first case. Thus clearly, optimal conditions exists for the pulsation parameters, and the mechanisms controlling this are related to the dynamics near the jet-hole exit.

1.3.3 Film cooling response surface

In figure 87, the contour lines of the space- and time-averaged film cooling effectiveness vs. DC and Tp are shown. The global optimum is shown by point $P1$ and its design parameters are at $DC = 0.14$ and $Tp = 1.16$, which are close to those of the first case discussed in the previous section including the mechanisms responsible for such a behavior. Local optimums are denoted by points $P2$ to $P5$. The coordinate of points $P1 - P5$ are their respective values of averaged film cooling effectiveness are given in table 12. From the computational point of view an important observation is the presence of local optimums. This non-convex behavior of the objective function versus the design variables renders the gradient-based optimization strategies inappropriate for this problem, since the gradient-based algorithms will converge to a local optimum depending on the initial guess. This can be partially remedied by using different initial guesses. However for the current problem each initial guess leads to several expensive DNS simulations. Nevertheless certainty in obtaining the global optimum cannot be guaranteed in such approaches. Moreover the direct numerical simulations required in gradient-based approaches, have to be carried out in sequence due to the inherent dependence of the updated guess to previous iterations. In contrast, in the current approach all sample points are independent of each other and all simulations can be carried out concurrently, resulting in a significant scale up in the total computation performance. Another advantage of the current approach, although not exploited in the this study, lies in the fact that the obtained response surface can play the role of a surrogate model and can be utilized in different design scenarios, such as optimization cases where the objective function is the film cooling effectiveness with the amount of the coolant penalized with different factors, or the amount of ingestion penalized and so on. Note that once the response surface is obtained, investigating different optimization problems can be carried out very quickly without incurring the computational cost of the DNS.

1.4 Conclusions

In this chapter, we investigated the influence of duty cycle and pulsation frequency on film cooling effectiveness for a 35-degree inclined jet in cross-flow with a plenum attached to the delivery pipe. we have presented an efficient computational strategy that combines high-fidelity simulations and construction of a response surface in the design space to find

DISTRIBUTION A: Distribution approved for public release.

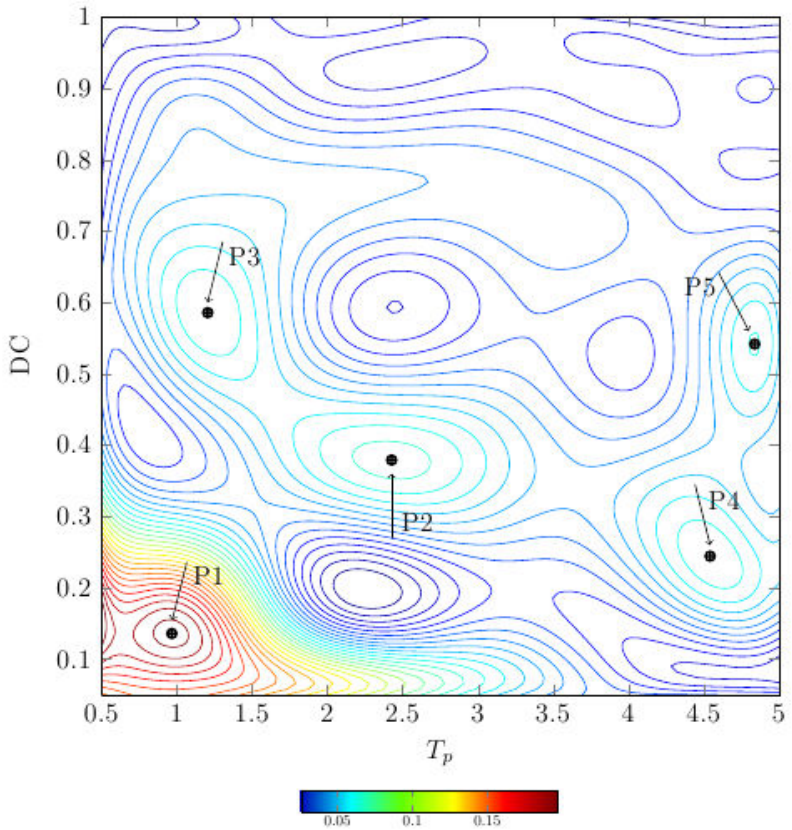

Figure 87: Contours of averaged film cooling effectiveness. Local and global maxima are shown with $P1$ being the global maximum and $P2$ to $P5$ are local maxima ordered with decreasing value. maxima ordered with decreasing value.

Table 12: Optimal design points

Point	DC	T_p	St	$\eta_N(\xi)$
$P1$	0.14	0.97	1.03	0.18
$P2$	0.38	2.43	0.41	0.08
$P3$	0.56	1.21	0.83	0.076
$P4$	0.24	4.54	0.22	0.075
$P5$	0.54	4.84	0.21	0.071

DISTRIBUTION A: Distribution approved for public release.

the optimal forcing parameters that maximizes the film cooling effectiveness. We carried out 73 direct numerical simulations and obtained the response surface of the averaged film cooling effectiveness as a function of the two design variables of duty cycle and pulsation period for a wide range of $DC \in [0.05, 1]$ and $Tp \in [0.5, 5]$. In summary the findings of this study are:

1. The optimal film cooling effectiveness occurs in the lower-left quadrant of the$DC-Tp$ design space, and at lower duty cycles ($DC = 0.14$) and higher frequencies ($St \sim 1$). During the off-period of coolant injection, flow adjustment near the delivery tube include ingestion of the mainstream flow into the tube and the propagation of this ingested front that pushes the coolant in the delivery tube to be squeezed out from the downstream edge of the hole. Thus coolant continues to spill out during the off-period, stays close to the surface, and provides improved coverage. For these cases a double-deck vortical structures were detected, with a hairpin vortex in the upper deck riding on top of a counter rotating vortex pair in the lower deck. The vertical velocity induced by each pair of vortices is small, leading to an attached coolant to the surface.

2. High duty cycles result in forming distinct vortex rings that are detached from the surface and lead to increased entrainment of the cross-flow and thus poor coverage.

3. High pulsation periods causes the penetration of the cross-flow to the delivery-tube trailing surface and causes a significant temperature rise in the delivery tube and an unfavorable effect on the film cooling effectiveness.

4. At lower pulsation periods, the ingested gas does not penetrate all the way to the trailing surface of the delivery tube, and does not cause an increase in the trailing wall temperature inside the tube.

5. Several local optimums were found, rendering the gradient-based optimization strategies inadequate for the current problem.

DISTRIBUTION A: Distribution approved for public release.

2 Canonical Systems Reduced Order Models

In this chapter, two-dimensional canonical flows, a two-sided lid driven cavity and a cylinder in cross-flow, are investigated. This is used to develop the necessary numerical tools and understanding of the POD-Galerkin model reduction method.

2.1 POD-Galerkin Method

The POD-Galerkin method is a combination of two operations providing a set of ordinary differential equations approximating the flow and temperature field empirical solutions. The resulting reduced order model equations for an unactuated flow are for the velocity field:

$$\dot{a_r}(t) = \sum_{i=1}^{N_V} \left(C_{i,0}^r + \frac{1}{Re} D_i^r \right) a_i(t) + \sum_{i=1}^{N_V} \sum_{j=1}^{i} C_{i,j}^r a_i(t) a_j(t) + \left(C_0^r + \frac{1}{Re} D_0^r \right) + P_r(t) \quad (1)$$

where

$$\vec{u} = \vec{\overline{u}} + \vec{u'} = \vec{\overline{u}} + \sum_{n=1}^{N_V} a_n(t) \vec{\varphi}_n(x)$$

$$C_0^r = -\left(\left(\vec{\overline{u}}.\nabla \right) \vec{\overline{u}}, \vec{\varphi}_r \right) = -\int_{\Omega_x} \overline{u}_l \frac{\partial}{\partial x_l} \left(\overline{u}_m \right) \varphi_{r,l} dx$$

$$D_0^r = \left(\triangle \vec{\overline{u}}, \vec{\varphi}_r \right) = \int_{\Omega_x} \frac{\partial}{\partial x_m \partial x_m} \left(\overline{u}_l \right) \varphi_{r.l} dx$$

$$C_{i,0}^r = -\left(\left(\vec{\overline{u}}.\nabla \right) \vec{\varphi}_i, \vec{\varphi}_r \right) - \left(\left(\vec{\varphi}_i.\nabla \right) \vec{\overline{u}}, \vec{\varphi}_r \right) = -\int_{\Omega_x} \left(\overline{u}_m \frac{\partial}{\partial x_m} \varphi_{i,l} + \varphi_{i,m} \frac{\partial}{\partial x_m} \overline{u}_l \right) \varphi_{r,l} dx$$

$$D_i^r = \left(\triangle \vec{\varphi}_i, \vec{\varphi}_r \right) = \int_{\Omega_x} \frac{\partial}{\partial x_m \partial x_m} \left(\varphi_{i,l} \right) \varphi_{r,l} dx$$

$$C_{i,j}^r = -\left(\left(\vec{\varphi}_i.\nabla \right) \vec{\varphi}_j, \vec{\varphi}_r \right) = -\int_{\Omega_x} \left(\varphi_{i,m} \frac{\partial}{\partial x_m} \varphi_{j,l} + \varphi_{j,m} \frac{\partial}{\partial x_m} \varphi_{i,l} \right) \varphi_{r,l} dx$$

$$P_r(t) = -\left(\nabla P(t), \vec{\varphi}_r \right)$$

and for the temperature field:

$$\dot{b}_s(t) = \sum_{i=1}^{N_V} E_{s,0}^i a_i(t) + \sum_{j=1}^{N_T} \left(E_{s,j}^0 + \frac{1}{Pr} \frac{1}{Re} F_{s,j} \right) b_j(t) + \sum_{i=1}^{N_V} \sum_{j=1}^{N_T} E_{s,j}^i a_i(t) b_j(t) + \left(E_{s,0}^0 + \frac{1}{Pr} \frac{1}{Re} F_{s,0} \right) \quad (2)$$

where

DISTRIBUTION A: Distribution approved for public release.

$$T = \overline{T} + T' = \overline{T} + \sum_{m=1}^{N_T} b_m(t)\psi_m(x)$$

$$E^0_{s,0} = -\left(\left(\vec{\overline{u}}.\nabla\right)\overline{T}, \psi_s\right) = -\int_{\Omega_x} \overline{u}_m \frac{\partial}{\partial x_m}\left(\overline{T}\right)\psi_s dx$$

$$F_{s,0} = \left(\triangle\overline{T}, \psi_s\right) = \int_{\Omega_x} \frac{\partial}{\partial x_m \partial x_m}\left(\overline{T}\right)\psi_s dx$$

$$E^i_{s,0} = -\left(\left(\vec{\varphi}_i.\nabla\right)\overline{T}, \psi_s\right) = -\int_{\Omega_x} \varphi_{i,m} \frac{\partial}{\partial x_m}\left(\overline{T}\right)\psi_s dx$$

$$E^0_{s,j} = -\left(\left(\vec{\overline{u}}.\nabla\right)\psi_j, \psi_s\right) = -\int_{\Omega_x} \overline{u}_m \frac{\partial}{\partial x_m}\left(\psi_j\right)\psi_s dx$$

$$F_{s,j} = \left(\triangle\psi_j, \psi_s\right) = \int_{\Omega_x} \frac{\partial}{\partial x_m \partial x_m}\left(\psi_j\right).\psi_s dx$$

$$E^j_{s,i} = -\left(\left(\vec{\varphi}_i.\nabla\right)\psi_j, \psi_s\right) = -\int_{\Omega_x} \varphi_{i,m} \frac{\partial}{\partial x_m}\left(\psi_j\right)\psi_s dx$$

In both equations, $\overline{u}_m$ corresponds to the m^{th} component of the vector $\vec{\overline{u}}$ and $\varphi_{r,l}$ corresponds to the l^{th} component of the vector $\vec{\varphi}_r$. Redundant indexes imply summation on those indexes according to Einstein notation.

Provided with initial values for $A(t_0) = [a_1(t_0), \ldots, a_{N_V}(t_0)]^\top$ and $B(t_0) = [b_1(t_0), \ldots, b_{N_T}(t_0)]^\top$ the set of ODEs can be integrated to obtain a prediction of the velocity and temperature field.

Both projected momentum and energy equations *RHS* are quadratic functions in terms of the coefficients a_i and b_j. Similarly to the full incompressible Navier Stokes and energy equations, the equations are only one-way coupled. The velocity equations are self-sufficient, while the temperature solution depends on the velocity field.

In the rest of this document, we will use indifferently a_i, a_i^{Vel} or a_i^V for the velocity POD temporal coefficients, and b_i, a_i^{Temp} or a_i^T for the temperature POD temporal coefficients.

In order to develop the methodology, the algorithms and the understanding of the POD-Galerkin reduced order modeling method, simple problems were first investigated.

2.2 Two-dimensional Two-sided Lid Driven Cavity

In order to develop the methodology, the algorithms and the understanding of the POD-Galerkin reduced order modeling method, simple problems were first investigated. The first investigated problem is a simple rectangular uniform cartesian grid, corresponding to a closed domain with homogeneous boundary conditions, low energy fluctuations and rather uniform length scales. In addition, to simplify and speed up the numerical simulations, the problem is chosen to be two-dimensional. These considerations lead the choice of a two-sided lid driven cavity flow (2D-2SLDC or 2SLDC).

DISTRIBUTION A: Distribution approved for public release.

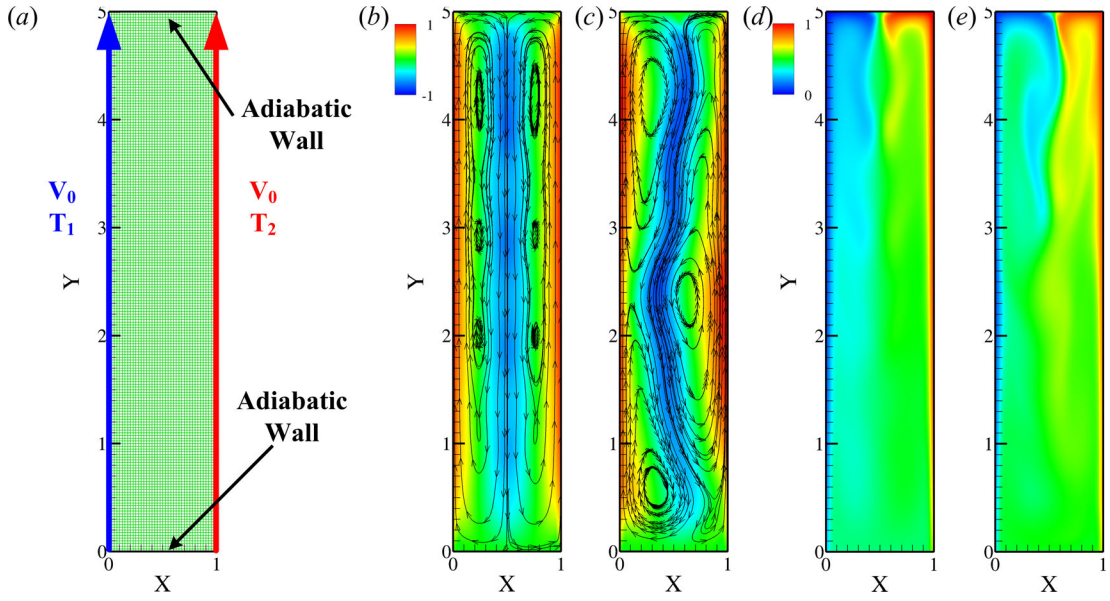

Figure 88: (a) Numerical domain and applied boundary conditions for the 2SLDC problem. (b) Time averaged flow field with V-velocity contours and U-V streamlines; (c) Instantaneous normalized flow field with V-velocity contours and U-V streamlines; (d) Time averaged normalized temperature field; (e) Instantaneous temperature field.

2.2.1 Numerical Setup

The numerical setup for this system is presented in figure 88. The domain is a rectangular domain of dimensions $1 \times 5m$ with a uniform mesh of 40×200 cells for a total of 8000 interior cells . The two "long" walls at $X = 0$ and $X = 1$ are driven at the same velocity of $V_0 = 0.05m.s^{-1}$ in the same direction but are maintained at two different temperatures of $T_1 = 300K$ and $T_2 = 350K$. The corresponding Reynolds number based on the cavity height $Re = V_0 h/\nu$, was approximately 1600. The two remaining "short" boundaries are adiabatic wall. This is a closed system without any mass going in or out the domain. The numerical model used was a two-dimensional approximation of Large Eddy Simulation model as implemented in Ansys Fluent^{TM}. The solver was second order in space and time. The time step used was of $\Delta t = 0.25s$ corresponding to a convective time step of $\Delta t_c = 2.5 \times 10^{-3}$ ($t_c = tV_0/h$) and resulting in maximum Courant's number ($u\Delta t/\Delta x$) of less than 0.5. In the rest of this section, the reported quantities will be normalized velocities $u = u^*/V_0$, $v = v^*/V_0$ and temperature $\theta = (T - T_1)/(T_2 - T_1)$.

2.2.2 Base Flow

Although not of particular interest in the current study, the base flow is rapidly described to put the results in the next sections in perspective. At low Reynolds numbers ($V_0 \approx 5 \times 10^{-3}$, $Re \approx 160$), the flow was found to be stable and stationary. In this regime, the flow field consisted of two large scale recirculation regions on each side of the problem symmetry line at $X = 0.5$. This configuration did not serve our purposes as some unsteadiness was required to obtain a meaningful reduced order model. As the value of the Reynolds number

DISTRIBUTION A: Distribution approved for public release.

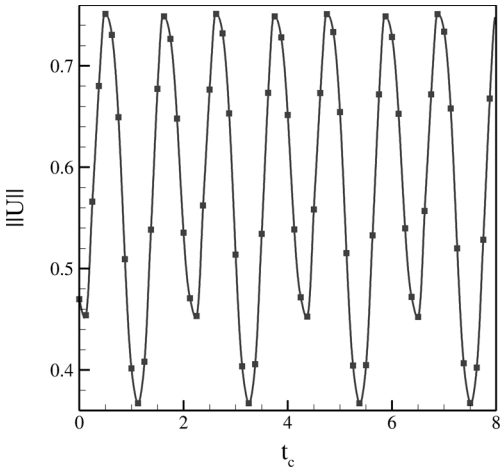

Figure 89: Velocity magnitude signal from probe located inside the cavity at $X = 0.5, Y = 2.5$ as a function of time.

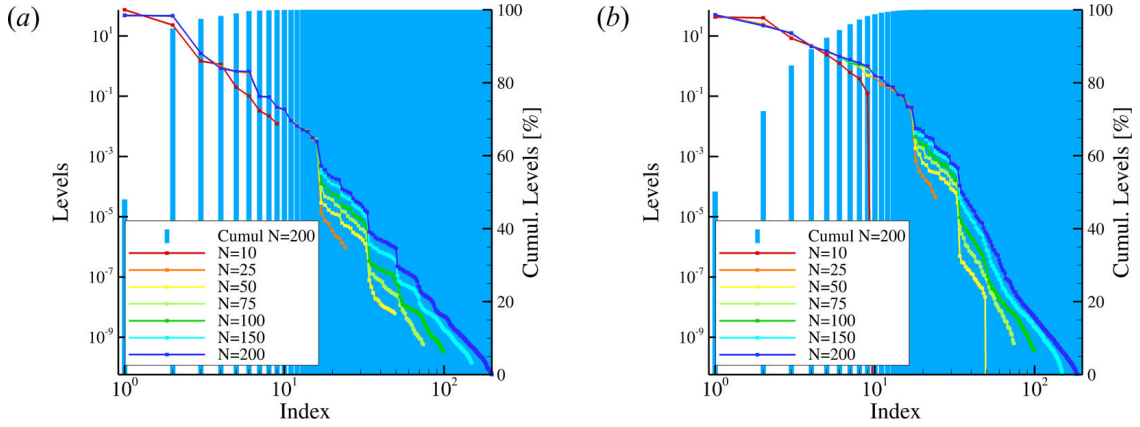

Figure 90: POD Energy distribution for different number N of snapshots included in the computation for (a) Velocity; (b) Temperature fields.

was increased to values of $V_0 = 0.05m.s^{-1}$ instability started to develop and the recirculation cells started to be convected from the top domain to the bottom in a quasi-periodic manner. Figure 88(b) shows the time averaged velocity field with three distinct pairs of symmetric recirculation cells with respect to the center-line. An instantaneous snapshot in figure 88(c) shows three recirculation cells and highlights the fact that the instantaneous flow field is not symmetric. The associated time averaged and instantaneous temperature fields are also provided in figure 88$(d,\ e)$. This flow configuration was judged suitable for experimenting with reduced order modeling methods. A probe was placed inside the flow at the center of the domain $(X = 0.5, Y = 2.5)$ to record the velocity magnitude throughout the simulations. The signal is presented in figure 89. This signal shows that the flow is quasi-periodic with a dominant frequency of $9.25\times10^{-3}Hz$ corresponding to a scaled frequency of $St = St_0 = 0.925$ where St is the Strouhal number $St = fh/V_0$. This signal is also modulated at subharmonic frequency of $St_0/2 = 0.463$.

DISTRIBUTION A: Distribution approved for public release.

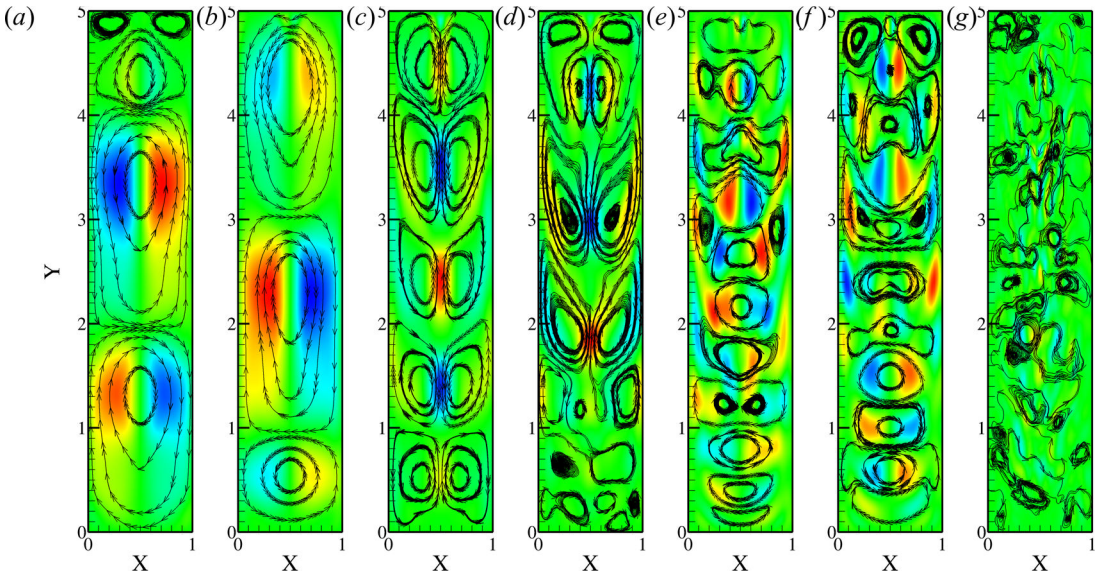

Figure 91: Velocity POD modes: (a) Mode1; (b) Mode2; (c) Mode3; (d) Mode4; (e) Mode5; (f) Mode6; (g) Mode20 for $N = 200$. U-V streamlines and V contours.

2.2.3 Proper Orthogonal Decomposition

Proper Orthogonal Decomposition is carried out using Sirovich Snapshot method on the fluctuation signal. Several decompositions including successively 10, 25, 50, 75, 100, 150 and 200 snapshots are investigated to observe the impact of the number of snapshots on the decomposition metrics. The snapshots are separated by 50 time steps for an equivalent convective time step of $\Delta t_c = 0.125$. This sampling is materialized by the symbols in figure 89 against the probe signal. Figure 90 shows the energy repartition for the different computations. The energy distribution converges rather rapidly to a unique distribution for the lower order modes (highest energy content) for $N > 50$ for the velocity field, but settles only for $N > 150$ for the temperature decomposition. This is a result of the non-optimality of the POD for the temperature signal since the thermal energy does not scale with the square of the temperature. In the rest of this section, the computations are carried out using the $N = 200$ POD modes for both temperature and velocity fields, in order to prevent any bias on the reduced order models introduced by an inaccurate temperature POD. For $N = 200$, the two first velocity POD modes carry as much as 94% of the total turbulent kinetic energy and a total of 5 and 9 modes are necessary to reconstruct respectively 99% and 99.9% of the total turbulent kinetic energy. On the other hand, the first two temperature modes carry "only" 73% of the total temperature signal fluctuation energy (pseudo-thermal energy) and a total of 11 and 15 POD modes are necessary to reconstruct respectively 99% and 99.9% of the total pseudo-thermal energy. These numbers are comparable to previous two-dimensional systems with simple flows.

The POD modes for the velocity and temperature are presented in figure 91 and figure 92 respectively. The first two modes are antisymmetric with respect to the flow center-line and exhibit three large recirculation regions. According to figure 90(a), they carry comparable amounts of energy, respectively 48% and 47% of the total energy. Peaks of identical sign

DISTRIBUTION A: Distribution approved for public release.

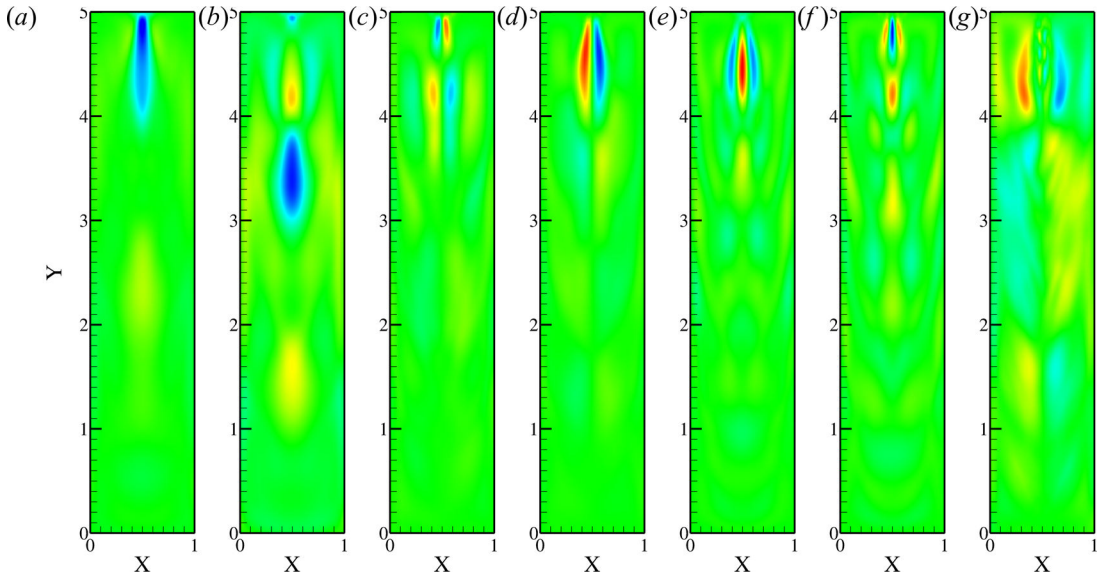

Figure 92: Temperature POD modes: (a) Mode1; (b) Mode2; (c) Mode3; (d) Mode4; (e) Mode5; (f) Mode6; (g) Mode20 for $N = 200$.

between modes 1 and 2 are however shifted in the Y-direction of approximately a quarter of a wavelength (mainly in the core of the flow). In addition, the temporal coefficients a_1 and a_2 in figure 93 appear identical with a phase shift of a quarter wavelength as well. These combined characteristics (identical energy levels, shape function and temporal coefficients shifted of a quarter of a wavelength) are typical of POD modes describing the convection of flow structures in a particular direction. Indeed, the sum of the two partial velocity fields $a_1\varphi_1$ and $a_2\varphi_2$ in the reconstructed signal results in the convection of the recirculation cells observed in the shape functions. Modes 3 and 4 on the other hand are symmetric and do not carry the same amount of energy. They describe the convection of smaller scale recirculation cells on each side of the symmetry line (2 cells per domain width). Modes 5 and 6 are again antisymmetric and of comparable energy content, and represent convection of again smaller scale recirculation cells (3 cells per domain width). As for modes 1 and 2, the temporal coefficients for modes 3 and 4 as well as for modes 5 and 6 have respectively similar frequencies but a quarter wavelength phase shift. Finally, mode 20 captures the dynamics of rather small scales and no real coherence can be found. The decrease in length scale captured by the successive modes is a classic and essential feature of the POD which by nature constructs a set of basis function with decreasing energy content, thus captures ever smaller fluctuations and length scales in higher order modes. This feature is in fact a key element in the process of reduced order modeling using truncated POD series to a finite number of POD modes therefore retaining only the lower order modes with the highest energy content susceptible to govern and represent the best the flow dynamics. Overall, the velocity shape functions appear to be organized in pairs of symmetric and antisymmetric modes with comparable energy content and temporal coefficient dominant frequency. The POD modes for the temperature decomposition show some similarities with the velocity decomposition. The first two POD modes capture rather large scale fluctuation areas, yet the decrease in length scale with increasing mode order is not as obvious as it is in the

DISTRIBUTION A: Distribution approved for public release.

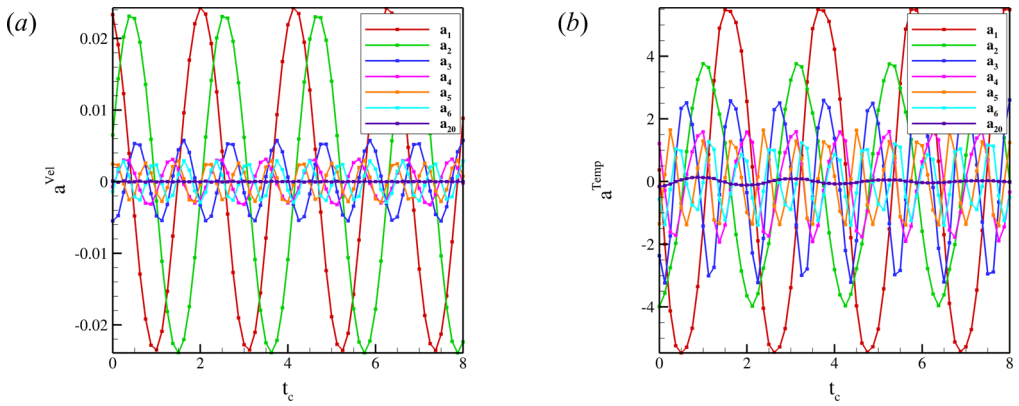

Figure 93: Temporal POD coefficients: (a) a_i^{Vel}; (b) a_i^{Temp} as a function of t_c for $N = 200$.

velocity decomposition. Similarly, the energy decay rate of energy distribution in figure $90(b)$ is not as significant as the velocity one. POD modes still appear to be associated in pairs of alternating symmetric and antisymmetric, yet the energy repartition between the individual modes of every pair is not as even as the one in the velocity decomposition. Once again, these results are attributed to the non-optimality of the POD to the decomposition of temperature signals.

The temporal coefficients a_i^{Vel} and a_i^{Temp} are presented in figure 93 and show that not only the temporal coefficients corresponding to a same pair of modes have similar amplitude (i.e. energy) and frequency, but that the frequency captured by the different pairs is increased with increasing modes orders. Modes 1 and 2 capture dynamics with a fundamental frequency of $St = 0.47 \approx St_0/2$, modes 3 and 4 with a frequency 1.5 times higher of $St = 0.705$, and modes 5 and 6 with a frequency twice as high $St = 0.94 \approx St_0$ where St_0 is the fundamental frequency directly evidenced in the probe signal of figure 89.

2.2.4 Reduced Order Model

Reduced order models are obtained for several combinations of the pair of values (N_V, N_T), respectively the number of velocity and temperature POD modes used in the reconstruction of the fields. The Galerkin projection is carried out on the POD results including 200 velocity fields and 200 temperature fields. The spatial derivatives of the respective POD modes are calculated using Tecplot$^{\text{TM}}$, utilizing a centered second order accurate scheme. Although the derivation scheme used by Tecplot to obtain the derivatives is most likely not identical to the one implemented in the Fluent solver, the error introduced by the change in scheme is deemed negligible with respect to the dropped POD terms in the velocity and temperature fields reconstructions. Moreover, the relatively refined mesh used in this simulation ensured local errors of the order, or inferior to, $\Delta x^2 \sim 6.10^{-4}$. The Galerkin coefficients of equations 1 and 2 are evaluated using the trapezoidal integration approximation. In this particular case, the velocity field and temperature fields are homogeneous at the boundary so that the pressure term $P_r(t)$ in equation 1 vanishes and does not require any additional calculations. The set of ODEs are integrated using both a 5^{th} order Runge-Kutta solver (Dormand-Prince pair 4/5 24 - DP45) and a variable order Adams-Bashforth-Moulton PECE solver (see 69) with a relative tolerance between 10^{-8} and 10^{-2}. The sensitivity of both solvers on

DISTRIBUTION A: Distribution approved for public release.

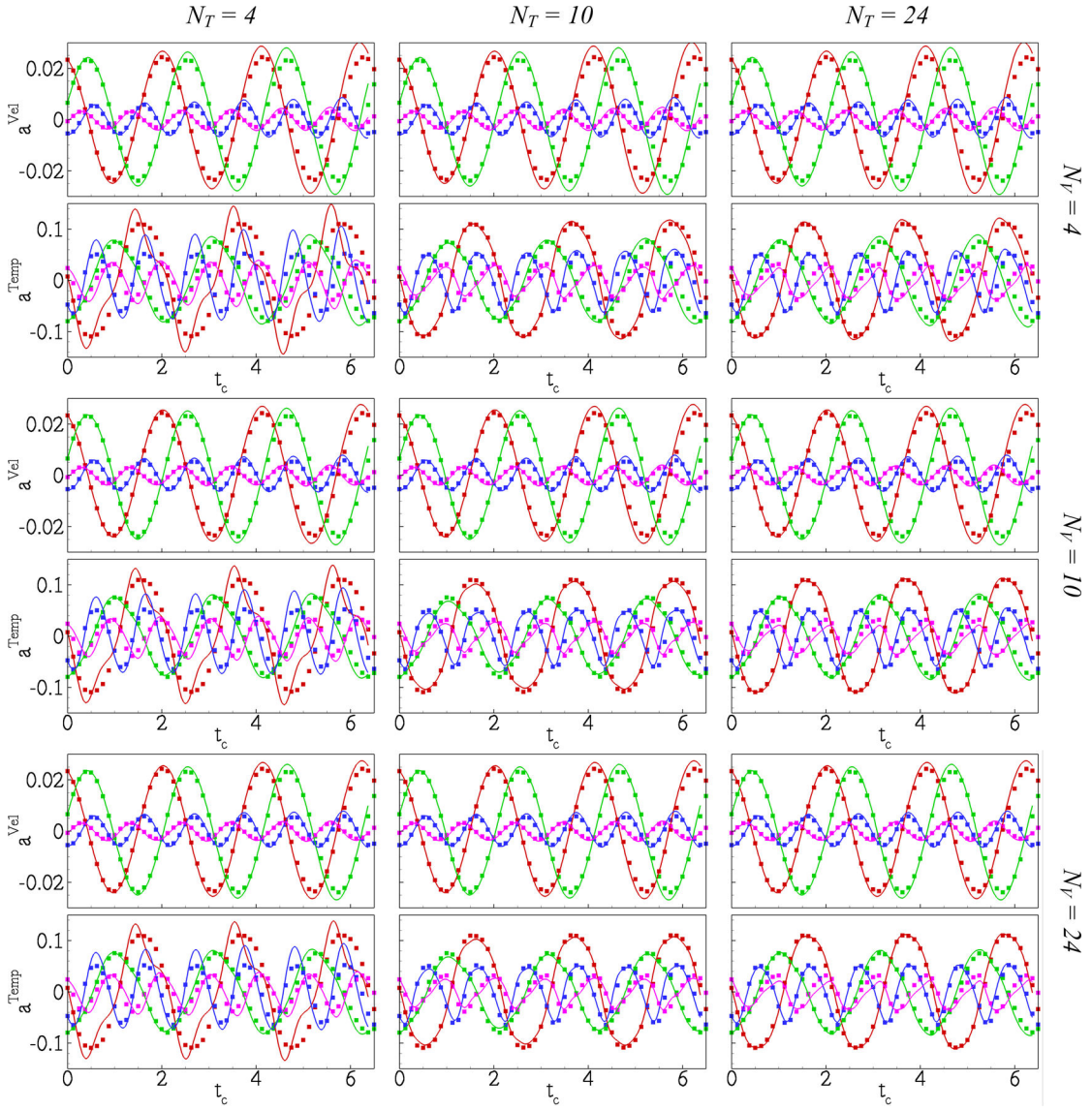

Figure 94: First four ROM temporal coefficients for the velocity and temperature fields obtained for several values of N_V and N_T (*solid lines*) along with corresponding POD temporal coefficients (*symbols*). a_1 (*red*), a_2 (*green*), a_3 (*blue*), a_4 (*magenta*).

DISTRIBUTION A: Distribution approved for public release.

the tolerance parameter was investigated and the solution did not evidence any significant differences beyond a tolerance of 10^{-4}. The presented following results are the one obtained using the DP45 algorithm with a relative tolerance of 10^{-4}. Both projected momentum and energy equations are solved simultaneously in a system of $N_V + N_T$ coupled ODEs.

The results from the integration of the reduced order model obtained from the Galerkin projection method are presented in figure 94 for several values of N_V and N_T, along with the corresponding POD coefficients corresponding to the projected LES data onto the POD basis. The results for the first four temporal coefficients show relatively good tracking for the velocity over the first periods corresponding to the dominant frequency as soon as $N_V = 4$. While the fidelity of the model appears to be improved by increasing the number of velocity POD modes to $N_V = 10$, no obvious improvement seems to occur between $N_V = 10$ and $N_V = 24$. This shows that the model is fully converged with 10 modes and that the remaining error is to be attributed to the numerous approximations made to obtain the set of ODEs including but not limited to, errors introduced by the solver numerical integration scheme, inaccuracy of the solution due to domain discretization, errors introduced by the mismatch in derivation scheme between the solver and the post-processing software, integrals approximations with the trapezoidal rule, etc. As expected from the fact that the velocity solution is decoupled from the temperature one, the changes in the value of N_T at fixed values of N_V do not visually affect the fidelity of the velocity ROM.

The impact of N_V and N_T on the temperature ROM fidelity is also evidenced in figure 94. With $N_T = 4$, the accuracy of the temperature ROM is poor and the tracking mediocre. However, the quality of the ROM is greatly improved for $N_T = 10$. When including 24 temperature modes, no significant improvement is observed on the first three coefficients and a certain degradation of the profile of the fourth coefficient occurs. Conversely to the velocity ROM, the changes in values of N_V at fixed N_T have a moderate yet visible influence on the temperature ROM tracking, in particular the "long term" accuracy of the model appears to be improved for increased number of velocity POD modes included.

Overall, very satisfying results are obtained using only 22 velocity modes and 6 temperature modes.

2.3 Two-dimensional Cylinder in a Cross-flow

While 2D-2SLDC problem constituted a good starting point, this flow was very well behaved and corresponded to a closed-flow configuration. To investigate open flow systems, a two-dimensional cylinder in a cross-flow is selected to assess the impact of neglecting the pressure terms in equation 1. In addition, the extensive documentation on this type of flow makes it an excellent candidate.

2.3.1 Numerical Setup

The numerical setup for the cylinder in cross-flow consists of a cylinder inside of diameter $D = 1m$ and a rectangular domain $16D$ wide (in the X direction) and $33D$ long (in the Y direction). A close-up view of the domain is provided in figure $95(a)$. The origin of the domain is located at the center of the cylinder and the inlet of the domain is at $Y = -8D$, therefore the outlet at $Y = 33D$. The grid is multi-block with an O-grid of $3D$ diameter surrounding the cylinder. The cell height at the cylinder wall is $2 \times 10^{-4}D$ for corresponding y^+ values of less than 0.25, well inside the boundary layer viscous sub-layer. The mesh

DISTRIBUTION A: Distribution approved for public release.

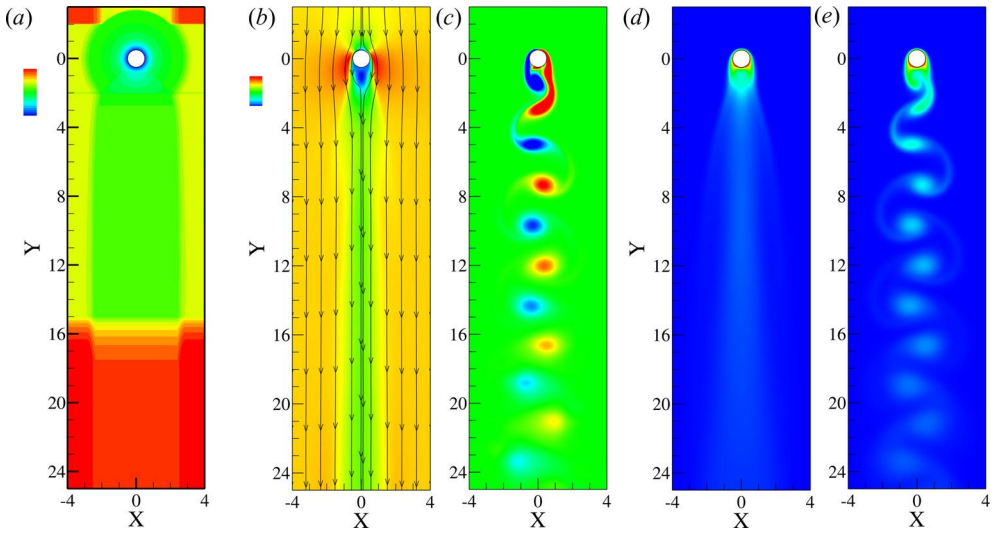

Figure 95: (a) Numerical domain and local cell surface area from $10^{-5}D^2$ $(blue)$ to $10^{-3}D^2$ (red). (b) Time averaged flow field with U-velocity contours and U-V streamlines; (c) Instantaneous normal vorticity; (d) Time averaged normalized temperature field; (e) Instantaneous temperature field.

counts a total of $250,000$ cells. Because of the high density of the mesh, the surface area of the individual cells is presented in figure $95(a)$, instead of the mesh itself, and still provides a good overview of the mesh distribution. At the inlet of the domain, normal velocity is imposed at $V_0 = 2.235 \times 10^{-3} m.s^{-1}$ for a corresponding Reynolds number ($Re_D = V_0 D/\nu$) of 150, within the unstable two-dimensional laminar regime. At the outlet of the domain, an outflow boundary condition is imposed. The sides of the domains are taken far away from the core of the flow and periodic boundary conditions are applied to them. A constant temperature of $T = T_1 = 300K$ is imposed at the domain inlet and a constant temperature of $T = T_2 = 350K$ is imposed at the cylinder wall. The numerical model used is a 2D approximation of the Large Eddy Simulation model as implemented in Ansys Fluent™ with a dynamic Smagorinsky-Lilly sub-grid scale model. The discretization scheme for the pressure, momentum and energy equation are respectively second order upwind, second order bounded central-differences and QUICK (Quadratic Upstream Interpolation for Convective Kinematics). The time discretization scheme is also second order. The integration time step used during the simulations is $\Delta t = 1s$ corresponding to a convective time step of $\Delta t_c = 2.2 \times 10^{-2}$ with $t_c = tV_0/D$. The maximum Courant's number ($u\Delta t/\Delta x$) is less than 0.9.

2.3.2 Base Flow

The base flow for this problem is well documented (see 75 for instance) and will only be described to put in perspective the following results. A recirculation region is located directly downstream of the cylinder (see figure $95b$) and contains a pair of vortical regions of opposite vorticity (see figure $95c$). At Reynolds numbers above the Hopf Bifurcation stability margin ($Re_D \approx 40$), the wake becomes unstable and the vortices composing the wake starts shedding

DISTRIBUTION A: Distribution approved for public release.

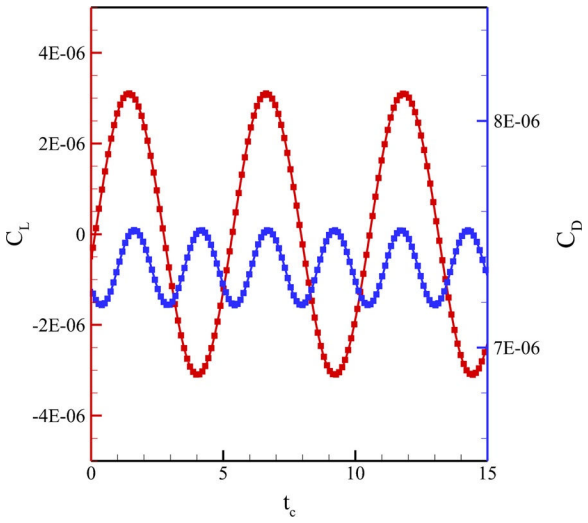

Figure 96: Integrated drag C_D and lift C_L coefficients as a function of convective time t_c. Symbols represent the sampling used for POD.

in an alternating periodic manner to form the well known Kármán vortex street observed in figure 95(c). The wake is characterized by the Strouhal number ($St = fD/V_0$) associated with the shedding frequency of the vortices, which is a function of the Reynolds number. In the current simulations at $Re_D = 150$, the fundamental shedding frequency is found to be $St_0 = 0.198$ in the lift coefficient C_L history of figure 96 while the drag coefficient C_D signature exhibits a fundamental twice as high. This is in agreement with previous findings from (71). For additional information on the velocity field of flows past circular cylinder, the reader is referred to (75). The temperature field is also presented in figure 95(d-e). Since the cylinder wall is the only surface at a prescribed temperature above cross-flow temperature, the average field shows that the only areas with elevated temperatures are the surroundings of the cylinder and the wake. The instantaneous temperature field in figure 95(e) is highly correlated to the vorticity field in figure 95(c) highlighting the thermal convection from the shedding wake vortices.

2.3.3 Proper Orthogonal Decomposition

As for the previous case, the proper orthogonal decomposition is carried out using the snapshot method. A sampling of $\Delta t_c = 5.5 \times 10^{-2}$, corresponding to 50 time steps, is used which is equivalent to 45 snapshots per period of the fundamental frequency and evidenced by the symbols in figure 96. Four decompositions including 45, 68, 90 and 135 snapshots are made for both the velocity and temperature fields in order to evaluate the influence of the number of snapshots on the convergence of the decomposition. Figure 97 presents the energy distribution from the decomposition of the velocity and temperature fields. For the velocity, the first 10 POD modes are identical for the decompositions including integer numbers of periods whereas the decomposition including a non-integer number of periods appears slightly different beyond the second mode. This is a well known result concerning POD decomposition of periodic flows, which in order to be accurate and optimum, requires an integer number of periods during the sampling (see 65). For the rest of this section, the

DISTRIBUTION A: Distribution approved for public release.

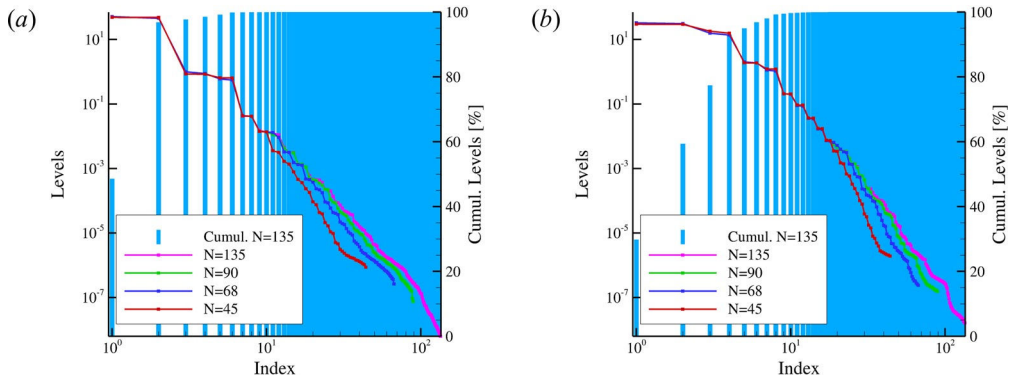

Figure 97: POD Energy distribution for different numbers of snapshots included in the computation for (a) Velocity; (b) Temperature fields.

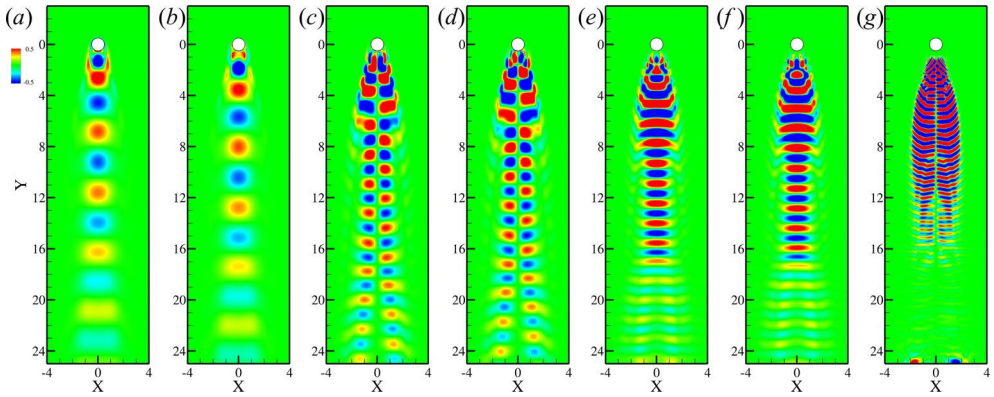

Figure 98: Vorticity from the velocity POD modes: (a) Mode1; (b) Mode2; (c) Mode3; (d) Mode4; (e) Mode5; (f) Mode6; (g) Mode20 for $N = 135$.

decomposition including 135 snapshots is used for reduced order modeling purposes, covering 3 shedding cycles, therefore allowing us to estimate the long term behavior of the ROMs. The first two velocity POD modes carry approximately 47% of the total turbulent kinetic energy each. A total of 5 and 8 velocity POD modes are required to respectively capture 99% and 99.9% of the total turbulent kinetic energy.

The difference between integer and non-integer sampling of the period is less obvious in the temperature decomposition yet remain visible. The first 18 modes for the temperature decomposition including an integer number of periods appear to be identical when including 1, 2 or 3 periods. Indeed, the energy distribution of the temperature decomposition is less optimal than the one in the velocity decomposition and the first two modes carry "only" 30% of the total pseudo-thermal energy. A total of 8 and 14 temperature POD modes are required to capture respectively 99% and 99.9% of the total pseudo-thermal energy which is significantly higher than for the velocity field decomposition. Once again, these observations evidence that while the POD is optimal in the sense of the kinetic energy, it is not in the sense of the thermal energy, therefore providing modes with lower energy content for the temperature decomposition.

DISTRIBUTION A: Distribution approved for public release.

The normal vorticity extracted from the shape functions of the velocity field decomposition is presented in figure 98. As for the 2SLDC results, the decomposition yields pairs of modes which are similar in terms of the size and shape of the vortical features they capture. The first mode in figure 98(a) is symmetric with respect to the flow symmetry line ($X = 0$) and captures vortical structures with scales of the order of the cylinder diameter, with alternating vorticity sign. The second mode is almost identical to the first one, with a shift in the pattern of a quarter wavelength towards the downstream direction. This shift, coupled with the $\pi/4$ shift in the phase of the temporal coefficient of mode 2 with respect to the one of mode 1 in figure 99, results in the downstream convection of vortical cells in the reconstructed signal $a_1(t)\varphi_1(x) + a_2(t)\varphi_2(x)$. This is comparable to the results obtained in the 2SLDC configuration. Modes 3 and 4 are the first antisymmetric modes and contain vortical cells of opposite sign on each side of the symmetry line with alternating sign in the downstream direction. The vorticity levels are rather high close to the recirculation region and decrease in intensity beyond $Y = 16$, with in addition, a bifurcation in the vortical structures trajectories beyond this point. It is rather unclear if this is to be related to the mesh density change beyond $Y = 16$ (visible in figure 95a) or to the natural decay of the vorticity due to diffusion. As for modes 1 and 2, the temporal coefficients for modes 3 and 4 are comparable in amplitude and frequency with a $\pi/4$ phase shift. Modes 5 and 6 exhibit a symmetric pattern similar to the one of modes 1 and 2, with yet twice as many changes in vorticity sign it the wake region. The vortical cells are rather elongated in the X-direction. The shape functions contain single cells with high vorticity up to $Y = 16$ and double cells on each side of the symmetry line with lower vorticity levels beyond that point. The temporal coefficients of modes 5 and 6 also exhibit a quarter period shift. Finally, mode 20 exhibits small scale fluctuations in the wake of the cylinder but, conversely to the 2SLDC results, conserves symmetry and coherence. It is worth noting that this latter mode also captures rather large scale structures (at least when compared to the ones directly downstream of the cylinder) near the domain outlet. This is a good example of the potential issues faced when using POD on flows involving various length and energy scales. Indeed, it is observed in figure 95(c) that the vorticity levels, and therefore the energy content, of the structures located directly downstream of the cylinder are significantly higher than the ones of the previously convected vortices on which diffusion has had an effect. Consequently, the POD will have a tendency to capture across the first POD modes the vortical structures in the near-field of the cylinder (as evidenced in figure 98a-f) and across the higher order modes the less energetic far-field structures. However, there is a certain overlap such that in mode 20, the far-field structures are captured along with smaller features of the near-field structures carrying less energy.

The POD modes for the temperature decomposition presented in figure 100 show strong similarities with the velocity ones. In particular modes 1 and 2 are symmetric with respect to the flow center-line, shifted in the downstream direction of a quarter wavelength with respect to each other and show strong similarities with the vorticity field of modes 5 and 6 from the velocity field decomposition. Modes 3 and 4 as well as 5 and 6 are antisymmetric. Once again, the higher order modes such as mode 20, capture simultaneously increasingly smaller scale features in the near-field but also larger, less energetic ones in the far-field.

The temporal coefficients for the velocity and temperature decompositions are presented in figure 99(a) and 99(b) respectively. While both decompositions result in series of pairs of coefficients with identical fundamental frequency and a $\pi/4$ phase shift, the fundamental frequency of the dominant velocity and temperature modes are different. While modes 1 and

DISTRIBUTION A: Distribution approved for public release.

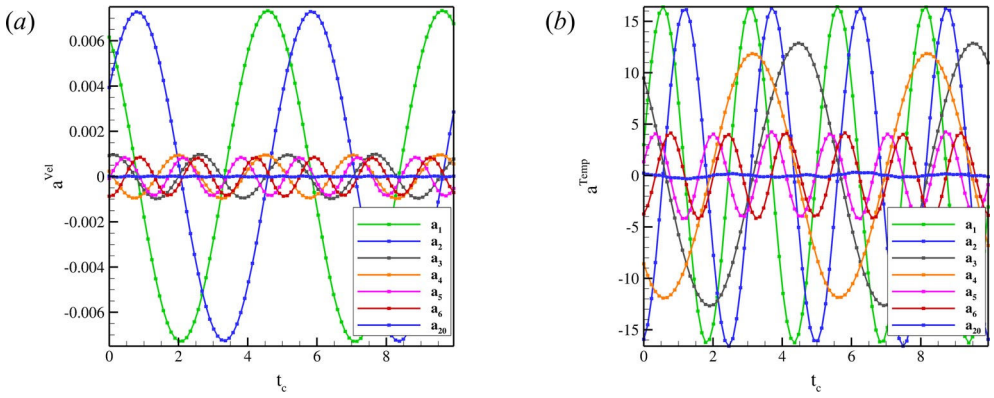

Figure 99: Temporal POD coefficients: (a) a_i^{Vel}; (b) a_i^{Temp} as a function of t_c for $N = 135$.

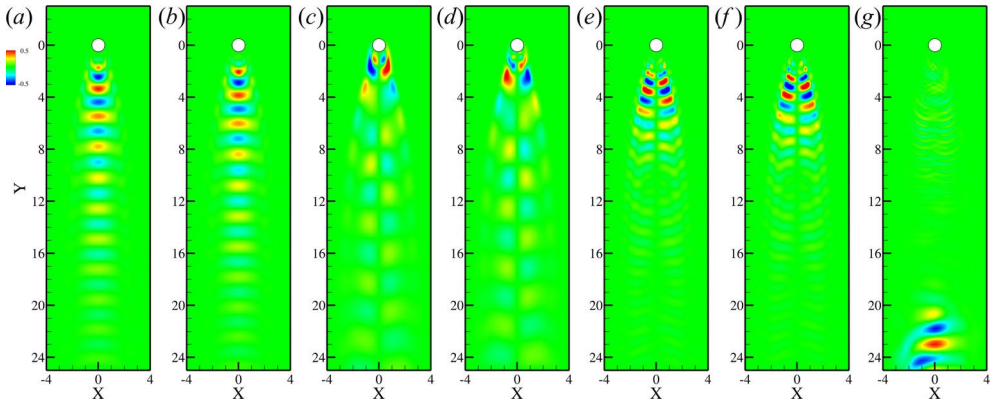

Figure 100: Temperature POD modes: (a) Mode1; (b) Mode2; (c) Mode3; (d) Mode4; (e) Mode5; (f) Mode6; (g) Mode20 for $N = 135$.

2 from the velocity field decomposition have a fundamental frequency equal to $St_0 = 0.198$ identical to the one found in figure 96 for the lift coefficient C_L, the first two temperature POD modes have a fundamental frequency of $2St_0$ corresponding to the one of the drag coefficient C_D in the same figure. Velocity modes 3 (and 4), modes 5 (and 6) and mode 20 have fundamental frequencies of respectively $2St_0$, $3St_0$ and $8St_0$ while temperature modes 3 (and 4), modes 5 (and 6) and mode 20 have respective fundamental frequencies St_0 and $4St_0$ and $5St_0$. Conversely to the 2SLDC decompositions, the fundamental frequencies captured by the "corresponding" velocity and temperature POD modes do not match. This is a reminder that although the velocity and temperature POD series are calculated based on the same data set of corresponding velocity and temperature fields, the obtained POD modes are decoupled from one another and there is no one-on-one equivalent between the velocity and temperature decompositions.

2.3.4 Reduced Order Model

Reduced order models are obtained for several combinations of the values N_V and N_T, respectively the number of POD modes used in the velocity and the temperature reconstruc-

DISTRIBUTION A: Distribution approved for public release.

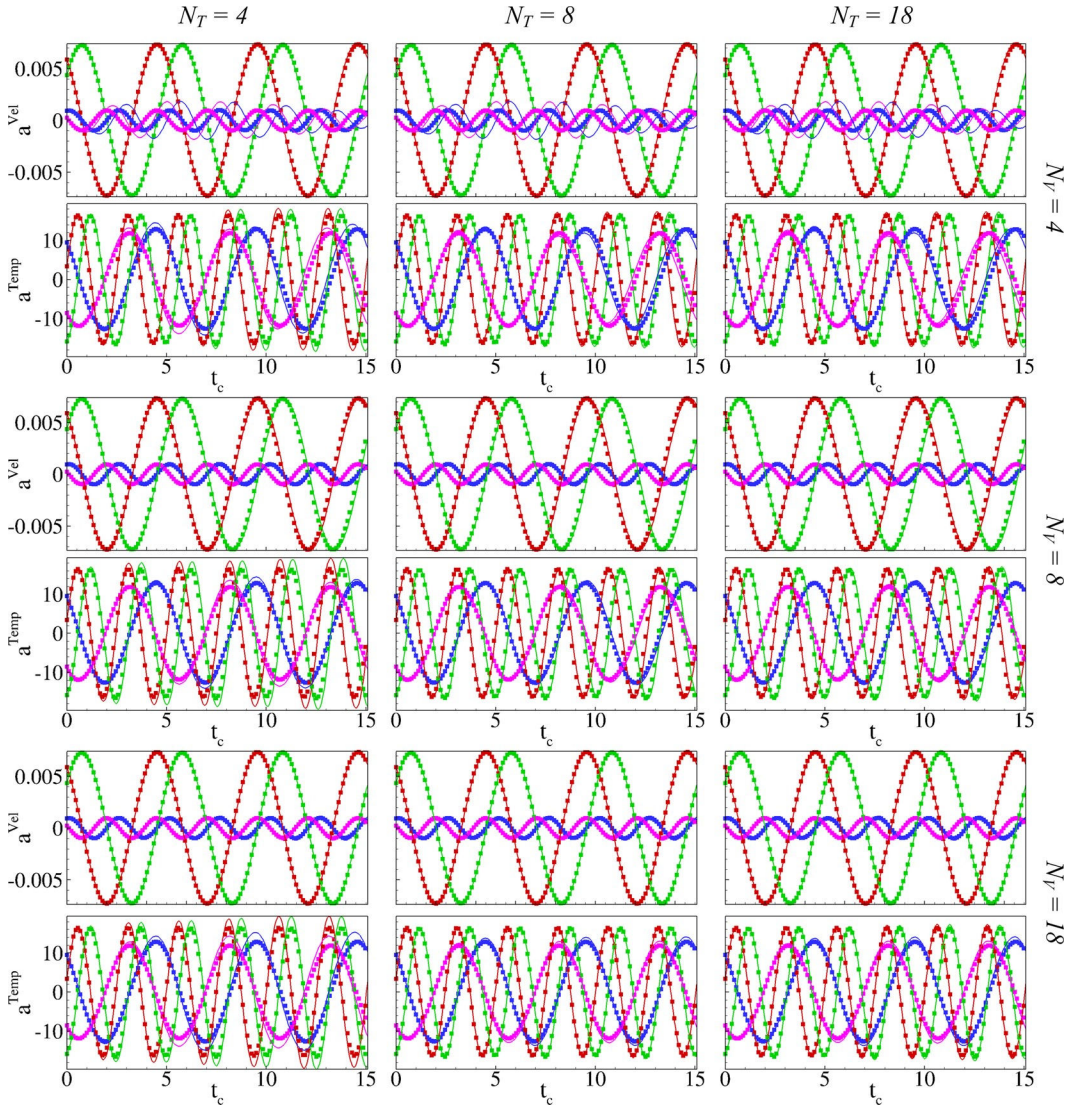

Figure 101: First four ROM temporal coefficients for the velocity and temperature fields obtained for several values of N_V and N_T (*solid lines*) along with corresponding POD temporal coefficients (*symbols*). a_1 (*red*), a_2 (*green*), a_3 (*blue*), a_4 (*magenta*).

tions, based on the decomposition including 135 snapshots described previously. As for the 2SLDC problem, the derivatives of the POD shape functions are obtained using Tecplot. A trapezoidal integration approximation is used to evaluate the Galerkin coefficients in equations 1 and 2 while the pressure term $P_r(t)$ in equation 1 is neglected. The ODEs are integrated using both the DP45 and ABM-PECE algorithms, with tolerance parameters of 10^{-8} to 10^{-2}. Once again, no significant differences are observed between both solvers and the integration results are sensibly identical beyond a relative tolerance of 10^{-4}. In the following, the equations for the velocity and the temperature are solved simultaneously using the DP45 algorithm with a tolerance of 10^{-4}.

DISTRIBUTION A: Distribution approved for public release.

The results from the integration of reduced order models are presented in figure 101 as a function of the parameters N_V and N_T for the first four temporal coefficients along with the corresponding POD coefficients (projected LES data). The results for the velocity ROM show excellent tracking over two periods for the first two temporal coefficients as early as $N_V = 4$. The accuracy of the ROM remains excellent for the following two modes with $N_V = 8$ and $N_V = 18$. As for the 2SLDC velocity ROM, no visible influence of N_T on the velocity solution is observed at fixed values of N_V. For $N_T = 4$, the temperature ROM is somewhat less accurate than its velocity counterpart on modes 1 and 2, but surprisingly good on mode 3 and 4. The ROM starts to diverge in the third period and the influence of N_V on the temperature ROM appears to be weak. For $N_T = 8$, the accuracy of the temperature ROM is greatly improved for the first two temporal coefficients over the $N_T = 4$ solution. The influence of N_V is however visible between $N_V = 4$ and $N_V = 8$, in particular for the third and fourth temporal coefficients. Finally, the results for $N_T = 18$ show reasonable accuracy at $N_V = 4$ and excellent qualitative tracking for $N_V = 8$ and $N_V = 18$. It is however worth noting that the accuracy in the third period appears to be slightly worse for the case with higher N_V, especially on the third and fourth modes. Overall good qualitative tracking of both velocity and temperature ROMs is obtained for $N_V = 8$ and $N_T = 8$.

Overall, good qualitative and quantitative agreement with the projected LES data is obtained using $N_V = 8, N_T = 18$, even though the pressure terms are being neglected.

DISTRIBUTION A: Distribution approved for public release.

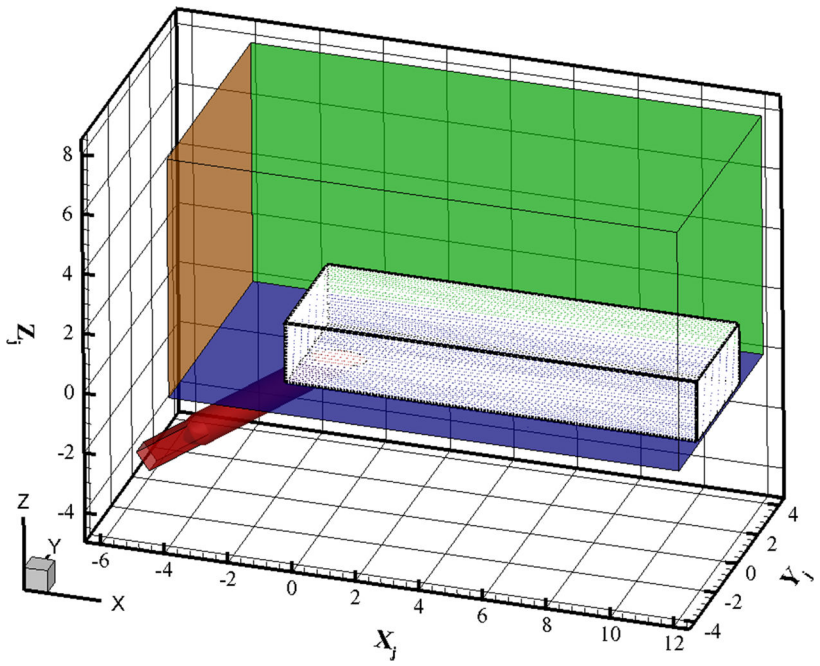

Figure 102: Proper Orthogonal Decomposition domain.

3 Film Cooling Jets Reduced Order Models

3.1 Preliminary Statistical POD Analysis of Film Cooling Jets

Before using the POD for reduced order modeling purposes, the decomposition is used for its flow analysis capabilities in order to isolate the dominant flow vortical structures in a quantitative way and identify any potential shortcomings of the method. POD is applied to both unforced and forced inclined jets described in the previous chapter. In this section, the Proper Orthogonal Decomposition is carried out on the complete velocity and temperature signals, without beforehand separating them into time averaged and fluctuation components.

3.1.1 Unforced Jets

The three-dimensional flow field and temperature field from LES at $BR = 0.15$ are analyzed using the snapshot method described in Chapter 4. A set of 200 statistically independent flow and temperature fields with a spatial density of 10 points per jet diameter is used. It is found that at the considered low turbulence levels, 300 snapshots and 20 vectors per jet diameters lead to sensibly identical results with yet considerably longer computation times. The analyzed sub-domain is presented in figure 102 and is such as $\{-1 \leq X_j \leq 12, -2 \leq Y_j \leq 2, 0 < Z_j \leq 2\}$ yielding 106,600 spatial points at the lowest resolution.

Figures 103(a-c), 104(a, b) present slices of the first four velocity POD modes (including the mean flow field) as well as the corresponding λ_2 (2^{nd} invariant of the velocity divergence tensor) iso-surfaces. The time averaged flow field exhibits the classical features of inclined jet in cross-flow and compares qualitatively well with previously reported results of (10). In particular the presence of a pair of counter-rotating vortices (CRVP) is visible in the $X_j = 6$

DISTRIBUTION A: Distribution approved for public release.

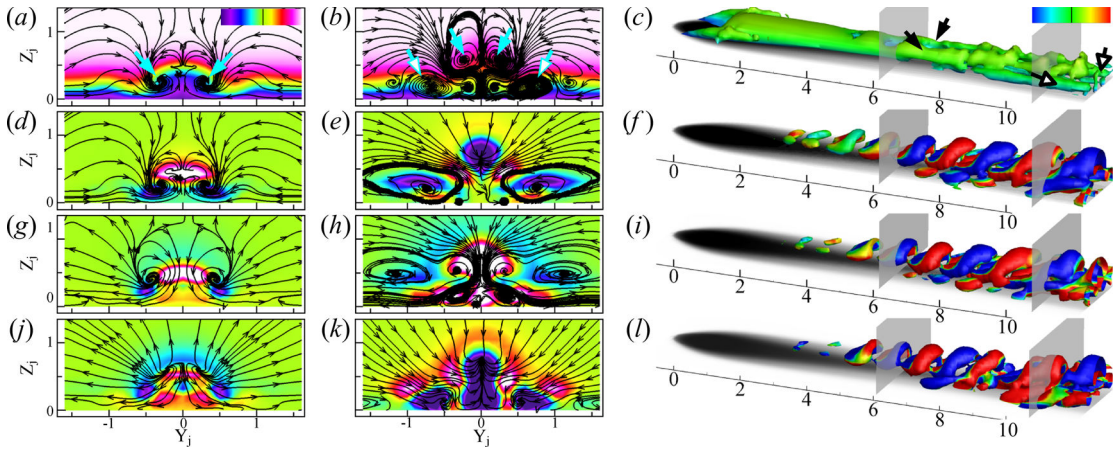

Figure 103: Mean flow (0^{th} POD Mode) and first 3 velocity POD modes at $BR = 0.15$ (a-c) Mode0; (d-f) Mode1; (g-i) Mode2; (j-l) Mode3. Slices at $X_j = 6$ (*left*), $X_j = 10.6$ (*center*) with U velocity contours and V-W streamlines. λ_2 iso-surfaces (*right*) computed from the corresponding POD modes colored by U velocity and mean wall temperature contours (*gray scale*).

and 10.6 slices (solid arrows) as well as in the $Z_j = 0.25$ slice with upward motion around the $Y_j = 0$ line surrounded by two lines of downward motion at $Y_j = \pm 0.5$. The CRVP is generated in the average field by the downstream convection of the shear layer hairpin vortices legs as for the vertical jet configuration. In addition at $X_j = 10.6$ a secondary pair of counter-rotating streamwise vortices (hollow arrows) of opposite vorticity is formed near the wall on each side of the jet, corresponding to the side vortices observed in figure 29. The side vortices are observed in figure 103(c) for $X_j > 9$ and materialized in the average flow field by vortex tubes along the jet core as well as in figure 104(b) through the formation of another 'stripe' of positive vertical motion at $Y_j = \pm 0.9$.

The remaining POD modes provide an orthogonal decomposition of the fluctuation part of the velocity. According to figure 105(a), the first two POD modes virtually capture the same amount of energy while being also very similar in shape when comparing figure 103(f) and 103(i), as well as figure 104 (c, d) and 104 (e, f) with a phase shift in the streamwise direction. Both modes exhibit alternating changes in the sign of the velocity components in the downstream direction. Hence, the cumulative effects of Mode1 and 2 alternating positive and negative velocity regions combined with the phase shifted variations in the signs of a_1^{Vel} and a_2^{Vel} in figure 105(b), generates a downstream motion. In the present case, this behavior is associated with the convection of the shear layer hairpin vortices which are the principal structures observed in the attached jet configuration, supported by λ_2 iso-surfaces in figures 104(f) and 104(i) exhibiting hairpin shapes similar to the one of hairpin vortices. The velocity vector field associated with the first two POD modes also exhibits in figures 104(c) and 104(e) focus points corresponding to the hairpins legs. It is also observed that the first modes are strong rather far away from the jet exit but not particularly significant near the jet exit. This is explained by the fact that proper orthogonal decomposition 'sorts' the modes with respect of the amount of kinetic energy they contain, thus sorting the scales of the structures as well, such that the most energetic modes (first modes) will usually represent

DISTRIBUTION A: Distribution approved for public release.

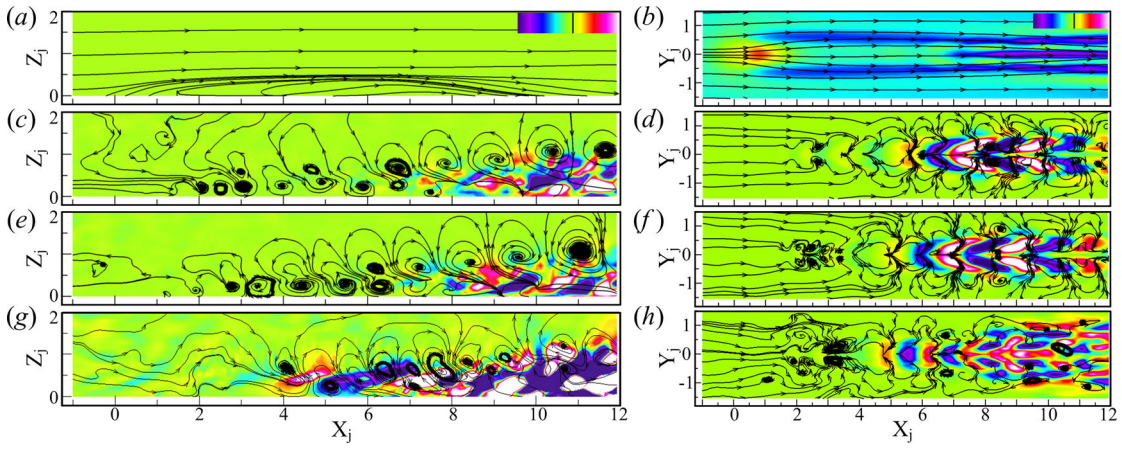

Figure 104: Mean flow and first 3 velocity POD modes at BR=0.15 (*a, b*) Mode0; (*c, d*) Mode1; (*e, f*) Mode2; (*g, h*) Mode3. Slices at $Y_j = 0$ with V velocity contours and U-W streamlines (*left*) and slices at $Z_j = 0.25$ with W velocity contours and U-V streamlines (*left*).

the largest structures. The third mode presented in figure 103(*k-m*) and 104(*g, h*) exhibits similarities with the first two modes with alternating positive and negative vertical velocity in the plane $Z_j = 0.25$, though the pattern appears less regular. In the plane $Y_j = 0$ of figure 104(*g*), the streamlines clearly show the formation of rollups in the jet upper shear layer. A strong negative streamwise velocity region is located near the symmetry plane ($Y_j = 0$) between the hairpin legs which is visible in the plane $X_j = 10.6$ as well. While streamwise vorticity from the fluctuations of the CRVP and side vortices is captured in the first two modes, no significant x-vorticity appears to be contained in the third mode at $X_j = 6$ or 10.6. Although according to figure 105(*a*) several other modes appear to carry a significant amount of energy, they will not be presented in the current document for the sake of brevity. However, it should be noted that the fourth mode resembles closely the third one yet with a 'phase shift' in the same way the first and second modes were related. The additional modes ($N \geq 5$) describe principally the dynamics of the near-wall region, particularly the side vortices and their interaction with the hairpin vortices.

The temperature field is analyzed as well using POD. Although the norm used in the standard proper orthogonal decomposition does not maximize the thermal energy, this method has been used in previous studies to provide a set of orthonormal functions that can be used to obtain a reduced order model of the temperature field (see previous sections). However, it can be argued that the decomposition may not be as 'optimal' as the one obtained for the velocity field in terms of energy. The 0^{th} mode (average temperature field) is presented in figure 106(*a-c*), and 107(*a, b*). The temperature field at the wall (figure 107*b*) is consistent with the one presented in figure 30(*a*). The contours in figure 106(*a, b*) show the averaged impact of the CRVP and the side-vortices on the temperature field. While the CRVP entrains hot cross-flow fluid near the wall, the side-vortices tend to increase the spread by varying jet fluid away from the jet core as the two lumps of cooler fluid at $Y_j = \pm 1$ suggest. In figure 105(*a*), the two first modes carry equivalent pseudo-thermal energy while figures 106(*f*) and 106(*i*) show that both modes, related to the hairpin shear

DISTRIBUTION A: Distribution approved for public release.

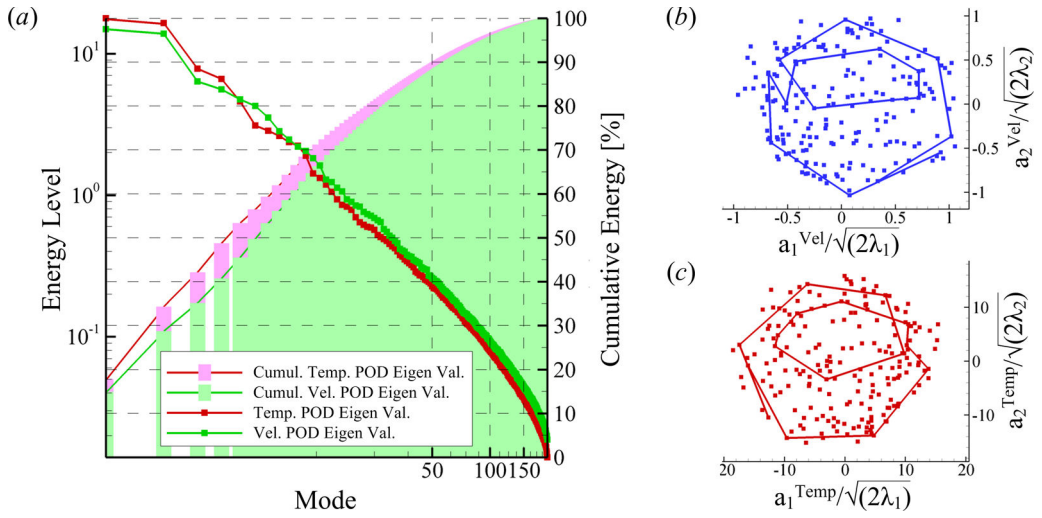

Figure 105: POD decomposition metrics for $BR = 0.15$ (a) POD modes eigenvalues and cumulative temperature and velocity energies; (b) First two velocity POD coefficients a_1^{Vel} and a_2^{Vel}; (c) First two temperature POD coefficients a_1^{Temp} and a_2^{Temp}.

layer vortices according to the shape of their iso-surfaces, are overall identical with a phase shift in the streamwise direction. Based on these considerations and given the distribution of the phase diagram in figure 105(c) showing alternating signs for a_1^{Temp} and a_2^{Temp}, it appears clearly that the first two modes describe the convective effect of the hairpin vortices on the temperature field. Near the wall at $Z_j \approx 0$ (figure 107d, f), the two modes exhibit similar shifted patterns yet a noticeable difference exists near $X_j = 10$ with the presence in the second mode of a pair of patches with a negative value (dark) on each side of the jet (around $Y_j = \pm 1$) which counterpart is not clearly found in the first mode. A comparable discrepancy between the two first modes is found in the same plane around $X_j = 8$, where in Mode1 a pair of patches of rather high positive values (white) near $Y_j = \pm 1$ are present yet no equivalent counter part is found in Mode2. These differences can be attributed to 'quasi-stationary' events occurring near the wall where the velocity is low and the convective effects are not as strong. Thus, while the positive patches in Mode1 appear to correspond to the effect of the hairpin vortices on the pinching of the jet coverage observed in the mean temperature field and attributed to cross-flow entrainment from the legs of the structures, the negative patches in Mode2 are likely to be associated to the spreading of the jet coverage due to the effects of the side vortices. For the sake of brevity, the 3^{rd} and 4^{th} modes are not presented here as they appeared very similar to the two first modes although at smaller length scales.

The 5^{th} mode, however associated with a lower eigenvalue (figure 105a), captures a different behavior as shown in figure 106(k-m) and figures 107(g, h). At $X_j = 6$ and $X_j = 10.6$, Mode5 exhibits two continuous zones in the streamwise direction with positive and negative values. This mode appears to capture a different type of mixing since conversely to Mode1 and 2 the spatial distribution of the mode is not alternating signs in the downstream direction and no other POD mode was found to assume a similar distribution. These observations suggest Mode5 is associated with the mixing behavior induced by the CRVP rather than the downstream convective effect of the hairpin vortices. Hence, the stacking

DISTRIBUTION A: Distribution approved for public release.

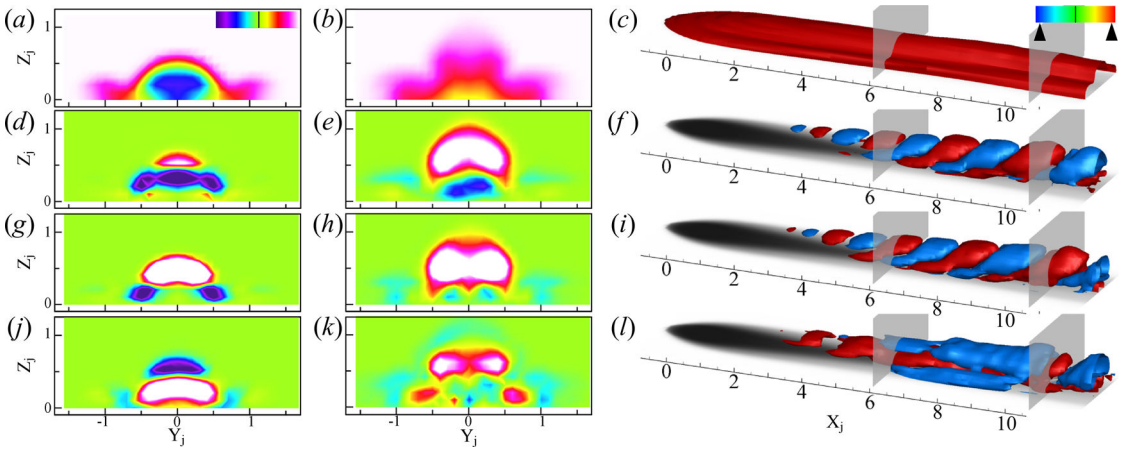

Figure 106: Mean temperature field (0^{th} POD mode) and first significant temperature POD modes at $BR = 0.15$ (*a-c*) Mode0; (*d-f*) Mode1; (*g-i*) Mode2; (*j-k*) Mode5. Slices $X_j = 6$ (*left*), $X_j = 10.6$ (*center*) with temperature contours. Iso-temperature surfaces (*right*) computed from corresponding POD modes (*red*: positive *blue*: negative) and mean wall temperature contours (*gray scale*).

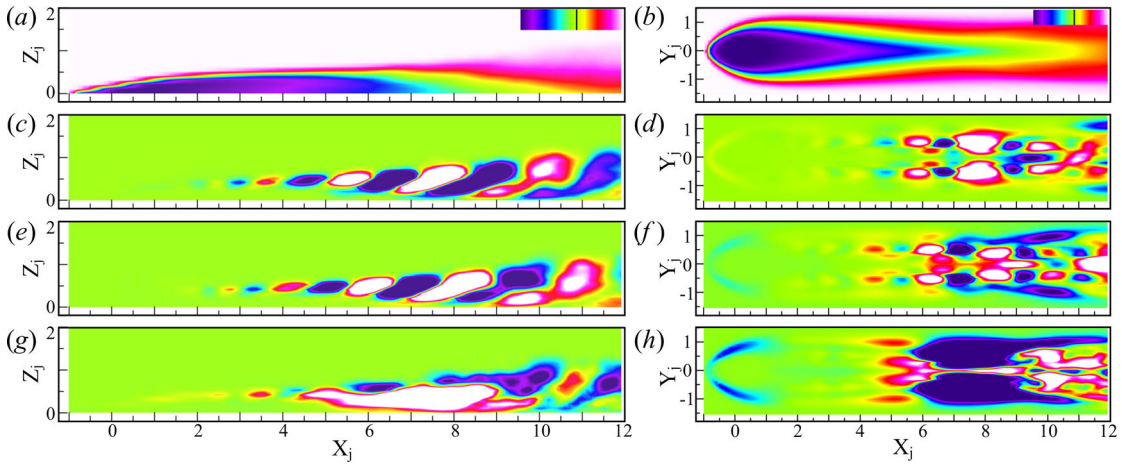

Figure 107: Mean temperature field and first significant temperature POD modes at $BR = 0.15$ (*a, b*) Mode0; (*c, d*) Mode1; (*e, f*) Mode2; (*g, h*) Mode5. Slices at $Y_j = 0$ with temperature contours (left) and slices at $Z_j = 0$ with temperature contours (*right*).

DISTRIBUTION A: Distribution approved for public release.

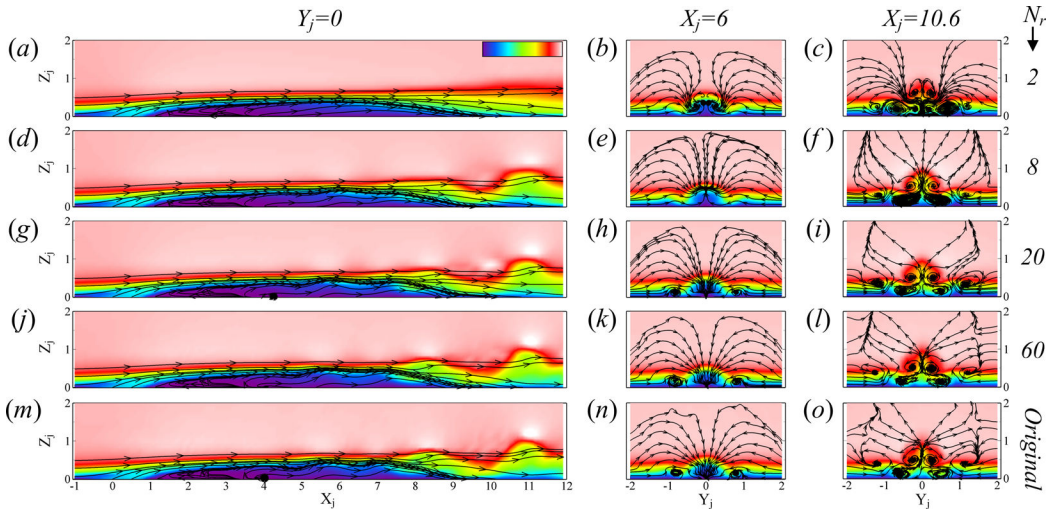

Figure 108: Reconstructed velocity field for multiple values of N_r. Stream traces correspond to in-plane velocity, contours to streamwise velocity.

of an area with negative values on top of one with positive values can be interpreted by the CRVP bringing cooler fluid to the upper part of the domain while entraining hotter fluid near the wall and toward the symmetry plane. Near the wall in figure 107(h), a large area of negative values is visible around $X_j = 8$, $Y_j = \pm 0.5$ where the jet coverage starts to degrade due to cross-flow entrainment. A similar distribution is found near the wall in Mode4 although the rest of the distribution is more consistent with the Mode3. From these observations, it can be argued that the temperature POD modes are more correlated than the velocity modes and part of the information associated with specific phenomena can be captured across several modes.

Figure 105(a) provides an estimation of the total amount of kinetic and pseudo-thermal energies captured by the POD modes as well as the cumulative energy captured by the N first modes. According to the latter, 61 velocity POD modes and 53 temperature POD modes are required to gather at least 90% of the total energy and respectively 156 and 163 modes to gather 99% while modes beyond respectively $N_V = 17$ and $N_T = 15$ carry less than 1% of the total energy.

In figure 108 an instantaneous velocity field is reconstructed from truncated POD series to assess the number of modes necessary to rebuild the dominant flow features. In the plane $Y_j = 0$, the first reconstruction using only 2 modes does not render the formation of the individual hairpin vortex present in the original snapshot at $X_j = 10.6$. This was to be expected due to the absence of information carried by higher order modes with respect to the hairpin vortices as seen in 103(l), thus justifying the lack of accuracy of the reconstructed field. The individual hairpin vortex is observed for $N_r \geq 8$. In the near field of the jet ($X_j < 6$) the reconstruction appears relatively close to the original field with as few modes as 8, due to the low fluctuation levels and limited length scales of the structures in this region. In the plane $X_j = 6$ however, the features of the original flow such as the two counter rotating vortices located at $Z_j = 0.3$, $Y_j = \pm 1$ are only consistently reconstructed for $N_r \geq 20$. Similarly in the plane $X_j = 10.6$, the location and scale of the multiple structures present in the original snapshot are only captured in reconstructions including

DISTRIBUTION A: Distribution approved for public release.

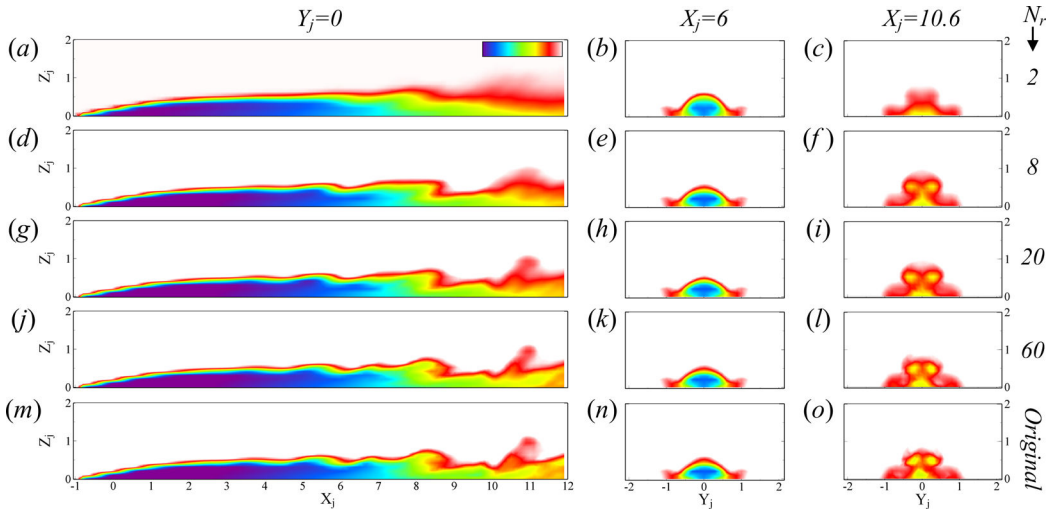

Figure 109: Reconstructed temperature field for multiple values of N_r.

20 modes or more. Overall, although closer from the actual snapshot, the reconstruction using 60 modes does not appear to constitute a significant improvement over the one with 20 modes in terms of the dominant features.

Figure 109 shows reconstructed and original temperature fields corresponding to figure 108. Overall in the plane $Y_j = 0$, the reconstructed temperature field appears to render individual structures beyond $N_r = 8$, with a relatively satisfying definition for $Nr \geq 20$. Similarly, in the planes $X_j = 6$ and $X_j = 10.6$, the reconstructed fields show very little differences. Beyond the qualitative examination of the reconstructed fields, time averaged error distributions with respect to the original field were also calculated to assess the quantitative accuracy obtained with a given number of POD modes. For the velocity field, the error in local kinetic energy. This choice has the advantage of combining all three velocity components into a single figure of merit in addition of being directly related to the norm used for the orthogonal decomposition. However, as the 0^{th} mode corresponds to the time averaged velocity field, not carrying any intrinsic error, it appears more adequate to monitor the error on the turbulent kinetic energy (TKE) rather than the total kinetic energy. The errors distributions on the turbulent kinetic energy are presented in figure 110. In the plane $Y_j = 0$, two zones can be identified. Beyond $X_j = 6$ the error on the decreases significantly to be almost zero for $N_r = 60$. However for $X_j < 6$, the error, although decreasing, stays significant in the jet shear layers even with as many as 100 POD modes. It should also be noted that the extent of this zone of relatively high error decreases with increasing number of POD modes included in the decomposition. This can be explained by the nature of the proper orthogonal decomposition and the norm associated with it, imposing a hierarchy of the modes based on the amount of kinetic energy they capture so that the first modes will capture the large scale structures of the domain. In jets in cross-flow, the principal instability responsible for the formation of the shear layer hairpin vortices is of the convective type and exhibits multiple length scales as it develops in the downstream direction to reach maximum intensity in the far-field. The POD modes thus capture first the downstream motion carrying the largest amount of energy and then progressively capture the lower shear layer fluctuations by going in a reverse direction to the development of the

DISTRIBUTION A: Distribution approved for public release.

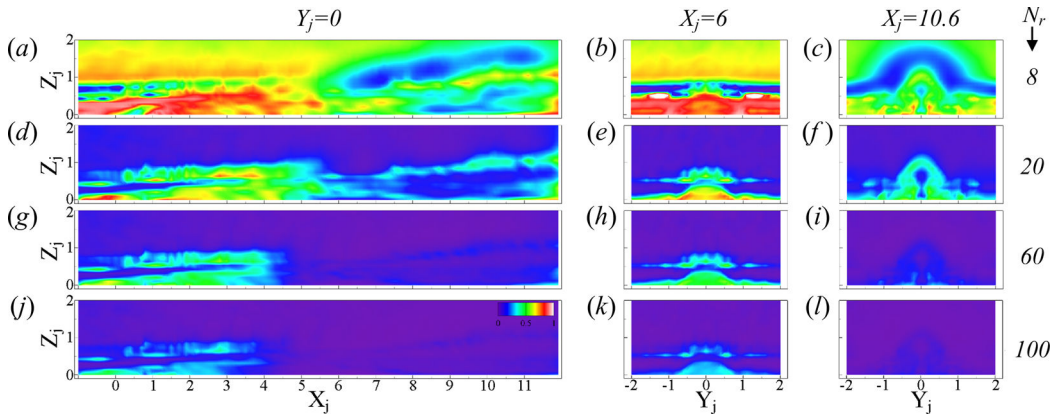

Figure 110: Average TKE error of the reconstructed fields for various values of N_r. Maximum contour value 1 (*white*).

instability thus justifying the relatively poor quality of the reconstruction in the near field of the jet. This constitutes one of the limitations of the standard POD which may lead to dynamical inaccuracy when trying to implement a reduced order model of the flow as pointed out by (36).

Since no perturbation on the temperature field is imposed at the inlets of the domain and by nature the energy equation is free of an explicit non-linear term in T capable of producing or sustaining fluctuations, in a large part of the domain the true temperature fluctuation is extremely low, even null, and thus induced extremely high errors on the fluctuation value when monitoring the reconstructed temperature field. Based on these considerations, it is decided to monitor the absolute relative error on the total temperature field rather than the fluctuation part, reported in figure 111. The error on the temperature field decreases consistently with increasing number of POD modes included in the reconstruction. Most of the error is concentrated beyond $X_j = 5$ where most of mixing and temperature fluctuations occur. It should be noted that similarly to the turbulent kinetic energy, the error in the shear layer of the near-field, appears to decrease at a slower rate than in the far-field. Overall with $N_r = 20$, the maximum error was found to be inferior to 2%, decreasing to less than 1% with $N_r = 60$.

3.1.2 Forced Jets

As for the steady state, LES flow fields and temperature fields for *Case X* at $St_\infty = 0.016$ are analyzed using 3D-POD. The domain and spatial sampling used for the forced cases are identical to the one described in the previous section. Based on the work of (73) on 2D-POD of a pulsed detached jet in cross-flow, an initial temporal sampling of 25 phase locked positions over 10 periods is considered. However, given that the forcing signal used in (73) was a sinusoidal, thus significantly different from the square wave used in the current study, a finer sampling of 50 phase locked positions over 10 cycles is preferred. The POD is computed on both the full time sequence and the phase averaged signal. As seen in figure 114, both methods provide sensibly similar results for the first 20 modes and starts to diverge for higher order modes. This result is expected and consistent with the findings of (73). Indeed, when considering the complete time sequence, the fluctuation part due to more fine-grained

DISTRIBUTION A: Distribution approved for public release.

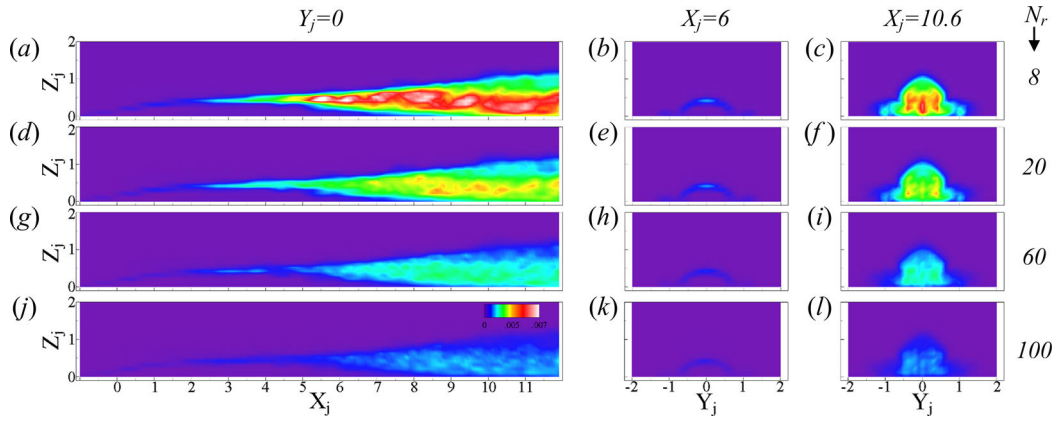

Figure 111: Average temperature error of the reconstructed field at various N_r values. Maximum contour value: 7.10^{-3} (*white*).

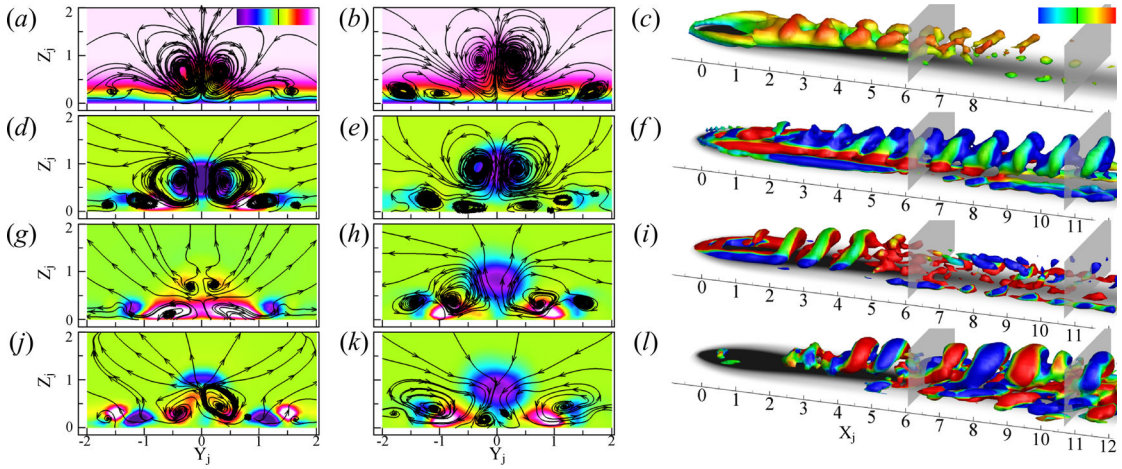

Figure 112: Mean flow (0^{th} POD Mode) and first significant velocity POD modes for *Case X* at $St_\infty = 0.016$ (*a-c*) Mode0; (*d-f*) Mode1; (*g-i*) Mode2; (*j-l*) Mode6. Slices at $X_j = 6$ (*left*), $X_j = 10.6$ (*right*) with U-velocity contours and V-W streamlines. λ_2 iso-surfaces (*right*) from corresponding POD modes colored by U-velocity and mean wall temperature contours (*gray scale*).

DISTRIBUTION A: Distribution approved for public release.

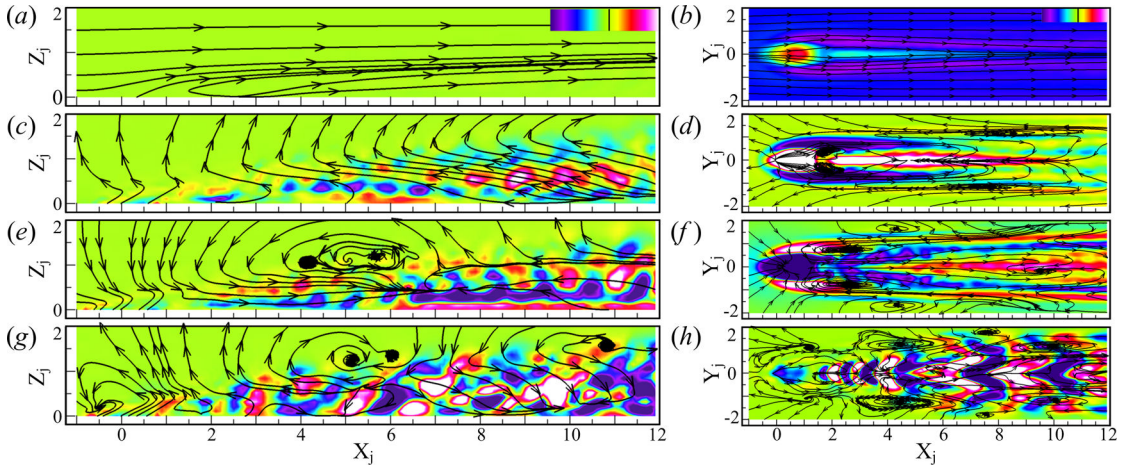

Figure 113: Mean flow and first significant velocity POD modes for *Case X* at $St_\infty = 0.016$; (*a, b*) Mode0; (*c, d*) Mode1; (*e, f*) Mode2; (*g, h*) Mode6. Slices at $Y_j = 0$ with V-velocity contours and U-W streamlines (*left*) and slices at $Z_j = 0.25$ with W-velocity contours and U-V streamlines (*right*).

turbulence is included in the signal and requires a large number of modes to be fully resolved. On the other hand, when analyzing the phase averaged signal, the turbulent fluctuation is removed from the signal thus requiring fewer modes to capture the bulk flow fluctuations (phase averaged). While in the steady state POD analysis, the turbulent fluctuations were considered important to model the flow behavior, in the pulsed system, the significant part was considered to be the phase averaged variation thus the results presented in this paper are based on the POD analysis of the phase averaged signal.

For the sake of brevity, figures 112 and 113 only present modes 0, 1, 2 and 6 issued from the decomposition of *Case X* at $St_\infty = 0.016$. As for the steady state, the 0^{th} mode corresponds to the average flow field. Based on the interpretations of the velocity shape functions it is possible to qualitatively identify which features of the forced jet are being captured by individual modes. The 1^{st} mode corresponds to the bulk flow fluctuation associated with the change in blowing ratio and captures the global jet expansion and shrinking occurring during a cycle. No evidence of a vortical structure is observed in the upper shear layer in figure 113(c), although a counter rotating vortex pair is visible in the constant X_j slices of figure 112(d) and 112(e). The 2^{nd} mode exhibits large scale structures in the jet upper shear layer in figure 113(e), converging velocity field toward the jet exit as well as strong vertical vorticity in the plane $Z_j = 0.25$ of figure 113(f), and is predominantly significant in the near field of the jet in figure 112(i). These considerations suggest that Mode2 is correlated to the large scale structures introduced at the transition from BR_l to BR_h and from BR_h to BR_l, being starting vortices and/or ingestion as described in the previous chapter. It should be noted that in this forced case, the cumulative captured kinetic energy of modes 1 and 2 is equivalent to 53% of the total kinetic energy which is to be put in perspective with the 30% in the steady state case at $BR = 0.15$. Modes 3 to 5 were very similar to the 2^{nd} mode with finer scales were considered as to capture smaller features associated with the introduction of the transient regimes and thus were not presented here for brevity. However, Mode6 in figure 113(g) evidences the presence of shear layer vortices consistent with the natural hairpin

DISTRIBUTION A: Distribution approved for public release.

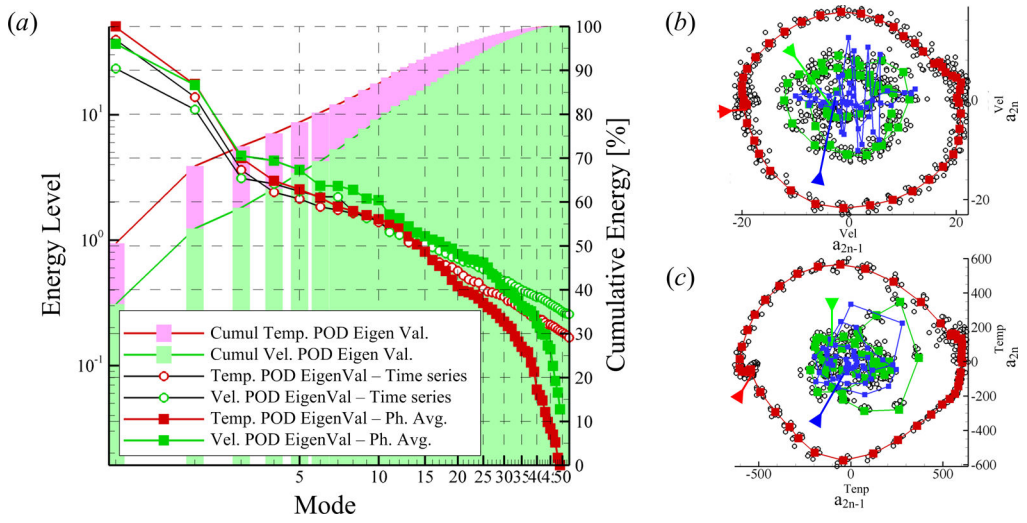

Figure 114: POD decomposition metrics for *Case X* at $St_\infty = 0.016$ (a) Temperature and velocity POD modes eigenvalues and cumulative energy; (b) Velocity POD coefficients; (c) Temperature POD coefficients. Open symbols correspond to full time sequence POD. Arrow points toward $t^* = 0$ in the time sequence.

vortices encountered in unforced conditions, and the λ_2 iso-surfaces of figure 112(m) are very comparable to the one found in dominants modes at $BR = 0.15$ (see previous section). This implies that the 6^{th} mode is likely related to the quasi-unforced behavior during either the low or high part of the cycle. This last point will be developed later and lead to the observation of the POD mode segregation. Conversely to the steady state, the circular shape of the phase diagram in figure 124(b) should not be interpreted as a sign of correlation between the 1^{st} and 2^{nd} modes since the signal is by nature periodic. However, the circular shape shows that both modes operate at the same frequency and with almost equal influence. Interestingly, clusters of points can be observed before the beginning (red arrow) of the cycle and before the transition from high to low blowing ratio (diametrically opposed to the red arrow) where both 1^{st} and 2^{nd} mode values stagnate, the former at a maximum (or minimum) and the latter at a zero value. This observation confirms the qualitative interpretation previously made where Mode1 would correspond to the bulk modulation of the jet envelope thus would be predominant away from the transition points, and Mode2 would correspond to the large scale structures of the transition and would have high values at the transitions.

The temperature field is analyzed as well using POD, the results of which are presented in figure 115 and 116. Similarly to the velocity field decomposition, the 0^{th} mode in figure 115(a-c), 116(a, b) corresponds to the average temperature field, while Modes 1 and higher correspond to the fluctuations around this time averaged field. As for the velocity decomposition, the 1^{st} mode, which is the most energetic, appears to describe the global temperature fluctuations due to the change in penetration associated with jet forcing. The 2^{nd} mode shows a more localized distribution with positive values in the vicinity of the jet exit and negative values in the far field. The phase diagram in figure 114(c) shows strong similarities with the one of the velocity field and suggests that while Modes1 and 2 have similar overall impact in terms of amplitude and frequency, the moments at which they

DISTRIBUTION A: Distribution approved for public release.

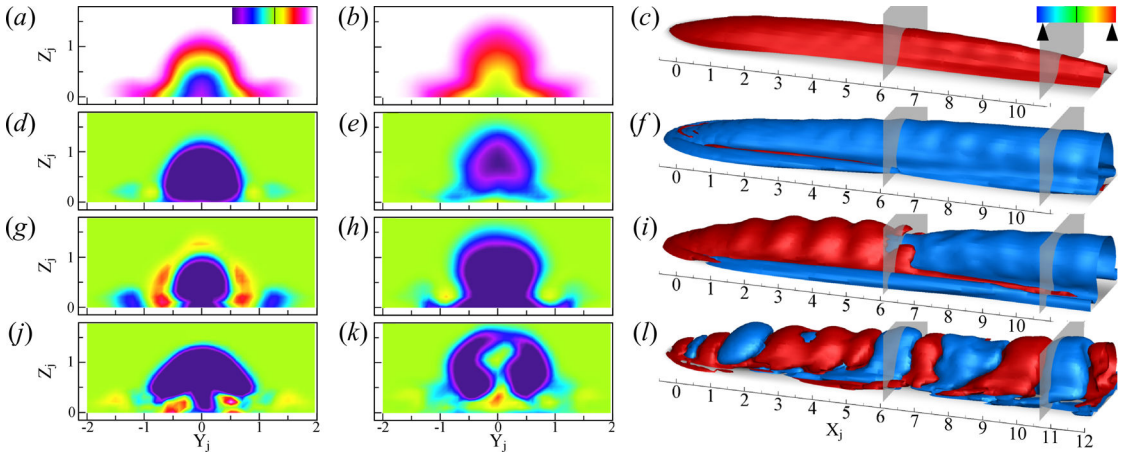

Figure 115: Mean temperature field (0^{th} POD mode) and first significant temperature POD modes for *Case X* at $St_\infty = 0.016$ (*a-c*) Mode0; (*d-f*) Mode1; (*g-i*) Mode2; (*j-l*) Mode10. Slices at $X_j = 6$ (*left*), $X_j = 10.6$ (*center*) with temperature contours. Iso-temperature surfaces (*right*) computed from the corresponding POD modes and mean wall temperature contours (*gray scale*).

are acting on the flow are different. Hence Mode1 has a stronger influence away from the transitions while Mode2 affects the flow mainly at the transitions moments. Modes 3 to 9 exhibited distributions similar to the one of Mode2 with yet smaller length scales and were considered to describe the smaller scale perturbations introduced by the transients thus not presented here. The 10^{th} mode though shows fluctuations in the jet shear layer further away from the jet exit which are consistent with the one observed in unforced conditions at $BR = 0.15$. This suggests that this mode captures the quasi-unforced nature of the jet away from the transitions. The energy distribution in figure 114(a) shows that a total of 41 velocity modes and 33 temperature modes are required to gather 99% of the total fluctuation energy.

To confirm the qualitative interpretations of the POD modes the coefficients a_1, a_2, a_6 for the velocity field and a_1, a_2, a_{10} for the temperature field were plotted in figure 117(a) versus t^* along with the phase averaged blowing ratio profile. In both decompositions, a_1 has broad periods of maxima in absolute value beyond $t^* = 0.20$ up to $t^* = 0.55$ and from $t^* = 0.80$ to $t^* = 1$, both corresponding to the respective established quasi-unforced regimes while a_2 exhibits more localized maxima, directly after the transitions, from one part of the cycle to the other. Modes 6 for velocity and 10 for temperature have significant values during the quasi-unforced regime in the high part of the cycle also confirming the qualitative analysis. The plots of intermediate coefficients (a_3 to a_5 for velocity and a_3 to a_9 for temperature) showed that their support of action was also localized within the transient regions of the cycle and the amplitude of their respective maxima was decreasing along with the width of the peak, exposing a more localized and finer scale influence. Although the transient and the high quasi-steady regimes are captured by modes 1 to 6, none of the first significant modes, except for the first one describing the bulk flow modulations, seem to have significant non-zero values during the low quasi-steady part of the cycle. Only modes beyond the 40^{th} one have their support of action localized during this part of the cycle as seen in figure 117(a) for

DISTRIBUTION A: Distribution approved for public release.

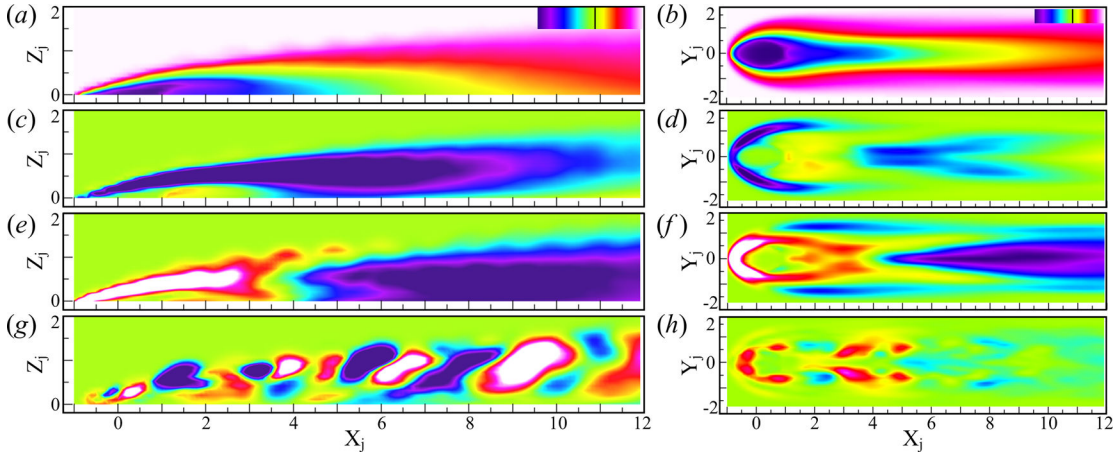

Figure 116: Mean temperature field and first significant temperature POD modes for *Case X* at $St_\infty = 0.016$ from LES; (a, b) Mode0; (c, d) Mode1; (e, f) Mode2; (g, h) Mode10. Slices at $Y_j = 0$ with temperature contours (*left*) and slices at $Z_j = 0$ with temperature contours.

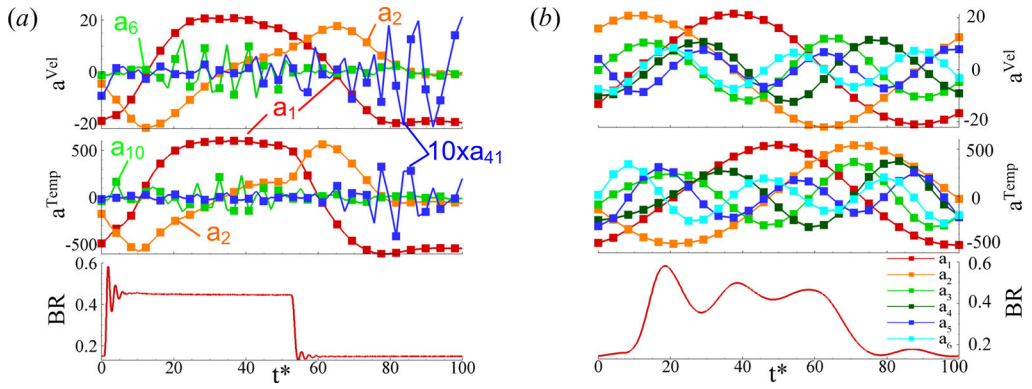

Figure 117: Temporal evolution of the POD modes coefficients a_i^{Vel} for the velocity (*top*) and a_i^{Temp} for temperature (*middle*) decompositions along with forcing blowing ratio profile (*bottom*) at (a) $St_\infty = 0.016$; (b) $St_\infty = 0159$. The values of a_{41} in (a) are multiplied by a factor 10 for increased visibility.

a_{41} (multiplied by 10 to increase visibility). This can be explained by the fact that vortical structures formed during the low quasi-unforced part of the cycle are relatively energetically weak, compared to the transient vortical structures or even the one formed during the quasi-steady high part of the cycle, thus are relegated to the end of the POD spectrum as weak perturbations.

Figure 118 shows the phase locations of the maximum and minimum values of the modal coefficients for each mode revealing the moment in the cycle where they have maximum influence. For both velocity and temperature, a clear pattern appears in the distribution of the maxima and minima. Indeed most of the 40 first modes have an influence on the high part of the cycle with some of them, similarly to Mode2 described previously, having effects at the transition from BR_h to BR_l as well. However, the support for modes 40 and above is

DISTRIBUTION A: Distribution approved for public release.

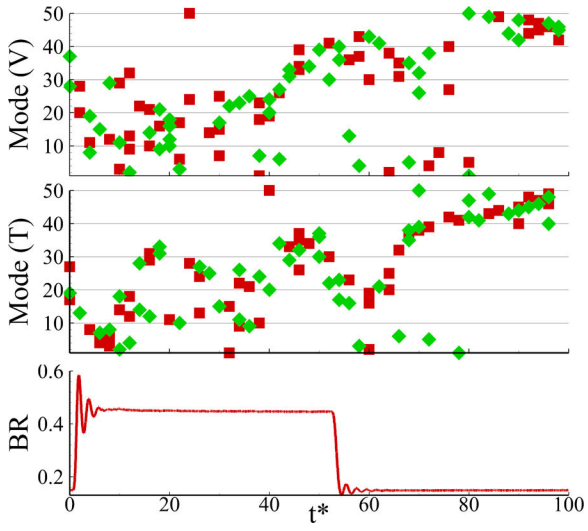

Figure 118: Phase distribution of the minima (*green diamond*) and maxima (*red squares*) associated with the POD modes coefficients a_i^{Vel} for the velocity (*top*) and a_i^{Temp} for the temperature (*middle*) along with phase averaged forcing signal (*bottom*).

almost exclusively located in the low quasi-unforced part of the cycle. Such segregation of the POD modes could have a negative impact on the reconstructed flow field as well as on a reduced order model resulting from truncation of the POD series as it would obliterate a significant part of the cycle.

Although Modes 1 and 2 are the most energetic, the complexity of the flow field generated at the transitions from one part of the cycle to the other prevents us from drawing definitive conclusions based only on the observation of these modes. They however provide a first order estimate of the impact of jet forcing on the temperature field, and particularly at the wall from a film cooling point of view. The first order effect of jet forcing on the wall temperature (corresponding to Mode1 in figure 115*d-f*, and 116*c, d*) appears to be located directly around the jet exit and corresponds to the increase in spread observed in figure 44(*a*) at the jet onset as well as directly downstream of the jet exit due to increase in coolant mass flow. Because a_1 changes sign throughout the cycle (positive over the high part and negative over the low part), the first order effect of jet forcing is a decrease in wall temperature during the high part and an increase during the low part. Overall, the highest values for Mode1 are located away from the wall suggesting a considerable waste of coolant in the free-stream. The second order effect represented by Mode2 shows that the transitional regime (during which Mode2 is dominant) affects more strongly the wall temperature than the bulk effect of forcing. The effect of the jet onset ($a_2 < 0$) over the average temperature field is to decrease the wall temperature locally around the jet exit due to local increase in spread, but increase it further downstream probably due to the increased entrainment associated with the starting structures lifting off of the wall. At the jet shutdown ($a_2 > 0$), the temperature around the jet increases due to the shrinking of the jet coverage associated with the decrease in coolant mass flow and the ingestion of cross-flow fluid. The downstream effect on the wall temperature is overall positive as the weaker vortical structures generated during the low part of the cycle do not entrain as much cross-flow and tend to remain attached to the wall.

DISTRIBUTION A: Distribution approved for public release.

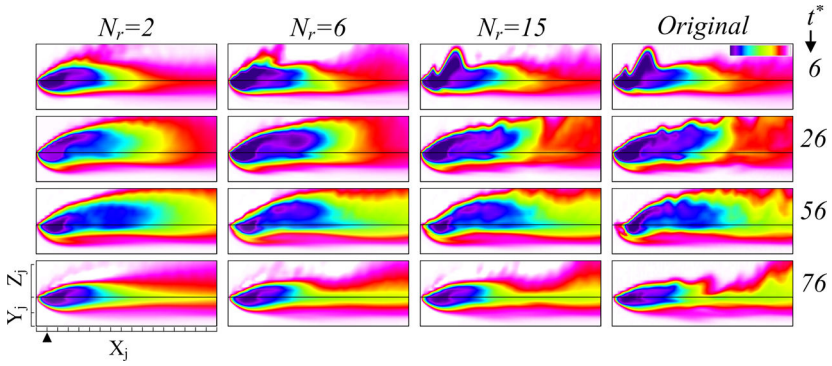

Figure 119: Reconstructed temperature field for multiple values of N_r at four different phase locations: $t^* = 0.06, 0.26, 0.56, 0.76$.

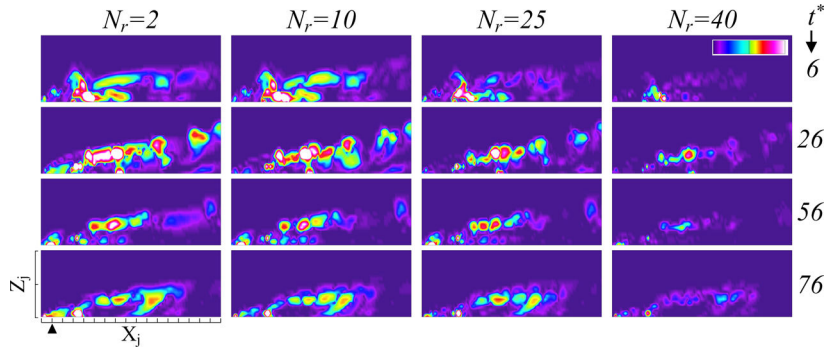

Figure 120: Error on the reconstructed velocity field for different N_r values estimated with phase averaged fluctuation of kinetic energy at $t^* = 0.06, 0.26, 0.56, 0.76$. Maximum value (*white*) is 9%.

Figure 119 presents the reconstructed temperature fields with $N_r = 2$, 6, and 15 modes along with the original temperature field at four phase locked positions. Overall the temperature field appears relatively well reconstructed with only 15 POD modes. However, while the increase from 2 to 15 modes brings significant improvement in the first 3 phase positions, the reconstruction at $t^* = 0.76$ does not show the same details as the one at $t^* = 0.06$ for $N_r = 15$. This is an illustration of the effect of the absence of the higher order modes capturing the behavior in the quasi-steady low part of the cycle. It should be noted that the reconstructed temperature field at the wall does exhibit the dominant features of the original field with only 6 modes.

Although the reconstructed velocity field is not presented, an estimate of the error on the reconstruction is shown in figure 120. Because the POD analysis was performed on the phase averaged signal, it is impossible to base the estimate of the error on the turbulent kinetic energy. Instead, the error (e_r) is estimated on the kinetic energy of the phase average fluctuation normalized by the total kinetic energy. Using $U_r = \bar{U} + \tilde{U}_r$ where U_r is the total reconstructed phase averaged field, $\bar{U}$ is the time averaged signal (equal to the true LES time averaged field) and $\tilde{U}_r$ the reconstructed phase averaged fluctuation using N_r POD modes.

DISTRIBUTION A: Distribution approved for public release.

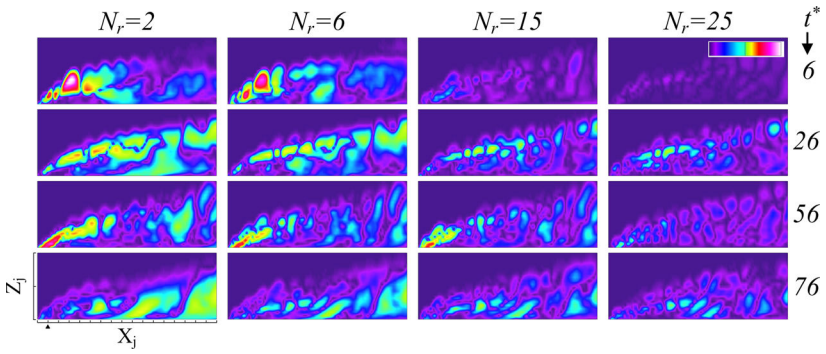

Figure 121: Error on the reconstructed temperature field for different values of N_r estimated using the total value of the temperature at $t^* = 0.06,\ 0.26,\ 0.56,\ 0.76$. Maximum value (*white*) is 9%.

Similarly, the true phase averaged velocity field can be decomposed into $U = \bar{U} + \tilde{U}$. The expression for the error on the phase averaged fluctuation is then:

$$e_r = \frac{\tilde{U_r}^2 + \tilde{V_r}^2 + \tilde{W_r}^2 - (\tilde{U}^2 + \tilde{V}^2 + \tilde{W}^2)}{U^2 + V^2 + W^2}$$

Figure 120 shows that the error decreases consistently with increasing numbers of modes although not equally across all phase positions. Indeed while the error decreases significantly from $N_r = 2$ to $N_r = 25$ at $t^* = 0.06$, it still stays relatively high for the other phase locations until $N_r = 40$. Even with $N_r = 40$, the reconstructions at $t^* = 0.26$ and 0.76 still show some error due to the truncation although in absolute value below 4% of the total instantaneous kinetic energy.

As for the steady state, the error on the reconstructed temperature field is estimated based on the relative error on total temperature (mean and fluctuation) and is presented in figure 121. Similarly to the velocity field, the error decreases consistently with increasing number of POD modes used in the reconstruction, although not homogeneously across all the phase positions. While the maximum error at $t^* = 0.06$ decreases from 9.2% at $N_r = 2$ to 0.2% at $N_r = 25$, corresponding to a factor of 46, it decreases at $t^* = 0.26$, 0.56 and 0.76 only by factors of respectively 2, 5, and 1.75. Nevertheless, the relative error does not exceed a maximum of 4% across the cycle with $N_r = 10$ and 2% with $N_r = 25$ and above. On both velocity and temperature fields, it is verified that the error asymptotically converges towards 0 when using all the modes for the reconstruction so that no loss of information is introduced by the proper orthogonal decomposition.

Simulation results from *Case X* at $St_\infty = 0.159$ are analyzed using 3D-POD as well. Identical domain and spatial samplings are used. The temporal sampling consists here of 25 phase locked positions over 10 cycles accounting for a total of 250 snapshots. As for the previous forced case, the decomposition is carried out on both the complete time sequence and the phase averaged signal. The complete energy distribution and the phase diagrams for the first 6 pairs of modes are presented in figure 124. Once again, decompositions of instantaneous and phase averaged flows are identical up to the 10^{th} POD mode and diverge for higher order modes due to the presence of the turbulent fluctuation in the full time sequence series. As for the previous case at $St_\infty = 0.016$, the decomposition on the phase averaged

DISTRIBUTION A: Distribution approved for public release.

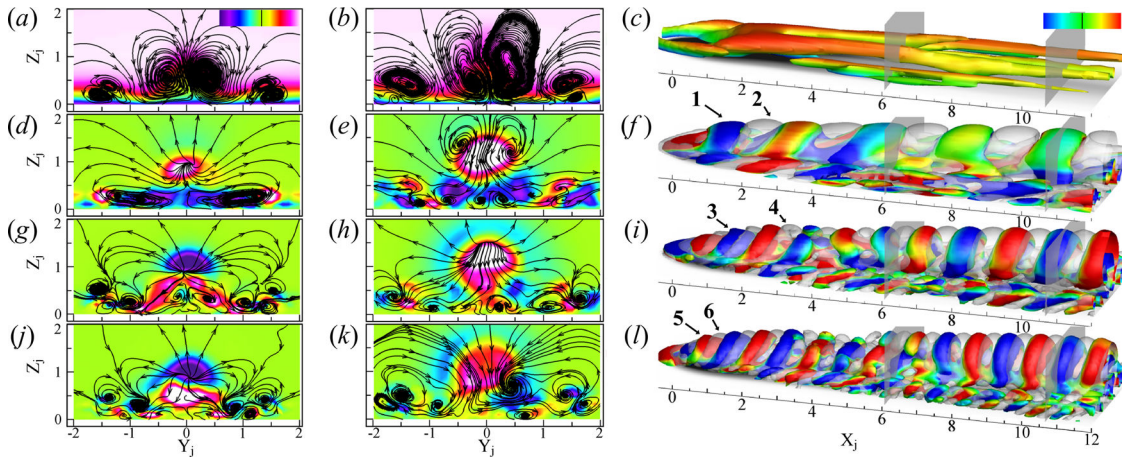

Figure 122: Mean flow (0^{th} POD Mode) and first significant velocity POD modes for *Case X* at $St_\infty = 0.159$ (*a-c*) Mode0; (*d-f*) Mode1; (*g-i*) Mode3; (*j-l*) Mode5. Slices at $X_j = 6$ (*left*), $X_j = 10.6$ (*center*) with U-velocity contours and V-W streamlines. λ_2 iso-surfaces (*right*) computed from corresponding POD modes and correlated mode (*white*) colored by the corresponding U-velocity and mean wall temperature contours (*gray scale*).

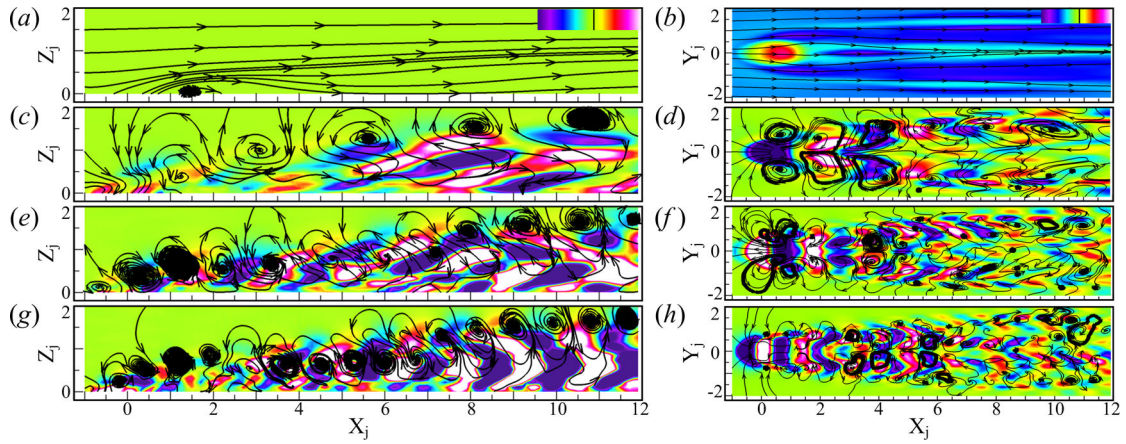

Figure 123: Mean flow and first significant velocity POD modes for *Case X* at $St_\infty = 0.159$ (*a, b*) Mode0; (*c, d*) Mode1; (*e, f*) Mode3; (*g, h*) Mode5. Slices at $Y_j = 0$ with V-velocity contours and U-W streamlines (*left*) and slices at $Z_j = 0.25$ with W-velocity contours and U-V streamlines (*right*).

DISTRIBUTION A: Distribution approved for public release.

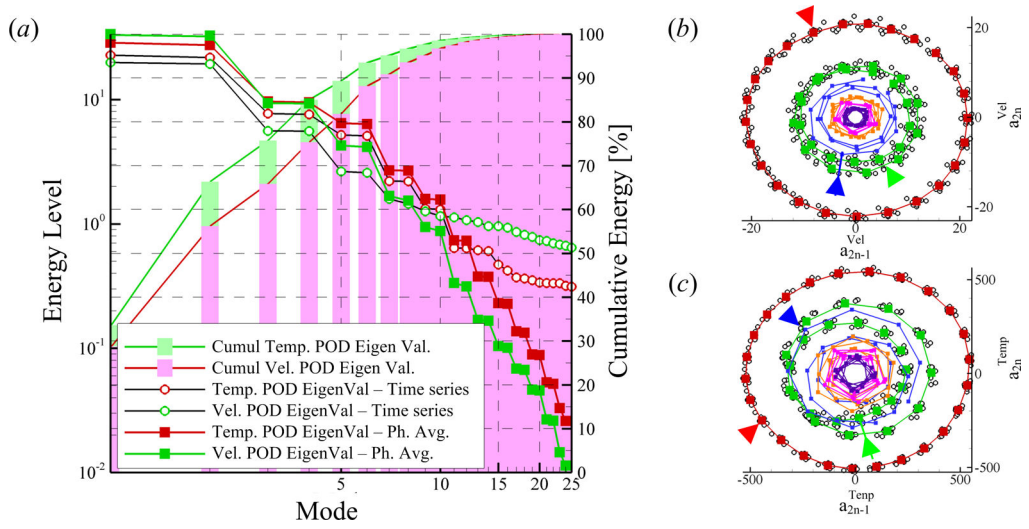

Figure 124: POD decomposition metrics for *Case X* at $St_\infty = 0.159$ from LES (a) POD modes eigenvalues and cumulative energy for temperature and velocity; (b) Velocity POD coefficients; (c) Temperature POD coefficients. Open symbols correspond to full time sequence POD. Arrow points toward $t^* = 0$ in the time sequence.

signal is preferred. The first noticeable difference between the two forced cases is found in the shape of the captured energy distribution. While in figure 114(a) at $St_\infty = 0.016$, the energy distribution does not exhibit a particular shape, the one at $St_\infty = 0.159$ assumes a clear stair-like shape. It should also be noted that the cumulative kinetic energy captured by the first two POD modes correspond to more than 65% of the total energy. Although in the presence of a forced case where the POD modes are automatically correlated to the forcing signal, the quasi-prefect circular distribution of the successive pairs of modes presented in the phase diagrams of figure 124(b) and 124(c) is a consequence of the stream-wise homogeneity of the flow making POD modes converge toward Fourier modes (see 34). This result is a consequence of the fact that at $St_\infty = 0.159$, multiple forcing cycles affect the flow field and that the dominant events are the generation and convection of the starting vortices. Hence the problem involves less length and time scales compared to the lower frequency case where the jet exhibited four distinct regimes each with distinct time and length scales.

POD modes issued from the decomposition of the velocity fields are presented in figures 122 and 123. While the 0^{th} POD mode corresponds to the average flow field, the 1^{st} and 2^{nd} are virtually identical with the exception of a phase shift in the downstream direction as seen in the superposition of λ_2 iso-surfaces in figure 122(f). Both modes assume the shape of multiple large scale hairpin vortices penetrating deeply in the free stream. A set of side vortices is visible in the λ_2 iso-surfaces as well as in the $X_j = 6$ slice of the flow field in figure 122(c). These correspond to the large scale side vortices formed near the wall close to the starting vortices and observed in instantaneous snapshots of figure 44. The third and fourth modes, also largely identical with a shift in phase, correspond to the first harmonic of the 1^{st} and 2^{nd} modes respectively. The phase diagram corresponding to these modes in 124(b) shows that while a_1^{Vel} and a_2^{Vel} complete a single revolution during a cycle, a_3^{Vel} and a_4^{Vel} complete two. Similarly, Modes 5 and 6 are the second harmonics of Modes 1 and 2

DISTRIBUTION A: Distribution approved for public release.

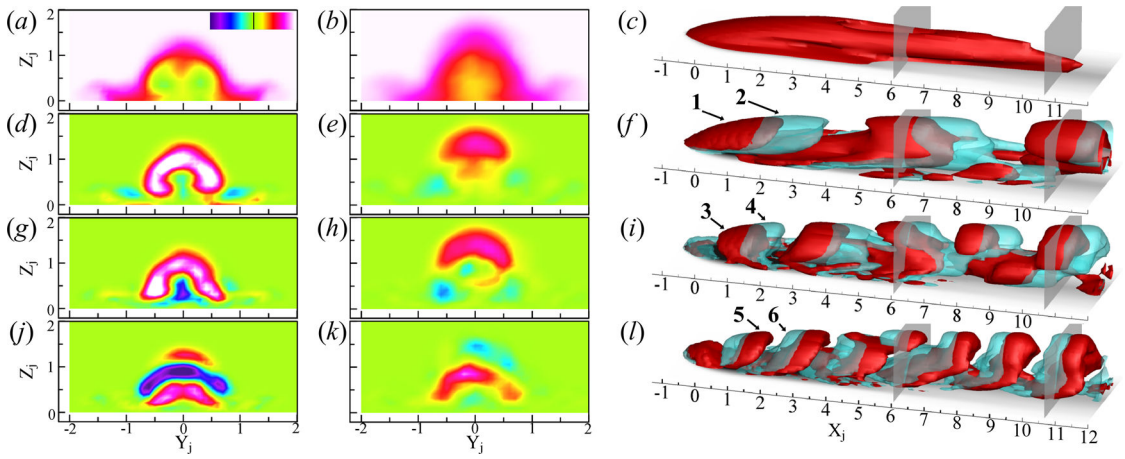

Figure 125: Mean temperature field (0^{th} POD mode) and first significant temperature POD modes for *Case X* at $St_\infty = 0.159$ (*a-c*) Mode0; (*d-f*) Mode1; (*g-i*) Mode3; (*j-l*) Mode5. Slices at $X_j = 6$ (*left*), $X_j = 10.6$ (*center*) with temperature contours. Iso-T surfaces (*right*) computed from corresponding pairs of POD modes (*transparent*) and mean wall temperature contours (*gray scale*).

respectively. The energy distribution in figure 124(a) shows that a total of 12 velocity modes and 15 temperature modes are required to reconstruct 99% of the total fluctuation energy.

As for the previous pulsed case, the modal coefficients a_1^{Vel} through a_6^{Vel} are plotted versus time along with the forcing signal in figure 117(b). The phase shift between the correlated pairs of modes is easily quantifiable and corresponds to a quarter of the period for the first two, an eighth for modes 3 and 4 and a sixteenth for modes 5 and 6. Conversely to the $St_\infty = 0.016$ case, none of the modes appears to dominate over one particular part of the forcing cycle and the coefficient converge towards cosine and/or sine functions.

The POD modes corresponding to the temperature field analysis are presented in figures 125 and 126. As in the velocity POD, the first two modes are quasi-identical with a shift in the stream-wise direction. The iso-surfaces in figure 125(f) have a hairpin-like shape, alternating positive and negative values in the stream-wise direction as in the unforced case at $BR = 0.15$. Higher order modes are paired similarly to the velocity field decomposition and correspond the successive harmonics of the first two modes. The evolution of the modal coefficients a_1^{Temp} through a_6^{Temp} with respect to time in figure 117(b) appears almost identical to the one obtained for the velocity field.

In opposition to the lower forcing frequency case, the impact of the different modes on the wall temperature decreases in scale and amplitude as mode order increases. Almost no impact on the wall temperature is observed beyond $X_j = 6$. In the vicinity of the jet exit, the 1^{st} temperature POD mode shows alternating positive and negative values due to the formation and convection of the starting structures. A band of high positive values covering part of the upstream edge of the jet exit is associated with the successive cross-flow ingestions and coverage increases occurring periodically at the jet shutdown and onset.

The reconstructed temperature field using 2, 4 and 6 POD modes is presented in figure 127. The reconstruction quality is homogeneous with time and although the finest details are not represented, the fields including 4 and more modes provide qualitatively a reasonably

DISTRIBUTION A: Distribution approved for public release.

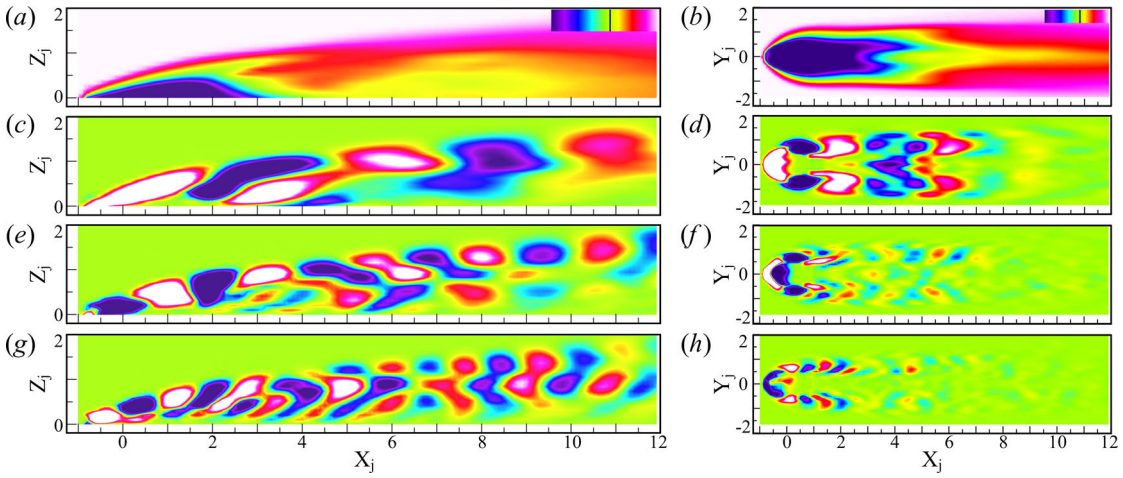

Figure 126: Mean temperature field and first significant temperature POD modes for *Case X* at $St_\infty = 0.159$ (*a, b*) Mode0; (*c, d*) Mode1; (*e, f*) Mode3; (*g, h*) Mode5. Slices at $Y_j = 0$ with temperature contours (*left*) and slices at $Z_j = 0$ with temperature contours (*right*).

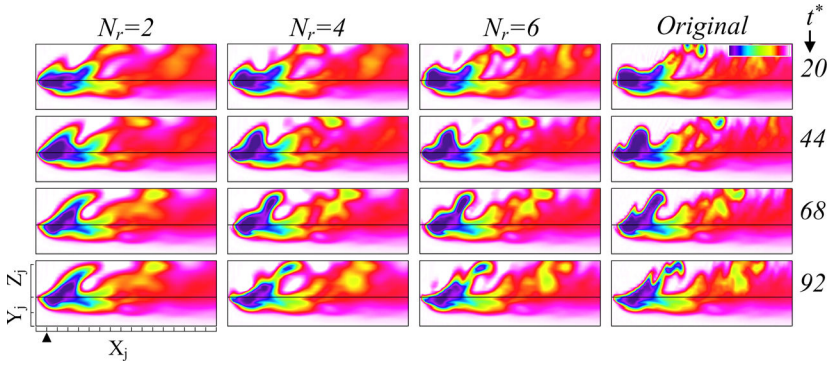

Figure 127: Reconstructed temperature field for multiple values of N_r at different phase location: $t^* = 0.2, 0.44, 0.68, 0.92$.

DISTRIBUTION A: Distribution approved for public release.

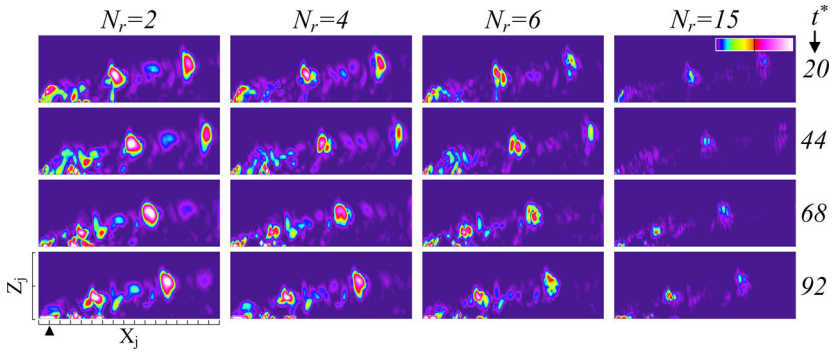

Figure 128: Error on the reconstructed velocity field for different N_r values estimated using the phase averaged fluctuation of kinetic energy at $t^* = 0.2, 0.44, 0.68, 0.92$. Maximum value (*white*) is 6%.

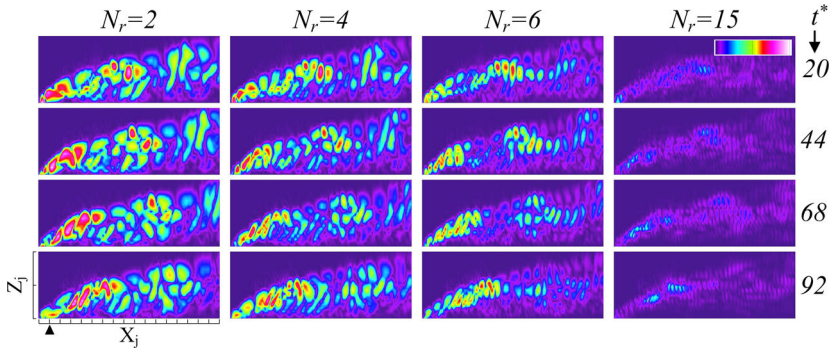

Figure 129: Error on the reconstructed temperature field for different values of N_r estimated using the total value of the temperature at $t^* = 0.2, 0.44, 0.68, 0.92$. Maximum value (*white*) is 6%.

good reconstruction. The error on the reconstructed velocity field and temperature fields are also investigated using different values of N_r. In figure 128 the error on the velocity field is estimated in the same way as for the lower forcing frequency case. The bulk of the error resides in the region where the core of the starting vortex is located which also corresponds to the regions of higher velocity fluctuations. In this higher forcing frequency case, the relative error decreases consistently with increasing number of included POD modes at all time steps. For $N_r = 15$, the overall maximum error does not exceed 4%. Finally, the error on the temperature field is also evaluated and presented in figure 129. As for the velocity reconstruction, the error decreases at all phase locations consistently with increasing number of POD modes included in the reconstruction. The effect of the individual modes is clearly visible on the reduction of the error as the scale of 'error patches' decreases with increasing values of N_r involving higher harmonics thus lower length scales. Six modes are required to obtain a maximum error inferior to 4% while 10 modes ensure a maximum error on the temperature field of the order of 2%.

These results evidence the sorting mechanism associated with proper orthogonal decomposition in both unforced and forced jets. In particular, in forced jet conditions, it is found

DISTRIBUTION A: Distribution approved for public release.

that the flows forced at low frequencies have decompositions which are much different from the ones at higher forcing frequencies when all other parameters are maintained fixed. In addition, due to the discrete length and energy scales introduced in forced jet conditions, the energy distribution of velocity and temperature decompositions are much more organized and exhibits a much more pronounced hierarchy compared to the unforced jet, even at the lowest blowing ratio.

3.2 Reduced Order Models

3.2.1 Stabilization Methods

The POD-Galerkin method was essentially applied to the film cooling jet simulations, although the three-dimensional, turbulent character of realistic film cooling flows can greatly affect the reduced order model accuracy and stability. Several stabilization methods were developped and applied to the unfoced and forced jets.

- *Local Linear Cazemier* stabilization - The first method implemented was developped by (15) and consist in a linear term added to the momentum equations. In the current study, similar considerations to the ones proposed by (15) were used in the heat equation to develop stabilizing parameters for the temperature ROM as well. The damped velocity model was then:

$$\begin{aligned} \dot{a_r}(t) = &\sum_{i=1}^{N_v} \left(C_{i0}^r + \frac{1}{Re_j} D_i^r \right) a_i(t) \\ &+ \sum_{i=1}^{N_v} \sum_{j=1}^{i} C_{ij}^r a_i(t) a_j(t) \\ &+ \left(C_0^r + \frac{1}{Re_j} D_0^r \right) + a_r(t) S_r^V \end{aligned} \tag{3}$$

with

$$S_r^V = -\frac{1}{\lambda_r} \sum_{i=1}^{N_V} \sum_{j=1}^{i} C_{ij}^r \left\langle a_i(t) a_j(t) a_r(t) \right\rangle - \left(C_{r0}^r + \frac{1}{Re_j} D_r^r \right) \tag{4}$$

DISTRIBUTION A: Distribution approved for public release.

The temperature model was then:

$$\begin{aligned}\dot{b}_s(t) = &\sum_{i=1}^{N_V} E^i_{s0} a_i(t) \\ &+ \sum_{j=1}^{N_T} \left(E^0_{sj} + \frac{1}{Pr}\frac{1}{Re_j} F_{sj} \right) b_j(t) \\ &+ \sum_{i=1}^{N_V}\sum_{j=1}^{N_T} E^i_{sj} a_i(t) b_j(t) \\ &+ \left(E^0_{s0} + \frac{1}{Pr}\frac{1}{Re_j} F_{s0} \right) + b_s S^T_s \end{aligned} \tag{5}$$

with

$$S^T_s = -\frac{1}{\sigma_s}\left(\sum_{i=1}^{N_V} E^i_{s0} \left\langle a_i(t) b_s(t) \right\rangle + \sum_{i=1}^{N_V}\sum_{j=1}^{N_T} E^i_{sj} \left\langle a_i(t) b_j(t) b_s(t) \right\rangle \right) - \left(E^0_{ss} + \frac{1}{Pr}\frac{1}{Re_j} F_{ss} \right) \tag{6}$$

- *Broad Linear Cazemier* stabilization - Another stabilization formulation was proposed, based on Bousinesq's eddy viscosity formulation and using Cazemier's energy conservation consideration. The damped model for the velocity was then:

$$\begin{aligned}\dot{a_r}(t) = &\sum_{i=1}^{N_v} \left(C^r_{i0} + \left(\frac{1}{Re_j} + \nu^r_T \right) D^r_i \right) a_i(t) \\ &+ \sum_{i=1}^{N_v}\sum_{j=1}^{i} C^r_{ij} a_i(t) a_j(t) \\ &+ \left(C^r_0 + \left(\frac{1}{Re_j} + \nu^r_T \right) D^r_0 \right) \end{aligned} \tag{7}$$

with

$$\nu^r_T = \frac{-1}{\lambda_r D^r_r}\left(\sum_{i=1}^{N_v}\sum_{j=1}^{i} C^r_{ij} \left\langle a_i(t) a_j(t) a_r(t) \right\rangle + \lambda_r \left(C^r_{r0} + \frac{1}{Re_j} D^r_r \right) \right) \tag{8}$$

DISTRIBUTION A: Distribution approved for public release.

The temperature model is then:

$$\begin{aligned}\dot{b}_s(t) = &\sum_{i=1}^{N_V} E^i_{s0} a_i(t) \\ &+ \sum_{j=1}^{N_T} \left(E^0_{sj} + \left(\frac{1}{Pr} + \alpha^s_T \right) \frac{1}{Re_j} F_{sj} \right) b_j(t) \\ &+ \sum_{i=1}^{N_V} \sum_{j=1}^{N_T} E^i_{sj} a_i(t) b_j(t) \\ &+ \left(E^0_{s0} + \left(\frac{1}{Pr} + \alpha^s_T \right) \frac{1}{Re_j} F_{s0} \right) \end{aligned} \tag{9}$$

with

$$\alpha^s_T = \frac{-1}{\frac{\sigma_s}{Re_j} F_{sj}} \left(\sum_{i=1}^{N_V} \sum_{j=1}^{N_T} E^i_{sj} \left\langle a_i(t) b_j(t) b_s(t) \right\rangle + \sum_{i=1}^{N_V} E^i_{s0} \left\langle a_i(t) b_s(t) \right\rangle + \left(E^0_{sj} + \frac{1}{Pr} \frac{1}{Re_j} F_{sj} \right) \sigma_s \right) \tag{10}$$

A relationship between the terms S^V_r, S^T_s, ν^r_T and α^s_T was established:

$$S^V_r = \frac{\nu^r_T}{D^r_r}, \qquad S^T_s = Re_j \frac{\alpha^s_T}{F_{ss}}$$

3.2.2 Unforced Jets

The first reduced order models obtained are based on unforced jets results. Two regimes, attached and transitional, are investigated. Due to the unlikelihood of the detached regime to benefit any film-cooling application, reduced order modeling of these flows is not pursued. In the perspective of obtaining a reduced order model for flow control, the complete domain has to be considered, in particular the jet pipe and its inlet plane which corresponds to the input plane for the control action.

3.2.2.1 Attached Regime The $BR = 0.15$ unforced jet is the first one investigated. The LES simulations are carried out using the parameters described in Chapter 3. A POD analysis is performed using a set of $1,000$ POD modes following Sirovich snapshot method. This represents a significant increase with respect to the preliminary study presented in the previous section which is justified by the extended domain in the downstream direction, the inclusion of the jet pipe in the decomposition, and the increased grid resolution. Snapshot sampling is done with an equivalent sampling frequency of $300Hz$ ($St_s = 4.8$). The POD metrics are presented in figure 130 for both the velocity and temperature fields decompositions. The first 6 to 8 POD velocity and temperature modes are organized in pairs carrying equivalent energy. The first two velocity modes carry each a little more than 5% of the total kinetic energy and the first two temperature modes carry each a little less than 10% of the total pseudo-thermal energy. To capture 99% of the kinetic energy, a total of 395 modes is

DISTRIBUTION A: Distribution approved for public release.

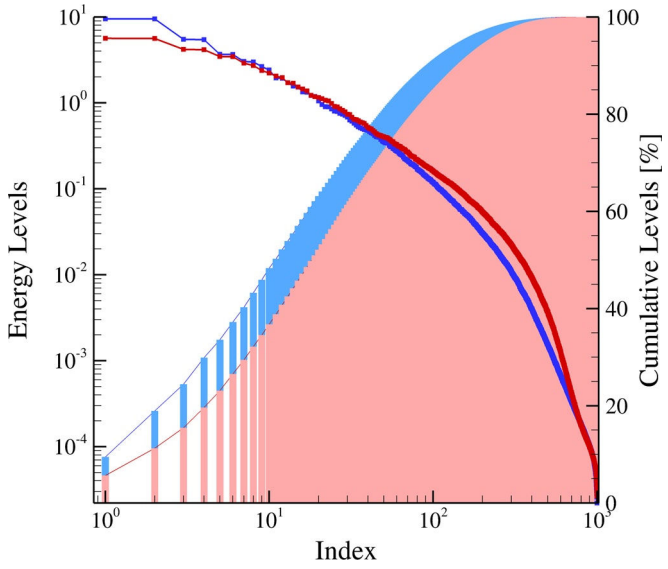

Figure 130: POD decomposition metrics for velocity (*red*) and temperature (*blue*) fields with $N = 1,000$ at $BR = 0.15$.

required, while 99% of the thermal energy is captured by the first 313 temperature modes. These constitute rather large numbers of modes and could pose an issue when integrating the reduced order models ordinary differential equations. The first 14 velocity POD modes λ_2 iso-surfaces are presented in figure 131 and confirm that the first POD modes are associated in pairs, shifted by a quarter of wave length in the downstream direction. Conversely to the preliminary decomposition, the first mode pair does not correspond to the hairpin vortices, but rather the near-wall side vortices. This is due to the ROM grid being extended in the downstream direction, therefore capturing more of the developing wall structures, which highlights the impact of the POD domain selection onto the hierarchy of the captured vortical structures. The first two modes also exhibit vortical structures in the jet tube developing due to the perturbations imposed at the jet inlet during the simulations. Hairpin vortices start appearing in the second pair of velocity modes, in particular in the mid-field. Higher order modes show structures similar to the ones of modes 1, 2 and 3, 4 or a combination of them at either higher spatial frequencies (modes 5, 6) or different locations (modes 13, 14). The first temperature modes in figure 132 are also associated in pairs of similar modes shifted in the downstream direction by a quarter wavelength, which is consistent with the preliminary statistical POD analysis. The first two modes capture the convective effect of the hairpin vortices on the temperature field, while modes 3 and 4 seem to capture temperature fluctuations closer to the wall and may be associated to the effects of the side vortices. Although the first pair of temperature modes captures fluctuations primarily in the mid-field, higher order modes capture features in both the near-field and far-field. Interestingly, modes 7 and 8 seem to represent fluctuations in the transverse planes, likely attributed to the darft of the hairpin vortices legs towards the symmetry plane.

Reduced order models are obtained using the Galerkin projection method described in the previous chapter. For all the following ROMs, the pressure terms arising in equation 1 at the boundaries have been neglected. Given the extent of the domain, not all Galerkin

DISTRIBUTION A: Distribution approved for public release.

coefficients corresponding to all $1,000$ POD modes are computed. In addition, the integration cost of more than $1,000$ non-linear coupled ODEs seem prohibitive and a maximum limit of 500 equations for the velocity and 500 temperature ROMs is set. Given the large domain and the important number of modes to be included, a parallel MPI code in Fortran 90 was developed to perform the projection across multiple platforms.

Evaluations of the error levels with respect to the true velocity and temperature fields showed that an optimum number of modes is found for all three time frames at approximately $N_V = 250$, 400 and 500 for respectively the short, medium and long term error estimates. The temperature error estimates also showed that a local minimum was found at $N_V = 250$, $N_T = 120$. The error levels of the medium and long term estimates decreased monotonously with increasing number of velocity POD modes, and increases monotonously with increasing number of temperature modes.

Figure 133 shows the integrated temporal coefficients a_i^V for the velocity ROM and a_i^T for the temperature ROM at $N_V = 250$ and $N_T = 120$, along with the corresponding projected LES results (POD temporal coefficients). Both velocity and temperature ROMs show reasonable agreement with the projected LES data up to $t_c = 1$ but start diverging from them beyond that point. The divergence occurs both in amplitude and phase and is particularly obvious in the first temperature coefficients. Several explanations can be thought of to justify the diverging behavior of the velocity and temperature modes. The first one comes from the truncation of the POD series and the presence of unresolved modes, potentially leading to less accurate models. Error estimates showed that increasing the number of POD modes does not necessarily lead to more accurate models. Another potential source of error could arise from neglecting the pressure term initially present in the equations. To verify the influence of the pressure term, an empirical pressure correction method as described in 58 is implemented and the complete ROM equations are integrated over identical time frames. The results are presented in figure 133 and show only very little difference with the non-corrected ROM. This provides an a posteriori confirmation of the original assumption of neglecting the pressure term. Another source of error can also come from the chaotic character of turbulent Navier Stokes equations which can lead two sets of infinitely close initial conditions towards two significantly different sets of solutions. Unfortunately, such chaotic behavior is intrinsic to turbulent fluid flows and can only be kept in mind when assessing the accuracy of reduced order models. Finally, a more fundamental source of error can originate from the initial set of snapshots considered to generate the POD basis. First, the sampling frequency used to collect the velocity and temperature fields snapshots acts as a temporal filter and cannot realistically provide a good representation of the vortical structures with a characteristic time-scale of the order of twice the sampling period according to Nyquist criterion. Moreover, the snapshots used in the current study being extracted from LES simulations, suffer from the inherent spatial and temporal filtering introduced by the LES model at the sub-grid scale level. Both temporal, and spatial filters introduced by the sampling but also the chosen turbulence model affect the representation of the smaller dissipative scales and can, combined with the POD series truncation, lead to significant underestimates of the effective momentum and thermal diffusivities.

To try to alleviate the underestimated diffusion, both local and broad linear stabilization methods are used to integrate the velocity and temperature ROMs at multiple values of N_V and N_T. Estimated error levels for the stabilized models on both the velocity and temperature fields drops significantly when using either one of the stabilization methods. The stabilized models evidence an optimum set of $(N_V, N_T) = (275, 100)$ at which minimum

DISTRIBUTION A: Distribution approved for public release.

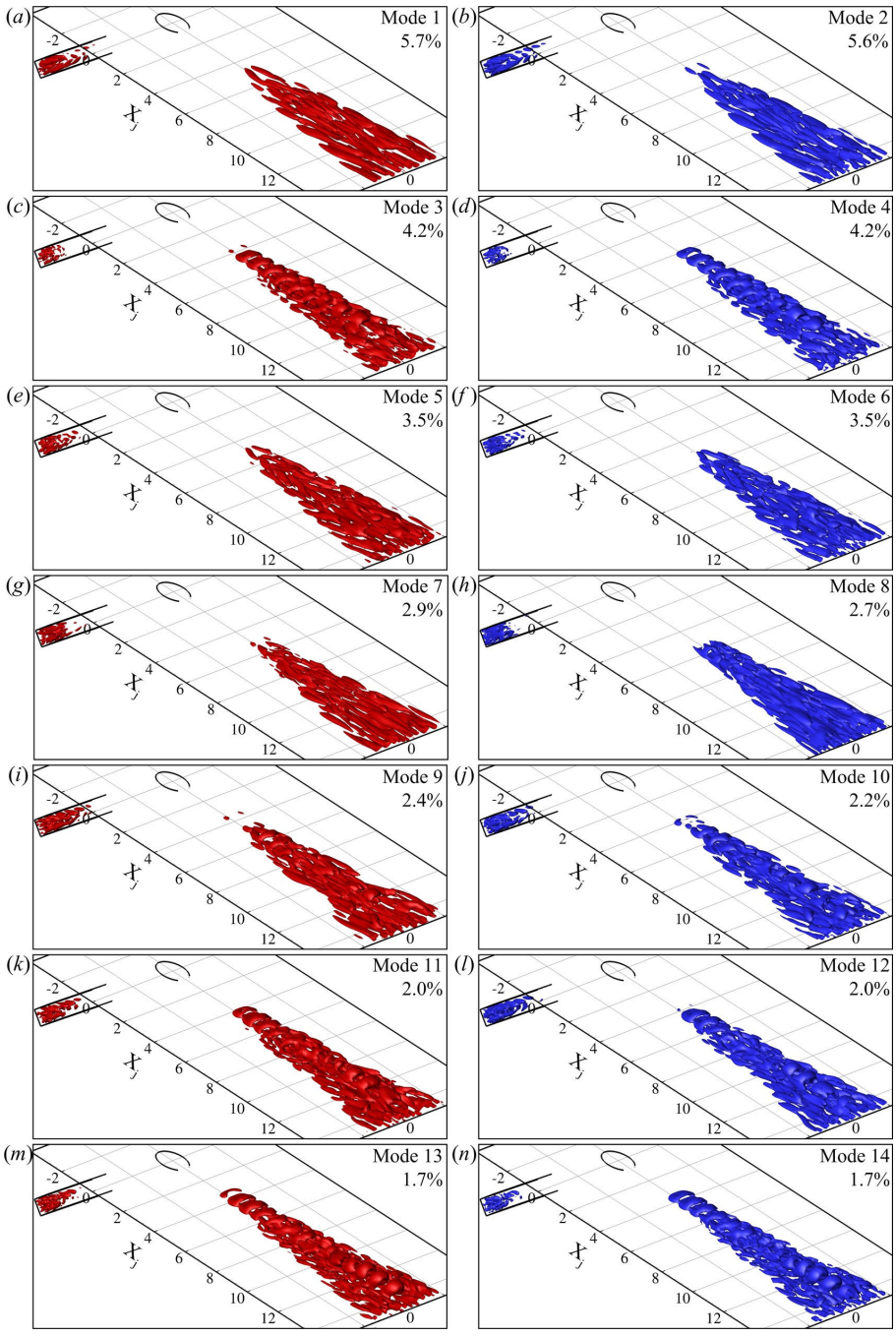

Figure 131: First 14 velocity POD modes λ_2 iso-surfaces for POD decomposition at $BR = 0.15$. Mode energy provided in percent of the total energy.

DISTRIBUTION A: Distribution approved for public release.

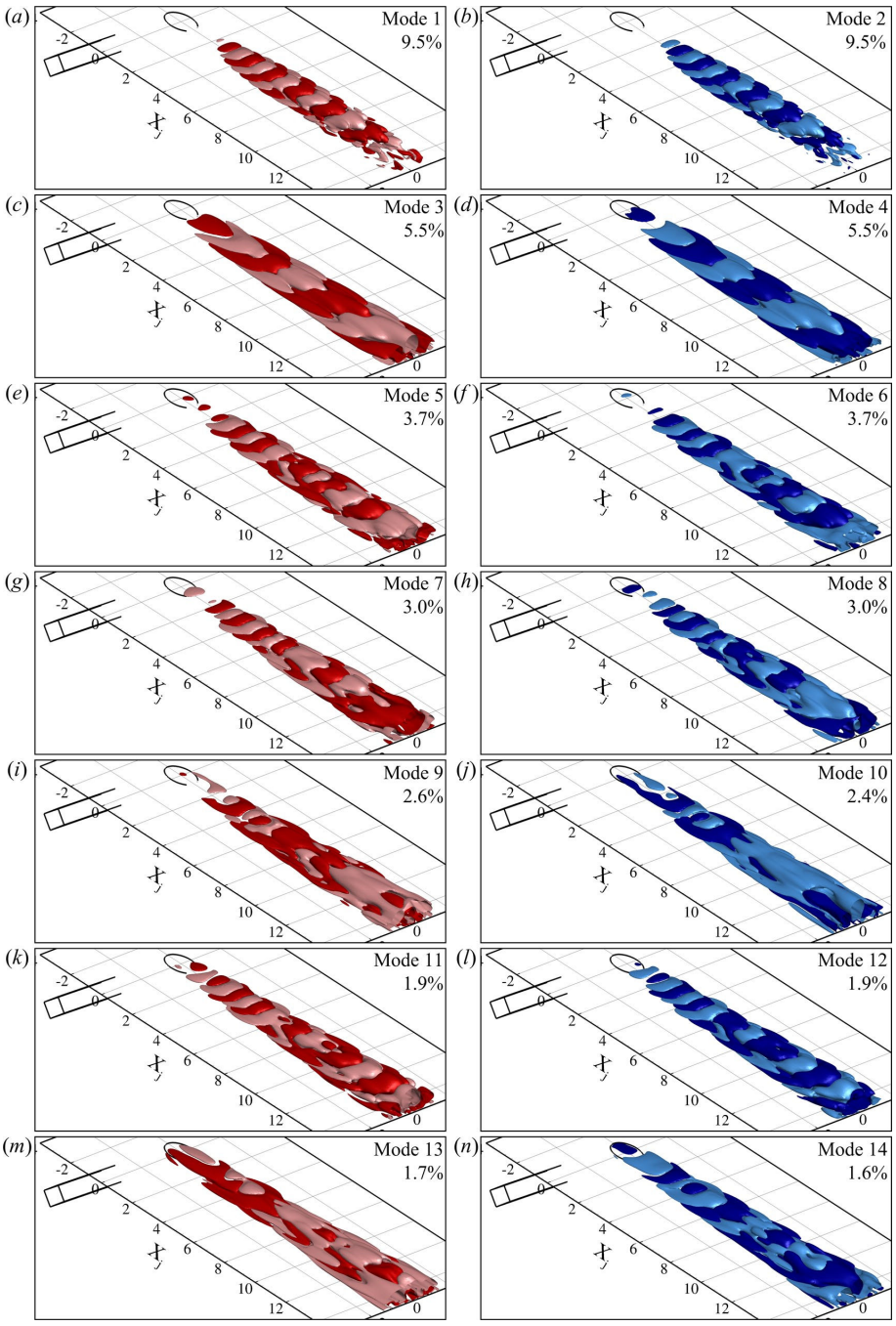

Figure 132: First 14 temperature POD modes iso-surfaces for POD decomposition at $BR = 0.15$. Pink and cyan contours are for negative values, red and blue for positive ones. Mode energy provided in percent of the total energy.

DISTRIBUTION A: Distribution approved for public release.

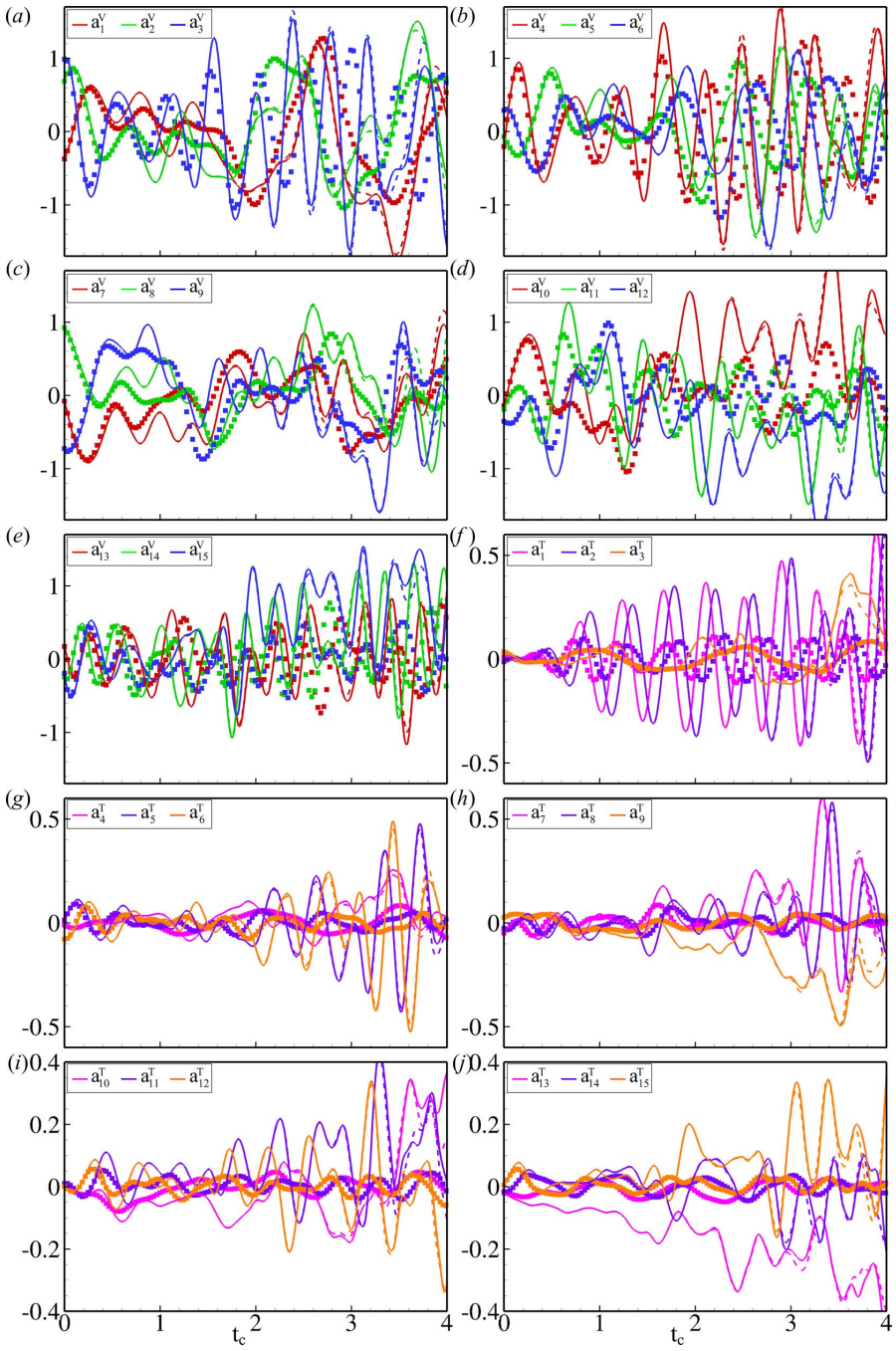

Figure 133: $BR = 0.15$ ROM temporal coefficients for the velocity and temperature fields obtained at $N_V = 250$, $N_T = 120$ without pressure correction (*solid lines*) and with pressure correction (*dashed lines*) along with corresponding POD temporal coefficients (*symbols*).

DISTRIBUTION A: Distribution approved for public release.

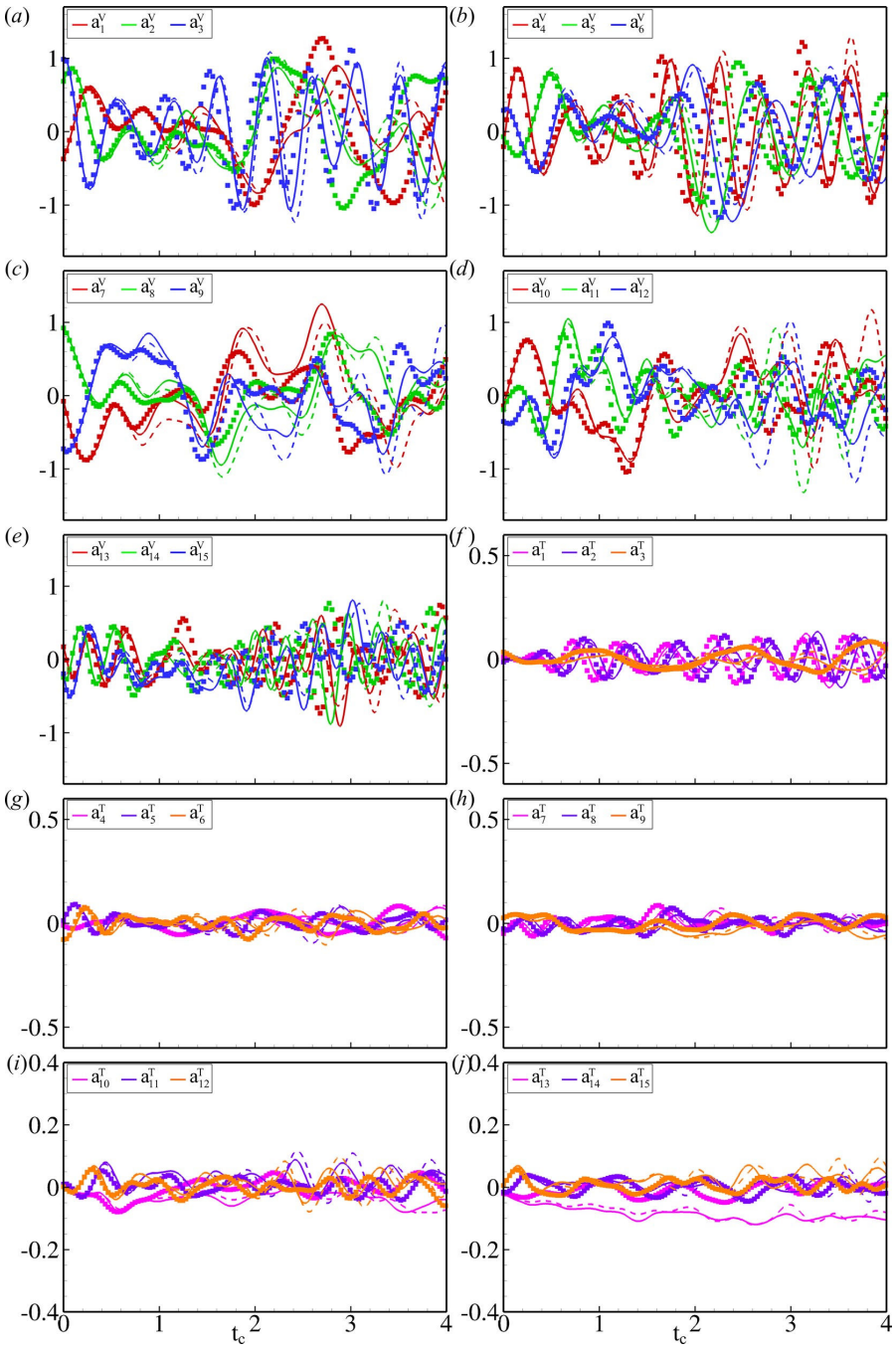

Figure 134: $BR = 0.15$ ROM temporal coefficients for the velocity and temperature fields obtained at $N_V = 275$, $N_T = 100$ with local linear stabilization (*solid lines*) and broad linear stabilization (*dashed lines*) along with corresponding POD temporal coefficients (*symbols*).

DISTRIBUTION A: Distribution approved for public release.

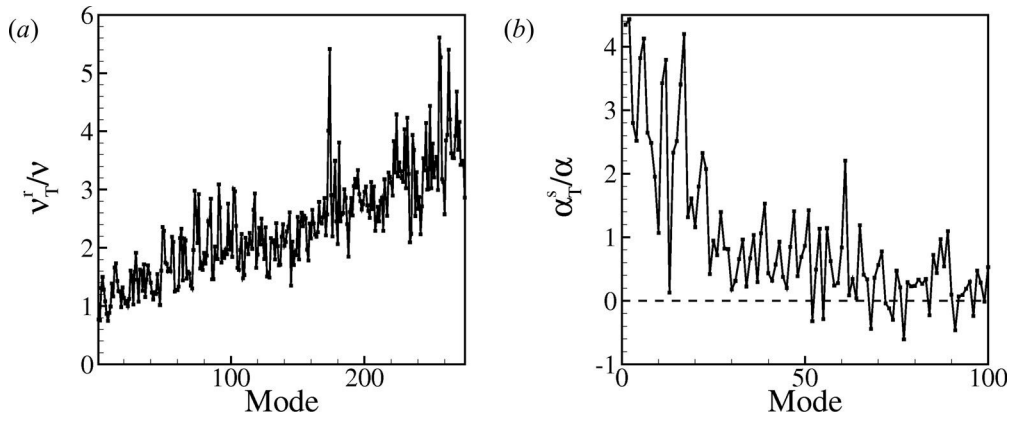

Figure 135: $BR = 0.15$ ROM (a) normalized turbulent momentum diffusivity ν_T^r/ν and (b) normalized turbulent thermal diffusivity α_T^s/α calculated for $N_V = 275$ and $N_T = 100$.

error levels are reached for both ROMs. Although they are comparable in magnitude, the error levels for the local stabilization are consistently slightly inferior to the corresponding ROMs integrated using the broad stabilization.

The best performing stabilized ROM, with $N_V = 275$, and $N_T = 100$, is presented in figure 134 for the velocity and temperature models integrated using both the local and broad damping methods. For the velocity, the agreement with the LES data is clearly improved over the non-stabilized ROM of figure 133 and reasonably good tracking is now obtained up to 3 convective time scale units. The temperature ROM accuracy is also enhanced, and in particular the amplitude divergence observed in the non-stabilized model is no longer visible. Once again, the local and broad stabilization methods provide very comparable ROMs although the former seems to outperform the latter by a small margin.

Finally, the normalized turbulent momentum (ν_T^r/ν) and thermal (α_T^s/α) diffusivities for the stabilized ROM calculated using equations 8 and 10 for $N_V = 275$ and $N_T = 100$ are presented in figure 135. The turbulent viscosity is always positive and increases consistently with the mode order. This confirms the fact that low order modes suffer from poorer modeling of the effective flow diffusivity and require more viscous damping. Indeed, while from the lower order mode point of view (larger scales), the energy cascade appears relatively accurately modeled, from the point of view of the higher order modes (smaller scales), closer to the truncation point, the energy cascade becomes less and less realistic and the absence of smaller dissipative scales or inaccuracies are more and more significant. The turbulent thermal diffusivity is for most of the modes positive but decreases in amplitude with increasing mode rank. Higher order modes even evidence negative turbulent thermal diffusivity values, effectively acting as a source term in the energy equation. This is to be expected since the truncated temperature POD series and the LES model prevent the modeling of heat generation through viscous dissipation.

3.2.2.2 Transitional Regime Simulations at $BR = 0.5$ are now used to obtain a reduced order model of the transitional jet. Simulations are obtained using the ROM grid and parameters described in Chapter 3. The POD analysis is performed using the same parameters as for the attached jet decomposition, including $1,000$ snapshots and an

DISTRIBUTION A: Distribution approved for public release.

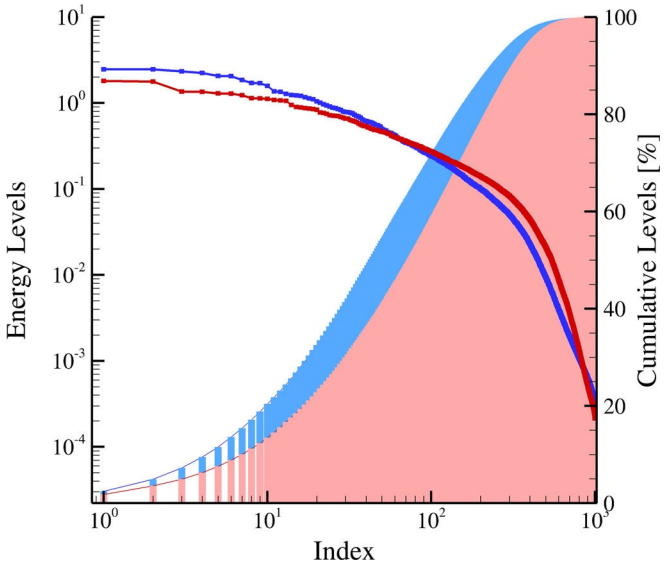

Figure 136: POD decomposition metrics for velocity (*red*) and temperature (*blue*) fields with $N = 1,000$ at $BR = 0.5$.

equivalent sampling frequency of $300Hz$ ($St_s = 4.8$) based on Sirovich snapshot method. The POD metrics are presented in figure 136 for both velocity and temperature decompositions. Compared to the previous case at $BR = 0.15$, both energy distributions are fuller which is a sign of a more turbulent flow involving a wider range of length scales. The first two POD modes have comparable energy content at approximately 1.75% each, while the first two temperature modes capture approximately 2.5% of the total pseudo-thermal energy. This is to be put in perspective with the respective 5% and 10% obtained at $BR = 0.15$. The 99% energy threshold is reached using 592 velocity modes and 521 temperature modes. This is beyond the limit which was set at 500 modes for each individual decomposition, though not by a large extent, so that effectively 97.8% of the total kinetic energy and 98.8% of the total pseudo-thermal energy can still be captured using 500 velocity and temperature modes. These numbers are assumed to be high enough to capture the significant dynamics of the flow. The velocity POD modes λ_2 iso-surfaces are presented in figure 137. As for the lower blowing ratio case, the first 12 modes are mostly associated in pairs of two modes with equivalent energy content, with features shifted in the downstream direction by a quarter of a wavelength from one mode to the other. The first pair captures large scale structures such as hairpin and wall vortices predominantly in the far-field. On the other hand, the second and third pairs represent comparable features but mostly in the mid-field. Higher order modes are grasping ever smaller structures throughout the domain, including the near-field. When comparing the POD modes obtained at $BR = 0.15$ and those obtained at $BR = 0.5$, it is interesting to notice how much "busier" the latter look and how all the modes at $BR = 0.5$ possess features across the complete flow domain. This is a result of the increased range of length and energy scales present in the higher blowing ratio case and is once more characteristic of more turbulent flows. The temperature POD modes are shown in figure 138 and present some interesting characteristics of their own. While in the $BR = 0.15$ case, the predominant modes were capturing fluctuations in the streamwise direction, the first two pairs of modes

DISTRIBUTION A: Distribution approved for public release.

at $BR = 0.5$ evidence simultaneously streamwise fluctuations in the far field and transverse ones in the near field close to the jet exit. This shows an evolution of the dominant convective mechanisms which at $BR = 0.15$ were primarily present in the far-field and associated to the hairpin vortices heads and side-vortices, but are now at $BR = 0.5$ also very strong in the near-field and associated with the counter-rotating vortex pair (through the hairpins legs). The temperature POD modes can also generally be matched in pairs of equivalent shape and energetic content, though some pairs having comparable energy levels can be mixed. For example, it appears rather clearly that modes 5 and 8 form a pair while modes 6 and 7 form another one which is "inserted" in between modes 5 and 8.

Reduced order models of the transitional unforced jet are obtained using the POD-Galerkin method. The ROM sensitivity to N_V and N_T was evaluated using estimates of the error surfaces for the velocity and temperature models for N_V and N_T values in the range $[30, 500] \times [30, 500]$. All surfaces exhibit missing areas corresponding to pairs of (N_V, N_T) values at which the ROM integration diverged within the time frame considered for the error evaluation. The primary reason for divergence resides in the velocity ROM instability, and only a few integrations with $N_V \leq 100$ were successful all the way to the $t_c = 6$ limit. The error levels on the velocity ROM, even in the short term, are considerable, conversely to the one on the temperature which are quite reasonable when compared to the non-stabilized results at $BR = 0.15$. Once again, considering the extent of the error levels, looking at medium and long term results would be rather hasty, and focus will be brought to the short term performance. The velocity ROM has a minimum error for $N_V = 350$, while the temperature ROM reaches minimum error on the modeled flow for $(N_V, N_T) = (350, 30)$ and minimum total error for $(N_V, N_T) = (30, 350)$. Figure 139 shows the integrated optimum ROMs. The model clearly diverges beyond $t_c = 2.5$ and the discrepancy appears to originate from the higher order velocity modes which amplitudes are growing significantly beyond $t_c = 1.5$. As the error propagates in the system, the lower order velocity and temperature modes are eventually diverging as well. It should be noted that since the integrated systems presented in figure 139 are not corresponding to each other, the diverging point do not clearly match. Nevertheless, both the velocity and temperature ROMs evidence rather good agreement with the projected LES data before the system starts to diverge ($t_c \leq 1$), which is an encouraging feature.

Following what was done in the attached jet model reduction, stabilizing terms are calculated and added to the velocity and temperature ROMs which are integrated using both local and broad stabilization formulations. Evaluated error surfaces for both methods showed that the ROM integrated with the local stabilization method to diverged more often than the ones integrated at the same values of (N_V, N_T) using the broad stabilization. This is especially the case for large values of N_V. In fact, none of the locally stabilized ROMs including more than 350 velocity modes can be integrated up to $t_c = 2$ (short term time frame) whereas it is possible to include all 500 velocity modes using the broad stabilization and integrate up to at least $t_c = 4$ (medium term time frame). Looking back at the $BR = 0.15$ stabilized ROMs, it appeared also impossible to obtain a converged solution for $N_V > 400$ when using the local stabilization, whereas $N_V = 500$ ROMs could be successfully integrated using the broad formulation stabilization. Overall, the minimum error levels attained for the velocity ROM are found to be on average one to two orders of magnitude lower when using broad stabilization compared to local stabilization. While the error on the modeled part of the velocity increases with increasing number of velocity modes before reaching a maximum around $N_V = 100$ and decreases again beyond that point, the total

DISTRIBUTION A: Distribution approved for public release.

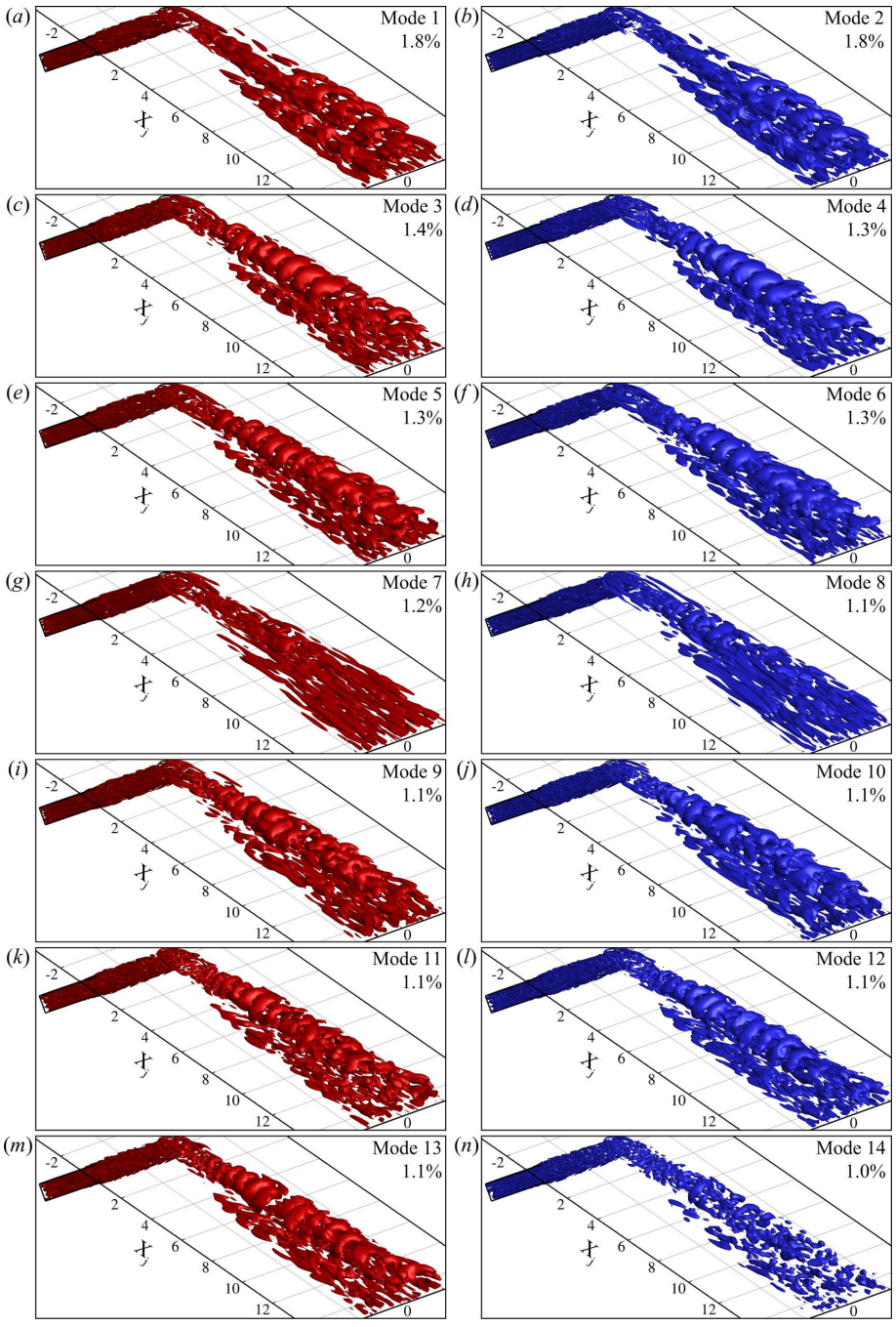

Figure 137: First 14 velocity POD modes λ_2 iso-surfaces for POD decomposition at $BR = 0.5$. Mode energy provided in percent of the total energy.

DISTRIBUTION A: Distribution approved for public release.

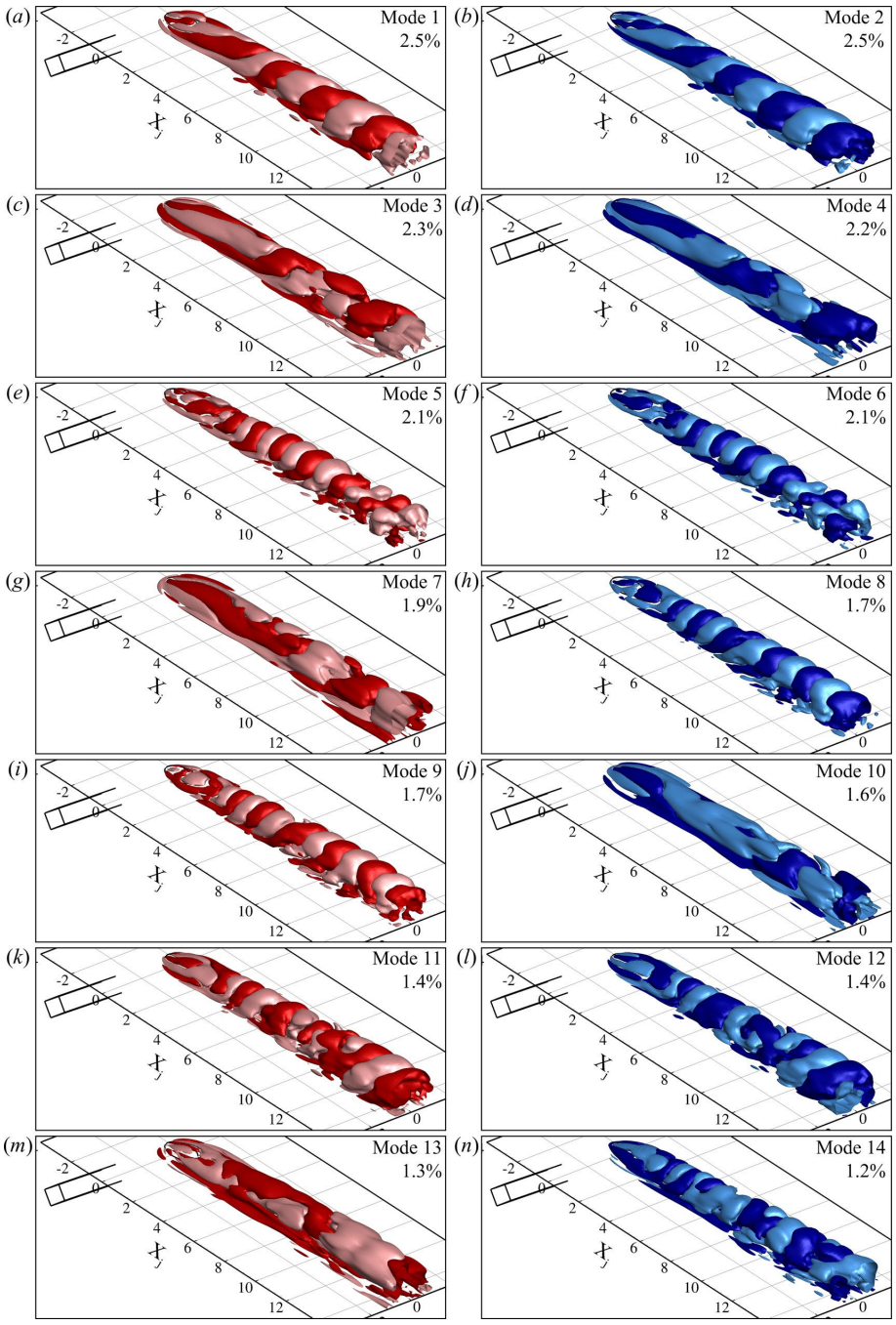

Figure 138: First 14 temperature POD modes iso-surfaces for POD decomposition at $BR = 0.5$. Pink and cyan contours are for negative values, red and blue for positive ones. Mode energy provided in percent of the total energy.

DISTRIBUTION A: Distribution approved for public release.

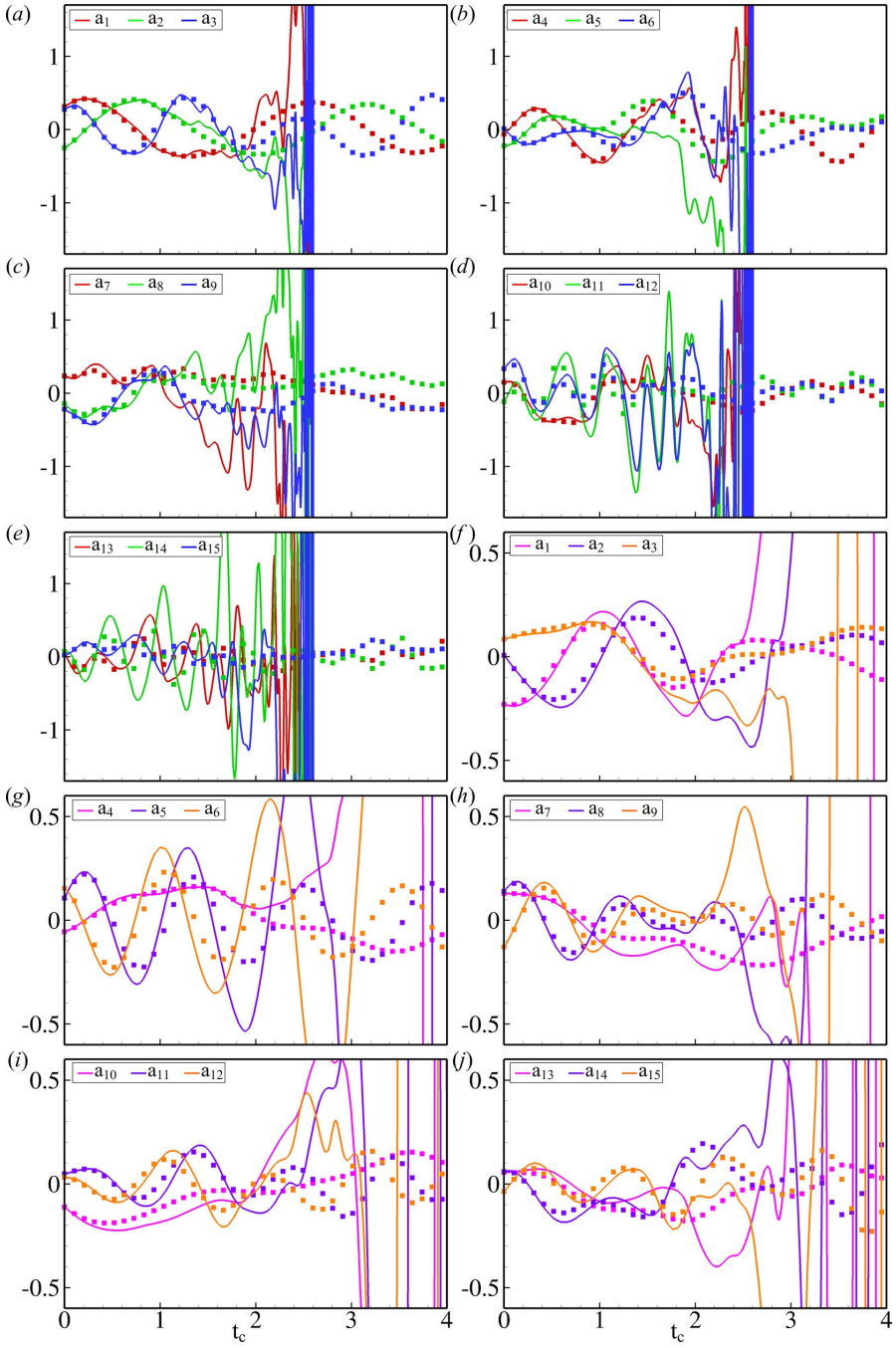

Figure 139: $BR = 0.5$ ROM temporal coefficients for the velocity at $N_V = 350$ and temperature fields obtained at $(N_V, N_T) = (30, 350)$ (*solid lines*) along with corresponding POD temporal coefficients (*symbols*).

DISTRIBUTION A: Distribution approved for public release.

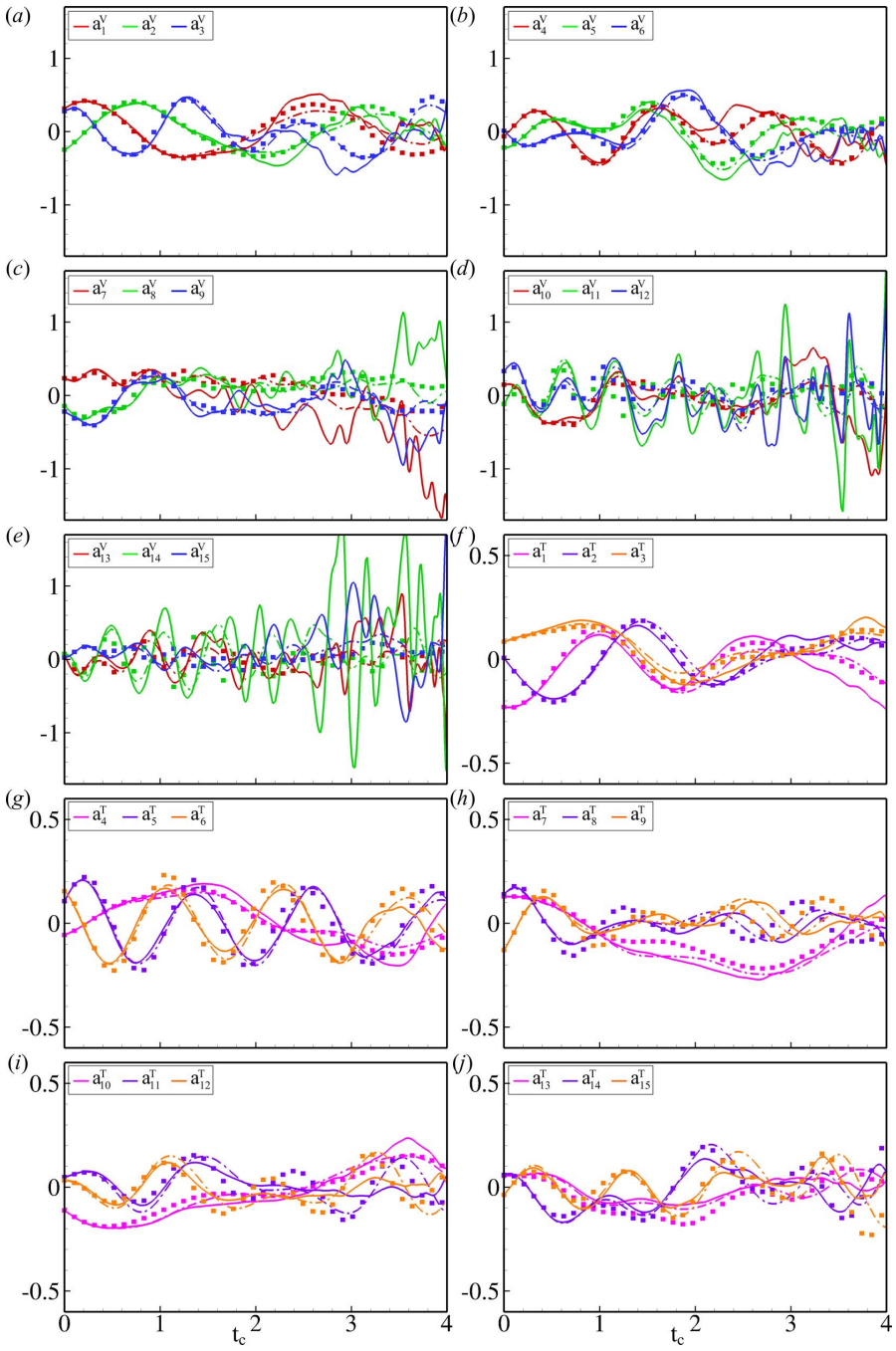

Figure 140: $BR = 0.5$ ROM temporal coefficients for the velocity and temperature fields obtained at $N_V = 350$, $N_T = 350$ with local linear stabilization (*solid lines*) and $N_V = 500$, $N_T = 300$ with broad linear stabilization (*dashed lines*) along with corresponding POD temporal coefficients (*symbols*).

DISTRIBUTION A: Distribution approved for public release.

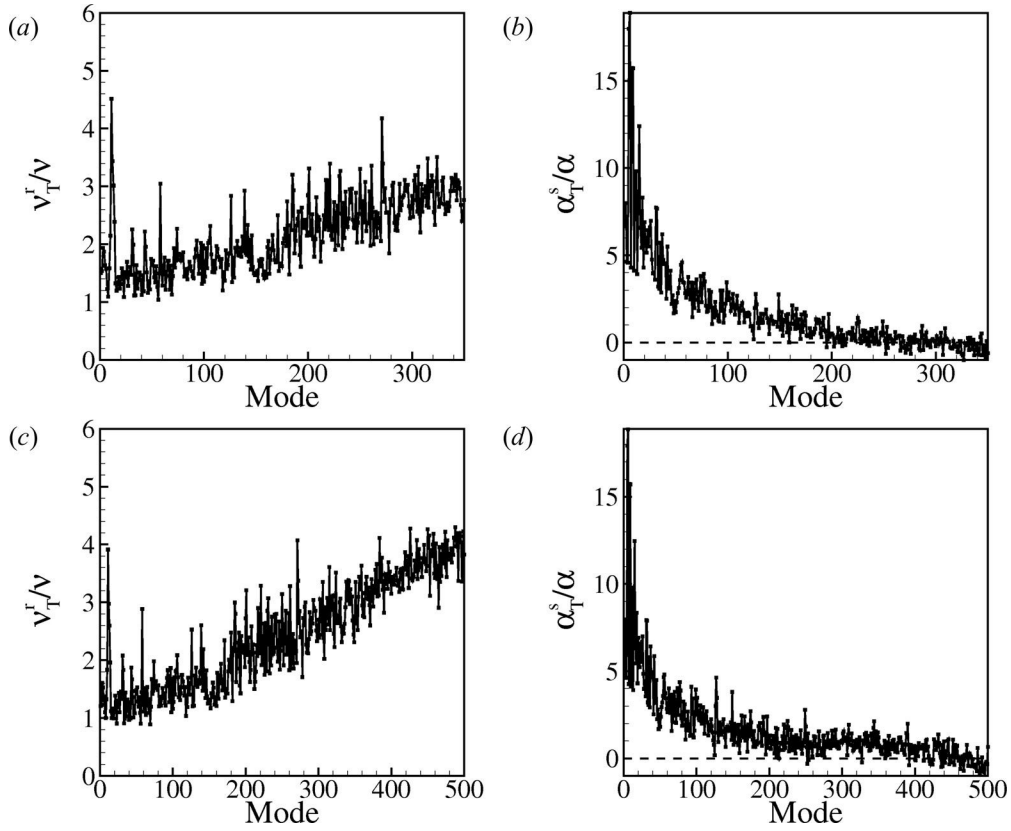

Figure 141: $BR = 0.5$ ROM $(a,\ c)$ normalized turbulent momentum diffusivity ν_T^r/ν and $(b,\ d)$ normalized turbulent thermal diffusivity α_T^s/α calculated for $(a,\ b)$ $N_V = 350$ and $N_T = 350$ and $(c,\ d)$ $N_V = 500$, $N_T = 300$.

error consistently decreases with increasing number of velocity modes. Thus, and because of the improved stability of the broadly stabilized ROMs, lower values of error can be reached for $N_V = 500$ which are unattainable by ROMs using the local stabilization method. The temperature ROM appears to be much less sensitive to the stabilization method used and the error levels using both methods are comparable in the short term, yet with a slight advantage to the broad stabilization method. This is due to the fact that the temperature ROMs for the transitional jet are almost insensitive to the value of N_V and can reach the lowest error levels with only a few velocity modes. In the medium and long term, the broad stabilization method also shows improved performance over the local one. Overall in the short term, the locally stabilized ROM reach minimum values value at $(N_V, N_T) = (350, 350)$ while the broadly stabilized ROM reach a minimum error values for $(N_V, N_T) = (500, 300)$. Similarly, the medium term error estimates show a minimum at $(N_V, N_T) = (350, 140)$ for the former and $(N_V, N_T) = (500, 200)$ for the latter.

Figure 140 presents the integrated ROMs using both local stabilization at $(N_V, N_T) = (350, 350)$ and broad stabilization for $(N_V, N_T) = (500, 300)$. The results show a clear improvement over the non-stabilized ROM in figure 139. No divergence of the extent of the one observed in the non-stabilized equations is found in the stabilized velocity ROMs though the amplitudes of the higher order modes of the locally stabilized equations start to increase

DISTRIBUTION A: Distribution approved for public release.

significantly beyond $t_c = 3$. This is clearly not the case for the broadly stabilized model which seems to follow the projected LES data all the way up to $t_c = 4$ (medium term). Less obvious differences are visible in the temperature ROMs which seem qualitatively very well behaved and follow the projected data nicely. A growing discrepancy is observed for the locally stabilized ROM towards the end of the considered time span $t_c \sim 4$, and is most likely a result of the growing amplitude of the corresponding high order velocity modes. Overall the broad stabilization method provides more stable and more accurate models of the transitional jet, in particular when including large numbers of POD modes compared to the locally stabilized method. The turbulent viscosity and thermal diffusivity for the optimum locally and broadly stabilized ROM are shown in figure 141. The trends for the turbulent viscosity ν_T are consistent with the one obtained for the attached jet, with increasing positive turbulent diffusivity for increasing mode order. The thermal diffusivity trends also follow the ones of the $BR = 0.15$ case, with positive values for lower order modes decreasing with mode rank. The higher order temperature modes evidence negative thermal diffusivity, accounting for heat generation due to viscous dissipation through the smaller scales.

3.2.3 Forced Jets

3.2.3.1 Instantaneous Flow Instantaneous velocity and temperature fields were the first one to be investigated in view to obtain a reduced order model of the forced flow.

Although reasonably good reduced order models were obtained for the unforced jet, it is unlikely those models will be able to capture and reproduce the dynamics of forced jets in cross-flow, and in particular the starting structures, which are generated in actuated conditions. To capture those dynamics, forced jet simulations were used to generate reduced order models by means of the POD-Galerkin method. The models for velocity and temperature fields were modified according to the decomposition proposed by (29). The velocity model was then:

$$\begin{aligned} \dot{a_r}(t) &= \sum_{i=1}^{N_V} \left(\tilde{C}^r_{i,0} + \frac{1}{Re_j} \tilde{D}^r_i \right) a_i(t) + \sum_{i=1}^{N_V} \sum_{j=1}^{i} \tilde{C}^r_{i,j} a_i(t) a_j(t) + \left(\tilde{C}^r_0 + \frac{1}{Re_j} \tilde{D}^r_0 \right) + P_r(t) \\ &+ \gamma(t) \left[\tilde{H}^r_0 + \frac{1}{Re_j} \tilde{L}^r_0 + \sum_{i=1}^{N_V} \tilde{H}^r_{i,0} a_i(t) \right] + \gamma^2(t) \tilde{K}^r_0 + \frac{d\gamma(t)}{dt} \tilde{G}^r_0 \end{aligned} \tag{11}$$

where

DISTRIBUTION A: Distribution approved for public release.

$$\vec{u} = \vec{\overline{u}} + \gamma(t)\vec{u}_{ref} + \vec{u'} = \vec{\overline{u}} + \gamma(t)\vec{u}_{ref} + \sum_{n=1}^{N_V} a_n(t)\vec{\varphi}_n(x)$$

$$\tilde{C}_0^r = -\left(\left(\vec{\overline{u}}.\nabla\right)\vec{\overline{u}}, \vec{\varphi}_r\right) = -\int_{\Omega_x} \overline{u}_l \frac{\partial}{\partial x_l}\left(\overline{u}_m\right)\varphi_{r,l}dx$$

$$\tilde{D}_0^r = \left(\triangle\vec{\overline{u}}, \vec{\varphi}_r\right) = \int_{\Omega_x} \frac{\partial}{\partial x_m \partial x_m}\left(\overline{u}_l\right)\varphi_{r.l}dx$$

$$\tilde{C}_{i,0}^r = -\left(\left(\vec{\overline{u}}.\nabla\right)\vec{\varphi}_i, \vec{\varphi_r}\right) - \left(\left(\vec{\varphi}_i.\nabla\right)\vec{\overline{u}}, \vec{\varphi}_r\right) = -\int_{\Omega_x}\left(\overline{u}_m \frac{\partial}{\partial x_m}\varphi_{i,l} + \varphi_{i,m}\frac{\partial}{\partial x_m}\overline{u}_l\right)\varphi_{r,l}dx$$

$$\tilde{D}_i^r = \left(\triangle\vec{\varphi}_i, \vec{\varphi}_r\right) = \int_{\Omega_x} \frac{\partial}{\partial x_m \partial x_m}\left(\varphi_{i,l}\right)\varphi_{r,l}dx$$

$$\tilde{C}_{i,j}^r = -\left(\left(\vec{\varphi}_i.\nabla\right)\vec{\varphi}_j, \vec{\varphi}_r\right) = -\int_{\Omega_x}\left(\varphi_{i,m}\frac{\partial}{\partial x_m}\varphi_{j,l} + \varphi_{j,m}\frac{\partial}{\partial x_m}\varphi_{i,l}\right)\varphi_{r,l}dx$$

$$P_r(t) = -\left(\nabla P(t), \vec{\varphi}_r\right)$$

$$\tilde{H}_0^r = -\left(\left(\vec{\overline{u}}.\nabla\right)\vec{u}_{ref}, \vec{\varphi}_r\right) - \left(\left(\vec{u}_{ref}.\nabla\right)\vec{\overline{u}}, \vec{\varphi}_r\right) = -\int_{\Omega_x}\left(\overline{u}_m \frac{\partial}{\partial x_m}u_{ref,l} + u_{ref,m}\frac{\partial}{\partial x_m}\overline{u}_l\right)\varphi_{r,l}dx$$

$$\tilde{L}_0^r = \left(\triangle\vec{u}_{ref}, \vec{\varphi}_r\right) = \int_{\Omega_x} \frac{\partial}{\partial x_m \partial x_m}\left(u_{ref,l}\right)\varphi_{r,l}dx$$

$$\tilde{H}_{i0}^r = -\left(\left(\vec{u}_{ref}.\nabla\right)\vec{\varphi}_i, \vec{\varphi}_r\right) - \left(\left(\vec{\varphi}_i.\nabla\right)\vec{u}_{ref}, \vec{\varphi}_r\right) = -\int_{\Omega_x}\left(u_{ref,m}\frac{\partial}{\partial x_m}\varphi_{i,l} + \varphi_{i,m}\frac{\partial}{\partial x_m}u_{ref,l}\right)\varphi_{r,l}dx$$

$$\tilde{K}_0^r = -\left(\left(\vec{u}_{ref}.\nabla\right)\vec{u}_{ref}, \vec{\varphi}_r\right) = -\int_{\Omega_x} u_{ref,l}\frac{\partial}{\partial x_l}\left(u_{ref,m}\right)\varphi_{r,l}dx$$

$$\tilde{G}_0^r = -\left(\vec{u}_{ref}, \vec{\varphi}_r\right) = -\int_{\Omega_x} u_{ref,l}\varphi_{r,l}dx$$

where $\gamma(t)$ is the control function, $\vec{u}_{ref}$ a reference velocity field, $\vec{\overline{u}}$ the average field and $\vec{u'}$ the fluctuation. In this study, $\gamma(t)$ is a square wave of amplitude 1. The reference velocity field is a time independent field chosen to represent the global impact of the control function on the flow. Effectively this term is used to homogenize the velocity at the control surface (jet inlet). For this particular study, the reference field $\vec{u}_{ref}$ is defined as:

$$\vec{u}_{ref} = \vec{\overline{u}}(BR = BR_h) - \vec{\overline{u}}(BR = BR_l) \tag{12}$$

The temperature model:

DISTRIBUTION A: Distribution approved for public release.

$$\dot{b}_s(t) = \sum_{i=1}^{N_V} \tilde{E}^i_{s,0} a_i(t) + \sum_{j=1}^{N_T} \left(\tilde{E}^0_{s,j} + \frac{1}{Pr}\frac{1}{Re_j}\tilde{F}_{s,j} \right) b_j(t) + \sum_{i=1}^{N_V}\sum_{j=1}^{N_T} \tilde{E}^i_{s,j} a_i(t) b_j(t) + \left(\tilde{E}^0_{s,0} + \frac{1}{Pr}\frac{1}{Re_j}\tilde{F}_{s,0} \right) + \gamma(t) \left[\tilde{N}^0_{s,0} + \sum_{j=1}^{N_T} b_j \tilde{N}^0_{s,j} \right] \quad (13)$$

where

$$T = \overline{T} + T' = \overline{T} + \sum_{m=1}^{N_T} b_m(t)\psi_m(x)$$

$$\tilde{E}^0_{s,0} = -\left(\left(\vec{\overline{u}}.\nabla\right) \overline{T}, \psi_s \right) = -\int_{\Omega_x} \overline{u}_m \frac{\partial}{\partial x_m}\left(\overline{T}\right)\psi_s dx$$

$$\tilde{F}_{s,0} = \left(\triangle \overline{T}, \psi_s \right) = \int_{\Omega_x} \frac{\partial}{\partial x_m \partial x_m}\left(\overline{T}\right)\psi_s dx$$

$$\tilde{E}^i_{s,0} = -\left(\left(\vec{\varphi}_i.\nabla\right) \overline{T}, \psi_s \right) = -\int_{\Omega_x} \varphi_{i,m} \frac{\partial}{\partial x_m}\left(\overline{T}\right)\psi_s dx$$

$$\tilde{E}^0_{s,j} = -\left(\left(\vec{\overline{u}}.\nabla\right) \psi_j, \psi_s \right) = -\int_{\Omega_x} \overline{u}_m \frac{\partial}{\partial x_m}\left(\psi_j\right)\psi_s dx$$

$$\tilde{F}_{s,j} = \left(\triangle \psi_j, \psi_s \right) = \int_{\Omega_x} \frac{\partial}{\partial x_m \partial x_m}\left(\psi_j\right).\psi_s dx$$

$$\tilde{E}^j_{s,i} = -\left(\left(\vec{\varphi}_i.\nabla\right) \psi_j, \psi_s \right) = -\int_{\Omega_x} \varphi_{i,m} \frac{\partial}{\partial x_m}\left(\psi_j\right)\psi_s dx$$

$$\tilde{N}^0_{s,0} = -\left(\left(\vec{u}_{ref}.\nabla\right) \overline{T}, \psi_s \right) = -\int_{\Omega_x} u_{ref,m} \frac{\partial}{\partial x_m}\left(\overline{T}\right)\psi_s dx$$

$$\tilde{N}^0_{s,j} = -\left(\left(\vec{u}_{ref}.\nabla\right) \psi_j, \psi_s \right) = -\int_{\Omega_x} u_{ref,m} \frac{\partial}{\partial x_m}\left(\psi_j\right)\psi_s dx$$

This decomposition carried out onto the temperature field evidenced the fact that the velocity control function $\gamma(t)$ appeared explicitely in the temperature model and therefore suggest that the temperature field could be (indirectly) controlled through the velocity field.

3.2.3.1.1 Reduced Order Models Based on the preliminary POD results, it was decided that forced cases at rather high forcing frequencies would constitute a good starting point to obtain a first reduced order model. In addition, it is believed that these flows could benefit more from controlled based tuning than lower forcing frequency ones, where the quasi-unforced parts of the cycle play too significant of a role and the error arising from the mode segregation evidenced previously could affect the stability and accuracy of the ROMs.

Forced jet simulations are carried out using the ROM grid described in Chapter 3 at forcing conditions corresponding to *Case IV* at $St_\infty = 0.159$. The jet inlet velocity is

DISTRIBUTION A: Distribution approved for public release.

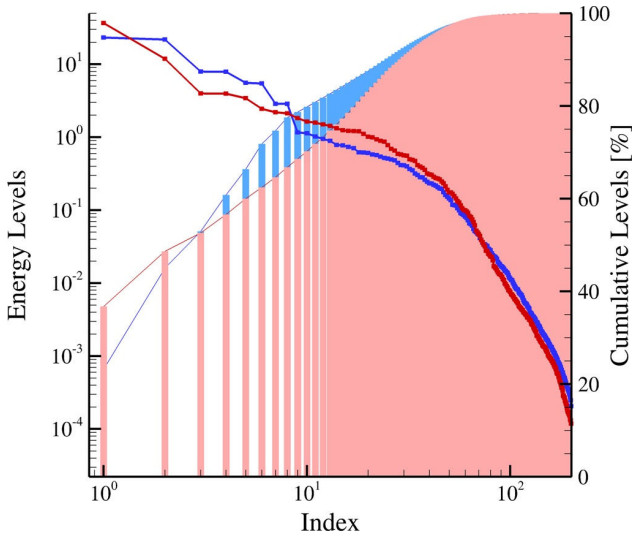

Figure 142: POD decomposition metrics for velocity (*red*) and temperature (*blue*) fields with $N = 200$ for *Case IV* at $St_\infty = 0.159$.

modulated using a square wave signal between $BR_h = 0.50$ and $BR_l = 0.150$. Snapshots are collected at 50 equally spaced phase-locked positions (equivalent sampling frequency $500Hz$ or $St_s = 7.9$) over four cycles for a total of 200 snapshots. In the following section, the transition from BR_l to BR_h occurs at $t_c = 0$.

The POD metrics are presented in figure 142 for both velocity and temperature decompositions. While the temperature metrics evidence the stair-like distribution of the energy levels mentioned in the POD preliminary study with the first two modes at 22% of the total pseudo-thermal energy each, the velocity distribution shows a clearly dominant first mode with 36% of the total kinetic energy while the second mode only carries 11%. This is due to the modified velocity decomposition including the control signal $\gamma(t)\vec{u}_{ref}$, which prevents from direct comparisons with the preliminary study. Overall, 65 velocity POD modes are required to reconstruct 99% of the total kinetic energy from $\vec{u}'$, and 70 temperature modes to reconstruct 99% of the total pseudo-thermal energy of T'.

The velocity POD modes λ_2 iso-surfaces are presented in figure 143, also including for reference the λ_2 iso-surfaces for the fields $\overline{\vec{u}}$ and $\vec{u}_{ref}$. The first two velocity POD modes capture predominantly large scale features at the jet exit likely corresponding to the starting structures, whereas higher order modes such as modes 3, 4, 5 and 6 also capture hairpin vortices in the mid and far-fields with increasing frequency. Interestingly, modes 7 to 12 appear to capture wall structures, predominantly in the far-field. The POD temporal coefficients in figure 145 show dynamics much different from the one of the preliminary POD at equivalent forcing conditions, which was again expected due to the different decomposition used in this section. The temperature POD modes in figure 144 are however much more similar to the ones observed in figure 125 in the preliminary study. The first modes exhibit large scale temperature fluctuation areas, associated with the convection of the starting vortex, while higher order modes correspond to higher harmonics of the first two modes, although the last temperature modes appear to capture anti-symmetric dynamics in the far-field region.

DISTRIBUTION A: Distribution approved for public release.

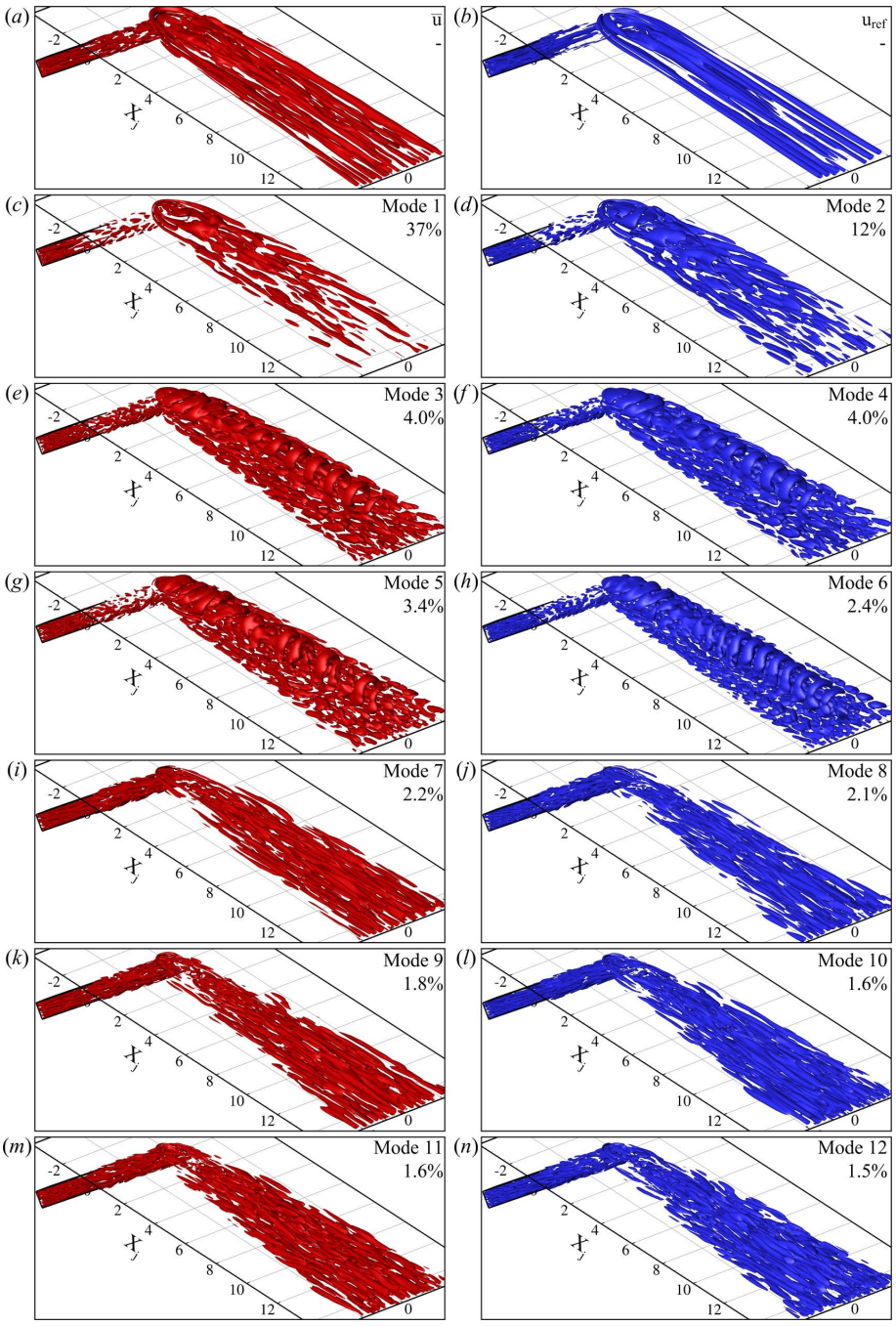

Figure 143: First 12 velocity POD modes along with $\vec{u}_m$ and $\vec{u}_{ref}$ λ_2 iso-surfaces for POD decomposition for *Case IV* at $St_\infty = 0.159$. Mode energy provided in percent of the total energy.

DISTRIBUTION A: Distribution approved for public release.

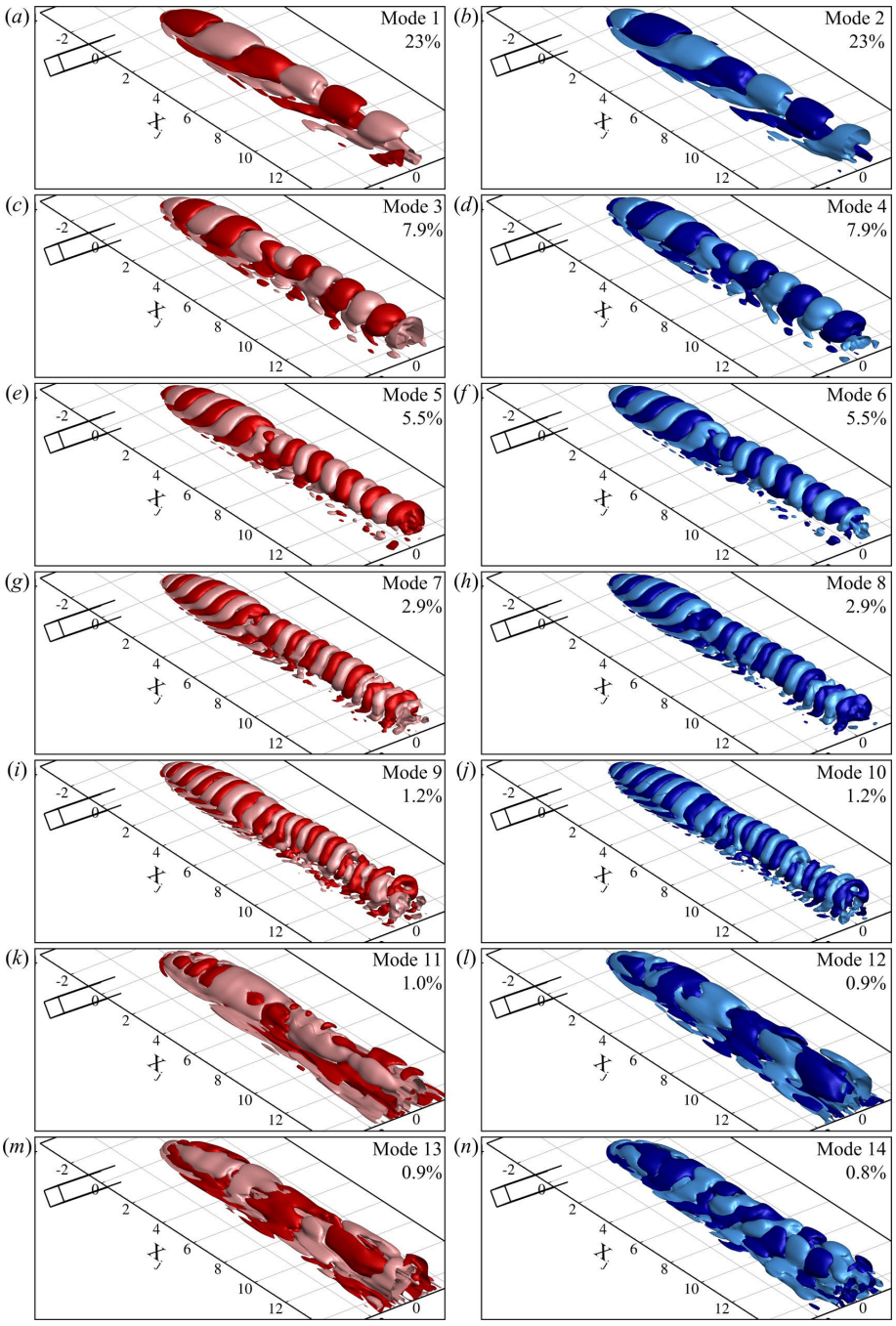

Figure 144: First 14 temperature POD modes iso-surfaces for POD decomposition for *Case IV* at $St_\infty = 0.159$. Pink and cyan contours are for negative values, red and blue for positive ones. Mode energy provided in percent of the total energy.

DISTRIBUTION A: Distribution approved for public release.

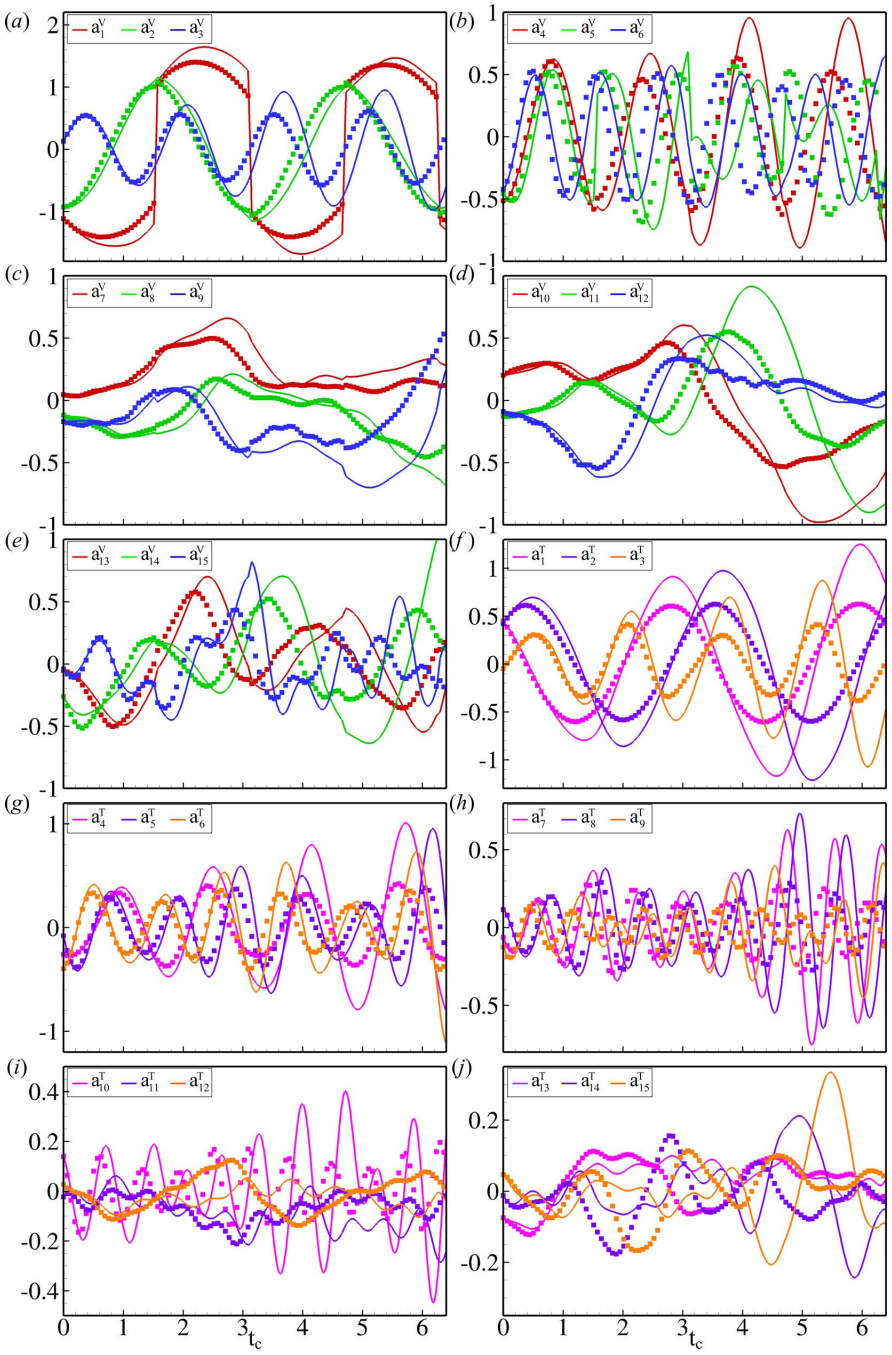

Figure 145: *Case IV* at $St_\infty = 0.159$ ROM temporal coefficients for the velocity ($N_V = 25$) and temperature ($(N_V, N_T) = (15, 45)$) fields (*solid lines*) along with corresponding POD temporal coefficients (*symbols*).

DISTRIBUTION A: Distribution approved for public release.

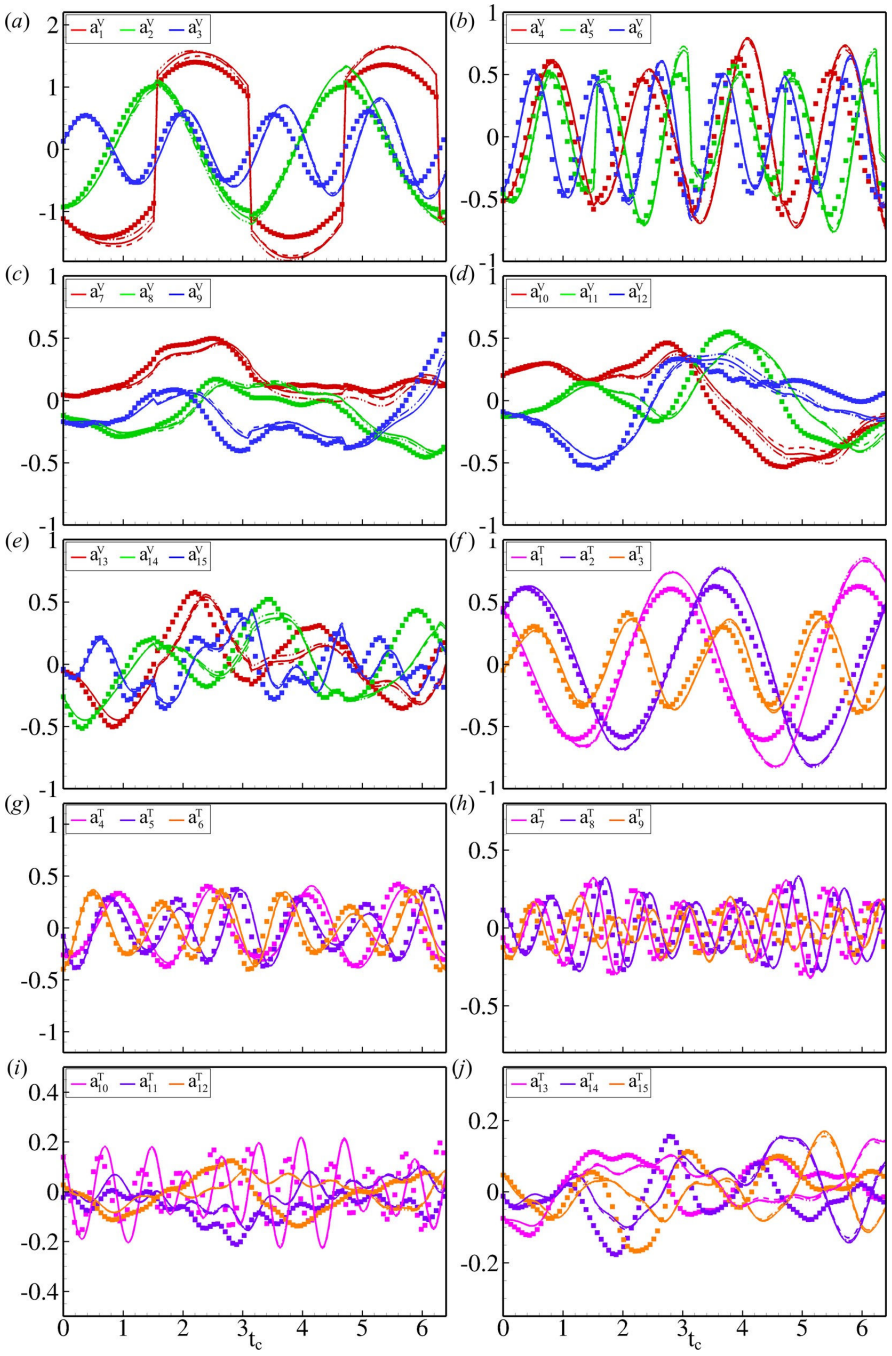

Figure 146: *Case IV* at $St_\infty = 0.159$ ROM temporal coefficients for the velocity ($N_V = 35$) and temperature ($(N_V, N_T) = (10, 30)$) fields using partial local (*solid*) partial broad (*dashed*) and asymptotic (*dash dot dot*) linear damping along with corresponding POD temporal coefficients (*symbols*).

DISTRIBUTION A: Distribution approved for public release.

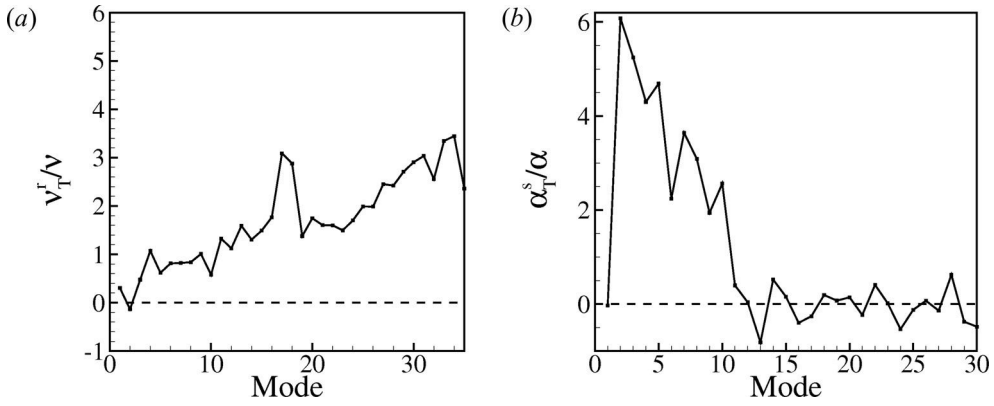

Figure 147: *Case IV* ROM (a) normalized turbulent momentum diffusivity ν_T^r/ν and (b) normalized turbulent thermal diffusivity α_T^s/α calculated for $N_V = 35$ and $N_T = 30$.

Reduced order models using the POD-Galerkin method are derived according to the method described in the previous section. Once again, the pressure term in equation 11 is neglected since ROMs integrated using empirical pressure correction term did not provide any noticeable improvement. In this case, it is possible to compute coefficients for all the velocity and temperature modes so that the complete set of ODEs representing 100% of the flow energy could be integrated. Error estimates are computed for (N_V, N_T) in $[10, 200] \times [10, 200]$ over one, two and three cycle periods and show that the error with respect to both the modeled flow and the total flow increases consistently with increasing number of velocity POD modes. However, the error levels for the best performing velocity and temperature ROMs are rather low, respectively around 8% and 16% over the first cycle period, especially when compared to non-stabilized unforced jets in the previous sections. It also seems that none of the ROMs including more than 125 velocity POD modes could be integrated over a full cycle, while ROMs including more than 90 velocity modes diverged before the end of the second cycle and those with more than 70 modes diverged before the end of the third one. Based on the total error $\overline{E_V^2}$, an optimum number of velocity modes of $N_V = 25$ for the velocity ROM is identified and based on $\overline{E_2^T}$ an optimum pair $(N_V, N_T) = (10, 45)$ for the temperature ROM corresponding to minimum total error is found. Both solutions are presented in figure 145. Overall, the agreement between both ROMs and the projected LES data is reasonably good. The most striking discrepancy resides in the first velocity equation, where the model diverges from the projected data systematically at the end of each part of the cycle, but is most of the time brought back into agreement at the next transition. The velocity model is performing reasonably well over two forcing cycles, although the agreement with the projected LES data clearly starts to be affected towards the end of the second cycle with significant discrepancy in amplitude and phase, even more so for the higher order modes. Similarly, rather good agreement between the temperature ROM and the projected data can be observed over at least the first cycle but phase and amplitude start diverging towards the end of the second cycle, in particular for higher order temperature modes.

Following the method used in the unforced jet configuration, the velocity and temperature reduced order models are integrated using partial local, broad and asymptotic stabilization methods. Corresponding error surfaces were computed and showed that all three methods had virtually identical minimum error level values, and stabilized ROMs integrations with

DISTRIBUTION A: Distribution approved for public release.

200 velocity modes over a full period (compared to a maximum of $N_V = 125$ for the non-stabilized ROMs). While the local and broad methods only permits to integrate ROMs with $N_V \leq 150$ over more than two periods (compared to $N_V \leq 75$ for the non-stabilized ROMs), the asymptotic method permits to integrate ROMs with $N_V \leq 190$ over two periods, and $N_V \leq 180$ over three periods, therefore showing the latter stabilizes systems with large number of velocity modes better. Minimum error levels for all methods are consistently lower than the non-stabilized ROMs by approximately a factor 4 for the velocity ROMs and by a factor 3 in the short term and a factor 60 in the long term for the temperature ROMs. Optimum values for the number of velocity and temperature POD modes correspond to $N_V = 35$ for the velocity ROM and$(N_V, N_T) = (10, 30)$ for the temperature ROM. The temporal coefficients for those integrated reduced order models are presented in figure 146. While the behavior of the first velocity mode is only marginally improved, most of the amplitude and phase discrepancies growing during the second forcing cycle are significantly reduced when using any of the stabilization methods. Overall, the dynamics of the stabilized ROMs using any of the damping methods are quite satisfying over at least 2 cycles.

Finally, the values for the turbulent viscosity and turbulent thermal diffusivity for the stabilized ROMs are presented in figure 147. Interestingly, while most of the velocity modes have a positive turbulent viscosity, the second one actually requires a negative value. Similarly, the first temperature mode requires a negative turbulent thermal diffusivity which is quite different from the unforced jets results. At this point, it should be kept in mind that first, the decomposed (and therefore integrated) signal does not correspond to the overall velocity fluctuation, but rather to the deviation from the reference signal $\gamma(t)\vec{u}_{ref}$ and therefore cannot be directly interpreted as a physical field. Then, it is reminded that the stabilization method adopted here is only an asymptotic (partial) method and only takes care of the under-diffusive character of the uncontrolled flow. Because of this, it is believed that a more complete formulation of the energy conservation constraints (including conservation for $\frac{d\gamma}{dt} \neq 0$) would greatly improve the ROM dynamics and in particular the deviations of the first mode.

3.2.3.2 Phase Averaged Flow Based on the results from the preliminary POD, study showing only little difference between instantaneous and phase averaged flow POD decompositions, the question of whether or not it is possible to obtain a reduced order model for the phase averaged flow is posed. In other terms, if most of the turbulent fluctuation part of the instantaneous velocity field is removed in the process of truncating the POD series, why not only model the dominant phase averaged features in the first place ? A similar approach to the one described in the instantaneous forced flow was applied to the phase averaged signal.

3.2.3.2.1 Reduced Order Models A phase averaged flow is obtained using the same parameters as for the instantaneous flow, for a solution integrated over 10 forcing cycles. The flow is then phase averaged at the same 50 discrete phase locations as for the previous decomposition, thus providing a set of 50 POD snapshots. The transition from BR_l to BR_h occurs at $t_c = 0$. The POD metrics are presented in figure 148. Overall, the energy distributions for both velocity and temperature POD modes are very comparable to the one in figure 142 for the instantaneous flow, in particular for the dominant mode. This is in agreement with the results from the preliminary POD analysis. The first velocity mode is dominant with 37% of the energy which is equivalent to the energy content of the first mode in the instantaneous decomposition. The second mode is significantly weaker with 17% of the

DISTRIBUTION A: Distribution approved for public release.

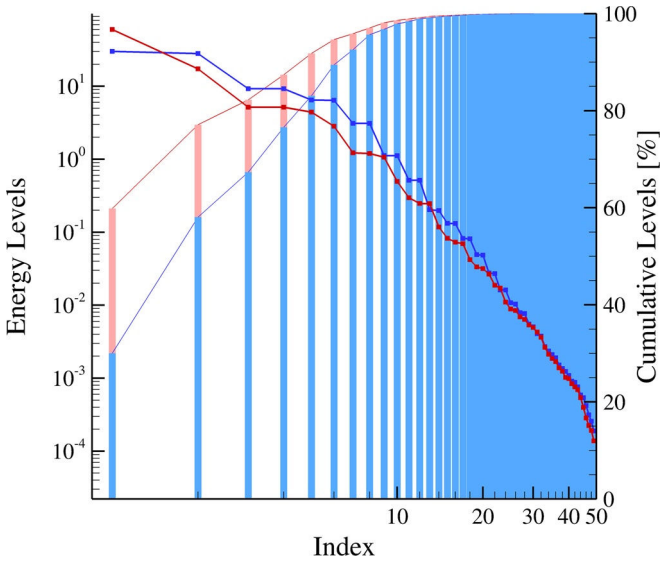

Figure 148: POD decomposition metrics for velocity (*red*) and temperature (*blue*) fields with $N = 200$ for *phase average Case IV* at $St_\infty = 0.159$.

total kinetic energy, against 11% for the second mode of the instantaneous decomposition. The temperature energy levels also exhibit a stair-like distribution, characteristic of flows dominated by strong convective mechanisms. The energy content from the phase averaged temperature field decomposition is globally higher than corresponding modes from the instantaneous one. The 99% total kinetic energy and pseudo-thermal cumulative energy thresholds are reached when including 12 velocity modes and 12 temperature modes respectively. In comparison, thresholds for their instantaneous fields counterparts were corresponding to 65 modes for the velocity field and 70 modes for the temperature field. The phase average values agree also quite well with the ones obtained in the preliminary study (respectively 12 and 15). The POD shape functions for the velocity and temperature are presented in figure 149 and 150. The first 6 velocity modes and 10 temperature modes bear strong resemblance with the instantaneous decompositions in the previous section. However, higher order modes, which here correspond to higher harmonics of the lower order ones, differ quite significantly from their counterparts in the instantaneous decomposition which are capturing either wall structures or anti-symmetric behavior.

Reduced order models corresponding to the non-stabilized equations are integrated for multiple values of (N_V, N_T) in the range $[5, 50] \times [5, 50]$ and corresponding error surfaces were generated. All the ROMs are successfully integrated up to three forcing cycles including all 50 velocity and temperature modes. In general, increasing the number of velocity modes has a negative impact on velocity and temperature error levels, and increasing the number of temperature modes also has a rather negative impact on the temperature error levels. However, the overall error levels are quite low when compared to the instantaneous ROMs with as much as an order of magnitude difference on the total velocity error in the short term. Because the error levels are overall low, it was decided to present in figure 151 the best performing integrated ROMs, such that $N_V > 12$ and $N_T > 12$, corresponding to the 99% energy threshold values from the POD. For the velocity model, this corresponds to $N_V = 14$

DISTRIBUTION A: Distribution approved for public release.

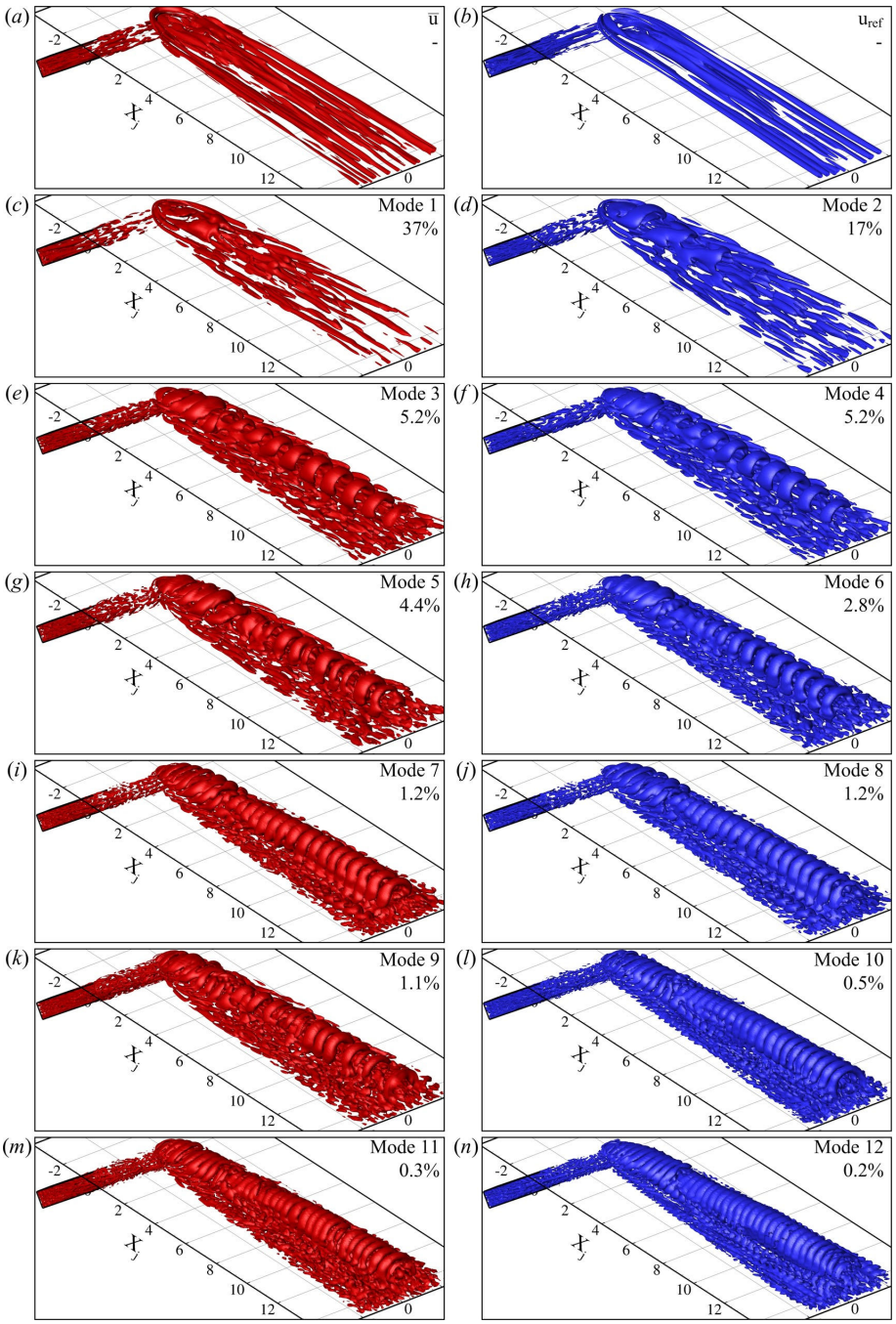

Figure 149: First 12 velocity POD modes along with $\vec{u}_m$ and $\vec{u}_{ref}$ λ_2 iso-surfaces for POD decomposition for *phase averaged Case IV* at $St_\infty = 0.159$. Mode energy provided in percent of the total energy.

DISTRIBUTION A: Distribution approved for public release.

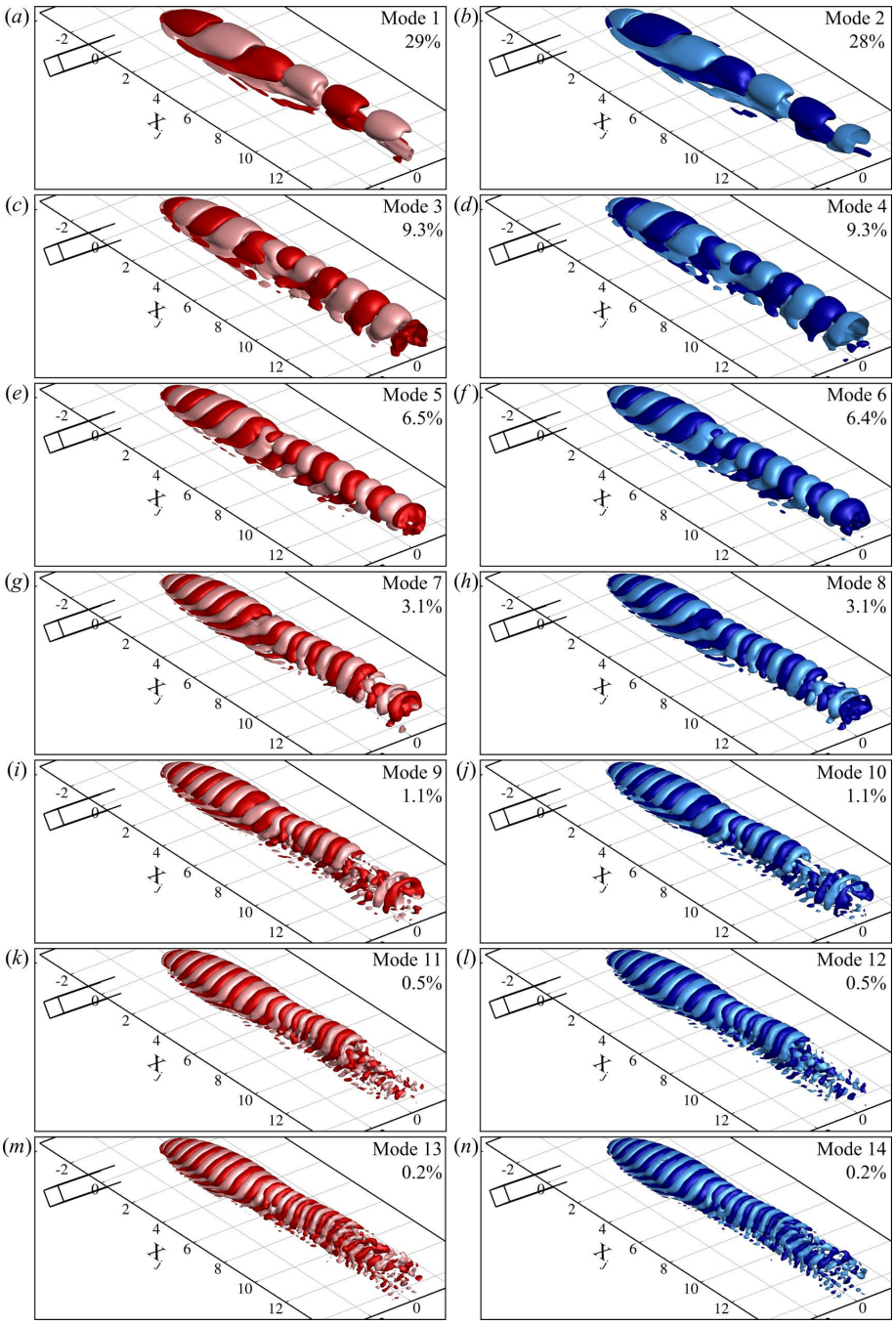

Figure 150: First 14 temperature POD modes iso-surfaces for POD decomposition for *phase averaged Case IV* at $St_\infty = 0.159$. Pink and cyan contours are for negative values, red and blue for positive ones. Mode energy provided in percent of the total energy.

DISTRIBUTION A: Distribution approved for public release.

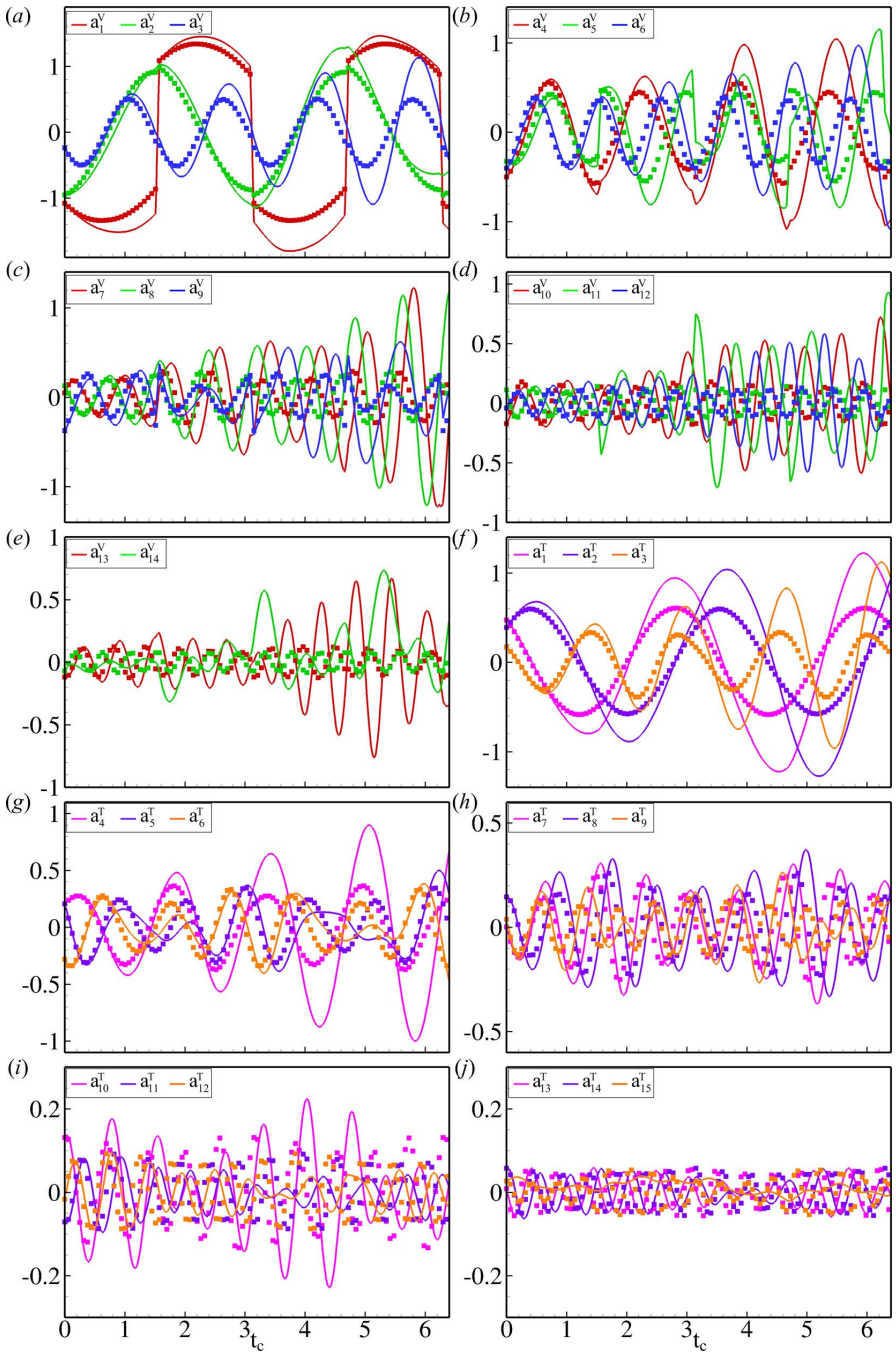

Figure 151: *phase averaged Case IV* at $St_\infty = 0.159$ ROM temporal coefficients for the velocity ($N_V = 14$) and temperature ($(N_V, N_T) = (25, 15)$) fields (*solid lines*) along with corresponding POD temporal coefficients (*symbols*).

DISTRIBUTION A: Distribution approved for public release.

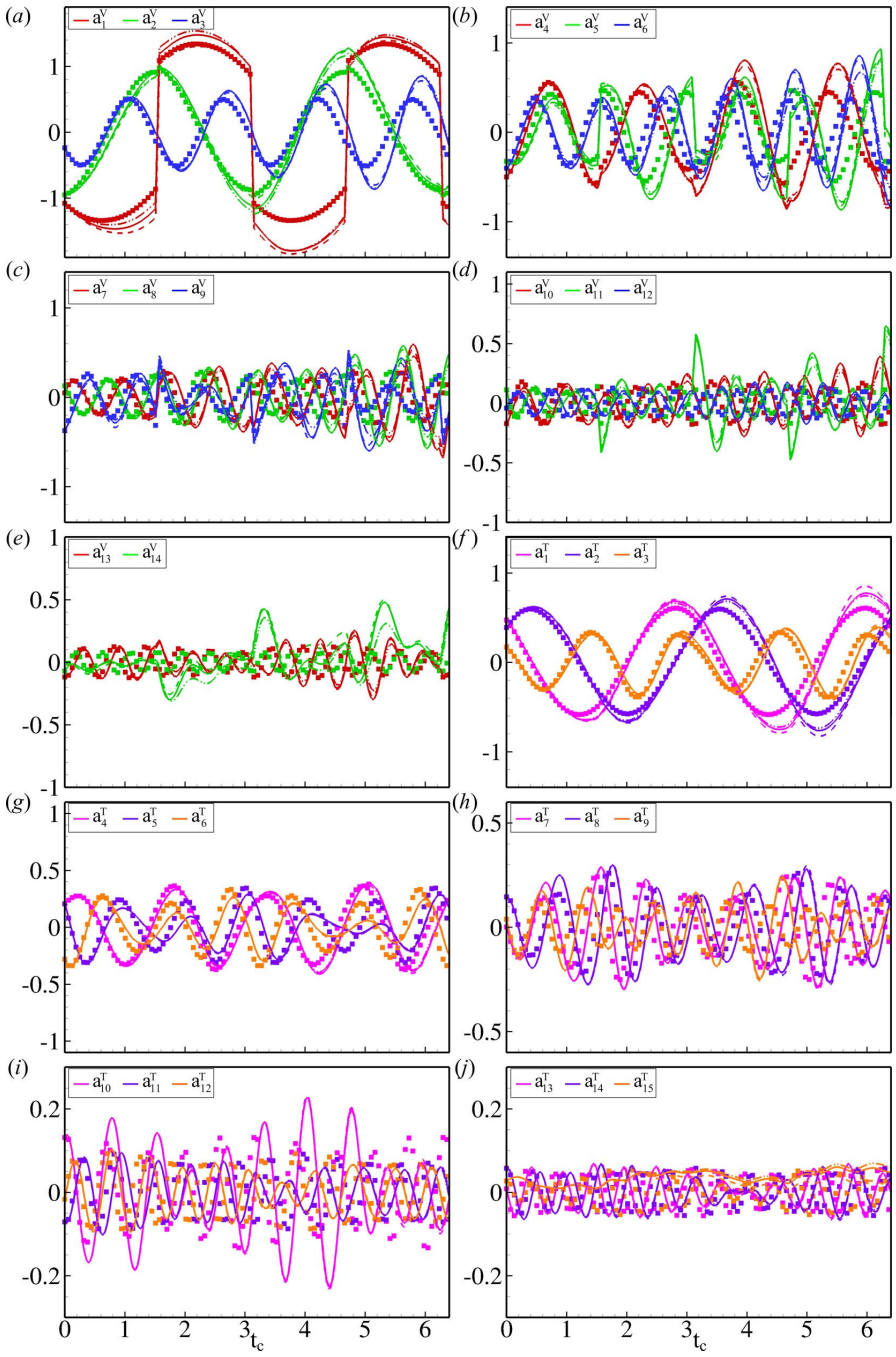

Figure 152: *phase averaged Case IV* at $St_\infty = 0.159$ ROM temporal coefficients for the velocity ($N_V = 14$) and temperature ($(N_V, N_T) = (25, 15)$) fields using partial local (*solid*), partial broad (*dashed*) and asymptotic (*dashed dot dot*) linear damping along with corresponding POD temporal coefficients (*symbols*).

DISTRIBUTION A: Distribution approved for public release.

and for the temperature model to $(N_V, N_T) = (25, 15)$.The agreement between projected LES data and ROM integrated results is qualitatively comparable to the one obtained for the instantaneous flow field, with however only half the number of modes. Once again, a clear discrepancy in the first velocity mode is observed. Amplitude and phase are starting to diverge during the second cycle, although the amplitudes appear to grow less for the higher orders in the phase averaged field than the instantaneous one. While slowly deteriorating, the agreement between the reduced order model the projected LES data over two forcing cycles is found to be reasonably good.

The reduced order models are then integrated using local, broad and asymptotic stabilization methods and the corresponding error surfaces are computed. All three stabilization methods exhibit comparable error levels, although in the long term, ROMs with $N_T = 50$ stabilized using the local and asymptotic methods start diverging in the second cycle. The asymptotic formulation provides more stability to the systems integrated using large numbers of velocity modes and slightly better performance in the long term when compared to the other two. Minimum total error levels on the velocity fields for the stabilized ROMs are on average two time lower in the short term, and almost ten times lower in the long term than comparable non-stabilized ROMs. The effect of the stabilization is even greater on the temperature field with total error levels decreased by a factor 10 in the short term and a factor 100 in the long term. The stabilized reduced order models corresponding to the ones presented previously are shown in figure 152. Overall, the agreement between LES projected data and integrated ROMs is clearly improved over the non-stabilized models with exception of the first velocity POD mode which is left quasi-unchanged. The asymptotically stabilized velocity ROM seems to have slightly better performance towards the end of the second cycle, in particular when considering higher order modes, though the difference is not significant enough to draw any definitive conclusion. The temperature ROM is almost completely insensitive to the type of stabilization method used, yet shows clearly improved agreement with the projected data. Finally, the computed turbulent viscosity and thermal diffusivity are presented in figure 153. Although not many points are shown here because of the low values of N_V and N_T, the trends appear to be similar to the ones obtained for the instantaneous fields, with globally increasing values of the turbulent viscosity and decreasing values of the turbulent thermal diffusivity for increasing mode ranks.

3.3 Conclusion

The preliminary POD analysis of the inclined film cooling jet at $BR = 0.15$ described in this section showed that when considering only part of the physical domain and at such low blowing ratios, POD converged when using 200 snapshots. A total of 78 velocity modes and 76 temperature modes were necessary to gather 99% of the total fluctuation energy. The most energetic velocity POD modes were found to be associated with the convection of the shear layer vortices encountered at this blowing ratio while higher order modes accounted for their interaction with side vortices located near the wall. The temperature analysis led to a more convoluted decomposition, due to the non-optimality of the norm associated to standard POD. The reconstruction of both fields has shown that satisfactory results can be obtained by including a total of 20 POD modes. However, due to the nature of the proper orthogonal decomposition, the relative error in the vicinity of the jet exit remains high and could potentially affect the behavior of a reduced order model based on a truncated series. Preliminary proper orthogonal decomposition analysis was also carried on the pulsed

DISTRIBUTION A: Distribution approved for public release.

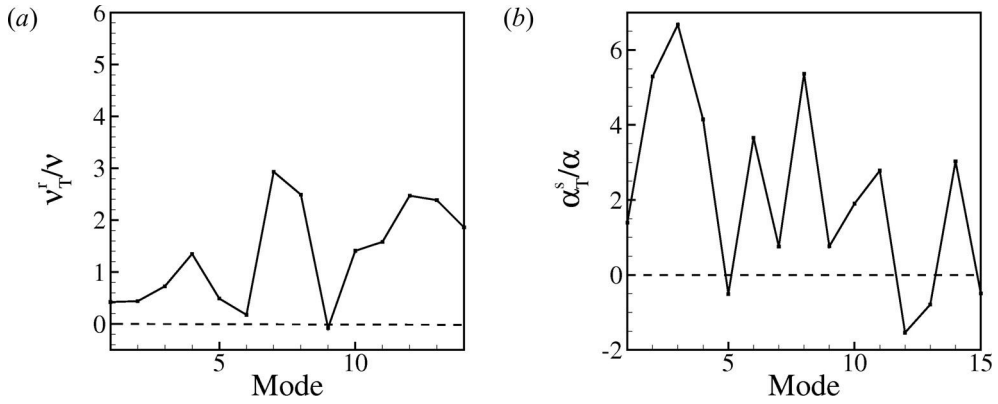

Figure 153: *phase averaged Case IV* ROM (a) normalized turbulent momentum diffusivity ν_T^r/ν and (b) normalized turbulent thermal diffusivity α_T^s/α calculated for $N_V = 14$ and $N_T = 15$.

jet at two distinct forcing frequencies. The analysis of the lowest frequency case ($St_\infty = 0.016$) included 50 phase averaged snapshots and showed that a total of 41 velocity and 33 temperature modes were required to gather more than 99% of the fluctuation energy. The different POD modes had a distinct support of action due to the presence of multiple flow regime within a single forcing cycle. Because of the segregation of the POD modes to specific cycle parts, the POD series truncation for the forced flow could lead to the suppression of the dynamics of part of the cycle. The higher forcing frequency ($St_\infty = 0.159$) analysis included 25 phase averaged modes and required 12 velocity and 15 temperature modes to capture more than 99% of the total fluctuation energy. The POD revealed the homogeneity of the flow in the streamwise direction due to the limited range of length and time scales present in the domain. Because of the significantly greater complexity of the problem at low forcing frequency, 40 POD modes were required to obtain less than 4% relative error on the velocity field, while the same error levels were reached with only 15 modes in the higher frequency case. The temperature field required fewer modes and respectively 10 and 6 modes were necessary at $St_\infty = 0.016$ and $St_\infty = 0.159$ to reach identical accuracy levels.

Reduced order modeling efforts were carried out using a refined grid and over the complete simulation domain, following the POD-Galerkin method described in the previous chapter. Stabilization methods, necessary in realistic three dimensional flows, were discussed and an extension of the model introduced by 15 was proposed. Unforced jets were first considered in both attached and transitional regimes. In the attached jet regime, the effects of the POD domain selection were evidenced by the change of the dominant structures from hairpin vortices to wall vortices between the preliminary analysis and the full domain decomposition. Although decreasing with increasing number of modes, the error levels on the total velocity field of the non-stabilized reduced order models were found to be quite significant. In the short term ($\Delta t_c < 2$), minimum error levels were reached for $(N_V, N_T) = (250, 120)$ but tracking was found to be qualitatively poor beyond $t_c = 1$. A growing divergence in the amplitude and phase of the ROMs was attributed to the interruption of the energy cascade introduced by the POD series truncation, the turbulence model used in the simulations, and the sampling frequency used in the snapshot collection. Stabilized ROMs using either local or broad linear stabilization methods evidenced greatly improved performance over

DISTRIBUTION A: Distribution approved for public release.

non stabilized ones, with error levels over 30 times lower for the velocity field and 200 times lower in the long term for the temperature ROM. Minimum error levels were reached for the stabilized ROMs using $(N_V, N_T) = (275, 100)$. Stabilized ROMs showed reasonable agreement with the projected LES data up to three convective time scale units. In the transitional jet regime, the POD reflected well the increased turbulent character of the flow, with fuller energy distributions and busier POD modes. Non stabilized reduced order models were derived and integrated for values of (N_V, N_T) in the range $[30, 500] \times [30, 500]$. The equations corresponding to the higher order modes were found to diverge rather rapidly beyond $t_c = 1$ and cause the entire system, including the temperature ROM, to diverge around $t_c = 2.5$, preventing any integration past this point. Consequently, error levels for the velocity ROMs in the short term were found to be extremely high, while corresponding temperature error levels were found to be surprisingly lower than comparable results in the attached configuration. Reduced order models including local and broad stabilization terms exhibited much improved error levels. It was found that the broad stabilization method was much more effective when integrating systems including large number of velocity POD modes and therefore permitted to further reduce error levels on the velocity field, even more so in the long term. The temperature ROMs were however much less sensitive to the type of stabilization method used than the velocity models. Qualitatively, both stabilization methods provided much improved ROMs dynamics with an advantage to the broadly stabilized reduced order models which showed very good agreement with the projected LES data at least up to $t_c = 4$.

Reduced order models for instantaneous and phase averaged forced flows at $BR_h = 0.5$, $BR_l = 0.15$, $DC = 50\%$ and $St_\infty = 0.159$ were obtained and integrated. Instantaneous flows were decomposed using (29) formulation. While the POD metrics and shape function of the temperature field were quite similar to the ones of the preliminary study, the POD for the velocity was found to be different due to the use of a different velocity field decomposition. Non-stabilized ROMs showed reasonable agreement with the projected LES data, although divergence started to grow during the second forcing cycle. Three stabilization methods were proposed (two partial and one complete asymptotic) and applied to the velocity and temperature models. All three methods provided significant improvement over the non-stabilized equations with yet a small advantage to the asymptotic stabilization when dealing with systems including larger numbers of velocity modes. Overall any of the stabilized model provided satisfying representation of the flow over at least two cycle periods. Reduced order model equations for the phase averaged flow were derived by neglecting a priori the Reynolds stresses and correcting for those a posteriori when using stabilization methods. Overall, reduced order models of the phase averaged flow were found to perform at least as well as the ones for the instantaneous flow using only half as many modes, thus reducing the computational cost associated with the integration of reduced order models. The stabilized equations provided significant improvement over the non stabilized ones, in particular for the temperature model. It appears clear that the introduction of discrete, strong vortical structures through jet actuation, provided a much better defined and more distinct POD basis responsible for the better accuracy of the forced ROMs over the unforced ones.

These results show that reasonably accurate reduced order models could be obtained for the attached and transient unforced regimes and quite accurate models could be obtained for both the instantaneous and phase averaged flows. Phase averaged models provided comparable error levels to those of instantaneous ones using only half the number of velocity and temperature modes. In all the investigated cases, stabilization methods were found to

DISTRIBUTION A: Distribution approved for public release.

be beneficial, if not necessary. In unforced conditions, the local linear stabilization of (15) and the proposed broad linear stabilization methods exhibited comparable performances, yet the broad formulation usually resulted in more stable equations allowing the integration of larger system and leading to lower error levels. This was particularly true for the more turbulent transient jet regime. In forced conditions, all three proposed methods, damping either only the base flow or both the base and controlled flows in an asymptotic way, provided comparable results in terms of the global error estimates and the agreement of the ROMs dynamics with the projected LES data. The asymptotic formulation seemed to provide some improved stabilization for models including large numbers of modes, compared to the other two. Further improvement of the reduced order models in both unforced and forced conditions will require more sophisticated stabilization methods, in particular with time-dependent capabilities. This is especially true for the forced jet. However, as it stands, it is believed the presented methods provide acceptable models in unforced conditions and relatively good ones in forced conditions, so that they can serve as an initial set of governing equations for the development of a flow controller.

DISTRIBUTION A: Distribution approved for public release.

4 Flow Control

4.1 Jet in Cross-flow Modeling

We consider the 3D Navier-Stokes (N-S) and continuity equations for an incompressible Newtonian fluid as the fluid flow model

$$\frac{\partial \mathbf{u}}{\partial t} + (\mathbf{u} \cdot \nabla)\,\mathbf{u} = -\nabla P + \frac{1}{Re}\nabla^2 \mathbf{u} \tag{14}$$

$$\nabla \cdot \mathbf{u} = 0 \tag{15}$$

where $\mathbf{u} = [u(x,y,z,t) \quad v(x,y,z,t) \quad w(x,y,z,t)]^T$. The problem setup consists of a computational box of dimensions $17D \times 10D \times 3D$ with a cross section in the xy plane along $z = 1.5D$ shown in Figure 154.

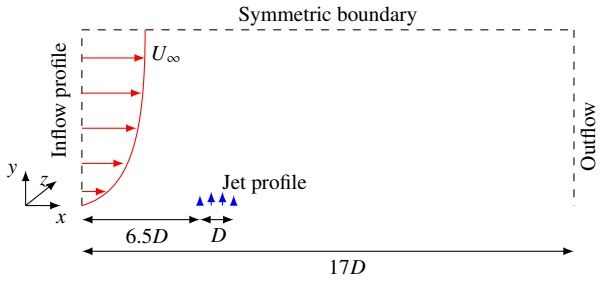

Figure 154: Jet in cross-flow setup

The following physical Dirichlet boundary conditions are prescribed

$$\mathbf{u}(\mathbf{x},t) = \begin{cases} \tilde{c}(t)\tilde{\mathbf{h}}_1(\mathbf{x}), & \text{jet inflow} \\ \tilde{a}_0(t)\tilde{\mathbf{h}}_0(\mathbf{x}), & \text{inflow} \\ 0, & \text{wall} \end{cases} \tag{16}$$

with the inflow boundary condition given by the Blasius solution. The jet inlflow boundary condition is implemented as

$$\tilde{\mathbf{h}}_1(\mathbf{x}) = \begin{bmatrix} 0 & (1-r^2)\,e^{-\left(\frac{r}{0.7}\right)^4} & 0 \end{bmatrix}^T,$$

where r is the distance from the jet center in the xz plane. Notice that this model corresponds to a vertical jet. This expression is intended to model the parabolic velocity profile of pipe Poiseuille flow and is used in several studies, including (5) and (37). At the outflow, a non-reflective boundary condition is used where the gradient of the velocity normal to the boundary is assumed to be zero. On the top of the domain, the boundary condition is given by $\frac{\partial u}{\partial y} = 0, v = 0$.

In this setup the following variables are used to non-dimensionalize the problem: U_∞, the free stream cross-flow velocity, V, the peak inflow velocity of the jet, D, the jet diameter, and ν, the kinematic viscosity. We characterize the jet in cross-flow with the 2 independent

DISTRIBUTION A: Distribution approved for public release.

dimensionless parameters: $Re = \frac{U_\infty D}{\nu}$, the free stream Reynolds number, and $R = \frac{V}{U_\infty}$, the velocity ratio.

4.1.1 Numerical Method

We use the hybrid staggered/semi-staggered finite difference algorithm described in (4) to numerically solve the N-S equation in a parallel computing environment. This direct numerical simulation (DNS) algorithm uses the fractional step method to advance the solution in time in two steps: 1) A semi-staggered grid structure is used to discretize the momentum equations and solve for an intermediate velocity with the pressure gradient term absent, and 2) A staggered grid is used to discretize the Poisson-Neumann equation that adds the pressure gradient to the projection step. All the components of velocity are stored at the cell vertices and pressure is stored at the cell centers. The momentum equations are discretized at cell vertices thus providing a consistent discretization of the diffusive and convective terms as the boundaries are approached. The discrete divergence and gradient operators of the projection step are constructed on a staggered gird layout leading to the exact satisfaction of the discrete continuity equation. It is important to note that the solution of the Poisson-Neumann equation in the projection step is free of any spurious eigenmodes.

A grid with 1,479,072 vertices as shown in Figure 155 was used for the simulations. Using 8 Intel XeonE5620 2.4Ghz, 12M cache processors, it took about 8s to advance the solution one time-step.

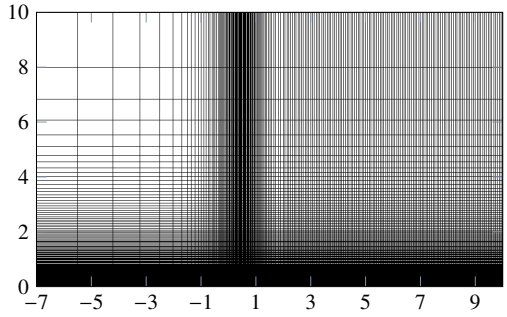

Figure 155: Grid used for simulations

4.1.2 Reduced Order Model Based on POD/Galerkin Projection

We now give a brief overview of the the well-known POD/Galerkin projection method for obtaining reduced order models of the N-S equation. For a detailed treatment of the POD and Galerkin projection, see (35, 43, 70) and the references therein.

We start out with a given solution flow field ensemble $\mathcal{U} = \{\mathbf{u}_1, \ldots, \mathbf{u}_N\}$, where $\mathbf{u}_i = \mathbf{u}(\mathbf{x}, t_i)$, and N is the number of solutions that has been generated by DNS. Given $\mathcal{U}$, the POD problem consists in finding orthonormal basis functions $\{\boldsymbol{\phi}_i\}_{i=1}^n$ that solve

$$\min_{\{\boldsymbol{\phi}_k\}_{k=1}^n} \sum_{i=1}^{N} \left\| \mathbf{u}_i - \sum_{j=1}^{n} (\mathbf{u}_i, \boldsymbol{\phi}_j)_J \boldsymbol{\phi}_j(\mathbf{x}) \right\|^2 \quad s.t. \quad (\boldsymbol{\phi}_i, \boldsymbol{\phi}_j) = \delta_{ij}, \tag{17}$$

DISTRIBUTION A: Distribution approved for public release.

where δ_{ij} is the Kronecker delta and $(\cdot,\cdot)$ is an inner product. The solution to the discretized version of (17) is given by a singular value decomposition (SVD) of the snapshot data matrix, $\mathcal{X} = [\mathbf{u}_1 \quad \mathbf{u}_2 \quad \cdots \quad \mathbf{u}_N]$, and the basis functions $\{\boldsymbol{\phi}_i\}_{i=1}^n$ are called *POD basis functions*.

The next step is to assume that $\mathbf{u}(\mathbf{x},t)$ admits a modal expansion of the form

$$\mathbf{u}(\mathbf{x},t) = \sum_{i=1}^{n} a_i(t)\boldsymbol{\phi}_i(\mathbf{x}) + \tilde{a}_0(t)\tilde{\mathbf{h}}_0(\mathbf{x}) + \tilde{c}(t)\tilde{\mathbf{h}}_1(\mathbf{x}) \tag{18}$$

where $\boldsymbol{\phi}_i, i = 1,\ldots,n$ are homogeneous on the boundary POD basis functions and $\tilde{\mathbf{h}}_0$ and $\tilde{\mathbf{h}}_1$ are control basis functions. The control basis functions are divergence-free extensions of the boundary conditions in (16) (i.e., they match boundary conditions and are divergence-free in the domain). Since there is no danger of confusion, we refer to the spatial component of the boundary conditions and the control basis functions by the same symbol. The following procedure is a simple and straightforward way to construct the control basis functions: Denote $\mathbf{u}_{unact}(\mathbf{x},t)$ an *unactuated solution* when it is a solution obtained with boundary conditions $\tilde{c}(t) = 0$ and $\tilde{a}_0(t) = a_0$. Denote $\mathbf{u}_{act}(\mathbf{x},t)$ an *actuated solution* when it is a solution obtained with boundary conditions $\tilde{c}(t) \neq 0$ and $\tilde{a}_0(t) = a_0$. The term $\tilde{\mathbf{h}}_0(\mathbf{x})$ is taken as the time average of an unactuated solution and $\tilde{\mathbf{h}}_1(\mathbf{x})$ is taken as the time average of $\mathbf{u}_{act}(\mathbf{x},t) - \mathbf{u}_{unact}(\mathbf{x},t)$.

In the literature there are several other methods on how to compute the control basis functions, for example (59), (40), (60), (14), and (64). We could use any of these methods to obtain a ROM but we take a slightly different route. The reason is that we prefer to construct control basis functions that are orthonormal to the POD basis functions in order to simplify the ROM for controller design purposes. Inspired by the Gram-Schmidt algorithm, we use the following procedure to compute these orthonormal POD and control basis functions:

1. Let $\mathcal{X}_h$ denote a snapshot matrix corresponding to

$$\mathbf{u}(\mathbf{x},t) - \tilde{a}_0(t)\tilde{\mathbf{h}}_0(\mathbf{x}) - \tilde{c}(t)\tilde{\mathbf{h}}_1(\mathbf{x}). \tag{19}$$

   Note that $\mathcal{X}_h$ is homogeneous on the boundary.

2. Obtain the POD basis functions corresponding to $\mathcal{X}_h$, i.e., SVD factorization of $\mathcal{X}$. The POD basis will be zero on the boundary by construction.

3. Compute $\mathbf{h}_0 = \frac{\tilde{\mathbf{h}}_0 - \sum_{i=1}^{n}\left(\tilde{\mathbf{h}}_0,\boldsymbol{\phi}_i\right)\boldsymbol{\phi}_i}{\|\tilde{\mathbf{h}}_0 - \sum_{j=1}^{n}\left(\tilde{\mathbf{h}}_0,\boldsymbol{\phi}_j\right)\boldsymbol{\phi}_j\|}$.
   Compute $\mathbf{h}_1 = \frac{\tilde{\mathbf{h}}_1 - \sum_{j=1}^{n}\left(\tilde{\mathbf{h}}_1,\boldsymbol{\phi}_j\right)\boldsymbol{\phi}_j - \left(\tilde{\mathbf{h}}_1,\mathbf{h}_0\right)\mathbf{h}_0}{\|\tilde{\mathbf{h}}_1 - \sum_{j=1}^{n}\left(\tilde{\mathbf{h}}_1,\boldsymbol{\phi}_j\right)\boldsymbol{\phi}_j - \left(\tilde{\mathbf{h}}_1,\mathbf{h}_0\right)\mathbf{h}_0\|}$.

Note that $\mathbf{h}_0$ and $\mathbf{h}_1$ are orthogonal to the POD basis by the construction in step 3. We denote the final orthonormal modal expansion as

$$\mathbf{u}_{ROM}(\mathbf{x},t) = \sum_{i=1}^{n} a_i(t)\boldsymbol{\phi}_i(\mathbf{x}) + a_0(t)\mathbf{h}_0(\mathbf{x}) + c(t)\mathbf{h}_1(\mathbf{x}) \tag{20}$$

where $\mathbf{h}_0(\mathbf{x})$ is called the *inflow basis* and $\mathbf{h}_1(\mathbf{x})$ is called the *control basis*.

DISTRIBUTION A: Distribution approved for public release.

Finally, a standard Galerkin projection with POD, inflow, and control basis functions can be carried out to derive the ROM. This is done by projecting (14), the N-S equation, to the i^{th} POD basis function as follows

$$\int_\Omega \frac{\partial \mathbf{u}}{\partial t} \cdot \boldsymbol{\phi}_i d\mathbf{x} + \int_\Omega \mathbf{u} \cdot \nabla \mathbf{u} \cdot \boldsymbol{\phi}_i d\mathbf{x} = -\int_\Omega \nabla P \cdot \boldsymbol{\phi}_i d\mathbf{x} + \int_\Omega \frac{1}{Re} \nabla^2 \mathbf{u} \cdot \boldsymbol{\phi}_i d\mathbf{x}, \tag{21}$$

where the integration is done over the whole spatial domain, Ω. Using integration by parts on the term $\int_\Omega \frac{1}{Re} \nabla^2 \mathbf{u} \cdot \boldsymbol{\phi}_i d\mathbf{x}$ and noting that the POD basis functions are divergence-free and homogeneous on the boundary, we obtain

$$\int_\Omega \frac{\partial \mathbf{u}}{\partial t} \cdot \boldsymbol{\phi}_i d\mathbf{x} + \int_\Omega \mathbf{u} \cdot \nabla \mathbf{u} \cdot \boldsymbol{\phi}_i d\mathbf{x} + \frac{1}{Re} \int_\Omega \nabla \mathbf{u} \cdot \nabla \boldsymbol{\phi}_i d\mathbf{x} = 0. \tag{22}$$

Recall that the POD basis functions are divergence-free, therefore (15), the continuity equation, is automatically satisfied. Finally, we substitute $\mathbf{u}$ with its truncated orthonormal modal expansion (20) and insert it into (22) to obtain the nonlinear system of differential equations:

$$\begin{aligned} \dot{\bar{\chi}} = \bar{A}\bar{\chi} + \bar{B}\bar{u} + \begin{bmatrix} \bar{\chi}^T \bar{N}_1 \bar{\chi} \\ \vdots \\ \bar{\chi}^T \bar{N}_n \bar{\chi} \end{bmatrix} + \begin{bmatrix} \bar{\chi}^T \bar{M}_1 \bar{u} \\ \vdots \\ \bar{\chi}^T \bar{M}_n \bar{u} \end{bmatrix} + \begin{bmatrix} \bar{u}^T \bar{K}_1 \bar{u} \\ \vdots \\ \bar{u}^T \bar{K}_n \bar{u} \end{bmatrix} + a_0 \bar{D}_1 \bar{\chi} \\ + a_0 \bar{D}_2 \bar{u} + \bar{D}_3 a_0 + \bar{D}_4 a_0^2 \end{aligned} \tag{23}$$

with matrices

$$\begin{aligned} \bar{A}_{ij} &= -\frac{1}{Re} \left(\nabla \boldsymbol{\phi}_j, \nabla \boldsymbol{\phi}_i \right), \bar{B}_{i1} = -\frac{1}{Re} \left(\nabla \mathbf{h}_1, \nabla \boldsymbol{\phi}_i \right), \\ \bar{N}_{i_{jk}} &= -\left(\boldsymbol{\phi}_j \cdot \nabla \boldsymbol{\phi}_k, \boldsymbol{\phi}_i \right), \bar{M}_{i_{j1}} = -\left(\boldsymbol{\phi}_j \cdot \nabla \mathbf{h}_1, \boldsymbol{\phi}_i \right) - \left(\mathbf{h}_1 \cdot \nabla \boldsymbol{\phi}_j, \boldsymbol{\phi}_i \right), \\ \bar{K}_i &= -\left(\mathbf{h}_1 \cdot \nabla \mathbf{h}_1, \boldsymbol{\phi}_i \right), \bar{D}_{1_{ij}} = -\left(\mathbf{h}_0 \cdot \nabla \boldsymbol{\phi}_j, \boldsymbol{\phi}_i \right) - \left(\boldsymbol{\phi}_j \cdot \nabla \mathbf{h}_0, \boldsymbol{\phi}_i \right), \\ \bar{D}_{2_{i1}} &= -\left(\mathbf{h}_0 \cdot \nabla \mathbf{h}_1, \boldsymbol{\phi}_i \right) - \left(\mathbf{h}_1 \cdot \nabla \mathbf{h}_0, \boldsymbol{\phi}_i \right), \tilde{D}_{3_i} = -\frac{1}{Re} \left(\nabla \mathbf{h}_0, \nabla \boldsymbol{\phi}_i \right), \\ \tilde{D}_{4_i} &= -\left(\mathbf{h}_0 \cdot \nabla \mathbf{h}_0, \boldsymbol{\phi}_i \right). \end{aligned}$$

It is clear that $\bar{\chi}(t)$ is the n-dimensional state vector consisting of $\{a_i(t)\}_{i=1}^n$ as its elements, and $\bar{u}(t)$ is the scalar input signal $c(t)$. We highlight that since the inflow and control basis are orthogonal to the POD basis, the terms $\dot{a}_0$ and $\dot{c}$ are zeroed out.

There will be an error associated with the ROM solution and the DNS solution. The relative error difference between the DNS and ROM solution that we focus on is the same

DISTRIBUTION A: Distribution approved for public release.

one that we consider for the POD problem, i.e.,

$$E_{\mathbf{u}} = \left(\frac{\sum_{i=1}^{N} \|\mathbf{u}_{DNS}(t_i) - \mathbf{u}_{ROM}(t_i)\|^2}{\sum_{i=1}^{N} \|\mathbf{u}_{DNS}(t_i)\|^2} \right). \tag{24}$$

It is important to note that due to the inclusion of the inflow and control basis, the modal expansion in (20) is not optimal in the POD sense anymore, although we will see in Section 4.3 that the error is not significant.

4.2 Feedback Control

4.2.1 Problem Statement

The problem we consider is a ROM-based velocity tracking problem. Specifically, we wish for the flow field in the domain to asymptotically track a time-invariant solution of the N-S equation, i.e,

$$\lim_{t\to\infty} (\mathbf{u}(\mathbf{x}, t) - \mathbf{u}_d(\mathbf{x})) = 0$$

or equivalently in the ROM state-space

$$\lim_{t\to\infty} (\bar{\chi}(t) - \bar{\chi}_d) = 0.$$

A straightforward approach would be to select a small enough Re and constant R and let the dynamics evolve so that a time-invariant solution is obtained. A time-invariant solution obtained with a constant inflow boundary condition and velocity ratio is called an *operating point* and denoted by $(\bar{\chi}_d, \bar{u}_d)$. It is crucial to note that this approach would yield a stable operating point since even in the presence of perturbations, this is the solution that the flow converges to. Our objective is to stabilize the flow to an unstable operating point, i.e., one that cannot by reached by simply evolving the fluid dynamics. The problem of designing a stabilizing feedback controller is compounded by the fact that the ROM is a nonlinear system. In this case a popular approach is to linearize the dynamics around an operating point and design a linear controller that will locally stabilize the ROM. While this is a simple and effective solution, the shortcoming of this method is that the designer does not have a verifiable check to guarantee that the linear controller will stabilize the operating point of the nonlinear system. In the control literature this is formally known as providing an estimate of the RoA. Roughly speaking, the region of attraction is the set of initial conditions of the ROM that are guaranteed to converge to an operating point. Therefore the problem we consider is to design a controller that achieves velocity-tracking with a guaranteed estimate of the RoA.

4.2.2 Controller Design

The first step in the design process is to define a new system, called the perturbation ROM, with the operating point that we want to stabilize, $(\bar{\chi}_d, \bar{u}_d)$, as its origin. Let $\chi = \bar{\chi} - \bar{\chi}_d$

DISTRIBUTION A: Distribution approved for public release.

and $u = \bar{u} - \bar{u}_d$. Then the perturbation ROM is given by

$$\dot{\chi}(t) = f(\chi, u) = A(\bar{\chi}_d, \bar{u}_d)\chi(t) + B(\bar{\chi}_d, \bar{u}_d)u(t) + Q[\chi(t), u(t)] \tag{25}$$

where

$$A = \bar{A} + a_0\bar{D}_1 + \begin{bmatrix} \bar{\chi}_d^T N_1 \\ \vdots \\ \bar{\chi}_d^T N_n \end{bmatrix} + \begin{bmatrix} \bar{u}_d^T \bar{M}_1^T \\ \vdots \\ \bar{u}_d^T \bar{M}_n^T \end{bmatrix},$$

$$B = \bar{B} + a_0\bar{D}_2 + \begin{bmatrix} \bar{\chi}_d^T \bar{M}_1 \\ \vdots \\ \bar{\chi}_d^T \bar{M}_n \end{bmatrix} + \begin{bmatrix} \bar{u}_d^T K_1 \\ \vdots \\ \bar{u}_d^T K_n \end{bmatrix},$$

and $Q[\cdot, \cdot]$ is a quadratic term given by

$$Q[\chi, u] = \begin{bmatrix} \chi^T \bar{N}_1 \chi \\ \vdots \\ \chi^T \bar{N}_n \chi \end{bmatrix} + \begin{bmatrix} \chi^T \bar{M}_1 u \\ \vdots \\ \chi^T \bar{M}_n u \end{bmatrix} + \begin{bmatrix} u^T \bar{K}_1 u \\ \vdots \\ u^T \bar{K}_n u \end{bmatrix},$$

with matrices $N_i = \bar{N}_i^T + \bar{N}_i$ and $K_i = \bar{K}_i^T + \bar{K}_i$. Note that in this case $\bar{\chi}_d$ and $\bar{u}_d$ are constant, hence A and B are time-invariant. We could also consider stabilization to a trajectory, $\bar{\chi}_d(t)$ and $\bar{u}_d(t)$, in which case $A(\cdot)$ and $B(\cdot)$ will be time varying.

The perturbation ROM (25) with linear state feedback $u(t) = Fx(t)$ is given by

$$\dot{\chi}(t) = f_F(\chi, F\chi) = A_F\chi(t) + Q[\chi(t), F\chi(t)], \;\; \chi(0) = \chi_0 \tag{26}$$

where $A_F = A + BF$. We model the quadratic nonlinearity as a lumped uncertain term, $\Delta(t)$, which allows us to rewrite (26) as

$$\dot{\chi}(t) = f_\Delta(\chi, F\chi, \Delta), \;\; \chi(0) = \chi_0 \tag{27}$$

Specifically, the time-varying uncertainty is of the following form

$$\Delta(t) = \begin{bmatrix} \chi^T & \chi^T F^T \end{bmatrix} \tag{28}$$

which allows us to write (27) as

$$\dot{\chi} = A_F\chi(t) + \begin{bmatrix} \Delta(t) \begin{bmatrix} N_1 & M_1 \\ 0 & K_1 \end{bmatrix} \\ \vdots \\ \Delta(t) \begin{bmatrix} N_n & M_n \\ 0 & K_n \end{bmatrix} \end{bmatrix} \begin{bmatrix} \chi \\ F\chi \end{bmatrix}. \tag{29}$$

A critical point is that we assume that $\Delta(t)$ belongs to the bounding set $\mathbf{\Delta} = \left\{\chi : \Delta^T(t)\Delta(t) \leq \delta^2 I\right\}$ and $\delta > 0$. As we will see later, this assumption is intimately related to the RoA. At this point we define the notion of quadratic stability which was originally introduced in the

DISTRIBUTION A: Distribution approved for public release.

robust control literature to deal with time-varying uncertainties (7). The definition we use is adapted from (19).

Definition 1. *[Quadratic Stability] Let $V(\chi) = \chi^T P \chi$ and $\mathbf{\Delta}$ be a bounding set. System (27) is quadratically stable at $\chi = 0$ if there exists a symmetric matrix $P > 0$ and a scalar $\alpha > 0$ such that the Lyapunov derivative $\dot{V}(\chi, \Delta)$ satisfies*

$$\dot{V}(\chi, \Delta) \leq -\alpha \left\|\chi\right\|^2 \text{ for all } \Delta \in \mathbf{\Delta}. \tag{30}$$

Note that quadratic stability implies the well-known asymptotic stability by Lyapunov's direct method. We now define the RoQA which will give us a verifiable check on the region of the ROM state-space in which our controller design method stabilizes the nonlinear ROM.

Definition 2. *[RoQA] If there exists an $\epsilon > 0$ such that $\mathcal{B}_P(\epsilon) \subseteq \mathbf{\Delta}$ then the RoQA is defined as $\left\{\chi_0 : \chi_0^T P \chi_0 < \epsilon\right\}$.*

The RoQA is therefore basically the largest ellipsoid that fits inside the region of the state-space of the ROM where the Lyapunov derivative is negative. The concept of a bounding set allows us to establish quadratic stability results since $\Delta(t)$ is used to model the terms related to $Q[\chi, F\chi]$ when these appear in the expression of the Lyapunov derivative of V. The driving design principle is to simultaneously determine a feedback gain F that enlarges the region of the state-space of the ROM where (30) holds, i.e., ϵ, and to determine the largest invariant ellipsoid that is contained in that region, i.e., the matrix P. In the context of the nonlinear control literature, the principle we follow is formally known as determining a regional *control Lyapunov function (clf)*, for more details see (45).

The design method can now be stated as follows.

Design method: Let $\Delta(t)$ be as in (28) with bounding set $\mathbf{\Delta} = \left\{\chi : \Delta^T(t)\Delta(t) \leq \delta^2 I\right\}$ and $\delta > 0$. The system (26) is quadratically stable if there exist solutions $Y = Y^T$ and Z to the linear matrix inequalities (LMIs)

$$Y > 0 \tag{31}$$

$$\begin{bmatrix} YA^T + AY + Z^T B^T + BZ + I & Y^T C^T + Z^T D^T \\ CY + DZ & -\frac{1}{\delta^2} I \end{bmatrix} < 0 \tag{32}$$

with RoQA $\mathcal{B}_P(\epsilon)$, where $\epsilon = \dfrac{\delta^2}{\lambda_{\max}\left(\begin{bmatrix} I \\ F \end{bmatrix} Y \begin{bmatrix} I & F^T \end{bmatrix}\right)}$ and $P = Y^{-1}$. The state feedback gain is given by $F = ZY^{-1}$.

Note: Several convex optimization packages are available which may be used to obtain the controller matrices Y and Z. Some of these are the Robust control toolbox in Matlab, `cvx` package for Matlab and `cvxopt` for Python.

Since the estimated RoQA of the perturbation ROM may be small, we propose a switching strategy combined with our design method to effectively enlarge the RoQA of the ROM if the operating points are 'close enough to each other'. This larger region is defined as follows.

Definition 3. *[Centered-ϵ-Cover] The state-space of the ROM is said to have a centered-ϵ-cover, if the center of each perturbation RoQA is contained inside a neighboring perturbation RoQA.*

DISTRIBUTION A: Distribution approved for public release.

Therefore, if the ROM has a centered-ϵ-cover, then each initial state $\bar{\chi}_0$ can be attracted to the center of the next perturbation RoQA by an appropriate state feedback control law. If we design a feedback gain F_i for each of these perturbation RoQAs we can switch the controller gain between the different F_is to semi-globally stabilize the ROM. This is illustrated in Figure 156 for a system with two operating points, one corresponding to ϵ_1 and another to ϵ_2.

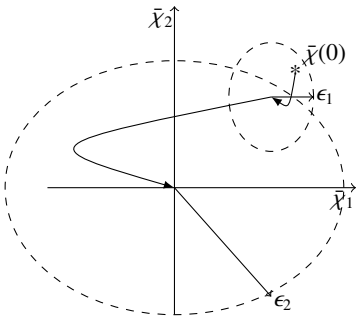

Figure 156: Equilibria path program example

For more details and formal proofs regarding this controller design method see (2).

4.3 Results

4.3.1 Open Loop Dynamics

We now present DNS and ROM simulation results for the system in open loop. The simulation results correspond to $Re = 650$ and $R = 1$ ($\bar{u} = 1, \bar{a}_0 = 1$). After about 7 flow-throughs, snapshots were collected and the POD and control basis functions were computed using the method described in Section 4.1.2. A total of 180 snapshots with a sampling period of $\Delta t = 0.0665$ were collected to compute the POD basis; this spans about 3.5 shedding cycles. The energy distribution in the POD modes is shown in Figure 157. We note that the singular values appear in pairs, a characteristic of flow systems with traveling structures (23).

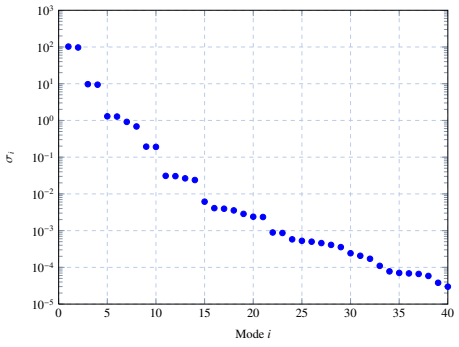

Figure 157: Energy in σ_i

Most of the energy is contained in the first 8 modes as shown in Table 13.

DISTRIBUTION A: Distribution approved for public release.

n	% Energy
8	92.9
16	98.1
32	99.7

Table 13: Energy captured by POD expansion

In Figures 158 and 159 we plot the λ_2-criterion, as defined in (38) and (16), of a selected number of POD basis functions and the control basis.

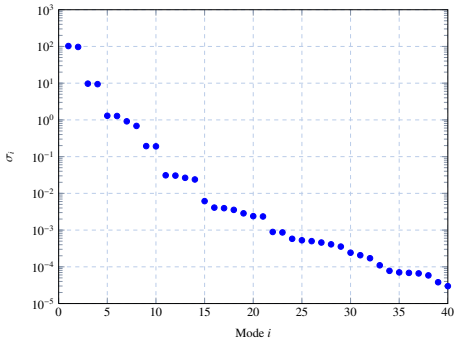

Figure 158: λ_2-criterion of POD basis functions ($\lambda_2 = -0.06$)

DISTRIBUTION A: Distribution approved for public release.

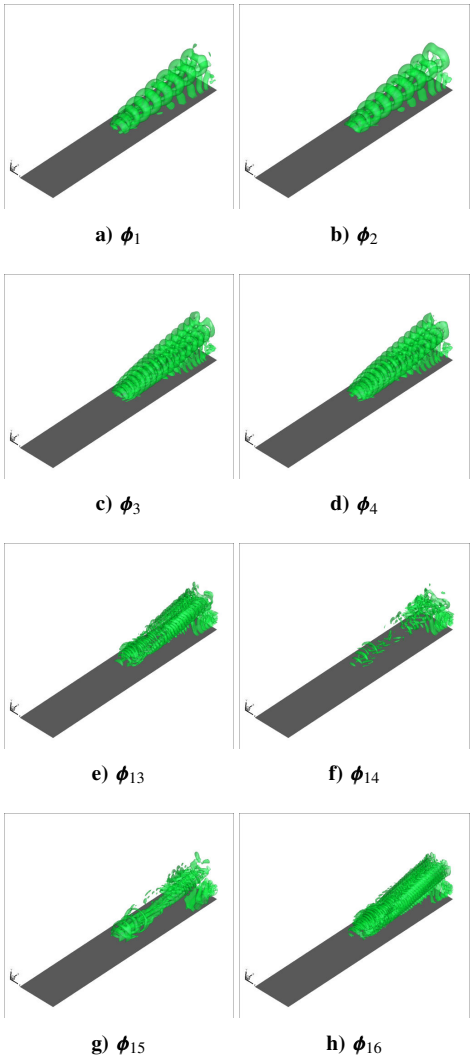

Figure 159: λ_2-criterion of control basis function ($\lambda_2 = -0.06$)

From the figures we can see the features of the coherent structures of the jet in cross-flow such as the horseshoe vortex, jet shear-layer vortices, and wake vortices. Figure 160 shows the x component of velocity at different time instants.

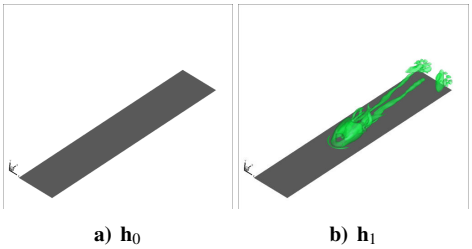

Figure 160: x-component of velocity. Top: DNS. Bottom: ROM, $n = 32$.

DISTRIBUTION A: Distribution approved for public release.

It is important to note that the fidelity of the ROM solution tends to decay as time advances. This becomes evident when the time history of $\bar{\chi}(t)$, or POD coefficients are visualized. Figure 161 shows the time history of the first and last 8 elements of $\bar{\chi}(t)$ as well as the projection of the DNS data to the POD coefficients $\{a_i(t)\}_{i=1}^{32}$. First, we notice that the ROM and DNS solutions match well at the beginning, and the time at which the DNS and ROM solutions start to diverge depends on the mode number. For example, the 7^{th} mode matches well up until $t = 5$, while the 1^{st} mode starts to diverge around $t = 1$. The figures also show that the amplitude of the higher modes grows in the ROM solution, while they stay 'small' in the projected DNS data. This behavior helps to explain the appearance of high frequency features in the flow in Figure 160. The solutions of the $n = 16$ ROM exhibit the same behavior but due to space limitations we do not present them. It is well known that ROMs usually diverge to a limit cycle not present in the original data as time advances, this has been reported in (17), (51), and chapter 5 in (66), among many others.

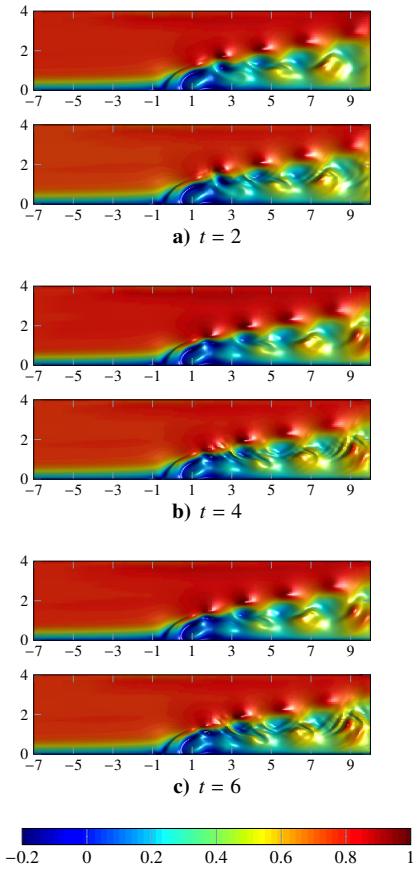

Figure 161: ROM (solid) and DNS (dotted) solution, $n = 32$

The error for the $n = 16$ model, as calculated in (24), is $E_{\mathbf{u}} = 1.99 \times 10^{-4}$ and the error for the $n = 32$ model is $E_{\mathbf{u}} = 1.95 \times 10^{-4}$. In addition, we plot the error in (24) as a function of time (i.e., the sequence) in Figure 162. Two observations that we obtain from that plot are that the difference in energy captured between a 16 and 32 order model is not significant

DISTRIBUTION A: Distribution approved for public release.

and that the difference is larger for low values of t. As time increases the error seems to converge to the same values for both $n = 16$ and $n = 32$.

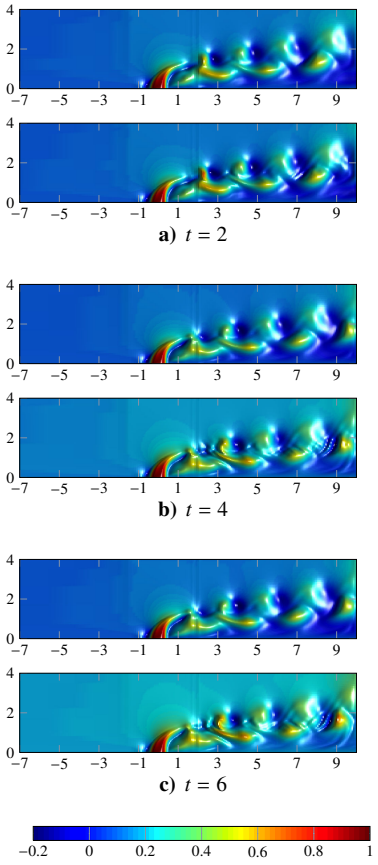

Figure 162: Error between DNS and ROM solution

4.3.2 Closed Loop Dynamics

Since the error dynamics for the $n = 16$ and $n = 32$ ROM are very similar, we focus on the $n = 16$ model for the controller design. The first issue we deal with is which operating point to pick. Using the MATLAB function `fsolve` we numerically solve

$$f(\bar{\chi}, \bar{u}, a_0) = 0$$

in (23) with $\bar{u} = 1$ and $a_0 = 1$ to obtain the desired operating point $\bar{\chi}_d^{(1)}$. To obtain the second operating point, $\bar{\chi}_d^{(2)}$, we set $\bar{u} = 1.0010$ and $a_0 = 1$. The values of the states for the first operating points is shown in Table 14. The second operating point is not reported due to space considerations.

DISTRIBUTION A: Distribution approved for public release.

State	Value		State	Value
$\bar{\chi}_{d_1}^{(1)}$	0.1804		$\bar{\chi}_{d_9}^{(1)}$	0.0112
$\bar{\chi}_{d_2}^{(1)}$	-0.2973		$\bar{\chi}_{d_{10}}^{(1)}$	0.0201
$\bar{\chi}_{d_3}^{(1)}$	-0.0015		$\bar{\chi}_{d_{11}}^{(1)}$	-0.0013
$\bar{\chi}_{d_4}^{(1)}$	0.0420		$\bar{\chi}_{d_{12}}^{(1)}$	0.0289
$\bar{\chi}_{d_5}^{(1)}$	0.0219		$\bar{\chi}_{d_{13}}^{(1)}$	0.0177
$\bar{\chi}_{d_6}^{(1)}$	-0.0690		$\bar{\chi}_{d_{14}}^{(1)}$	0.2212
$\bar{\chi}_{d_7}^{(1)}$	0.2815		$\bar{\chi}_{d_{15}}^{(1)}$	-0.4283
$\bar{\chi}_{d_8}^{(1)}$	0.3764		$\bar{\chi}_{d_{16}}^{(1)}$	-0.1707

Table 14: Operating point $\bar{\chi}_d^{(1)}$

With an operating point identified, we now study the stability of the operating point. Figure 163 clearly shows that if the ROM is solved with a small perturbation to $\bar{\chi}(0) = \bar{\chi}_d^{(1)}$, then the resulting solution eventually leaves the operating point.

To verify our intuition, Figure 164 shows the eigenvalues of the matrix A of the perturbation system at $\bar{\chi}_d^{(1)}$. The two pairs of eigenvalues on the right hand side of the imaginary axis reveal that the selected operating point is indeed unstable. The role of the feedback controller then is to shift the unstable eigenvalues to the left hand side of the imaginary axis and to enlarge the RoQA of the perturbation system.

Figure 165 shows the location of the eigenvalues of the matrix $A+BF$ of the perturbation ROM at $\bar{\chi}_d^{(1)}$ with the feedback gain F designed using the method in Section 4.2.

A similar argument holds for the perturbation system at $\bar{\chi}_d^{(2)}$, although we don't include the plots due to space constraints. The ROM solution of the perturbation system clearly depicts the stabilizing effect of the controller as shown in Figure 166.

We can see from Figure 166 that the RoQA is fairly small. This means that to stabilize the ROM, a fairly large number of switches will be required if the initial condition is far away from $\bar{\chi}_d^{(1)}$. However, this method provides us with an estimate of the RoQA while a simpler linearization study only provides local results, i.e., the RoQA may be vanishingly small. Figure 167 shows a two stage equilibria path simulation, from $\bar{\chi}_0$ to $\bar{\chi}_d^{(1)}$ and settling at $\bar{\chi}_d^{(2)}$.

The initial condition for the simulation is shown in Table 15. It is computed via our controller design method and lies in the maximized RoQA. The location of $\bar{\chi}_d^{(2)}$ is chosen such that $\bar{\chi}_d^{(1)}$ lies in the RoQA of $\bar{\chi}_d^{(2)}$. The switch occurs at $t = 12$ and clearly shows up in the plot of the control signal.

The result presented in Figure 167 corresponds to the setup shown in Figure 168 (a), i.e, the ROM. Once a state feedback F has been designed, it is inserted into a DNS simulation as shown in Figure 168 (b) and (c) to evaluate the performance of the controller in the full order model.

DISTRIBUTION A: Distribution approved for public release.

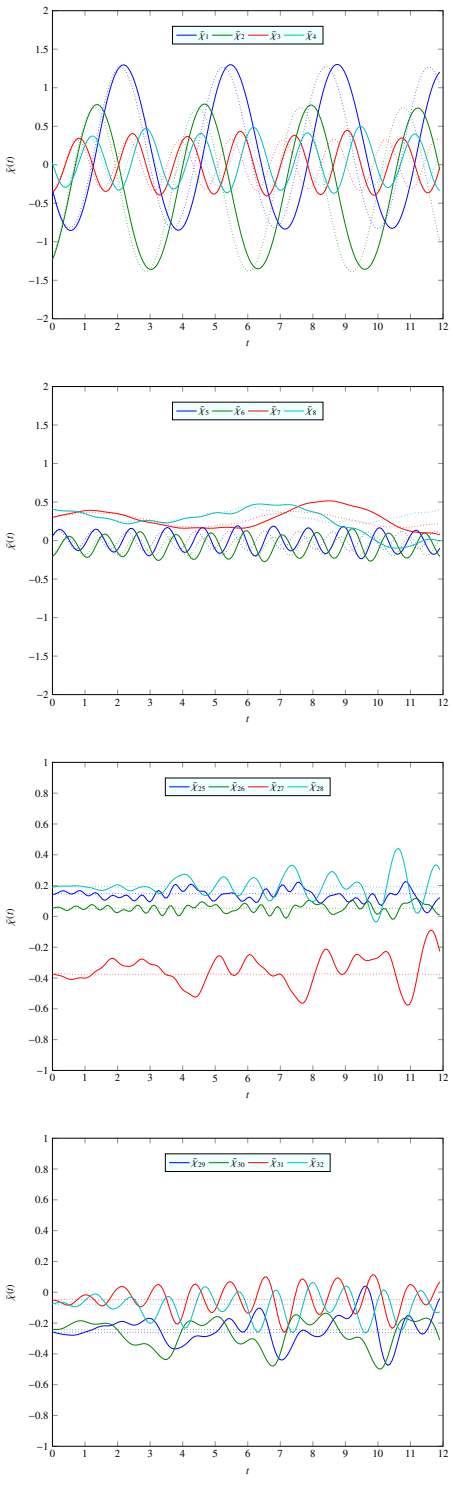

Figure 163: ROM solution with $\bar{\chi}_0 = \bar{\chi}_d^{(1)}$

DISTRIBUTION A: Distribution approved for public release.

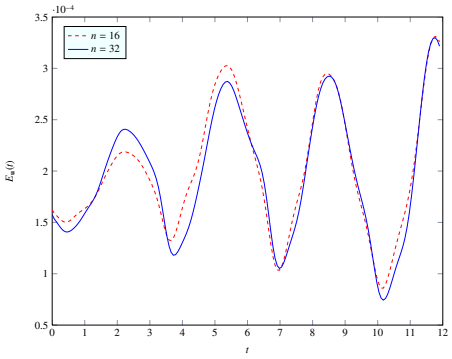

Figure 164: Eigenvalues of A (perturbation at $\bar{\chi}_d^{(1)}$)

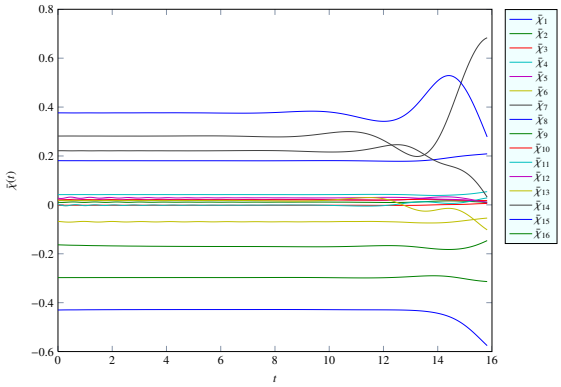

Figure 165: Eigenvalues of A+BF (perturbation at $\bar{\chi}_d^{(1)}$)

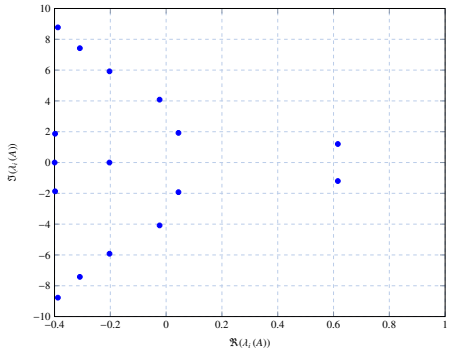

Figure 166: ROM solution in closed loop (perturbation at $\bar{\chi}_d^{(1)}$)

The results of the ROM and DNS in closed loop (implementation 1) are shown in Figure 169. There is a noticeable difference between the ROM and DNS solution starting at around $t = 2$ and from then onwards the DNS solution leaves the operating condition. In this sense, the behavior between the ROM and DNS solution is the same as in open loop, eventually the ROM solution loses fidelity. The solution using DNS implementation 2 behaves similarly

DISTRIBUTION A: Distribution approved for public release.

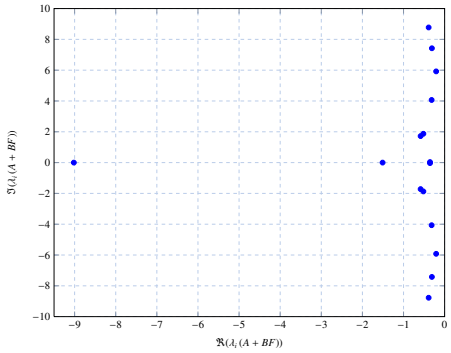

Figure 167: ROM solution in closed loop and input signal

State	Value		State	Value
$\bar{\chi}_1$	0.1807		$\bar{\chi}_9$	0.0108
$\bar{\chi}_2$	-0.2974		$\bar{\chi}_{10}$	0.0197
$\bar{\chi}_3$	-0.0015		$\bar{\chi}_{11}$	-0.0003
$\bar{\chi}_4$	0.0419		$\bar{\chi}_{12}$	0.0286
$\bar{\chi}_5$	0.0215		$\bar{\chi}_{13}$	0.0183
$\bar{\chi}_6$	-0.0688		$\bar{\chi}_{14}$	0.2212
$\bar{\chi}_7$	0.2815		$\bar{\chi}_{15}$	-0.4296
$\bar{\chi}_8$	0.3763		$\bar{\chi}_{16}$	-0.1657

Table 15: Initial condition for switched system simulation, $\bar{\chi}_0$

in the first few units of time, but the control signal calculated in this setup diverges from the signal $c_1(t)$ of Figure 168 (a) . After about $t = 2$ the control signal behaves erratically which illustrates the difficulty in implementing the control signal from the ROM to the DNS simulation.

4.4 Conclusion

We have presented a design method for feedback stabilization of a ROM of a jet in cross-flow. The proposed controller is linear and in addition to regionally stabilizing the nonlinear ROM, also enlarges the estimate of the RoQA. Stability is therefore guaranteed around a region of the operating point. The RoQA is computed by a simple formula based on the solution to a set of LMIs. The overall design consists of a sequence of linear controllers implemented in a switching strategy that regionally stabilize the desired equilibrium under the assumption that the system admits a centered-ϵ-cover. If this assumption is satisfied, then the switching controller will achieve semi-global stabilization of the nonlinear system. The controller that was designed based on the ROM was able to stabilize the flow to the selected operating point in DNS for a short time period until the DNS solution diverged to

DISTRIBUTION A: Distribution approved for public release.

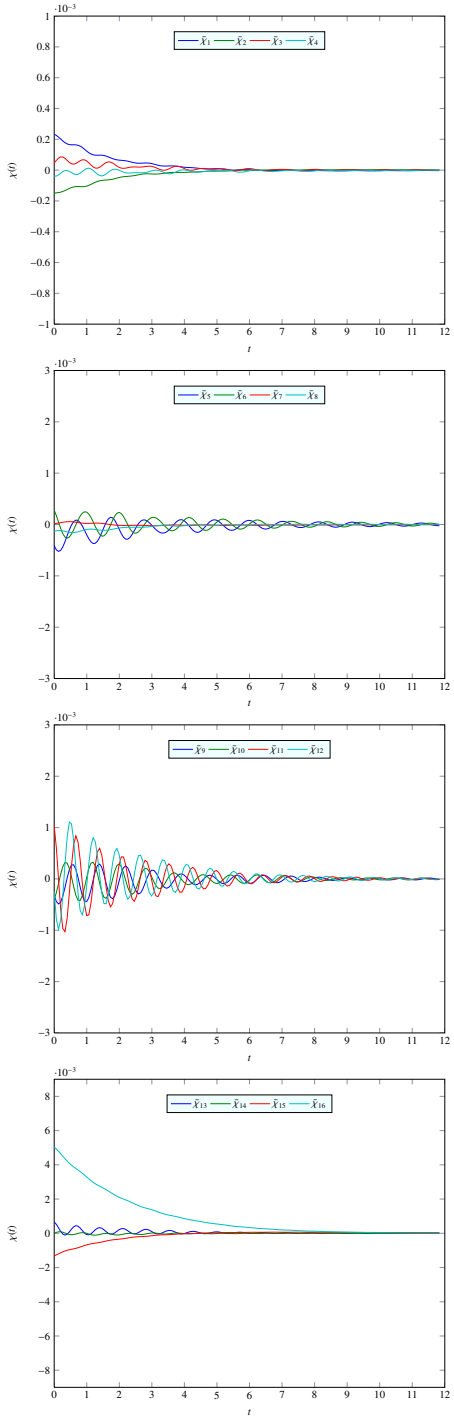

Figure 168: DNS closed loop implementations

another operating condition. This highlights the difficulties encountered when a controller is designed for a ROM and then implemented on the full system.

DISTRIBUTION A: Distribution approved for public release.

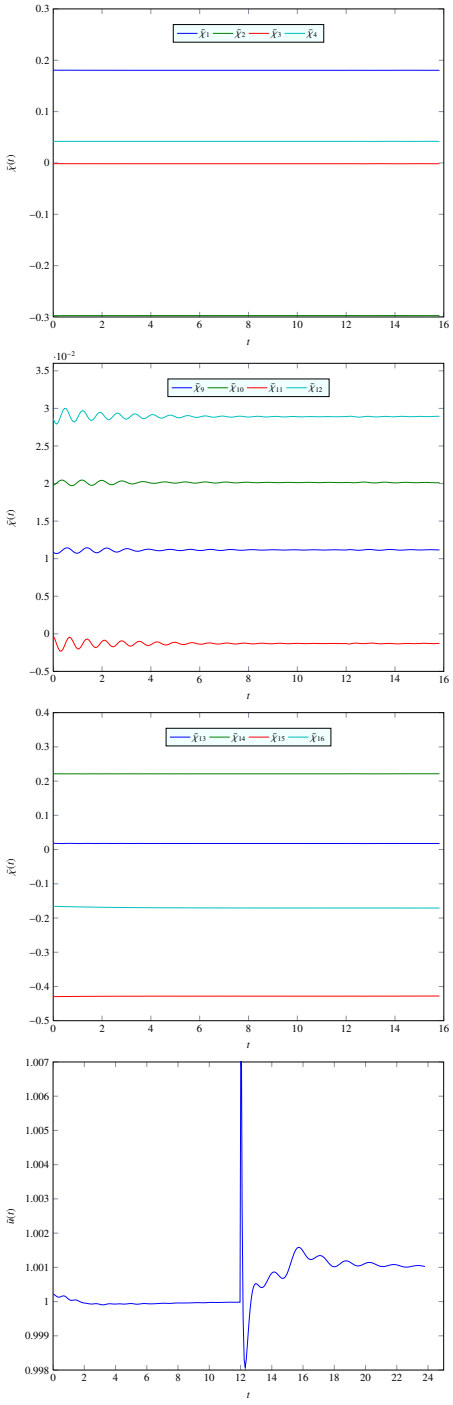

Figure 169: x-component of velocity in closed loop. Top: DNS. Bottom: ROM.

DISTRIBUTION A: Distribution approved for public release.

References

[1] S. Ahuja and C.W. Rowley. Feedback control of unstable steady states of flow past a flat plate using reduced-order estimators. *Journal of Fluid Mechanics*, 645:447–478, 2010.

[2] Luis Alvergue, Guoxiang Gu, and Sumanta Acharya. A generalized sector bound approach to feedback stabilization of nonlinear control systems. *International Journal of Robust and Nonlinear Control*, 23(14):1563–1580, 2013.

[3] M. Amitay, V. Kibens, D. Parekh, and A. Glezer. *The dynamics of flow reattachment over a thick airfoil controlled by synthetic jet actuators*. Aerospace Sciences Meetings. American Institute of Aeronautics and Astronautics, 1999. doi:10.2514/6.1999-1001.

[4] Hessam Babaee and Sumanta Acharya. A semi-staggered numerical procedure for the incompressible Navier-Stokes equations on curvilinear grids. In *ASME 2011 International Mechanical Engineering Congress and Exposition (IMECE2011)*, pages 927–936, 2011.

[5] Shervin Bagheri, Philipp Schlatter, Peter J. Schmid, and Dan S. Henningson. Global stability of a jet in crossflow. *Journal of Fluid Mechanics*, 624:33–44, 2009.

[6] Alexandre Barbagallo, Denis Sipp, and Peter J. Schmid. Closed-loop control of an open cavity flow using reduced-order models. *Journal of Fluid Mechanics*, 641:1–50, 2009.

[7] B. R. Barmish. Stabilization of uncertain systems via linear control. *IEEE Transactions on Automatic Control*, 28(8):848–850, 1983.

[8] C. M. Bell, P. M. Ligrani, W. A. Hull, and C. M. Norton. Film cooling subject to bulk flow pulsations: effects of blowing ratio, freestream velocity, and pulsation frequency. *International Journal of Heat and Mass Transfer*, 42(23):4333 – 4344, 1999.

[9] M. Bergmann, L. Cordier, and J-P. Brancher. Drag minimization of the cylinder wake by trust-region proper orthogonal decomposition. In Rudibert King, editor, *Active Flow Control*, volume 95 of *Notes on Numerical Fluid Mechanics and Multidisciplinary Design*, pages 309–324. Springer Berlin / Heidelberg, 2007.

[10] S. Bernsdorf, M. G. Rose, and R. S. Abhari. Modeling of film cooling—part i: Experimental study of flow structure. *Journal of Turbomachinery*, 128(1):141–149, 2006.

[11] Franco Blanchini. Set invariance in control. *Automatica*, 35(11):1747–1768, 1999.

[12] J. P. Bons, R. Sondergaard, and R. B. Rivir. Turbine separation control using pulsed vortex generator jets. *Journal of Turbomachinery*, 123(2):198–206, 2001.

[13] R. S. Bunker. A review of shaped hole turbine film-cooling technology. *Journal of Heat Transfer*, 127(4):441–453, 2005.

[14] John Burkardt, Max Gunzburger, and Hyung-Chun Lee. POD and CVT-based reduced-order modeling of Navier–Stokes flows. *Computer Methods Appl. Mech. Engrg.*, 196:337–355, 2006.

DISTRIBUTION A: Distribution approved for public release.

[15] W. Cazemier, R. W. C. P. Verstappen, and A. E. P. Veldman. Proper orthogonal decomposition and low-dimensional models for driven cavity flows. *Physics of Fluids*, 10(7):1685–1699, 1998.

[16] Pinaki Chakraborty, S. Balachandar, and Ronald J. Adrian. On the relationships between local vortex identification schemes. *Journal of Fluid Mechanics*, 535:189–214, 2005.

[17] Tim Colonius Clarence W. Rowley and Richard M. Murray. Model reduction for compressible flows using POD and Galerkin projection. *Physica D*, 189:115–129, 2004.

[18] Debora A Compton and James P Johnston. Streamwise vortex production by pitched and skewed jets in a turbulent boundary layer. *AIAA journal*, 30(3):640–647, 1992.

[19] Martin Corless. Robust stability analysis and controller design with quadratic Lyapunov functions. In Alan Zinober, editor, *Variable Structure and Lyapunov Control*, volume 193 of *Lecture Notes in Control and Information Sciences*, pages 181–203. Springer Berlin / Heidelberg, 1994.

[20] L. Cortelezzi and A. R. Karagozian. On the formation of the counter-rotating vortex pair in transverse jets. *Journal of Fluid Mechanics*, 446:347–373, 2001.

[21] S. M. Coulthard, R. J. Volino, and K. A. Flack. Effect of jet pulsing on film cooling-part i: Effectiveness and flow-field temperature results. *Journal of Turbomachinery*, 129(2):232–246, 2007.

[22] M. Couplet, C. Basdevant, and P. Sagaut. Calibrated reduced-order pod-galerkin system for fluid flow modelling. *Journal of Computational Physics*, 207(1):192–220, 2005.

[23] A. E. Deane, I. G. Kevrekidis, G. E. Karniadakis, and S. A. Orszag. Low dimensional models for complex geometry flows: Application to grooved channels and circular cylinders. *Physics of Fluids A*, 3(10):2337–2354, 1991.

[24] J. R. Dormand and P. J. Prince. A family of embedded runge-kutta formulae. *Journal of Computational and Applied Mathematics*, 6(1):19 – 26, 1980.

[25] S. V. Ekkad, S. Ou, and R. B. Rivir. Effect of jet pulsation and duty cycle on film cooling from a single jet on a leading edge model. *Journal of Turbomachinery*, 128(July 2006):564–571, 2006.

[26] T. F. Fric and A. Roshko. Vortical structure in the wake of a transverse jet. *Journal of Fluid Mechanics*, 279:1–47, 1994.

[27] Roberto Genesio, Michele Tartaglia, and Antonio Vicino. On the estimation of asymptotic stability regions: State of the art and new proposals. *IEEE Transactions on Automatic Control*, 30(8):747–755, 1985.

[28] S. Gopalan, B. M. Abraham, and J. Katz. The structure of a jet in cross flow at low velocity ratios. *Physics of Fluids*, 16(6):2067–2087, 2004.

DISTRIBUTION A: Distribution approved for public release.

[29] W. R. Graham, J. Peraire, and K. Y. Tang. Optimal control of vortex shedding using low-order models. part i - open-loop model development. *International Journal for Numerical Methods in Engineering*, 44(7):945–972, 1999.

[30] W. R. Graham, J. Peraire, and K. Y. Tang. Optimal control of vortex shedding using low-order models. part ii - model-based control. *International Journal for Numerical Methods in Engineering*, 44(7):973–990, 1999.

[31] X. Guo, W. Schroder, and M. Meinke. Large-eddy simulations of film cooling flows. *Computers & Fluids*, 35(6):587–606, 2006.

[32] L Hansen and J Bons. Flow measurements of vortex generator jets in separating boundary layer. *Journal of propulsion and power*, 22(3):558–566, 2006.

[33] FS Henry and H Pearcey. Numerical model of boundary-layer control using air-jet generated vortices. *AIAA journal*, 32(12):2415–2425, 1994.

[34] P. Holmes, J. L. Lumley, and G. Berkooz. *Turbulence, coherent structures, dynamical systems and symmetry*. Cambridge Univ Pr, 1998.

[35] Philip Holmes, John L. Lumley, and Gal Berkooz. *Turbulence, Coherent Structures, Dynamical Systems and Symmetry*. Cambridge University Press, 1996.

[36] M. Ilak and C. W. Rowley. Modeling of transitional channel flow using balanced proper orthogonal decomposition. *Physics of Fluids*, 20(3):034103–17, 2008.

[37] Miloš Ilak, Philipp Schlatter, Shervin Bagheri, and Dan S. Henningson. Bifurcation and stability analysis of a jet in crossflow: onset of global instability at a low velocity ratio. *Journal of Fluid Mechanics*, 696:94–121, 2012.

[38] J. Jeong and F. Hussain. On the identification of a vortex. *Journal of Fluid Mechanics*, 285:69–94, 1995.

[39] Sanjay S. Joshi, Jason L. Speyer, and John Kim. A systems theory approach to the feedback stabilization of infinitesimal and finite-amplitude disturbances in plane poiseuille flow. *Journal of Fluid Mechanics*, 332:157–184, 1997.

[40] Coşku Kasnakoğlu, Andrea Serrani, and Mehmet Önder Efe. Control input separation by actuation mode expansion for flow control problems. *International Journal of Control*, 81:1475–1492, 2008.

[41] R. M. Kelso, T. T. Lim, and A. E. Perry. An experimental study of round jets in cross-flow. *Journal of Fluid Mechanics*, 306:111–144, 1996.

[42] R. M. Kelso and A. J. Smits. Horseshoe vortex systems resulting from the interaction between a laminar boundary layer and a transverse jet. *Physics of Fluids*, 7(1):153–8, 1995.

[43] Michael Kirby. *Geometric Data Analysis: An Empirical Approach to Dimensionality Reduction and the Study of Patterns*. Wiley-Interscience, 2000.

DISTRIBUTION A: Distribution approved for public release.

[44] A. Krothapalli and L. Lourenco. Separated flow upstream of a jet in crossflow. *AIAA Journal*, 28(3):414–420, 1990.

[45] Miroslav Krstić, Ioannis Kanellakopoulos, and Petar V. Kokotović. *Nonlinear and Adaptive Control Design*. John Wiley & Sons, USA, 1995.

[46] P. S. Krueger, J. O. Dabiri, and M. Gharib. The formation number of vortex rings formed in uniform background co-flow. *Journal of Fluid Mechanics*, 556:147–166, 2006.

[47] Sang Woo Lee, Joon Sik Lee, and Sung Tack Ro. Experimental study on the flow characteristics of streamwise inclined jets in crossflow on flat plate. *Journal of turbomachinery*, 116(1):97–105, 1994.

[48] P. M. Ligrani, R. Gong, J. M. Cuthrell, and J. S. Lee. Bulk flow pulsations and film cooling - i. injectant behavior. *International Journal of Heat and Mass Transfer*, 39(11):2271–2282, 1996.

[49] P. M. Ligrani, R. Gong, J. M. Cuthrell, and J. S. Lee. Bulk flow pulsations and film cooling - ii. flow structure and film effectiveness. *International Journal of Heat and Mass Transfer*, 39(11):2283 – 2292, 1996.

[50] JC Lin, FG Howard, DM Bushnell, and GV Selby. Investigation of several passive and active methods for turbulent flow separation control. In *AIAA, Fluid Dynamics, 21st Plasma Dynamics and Lasers Conference, 21st, Seattle, WA, June 18-20, 1990. 17 p.*, volume 1, 1990.

[51] Xia Ma and George M. Karniadakis. A low-dimensional model for simulating three-dimensional cylinder flow. *Journal of Fluid Mechanics*, 458:181–190, 2002.

[52] Y. M. Marzouk and A. F. Ghoniem. Vorticity structure and evolution in a transverse jet. *Journal of Fluid Mechanics*, 575:267–305, 2007.

[53] K. T. McGovern and J. H. Leylek. A detailed analysis of film cooling physics: Part ii—compound-angle injection with cylindrical holes. *Journal of Turbomachinery*, 122(1):113–121, 2000.

[54] Keith R McManus, Hartmut H Legner, and Steven J Davis. Pulsed vortex generator jets for active control of flow separation. *AIAA paper*, (94-2218):5, 1994.

[55] D. E. Nikitopoulos, S. Acharya, J. Oertling, and F. H. Muldoon. On active control of film-cooling flows. In *ASME Turbo Expo*, 2006.

[56] D. E. Nikitopoulos and J. T. C. Liu. Nonlinear binary-mode interactions in a developing mixing layer. *Journal of Fluid Mechanics*, 179(1):345–370, 1987.

[57] D. E. Nikitopoulos and J. T. C. Liu. Nonlinear three-mode interactions in a developing mixing layer. *Physics of Fluids*, 13:966, 2001.

[58] B. R. Noack, P. Papas, and P. A. Monkewitz. The need for a pressure-term representation in empirical galerkin models of incompressible shear flows. *Journal of Fluid Mechanics*, 523:339–365, 2005.

DISTRIBUTION A: Distribution approved for public release.

[59] Bernd R. Noack, Gilead Tadmor, and Marek Morzyński. Actuation models and dissipative control in empirical galerkin models of fluid flows. In *2004 American Control Conference*, pages 5722–5727, 2004.

[60] Bernd R. Noack, Gilead Tadmor, and Marek Morzyński. Low-dimensional models for feedback flow control. part I: Empirical galerkin models. In *2nd AIAA Flow Control Conference*, 2004.

[61] M. Raffel, C. E. Willert, and J. Kompenhans. *Particle image velocimetry: a practical guide*. Springer Verlag, 1998.

[62] S. Raghunathan, J. Watterson, R. Cooper, and S. Lee. *Short wide angle diffuser with pulse jet control*. Aerospace Sciences Meetings. American Institute of Aeronautics and Astronautics, 1999. doi:10.2514/6.1999-280.

[63] S. S. Ravindran. Reduced-order adaptive controllers for fluid flows using pod. *Journal of Scientific Computing*, 15(4):457–478, 2000.

[64] S.S. Ravindran. Optimal boundary feedback flow stabilization by model reduction. *Computer Methods Appl. Mech. Engrg.*, 196:2555–2569, 2007.

[65] C. W. Rowley. Model reduction for fluids, using balanced proper orthogonal decomposition. *International Journal of Bifurcation Chaos in Applied Sciences and Engineering*, 15(3):997–1014, 2005.

[66] Clarence Rowley. *Modeling, Simulation, and Control of Cavity Flow Oscillations*. PhD thesis, California Institute of Technology, 2002.

[67] R. Sau and K. Mahesh. Dynamics and mixing of vortex rings in crossflow. *Journal of Fluid Mechanics*, 604:389–409, 2008.

[68] Onofrio Semeraro, Servin Bagheri, Luca Brandt, and Dan S. Henningson. Feedback control of three-dimensional optimal disturbances using reduced-order models. *Journal of Fluid Mechanics*, 677:63–102, 2011.

[69] L. F. Shampine and M. K. Gordon. *Computer solution of ordinary differential equations : the initial value problem*. San Francisco : W. H. Freeman, 1975. Includes index.

[70] Lawrence Sirovich. Turbulence and the dynamics of coherent structures part i: Coherent structures. *Quarterly of Applied Mathematics*, 45(3):561–571, 1987.

[71] M. Thompson, K. Hourigan, and J. Sheridan. Three-dimensional instabilities in the wake of a circular cylinder. *Experimental Thermal and Fluid Science*, 12(2):190–196, 1996.

[72] M. Tyagi and S. Acharya. Large eddy simulation of film cooling flow from an inclined cylindrical jet. *Journal of Turbomachinery*, 125(4):734–742, 2003.

[73] R. Vernet, L. Thomas, and L. David. Analysis and reconstruction of a pulsed jet in crossflow by multi-plane snapshot pod. *Experiments in Fluids*, 47:707–720, 2009. 10.1007/s00348-009-0730-6.

DISTRIBUTION A: Distribution approved for public release.

[74] C. Vezier. Dynamics of vortical structures in a low-blowing-ratio pulsed transverse jet. Master's thesis, Louisiana State University, 2009.

[75] C. H. K. Williamson. Vortex dynamics in the cylinder wake. *Annual Review of Fluid Mechanics*, 28(1):477–539, 1996.

[76] K. M. Womack, R. J. Volino, and M. P. Schultz. Combined effects of wakes and jet pulsing on film cooling. *Journal of Turbomachinery*, 130(4):041010–12, 2008.

[77] K. M. Womack, R. J. Volino, and M. P. Schultz. Measurements in film cooling flows with periodic wakes. *Journal of Turbomachinery*, 130(4):041008, 2008.

[78] Jie-Zhi Wu, Xi-Yun Lu, Andrew G Denny, Meng Fan, and Jain-Ming Wu. Post-stall flow control on an airfoil by local unsteady forcing. *Journal of Fluid Mechanics*, 371(1):21–58, 1998.

[79] C. H. N. Yuen and R. F. Martinez-Botas. Film cooling characteristics of a single round hole at various streamwise angles in a crossflow: Part i effectiveness. *International Journal of Heat and Mass Transfer*, 46(2):221 – 235, 2003.

DISTRIBUTION A: Distribution approved for public release.

AFOSR Final Performance Report

DISTRIBUTION A: Distribution approved for public release.

Project Title:	Towards Combined Active Control of Film Cooling and Turbine Blade Aerodynamics.
Award Number:	FA9550-08-1-0440
Dates Covered:	8/15/2008 - 8/14/2013
Program Manager:	Dr. Douglas Smith
Principal Investigator:	Dimitris E. Nikitopoulos Mechanical Engineering Department Louisiana State University Baton Rouge, Louisiana 70803 Tel: (225)-578-5903, email : medimi@lsu.edu
Co-Investigators:	Shengmin Guo, Guoxiang Gu, and Sumanta Acharya Mechanical Engineering Department Louisiana State University Baton Rouge, Louisiana 70803

Abstract:

In this study, actively controlled film cooling flows were investigated in view of improved film cooling metrics and increased adaptability. In the first place a mechanistic analysis was carried out on unforced and forced film cooling geometries of a vertical and an inclined jet in cross-flow, evidencing characteristic vortical systems and scaling parameters for those systems. A cutting edge linear cascade facility including a realistic wake generator was designed, fabricated and validated. PIV measurements and Mie scattering visualizations evidenced the effect of the wake on film cooling jets as it impinged the blade. The first Reduced Order Models (ROMs) of unforced and forced film cooling jets velocity and temperature fields were derived using the POD-Galerkin projection method. ROM stabilization techniques were developed and implemented to improve the models stability and accuracy. An optimization method using Direct Numerical Simulations was developed to identify optimum forcing parameters for improved film cooling metrics. Finally, a linear state feedback controller for stabilization of a POD-based ROM of film cooling system was developed and implemented. The designed controller was able to stabilize the flow to the selected operating point in DNS for a short time period until the DNS solution diverged to another operating condition.

DISTRIBUTION A: Distribution approved for public release.

DISTRIBUTION A: Distribution approved for public release.

REPORT DOCUMENTATION PAGE

Form Approved
OMB No. 0704-0188

The public reporting burden for this collection of information is estimated to average 1 hour per response, including the time for reviewing instructions, searching existing data sources, gathering and maintaining the data needed, and completing and reviewing the collection of information. Send comments regarding this burden estimate or any other aspect of this collection of information, including suggestions for reducing the burden, to the Department of Defense, Executive Service Directorate (0704-0188). Respondents should be aware that notwithstanding any other provision of law, no person shall be subject to any penalty for failing to comply with a collection of information if it does not display a currently valid OMB control number.

PLEASE DO NOT RETURN YOUR FORM TO THE ABOVE ORGANIZATION.

1. REPORT DATE *(DD-MM-YYYY)*	2. REPORT TYPE	3. DATES COVERED *(From - To)*
11/14/2013	Final	8/15/2008-8/14/2013

4. TITLE AND SUBTITLE
TOWARDS COMBINED ACTIVE CONTROL OF FILM COOLING AND TURBINE BLADE AERODYNAMICS

5a. CONTRACT NUMBER
FA9550-08-1-0440

5b. GRANT NUMBER
N/A

5c. PROGRAM ELEMENT NUMBER
N/A

6. AUTHOR(S)
Dimitris E. Nikitopoulos,
Guoxiang Gu,
Shengmin Guo,
Guillaume Bidan

5d. PROJECT NUMBER
N/A

5e. TASK NUMBER
N/A

5f. WORK UNIT NUMBER
N/A

7. PERFORMING ORGANIZATION NAME(S) AND ADDRESS(ES)
Louisiana State University System,
3810 W Lakeshore Drive, Room 107, System Bldg,
Baton Rouge, LA 70808

8. PERFORMING ORGANIZATION REPORT NUMBER
N/A

9. SPONSORING/MONITORING AGENCY NAME(S) AND ADDRESS(ES)
Air Force Office of Science and Research / JA
875 Randolph Street
Suite 325 Room 3112
Arlington, VA 22203

10. SPONSOR/MONITOR'S ACRONYM(S)
AFOSR / JA

11. SPONSOR/MONITOR'S REPORT NUMBER(S)

12. DISTRIBUTION/AVAILABILITY STATEMENT
Please withhold the distribution of this Final Report for 1 year, to allow for complete publication of the discussed results in peer-reviewed journal publications. After this period of time, Distribution A.

13. SUPPLEMENTARY NOTES

14. ABSTRACT
In this study, actively controlled film cooling flows were investigated in view of improved film cooling metrics and increased adaptability. In the first place a mechanistic analysis was carried out on unforced and forced film cooling geometries of a vertical and an inclined jet in cross-flow, evidencing characteristic vortical systems and scaling parameters for those systems. A cutting edge linear cascade facility including a realistic wake generator was designed, fabricated and validated. PIV measurements and Mie scattering visualizations evidenced the effect of the wake on film cooling jets as it impinged the blade. The first Reduced Order Models (ROMs) of unforced and forced film cooling jets velocity and temperature fields were derived using the POD-Galerkin projection method. ROM stabilization techniques were developed and implemented to improve the models stability and accuracy. An optimization method using Direct Numerical Simulations was developed to identify optimum forcing parameters for improved film cooling metrics. Finally, a linear state feedback controller for stabilization of a POD-based ROM of film cooling system was developed and implemented. The designed controller was able to stabilize the flow to the selected operating point in DNS for a short time period.

15. SUBJECT TERMS

16. SECURITY CLASSIFICATION OF:			17. LIMITATION OF ABSTRACT	18. NUMBER OF PAGES	19a. NAME OF RESPONSIBLE PERSON
a. REPORT	b. ABSTRACT	c. THIS PAGE			19b. TELEPHONE NUMBER *(Include area code)*

DISTRIBUTION A: Distribution approved for public release.

Contents

I Project Description **8**

1 Personnel **9**

2 Publications **9**
2.1 Theses and Dissertations 9
2.2 Archival Publications 10
2.2.1 Peer Reviewed Journal Publications: 10
2.2.2 Conference Proceedings 10

3 Motivations **11**

4 Initial Objectives **15**

5 Changes in research objectives **17**

6 Accomplishments/Findings **18**

II Mechanistic Analysis **21**

1 Vertical Jet in Cross-flow **22**
1.1 Experimental and Numerical Setup 22
1.1.1 Wind Tunnel Experiments 22
1.1.2 Numerical Simulations 23
1.2 Results 25
1.2.1 Unforced Jet 25
1.2.2 Forced Jet 33

2 Inclined Jet in Cross-flow **44**
2.1 Experimental and Numerical Setup 44
2.1.1 Wind Tunnel Experiments 44
2.1.2 Numerical Simulations 45
2.1.2.1 Mechanistic Analysis Grid 45
2.1.2.2 Reduced Order Modeling Grid 47
2.1.2.3 Inlet Conditions Grid 49
2.2 Unforced Jet 50
2.3 Forced Jet 55
2.3.1 Low-to-High Blowing Ratio Transition: Starting Vortices 57

DISTRIBUTION A: Distribution approved for public release.

3 Cascade Wind Tunnel **68**
3.1 Experimental Setup Design . . . 68
3.1.1 Wind tunnel design . . . 68
3.1.2 Test section design . . . 70
3.1.3 Wake generator design . . . 73
3.1.4 Additional equipment . . . 74
3.2 Linear Cascade Characterization without Wake Generator . . . 76
3.2.1 Pressure Distribution along the Wind Tunnel . . . 77
3.2.2 Test Section Velocity Distribution . . . 77
3.2.3 Test Section Spectral Content . . . 80
3.2.4 Pressure Profiles . . . 81
3.3 Linear Cascade Characterization with Wake Generator . . . 83
3.3.1 Test Section Velocity Distribution . . . 83
3.3.2 Test Section Spectral Content . . . 87
3.3.3 Pressure Measurements . . . 89
3.4 Particle Image Velocimetry and Mie scattering visualizations . . . 92

III Optimization, Reduced Order Modeling and Flow Control 99

1 Optimization of Forced Film Cooling Jets **100**
1.1 Methodology . . . 100
1.1.1 Optimization Problem . . . 101
1.2 Simulation details . . . 102
1.2.1 Computational Mesh . . . 102
1.3 Results and Discussion . . . 104
1.3.1 Effect of pulsation on film cooling performance . . . 104
1.3.2 Optimal and sub-optimal behavior . . . 106
1.3.3 Film cooling response surface . . . 113
1.4 Conclusions . . . 113

2 Canonical Systems Reduced Order Models **116**
2.1 POD-Galerkin Method . . . 116
2.2 Two-dimensional Two-sided Lid Driven Cavity . . . 117
2.2.1 Numerical Setup . . . 118
2.2.2 Base Flow . . . 118
2.2.3 Proper Orthogonal Decomposition . . . 120
2.2.4 Reduced Order Model . . . 122
2.3 Two-dimensional Cylinder in a Cross-flow . . . 124
2.3.1 Numerical Setup . . . 124
2.3.2 Base Flow . . . 125
2.3.3 Proper Orthogonal Decomposition . . . 126
2.3.4 Reduced Order Model . . . 129

DISTRIBUTION A: Distribution approved for public release.

3 Film Cooling Jets Reduced Order Models **132**
3.1 Preliminary Statistical POD Analysis of Film Cooling Jets 132
3.1.1 Unforced Jets 132
3.1.2 Forced Jets 139
3.2 Reduced Order Models 153
3.2.1 Stabilization Methods 153
3.2.2 Unforced Jets 155
3.2.2.1 Attached Regime 155
3.2.2.2 Transitional Regime 162
3.2.3 Forced Jets 170
3.2.3.1 Instantaneous Flow 170
3.2.3.1.1 Reduced Order Models 172
3.2.3.2 Phase Averaged Flow 179
3.2.3.2.1 Reduced Order Models 179
3.3 Conclusion 185

4 Flow Control **189**
4.1 Jet in Cross-flow Modeling 189
4.1.1 Numerical Method 190
4.1.2 Reduced Order Model Based on POD/Galerkin Projection 190
4.2 Feedback Control 193
4.2.1 Problem Statement 193
4.2.2 Controller Design 193
4.3 Results 196
4.3.1 Open Loop Dynamics 196
4.3.2 Closed Loop Dynamics 200
4.4 Conclusion 204

References **206**

DISTRIBUTION A: Distribution approved for public release.

Part I
Project Description

DISTRIBUTION A: Distribution approved for public release.

1 Personnel

Professors

- Dimitris, E., Nikitopoulos
- Guoxiang Guo
- Sumanta Acharya
- Guoxiang Gu

Graduate Students

- Clementine Vezier - M.Sc. (2009)
- Lemuel, A., Wells - M.Sc. (left before completing degree)
- Jean Philippe Junca-Laplace - M.Sc. (2011)
- Jason, W., Bitting - Ph.D. (expected 2015)
- Christopher, Foreman - M.Sc. (2012)
- Shiloh, M., Meyers - M.Sc. (expected 2014)
- Luis, D., Alvergue PhD (2012)
- Guillaume, F., Bidan - Ph.D. (2013)
- Hessam, Babbae - Ph.D. (2013)

2 Publications

2.1 Theses and Dissertations

All thesis and dissertations are available online at *etd.lsu.edu*

- C. Vezier, "Dynamics of Vortical Structures in a Low-Blowing-Ratio Pulsed Transverse Jet", M.Sc. Thesis, Louisiana State University, 2009.
- J.-P. Junca-Laplace, Design, Fabrication, and Characterization of a New Wind Tunnel Facility - Linear Cascade with a Wake Simulator", M.Sc. Thesis, Louisiana State University, 2011.
- L., D., Alvergue, "Feedback Control of Sector-Bound Nonlinear Systems with Applications to Aeroengine Control", Ph.D. Dissertation, 2012.
- C. Foreman, "Characterization and Verification of a Closed Loop Wind Tunnel with a Linear Cascade and Upstream Wake Generator", M.Sc. Thesis, Louisiana State University, 2013.

DISTRIBUTION A: Distribution approved for public release.

- G., F., Bidan, "Mechanistic Analysis and Reduced Order Modeling of Forced Film Cooling Jets", Ph.D. Dissertation, Louisiana State University, 2013.

- H. Babaee, "Analysis and Optimization of Film Cooling Effectiveness ", Ph.D. Dissertation, Louisiana State University, 2013.

2.2 Archival Publications

2.2.1 Peer Reviewed Journal Publications:

- Guillaume Bidan and Dimitris E. Nikitopoulos, "Fundamental Study of Modulated Transverse Jets from a Film-Cooling Perspective", AIAA Journal, Vol. 49, No. 7 (2011), pp. 1498-1510, doi: 10.2514/1.J050903.

- Alvergue, Luis, Guoxiang Gu, and Sumanta Acharya, "A generalized sector-bound approach to feedback stabilization of nonlinear control systems", International Journal of Robust and Nonlinear Control (2012), Vol. 23, No. 14, pp.1563-1580, doi: 10.1002/rnc.2843.

- Guillaume Bidan, Clémentine Vézier and Dimitris E. Nikitopoulos, "Study of unforced and modulated film-cooling jets using proper orthogonal decomposition–part I: unforced jets", Journal of Turbomachinery, Vol. 135, No. 2 (2013), pp. 021037, doi: 10.1115/1.4006599.

- Guillaume Bidan, Clémentine Vézier and Dimitris E. Nikitopoulos, "Study of unforced and modulated film-cooling jets using proper orthogonal decomposition–part II: forced jets", Journal of Turbomachinery, Vol. 135, No. 2 (2013), pp. 021038, doi: 10.1115/1.4006600.

- Guillaume Bidan and Dimitris E. Nikitopoulos, "On steady and pulsed low-blowing ratio transverse jets", Journal of Fluid Mechanics, Vol. 714 (2013), pp. 393-433, doi: i:10.1017/jfm.2012.482.

- Luis Alvergue, Guoxiang Gu, and Sumanta Acharya, "A Generalized Sector Bound Approach to Feedback Stabilization of Nonlinear Control Systems", International Journal of Robust and Nonlinear Control, Vol. 23, No. 14 (2013), pp. 1563-1580.

2.2.2 Conference Proceedings

- Guillaume Bidan, Pierre-Emmanuel Bouladoux, Jeremiah E. Oertling, Dimitris E. Nikitopoulos, "Experimental and Numerical Study of Steady and Modulated Transverse Jets at Low Blowing Ratios", ASME Turbo Expo 2010, June 14th–18th 2010, Glasgow, UK, GT2010-23013, pp. 2525-2535, doi: 10.1115/GT2010-23013.

- Luis Alvergue, Guoxiang Gu, and Sumanta Acharya, "A Novel Feedback Controller for Reduced Order Fluid Flow Models", 30th Chinese Control Conference (CCC), July 22nd-24th 2011, Yantai, China, pages 711-716. 2

DISTRIBUTION A: Distribution approved for public release.

- Hessam Babaee and Sumanta Acharya, "A semi-staggered numerical procedure for the incompressible Navier-Stokes equations on curvilinear grids", ASME 2011 International Mechanical Engineering Congress and Exposition (IMECE2011), pp. 927-936.

- Guillaume Bidan, Clémentine Vézier and Dimitris E. Nikitopoulos, "Study of Unforced and Modulated Inclined Film-Cooling Jets Using Proper Orthogonal Decomposition: Part I-Unforced Jets", ASME Turbo Expo 2011, June 6th-10th 2011, Vancouver, British Columbia, Canada, GT2011-45400, pp. 1517-1528, doi: 10.1115/GT2011-45400.

- Guillaume Bidan, Clémentine Vézier and Dimitris E. Nikitopoulos, "Study of Unforced and Modulated Inclined Film-Cooling Jets Using Proper Orthogonal Decomposition: Part II-Forced Jets", ASME Turbo Expo 2011, June 6th-10th 2011, Vancouver, British Columbia, Canada, GT2011-46901, pp. 1809-1822, doi: 10.1115/GT2011-46901.

- Alvergue, Luis, and Guoxiang Gu., "Feedback Control for Quadratic Nonlinear Systems", 24th Chinese Control and Decision Conference (CCDC), May 23rd-25th 2012, Taiyuan, China, pp. 2566- 2571.

- Hessam Babaee and Sumanta Acharya, "A Symmetric Finite Difference Discretization of Pressure-Poisson Equation on Curvilinear Grids", 42nd AIAA Fluid Dynamics Conference and Exhibit, June 25th-28th 2012, New Orleans, Louisiana.

- Luis D. Alvergue, Guoxiang Gu, and Sumanta Acharya, "A Generalized Sector Bound Approach to Feedback Stabilization of Nonlinear Control Systems", 2012 American Control Conference, June 27th-29th 2012, Montreal, Canada, pp. 2583-2588.

- Guillaume Bidan, Dimitris E. Nikitopoulos, "Film-Cooling Jets Analyzed with Proper Orthogonal Decomposition and Dynamic Mode Decomposition", AIAA 43rd Fluid Dynamics Conference and Exhibits, June 24th-27th 2013, San Diego, California, doi: 10.2514/6.2013-2970.

3 Motivations

Film cooling systems remain a critical component in jet engines both in terms of reliability and performance. The considerable and diverse benefits of an actively controlled film-cooling system on an intelligent power producing engine are summarized in the chart below (figure 1 - modified from (55)).

Apart from the obvious benefits from increases in Turbine Inlet Temperature (T41) and possible reduction of net coolant flow rates, an actively controlled thermal management system can lead to power producers that are more flexible in accommodating a broader range of fuels (with varying heating values and properties) without adverse effects on performance, serviceability and lifetime. This is becoming of increased importance as various fuels are entering the mainstream in power production; e.g. shale gas, LNG and synthetic gases from gasification of coal and a variety of bio-fuels such as bagasse and other biomasses. Controlling the temperature of gas-turbine components to within limits acceptable for their health, irrespectively of the fuel feed-stock, is feasible though an actively controlled cooling

DISTRIBUTION A: Distribution approved for public release.

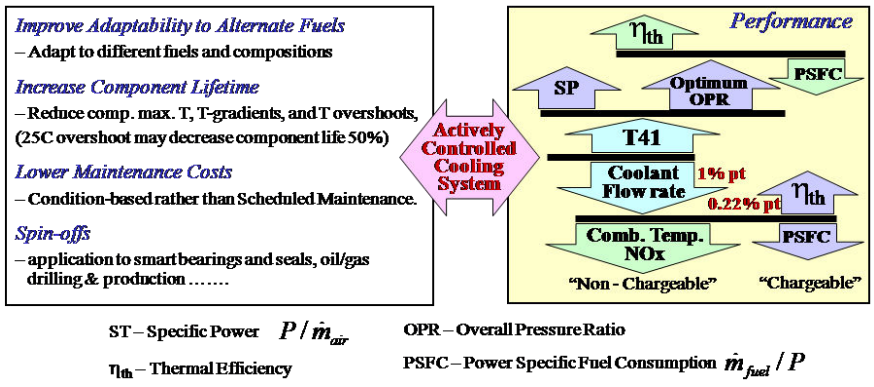

Figure 1: Benefits summary of Actively Controlled Cooling System.

system and very important (an overshoot of as little as 2% of blade critical temperature can lead to a decrease in the part lifetime of as much as 50%).

Film cooling systems involve arrays of continuously blowing jets located on the surface of the part to be cooled and supplied with cooler air diverted from the compressor through internal cooling channels. More 'intelligent' and adaptable systems could lead to a decrease in the overall amount of coolant necessary to operate and yield overall lower emissions and/or higher performance while maintaining system reliability. Although methods to improve film cooling systems through jet hole geometry optimization have been implemented (13), those systems remain passive in nature and lack adaptability to local or global changes in operating conditions. Investigations of the effects of cross-flow unsteadiness, for instance encountered by systems located beyond the turbine first stage, showed that bulk cross-flow pulsations can have a catastrophic effect on cooling performance due to passive jet pulsation (8, 48, 49, 77). Actively controlled film cooling systems using pulsed jets for instance, could provide adaptable jet exit conditions while mitigating the detrimental effects of cross-flow unsteadiness.

The four fundamental vortical structures involved in unforced jet cross-flow configuration have been previously established by (26, 41): the shear layer vortices (Slv), counter rotating vortex pair ($CRVP$), horseshoe vortex (Hv) and wake vortices (Wv) (figure 2). The shear layer vortices are near-field structures, generally considered to be the result of Kelvin-Helmholtz type instability of the jet cylindrical shear layer. The CRVP is the dominant mixing structure in transverse jets and has been the topic of many studies concerned with mixing enhancement or prevention. Formed downstream of the jet exit and dominating the far field, the CRVP consists of a pair of quasi-streamwise counter-rotating vortices. The horseshoe vortex constitutes the third characteristic vortical structure of transverse jets and is the result of cross-flow boundary layer separation upstream of the jet exit previously studied by (42, 44). Finally, the wake vortices are, according to (26), tornado like quasi-vertical vortices, located below the jet core and originating from cross-flow boundary layer separation due to the adverse pressure gradient past the jet column. Numerous studies have dealt with the characterizations of general quantities such as jet penetration, spread, mixing rate, and have identified the jet-to-cross-flow mass-flux ratio (blowing ratio BR) and the jet-to-cross-flow momentum ratio as two of the principal scaled parameters for transverse jets. Since mixing enhancement and VSTOL propulsion have been the main concern in the

DISTRIBUTION A: Distribution approved for public release.

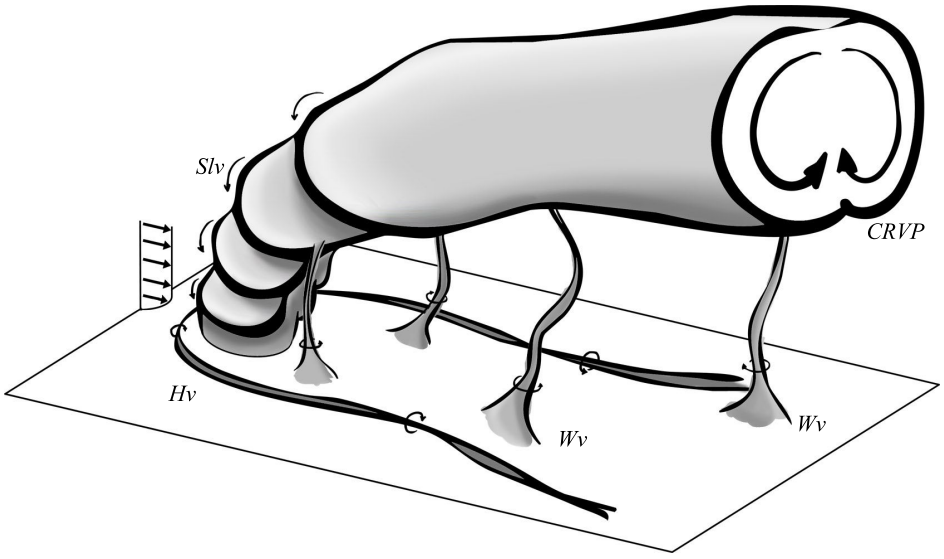

Figure 2: Jet in cross-flow dominant vortical structures

past, most of the studies have been focusing on rather high blowing ratio, vertical jets while only few studies have considered blowing ratios less than 1.0, or inclined jets.

A substantial amount of research has been devoted so far to the control and suppression of boundary-layer separation under conditions prevailing in low-pressure turbine (LPT) airfoils. Vortex generator jets (VGJ) were initially demonstrated to have a significant effect on reducing separation by (50) and have configurations very similar to those used for film-cooling jets according to (3). Both experimental and computational studies from (18) and (33) indicate that this single vortex is very effective in bringing higher-momentum free-stream fluid close to the wall. This adds the kinetic energy necessary for the flow to overcome friction and the adverse pressure gradient near the wall, and thus delay or suppress separation. This mechanism has also been demonstrated computationally with large vortices generated by pulsed normal jets as agents of the momentum transfer from the free stream to the wall region in (78). Jet injection combined with pulsing has been used to suppress separation of wall-bounded flows for several applications. Separation control through the use of pulsed injection through non-zero compound angled VGJs has been successfully realized by several studies (see (54)) including applications to diffusers in (62) and to LPT blade separation control in (12, 32). For the latter case of the LPT application detailed investigations have been conducted on the effect of jet pulsing frequency by (3) indicating that the highest effectiveness in separation control was achieved at low frequencies (relative to the characteristic separated flow frequencies) because of the relatively long relaxation time of the boundary layer as it resumes its separated state. This low-frequency effectiveness together with observations from (47), and analysis of (55), pointing towards a low-frequency envelope for improved film-cooling, provide substantial motivation to investigate the possibility of combined film-cooling and separation control. It also indicates that should the film-cooling system be used for separation control on the HPT airfoils it is likely that the control action is not going to compromise the film-cooling performance. Both of these issues are subjects of the proposed investigation.

DISTRIBUTION A: Distribution approved for public release.

Previous studies by (25, 21) on forced film cooling jets in steady cross-flow environment gave mixed results with both improved and degraded performance over comparable steady state jets. Comparable systems coupled with a spoked wheel wake generator were also studied by (76), in an attempt at counter-balancing large scale cross-flow perturbations and lead to the conclusion that forced jets did not provide amelioration of the film cooling performance. Given the overwhelming number of actuation parameters available (high blowing ratio - BR_h, low blowing ratio - BR_l, forcing frequency - f_f, duty cycle - DC, phase difference - φ ... to name a few) and the highly non-linear character of forced film cooling flows, it appears almost impossible to identify optimum forcing conditions through linear test matrices. This suggests that improved film cooling metrics can only be achieved through 'smarter', self-tuning systems with closed loop control.

Such systems necessitate flow governing equations and/or models in order to operate. Although advances in computational fluid dynamics have led to significant improvement in the results accuracy through large eddy simulations (LES) and direct numerical simulations (DNS), such models require considerable computing power to simulate only a small fraction of time. More reasonable reduced order models (ROM) of the flow are therefore preferable in order to be implemented in closed loop, time-resolved actuation systems. Such ROM-based controlled systems have been successfully implemented for flow systems in (63, 66, 9, 29, 30), to name a few, leading to improved desired metrics. Reduced order modeling is generally achieved in two steps, consisting of first extracting a spatially dependent orthogonal set from experimental data, and then using a subset in a Galerkin projection method onto the Navier-Stokes and energy equations to obtain a set of governing non-linear first order differential equations, providing approximations of the flow and temperature fields.Although the method is well established and successful in two-dimensional low Reynolds number flows, it has been found to often lead to models with low accuracy or even fail in complex three-dimensional systems (22, 65). Indeed, such systems often involve multiple length and energy scales which can create some difficulties when the turbulent interactions are not always captured by the POD-Galerkin method. In the literature there are many works concerned with stabilizing a perturbation of a flow to an equilibrium point using the ROM methodology. For example, (1) studies the linearized dynamics of flow past a flat plate and the stabilization of unstable steady states via balanced Proper Orthogonal Decomposition (POD) ROMs. The application is to regulate vortices in separated flows behind low aspect-ratio wings. Investigating the growth of Tollmien-Schlichting waves in the linearized Navier-Stokes equation, and their attenuation to a steady state using feedback control is considered in (68). In (6), a feedback controller is designed to stabilize a linearized open cavity flow to a steady flow. Global modes, POD, and balanced POD modes are used as expansion bases for the ROM and their performance is compared. The article (64) considers feedback stabilization of flow past an airfoil by a POD/Galerkin ROM. The feedback controller stabilizes the ROM solution but it stops short of implementing the controller in the full order model. With respect to the jet in cross-flow, in (37) the transition from steady to unsteady flow of a jet in cross-flow is analyzed. It applies the tools of linear stability analysis to characterize the critical value of blowing ratio that destabilizes the flow from an equilibrium point.

A common practice for controller design is to linearize the dynamics about a steady state solution (also called an operating point) and apply linear controller design methods. There are many investigations which follow this line of research and they have shown to be effective (39, 1, 64, 40), however the resultant feedback stability is only a local property that may not be applicable to solving practical flow control problems. The main limitation is the lack

DISTRIBUTION A: Distribution approved for public release.

of a characterization of the region of attraction (RoA), which roughly speaking is the set of initial conditions for which the closed loop system is stable. The RoA is an invariant set that is typically difficult to represent and much effort has been devoted to methods for estimating the RoA (11, 27).

In view of the past studies on forced film cooling systems, the identification of ideal forcing parameters to obtain increased film cooling performance using results from a predetermined test matrix appears as a challenging if not impossible task, particularly when considering the rather poor knowledge of the fluidics associated with forced film cooling flows. Active control of the film cooling jets subjected to a closed loop controller appears as a viable solution to converge towards optimum forcing conditions in steady but particularly unsteady cross-flow environment. It was established previously that integration of the complete Navier-Stokes equations is neither desirable, nor feasible, when considering the design of a controller-based system. Thus, one of the key steps in the implementation of a close-loop controlled system resides in the derivation of low order equations representative of the flow of interest, here in particular film cooling flows. The final step is the design of a close loop feedback control strategy, adapted to film cooling metrics.

4 Initial Objectives

The general objectives of the proposed research were to: (A) investigate the physics of the interaction between pulsed film-cooling flow and the downstream separation-prone flow-field on the suction side of gas-turbine blades, (B) examine the possibility of achieving combined improvement of film-cooling and separation suppression, under unsteady upstream conditions (e.g. caused by rotor wake passage), (C) develop and implement an active feedback-control system and algorithm(s) to this effect and assess their performance, (D) lay the foundations for future implementation of active control of the flows of interest using distributed sensing and actuation. These objectives were to be achieved through the combination of an experimental investigation, numerical simulations, and a parallel theoretical effort geared towards development of reduced-order models (ROMs) of the physical processes and appropriate feedback-control algorithms. The experimental effort was to consist of cold-flow studies performed on a scaled-up cascade with realistic vanes and film-cooling geometry, including a wake-passage unsteadiness simulator device and a film-cooling-flow pulsing system. The tasks of this phase were to:

1. Address general objectives A and B above, using an array of pulsed film-cooling jets located on the vane suction surface near the shower-head region. The pulsing control parameters (frequency, amplitude, duty cycle, phase) were to be selected considering the characteristics of the wake-passage unsteadiness characteristics and on the basis of current and past research on the independent improvement of film-cooling and separation suppression.

2. Address general objective B above in determining the existence of pulsing control parameters for which the film-cooling flow (e.g. in terms of limiting lift-off and maintaining film coverage) and separation prevention are optimized. This task of the experimental investigation was to be closely tied to the simulation and feedback controller development tasks.

DISTRIBUTION A: Distribution approved for public release.

3. Contribute to the development of ROMs for the relevant flow-field from velocity-field data in support of general objective C. This task was also to be intimately tied to the feedback controller task, because control actions in general influence the ROM, necessitating the understanding of this interaction

4. Provide experimental data needed to set realistic boundary conditions for the numerical simulations and the validation of simulation results.

5. Implement, validate and assess the feedback control scheme/algorithm on the physical experiment in support of general objectives B and C.

The theoretical control work had the following tasks:

1. Develop a feedback flow-control algorithm utilizing ROMs emanating from corresponding tasks of the experimental and numerical efforts. Part of this task was also to be directed to the development of the ROMs themselves.

2. Support the implementation of this algorithm on the physical as well as on the numerical experiments and assess its performance.

The numerical effort was to employ DNS and/or LES of the flow of interest including heat transfer and will be tightly integrated with the experimental and theoretical ones. Its tasks were to:

1. Address general objectives A and B above, by conducting numerical simulations of flow and heat-transfer for the geometry and conditions of the physical experiments. This task was also to contribute to the understanding of the coupling between flow and heat transfer in the film-cooling region.

2. Implement and assess the feedback control scheme/algorithm through numerical simulation experiments and provide guidance for the physical experiments and the theoretical control effort, in support of general objectives B and C.

3. Address general objective B in searching for the existence of pulsing control parameters for which film-cooling performance and separation prevention are mutually optimized.

4. Investigate in detail the influence of control actions on the ROMs and contribute to their development from simulation data in support of general objective C.

The experimental and numerical efforts were to be conducted in a mutually complementary fashion, as reflected by the commonality of scope in their respective tasks. The technical results obtained though the proposed combined effort were to provide the knowledge and experience base for future implementation of control of these flows in the hot gas path employing local rather than global actuation coupled with local sensing, as per the longest term general objective D.

DISTRIBUTION A: Distribution approved for public release.

5 Changes in research objectives

The experimental work has been delayed by a period of approximately 20 months starting shortly after the beginning of the grant. There are two major reasons for the delay. First, a leak on the roof of the wind-tunnel laboratory building caused by a tree fall during hurricane Gustav (9/2008) destroyed the pulsed laser used for visualizations and PIV and caused the warping of the wind-tunnel screen and contraction sections, which resulted in unacceptably poor flow quality for experiments. The second cause for this delay was the subsequent renovation of the building in which the Wind-Tunnel is located, and in which the cascade facility for this project would be located. The construction shut down operations from 1/2009-7/2010. These problems and delays were documented in the annual reports for the project as they occurred. During this period no experiments could be conducted, and indeed they did not start in earnest until 9/2010 after the laboratory was cleaned and the equipment reconnected and tested.

1. Heat transfer measurements on the cascade facility were not possible and were not carried out;

2. A new cascade facility was designed and built in view of an existing one not being adequate for the purpose and not being serviceable. The latter was dismantled and rendered not operational because of it being transferred to another building. Furthermore, the wake generator of this facility did not meet the desired requirements. This in addition to the aforementioned delays resulting from the damages caused by hurricane Gustav and construction work, significantly affected the progress of experimental measurements on realistic film cooling systems. For these reasons, investigations on interactions between film cooling jets and flow separation region were not possible, and focus was kept on investigation of forced film cooling physics, their optimization and reduced order modeling.

3. The fundamental scope of work was substantially expanded in order to meet the challenges of developing 3D reduced order models for the complex film-cooling flows addressed by the project. This was deemed necessary in order to lay the groundwork towards the combined active control of film cooling flows and turbine blade aerodynamics.

Based on these considerations, the initial objectives were changed to:

- Experimental investigations:

    1. To perform a fundamental mechanistic analysis of unforced and forced low blowing ratio jets in cross-flow. To this end, both vertical and inclined low blowing ratios forced and unforced jets in cross-flow will be investigated in an effort to extend the otherwise extensive literature concerning those flows at high blowing ratios.
    2. To develop, build and characterize a realistic film cooling linear cascade type capable of producing engine like Reynolds numbers ($Re \simeq 500,000$) with realistic incoming wake signatures. This facility would be capable of reproducing engine conditions in the turbine stages beyond the first nozzle guide vanes. This facility will be designed around an AFRL L1-A profile, equipped with film cooling holes.

DISTRIBUTION A: Distribution approved for public release.

3. To provide support in developing a reduced order model of unforced and forced film cooling velocity and temperature fields.

- Numerical effort:

1. To identify optimum forcing conditions for forced film cooling systems. To this end, Direct Numerical Simulations of film cooling systems will be carried out and a methodology for the identification of optimum forcing parameters will be developed.
2. Investigate in detail the influence of control actions on the ROMs and contribute to their development from simulation data.
3. Implement and assess the feedback control scheme/algorithm through numerical simulation experiments.
4. To develop a reduced order model of unforced and forced film cooling velocity and temperature fields.

- Theoretical control:

1. Develop a feedback flow-control algorithm utilizing ROMs emanating from corresponding tasks of the experimental and numerical efforts. Part of this task was also to be directed to the development of the ROMs themselves.
2. Support the implementation of this algorithm on the physical as well as on the numerical experiments and assess its performance.

6 Accomplishments/Findings

- Investigation of the fundamental forced film cooling systems using experimental and numerical (LES) methods:

  – Identification and detailed description of the vortical system developing in unforced low blowing ratio transverse jets (90 degrees injection angle). In particular, description of a stable inner vortex vortex inside the jet pipe for blowing ratios below 0.275 interacting with the well-known horseshoe vortex system. The destabilization of this structure is responsible for transition of the jet from attached to detached configuration and clear film cooling performance degradation.

  – Experimental verification of the vortical system formed in forced transverse jets with non-zero low blowing ratio, and definition of the proper scaling parameters for such jets. Experiments allowed to confirm the existence of four starting vortex regimes in agreement with previous numerical studies. Additional investigations revealed the proper scaling parameters to be used in forced transverse jets with residual low flow-rate were (BR_h, SR_h). Experiments showed that previous numerical studies over predicted the threshold values between different starting vortex regimes by as much as a factor 3.

DISTRIBUTION A: Distribution approved for public release.

- Experimental and numerical investigations and detailed description of the vortical system developing in low blowing ratio film cooling geometries and their impact on adiabatic effectiveness.
- First time description of the vortical system born from jet forcing in forced film cooling setups. Identification of 6 vortical regimes, and derivation of the proper scaling parameters (BR_h, SR_h) based on PIV measurements. Forced film cooling systems were found to have lower performances compared to unforced systems when actuated in "open loop" fashion.Investigation of realistic film cooling systems using cascade wind tunnel experiments and realistic wake generator:
- Complete design, fabrication and validation of a linear cascade setup with realistic flow conditions ($Re \simeq 500,000$) and realistic incoming wake profiles, equipped with L1-A two dimensional profiles.
- Characterization of the L1-A wake profile and characteristic frequency under unsteady cross-flow conditions.
- Mie scattering visualizations and PIV measurements evidencing the impact of the wake on film cooling jet behavior.

- Numerical simulations and forced film cooling optimization:
  - An optimization strategy combining high-fidelity simulations with response surface construction, was applied to pulsed film cooling for turbine blades. The response surface was constructed for the film cooling effectiveness as a function of duty cycle, in the range of DC between 0.05 and 1, and pulsation frequency St in the range of 0.2-2, using a pseudo-spectral projection method. 73 direct numerical simulations (DNS) using spectral element method were performed to sample the film cooling effectiveness on a Clenshaw-Curtis grid in the design space and evidenced a global optimum at DC = 0.14 and St = 1.03.
  - Extraction of the first known reduced order models of unforced film cooling systems velocity and temperature fields at $BR = 0.15$ and $BR = 0.5$, using the POD-Galerkin projection modeling method. Implementation of known and new stabilization techniques for improved model reliability.
  - Extraction of the first known reduced order models of forced film cooling systems instantaneous and phase averaged velocity and temperature fields, using the POD-Galerkin projection modeling method. Implementation of known and new stabilization techniques for improved model reliability.
  - Description of the impact of forcing frequency on film cooling reduced order models through mode segregation mechanism at low forcing frequencies.
  - Description of the impact of blowing ratio on unforced film cooling reduced order models and emphasis of the necessity to implement efficient stabilization methods at high blowing ratios.

- Feedback flow control of film cooling systems:
  - Development of a generalized sector bound approach to feedback stabilization of nonlinear control systems described by state-space models. Regional stabilization

DISTRIBUTION A: Distribution approved for public release.

of the nonlinear dynamics and maximization of the estimated region of quadratic attraction.

– Development of a sequence of linear controllers regionally stabilizing the desired equilibrium using a a switching strategy based on the assumption of a centered-epsilon-cover equilibria path. The controller was used to successfully stabilize a reduced order model (ROM) of a jet in cross-flow to a steady low kinetic energy flow.

DISTRIBUTION A: Distribution approved for public release.

Part II
Mechanistic Analysis

DISTRIBUTION A: Distribution approved for public release.

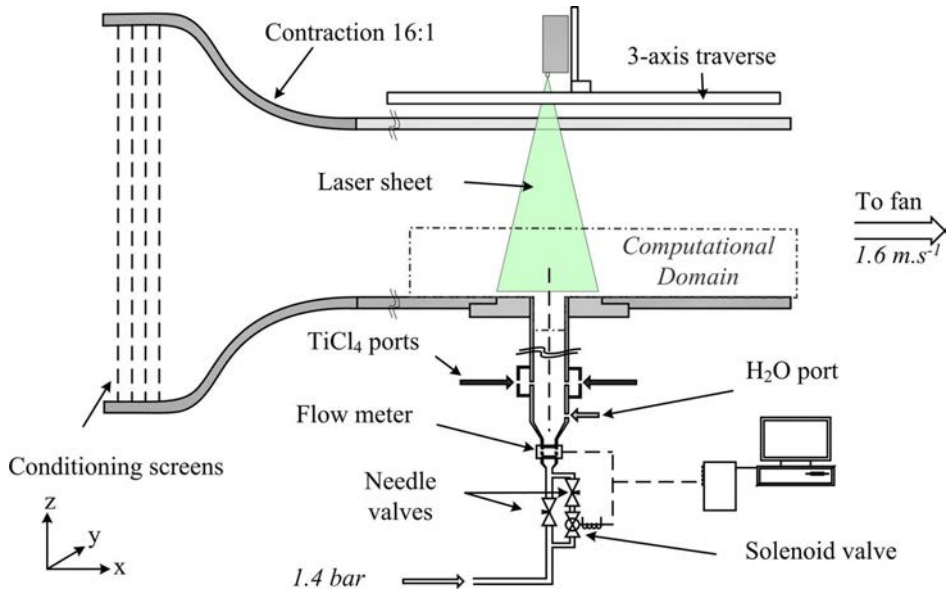

Figure 3: Vertical jet experimental apparatus.

1 Vertical Jet in Cross-flow

In order to gain physical insight on forced film cooling jets, the vortical structures generated in low blowing ratio partly modulated vertical jets in cross-flow are investigated first. Though not strictly application-relevant when it comes to film cooling, these jets offer the advantage of having been well documented in the past, though at blowing ratio values usually relatively high, and constitute a good starting point for a mechanistic analysis and understanding of forced film cooling flows.

First, a detailed unforced survey was conducted to provide a description of the vortical structures found in low blowing ratio transverse jets as well as their evolution as the blowing ratio was increased to reach a more commonly studied detached configuration. Then, partially modulated transverse jets were investigated with a particular focus on the transient regimes introduced by jet forcing. These results were based on experimental results using hot wire anemometry and Mie scattering visualizations while monitoring the jet flow rate in a time-resolved manner. Large Eddy Simulation (LES) as implemented in Ansys Fluent™ was also used to provide additional insights on the behavior of the vortical structures. Film cooling performance was evaluated from the numerical simulations for the forced jets and compared to the unforced results.

1.1 Experimental and Numerical Setup

1.1.1 Wind Tunnel Experiments

Experiments were conducted in an open loop aerodynamic wind tunnel with a $9m$ long test section and a $0.9 \times 0.6m$ cross-section, schematically presented in figure 3. A set of four conditioning screens followed by a contraction with an area ratio of $16:1$ were located directly upstream of the test section to provide stable inlet conditions during the experiments.

DISTRIBUTION A: Distribution approved for public release.

Optical access was available through a set of transparent acrylic walls constituting the top and one of the side walls of the test section, respectively allowing visualizations in planes parallel to the bottom wall (X-Y) and parallel to the jet symmetry plane (X-Z). The coordinates x, y, and z are respectively associated with the stream-wise, span-wise and vertical directions of the flow as shown in figure 3, the origin is taken at the center of the jet exit and the quantities X_j, Y_j, and Z_j correspond to the normalized coordinates with respect to the jet diameter D_j (resp. x/D_j, y/D_j and z/D_j). The free stream flow in the test section had turbulence intensity levels of less than 0.5%, with a boundary layer Reynolds number at the jet level of $Re_\infty = U_\infty \delta/\nu = 1,700$ (with δ the 99% boundary layer thickness and ν the air kinematic viscosity). The jet exited from a $25.4mm$ (D_j) round exit located $762mm$ downstream of the test section inlet and was mounted flush to the bottom wall. At the jet inlet, the setup was composed of two branches, a principal and a bypass, each comporting a metering needle valve to control the flow in the branch. The bypass also comported a computer-controlled solenoid valve which is used to pulse the flow during forced flow experiments (see figure 3). This system provided the ability to independently and accurately set the low (BR_l) and high (BR_h) jet blowing ratios in forced experiments, recorded in a time resolved manner by an inline flow-meter. The jet and cross-flow were at ambient temperature therefore the density ratio was approximately one. The experimental setup is studied using laser sheet Mie scattering visualizations, hot wire anemometry and time resolved flow rate records.

1.1.2 Numerical Simulations

Numerical simulations were carried out in parallel to the experiments in order to provide more detailed information on the vortical structures and their formation mechanisms under forced and unforced conditions. A commercial solver (Ansys Fluent™) was used to simulate the unsteady, turbulent flow through incompressible Large Eddy Simulation (LES) using a dynamic Smagorinsky sub-grid scale model with second order accuracy for both spatial and temporal discretizations. Figure 4 shows the simulated domain consisting of a rectangular box representing a part of the wind-tunnel test section and of the jet pipe as well as the applied boundary conditions. The main computational domain was $18D_j$ long (stream-wise x-direction), $8D_j$ wide (span-wise y-direction) and $6D_j$ tall (vertical z-direction) and accounts for $174 \times 92 \times 76$ cells along the respective dimensions. The jet exit center was located $6D_j$ downstream from the domain inlet and the jet pipe domain is $8D_j$ long to allow development of the artificial inlet boundary conditions, the parameters of which are adjusted to approximate the natural flow induced during experiments. The jet tube mesh consisted of an O-grid type mesh with 3060 cells in the cross-section and 150 cells along the pipe axis. The full mesh was structured and contained overall 1.8 million cells. The first cells in contact with solid walls were on average $0.03D_j$ tall in the normal direction for y^+ values below or close to unity. To obtain statistically significant data, the flow was integrated over several thousands iterations for each case on high performance computing platforms at Louisiana State University (IBM Power5+ at $1.9GHz$), using an average of 24 processors per run. Velocity characteristics and boundary layer profiles for the inlet of the computational domain were obtained from hot wire measurements performed in the wind tunnel as summarized in table 1, where δ^*, θ and H correspond respectively to the boundary layer displacement, momentum thickness and shape factor.

DISTRIBUTION A: Distribution approved for public release.

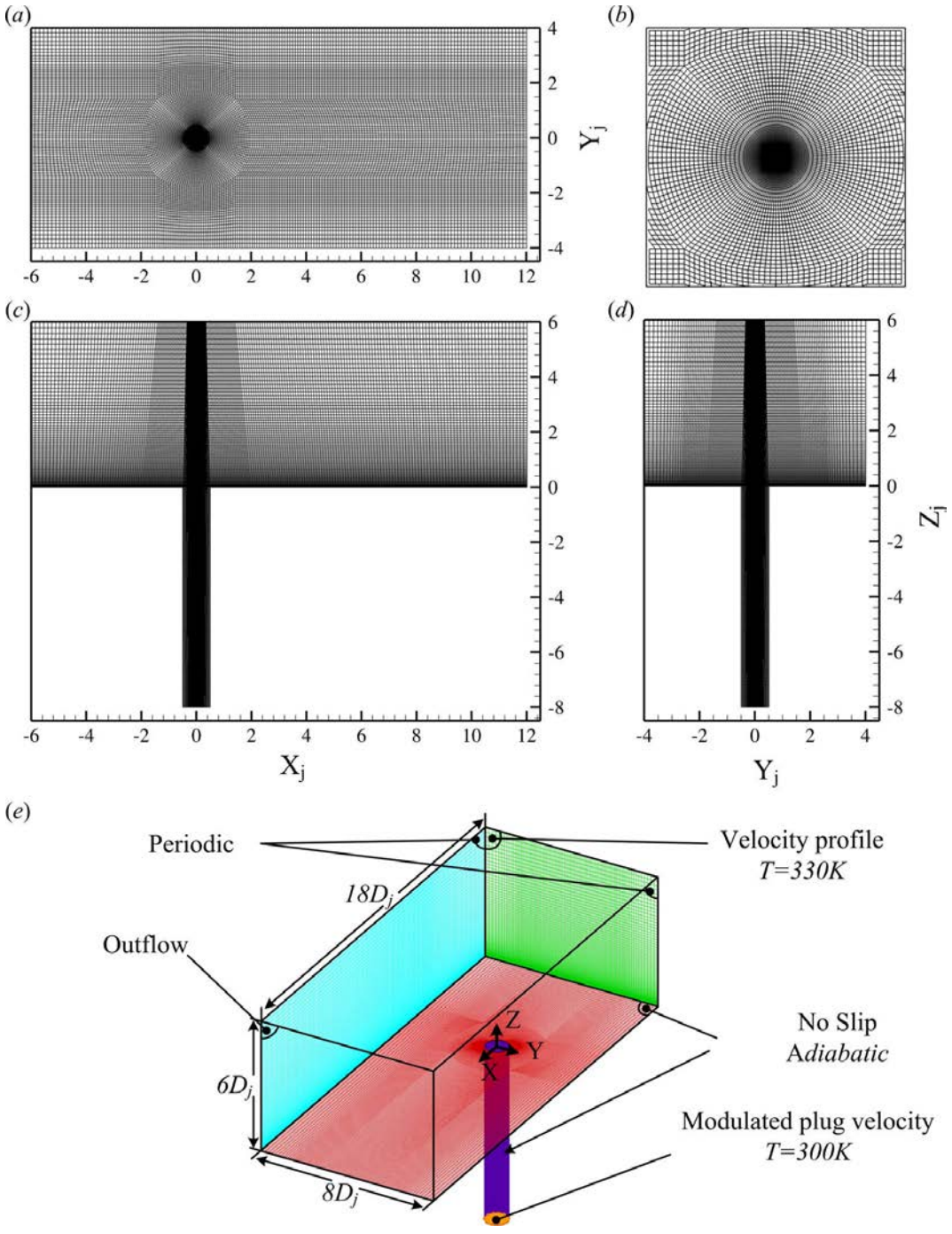

Figure 4: Vertical jet numerical grid details and boundary conditions. (a) X-Y view, (b) X-Y view detail, (c) X-Z view, (d) Y-Z view, (e) global view and imposed boundary conditions.

DISTRIBUTION A: Distribution approved for public release.

Table 1: Inlet boundary layer characteristics at $X_j = -6$, $Y_j = 0$.

U_∞	Ti	δ/D_j	δ^*/D_j	θ/D_j	H
$1.6ms^{-1}$	$< 0.5\%$	0.630	0.172	0.077	2.23

At the inlet of the jet pipe, uniform velocity was set so as to equal the volumetric flow rate of the experiment. In the pulsed jet simulations, the velocity was modulated by using the signal of the unsteady volumetric flow rate measurement from the flow-meters during experiments. Spatial profile perturbations were provided using the spectral synthesizer method implemented in Fluent with a characteristic length scale equal to D_j and a cross-flow characteristic boundary layer length scale equal to 0.4δ. Based on the experimental measurements presented in table 1, a 0.5% perturbation level was imposed at the cross-flow inlet. Because the experimental setup does not allow measurements $8D_j$ inside the jet pipe, the perturbation levels at the jet inlet were adjusted so that simulated and experimental perturbation levels at the jet exit would match. The jet and test section walls were set as adiabatic. Periodic boundary conditions were applied to the side boundaries of the test section box and a standard convective outflow boundary condition was used on the outlet plane. Finally, conversely to the experiment, the jet and cross flow fluids were maintained at constant temperatures of respectively 300 and $330K$ similarly to what was done in the experiments of (25). The density difference associated with those temperature gradients was sufficiently low as to not affect the velocity field.

Figure 5 shows a comparison between experimentally measured and predicted velocity magnitude profiles at two stream-wise locations, $X_j = 1.0$ and $X_j = 3.5$ in the symmetry plane $Y_j = 0$ for three values of the blowing ratio. Because experimental profiles were obtained using single component hot wire anemometry, no distinction could be made between stream-wise and vertical velocity components, thus velocity magnitudes were chosen as a comparison basis. In addition, recirculatory flow present near the wall at $X_j = 1.0$ could be measured accurately because of hot wire signal rectification, thus no experimental data is reported in this region. The velocity profiles in figure 5 compare reasonably well at $BR = 0.15$ and $BR = 0.465$ for both stream-wise locations, while at $BR = 0.25$, the simulations appear to under predict the velocity magnitude in the jet wake. This result is consistent with a mismatch in the transition behavior between experimental and numerical data which will be described later. Overall, the agreement of the rudimentary mean flow comparisons between simulation and experimental results is quite good and re-enforces the qualitative and mechanistic comparisons between the simulation results and the visualizations presented in the following sections. Thus, both physical and simulated flows are deemed comparable enough to be used concurrently in interpreting and understanding fundamental processes.

1.2 Results

1.2.1 Unforced Jet

A rather extensive study of the unforced jet over a wide range of blowing ratios from $BR = 0.150$ to $BR = 4.3$ was conducted as a baseline for the subsequent pulsed jet study. Based on the characteristic vortical structures of the jet at various blowing ratios, attached and detached jet regimes were identified at blowing ratios below 0.275 and above 0.6 respectively.

DISTRIBUTION A: Distribution approved for public release.

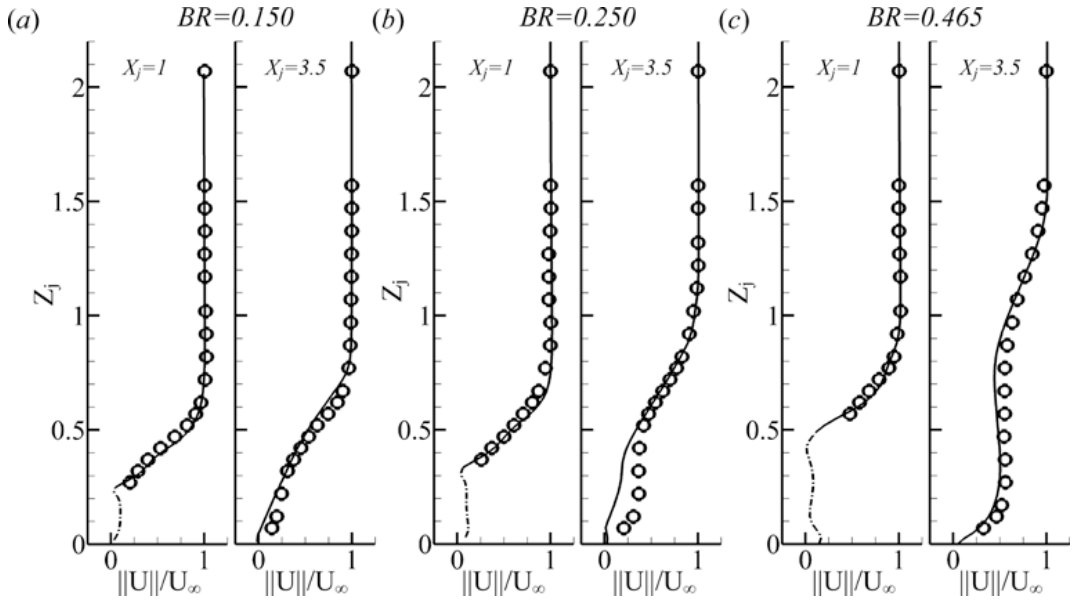

Figure 5: Experimental (*symbols*) and simulated (*solid line*) velocity magnitude profiles in the symmetry plane at $X_j = 1$ and $X_j = 3.5$ for (a) $BR = 0.15$, (b) $BR = 0.25$, (c) $BR = 0.465$.

The latter exhibited classic transverse jet vortical structures (horseshoe vortex, ring shear layer vortices, wake vortices). At intermediate values of the blowing ratio ($0.275 \leq BR < 0.600$) the transition cases exhibited features from both types of flows.

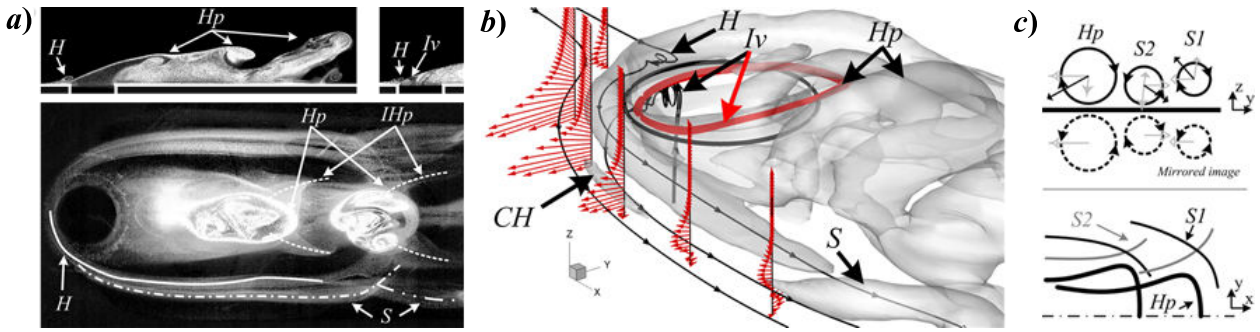

Figure 6: (a) Reactive Mie scattering visualization in the plane $Y_j = 0$ (top) and $Z_j = 0.5$ (bottom) at $BR = 0.188$; (b) Laplacian of the pressure iso-surface at $\Delta P = 1kPa.m^{-2}$ and local velocity profiles with spanwise and vertical component only, in the vicinity of the jet exit from LES at $BR = 0.188$; (c) Induction effects between hairpin (*Hp*) and side vortices (*S1* and *S2*) and their respective mirrored images. *H* - Horseshoe vortex, *CH* - Counter-horseshoe vortex, *Iv* - Inner vortex, *Hp* - Hairpin vortices, *S* - Side vortices (*dash-dot line*), *IHp* - Inverted hairpin vortices (*dashed line*).

DISTRIBUTION A: Distribution approved for public release.

The regime most relevant to film cooling application, the attached jet, was investigated in great details for the first time in this study, and a set of characteristic vortical structures were identified:

- *Recirculation region* - A recirculation region was identified directly downstream of the jet exit in both experimental visualizations and numerical results (figure 6*a*). Time-averaged streamlines from LES, showed that the recirculation region was mainly supplied by jet fluid issuing from the sides of the jet tube, although a certain amount of cross-flow fluid (moist air in the experiment) was entrained and reacted to generate the seed particles in the visualizations as well.

- *Shear layer hairpin vortices* - The dominant shear layer structures were found to be of the interlocked hairpin type (*Hp* in figure 6). These vortices were formed periodically in the lower shear layer with increasing formation frequency as the blowing ratio was increased. Multiple self-induction and mirrored induction effects dictated the behavior of the hairpin vortices as they were convected downstream by the cross-flow momentum.

- *Horseshoe vortex* - A stable horseshoe vortex was located above and on the leading edge of the jet exit (*H* in figure 6). Relatively small at the lowest blowing ratios, (approximately $0.19D_j$ in radius at $BR = 0.15$), the primary vortex became larger in diameter with increasing values of the blowing ratio (up to $0.26D_j$ at $BR = 0.275$), while being pushed further upstream from the leading edge of the jet. Seeding particles entrained from the upper lip of the jet into the horseshoe vortex system in experimental visualizations, evidenced transport of jet fluid by the structure. Cases with blowing ratios in the range $0.225 \leq BR \leq 0.275$, exhibited irregular transport of the horseshoe vortex, which was convected downstream on top of the jet upper shear layer. This destabilization was likely provoked by an interaction between the horseshoe vortex and the inner vortex. Although not immediately seeded and entirely visible, a second horseshoe vortex very quickly replaced the convected one in the cross-flow boundary layer upstream of the jet.

- *Side vortices* - Additional stream-wise wall vortices were found in both Mie scattering visualizations and numerical simulations (*S* in figure 6). In the near field, these side vortices, were located on the outside of the horseshoe vortex. The origins of these secondary vortices were explained by a strong positive spanwise (or locally radial outwards) velocity gradient in the vertical (wall-normal) direction due to jet fluid injected around the jet hole, as well as cross-flow deflection imposed by the jet blockage (figure 6*b*). Further downstream, both horseshoe and counter-horseshoe vortices interacted with the shear layer structures, to respectively form positive and negative side-vortices *S1* and *S2*. Due to their closeness to the wall and their opposite vorticity, both types of side-vortices behave differently as they are convected. Figure 6 (*c*) illustrates first order mutual induction effects as well as mirrored induction effects. As they were convected downstream, the negative side-vortices had a tendency to ride on top of the positive ones while converging toward the symmetry plane, whereas the latter diverged from the symmetry plane. The different relative motions of the side vortices resulted in "X-patterned" structures lying on each side of the jet core, which can be observed both in the Mie scattering visualizations and LES results.

DISTRIBUTION A: Distribution approved for public release.

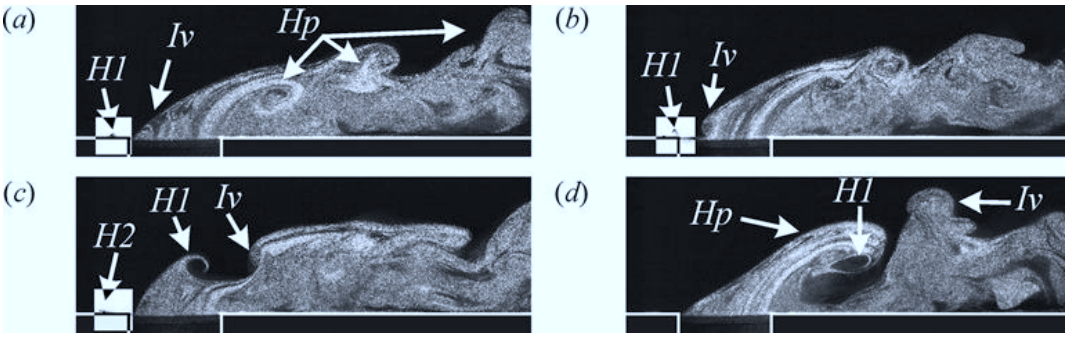

Figure 7: Fully Reacted Mie scattering visualizations at $Y_j = 0$ and $BR = 0.365$ (a) $t_c = t_0$; (b) $t_c = t_0 + 6$ $(95ms)$; (c) $t_c = t_0 + 7.9$ $(125ms)$; (d) $t_c = t_0 + 9.8$ $(155ms)$. Hn - Horseshoe vortex #n, *Iv* - Inner vortex, *Hp* - Hairpin vortices.

- *Inner vortex* - Amongst the few low-blowing-ratio studies of the past, (28) suggested that at low blowing ratios, the span-wise vorticity from the boundary layer, resulting in the formation of the horseshoe vortex, interacted with the jet upper shear layer vorticity and ultimately canceled it so that, conversely to the higher blowing ratio cases, the upstream shear layer was not rolling and no vortical structure was formed at the leading edge of the jet. The current study showed the presence of a stable rollup of reacted seed, or inner vortex (*Iv* in figure 6), resulting from jet flow separation inside the pipe and located at the leading edge. The shedding of this vortex was prevented by the blockage exerted by the cross-flow on the jet as suggested by the relatively advanced position of the horseshoe vortex. Accordingly, LES showed a high pressure region located upstream and above the jet exit, creating an adverse pressure gradient for part of the jet fluid exiting from the pipe, thus forcing it to roll up at the jet leading edge. Jet fluid from the upstream region of the jet was found to exit on the sides of the jet pipe as well as upstream, underneath the primary horseshoe vortex. The inner vortex and the consecutive hairpin vortices formed a series of interlocked rings, sharing the upstream part. For blowing ratios between 0.275 and 0.6, inner vortex started to shed, as the jet entered the the transitional regime. A typical convection sequence of this vortical structure is presented in figure 7. The inner vortex (Iv), still partly inside the jet tube in figure 7(a), is convected in figure 7(b), which is followed by an ingestion of cross-flow fluid inside the jet pipe at the leading edge. The perturbation of the jet/cross-flow interface also triggered the transport of the horseshoe vortex (*H1*) in figure 7(c), followed by the formation of a large hairpin vortex (Hp) in figure 7(d). At values of the blowing ratio approaching 0.6, the size of the transported inner vortex became comparable to the downstream shear layer vortices and the ingestion of cross-flow fluid that followed the inner vortex transport, was gradually decreased, until it completely disappeared beyond $BR = 0.6$.

- *Counter Rotating Vortex Pair (CRVP)* - In time averaged stream-wise vorticity field, a pair of stream-wise counter-rotating vortices was located on each side of the symmetry plane (*filled arrows*). This result is a common feature in transverse jets and is usually identified as the CRVP. According to the instantaneous observations, the vorticity of this vortex pair was generated by the hairpin vortices. Although close from the usual

DISTRIBUTION A: Distribution approved for public release.

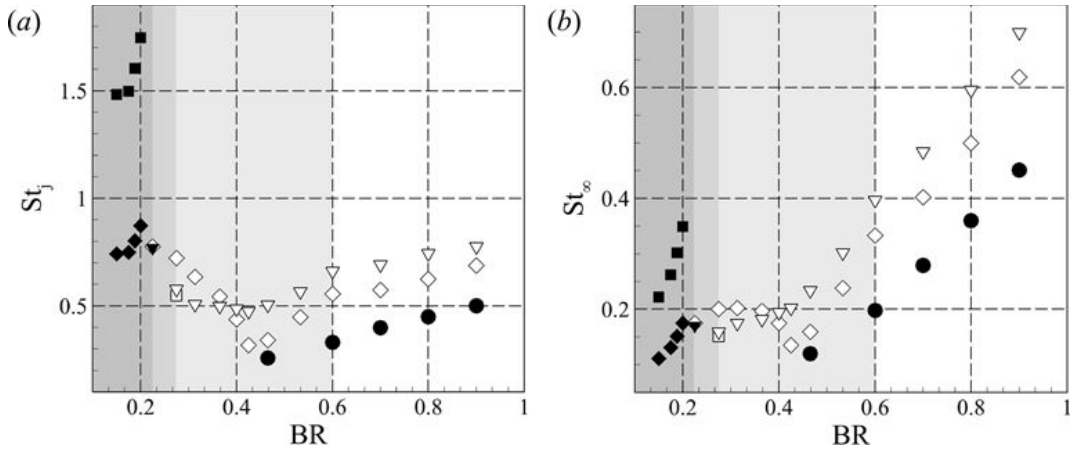

Figure 8: Fundamental frequencies scaled using (a) time averaged jet velocity; (b) cross-flow velocity. In the experiment these were identified from hot wire records using wavelet analysis. The symbol $\diamond$ corresponds to the jet exit ($X_j = 0$, $Z_j = 0$); $\triangledown$ is from location ($X_j = 0$, $Z_j = 0.25$) and $\blacktriangledown$ from location ($X_j = 0$, $Z_j = 0.5$), both inside the upper shear layer; $\blacksquare$ corresponds to the fundamental and $\blacklozenge$ to its subharmonic from downstream location ($X_j = 3.5$, $Z_j = 0.75$); $\square$ is from location ($X_j = 3.5$, $Z_j = 1.25$). The symbol $\bullet$ indicates characteristic frequencies from the LES at the center of the jet exit ($X_j = 0$, $Z_j = 0$).

CRVP structure described in most high blowing ratio jets in cross-flow studies, the attached jet CRVP was found to be instantaneously discontinuous since induced by hairpin vortices, and was not the dominant feature of the far field, where the vorticity in the CRVP was twice as low as the one in the average side vortices found near the wall.

- *Characteristic frequency modes* - Single component hot wire measurements were performed at select locations, chosen based on the visualizations in order to identify frequency modes associated with the previously described structures. The velocity signals were subjected to both Fourier and wavelet spectral analysis, the latter between 0 and $50Hz$ (corresponding to Strouhal numbers St_∞ between 0 and 0.794), guided by the results from the former. The results presented in figure 8, summarize the fundamental frequencies found at each location scaled by jet diameter and mean jet velocity ($St_j = f.D_j/U_j$) in figure 8(a) and scaled by jet diameter and cross-flow velocity ($St_\infty = f.D_j/U_\infty$) in figure 8($b$). Results from the attached jet regime showed an increase in Strouhal number with increasing blowing ratio, corresponding to the rate of formation of hairpin vortices. Similarly, results from the detached jet at $BR = 0.6$ showed a nearly linear rate of increase in Strouhal number with blowing ratio at both locations, corresponding to the formation rate of ring vortices. The simulation results showed an identical trend but with overall lower frequencies and a slightly lower rate of increase. Overall, the value of St_∞ appeared relatively constant around 0.2 over the range $0.225 < BR < 0.425$, while St_j decreased continuously from 0.780 to 0.32 at the jet exit. This indicates that the dominant feature, in this case the transport of the horseshoe vortex and the inner vortex, were better scaled by the cross-flow velocity and

DISTRIBUTION A: Distribution approved for public release.

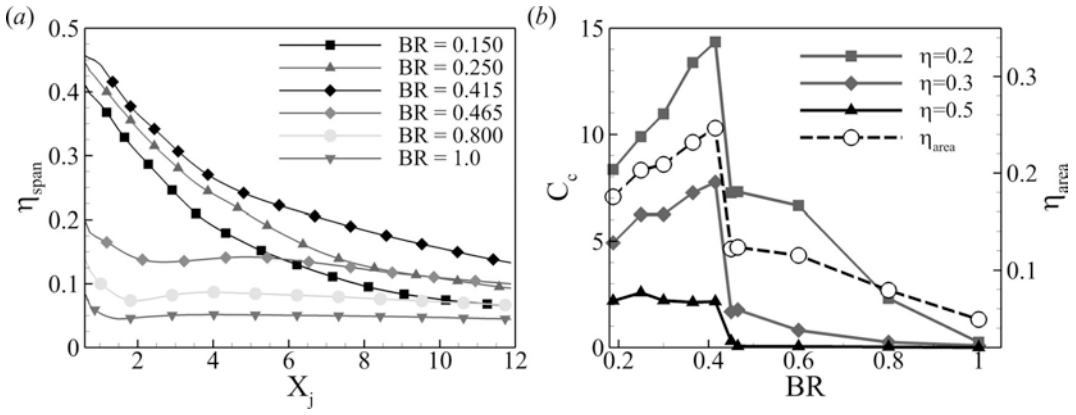

Figure 9: Film cooling performance: (a) Spanwise averaged adiabatic effectiveness; (b) Area averaged adiabatic effectiveness and coverage coefficient for thresholds $\eta = 0.2$, 0.3, 0.5 as a function of BR after LES.

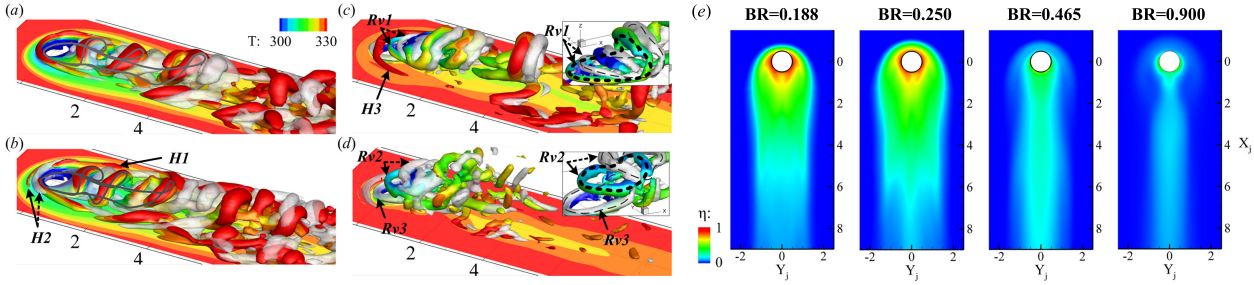

Figure 10: (a-d)ΔP iso-surfaces at two superposed time instants separated by Δt_c, first iso-surface colored by temperature: (a) $BR = 0.188$, $\Delta P = 1500$, $\Delta t_c = 1.25$; (b) $BR = 0.25$, $\Delta P = 2000$, $\Delta t_c = 2.2$; (c) $BR = 0.465$, $\Delta P = 5000$, $\Delta t_c = 0.6$; (d) $BR = 0.9$, $\Delta P = 1500$, $\Delta t_c = 0.6$. (e) Time averaged wall adiabatic effectiveness at: (a) $BR = 0.188$; (b) $BR = 0.25$; (c) $BR = 0.465$; (d) $BR = 0.9$.

thus suggested that the transport mechanism was initiated by the horseshoe vortex. On the other hand, for $0.425 \leq BR < 0.6$, St_j values tended to reach saturation, while St_∞ was clearly increasing, indicating a shift in the transport initiating structure from the horseshoe vortex to the inner vortex.

- *Film Cooling Performance* - Vortical structures influencing the wall temperature field were identified. The area of highest adiabatic effectiveness in the attached configuration was located in the recirculation region, which was essentially seeded by jet fluid (figure 10). The fluid forced to exit on the sides of the jet pipe by the high pressure region also provided additional coverage. The horseshoe vortex was found to entrain significant amounts of coolant upstream of the jet due to its position above the jet exit and have a positive effect on film cooling adiabatic effectiveness in this region. The counter-horseshoe and horseshoe vortices had an opposite impact on the jet spread at the wall

DISTRIBUTION A: Distribution approved for public release.

because of their respective velocity fields. Near the wall the horseshoe vortex had a velocity field pointing away from the symmetry plane and tend to entrain cooler fluid from the jet core region toward the wall, whereas the counter-horseshoe vortices had an associated opposite velocity field carrying free stream fluid near the bottom surface. Consequently, the formation of the X-patterned structures directly downstream of the hairpin vortices resulted in dramatic decrease in local wall adiabatic effectiveness. Along the symmetry plane, the legs of the hairpin vortices were responsible for the transport of most of the coolant. These results show the significant role of the horseshoe vortex and the inner vortex in the jet coverage near the wall. As the horseshoe vortex started to be convected beyond $BR = 0.25$, the coolant supply upstream of the jet exit was never interrupted and coverage was continuously provided to this area. As BR increases, the horseshoe vortex was strengthened and pushed further upstream from the jet exit, thus augmenting the jet coverage at the wall. Finally, the hairpin vortices at $BR = 0.25$ were stronger when compared to the lower blowing ratio cases, and stayed coherent further downstream, carrying more coolant along the symmetry plane. The transitional regime marked the beginning of coverage degradation. At $BR = 0.465$, the hairpin vortices' legs immediately lifted off of the wall after the jet exit because of increased mutual induction, as well as the shedding of the inner vortex. The consequent drop in coverage observed in the contours of adiabatic effectiveness (figure 10) was explained by the consecutive transports of the inner and horseshoe vortices, interrupting the coolant flow upstream and on the sides of the jet exit. In the detached configuration, at $BR = 0.9$, the shear layer ring vortices (R2) were formed on a periodic basis and were directly convected away from the wall, therefore not providing coverage. Conversely to the transitional regime, the horseshoe vortex formed ahead of the jet was not convected, though it oscillated as the shear layer ring vortices shed, and its impact on the wall temperature was only minor. Marginal amounts of coolant reached the jet wake region transported by the wake vortices as evidenced by the η contours as well as the presence of seed particles in experimental Mie scattering visualizations. An increase in spanwise averaged adiabatic effectiveness was found (figure $9a$) for increasing values of the blowing ratio until the transitional threshold was reached ($BR = 0.415$) and then dropped precipitously. As BR continued to increase, the effectiveness decreased asymptotically toward zero. A local minimum in η_{span} profiles for the transitional jet was observed downstream of the jet exit, corresponding to the location where the cross-flow recovered behind the jet and moved upstream toward the jet exit as BR increased. Maximum coverage was reached at $BR = 0.415$. The area averaged adiabatic effectiveness,η_{area}, (figure $9b$) was computed from the simulations, assessing the overall film cooling performance at a given blowing ratio. Accordingly to η_{span} trends, film cooling was improved for increasing values of BR below the transitional threshold, and decreased dramatically beyond this point.

Investigations of the unforced jet showed that the transitional threshold constitutes a limitation to the improvement of film cooling performance because of the transport of the inner vortex and the associated interruption of coolant supply to the upstream region. Based on the evolution of the film cooling metrics in the attached jet regime, delaying the transport of the inner vortex to higher values of BR could lead to improved overall coverage.

DISTRIBUTION A: Distribution approved for public release.

Table 2: Forced cases parameters †: No flow-meter record available, ‡: No experiments at these conditions, *: Simulations carried at these conditions.

$Case\#$	BR_m	BR_l	BR_h	BR_{pp}	$DC(\%)$
1^{*}	0.250	0.188	0.438	0.250	25
2	0.250	0.075	0.325	0.250	70
3^{*}	0.350	0.188	0.836	0.648	25
4^{*}	0.350	0.188	0.513	0.325	50
5	0.350	0.225	0.475	0.250	50
6	0.350	0.175	0.425	0.250	70
$7^{\dagger}$	0.750	0.200	2.20	2.00	25
$8^{\dagger}$	1.25	0.200	4.20	4.00	25
$9^{\ddagger *}$	1.25	0.200	2.20	2.00	50
$10^{\ddagger *}$	0.365	0.200	2.20	2.00	8
$11^{\ddagger *}$	1.28	0.700	3.00	2.30	25
12^{*}	0.465	0.188	0.712	0.524	50

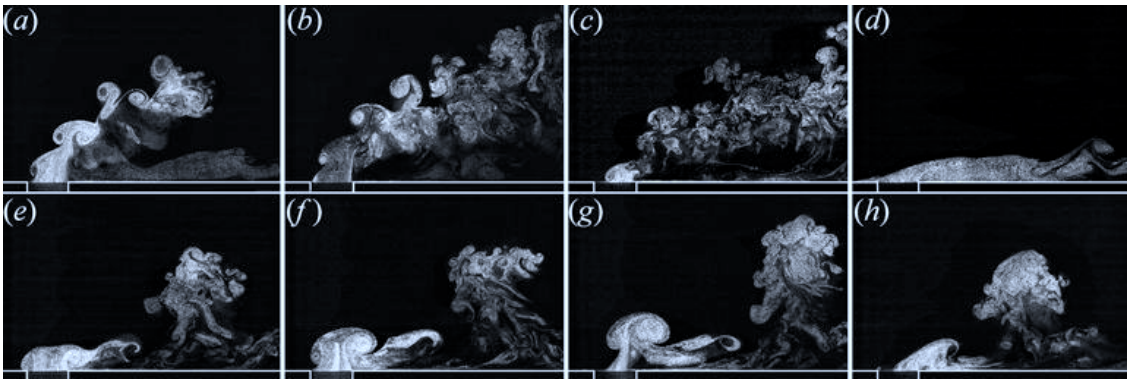

Figure 11: Mie scattering visualizations in the plane $Y_j = 0$ for *Case 3*, (a) $t^* = 0.1$; (b) $t^* = 0.2$; (c) $t^* = DC + 0.025$; (d) $t^* = DC + 0.63$ at $St_\infty = 0.016$ and (e) $t^* = 0.1$; (f) $t^* = 0.2$; (g) $t^* = DC + 0.025$; (h) $t^* = DC + 0.63$ at $St_\infty = 0.159$.

DISTRIBUTION A: Distribution approved for public release.

1.2.2 Forced Jet

Forced jet experiments were performed using a nominal square wave actuation signal for the solenoid valve shown in figure 3. A wide range of forcing parameters' values for BR_m, BR_l, BR_h, BR_{pp}, (respectively mean, low, high, peak to peak blowing ratios over a cycle) and DC (duty cycle) was covered and are summarized in table 2. Each individual case was observed at 4 distinct forcing frequencies (f_f) of 0.5, 1.0, 5.0 and $10.0Hz$, respectively corresponding to Strouhal numbers of $St_\infty = 0.008$, 0.016, 0.079 and 0.159. These were selected to stay below the shear layer natural frequencies of the unforced jet so as to minimize the potential of direct resonant amplification (see 55), although resonance with sub-harmonic and other lower harmonics giving rise to stronger non-linear effects (see 56 and (57)) cannot be ruled out. Phase locked Mie scattering visualizations, supplemented by hot wire anemometry and Large Eddy Simulations, were used to document the forced cases. Because of the large number of parameters attached to partly modulated transverse jets, the use of the cross-flow Strouhal number St_∞, defined in the previous sections, was preferred over the parameter St_j, necessitating the identification of characteristic velocity scales for each forced case. The dimensionless time $t^* = t \times f_f$ was used to report instants inside a cycle. Using this parameter, the transition from low to high blowing ratio occurred at $t^* = 0$, while the transition from high to low blowing ratio occurred at $t^* = DC$.

The typical forced jet in cross-flow cycle could be composed of up to four distinct phases.

- *Generation of a starting vortex system* at the transition from low to high blowing ratio with starting vortices (figure 11*a*), due to increased shear and mass surplus in the jet pipe.
- *Quasi-unforced plateau* in the high blowing ratio part of the cycle with typical structures encountered in the unforced jet at $BR = BR_h$ (figure 11*b*),
- *Cross-flow ingestion* inside the jet pipe at the transition from high to low blowing ratio with (figure 11*c*) due to mass deficit at the jet shutdown
- *Quasi-unforced plateau* in the low part of the cycle with typical structures encountered in the unforced jet at $BR = BR_l$ (figure 11*d*).

At higher forcing frequencies, only two overlapping phases were found: a transition from low to high blowing ratio with the formation of a starting structure (figure *11e, f*) and a transition from high to low blowing ratio with cross-flow ingestion inside the jet pipe (figure 11*g, h*).

- Starting vortices - At the high blowing ratio onset, a starting vortex was formed at the edge of the jet exit due to the higher shear generated across the jet/cross-flow interface by the bulk flow rate increase. These starting structures were observed and described in many pulsed jets in cross-flow experiments and simulations for their potential in mixing and penetration improvement, though generally at higher average blowing ratios and forcing frequencies than in this work. Over the range of forcing parameters covered in this study, four regimes of starting vortices could be observed:
  - *Single starting hairpin vortex* - formed at rather low BR_h values for short injection times. They were very similar to the one observed under unforced conditions, yet

DISTRIBUTION A: Distribution approved for public release.

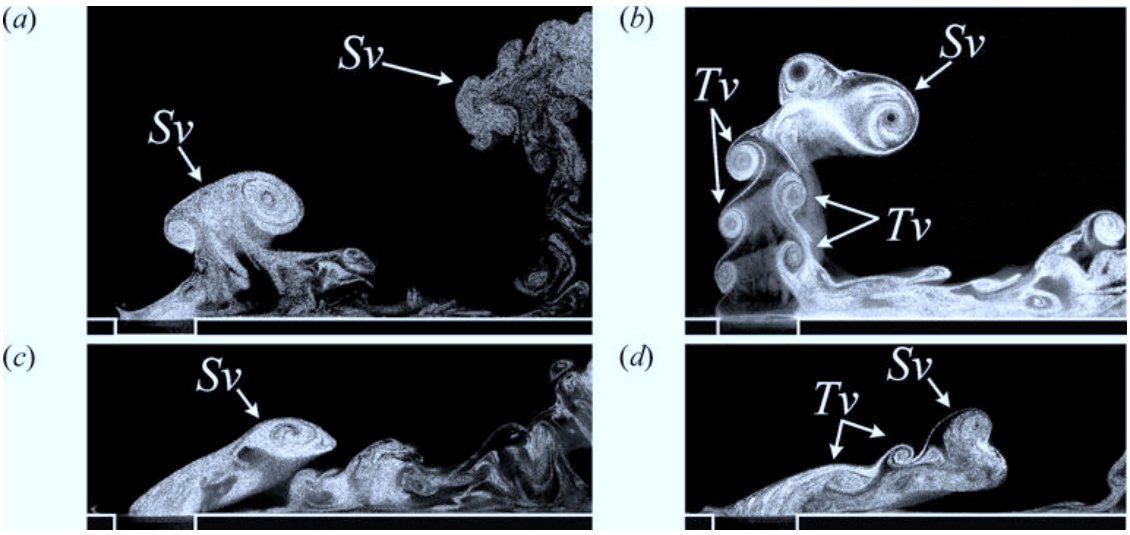

Figure 12: Mie scattering visualizations in the plane $Y_j = 0$ for (a) *Case 3* at $St_\infty = 0.159$ – Single starting vortex ring; (b) *Case 3* at $St_\infty = 0.016$ – Leading starting vortex ring and trailing vortices; (c) *Case 1* at $St_\infty = 0.159$ – Single starting hairpin vortex; (d) *Case 2* at $St_\infty = 0.079$ – Leading starting hairpin vortex and trailing hairpin vortices. (Sv) Starting vortex, (Tv) Trailing vortices.

considerably larger as shown in (figure 12c). Interestingly, these hairpin vortices were found to be formed even though the BR_h value ($BR_h = 0.438$ in *Case 1*) was significantly higher than the unforced jet transitional blowing ratio threshold ($BR_{tr} = 0.275$). This mechanism was attributed to transient dynamics of the horseshoe and inner vortices at the jet onset.

– *Starting hairpin vortex and trailing vortices* - formed at rather low BR_h values for long injection times (figure 12d). Their dynamics were found to be essentially identical to the ones in unforced conditions.

– *Single starting vortex ring* - formed at rather high values of BR_h and for short injection times (figure 12a). The starting vortex tilted towards the upstream direction as it was convected downstream and away from the wall. To observe the dynamics of single starting vortex rings, a forcing signal using an idealized square wave at $St_\infty = 0.159$ was used such that $BR_l = 0.200$, $BR_h = 2.20$, $DC = 8\%$ (identified as *Case 10* in table 2 figure 13). As the starting vortex departed from the bottom wall (figure 13b), the structure acquired an initial tilt angle toward the upstream direction which increased progressively. Under the action of the cross-flow, the vortex ring was deformed and progressively folded, the upstream and downstream parts approaching each other, while the side arms relatively dropped. The jet exit velocity profiles showed a continuous momentum and vorticity deficit at the leading edge, compared to the trailing edge, throughout the starting vortex formation process. This suggested that the circulation and initial convection velocity imbalances responsible for the tilting also originated from the characteristic skewness of the jet in cross-flow velocity profiles.

DISTRIBUTION A: Distribution approved for public release.

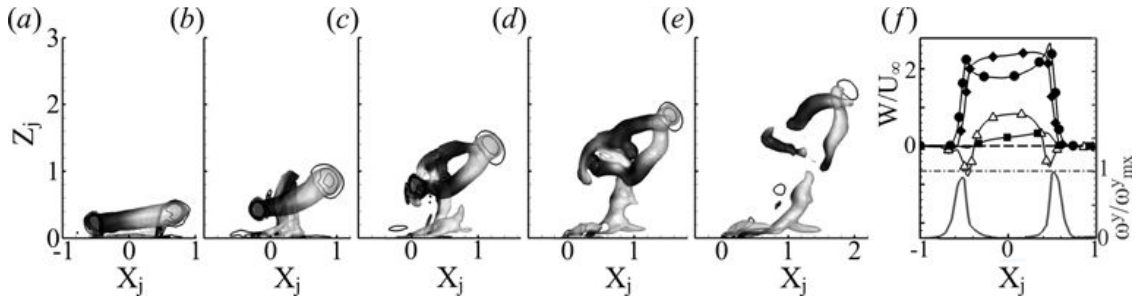

Figure 13: X-Z view of Laplacian of the pressure iso-surfaces at $\Delta P = 80kPa.m^{-2}$ for *Case 10* at $St_\infty = 0.159$ for time instants (a) $t^* = 0.085$; (b) $t^* = 0.19$; (c) $t^* = 0.29$; (d) $t^* = 0.39$; (e) $t^* = 0.49$, colored by spanwise vorticity from *black* (negative) to *white* (positive). (f) Jet exit velocity profiles at ($\blacksquare$) $t^* = 0^-$,($\diamond$) $t^* = 0.005$, ($\bullet$) $t^* = 0.075$, ($\triangle$) $t^* = DC + 0.005$ and spanwise vorticity profile (*gray*) at $t^* = 0.005$.

- *Starting vortex ring and trailing column* - formed at rather high values of BR_h and for long injection times (figure $12a$). In this configuration, the leading ring vortex was followed by a series of smaller vortex rings constituting a trailing column (figure $14a$). The leading vortex ring initially tilted in the upstream direction due to interaction with the cross-flow boundary layer and velocity distribution skewness. As it departed from the wall and the first trailing vortex ring was formed and the leading vortex ring tilting was reversed towards the downstream direction, "swallowing" the downstream part of the first trailing vortex. This "partial leapfrogging" of the first trailing vortex as well as the downstream tilting of the leading vortex ring could easily be explained by 2D inviscid considerations. The reorientation of the trailing vortices was found to be an important feature since it generated vertical vorticity from the side-arms of the trailing column ring vortices and therefore provided a source for the initialization of the CRVP. The simulated dynamics of the leading vortex ring and the trailing vortices for *Case 9* (figure 15), confirmed the partial leapfrogging of the trailing vortices as well as the tilting dynamics. Additional insight was gained on the behavior of the side arms of the trailing vortices as they were convected in the free stream and away from the wall. The first trailing vortex was distorted due to the rapid ingestion of its downstream rollup by the starting vortex ring. The trailing vortices (*Tv2*, *Tv3*, *Tv4* ...) followed similar dynamics so that the overall reorientation of the trailing vortices generated coherent vertical vorticity and resulted in the formation of a quasi-vertical vortex pair on the lee-side of the jet. This pair of vortices was consistent with the CRVP of the unforced jet observed in the experimental visualizations. Both experimental and numerical observations indicated a CRVP initiation mechanism based on trailing vortices partial leapfrogging combining tilting, stretching, and deforming in agreement with the mechanism described by (41), (20) or (52).

- Starting Vortices Classification - The different types of starting structures were sorted against two sets of parameters : (SR_h, BR_h) and (SR_{pp}, BR_{pp}) such as $SR_x = U_x\tau/D_j = BR_xU_\infty DC/(f_fD_j) = BR_xDC/St_\infty$with $x = pp$ or $x = h$. Overall, both

DISTRIBUTION A: Distribution approved for public release.

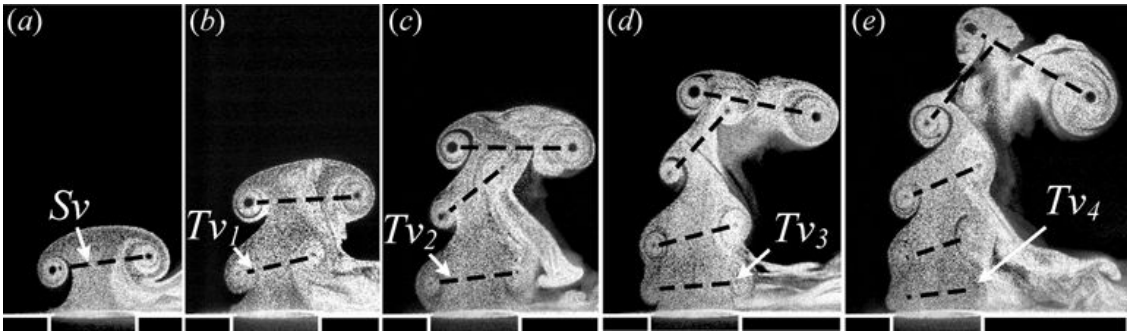

Figure 14: Mie scattering visualizations in the plane $Y_j = 0$ for *Case 8* at $St_\infty = 0.079$ showing leading vortex ring and trailing column formed at the jet transition from BR_l to BR_h. The first ring of the trailing column ($Tv1$) is ingested by the leading vortex ring (Sv).

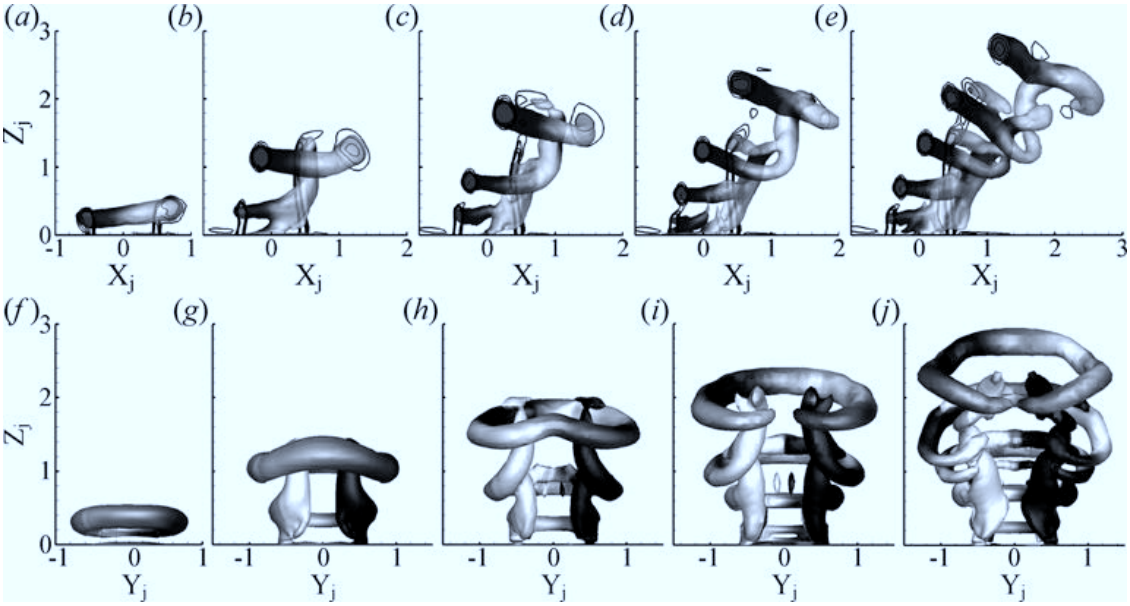

Figure 15: *Top*: *X-Z* view, *Bottom*: *Y-Z* view of Laplacian of the pressure iso-surfaces at $\Delta P = 100kPa.m^{-2}$ for *Case 9* at $St_\infty = 0.159$ for time instants (*a, f*) $t^* = 0.085$; (*b, g*) $t^* = 0.25$; (*c, h*) $t^* = 0.33$; (*d, i*) $t^* = 0.39$; (*e, j*) $t^* = 0.49$, colored by spanwise (*Top*) and vertical (*Bottom*) vorticity ranging from *black* (negative) to *white* (positive).

DISTRIBUTION A: Distribution approved for public release.

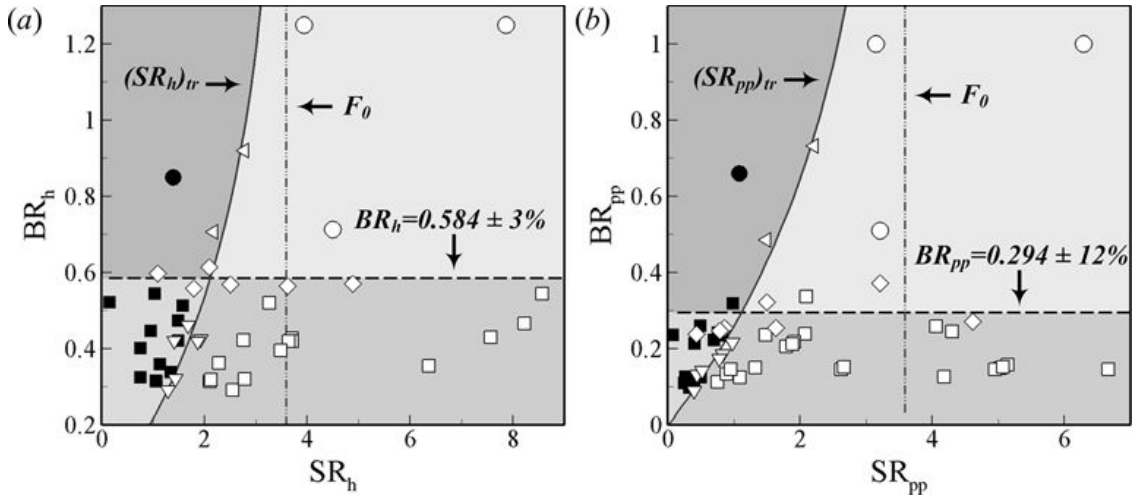

Figure 16: Classification of the starting vortices observed in forced experiments with respect to characteristic stroke ratios and blowing ratios (a) SR_h, BR_h; (b) SR_{pp}, BR_{pp}. ○ Leading vortex ring and trailing column; ● Single vortex ring; ▷ Limiting case vortex ring with/without trailing column; □ Leading hairpin vortex and trailing hairpins; ■ Single hairpin vortex; ◇ Limiting case hairpin/ring vortex; ▽ Limiting case hairpin vortex with/without trailing vortices. $F_0 = 3.6$ - Asymptotic formation number from (67). Transition stroke number fit $(SR_x)_{tr} = F_0 - A_1.exp(-A_2.BR_x)$ (a) $(SR_h)_{tr}$: $A_1 = 3.6$, $A_2 = 1.51$; (b) $(SR_{pp})_{tr}$: $A_1 = 3.6$, $A_2 = 1.26$.

sets of parameters exhibited a similar distribution to the one provided by (67), with a differentiation of the four different starting vortices. A better separation between the regimes was achieved when using the set (SR_h, BR_h) with less overlapping of the zones compared to the one obtained with (SR_{pp}, BR_{pp}). The distinction between the two principal starting structures regimes observed in figure 16(a) shows that hairpin vortices were formed in cases with $BR_h < 0.584 \pm 3\%$, while this separation occurred for cases with $BR_{pp} < 0.294 \pm 12\%$ in figure 16(b). Based on these observations, the set (SR_h, BR_h) appeared to provide a more precise classification map of the starting vortices. A better separation between the regimes is achieved when using the set (SR_h, BR_h) with less overlapping of the zones compared to the one obtained with (SR_{pp}, BR_{pp}). This was confirmed using with idealized square wave models of different amplitudes and pulse widths, simulated using LES. Based on a two dimensional assumption, the total circulation was computed at the jet exit by integrating the spanwise vorticity on the domains $\{\Omega_1 : -2 \leq X_j < 0, Y_j = 0, 0 < Z_j \leq 2.5\}$ and $\{\Omega_2 : 0 < X_j \leq 2, Y_j = 0, 0 < Z_j \leq 2.5\}$, respectively at the leading and trailing edges of the jet exit. Figure 17 shows that the high blowing ratio velocity U_h clearly provided a fixed proportional relationship between the scaled total circulation at the jet exit ($\Gamma^* = \Gamma/(U_c D_j)$ and the formation time ($t^* = tU_c/D_j$) for all forcing conditions, conversely to U_h, and was therefore the proper scaling parameter.

This study exhibited qualitatively good agreement with the observations from (67) in terms of the type of starting vortices generated and their dynamics, although a discrepancy

DISTRIBUTION A: Distribution approved for public release.

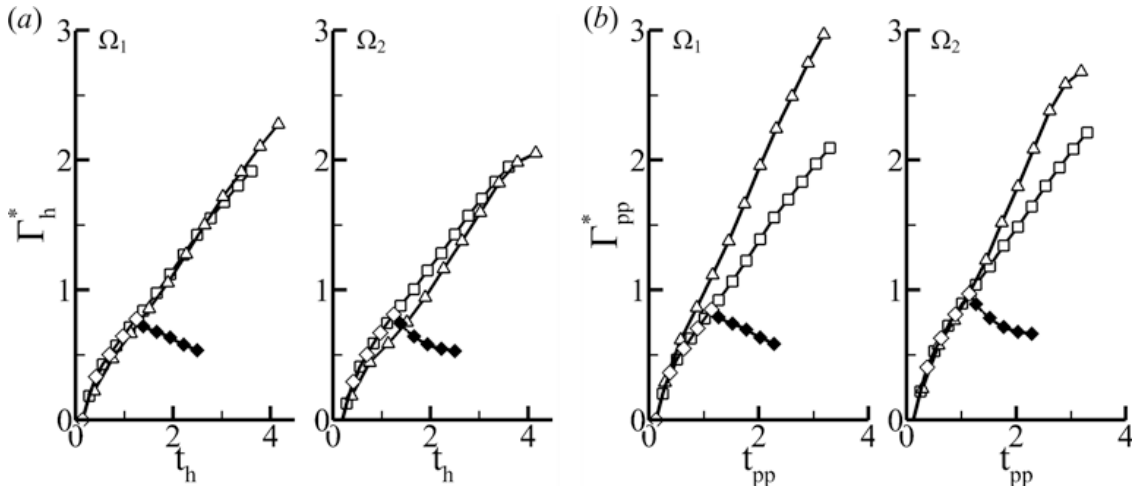

Figure 17: Total 2D circulation from LES scaled using (a) U_h and (b) U_{pp} for *Case 9* ($\square$), *Case 10* ($\diamond$ - high flow on; $\blacklozenge$ - low flow on), *Case 11* ($\triangle$) in domains Ω_1 and Ω_2.

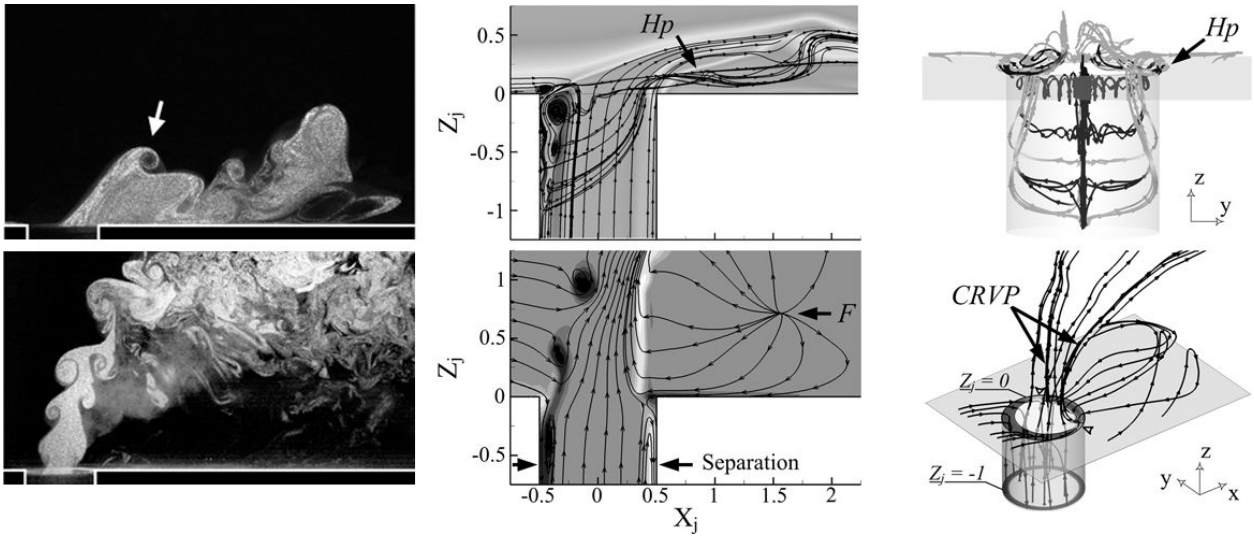

Figure 18: Top: leading edge ingestion; Bottom: Peripheral ingestion.

was found in the threshold value of BR_h between the formation of starting hairpin vortices and starting ring vortices. Indeed in (67) a threshold value of $BR_h = 2.0$ was established, whereas a value of $BR_h = 0.584$ was found in this study's experimental results.

- Cross-flow ingestion - At the jet shutdown, most of the cases with $BR_{pp} > 0.150$ exhibited clear ingestion of cross-flow fluid inside the jet feeding tube. As shown in figure 18, two types of ingestion could be observed.

  - *Leading edge ingestion* - At low BR_h values, the ingestion principally occurred at the leading edge of the jet exit and triggered the convection of the horseshoe vortex in the downstream direction. At the jet shutdown, the horseshoe vortex was

DISTRIBUTION A: Distribution approved for public release.

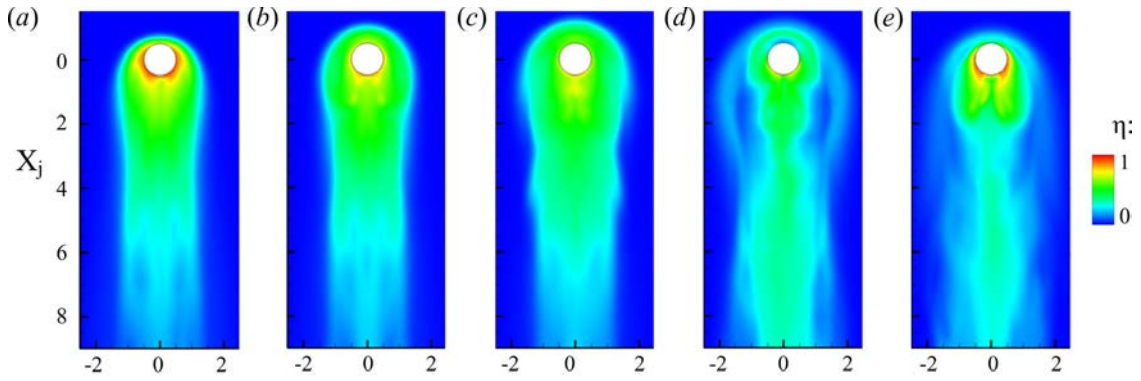

Figure 19: Instantaneous wall adiabatic effectiveness contours from LES. Top: $BR_m = 0.35$, $DC = 50\%$ (*Case 4*) at $St_\infty = 0.016$, time stamps: (a) $t^* = -0.03$; (b) $t^* = 0.08$; (c) $t^* = 0.20$; (d) $t^* = 0.43$; (e) $t^* = DC + 0.10$.

partially ingested inside the jet pipe, while the inner vortex was pulled further inside. Flow separation occurred at the jet leading and trailing edges and the higher shear introduced by the backward flow entrained the rollup of the jet shear layer, forming a complex vortical system, composed of three vortices of negative spanwise vorticity and two of opposite vorticity near the wall. Over time, the multiple inner vortices eventually paired, so that only one stable rollup persisted in the jet pipe, in the same fashion as the corresponding unforced regime. The BR_{pp} parameter, directly related to the mass deficit between high and low parts of the cycle, was found to play a significant role in the scaling of the ingestion extent. This is also supported by the experimental observations that no ingestion was observed for $BR_{pp} < 0.15$.

- *Peripheral ingestion* - For higher values of BR_h, the cross-flow ingestion occurred on the whole circumference of the jet exit. The lack of seed in the cross-flow and the absence of visibility in the jet pipe prevented a more detailed characterization of this transition using Mie scattering visualizations. Numerical simulations were then used to gain additional physical insight on these transient regimes. The flow inside the jet pipe separated over the total circumference of the jet, therefore reducing the effective flow area and increasing the effective blowing ratio. The jet shear layer was clearly disrupted with the formation of regions of vorticity opposite to the natural shear layer vorticity at the jet exit. Only two regions at the jet exit, maintained positive velocity values throughout this transient and corresponded to the location of the roots of the CRVP.

The extent of the separation regions in both cases and the evacuation of transient structures inside the feeding pipe explained the rather "chaotic" character of the flow during the early moments of the low part of the cycle.

- *Film cooling performance* - In the starting hairpin vortex regime, during the early stages of the BR_l to BR_h transient regime, jet fluid continuously flowed from the upstream

DISTRIBUTION A: Distribution approved for public release.

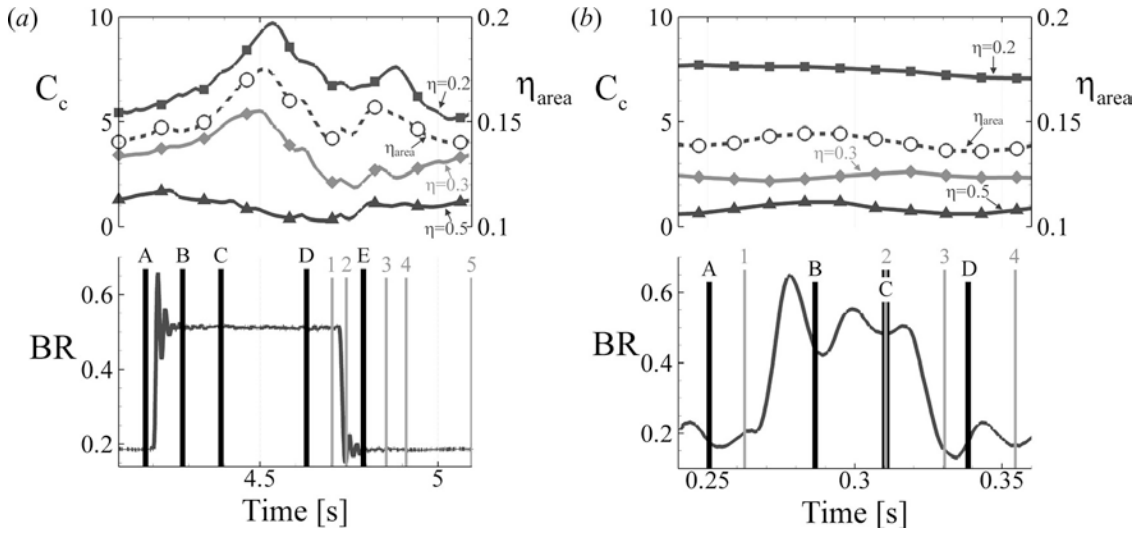

Figure 20: *Top*: Instantaneous coverage coefficient (*solid*) and area averaged adiabatic effectiveness (*dashed*); Bottom: Typical blowing ratio profile over a cycle for: (*a*) $BR_m = 0.35$, $DC = 50\%$ (*Case 4*) at $St_\infty = 0.016$ vertical bars represent snapshot instants for figure 19; (*b*) $BR_m = 0.35$, $DC = 50\%$ (*Case 4*) at $St_\infty = 0.0159$ vertical bars represent snapshot instants for figure 21.

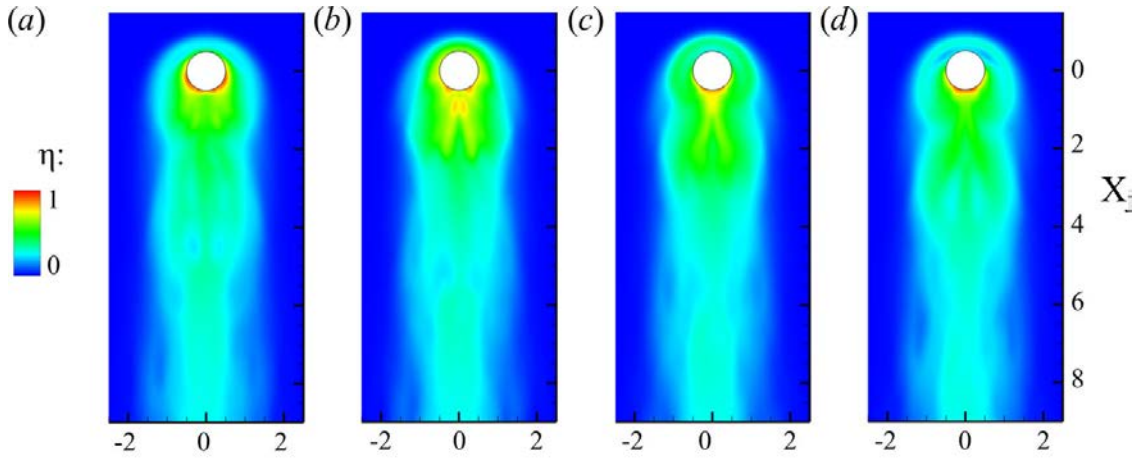

Figure 21: Instantaneous wall adiabatic effectiveness contours from LES. Top: $BR_m = 0.35$, $DC = 50\%$ (*Case 4*) at $St_\infty = 0.159$, time stamps: (*a*) $t^* = -0.16$; (*b*) $t^* = 0.20$; (*c*) $t^* = 0.44$; (*d*) $t^* = DC + 0.22$.

DISTRIBUTION A: Distribution approved for public release.

edge of the jet, weakening the inner vortex while slightly elevating and enhancing the principal horseshoe vortex, therefore temporarily preventing shedding of the inner vortex. An increase of the cooled area around the jet during the low-to-high transient part of the cycle was observed (figure 21*a-c*), relative to the previous low blowing ratio part. This was confirmed by the trends of the time dependent η_{area} and C_c values over a cycle (figure 20*a*). An increase in η_{area} and $C_c(\eta < 0.5)$ was observed immediately after the transition from low to high blowing ratio over one quarter of the cycle period ($t^* < 0.25$), compared to the values during the low part of the cycle. The supply of jet fluid to the upstream region was slowly disrupted as the pressure overshoot from the low-to-high blowing ratio transition settled and the difference in pressure increased across the jet/cross-flow interface. As the inner vortex was freed, the jet behaved in a quasi-unforced manner at $BR = 0.512$ and the coverage was dramatically decreased when the jet became transitional, and the values of η_{area} and C_c decreased continuously during the remaining high part of the cycle. These trends provide some guidance towards tailoring the forcing signal in order to improve film-cooling metrics. Truncating the high part of the cycle, before the quasi-unforced high blowing ratio state settles, could prevent the performance degradation after the transient associated with the arrival of the pulse has washed out, while retaining the initial improvement associated with the arrival of the pulse. At the high-to-low blowing ratio transition, ingestion of cross-flow fluid at the jet upstream lip occurred, and hot cross-flow fluid was entrained inside the jet pipe by the inner vortex and an instantaneous decrease in film coverage around the jet exit could be observed (figure 21*e*). As the jet settled in the low blowing ratio quasi-unforced regime, this pocket of hot fluid was slowly evacuated. This explained in part the lowest performance of the pulsed jet during the BR_h to BR_l transient part of the cycle relative to the unforced jet. This indicates that a smoother transition from BR_h to BR_l, for instance via a ramp signal, could suppress part of the ingestion by decreasing the mass deficit induced by the rapid jet draw down. At higher forcing frequency, injection of jet fluid in the upstream region occurred briefly at the jet onset but was not as prominent as the one observed at lower forcing frequency and was rapidly stopped as the jet shuts down. Instantaneous estimates of η_{area} and C_c (20*b*) showed almost no fluctuations throughout the cycle. Time averaged values for η_{span}, η_{area} and C_c extracted from simulated adiabatic effectiveness and presented in figure 22 and table 3 show that forced jets at $St_\infty = 0.016$ and $St_\infty = 0.159$ had very comparable performances in terms of spanwise averaged effectiveness and coverage, despite the significant fluctuations of instantaneous values of η_{span} and C_c observed in instantaneous trends at $St_\infty = 0.016$, compared to quasi-unforced values at $St_\infty = 0.159$. Overall, these two cases had spanwise averaged adiabatic effectiveness values approximately 30% lower than the corresponding unforced jet at equivalent mean blowing ratio ($BR = BR_m$). Accordingly, the coverage coefficients were on average 50% to 70% lower than corresponding unforced jet values at constant mass flow. The area averaged adiabatic effectiveness painted a similar picture. Simulations for *Case 3* showed significantly deteriorated performance compared to equivalent unforced results with 90% and 65% decrease in C_c and η_{area} respectively, attributed to the high value of BR_{pp}, yielding strong starting vortices and carrying coolant away from the wall, while generating large mass deficit at the jet shutdown and considerable cross-flow ingestion. The last two simulations at $BR_m = 0.45$, corresponding to *Case 12*, showed some improvement over the corresponding unforced jet results directly downstream of

DISTRIBUTION A: Distribution approved for public release.

Table 3: Coverage coefficient and area averaged adiabatic effectiveness from LES under forced conditions compared to equivalent mass flow rate unforced cases.

Conditions	C_c			η_{area}
	$\eta = 0.2$	$\eta = 0.3$	$\eta = 0.5$	
$BR = BR_m = 0.350 - St_\infty = 0$	12.82	7.02	2.15	0.226
$BR = BR_h = 0.513 - St_\infty = 0$	7.05	1.47	0.21	0.123
$Case\,4 - St_\infty = 0.016$	**7.22**	**3.23**	**0.81**	**0.162**
$Case\,4 - St_\infty = 0.159$	**7.26**	**2.63**	**0.66**	**0.145**
$BR = BR_h = 0.836 - St_\infty = 0$	1.91	0.21	0.05	0.071
$Case\,3 - St_\infty = 0.159$	**1.99**	**0.75**	**0.30**	**0.079**
$BR = BR_m = 0.450 - St_\infty = 0$	7.25	1.68	0.30	0.122
$BR = BR_h = 0.720 - St_\infty = 0$	3.96	0.47	0.08	0.093
$Case\,12 - St_\infty = 0.016$	**5.62**	**1.91**	**0.20**	**0.121**
$Case\,12 - St_\infty = 0.159$	**4.29**	**1.39**	**0.34**	**0.113**
$BR = 0.415 - St_\infty = 0$	14.42	7.87	2.17	0.247

the jet exit for $X_j < 4$. The coverage coefficients of the forced cases (table 3) matched or exceed the values of the unforced jet when $St_\infty = 0.159$, while the values of η_{area} were comparable to the unforced one. Overall, the forcing frequency appeared to have only a limited influence on film cooling performance of the jet for *Case 4* and *Case 12*. However, flow visualizations clearly showed that the degradation of the film cooling performance at $St_\infty = 0.016$ could be attributed to the settling of the jet in the high part of the cycle with transitional features such as the transport of the inner vortex, while at $St_\infty = 0.159$ the high entrainment of cross-flow fluid generated by the starting vortex was responsible for such performance decrease. Effectively the same outcome in terms of thermal performance was perpetrated by different flow dynamic mechanisms. Overall, jet forcing around an average value below the unforced transitional threshold had a greater influence (yet detrimental) on the film cooling metrics, than forcing around an average value beyond the transitional threshold. This shows that the beneficial effect of decreasing the blowing ratio below the transitional value during the low part of the cycle was less significant than the detrimental action of increasing it above this threshold.

DISTRIBUTION A: Distribution approved for public release.

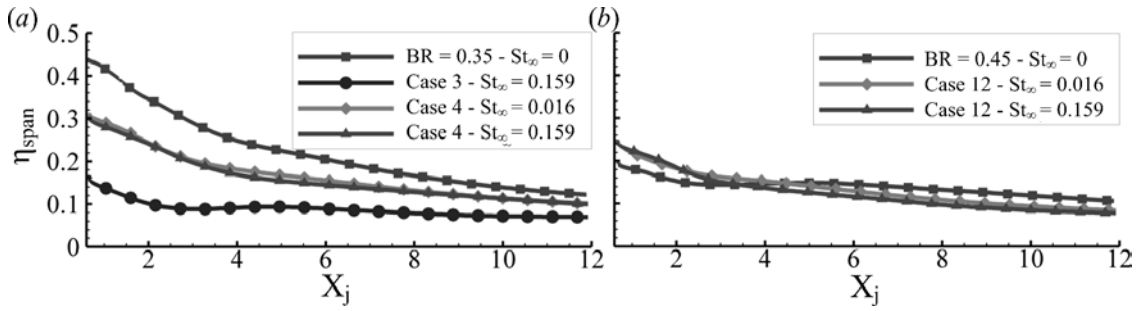

Figure 22: Spanwise averaged adiabatic effectiveness for forced jet in cross-flow and associated constant mass flow rate unforced jet results after LES.

DISTRIBUTION A: Distribution approved for public release.

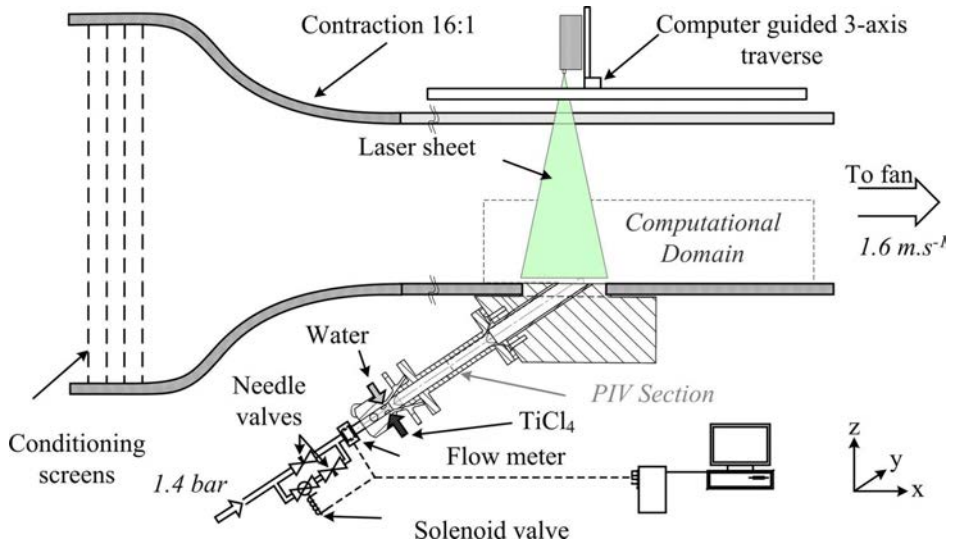

Figure 23: Inclined jet experimental apparatus.

2 Inclined Jet in Cross-flow

A more application-relevant geometry of a 35° inclined modulated jet over a flat plate is investigated using reactive Mie scattering visualizations, hot wire anemometry and PIV measurements, complemented by Large Eddy Simulations (LES) to provide details on the flow and temperature fields in the near-field of the jet exit. As for the vertical jet, the first part focuses on the characterization of the unforced jet baseline, while the second section investigates the specifics of modulated inclined jets.

2.1 Experimental and Numerical Setup

2.1.1 Wind Tunnel Experiments

The experiments for the 35° jet were carried out in the same wind tunnel as the one used in the 90° jet study. Notations and coordinate systems for the inclined jet were also identical to the previous chapter, taking the origin at the jet exit center. The only major difference between both configurations was the implementation of a PIV (Particle Image Velocimetry) section in the jet pipe consisting in a square acrylic tube of $6D_j$ long presented in figure 23. This section will be used in a close future for PIV (Particle Image Velocimetry) measurements in view of obtaining realistic inlet conditions for LES. The cross-flow conditions were identical to the 90° jet study and are provided in table 1. The jet exited from a $25.4mm$ round tube mounted flush to the bottom wall at an angle of 35° with respect to the cross-flow direction and zero compound angle. The tube length, including the PIV section was approximately $12D_j$. A seeding system injecting $TiCl_4$ and water inside the jet was also used during reactive and fully reacted Mie scattering visualizations. The jet supply system was identical to the one of the vertical jet with two branches one of which includes a computer-controlled solenoid valve used to pulse the flow (figure 23). The experiment was designed so that the jet natural frequencies would be relatively low ($< 100Hz \sim St_\infty = 1.5$) and forcing is applied at

DISTRIBUTION A: Distribution approved for public release.

Table 4: Simulation parameters for the ROM grid.

	$BR = 0.15$	$BR = 0.5$	$BR = 1.0$	*Case IV*
Fluctuation levels	30%	50%	60%	50%
Number of vortices	150	190	210	190
Time step	1×10^{-4}	5×10^{-5}	1×10^{-5}	1×10^{-5}

frequencies lower than these natural frequencies consistently with the scaled-down (relative to this work) experiments of (25) and theoretical assessments of (55).

In the forced jet experiment, an additional visualization plane (Y-Z) was acquired at four distinct streamwise locations of $X_j = 0$, 0.5, 1 and 1.5. For those visualizations, the camera was set downstream of the visualization plane at an angle of approximately 30° with the streamwise direction and the focus plane was adjusted using a Scheimpflug mount offsetting the lens axis from the camera sensor axis to satisfy the Scheimpflug condition (see (61)). The obtained images were then dewarped based on a linear transformation algorithm, using a previously acquired calibration image. These images (and the one in the $Y_j = 0$ plane for the forced jet) were obtained in a time resolved manner at 1000 frames per second (fps) using a Dantec Dynamics Nanosense MkIII camera with a 1280×1024 sensor. Finally, the forced jet was also documented using 2D-PIV measurements in the $Y_j = 0$ plane. These measurements were obtained using the same camera operated at $500fps$ with an average time delay between both laser shots of $\Delta t = 250ms$. An adaptive correlation algorithm was used with an initial interrogation window of 64 pixels, a final interrogation window of 16 pixels and a 50% overlap. At least 30 cycles were acquired for each forcing conditions to obtain accurate phase averages. Seeding for PIV measurements was achieved using $2\mu m$ porous silica particles with extremely low specific gravity and high reflectivity, following the flow very accurately.

2.1.2 Numerical Simulations

As for the previous configuration, numerical simulations were carried out in parallel to the experiments using Ansys Fluent$^{\text{TM}}$. Large Eddy Simulations (LES) with dynamic Smagorinsky sub-grid scale models were used. A set of three simulation grids was used in this part of the study. All three of them were built on the same principles as the vertical jet grid, representing a part of the jet pipe and of the wind-tunnel test section.

2.1.2.1 Mechanistic Analysis Grid The first grid corresponded to the one used in (74). This grid was primarily used for flow understanding and a preliminary statistical POD analysis. The domain consisted of a rectangular box representing a part of the wind-tunnel test section and part of the jet feeding tube. The computational domain was $18D_j$ long (x-direction), $8D_j$ wide (y-direction) and $8D_j$ tall (z-direction), respectively discretized into $160 \times 100 \times 90$ hexahedral cells, while the jet pipe feeding was $8D_j$ long, discretized by 2000 nodes in the cross-section and 120 nodes in the axial direction. The grid was structured and counted approximately 1.6 million hexahedral cells. The jet exit center was located $6D_j$ downstream from the domain inlet. The first cells in contact with the walls were approximately $0.03D_j$ tall, providing average y^+ values of the order of 1, thus reaching the

DISTRIBUTION A: Distribution approved for public release.

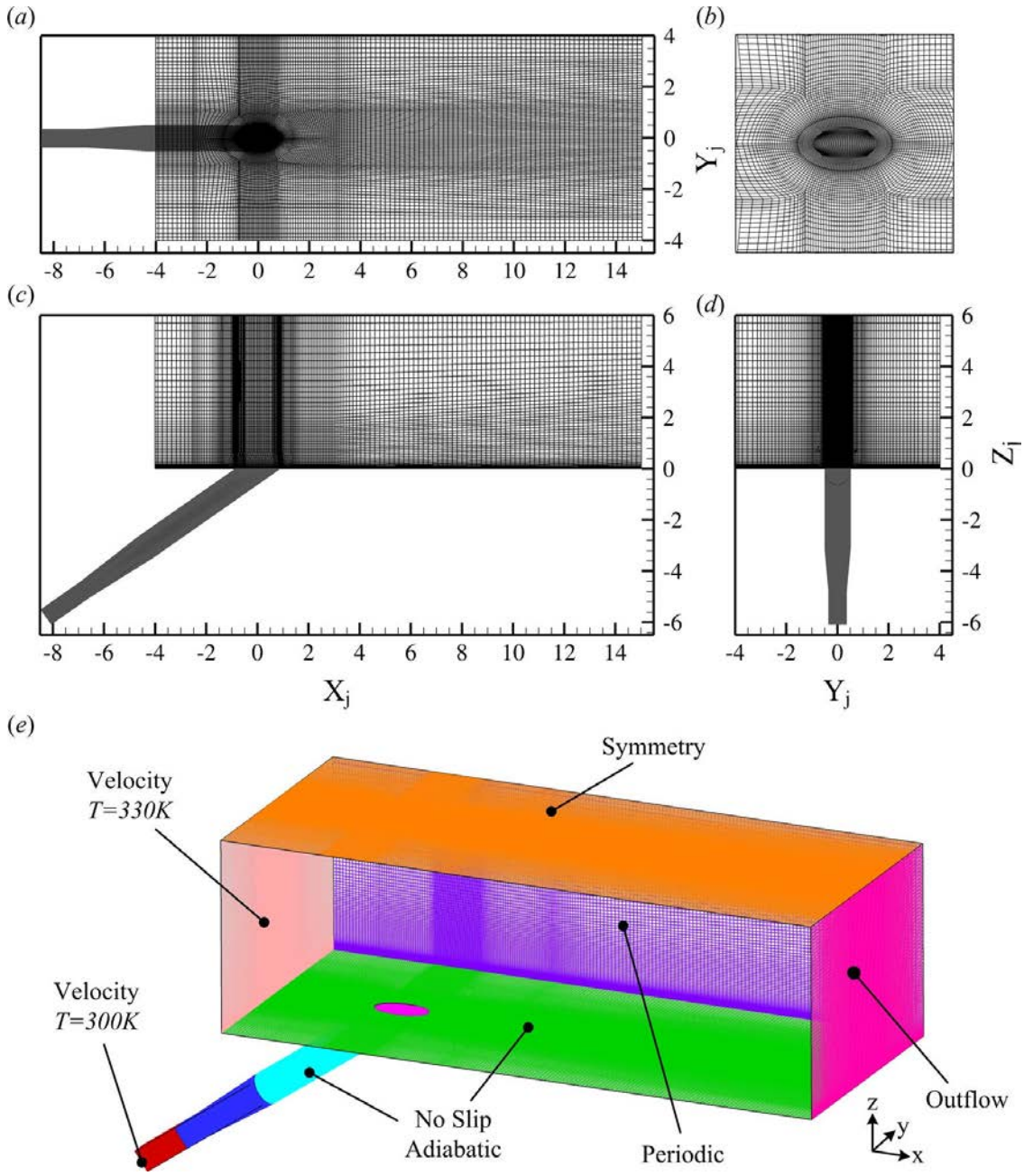

Figure 24: Inclined jet numerical grid details and boundary conditions. (a) X-Y view, (b) X-Y view detail, (c) X-Z view, (d) Y-Z view, (e) global view and boundary conditions.

DISTRIBUTION A: Distribution approved for public release.

viscous sub-layer and allowing direct solving of the wall shear stress from laminar stress-strain relationship, without using wall functions.

Velocity characteristics and boundary layer profiles for the inlet of the computational domain were obtained from hot wire measurements performed in the wind tunnel as summarized in table 1. The numerical solver used was pressure based with second order accuracy in time and space. The integration time steps used ranged from $5.10^{-5}s$ at $BR = 1.2$ to $5.10^{-4}s$ at $BR = 0.15$ so as to remain below the minimum Kolmogorov time scale in the domain. At the inlet of the jet pipe, uniform velocity profile was set so as to equal the volumetric flow rate of the experiment. The jet and cross flow fluids were maintained at constant temperature of respectively 300 and $330K$, not affecting the velocity field. A grid independence study was carried out using this particular grid and is available in (74).

2.1.2.2 Reduced Order Modeling Grid The second grid is presented in figure 24 and corresponded to a refined and extended version of the first grid. It was primarily used to obtain flow and temperature fields snapshots for reduced order modeling purposes. The domain was extended of $3D_j$ in the downstream direction and the jet exit relocated $4D_j$ downstream of the domain inlet to give a $19D_j$ long grid. The spanwise dimension was left unchanged while the height is brought down to $6D_j$. The pipe geometry was slightly modified to account for an updated, longer jet pipe PIV section. The main domain comported $240\times148\times75$ hexahedral cells in respectively the streamwise, spanwise and vertical directions. The jet pipe was meshed using an O-grid of 6500 cells in the cross-section and 175 cells in the pipe axis direction. This accounted for a total of over 4 million cells. The first cell in contact with the wall was on average $0.005D_j$ tall resulting in much less than unity y^+ values. The main domain inlet velocity profile was obtained from experimental measurements as summarized in table 1. The pipe inlet velocity profile was obtained from $k-\omega$ simulations in Fluent using the inlet condition grid described below. Perturbations to the velocity field were added at the pipe inlet using Fluent vortex method with a length scale of D_j. The perturbation levels and number of vortices were adjusted on a case-to-case basis so as to match point-wise hot wire measurements at the jet exit and are summarized in table 4. High perturbation levels had to be implemented to recreate the fluctuation levels introduced by the injection jets of the seeding system (see inlet condition grid below). The integration time step for each individual blowing ratio case was evaluated based on the Kolmogorov time-scale determined from initial $k-\epsilon$ RANS simulations. The corresponding time steps are summarized in table 4.

A series of constant temperature anemometry measurements were performed at blowing ratios of $BR = 0.15$, $BR = 0.5$ and $BR = 1.0$, at 4 different streamwise locations ($X_j = 0$, 2.5, 5, 10) and are presented in figure 25 along with extracted corresponding simulation results. Overall the LES results compared extremely well with the experimental measurements at all streamwise locations and at all three blowing ratio. Only a minor discrepancy was found directly at the jet exit at $BR = 0.15$ which could be attributed to rectification of the hot wire probe signal. Indeed, at such low blowing ratio, the seeding flow rate accounted for a large amount of the overall jet flow rate (more than 60%) and the fluctuation levels introduced by the seeding jets along the hot wire direction were likely non-negligible and could locally increase the sensed velocity magnitude. These validation measurements provided good confidence in the obtained numerical results.

DISTRIBUTION A: Distribution approved for public release.

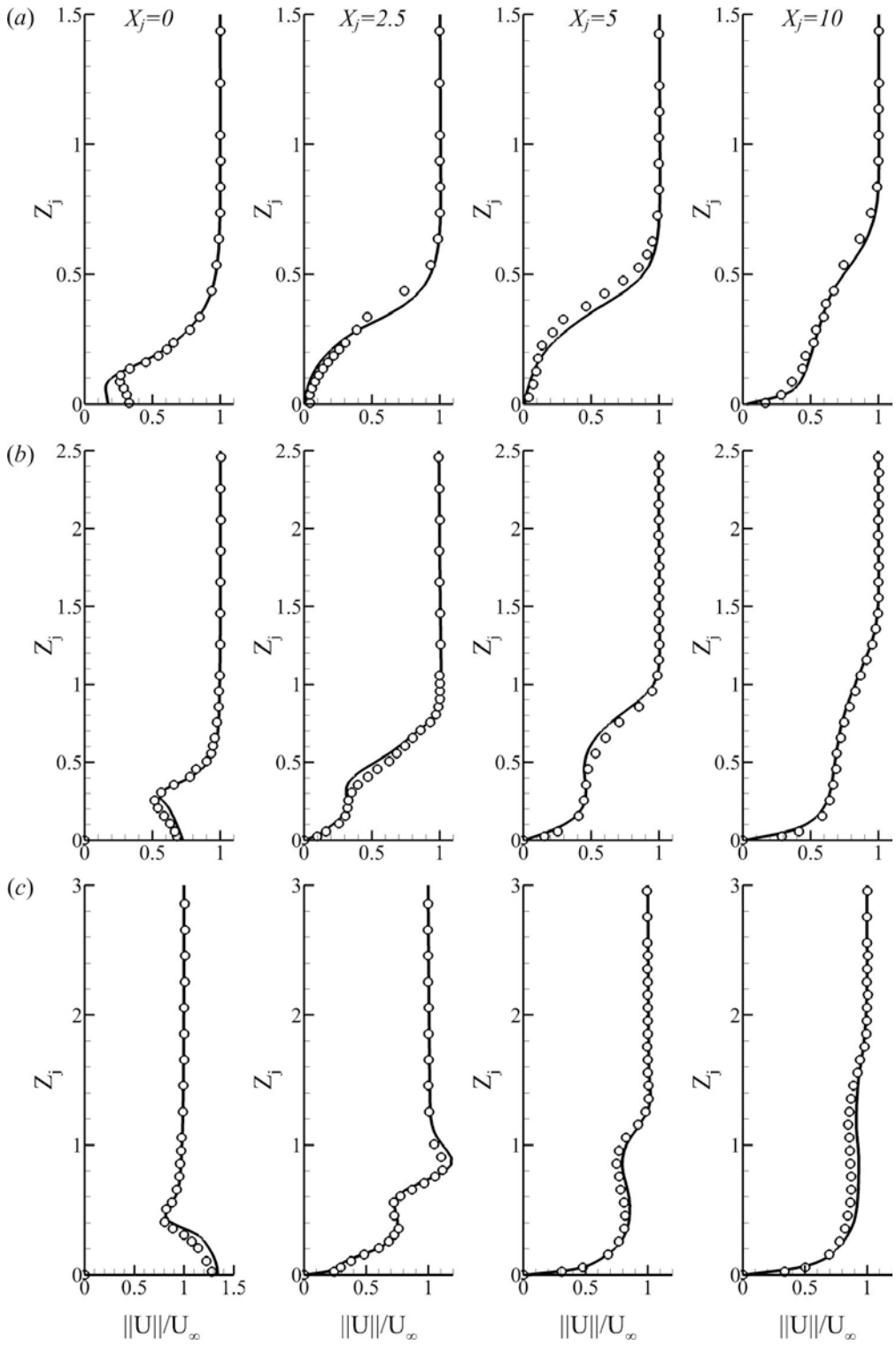

Figure 25: Experimental (*symbols*) and LES (*solid line*) time averaged velocity magnitude profiles at (*a*) $BR = 0.15$; (*b*) $BR = 0.5$; (*c*) $BR = 1.0$ at $X_j = 0$, 2.5, 5 and 10.

DISTRIBUTION A: Distribution approved for public release.

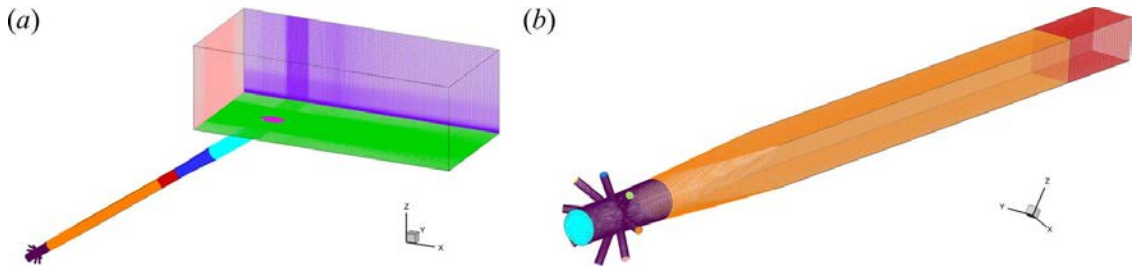

Figure 26: Extended inlet conditions grid.

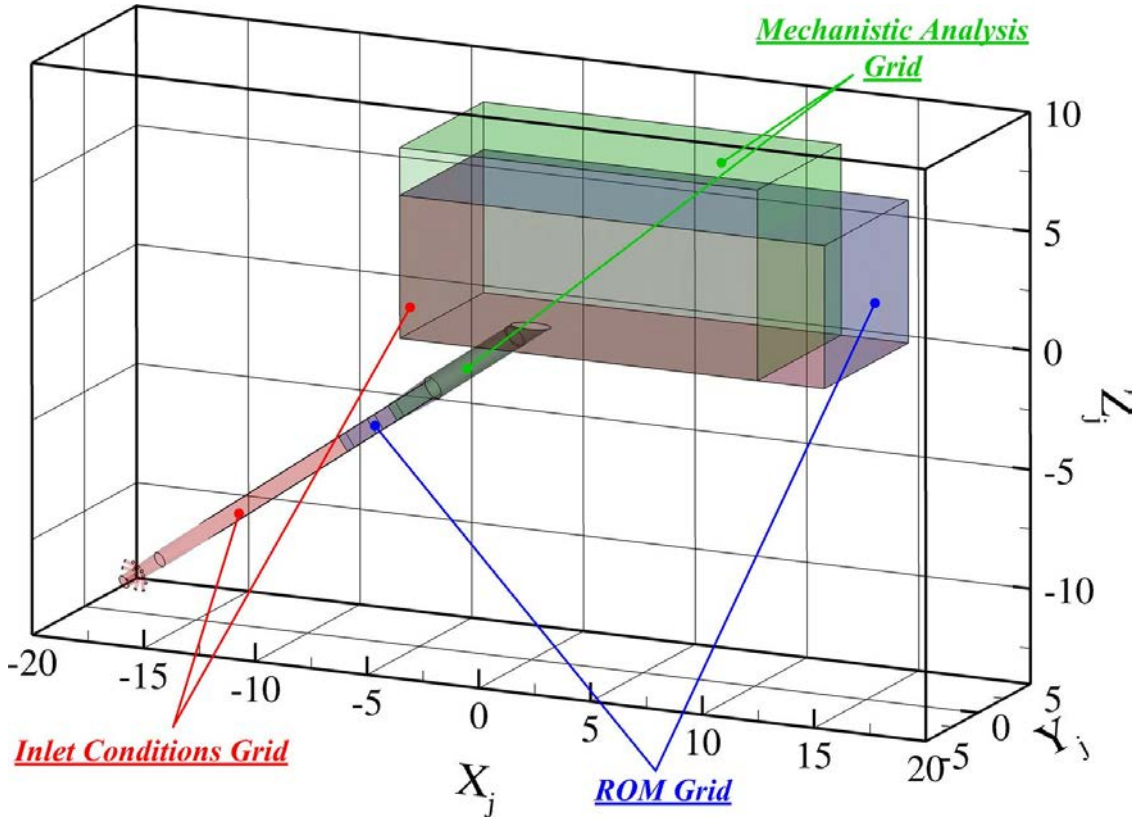

Figure 27: Geometries of the different grids.

2.1.2.3 Inlet Conditions Grid A third and last grid was used to obtain the jet inlet velocity profile. This grid was based on the previous one, with an extended pipe geometry, including the complete jet PIV section, seeding injection block and jets and an approximation of the flow-meter geometry. Figure 26 shows the extended pipe geometry. The complete mesh comported 5.7 million cells. The simulations were ran with a $k-\omega$ model with fully developed inlet velocity profiles for the main pipe inlet as well as the seed injection jets. Average velocity magnitude profiles were extracted at the location of the ROM grid inlet plane and used as inlet conditions for these simulations.

Finally, figure 27 shows the geometries of all the different grids for comparison purposes.

DISTRIBUTION A: Distribution approved for public release.

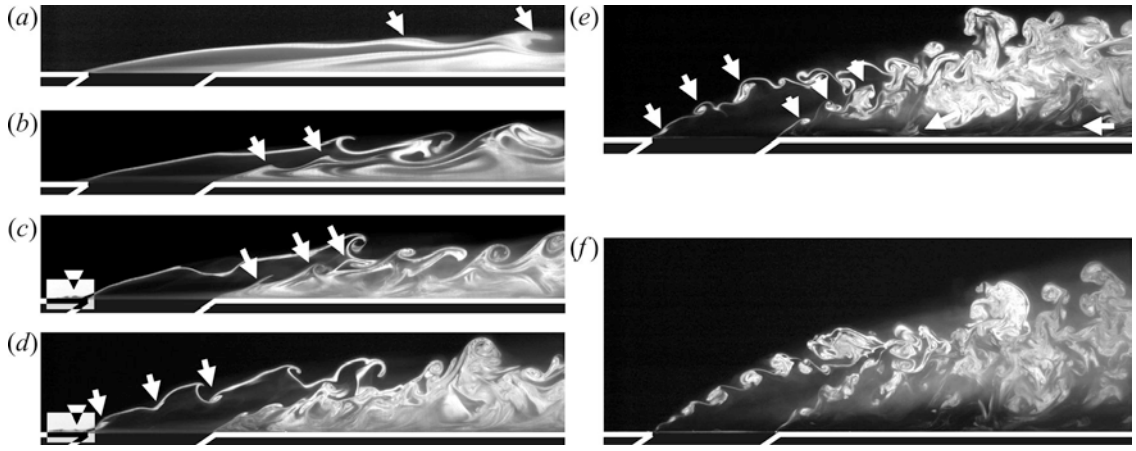

Figure 28: Experimental Mie scattering visualizations in the plane $Y_j = 0$ at (a) $BR = 0.15$; (b) $BR = 0.3$; (c) $BR = 0.4$; (d) $BR = 0.75$; (e) $BR = 1.1$; (f) $BR = 1.2$.

2.2 Unforced Jet

In unforced conditions, the jet was studied using reactive and fully reacted Mie scattering visualizations. Selected cases at $BR = 0.15$, 0.3, 0.4, 0.75, 1.0 and 1.2 were simulated with LES using the mechanistic analysis grid. Similarly to the vertical jet in cross-flow described in the previous section, several unforced jet regimes were observed. At low blowing ratios under $BR = 0.4$, the jet was fully attached to the wall while at blowing ratios above $BR = 1.0$, the jet was found to be completely detached from it. At intermediate blowing ratios, the jet exhibited vortical structures from both regimes.

The attached jet was the most relevant configuration to film cooling and shows strong similarities with the vertical jet configuration. A series of characteristic vortical structures were also identified:

- *Recirculation region* - Directly downstream of the jet exit, an area of reacted seed evidenced the characteristic recirculation region present in the attached jet configuration (figure 28a). This region, mainly supplied by jet fluid, was also observed in the LES results and corresponded to an area of lower temperatures encompassed by the hairpin vortices legs (in figure 29a, c). This region was found to be much smaller than the one found in the vertical jet configuration at comparable blowing ratio values.

- *Shear layer interlocked hairpin vortices* - The dominant shear layer vortical structures consisted in interlocked hairpin vortices observed in the experimental side-views as well as the LES renderings at $BR = 0.15$ (figures 28a 29a-b), developing as a result from Helmholtz or Landman-Saffman type of instability in the jet shear layers. At low blowing ratio ($BR = 0.15$), the instability developed sooner in the upper shear layer where the initial rollup occurred first, and eventually both upper and lower shear layers merged a few diameters downstream of the jet exit and the hairpin vortex fully formed. The dynamics of the hairpin vortices were comparable to those observed for the vertical jet and dictated by cross-flow convection as well as mutual, self, and mirrored inductions with respect to the bottom wall. At $BR = 0.3$ (figure 28b), instability in the lower shear layer started to develop and eventually at $BR = 0.4$ (figure 28c) both

DISTRIBUTION A: Distribution approved for public release.

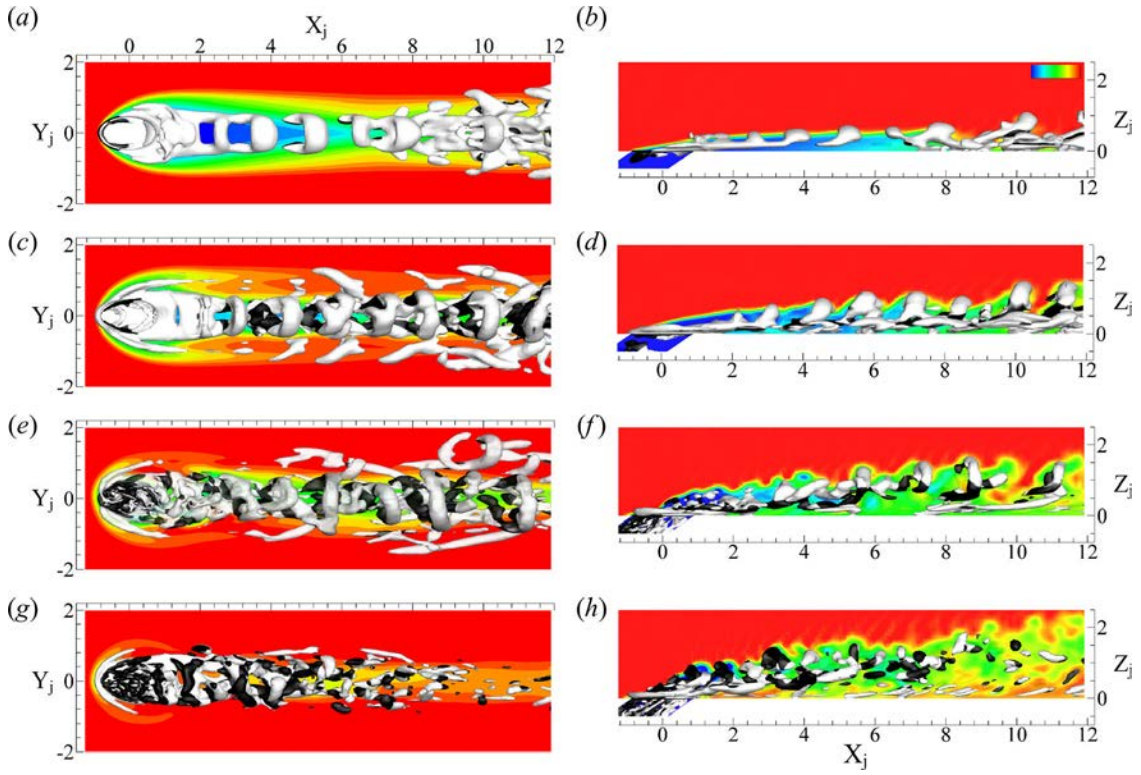

Figure 29: Laplacian of the pressure iso-surfaces from LES colored with spanwise vorticity contours from negative (*black*) to positive (*white*) at (*a*-*b*) $BR = 0.15$, $\Delta P = 0.4kPa.m^{-2}$; (*c*-*d*) $BR = 0.4$, $\Delta P = 0.7kPa.m^{-2}$; (*e*-*f*) $BR = 0.75$,$\Delta P = 2.5kPa.m^{-2}$; (*g*-*h*) $BR = 1.2$, $\Delta P = 5kPa.m^{-2}$ and instantaneous temperature contours in the planes $Z_j = 0$ (*left*) and $Y_j = 0$ (*right*).

DISTRIBUTION A: Distribution approved for public release.

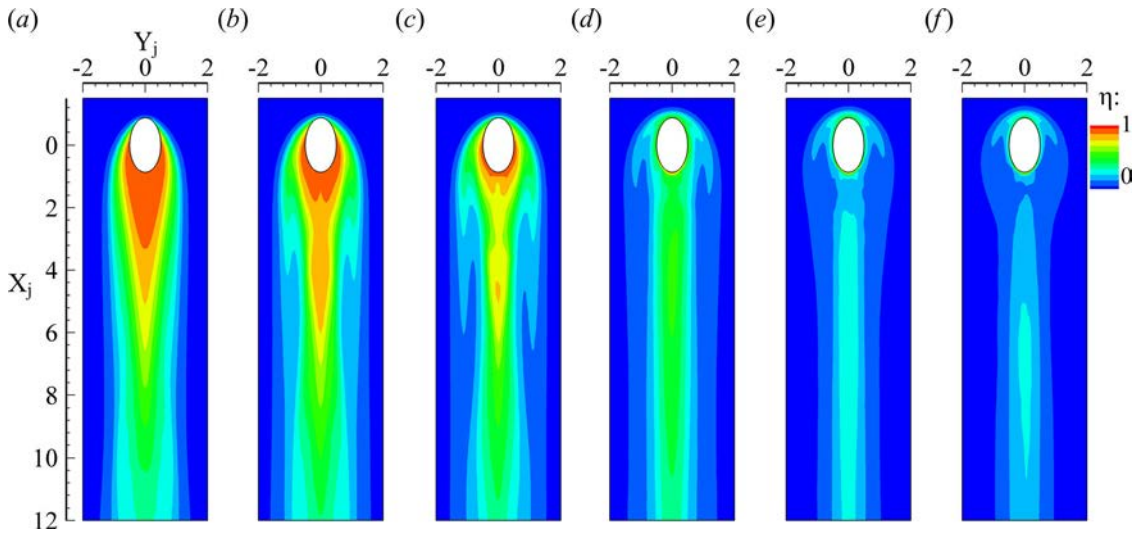

Figure 30: Wall adiabatic effectiveness contours from LES at (a) $BR = 0.15$; (b) $BR = 0.3$; (c) $BR = 0.4$; (d) $BR = 0.75$; (e) $BR = 1.0$; (f) $BR = 1.2$.

shear layers exhibited distinct rollups, each corresponding to a hairpin vortex, merging as they were convected downstream.

- *Horseshoe vortex* - Upstream of the jet exit, the horseshoe vortex system was absent from the experimental side visualizations at the lowest blowing ratios of $BR = 0.15$ and $BR = 0.3$, as well as from the LES results (figure $29a$). However, a pair of streamwise vortices containing vorticity coherent with the horseshoe vortex developed on the sides of the jet without connecting upstream in the usual U-shape as evidenced. This is identical to the mechanism responsible for the formation of the counter-horseshoe vortex and the side vortices in the 90° jet configuration. The absence of a full horseshoe vortex has been documented in previous studies such as (72) or (31) in cases where the cross-flow blockage due to the presence of the jet was weak. At $BR = 0.4$, the jet blockage was important enough to cause the cross-flow boundary layer to fully separate upstream of the jet exit and form a complete horseshoe vortex (figure $28c$ and $29c$). Conversely to the vertical jet, the horseshoe vortex was never found to be transported over the jet due to the absence of destabilizing interaction with the inner vortex in this setup.

- *Wall side vortices* - At $BR = 0.15$, in the far-field of figure $29(a)$ X-patterned structures were formed around $X_j = 10$, identical to the ones observed in the attached vertical jet setup. These became stronger and started forming earlier as the jet blowing ratio and the associated cross-flow deflection increased.

The inner vortex was found to be absent to the inclined jet configuration due to lower adverse pressure gradient for the flow exiting the jet pipe. It should be noted that conversely to the vertical jet, the horseshoe vortex was never found to be transported over the jet. This is also explained by the absence of destabilizing interaction with the inner vortex in this setup.

DISTRIBUTION A: Distribution approved for public release.

- *Film cooling performance* - The impact of the different vortical structures on the wall temperature and the film cooling performance were investigated using the results from the simulations. In the attached jet configuration, the shear layer vortical structures had a strong influence on the wall temperature field since they carried most of the coolant fluid from the jet while generating a velocity field responsible for entraining cross-flow fluid into the wall region (figure 29*c*-*d*). Jet fluid exited from the sides of the jet exit, very close to the wall to provide significant wall coverage as evidenced by the temperature contours of figure 29(*a*) and 29(*c*). Quantitative information was extracted from the numerical simulations to provide a performance benchmark to the forced results and was also compared to the vertical jet results. At $BR = 0.15$, (figure 30*a*), the area of high adiabatic effectiveness directly downstream of the jet exit corresponded to the recirculation region enclosed by the legs of the successive hairpin vortices. As the blowing ratio was increased up to $BR = 0.4$, the hairpin vortices legs with higher circulation lifted off the wall sooner due to self induction and therefore carried coolant away from the wall, resulting in film coverage breakup and entrainment of hot cross-flow fluid near the wall (figure 29*a*-*d*). On the other hand, from $BR = 0.15$ to $BR = 0.4$, a relative increase in spread was observed further away from the jet exit ($X_j \geq 7$) due to the beneficial effect of the side vortices and their favorable velocity field, as well as near the jet exit due to the strengthening and formation of the horseshoe vortex. However, due to the absence of inner vortex in the inclined jet configuration, the upstream region was almost not cooled at all. As the jet entered the transitional regime ($0.4 < BR \leq 0.9$), the wall coverage downstream of the hole was degraded due to lift off of the shear layer structures. The coverage finally became marginal in the detached configurations where the jet wake was the only region showing some form of cooling effect. Spanwise averaged adiabatic effectiveness η_{span} as well as center-line adiabatic effectiveness $\eta_{centerline}$ and comparable results from the vertical jet (figure 31*a*), showed that directly downstream of the jet exit ($X_j < 6$), the case at $BR = 0.15$ demonstrated best performance due to the presence of the steady recirculation region fed by jet fluid. However further downstream ($X_j > 6$) the case at $BR = 0.3$ provided best adiabatic effectiveness due to the increased coolant flow rate and spread over the case at $BR = 0.15$. As the blowing ratio was increased beyond 0.3, the spanwise averaged performance of the inclined jet decreased consistently. The center-line results for the inclined jet (figure 31*b*) showed similar trends. The local decrease in $\eta_{centerline}$ observed for $BR \geq 0.3$ directly downstream of the jet exit was attributed to early lift-off of the shear layer vortices. For $BR \leq 0.3$, the inclined jet showed greater spanwise averaged and center line adiabatic effectiveness, compared to the vertical jet. However, the inclined jet performance was degraded beyond $BR = 0.3$, which was not the case for the vertical jet where performance continued to increase up to $BR = 0.415$. Consequently, at $BR = 0.4$, the vertical jet exhibited greater η_{span} values than those of the inclined configuration. At higher blowing ratios ($BR \geq 0.75$), the inclined jet performed better than the vertical jet. The $\eta_{centerline}$ trends showed that the inclined jet always provided greater center-line effectiveness over the vertical jet. This confirmed that the overall better performance of the vertical jet at $BR = 0.4$ was essentially provided by a greater spanwise spread of the film. Area-averaged adiabatic effectiveness and coverage coefficient estimates for both inclined and vertical jets (figure 32), provided a global performance index at every blowing ratio. The η_{area} trends for the inclined jet exhibited a constant decrease in performance past

DISTRIBUTION A: Distribution approved for public release.

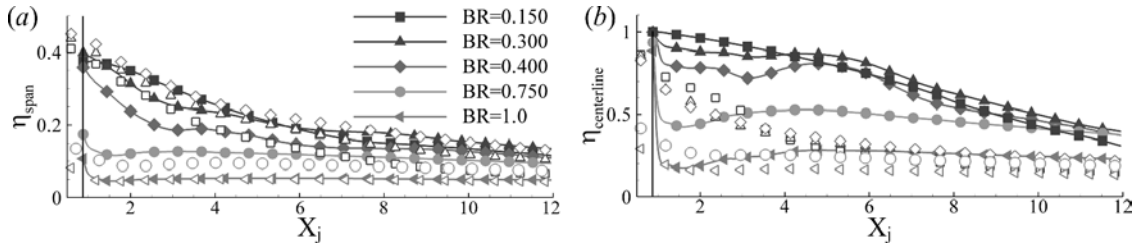

Figure 31: Film cooling performance: (a) Spanwise averaged adiabatic effectiveness η_{span}; (b) center-line adiabatic effectiveness $\eta_{centerline}$ after LES for the inclined jet (*solid line*, *filled symbols*) and the vertical jet (*open symbols*).

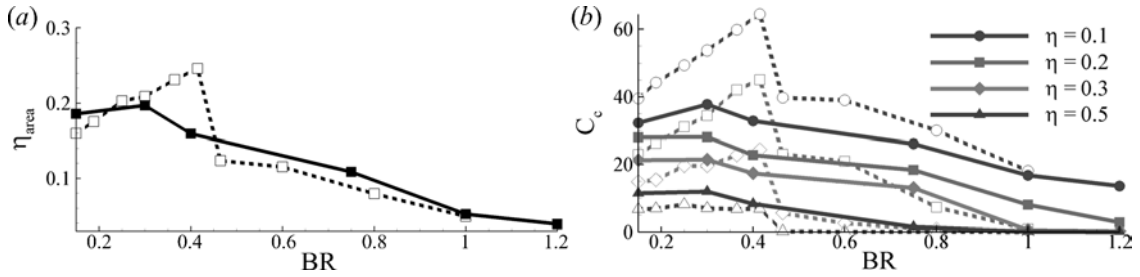

Figure 32: Unforced film cooling performance (a) Area averaged adiabatic effectiveness η_{area} for the inclined jet (*solid line*) and the vertical jet (*dashed line*); (b) coverage coefficient C_c for thresholds $\eta = 0.1, 0.2, 0.3, 0.5$.

$BR = 0.3$ with a slight improvement from $BR = 0.15$ to $BR = 0.3$. This result was consistent with observations based on η_{span} values. The improvement from $BR = 0.15$ to $BR = 0.3$ was attributed to an increase in η values beyond $X_j = 5$. A local maximum was found between $BR = 0.15$ and $BR = 0.3$ which was rather low for an inclined jet configuration and could be justified by the use of single jet in laminar cross-flow conditions. The comparisons with the vertical jet results showed that the expected performance degradation as the blowing ratio increased was less abrupt in the inclined configuration than in the vertical setup. Interestingly, the vertical jet performed better at $BR = 0.415$ with an area averaged adiabatic effectiveness of 0.225 within the considered field of view ($-1.2 < X_j < 12$). The coverage coefficient trends confirmed the above mentioned results with a consistent decrease in performance beyond $BR = 0.3$ for the inclined jet. Once again when compared to the vertical jet, the inclined jet provided more coverage at high effectiveness ($\eta \geq 0.5$) values. The vertical jet though provided significantly greater coverage at lower effectiveness levels (almost double in some cases), sign of increased spread at higher injection angles. Higher spread and performance in the neighborhood of the jet exit ($X_j < 12$) for high injection angles were previously reported in studies such as (79).

The overall greater performance of the vertical jet in this study should be put in perspective with respect of two considerations. First, the domain of the current study was limited to the near field ($X_j < 12$), which in (79) was the approximate streamwise location beyond which the inclined jet started to evidence better performance than the vertical one.

DISTRIBUTION A: Distribution approved for public release.

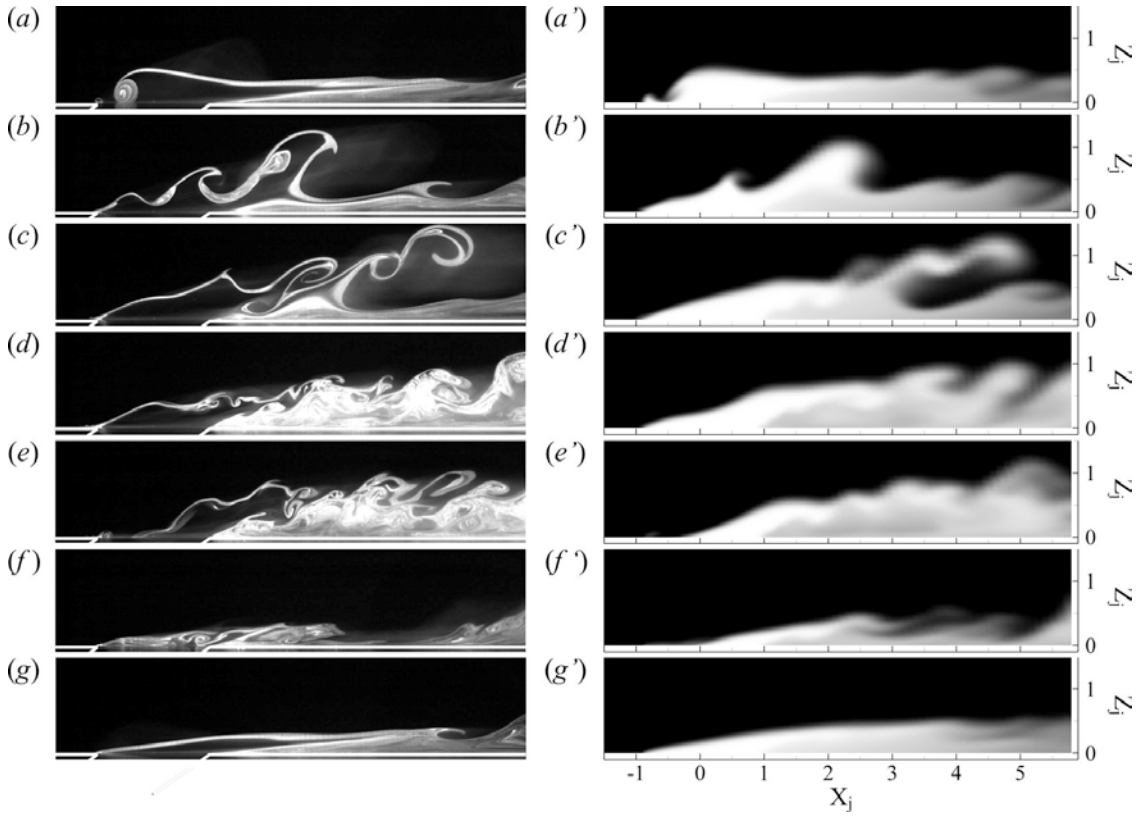

Figure 33: Instantaneous reactive Mie scattering visualizations in the plane $Y_j = 0$ (*left*) and temperature field from LES (*right*) at: (*a*) $t^* = 0.04$; (*b*) $t^* = 0.09$; (*c*) $t^* = 0.13$; (*d*) $t^* = 0.49$; (*e*) $t^* = DC + 0.07$; (*f*) $t^* = DC + 0.19$; (*g*) $t^* = DC + 0.47$ for *Case X* at $St_\infty = 0.016$.

Also, it was demonstrated in the vertical jet study that the sudden decrease in performance in the 90° injection configuration was due to a destabilization of the inner vortex formed inside the jet tube, extremely sensitive to both cross-flow and jet inlet conditions. Hence, it is expected that outside the laminar cross-flow boundary layer conditions used in this study, the transition for the vertical jet could happen significantly sooner, therefore leading to better performance for the inclined configuration.

2.3 Forced Jet

Forced jet experiments were carried out using a nominal square wave excitation according to the forcing parameters summarized in Table 5. Most of those cases were observed at 4 forcing frequencies of 0.5, 1.0, 5.0 and $10.0Hz$, respectively corresponding to Strouhal numbers of $St_\infty = 0.008$, 0.016, 0.079 and 0.159.

As for the the forced vertical jet configuration, a total of four phases can be identified during forced cycles.

DISTRIBUTION A: Distribution approved for public release.

Table 5: Forced inclined jet cases. *: Simulations carried at these conditions using mechanistic analysis grid, †: Simulations carried out at these conditions using ROM grid.

Case#	BR_m	BR_l	BR_h	BR_{pp}	$DC(\%)$
I	0.151	0.150	0.250	0.100	0.7
II	0.200	0.150	0.250	0.100	50
III	0.153	0.150	0.500	0.350	0.7
IV†	0.325	0.150	0.500	0.350	50
V	0.156	0.150	1.00	0.850	0.7
VI	0.575	0.150	1.00	0.850	50
VII	0.164	0.150	2.00	1.85	0.7
VIII	1.08	0.150	2.00	1.85	50
IX	0.171	0.150	3.00	1.85	0.6
X*	0.300	0.150	0.450	0.300	50
XI*	0.450	0.150	0.750	0.600	50
XII	0.875	0.750	1.00	0.250	50
XIII	1.08	0.650	1.50	0.850	50
XIV	1.58	1.15	2.00	0.850	50
XV	1.88	1.75	2.00	0.250	50

- *Starting vortices* - transient introduced at the transition from BR_l to BR_h consisting in the formation of a single or series of vortical structures (figure 33*a-c*).
- *Quasi-unforced regime established at high blowing ratio* - settled as the transient associated with the starting vortices was washed away and while the jet remained at high flow rate. In this phase, the jet behaves identically to an unforced jet at equivalent blowing ratio of BR_h (figure 33*d*).
- *Cross-flow ingestion* - transient triggered by the sudden decrease in mass-flow at the moment the solenoid valve is closed and the blowing ratio transitions from BR_h to BR_l. During this phase (figure 33*e*, *f*), cross-flow fluid is ingested inside the jet pipe and the jet flow is disrupted.
- *Quasi-unforced regime at low blowing ratio* - established as the transient dynamics from the ingestion are washed away while the jet remains in low flow rate. In this part of the cycle, the jet behaves similarly to an unforced jet at equivalent blowing ratio of BR_l (figure 33*g*).

As for the vertical jet, the two quasi-unforced regimes were not always observed depending on the duty cycle and forcing frequency which determine the duration of the low and high parts of the cycle and therefore the available time for the transients to be evacuated before the next transient is introduced. In the current study, a majority of the cases at $St_\infty = 0.008$ and $St_\infty = 0.016$ (respectively corresponding to 0.5 and $1Hz$) exhibits all four regimes while cases at $St_\infty = 0.08$ and $St_\infty = 0.159$ (respectively 5 and $10Hz$) only exhibits the transients.

DISTRIBUTION A: Distribution approved for public release.

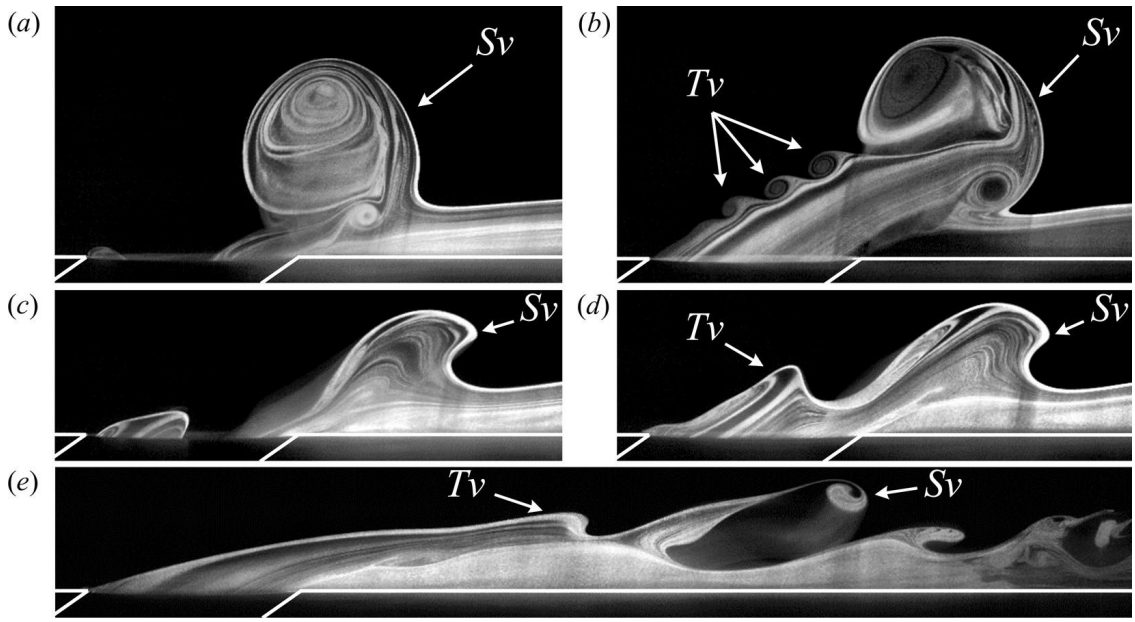

Figure 34: Mie scattering visualizations in the plane $Y_j = 0$ for (a) *Case V* at $St_\infty = 0.008$ – Single starting vortex ring; (b) *Case VIII* at $St_\infty = 0.008$ – Leading starting vortex ring and trailing vortices; (c) *Case III* at $St_\infty = 0.008$ – Single compound starting vortex; (d) *Case IV* at $St_\infty = 0.008$ – Compound starting vortex and trailing vortices; (e) *Case II* at $St_\infty = 0.008$ - Starting hairpin vortex and trailing vortex. (Sv) Starting vortex, (Tv) Trailing vortices.

2.3.1 Low-to-High Blowing Ratio Transition: Starting Vortices

- Starting vortices - In the forced inclined jet configuration, starting vortices were also observed as the blowing ratio transitioned from BR_l to BR_h due to the associated sudden increase in shear at the jet/cross-flow. While for the vertical jet only two principal regimes of starting structures/systems were identified, the inclined jet exhibited six dominant types of starting vortices presented in figure 34.

  - *Single starting hairpin vortex* - At the lower end of the investigated BR_h range, and for short injection times, the starting vortices consisted of a rather large hairpin vortex with dynamics were overall identical to the ones of the unforced jet. Because of the inclined geometry of the jet, the expansion wave generated at the valve opening reached the leading edge of the jet exit first and triggered the formation of a shear layer rollup with negative vorticity at the leading edge. However, due to the relatively low magnitude of the pulse, the vorticity generated at the leading edge remained low and the rollup was rapidly dissipated by the incoming boundary layer with opposite vorticity before it could accumulate enough circulation to be transported. The transition from low to high blowing ratio in those cases did not carry enough energy to force the jet shear layer to roll into a coherent starting vortex. However, the propagation of the expansion wave into the free stream acted as a perturbation for the natural jet shear layer

DISTRIBUTION A: Distribution approved for public release.

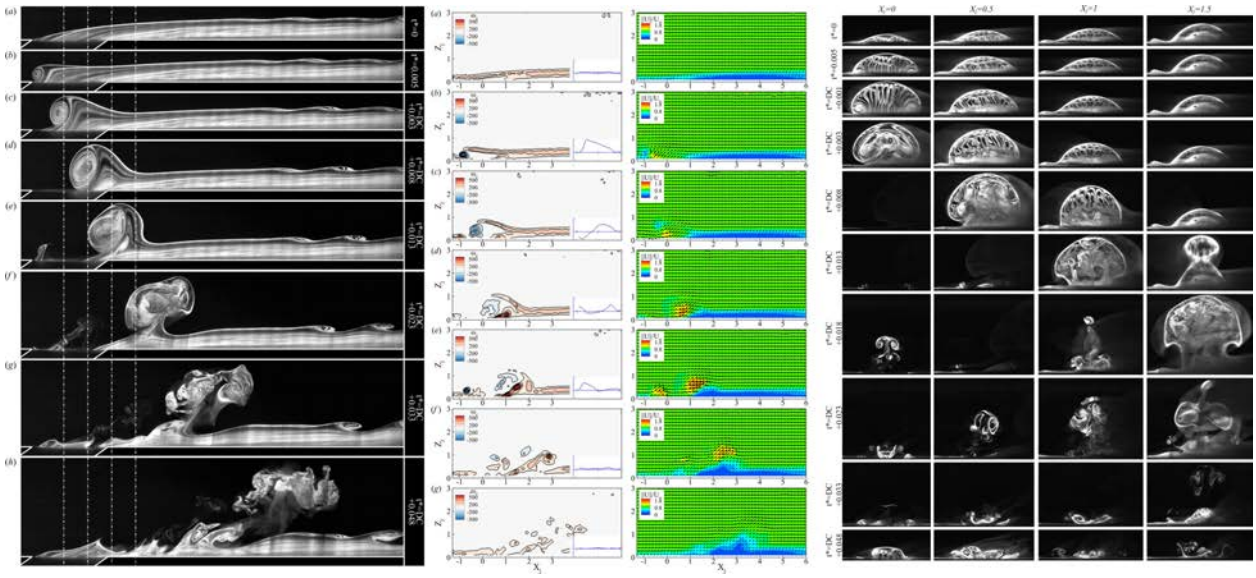

Figure 35: Single starting vortex ring (a) X-Z Mie scattering visualizations; (b) X-Z PIV; (c) Y-Z Mie scattering visualizations.

instability and triggered the formation of a large hairpin vortex. A similar regime was observed in the vertical jet study.

– *Starting hairpin vortex and trailing vortices* - For low BR_h values but with longer injection times, the leading starting hairpin vortex was followed by series of smaller hairpin vortices (figure 34*e*). A similar regime was observed in the vertical jet study.

– *Single starting vortex ring* - At high values of BR_h but for short injection times, only a single starting ring vortex was generated (figure 35). The upper shear layer started rolling up first due to the slanted nature of the jet geometry and the way the pressure wave traveled down the jet pipe, therefore creating a local increase in velocity at the jet leading edge. The upper rollup of the starting vortex departed the wall first while the lower shear layer rollup was just starting to form. However, as the upstream part of the starting vortex was convected above the jet exit, the pulse was interrupted and the actuation valve is closed leading to cross-flow ingestion and affecting the upstream part of the starting vortex ring, still located above the jet exit. The backward flow had strong impact on the starting vortex, interrupting its initial positive rotation and even reverting it. While convected, the weakened starting vortex started to dissipate and lose its coherence rapidly. A similar regime was observed in the vertical jet study, with yet different vortex dynamics.

– *Starting vortex ring and trailing column* - At high values of BR_h, for long injection times, the starting vortices were of the ring kind, followed by a series of smaller trailing ring vortices (figure 36). The leading starting vortex started to roll at

DISTRIBUTION A: Distribution approved for public release.

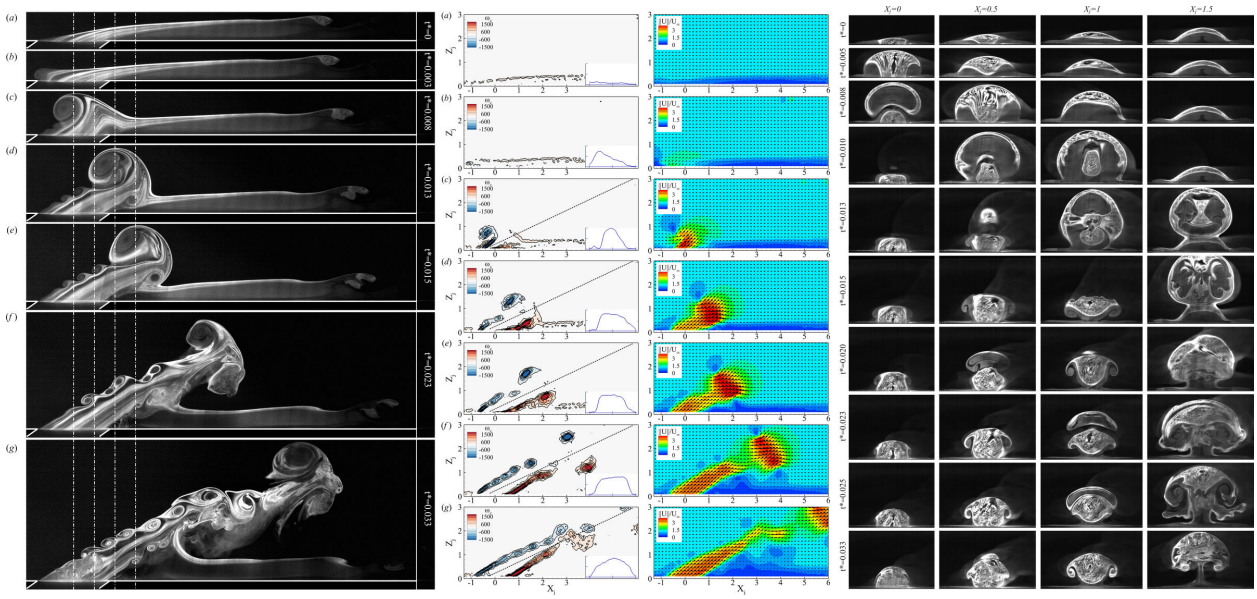

Figure 36: Leading vortex ring and trailing vortices (a) X-Z Mie scattering visualizations; (b) X-Z PIV; (c) Y-Z Mie scattering visualizations.

the leading edge due to the slanted geometry of the jet, and the shear layer progressively rolled up towards the downstream edge. Because of this delay, the formation process time-lines for the upstream and downstream part of the starting vortex ring were offset in time and the upstream part of the starting vortex departed the leading edge first after having accumulated sufficient amount of circulation, while the downstream part departed the wall later. Consequently, the starting vortex axis rotated continuously in the positive direction from 0° to approximately 50° at the moment of the departure of the downstream rollup and reached an equilibrium at approximately 60° while convected in the free stream. After the departure of the leading vortex ring, the jet shear layer rolled up into additional trailing vortices, smaller in size, yet in nature very similar to the starting vortex ring and following comparable trajectories. Conversely to the vertical jet, pairing of consecutive trailing vortices was clearly observed on both the upper and lower shear layers. The vortical system developing in the wake of the starting vortex took the form of a mushroom-like shape and a pair of strong counter-rotating vortices developed on the lower part of the jet body, coherent with the CRVP structure of high blowing ratio unforced detached jets. A similar regime was observed in the vertical jet study, with yet different vortex dynamics.

– *Compound starting vortex system and trailing vortices* - At intermediate values of BR_h, for long injection times the forced inclined jet could generate starting structures of a third, hybrid type. At the transition from BR_l to BR_h, the increased shear at the jet/cross-flow upstream interface triggered the rolling of the upper shear layer to form a starting vortex ring with relatively low vertical momentum. After shedding of the leading vortex, a region of positive velocity redeveloped

DISTRIBUTION A: Distribution approved for public release.

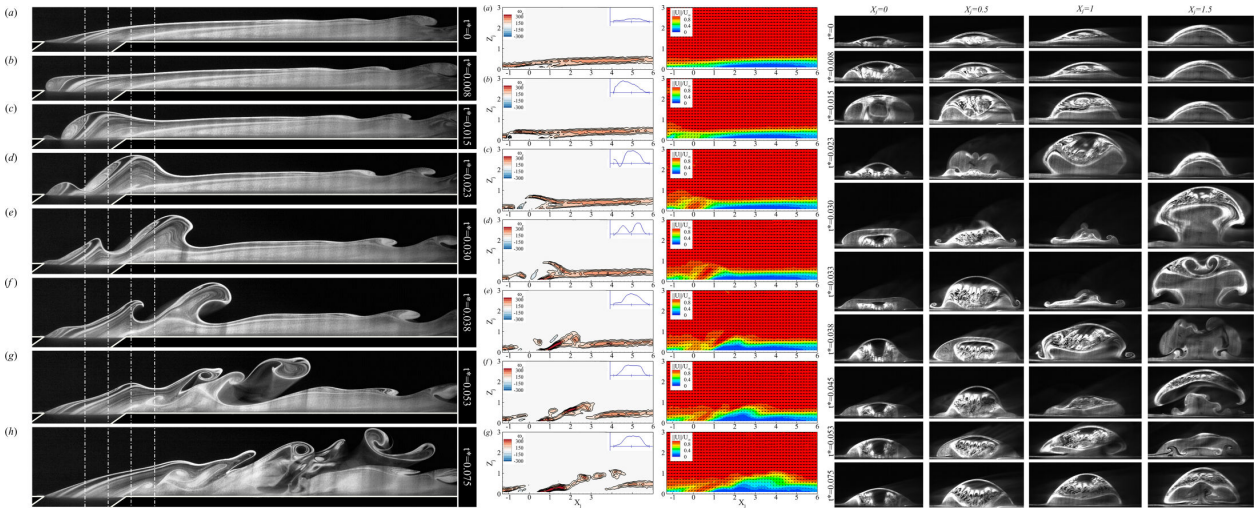

Figure 37: Compound starting vortex system and trailing vortices (a) X-Z Mie scattering visualizations; (b) X-Z PIV; (c) Y-Z Mie scattering visualizations.

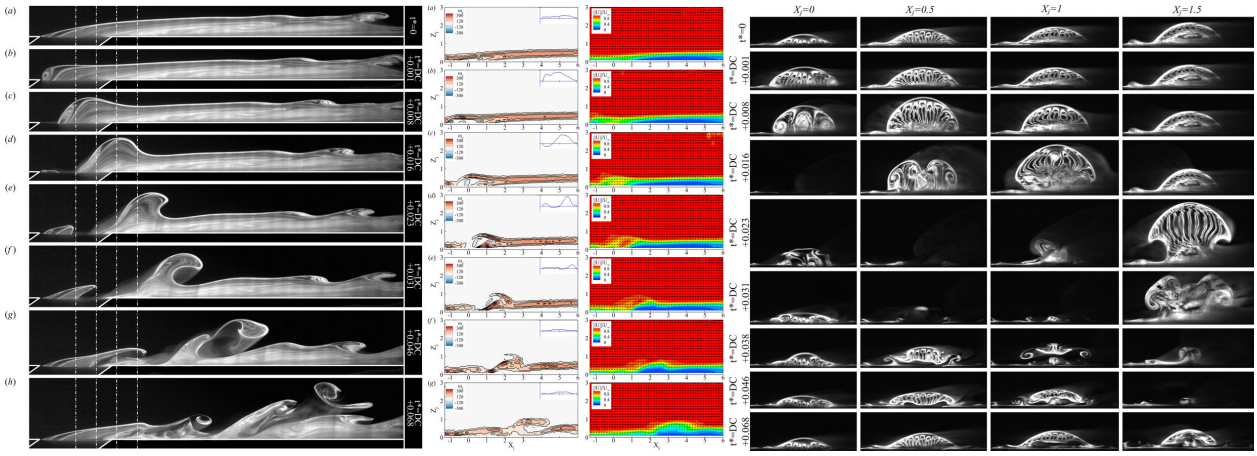

Figure 38: Single compound starting vortex system (a) X-Z Mie scattering visualizations; (b) X-Z PIV; (c) Y-Z Mie scattering visualizations.

at the leading edge and triggered the formation of a trailing structure. This pattern was repeated, though with less amplitude, until two trailing structures were formed in the wake of the leading starting vortex ring. As the starting vortex and its trailing vortices penetrated the free stream, secondary positive rollups originating from the jet upper shear layer natural vorticity, developed downstream of the convected upper shear layer rollups. These secondary structures eventually evolved into large hairpin vortices, subsisting while the primary starting vortex ring and trailing vortices were diffused by the overall positive vorticity.

– *Single compound starting vortex system* - This type of complex starting vortex was formed at intermediate values of BR_h and for short injection times (38). In this

DISTRIBUTION A: Distribution approved for public release.

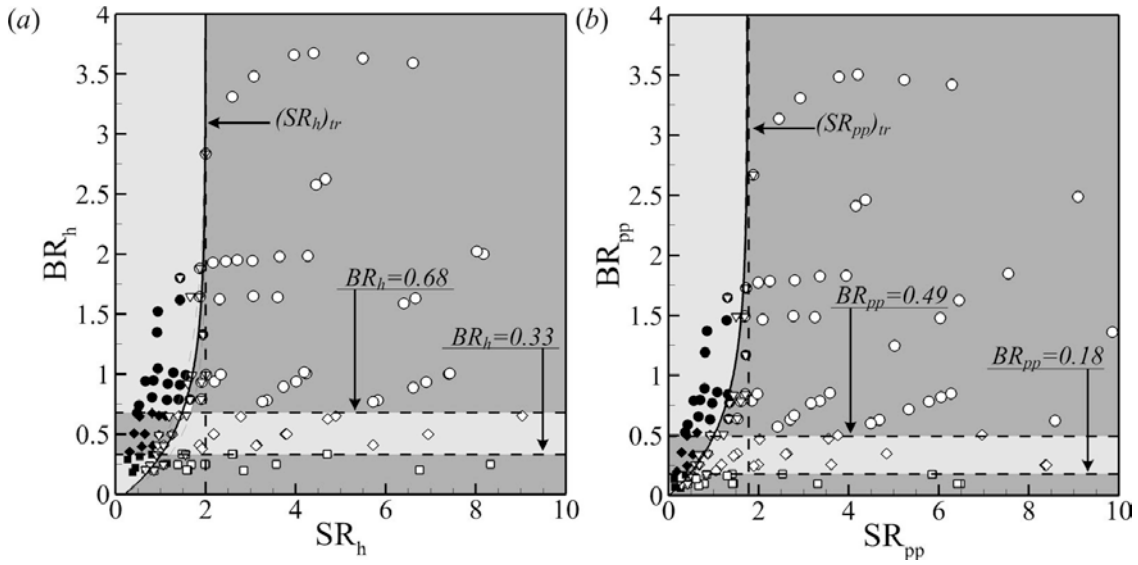

Figure 39: Classification of the starting vortices observed in forced experiments against characteristic stroke and blowing ratios (a) SR_h, BR_h; (b) SR_{pp}, BR_{pp}. ○ Starting vortex ring and trailing column; ● Single vortex ring; ▽ Limiting case single/multiple starting structures; □ Leading hairpin vortex and trailing hairpins; ■ Single hairpin vortex; ; Limiting case hairpin vortex with/without trailing vortices. Transition stroke number fit $(SR_x)_{tr} = F_0 - A_1.exp(-A_2.BR_x)$ (a) $(SR_h)_{tr}$: $F_0 = 2.0$, $A_1 = 1.8$, $A_2 = 1.82$; (b) $(SR_{pp})_{tr}$: $F_0 = 1.75$, $A_1 = 1.75$, $A_2 = 1.7$.

case, only the leading structures (primary ring and secondary hairpin) developed albeit with slightly modified dynamics compared to the previous regime. In this regime, as the upstream rollup of the primary starting vortex departed the jet exit leading edge, the actuation valve was closed, leading to cross-flow ingestion inside the jet pipe and affecting the trajectory of the primary the vortex ring, partly ingested in the jet pipe, and decreasing its circulation. A secondary hairpin vortex eventually developed downstream of the primary ring vortex which was later on dissipated by the overall positive cross-flow vorticity.

- Starting vortices classification - A classification similar to the one of the vertical jet was made, against scaling parameters (SR_h, BR_h) and (SR_{pp}, BR_{pp}) (figure 39). Both sets of parameters provided comparable and satisfactory maps. Using the (SR_h, BR_h) scaling, starting hairpin vortices were formed for BR_h values below 0.33, starting ring vortices formed for $BR_h > 0.68$ and compound vortices generated at intermediate values. The transition stroke ratio $(SR_h)_{tr}$ was found to decrease consistently with decreasing values of BR_h. A formation number (asymptotic value of $(SR_h)_{tr}$) of $F_0 = 2.0$ was identified, which was significantly lower than for the vertical jet (close to 3.6). The (SR_{pp}, BR_{pp}) classification showed identically shaped regions for the different starting structures. Overall the threshold values were so that starting hairpin vortices were formed for $BR_{pp} < 0.18$, starting ring vortices for $BR_{pp} > 0.49$, and compound

DISTRIBUTION A: Distribution approved for public release.

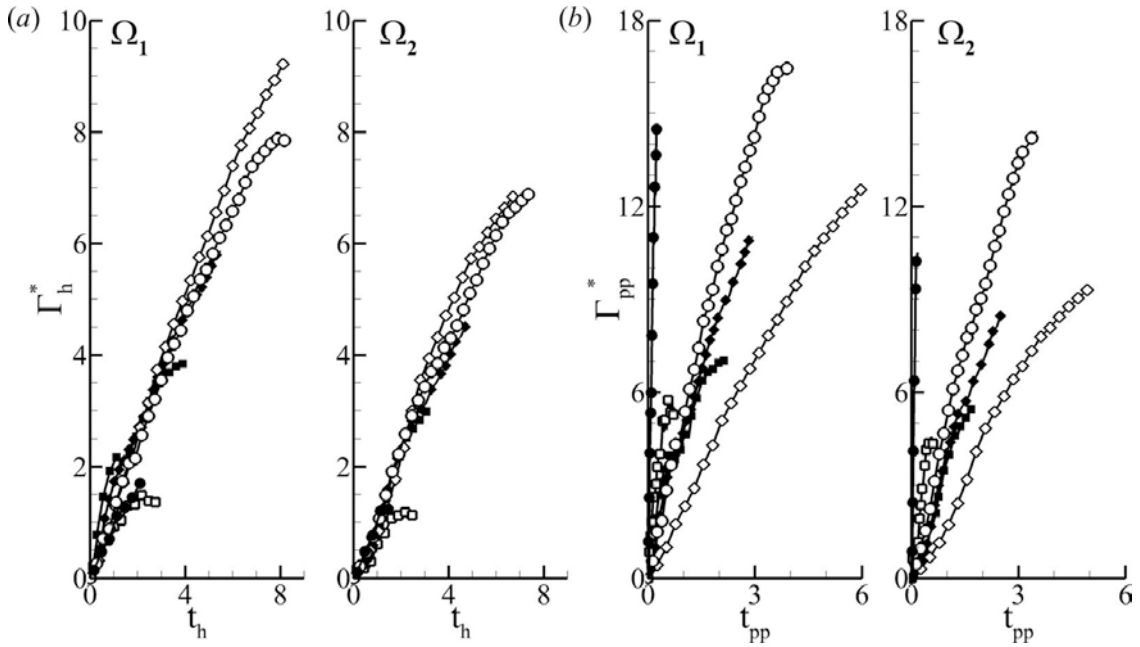

Figure 40: Total 2D circulation from PIV measurements, scaled using (*a*) U_h and (*b*) U_{pp} for *Case VI* (■), *Case VIII* (◊), *Case XII* (□), *Case XIII* (♦), *Case XIV* (○), *Case XV* (●).

starting vortices were formed at intermediate values. The transition stroke number $(SR_{pp})_{tr}$, was also found to decrease with decreasing values of BR_{pp} and the formation number was found at approximately $F_0 = 1.75$, also lower than the vertical jet value. Such decrease in the formation number was explained by the geometrical configuration of the inclined jet which led to higher co-flowing components of the velocity between the jet and the cross-flow compared to the vertical jet, in agreement with findings from (46) for co-flowing flows. As for the vertical jet, rates of generation of the circulation at both the leading and trailing edges were evaluated, this time based on PIV measurements, to identify the correct scaling parameter. The leading edge and trailing edge domains were taken to be the areas of the PIV domain, respectively Ω_1 above and Ω_2 below the line $Y_j = \frac{2.9}{6}X_j + 0.2$ which was found to accommodate all the considered cases. The results were scaled using experimentally determined values of BR_h and BR_{pp} and clearly showed that the scaled results using U_h caused the circulation trends on both domains to collapse nicely onto a single line, making (SR_h, BR_h) the proper scaling parameters for inclined partly modulated jets in cross-flow.

- Cross-flow Ingestion - At the transition from BR_h to BR_l, the rapid decrease in flow rate was accompanied by an ingestion of cross-flow fluid at the jet inlet leading edge, observed in both experiments and simulations (figure 41). The flow separated inside the jet pipe and cross-flow fluid was ingested at the upstream edge of the jet while the horseshoe vortex was convected downstream as the adverse pressure gradient caused by the presence of the jet vanished. The ingestion was more consequent in *Case XI* with a greater BR_h/BR_{pp} value since the mass deficit at the closing of the solenoid valve was more significant. Conversely to the vertical jet, no particular quasi-stationary

DISTRIBUTION A: Distribution approved for public release.

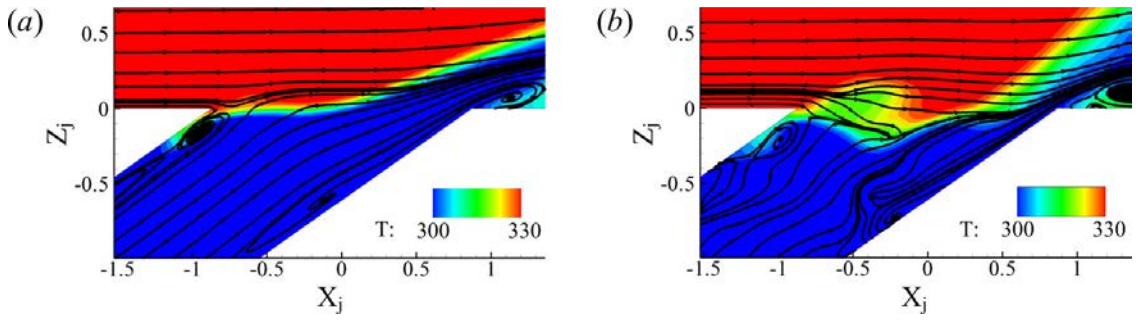

Figure 41: Temperature field and 2D U-W streamlines for (*a*) *Case X*; (*b*) *Case XI* at $t^* = DC + 0.03$.

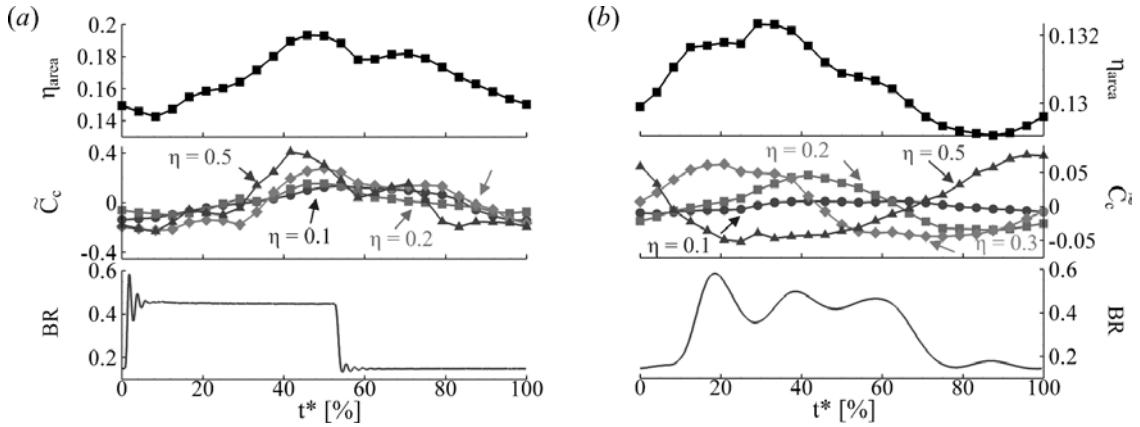

Figure 42: Phase Averaged η_{area} (*top*), relative coverage coefficient fluctuation for $\eta = 0.1$, 0.2, 0.3 and 0.5 (*center*), blowing ratio (*bottom*) for *Case X* at (*a*) $St_\infty = 0.016$; (*b*) $St_\infty = 0.159$.

vortical structures developed after the flow separation and all transients were directly evacuated. This was explained by the difference in pressure gradient across the jet exit between both configurations. Only a single ingestion mode corresponding to the leading edge ingestion was observed in the inclined jet configuration, even in high BR_h cases.

- Film Cooling Performance - The impact of the starting structures on the temperature field was investigated using LES results. Instantaneous wall adiabatic effectiveness and Laplacian of the pressure iso-surfaces for *Case X* (figure 33*b-d*), showed an increase in spread around the jet exit observed at the onset of the high blowing ratio, due to jet fluid exiting on the side of the jet exit. The coverage was also affected by draft induced by the secondary starting vortices and the associated cross-flow fluid entrainment. A 'pinch' in the coverage developed near the secondary starting structures legs as they were convected downstream. For *Case XI* (figure 33*j-l*) corresponding to a higher value of BR_h, although a relatively low increase in the spread could be observed, the cooling performance of the jet was significantly degraded as the jet lifted

DISTRIBUTION A: Distribution approved for public release.

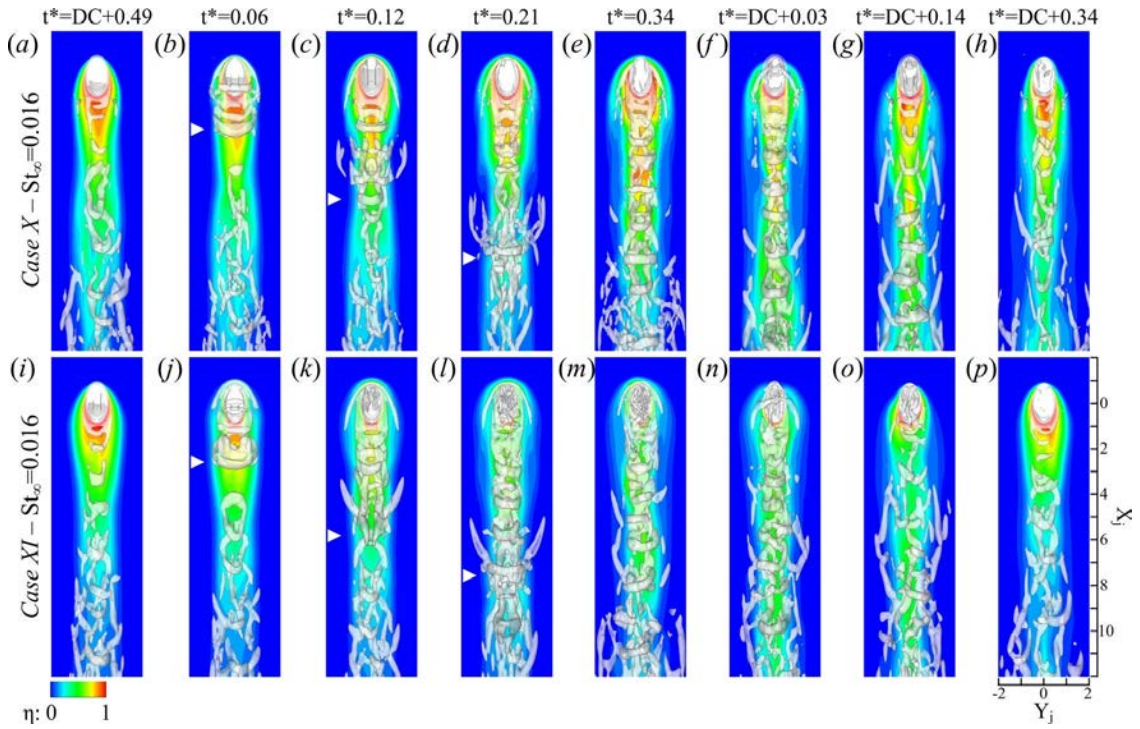

Figure 43: Instantaneous wall adiabatic effectiveness and Laplacian of the pressure isosurfaces from LES for (*a-h*) *Case X*; (*i-p*) *Case XI* (bottom) at $St_\infty = 0.016$ at $t^* = DC + 0.49$, 0.06, 0.12, 0.21, 0.34, $DC + 0.03$, $DC + 0.014$ and $DC + 0.34$.

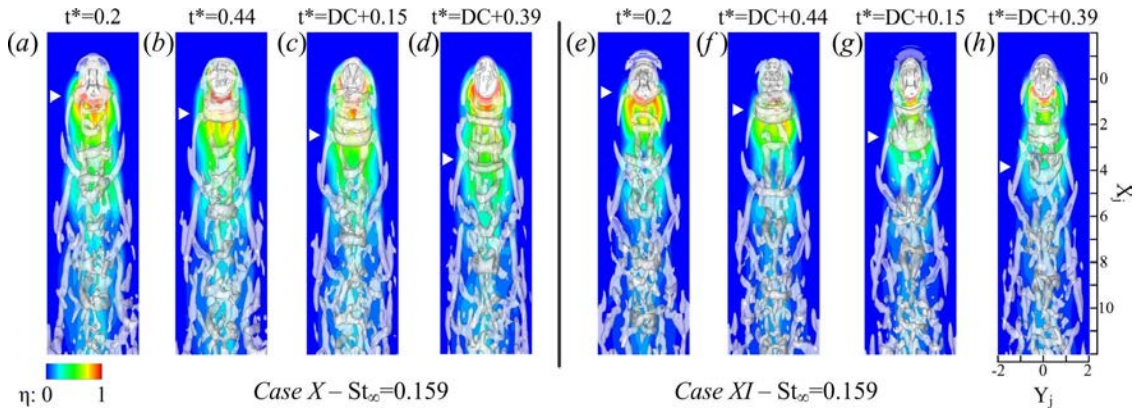

Figure 44: Instantaneous wall adiabatic effectiveness and Laplacian of the pressure isosurfaces from LES for (*a-d*) *Case X* and (*e-h*) *Case XI* at $St_\infty = 0.159$ during a forcing cycle.

DISTRIBUTION A: Distribution approved for public release.

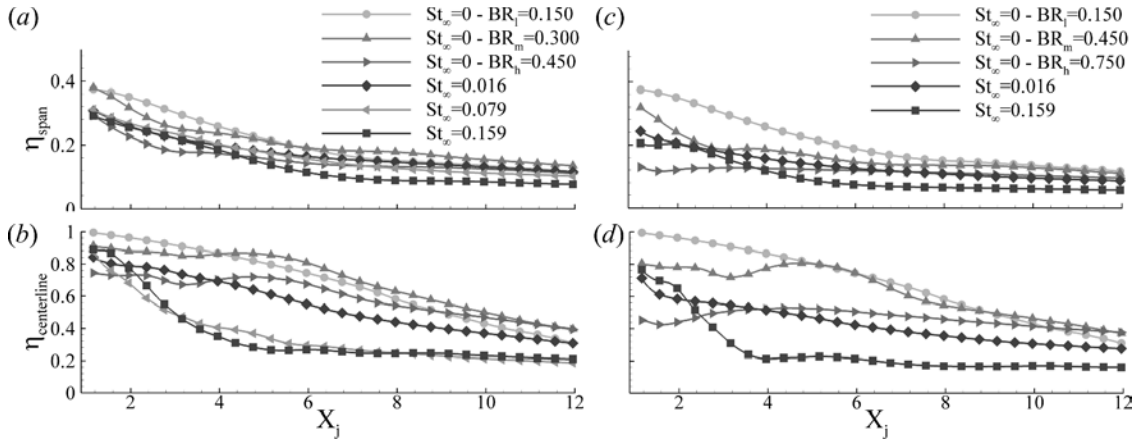

Figure 45: Film cooling performance: Spanwise averaged (*top*) and Center line (*bottom*) adiabatic effectiveness from LES for the forced inclined jet for (*a*, *b*) *Case X*; (*c*, *d*) *Case XI*.

partially off the wall shortly after the transition to BR_h. Simulations at a higher forcing frequency showed that coverage was brought to the wall essentially by the secondary starting vortices (figure 44) as they were convected downstream. In *Case X* ($BR_h = 0.45$), the coverage beyond $X_j = 6$ was marginal as the starting structures consistently lifted off the wall at this point. For *Case XI* ($BR_h = 0.75$), the average coverage breakup point was even closer to the jet exit, about $X_j = 4$, as the starting structures possessed more strength and vertical momentum compared to the lower blowing ratio case, thus lifting off the wall earlier. In both cases, large X-patterned structures from the combination of side vortices and wake vortices associated with the leading starting vortex velocity field, were formed downstream of the starting structures, and while the upper legs of the 'X' affected coverage negatively, the lower legs of the 'X' with opposite vorticity favored the spread, hence the "rosary-like" pattern observed at the wall from the succession of pinch/spread. Although the disruption of coolant at the jet shut down due to ingestion significantly affected the coverage during most of the low part of the cycle. The perturbation was even greater for larger values of the BR_{pp} parameter. Time averaged η_{span} and $\eta_{centerline}$ values for *Case X* and *XI*, were compared to relevant unforced jet trends at constant low, high and average blowing ratios. For forced jets at $BR_h = 0.45$, the span-wise average effectiveness trends showed that forced cases at $St_\infty = 0.016$ and $St_\infty = 0.079$ had performances comparable to the unforced case at $BR = BR_h = 0.45$ with yet center-line adiabatic effectiveness lower and decreasing consistently with increasing forcing frequency. Overall η_{span} and $\eta_{centerline}$ values decreased with increasing frequency, but suggested an increase in spread for the forced cases with overall more homogeneous wall adiabatic effectiveness values over the unforced jet. *At* $BR_h = 0.75$, although no improvement in η_{span} were found in forced cases over the $BR = BR_l$ and $BR = BR_m$ unforced jets, forcing the jet at $St_\infty = 0.016$ provided overall higher η_{span} values than the one of the unforced jet at$BR = BR_h$ particularly for $X_j < 6$. At $St_\infty = 0.159$ higher η_{span} values were achieved for $X_j < 4$ over the case at $BR = BR_h$ with lower values downstream of this point. Once again, forced jet center-line adiabatic

DISTRIBUTION A: Distribution approved for public release.

Table 6: Coverage coefficient and area averaged adiabatic effectiveness from LES under forced conditions compared to equivalent mass flow rate unforced cases. Values for the unforced jet are interpolated from figure 32.

Conditions	C_c			η_{area}
	$\eta = 0.2$	$\eta = 0.3$	$\eta = 0.5$	
$BR = BR_m = 0.3 - St_\infty = 0$	28.0	21.4	11.9	0.197
$BR = BR_h = 0.45 - St_\infty = 0$	22.2	16.8	7.29	0.152
$Case\,X - St_\infty = 0.016$	**25.5**	**17.9**	**8.96**	**0.168**
$Case\,X - St_\infty = 0.159$	**19.9**	**10.9**	**5.31**	**0.131**
$BR = BR_h = 0.75 - St_\infty = 0$	18.3	13.0	1.43	0.109
$Case\,XI - St_\infty = 0.016$	**20.3**	**13.0**	**4.42**	**0.129**
$Case\,XI - St_\infty = 0.159$	**10.4**	**6.47**	**3.07**	**0.091**

effectiveness were lower than those of unforced cases at $BR = BR_l$ and $BR = BR_m$ but higher $\eta_{centerline}$ values were achieved over the case $BR = BR_h$ for $St_\infty = 0.016$ and $St_\infty = 0.159$ for respectively $X_j < 4$ and $X_j < 2.5$. The phase averaged temporal evolutions of forced cases at $BR_h = 0.45$ showed high fluctuations of η_{area} at low forcing frequencies and in particular the the negative impacts of the ingestion transient and of the quasi-unforced high blowing ratio regime on film cooling performance. Fluctuations (and averages) were found to be much lower in the higher forcing frequency case and overall the coverage appeared relatively constant. Global performance for the forced jet summarized in table 6 along with relevant unforced jet performance. In all cases, forcing led to decreased performance over the equivalent unforced jet at constant mean blowing ratio ($BR = BR_m$). However, the forced cases at $St_\infty = 0.016$ performed systematically better than the equivalent unforced jets at fixed high blowing ratio ($BR = BR_h$). At fixed BR_h, BR_l and DC, the jets forced at the highest forcing frequency ($St_\infty = 0.159$) had systematically the lowest performance.

- Other studies put in perspective of the current findings - Studies from (25) and (21) (or 76 which has operating conditions identical to those of 21) were put in perspective of the current findings in terms of forced jet in cross-flow scaling parameters in a an attempt at explaining how they could have provided such disparities in their results. First of all, while they were carried out at comparable blowing ratios and forcing frequencies, the corresponding scaled parameters, using the scaling defined in the current study, show that both studies actually did not investigate the jet in the same conditions. When using the current study delimitation of the (SR_h, BR_h) map (figure 46), it appears rather clearly that some flow regimes have been sampled more extensively than others, in particular the starting ring vortex and trailing column regime, which, according to figure 36 appears poorly suited for film cooling purposes. On the other hand, only one data set was investigated in the hairpin vortex regime, and only one value of BR_h in the compound starting vortex regime. The current study also evidenced the differences in vortex dynamics between a vertical and inclined jet and suggest a great disparity between the physics of the jets involved in (25) (inclined jet

DISTRIBUTION A: Distribution approved for public release.

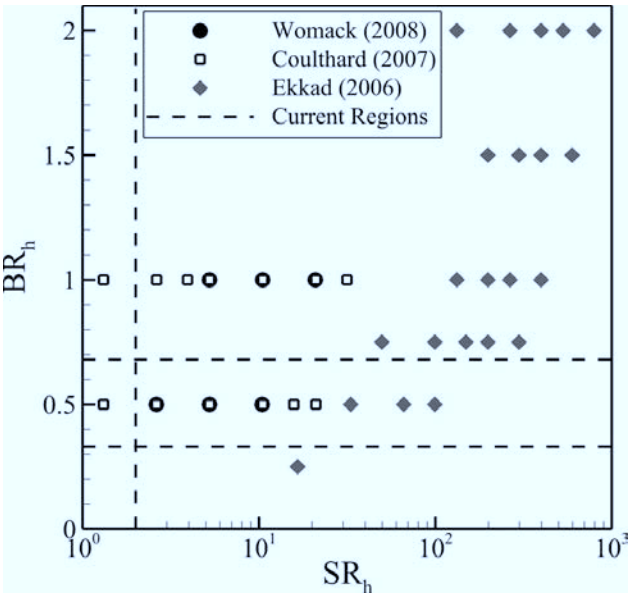

Figure 46: Scaled operating points for previous forced inclined jet studies from (25), (21), and (76) based on the scaling parameters identified in the current work.

with injection angle of 20° with respect to the streamwise direction, and a compound angle of 90°over a leading edge model) and (21) (row of inclined jets at 35° over a flat plate, similar to the one of the current study). Given the considerable impact the introduction of compound angles can have on unforced jets (see 53), it is strongly believed it will also affect the formation mechanisms and dynamics of the starting structures.

DISTRIBUTION A: Distribution approved for public release.

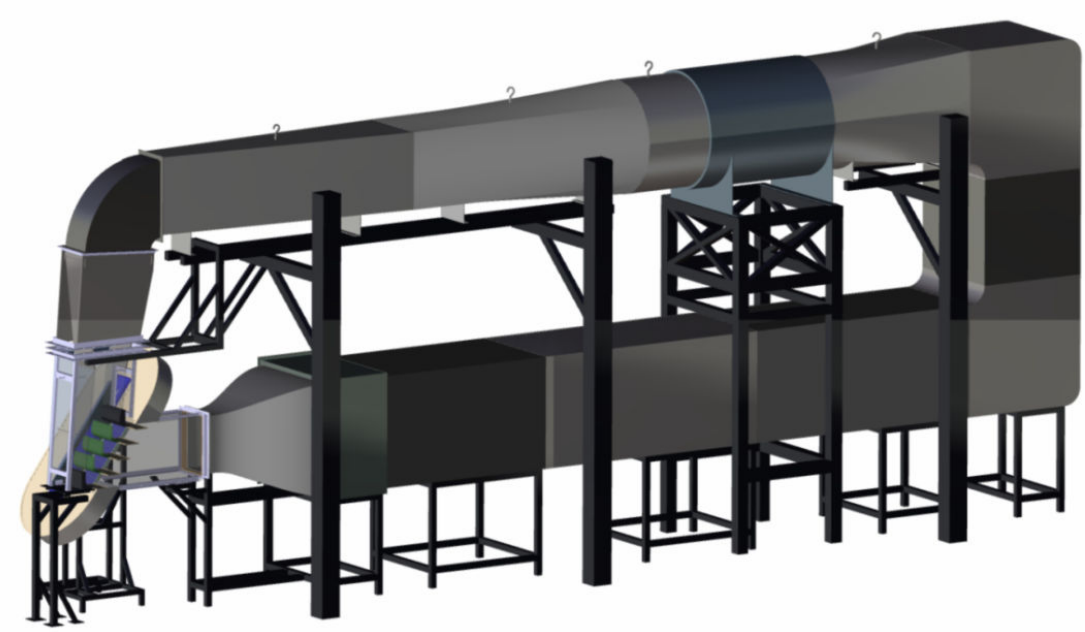

Figure 47: Global view of the wind tunnel

3 Cascade Wind Tunnel

3.1 Experimental Setup Design

3.1.1 Wind tunnel design

A new wind tunnel has been designed and constructed at the LSU Mechanical Engineering Laboratories. The objective was to design a test facility adapted to a wide range of experimental measurements on turbine blades. The test section consists of a 4 passage linear cascade composed of 3 full blades and 2 shaped wall blades (inner and outer blades). A conveyor setup was designed and fabricated to simulate passing wakes upstream of the cascade. Aerodynamic and heat transfer experimental tests were conducted in a relative frame with fixed rotor turbine blades while the nozzle guide vanes are rotating. This facility was designed to enable easy interchanges of different experimental setups. All the parts, as well as the complete assembly, have been fully designed using a Computer Aided Design (CAD) software. Figure 47 shows a general view of the 3D design.

The new test facility was chosen to be a closed-circuit wind tunnel to ensure a controlled return flow and to reach low levels of turbulence and unsteadiness in the test section. The whole wind tunnel is 33 feet long and 11 feet high. The fan diameter is 38 inches. After the test section, the flow is expanding through a first diverging duct and reaches the first corner vanes. Then 2 consecutive diffusers with equivalent cone angles of 5° expand the flow without separation before passing through the fan. The fan is surrounded by 2 flexible ducts to prevent excessive vibration propagation within the wind tunnel. After the fan, the flow passes through a last diffuser and expands into a 38 inches side square section duct. Then the flow goes through 2 more corners with 13 corner vanes in each. A heat exchanger with circulating chilled water is located in between the two bends to regulate the temperature

DISTRIBUTION A: Distribution approved for public release.

Table 7: Pressure losses estimation

Part	K_0	Total Losses (%)
Test section inlet	0.021	6.9
Cascade	0.0384	12.6
Test section outlet	0.0348	11.4
Divergent 1	0.0886	29.0
Corner 1	0.0377	12.3
Divergent 2 & 3	0.0187	6.1
Main duct	0.0017	0.6
Corner 2	0.0015	0.5
Corner 3	0.0015	0.5
Settling chamber	0.0615	20.0
Contraction cone	0.0005	0.2
TOTAL	0.3059	100

inside the wind tunnel during operation. A 19 feet long duct with constant section follows before the flow goes into the settling chamber. The settling chamber consists of a 2 inches thick honeycomb to straighten the flow and 5 screens to reduce turbulence levels. Then, the well-conditioned and uniformed flow enters the contraction cone and is accelerated to the test section inlet. The contraction cone consists of 2 matched cubic polynomial curves to guide the flow from a 38 in square duct to a $19.5in \times 12in$ rectangle duct, equivalent to a contraction ratio of 6.16.

Pressure Loss Estimation in the Wind Tunnel - In this closed-loop wind tunnel, the axial fan produces a rise in static pressure, which compensate for the total pressure losses in the rest of the tunnel. To estimate pressure losses through the different parts of the wind tunnel, the pressure loss coefficient K is used. This coefficient is defined as the ratio of pressure drop in static pressure ΔP over the mean flow dynamic pressure q.

Wattendorf (1938) developed a logical approach to calculate the different pressure losses in a closed circuit wind tunnel. This approach was to divide the wind tunnel into four different kinds of parts: (1) straight, constant area sections, (2) corners, (3) divergent sections, (4) contracting sections. Then, he referred all local losses to the "jet" dynamic pressure q0, greatest dynamic pressure in the wind tunnel. In our wind tunnel, this dynamic pressure q_0 occurs at the exit of the cascade. Then the coefficient of loss becomes:

$$K_0 = \frac{\Delta P}{q}\frac{q}{q_0} = K\frac{q}{q_0} = K\frac{D_0^4}{D^4}$$

Where: D_0 is the jet equivalent diameter, D is the local tunnel equivalent diameter.

Then, the wind tunnel energy ratio ER_t can be defined as:

$$ER_t = \frac{\text{Jet energy}}{\sum\text{Circuit losses}} = \frac{1}{\sum K_0}$$

Below is an estimation of the loss coefficients K_0 for each wind tunnel components, as suggested by Wattendorf:

DISTRIBUTION A: Distribution approved for public release.

The corresponding wind tunnel energy ratio was evaluated at $ER_t = 3.27$. An energy ratio of 3.27 is within the range of most closed circuit wind tunnels. Thus, this design can be seen as a good balance between flow quality, cost, and complexity of fabrication.

3.1.2 Test section design

The 2D blade shape profile of the cascade was provided by the Air Force Research Laboratories (AFRL). It is a High Lift Low Pressure Turbine (LPT) blade 'L1A' profile with a 1.34 incompressible Zweifel coefficient (figure 48). A 6-inch axial chord and 1 foot span were chosen. The span is chosen to be two times the axial chord to make sure we have a nominally 2D flow at the mid span. The solidity of the cascade, ratio of the axial chord to the spacing, is 1. The blade inlet air angle is 35 degrees from axial, and the exit angle is -60 degrees from axial, resulting in a 95 degrees total turning. The linear cascade inlet plane is 1 ft high and 2 ft wide. The nominal inlet velocity is $50m/s$ and was chosen as a reference, with the axial chord to determine the Reynolds number. Two inlet bleeds and two tailboards are placed upstream and downstream of the cascade to adjust the flow and obtain periodic cascade performances as specified by Eldrege and Bons (2004). The cascade inlet plane angle was adjusted from 35°, flow inlet angle of the cascade test blade to 36° to take into consideration the deviation of the mainstream airflow due to the wake simulator. The tangential velocity component induced by the wake generator can be estimated at $1m/s$, which is the nominal operating translation velocity of the moving plates. Considering a $50m/s$ nominal freestream velocity, a simple vector decomposition gives a velocity triangle with about 1° angle of deviation of the mainstream flow (figure 51). The designation used is the same as turbomachinery theory, the absolute velocity is C, the relative velocity is $W = 50m/s$ and U is the rotor blade speed $1m/s$. Then, the total turning angle of the cascade with wake simulator is 96°, which is 1° more than the deviation angle of the test blades.

- *Pressure Measurement Blade* - A pressure tap blade was constructed to measure the pressure profile on the central test blade and compare it to known results. The blade is an assembly of nine parts spanning 12 inches. The pressure tap sections are located at 3 inches, 6 inches, and 9 inches along the blade height. Each pressure tap section has forty-one pressure taps built into it totaling one hundred twenty three pressure taps. The large number of pressure taps enabled a high resolution capture of the pressure profile along the length of the blade. Having the taps spaced every three inches allowed the straightness of the blade to be validated by comparing the pressure acquired by each section. Because of its complexity, the pressure tap sections had to be manufactured using rapid prototyping process called stereolithography (SLA). This process uses an acrylonitrile butadiene styrene (ABS) like material called Accura 55 (details in Appendix II Data Sheets). GPI Prototype and Manufacturing Services, Inc. located in Lake Bluff, IL made the pressure tap sections. Two Scanivalve DSA3217 differential pressure scanners were used to measure the pressure profiles.

- *Film Cooling Blade* - The film cooling blade is shown in Figure 49. The film cooling blade was designed to accommodate measurements using PIV and IRT techniques. The blade has thirty 1/8" diameter film cooling holes connected to an internal plenum. The holes are angled 35° to the local tangent of the surface and are spaced 3/8"

DISTRIBUTION A: Distribution approved for public release.

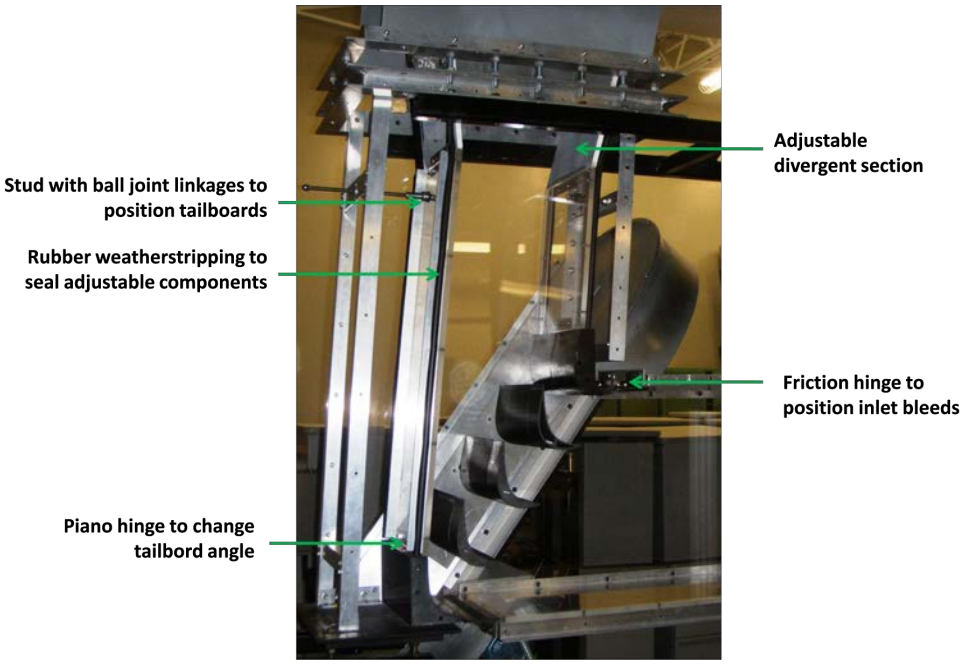

Figure 48: Cascade image

Table 8: Location of Pressure Taps as Percent of Axial Chord (X/C_x)

Suction Side						**Pressure Side**			
Tap #	% of C_x	**Tap #**	% of C_x	**Tap #**	% of C_x	**Tap #**	% of C_x	**Tap #**	% of C_x
1	1	**10**	35	**19**	65	**1**	1	**10**	71
2	3	**11**	40	**20**	67.5	**2**	3	**11**	76
3	5	**12**	45	**21**	70	**3**	5	**12**	81
4	7.5	**13**	50	**22**	72.5	**4**	11	**13**	86
5	10	**14**	52.5	**23**	77.5	**5**	21	**14**	91
6	15	**15**	55	**24**	82.5	**6**	31		
7	20	**16**	57.5	**25**	87.5	**7**	41		
8	25	**17**	60	**26**	92.5	**8**	51		
9	30	**18**	62.5	**27**	97.5	**9**	61		

DISTRIBUTION A: Distribution approved for public release.

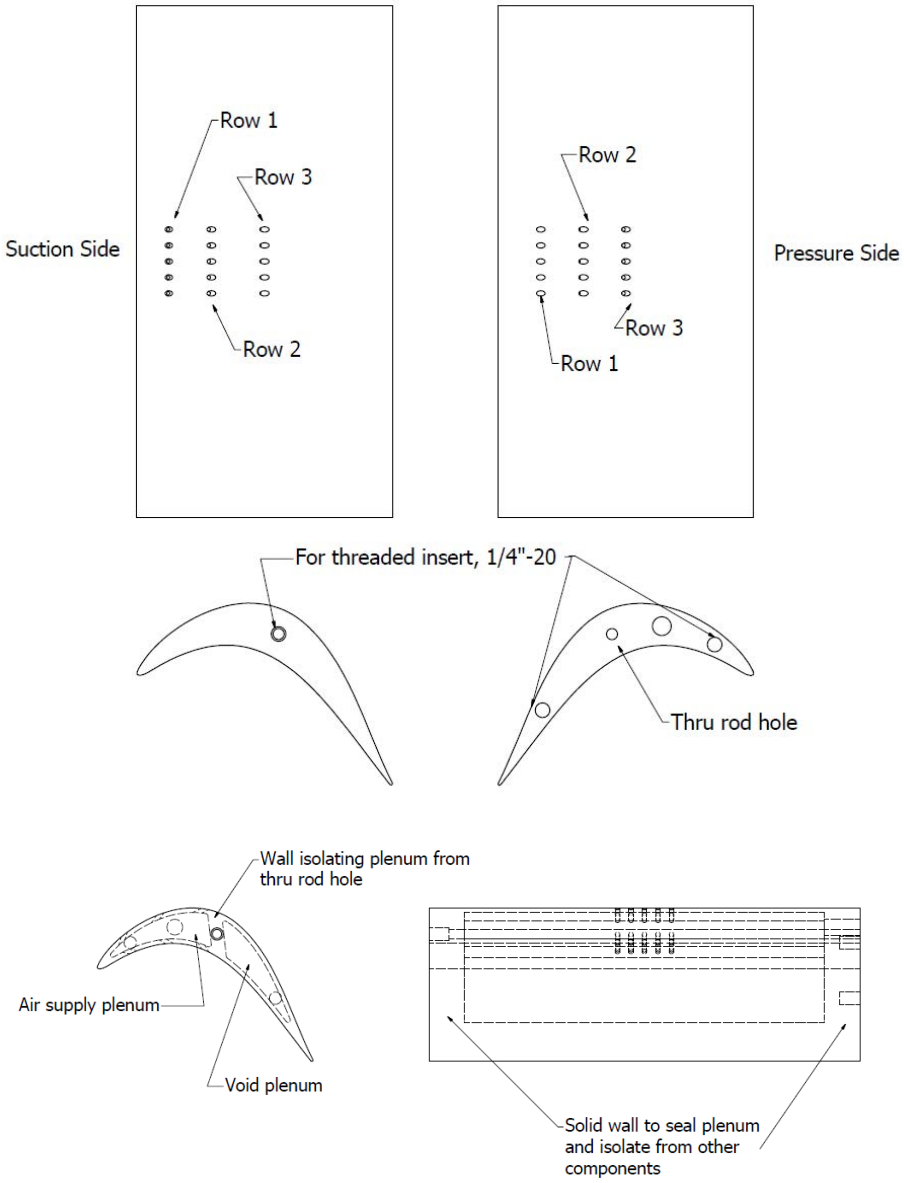

Figure 49: (Top) Suction/Pressure Side Views, (Middle) Left/Right Side Views, (Bottom) Left/Back View w/ Hidden Lines Shown of the Film Cooling Blade

laterally. The length to depth ratios of the holes are listed in Table 9 assuming a 1/8" diameter. The internal plenum is connected to an air supply via a $\frac{1}{4}$" NPT fitting and is completely isolated from the other components of the blade such as the thru-rod hole and the threaded insert holes as shown in Figure 49. The blade was manufactured using the same process, material and company as the pressure tap sections.

DISTRIBUTION A: Distribution approved for public release.

Table 9: Locations and L/D Ratio of Film Cooling Holes

Row/Side		% Chord Location (X/C_x)	Length to Diameter Ratio, L/D
Suction	1	12.5	1.816
	2	29.167	1.824
	3	50	1.880
Pressure	1	16.667	1.694
	2	33.333	1.664
	3	50	1.664

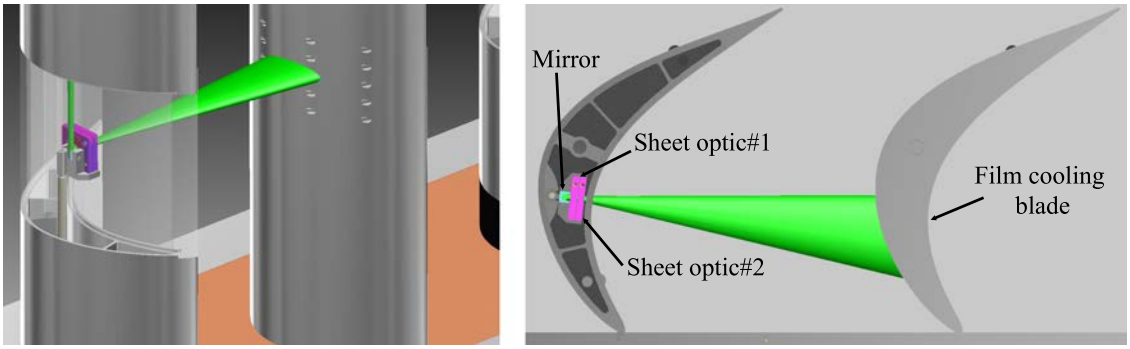

Figure 50: Assembled PIV Side Blade with optical setup for PIV measurements / Mie scattering visualizations

- *PIV Side Blades* - The PIV side blades were built to accommodate PIV measurements in the test section using the film cooling blade. There are two of them, one on either side of the central test blade in the cascade, and they are manufactured in five separate parts as shown in Figure 50 below. The plastic base spacer and acrylic sections are optically transparent to allow a laser sheet to pass through them. The blade was designed to allow the laser beam to enter from the left of the plastic base spacer, travel through the blade to mid-height of the blade. The beam is then redirected at 90° through a prism, and epxanded in one (2D-PIV)or two dimensions (3D-PIV) through cylindrical optics to generate a laser sheet or volume for PIV measurements. Finally, the sheet (or volume) illuminates the film cooling holes on the film cooling blade (figure 50). The entire mirror/optics ensemble can be traversed up and down the side blades using an in-house designed traverse system to illuminate different spanwise locations of the film cooling blade.

3.1.3 Wake generator design

Wakes are generated with aluminum plates in translation on a conveyor setup parallel to the mainstream airflow (figure 52 and 53). Those plates are 3/8 inch thick and are designed to be in size similar to the cascade test blades. The conveyor with the 17 moving plates is enclosed in an airtight shell. The design speed is 1 m/s but can be adjusted to study its influence. The plate length and pitch were chosen to be equal to the axial chord of

DISTRIBUTION A: Distribution approved for public release.

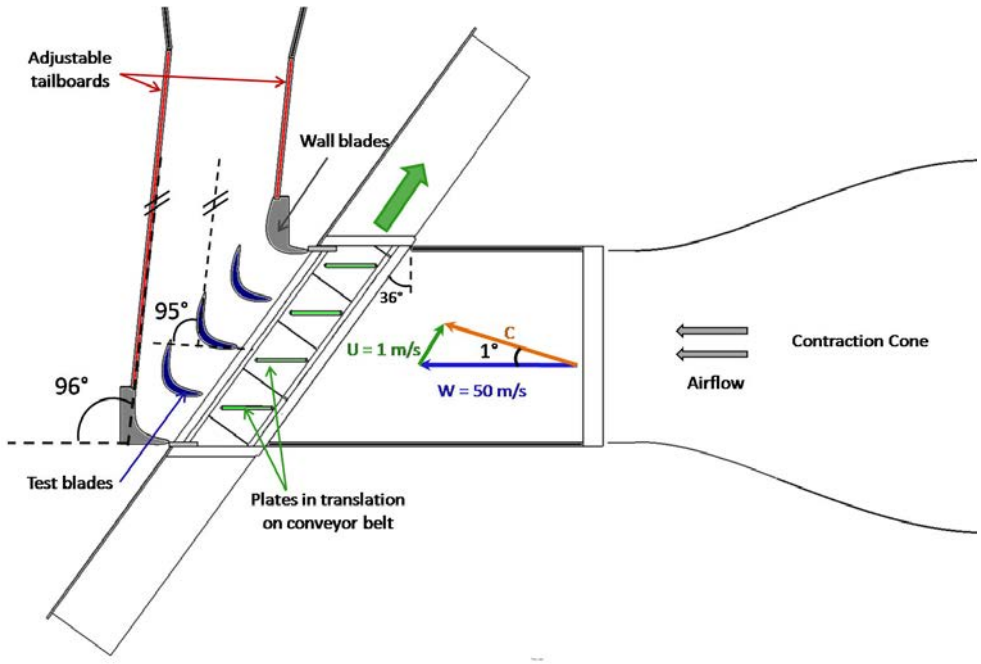

Figure 51: Cascade angles and velocity triangle.

the cascade blade (6 inches). The distance between the trailing edges of the plate and the cascade inlet plane is 2.4 inches, which is 40 % of their chord, and similar to engine stator-rotor stage spacing. Trailing and leading edges of the plates are interchangeable to study different configurations. In addition, plates are removable and can be substituted with more realistic airfoil profiles if required in the future.

The conveyor mechanism was specificaly designed and fabricated for this application. The conveyor belt and standard conveyor components such that spockets, wearstrips or shafts have been purchased from a company specialized in modular plastic conveyor belts, Intralox L.L.C. The frames, stand, cover and plate assemblies have been designed using a CAD software and built in house at the LSU Mechanical and Chemical Engineering machine shops with exception of the conveyor shell which was built by an external contractor, specialized in sheet metal work (BMR Metal Works LLC, Watson. LA).

The conveyor gearmotor is a combination of an AC electric motor, a gear unit to reduce the rotational speed and a Variable Frequency Drive (VFD) to control the output speed of the motor. This is a SEW-EURODRIVE gearmotor, model # KAF37DRE80M4 / MM11. The AC electric motor is a DRE80M4 model, 3-phase with a $1.5HP$ power. Coupled to a MM11 VFD, the output speed range of this gearmotor can vary from 19 to $189rpm$, with a $486in-lb$ nominal torque at $189rpm$. This RPM range corresponds to a belt velocity range from $0.28m/s$ to $2.76m/s$.

3.1.4 Additional equipment

Three axis linear traverse - A three axis linear traverse was designed and assembled to accommodate constant temperature anemometry (CTA) measurements. The possibility

DISTRIBUTION A: Distribution approved for public release.

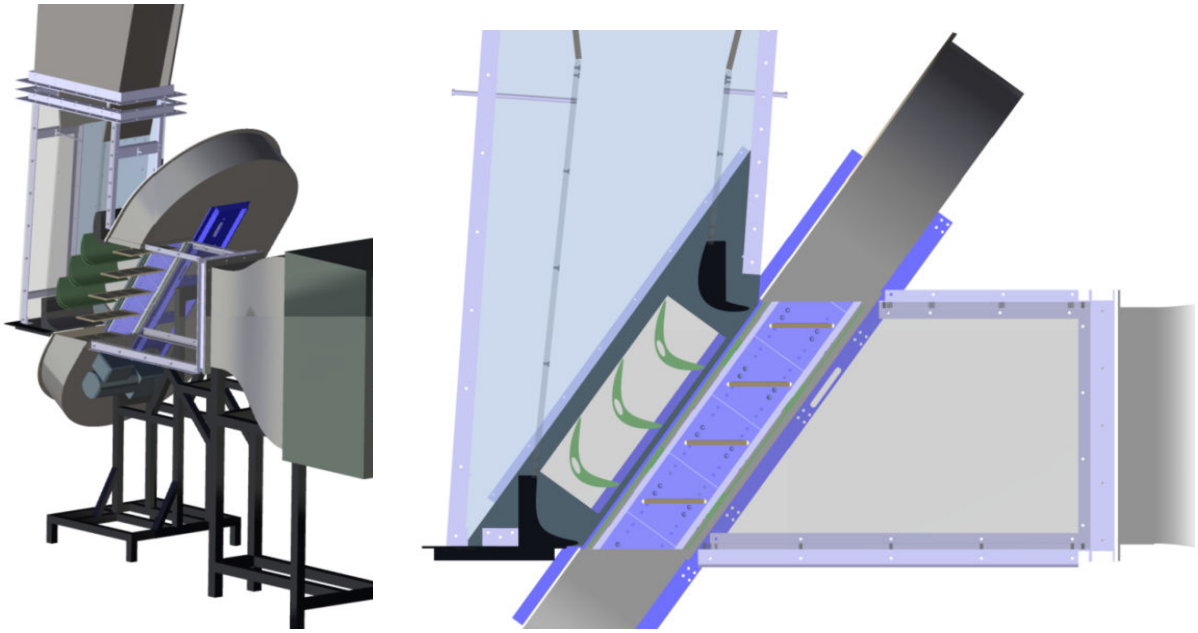

(a) (b)

Figure 52: Views of the wake simulator mechanism integrated to the test section.

(a) (b)

Figure 53: CAD view and picture of the wake simulator.

DISTRIBUTION A: Distribution approved for public release.

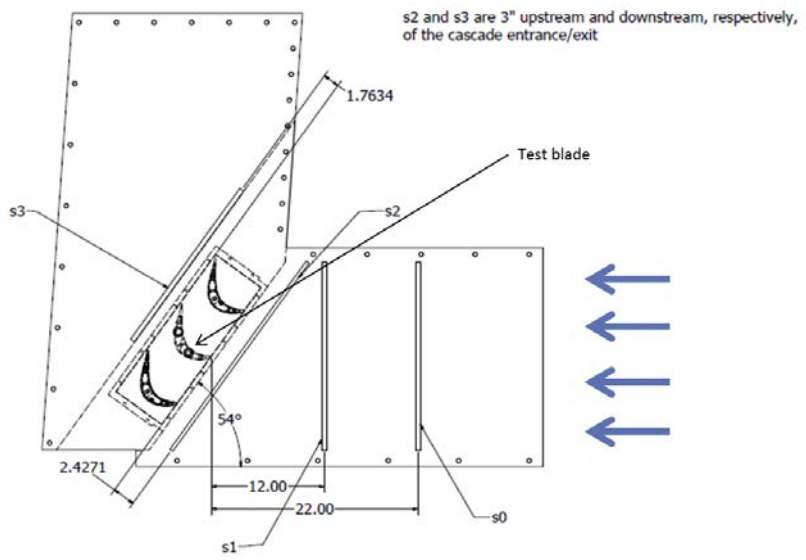

Figure 54: 2D Schematic of Test Section w/o Wake Generator w/ Labeled CTA Slots.

of other uses such as particle image velocimetry (PIV) and infrared thermography (IRT) measurement techniques was taken into account in its design as well. The traverse has two vertical axes coupled with a timing belt. A counter-weight system (not shown) was also implemented to increase the payload of the traverse by supporting the 60*lbs*. weight of the X and Y axes. (two 15*lbs* steel cylinders suspended on the far side of the traverse using a pulley). The linear stages that make up the individual axes are Velmex Bislides lead screw and ball design with 2 mm/rev leads. Stepper motors equipped with encoders (no encoder on Z axis) are used to power the axes of the traverse. NEMA 23 Danaher Motion stepper motors (Model # T22NRLG-LDN-NS-00) are used on the X and Y axes. A NEMA 34 Oriental Motors stepper motor (Model # PK296-03BA) is used on the Z axis. National Instruments quadrature encoders (Model # 15T-01SA-1000-N5RHV-F00-CE) are used on the X and Y axis, only.

3.2 Linear Cascade Characterization without Wake Generator

Experimental studies in wind tunnels generally aim at measuring various parameters of the airflow around aerodynamic bodies. In general, three main parameters are measured: velocity, pressure and temperature. These data measured over an area and through time can yield to more practical characteristics such as heat transfer or aerodynamic measurements, turbulence level or boundary layer profiles. In order to perform reliable measurements on different quantities in a wind tunnel, several steps are necessary: 1- Selection of equipment, 2- Experiment planning, 3- System configuration and installation, 4- Calibration, 5- Data acquisition, 6- Data reduction. Finally, data can be analyzed and some corrections can be applied if necessary. All these steps will be detailed in the following chapter.

DISTRIBUTION A: Distribution approved for public release.

3.2.1 Pressure Distribution along the Wind Tunnel

Static and dynamic pressures were measured with a Pitot tube linked to a handheld digital manometer at different locations along the flow path in the closed circuit wind tunnel. Figure $55a$) represents the variation of static, dynamic and total pressure along the wind tunnel for a mean velocity in the test section inlet of $53m/s$. The graph starts at the test section inlet (x=0 foot) and ends at the contraction cone outlet (x= 70 feet) to close the loop.

As expected, a permanent total pressure decrease along the wind tunnel occurs due to pressure losses. Static and dynamic pressures vary symmetrically, in function of the section areas. As predicted Part 2.3, most pressure losses occur around the cascade, where the dynamic pressure is the highest. Static pressure rises across the fan by 7 inches H_2O at this particular wind tunnel working point with a calculated flow rate of around 17,000 CFM.

3.2.2 Test Section Velocity Distribution

- *Test section inlet* - CTA measurements were used to characterize the contraction outlet plane 's0' and cascade inlet plane 's2' (figure 54).

  - *Contraction outlet* (s0) - The velocity variation in the core of the section was approximately $1m/s \pm 0.02m/s$ with a 95% confidence interval. Refined measurement in a corner of the same plane 's0' showed fluctuations of $\pm 1.5m/s$ in the corner flow for a 95% confidence interval. The turbulence intensity reached levels as low as 0.12% in the center of the cross-sectionand 7% in the corners. The incoming boundary layer profile was acquired for a mainstream flow velocity at $50m/s$ (figure 55). The boundary layer characteristics are summarized in table 10. Full velocity profiles were acquired at slot s0 in both the vertical (Z) and horizontal (Y) directions; s2 in the direction along the slot and in the horizontal direction. The velocity was uniform at $50m/s$ across about 95% of the cross-section in the vertical direction. The horizontal direction showed much of the same except with a slight drop of about $1m/s$ in the horizontal direction from $Y/H = 0.8$ to 0.95. The turbulence intensity in the freestream was about 0.20% for both cases.
  - *Cascade inlet* (s2) - The incoming air flow at slot s2 was beginning "feel" the effects of the leading edge of the cascade blades. The velocity varied from $50m/s$ upstream of the leading edge to $53m/s$ between the leading edges of the cascade blades. The variance between the velocities at the leading edge, $s/S = 0.25, 0.50, 0.75$, of the blades was approximately 1% of the freestream velocity. In the horizontal direction, the velocity was uniform from $Y/H = 0.05$ to 0.65. Beginning at $Y/H = 0.65$, the velocity dropped to about $49m/s$ and stayed there until $Y/H = 0.95$. The turbulence intensity was about 0.20% in the freestream again for both cases. The temperature (figure 56c) stayed at around $24°C$ from $Z/L = 0.20$ to 0.95. Starting at $Z/L = 0.05$ and extending to $Z/L = 0.20$, the temperature rose from $23°C$ to $24°C$. This temperature rise is most likely due to an increase in the overall, bulk temperature of the air flow in the wind tunnel.

- *Test section outlet* (s3)- The mean velocity values were measured at mid-span, 50% of the axial chord downstream of the cascade outlet plane at the slot 's3' . The inlet

DISTRIBUTION A: Distribution approved for public release.

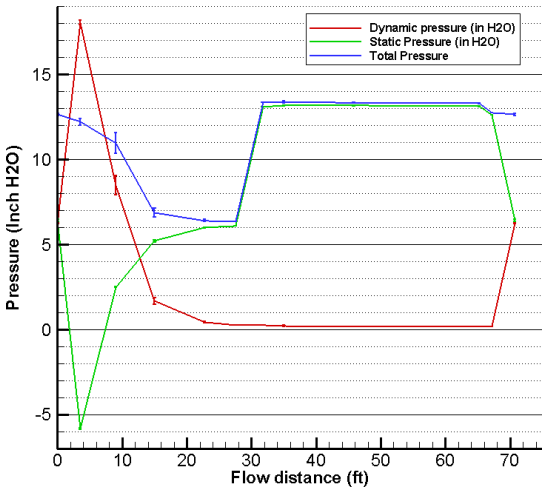

(a)

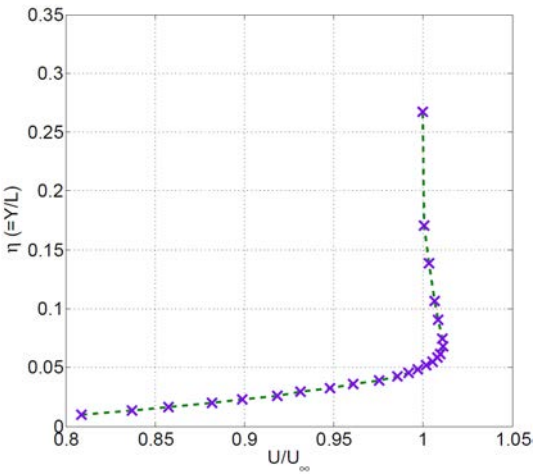

(b)

Figure 55: a) Variation of static dynamic and total pressure along the wind tunnel; b) Boundary Layer Profile.

Table 10: Inlet boundary layer characteristics at $X_j = -6$, $Y_j = 0$.

U_∞	Ti	$\delta_{99\%}/L$	δ^*/L	θ/L	H	Re_θ
$50ms^{-1}$	$< 0.12\%$	0.04	0.077	0.058	1.33	4,334

mean velocity U_∞ was $50m/s$, which gives a Reynolds number based on the blade axial chord of 450,000. The wake profile of the center blade of the cascade is shown Figure 57. The pressure side is on the right side of the graph and the suction side on the left. The wake profile in Figure 58a) had a periodic shape as hoped. The minimum velocity in the wake of each blade varied from $62m/s$ $(1.24U_\infty)$ to $59m/s$ $(1.18U_\infty)$, from $s/S = 0.25, 0.50, 0.75$. In between the blades, the velocity started at about $73m/s$ $(1.46U_\infty)$ then decreased in a curved, concave fashion to about $70m/s$ $(1.4U_\infty)$ on the edge of the blades wake. The turbulence intensity downstream of the cascade was approximately 0.25% in between the blades and peaked at about 2% downstream of the central test blade. The turbulence intensity downstream of the two side blades was about 1.5% each. The maximum turbulence intensity at the pressure side and suction side walls was about 10% and 2%, respectively The effect of altering the angle of attack on the central test blade was also investigated. Figure 58b showed decreasing the angle of attack from 0° to −2.5° decreased the velocity downstream of the trailing edge by about $1m/s$ and, in general, decreased the suction side wake velocity by about 2 m/s; the pressure side wake was reduced by $1m/s$. It also shifted the position of minimum velocity slightly to the left. When the angle of attack was increased from 0° to +2.5°, the minimum velocity in the wake was decreased by approximately $25m/s$ $(0.5U_\infty)$. This increase in angle of attack also created a wake about 350% larger than the 0° wake. A second measurement of the wake at a later time, shown in purple, produced a different result. In this case, the wake minimum velocity was about $15m/s$ $(0.3U_\infty)$ lower than the 0° angle of attack case. This result most likely occurred because the

DISTRIBUTION A: Distribution approved for public release.

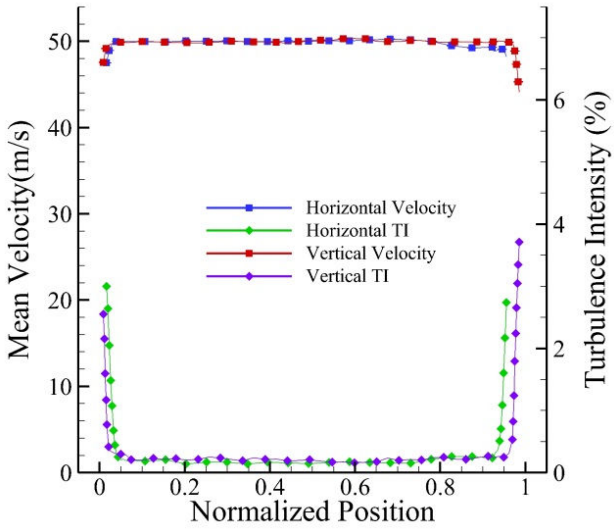

(a) Mean Velocity and Turbulence Intensity at Slot s0

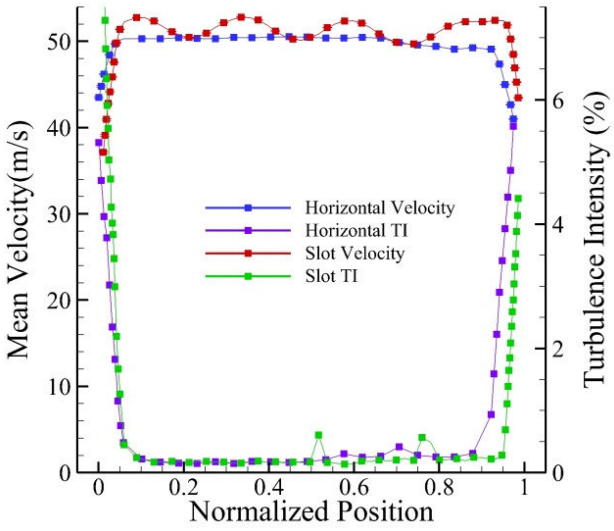

(b) Mean Velocity and Turbulence Intensity at Slot s2

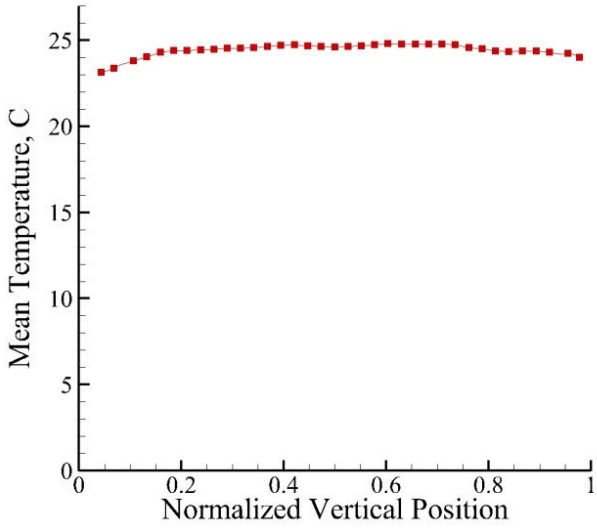

(c) Mean Temperature vs. Vertical Direction at Slot s0

Figure 56: Velocity, turbulence intensity and temperature profiles for slot s0 and s2.

DISTRIBUTION A: Distribution approved for public release.

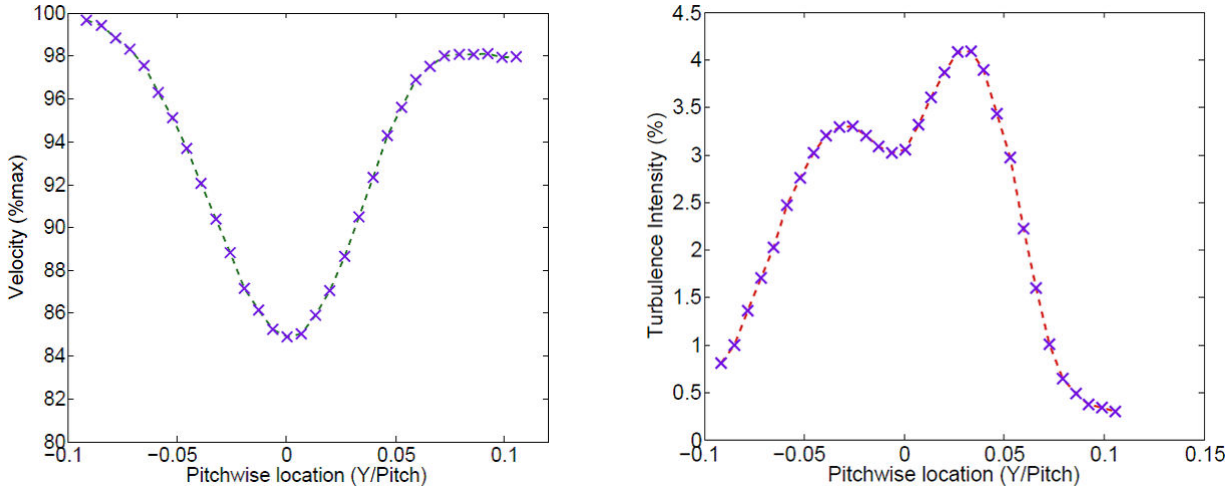

(a) (b)

Figure 57: a) Wake velocity profile on a L1A blade at $Re = 450,000$; b) Turbulence intensity profile on a L1A blade at $Re = 450,000$.

Table 11: Results of Frequency Analysis on Wind Tunnel Ducting and Test Section Walls

Location	Characteristic Length, $L_c(m)$	Natural Frequency, $\omega_n(Hz)$	Characteristic Frequency, $f(Hz)$
Upstream Duct	0.9652	180	10
Bottom & Top Wall	0.3048	570	164
Left & Right Wall	0.4953	350	100

blade was not at a $+2.5°$ angle of attack when the measurement took place, but instead was at an angle of attack slightly lower ($2.0°$). However, this is still useful because it shows the blade is very sensitive to an increasing angle of attack.

3.2.3 Test Section Spectral Content

- *Test section inlet* (s0) - The energy spectrum at all four walls and the center of the test section was measured in slot s0 (figure 59). In all cases, a peak occurred at $15Hz$. At the center of the test section, a peak occurred at $470Hz$ as well. A more distributed set of peaks also occurred from $200 - 300Hz$ in the center of the test section. The peaks in energy were compared to the natural frequency of the wind tunnel ducts, and test section walls (table 11). Based on those estimates, the $15Hz$ peak is consistent with the tunnel ducting and the $470Hz$ peak with the test section walls natural frequencies. The "hump" from $200 - 300Hz$ could arise from a combination of the natural frequency and the characteristic frequency of the test section walls.

DISTRIBUTION A: Distribution approved for public release.

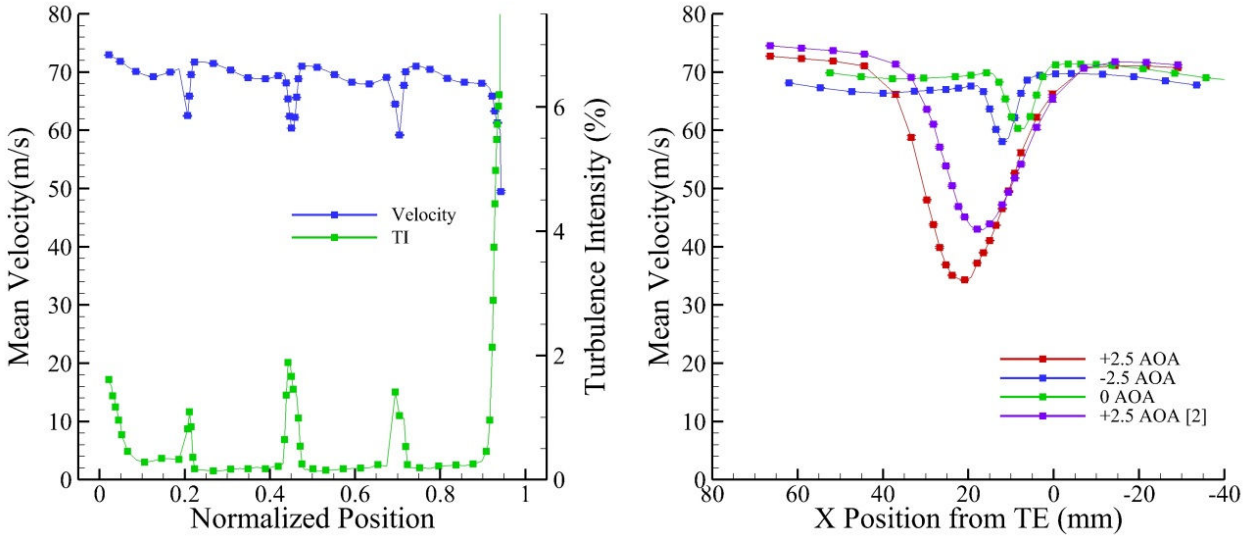

(a) Mean Velocity and Turbulence Intensity at Slot s3 (b) Comparison of Blade Wake Profiles at Different Angle of Attack

Figure 58: Wake velocity profiles at slot s3.

- *Test section outlet* (s3) - The energy spectrum of the central test blade wake was also investigated at different angles of angles of attack from $+2.5°$ to $-2.5°$ (figure 60). A small peak occurred at about $15Hz$ for the $0°$ and $-2.5°$ angle of attack cases, consistent with the one found at the test section inlet. For the $+2.5°$ case, a hump occurred from $200Hz$ to $500Hz$. This hump or peak in the energy spectrum is possibly the wake shedding frequency of an unstable or separated boundary layer. The supposed reason for the $+2.5°$ wake to produce two different energy spectra is an error in the blade position. It is believe the case labeled "+2.5 AOA" was actually at an angle of attack $+2°$. However, the fact that the hump disappeared when the angle of attack was slightly decreased shows the blade becomes very sensitive when the angle of attack is increased to $+2°$.

3.2.4 Pressure Profiles

Pressure profiles were acquired using the in-house designed pressure tap blade and two Scanivalve DSA 3217 Pressure Scanners. The pressure coefficient results were also put in perspective of provided AFOSR reference pressure profiles, and $k-\epsilon$ simulations using Ansys Fluent (figure 61). The experimental coefficient of pressure (C_P) shown has decent agreement with the AFOSR results but better agreement with the CFD results. The largest deviations occur on the suction side of the blade where the blade has high curvature, and at the trailing edge of the blade. The most likely cause of the discrepancies is the test section pressure bleeds which were opened to balance the flow at slot s2 and slot s3. The C_P trends were measured at three different incoming velocities (figure 61b), chosen because within 5% of the nominal incoming Reynolds number, and collapsed on top of each other as expected.

DISTRIBUTION A: Distribution approved for public release.

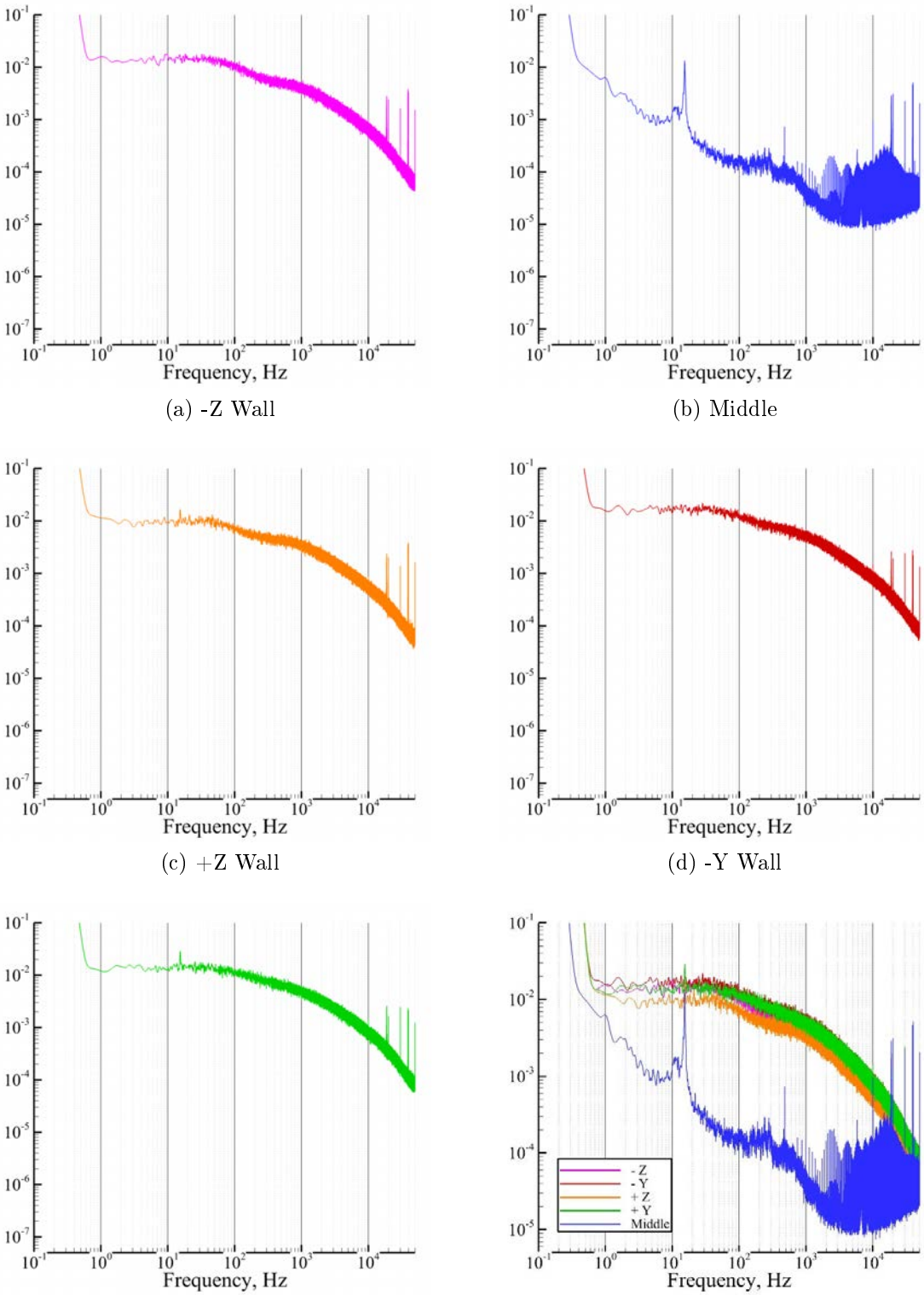

(a) -Z Wall (b) Middle

(c) +Z Wall (d) -Y Wall

(e) +Y Wall (f) Comparison of a-e

Figure 59: Energy Spectra at Slot s0

DISTRIBUTION A: Distribution approved for public release.

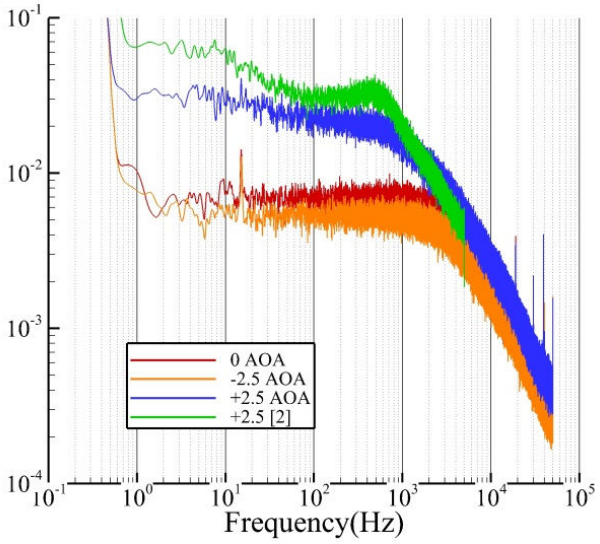

Figure 60: Central Test Blade Wake Spectra at +2.5°, 0°, and -2.5° Angle of Attack.

Similarly, C_P trends were measured at three different angles of attack and decreased on the suction side as the angle of attack was increased, and remained essentially constant on the pressure side (except near the leading and trailing edges). The C_P trends evidenced a boundary layer separation (figure 61c) when at +2.5°, consistent with the findings in the spectral measurements.

3.3 Linear Cascade Characterization with Wake Generator

Incoming velocity profiles were acquired at slot s0 (figure 62), Cascade wake measurements were acquired at the downstream slot located $3in$ from the cascade trailing edge plane. The slot was located $3in$ downstream of the cascade blade leading edges in the Z direction not the direction depicted in Figure 62.

All "running" results were acquired when the wake generator was running at a translation velocity of $1m/s$. This corresponds to a wake passing frequency of $6.5Hz$ based on a blade spacing of $6in$. Other results were acquired with the wake generator at a fixed position to compare with the running results. These results are labeled "aligned" and "misaligned" and the positions are depicted below in Figure 63.

The spacing between the leading edge of the cascade blades and the trailing edge of the wake generator blades was designed to be 40% of the axial chord or 2.4 inches.

3.3.1 Test Section Velocity Distribution

- *Test section inlet* (s0) - The velocity profiles and turbulence intensities at slot s0 (figure 64). Velocity profile and turbulence intensity were evaluated with the wake generator blades in the aligned, misaligned, and running positions. Velocity profiles are uniform across vertical and horizontal direction of the test section. A single point measurement of the velocity was acquired at slot s0 for fluctuation purposes. The mean velocity when

DISTRIBUTION A: Distribution approved for public release.

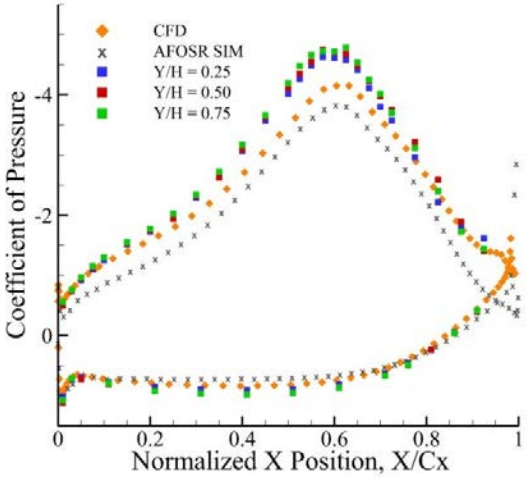

(a) $C_P$with AOA = 0° and $U_\infty = 49.04 \pm 0.11 m/s$ on the Cascade Blade Compared to an AFOSR Simulation at $Re_{Cx} = 500,000$ and a k-ε 3D Simulation at $Re_{Cx} = 500,000$.

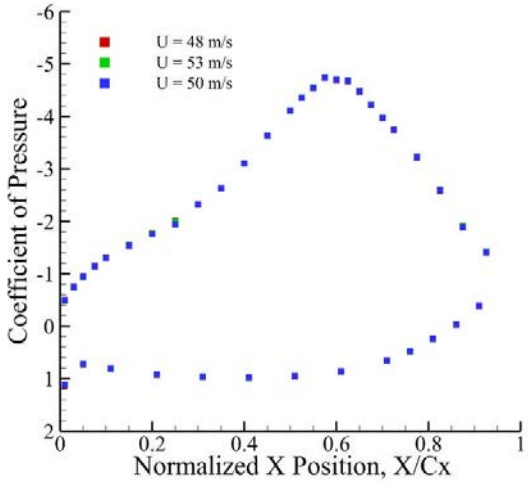

(b) Comparison of $Y/H = 0.50$ C_P at Different Incoming Velocities and 0° AOA

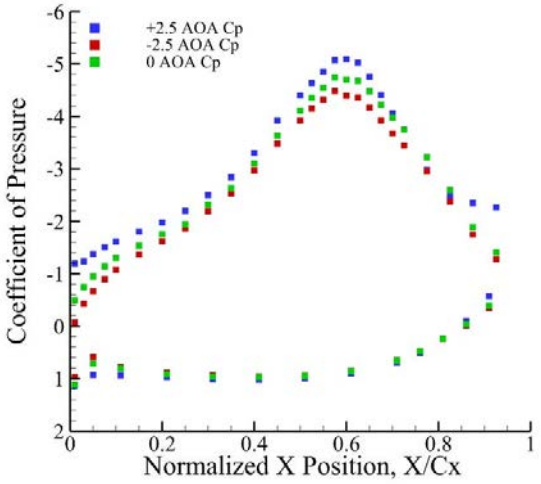

(c) Comparison of $Y/H = 0.50$ C_P at different Angle of Attack and $U_\infty = 48.71 \pm 0.33 m/s$.

Figure 61: Experimental, AFOSR and CFD pressure profiles.

DISTRIBUTION A: Distribution approved for public release.

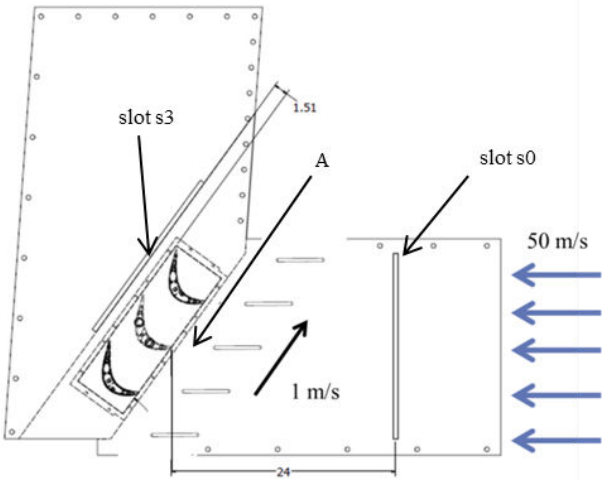

Figure 62: Illustration of Test Section with Wake Generator Installed and CTA Slots Labeled.

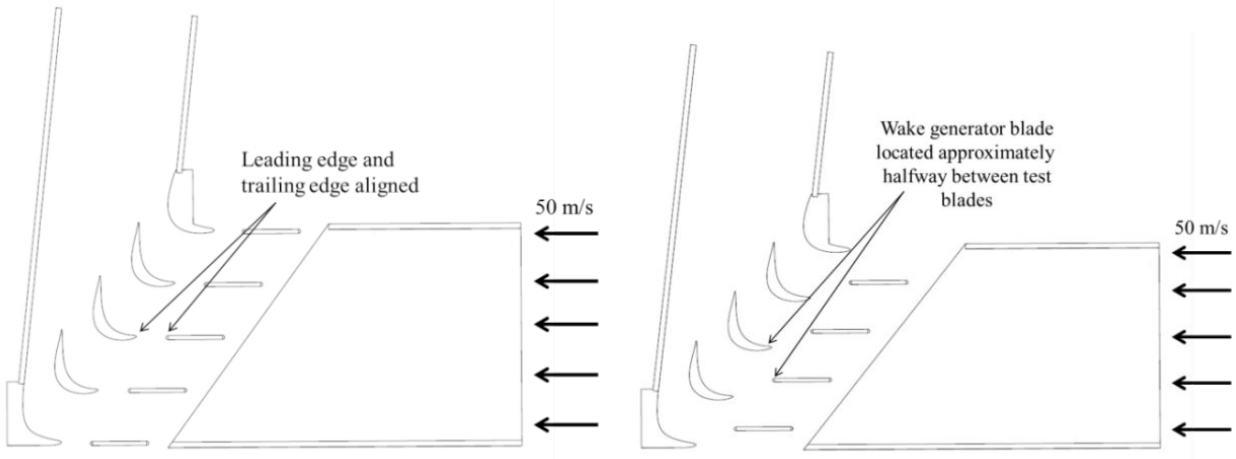

(a) (b)

Figure 63: Illustration of "Aligned" (left) and "Misaligned" (right) Configurations

DISTRIBUTION A: Distribution approved for public release.

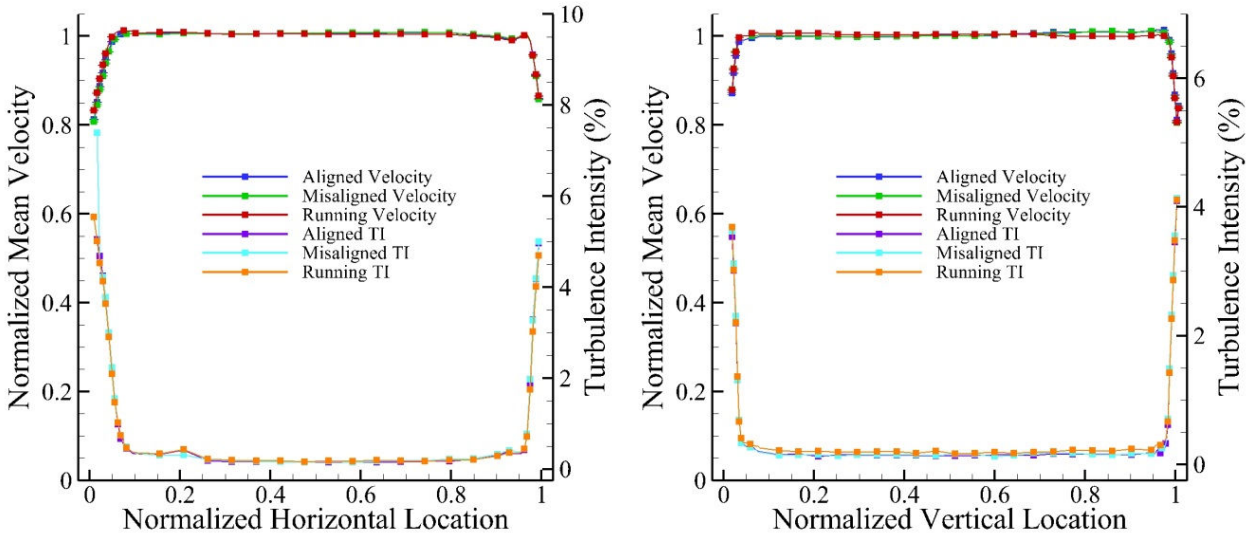

(a) Horizontal (b) Vertical

Figure 64: Velocity Profiles and Turbulence Intensities in Slot s0 for Different Cases.

the wake generator was aligned was $50.029 \pm 0.035 m/s$ and $49.972 \pm 0.037 m/s$ when it was misaligned. When the wake generator was running, the velocity varied from $49.991 m/s$ to $49.840 m/s$. However, phase averaged results acquired over 104 cycles at the same positions showed no cyclic pattern occurring with the wake generator running. The turbulence intensity in the freestream was about 0.20% with the wake generator running and about 0.15% with it off for the horizontal and vertical profiles. It increases, as expected, near the walls and in the boundary layer.

- *Test section outlet* (s3) - The wake of the cascade blades was acquired with the wake generator blades in the aligned and misaligned positions, and compared to the case without the wake generator installed. The velocity in the wake was slightly higher with the wake generator installed than without it (not shown in Figure 65). The test section bleeds changed the mass flow rate exiting the cascade and thus, caused a decrease in the overall velocity downstream of the cascade. With the wake generator installed, the bleeds were not used producing a higher mass flow rate; therefore, the velocity was also higher. The central test blade minimum velocity was about $5 m/s$ lower than the top and bottom test blades for the aligned case (figure 65). In this same case, the velocity between the blades started at about $80 m/s$ ($1.6 U_\infty$) on the pressure side and slowly decreased to about $78 m/s$ ($1.56 U_\infty$) on the suction side before the wake of the blades begins. The aligned profile was also shifted to the left by $l/L = 0.02$ and had a lower minimum velocity for each blade than the misaligned profile. The values there are from 0.50 compared to 0.25% in the "Velocity w/o Wake Generator" case. The overall velocity profile, in the misaligned case, decreased slightly with increasing position (from left to right) possibly due to flow restrictions caused by the wake generator blade locations. The aligned case turbulence intensity was larger

DISTRIBUTION A: Distribution approved for public release.

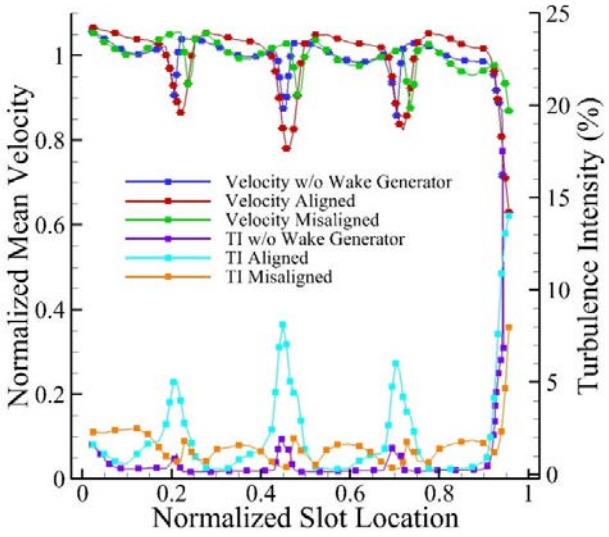

Figure 65: Comparison of the Velocity and Turbulence Intensity in the Wake of the Cascade Blades with the Wake Generator in Different Positions and without the Wake Generator Installed.

than the misaligned case with values of 5%, 9%, and 7% from bottom to top in the cascade (figure 65).

- *Phase averaged results in the wakes* - The results were phase averaged over 208 cycles for the central test blade and 104 cycles for the wake generator blade. The period of one cycle was calculated to be $T = 0.15385s$ based on the $6.5Hz$ wake passing frequency. The wake generator profile (figure 66a) was measured at the leading edge of the central test blade and shows an initial incoming velocity of $50m/s$ at $t0$ then a decrease starting at $t/T = 0.50$. The minimum velocity, $U = 38m/s$, occurred at $t/T = 0.7175$. After this time, the velocity increased back to $50m/s$ at $t/T = 1.0$. The effect of the passing wake on the central test blade wake (figure 66b) show that the wake profile initially looks very similar to the one of the misaligned case, then started to shift towards the suction side at $t/T = 0.50$ and grow wider, moving closer to the profile observed in the aligned case. The wake was about $l/L = 0.25$ wide at $t/T = 0$, and grew to $l/L = 0.41$ at $t/T = 0.75$. The minimum velocity was approximately $60m/s$ $(1.2U_\infty)$ and the wake very wide. After time $t/T = 0.75$, the wake shifts back towards the pressure side and eventually goes back to the same shape as at $t0$.

3.3.2 Test Section Spectral Content

- *Test section inlet* (s0) - The energy spectrums computed at the walls and center of slot s0 were acquired with the wake generator running and in the aligned position. The spectra at the test section walls (figure 67a) have the same very high frequency peaks observed without the wake generator at $1kHz$. The center of the test section

DISTRIBUTION A: Distribution approved for public release.

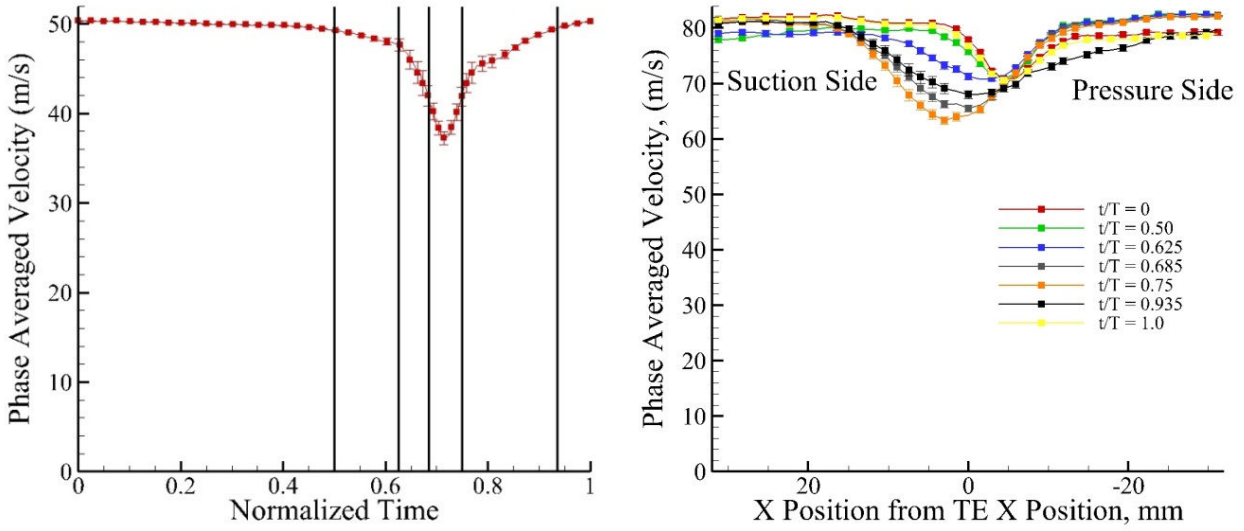

(a) (b)

Figure 66: (a) Phase Averaged Time Record of the Wake Generator Blade; (b) Phase Averaged Velocity Profile of the Central Test Blade Wake at Different Times

exhibited those same peaks, although at lower amplitude, and peaks at $11Hz$, $30Hz$ and $90Hz$ and lower overall energy levels due to lower turbulence level. While the $11Hz$ peak was consistent with the tunnel ducting, the 90 and $1000Hz$ peaks were associated with the insertion of the wake generator. In particular, the $1kHz$ peak was found to be close to a characteristic frequency based on the freestream velocity and the blade spacing, $2.5C_x$. This peak disappeared from the boundary layer spectrum as soon as the wake generator was immobilized in a steady position, while the rest of the spectra remained identical. The wake generator blade passing frequency ($6.5Hz$) was also clearly captured in the test section center rotating sprectra.

- *Test section outlet* (s3) - The wake of the central test blade (figure 68) was acquired with the wake generator blades aligned, misaligned and running; the wake of the wake generator blade was acquired in the aligned and running positions. The central test blade measurement was acquired at the location of the minimum velocity in the wake. The wake generator measurement was at $Y/H = 0.5$ and about $1in$ upstream of the leading edge of the central test blade ("A" in figure 62). The aligned case (figure 68a) has higher energy content compared to the misaligned case indicating a more turbulent wake. Peaks occured at about $30Hz$ and $900Hz$ in that case. Both of these peaks are most likely the same ones observed in the center of the test section. The $900Hz$ peak occured in the misaligned case as well, although shifted to slightly higher values since the distance from blade to vane was increased. The wake passing frequency was picked up along with the resulting harmonics in the running case. In Figure 68b, the expected $6.5Hz$ peak and its harmonics are present along with the same $900Hz$ peak observed upstream of the wake generator for the running case, yet with overall lower energy

DISTRIBUTION A: Distribution approved for public release.

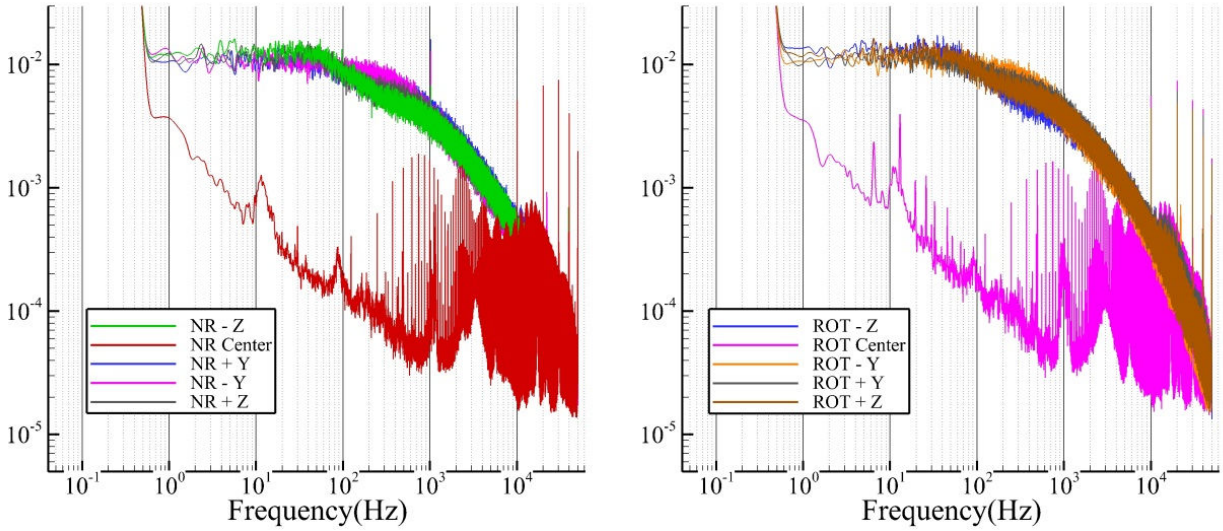

(a) Not Rotating (NR)

(b) Rotating (ROT)

Figure 67: Slot s0 Energy Spectrum at Different Positions.

content. The peak at $1000Hz$ in the aligned case was also a full order of magnitude larger than in figure 67 and 68a. For the running case, the peak at about $900Hz$ was actually wider and had lower peak energy because of the fluctuating blade spacing due to the blade motion.

3.3.3 Pressure Measurements

- *Time Independent Measurements* - Pressure measurements were acquired with the wake generator blades in the aligned and misaligned positions to compare with the phase averaged profiles acquired with the wake generator running. The coefficient of pressure distribution on the pressure tap blade at three locations along the blade height: $Y/H = 0.25, 0.50$ and 0.75 were acquired in the aligned and misaligned positions (figure 69). Overall the agreement was very good and the results were well within 10% of one another. Static comparisons (aligned and misaligned - figure 70) with AFOSR and CFD C_P values at $Y/H = 0.5$ show that the current experimental results agree very well with the CFD results and slightly less with the AFOSR results, in particular at the trailing edge. C_P on the suction side when the wake generator was not installed was the lowest compared to the aligned and misaligned cases, most likely due to the test section bleeds. As expected, the aligned case resulted in the highest coefficient of pressure on the suction side compared to the other two cases. The experimental results for the misaligned case followed the CFD curve almost exactly and wer only slightly shifted compared to the AFOSR results. In Figure 69, the coefficient of pressure distribution on the pressure tap blade is presented for three locations along the blade height: $Y/H = 0.25, 0.50$, and 0.75. The results are shown for the aligned and misaligned cases. In both cases, there is some slight disagreement between the spanwise sections on the

DISTRIBUTION A: Distribution approved for public release.

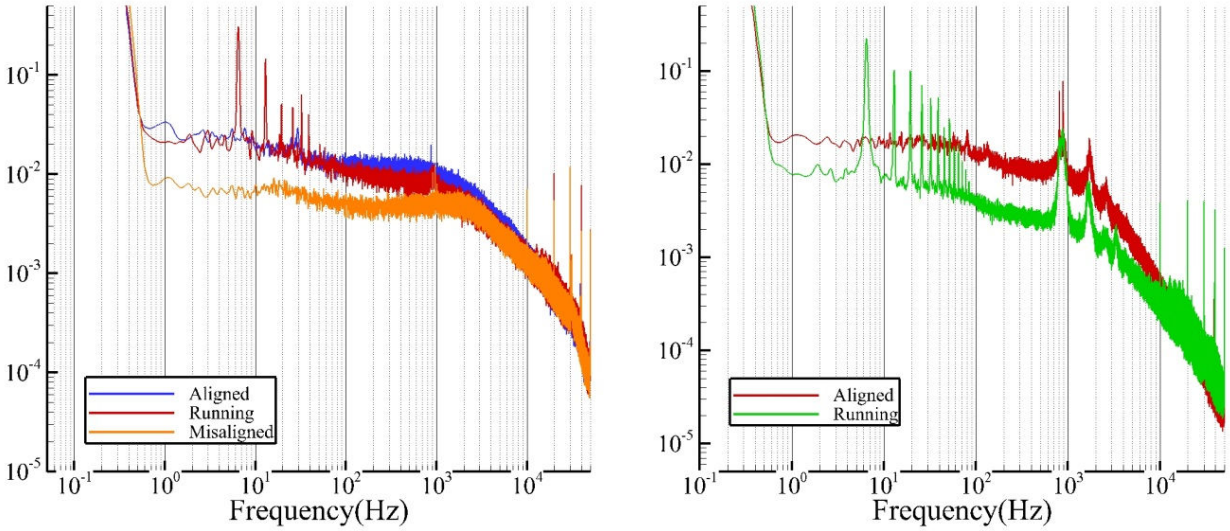

(a) Central Test Blade

(b) Wake Generator Blades

Figure 68: Energy Spectrum in the Wake of the Blades.

pressure side and on the suction side near the trailing edge. However, the overall agreement is very good and the results are well within 10% of one another. Figure 70 compares the experimental results with the previously presented computational and experimental results. Only the experimental results for the section at $Y/H = 0.50$ are presented to unclutter the graph. C_P on the pressure side appears to be the same for all cases, even at the leading edge. On the pressure side, the experimental results agree very well with the CFD results and slightly less with the AFOSR results. Again, the results at the trailing edge do not agree with the AFOSR data. C_P on the suction side when the wake generator is not installed is the lowest compared to the aligned and misaligned cases, most likely due to the test section bleeds. As expected, the aligned case resulted in the highest coefficient of pressure on the suction side compared to the other two cases; therefore, it the blade produced the least amount of lift in that case. The experimental results for the misaligned case follow the CFD curve almost exactly and are only slightly shifted compared to the AFOSR results.

- *Phase Averaged Results* - The pressure distribution on the blade profile was captured when the wake generator was running with a wake passing frequency of $6.5Hz$ over a total of 104 cycles (figure 71). The stagnation point at the leading edge of the blade fluctuated as the wake passed, varrying from 0.9, initially, to 1.0 then down to 0.8 at $t/T = 0.90$ and indicating that the freestream flow lost energy due to losses occurring in the wake of the wake generator blade. Overall, the C_P value increased homogeneously until about $t/T = 0.60$ as a result of the flow accelerating and recovering after a wake passage, and decreased as the wake passed. The suction side was first impacted by the wake and therefore C_P values decreased there first. The pressure side was impacted $t/T = 0.10$ later, with a decrease in C_P. Overall, the fluctuations were very small and did not affect the airfoil lift by much.

DISTRIBUTION A: Distribution approved for public release.

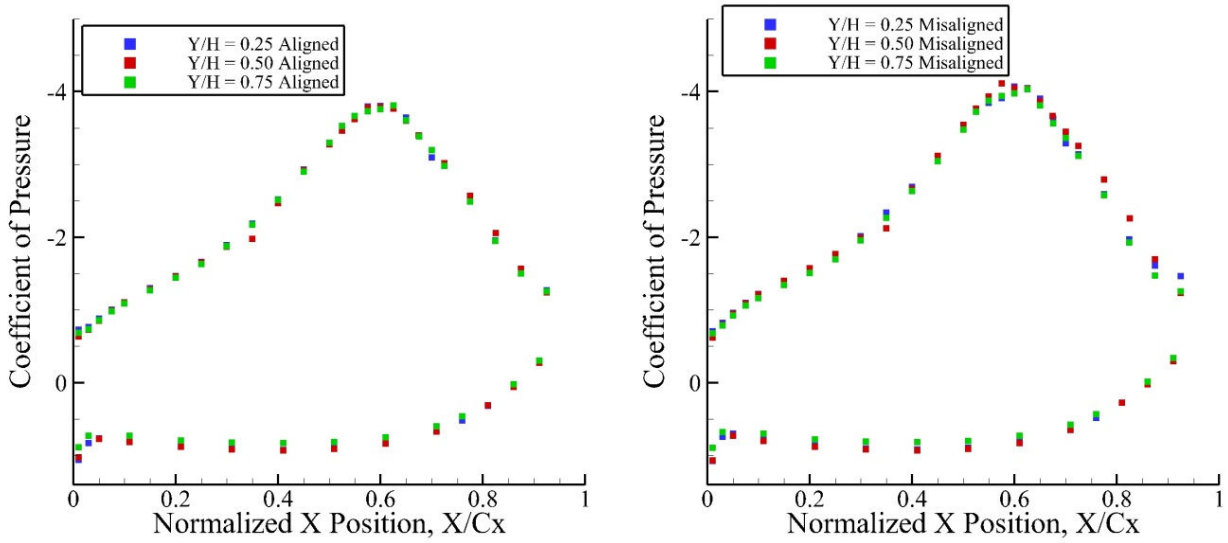

(a) Aligned (b) Misaligned

Figure 69: Coefficient of Pressure Distribution on the Pressure Tap Blade with the Wake Generator Blades in Different Positions.

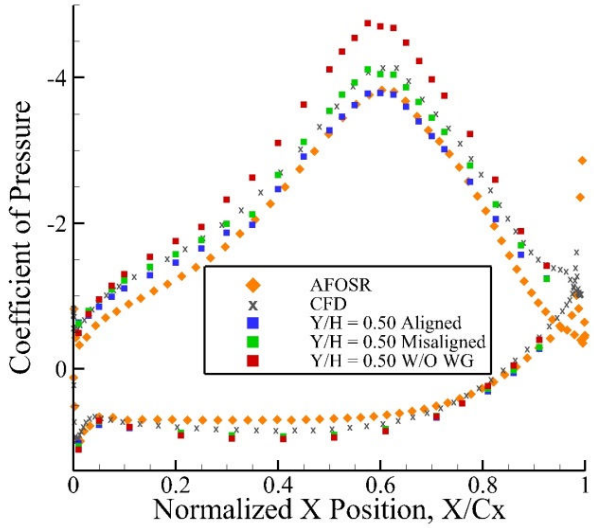

Figure 70: Comparison of the Coefficient of Pressure Distribution with the AFOSR and CFD Results.

DISTRIBUTION A: Distribution approved for public release.

3.4 Particle Image Velocimetry and Mie scattering visualizations

PIV measurements and Mie scattering visualizations were realized using the optical setup described previously. The reference field U_0 is shown in figure 72 with the conveyor off, and the wind tunnel operating at $Re = 450,000$. It shows the flow acceleration over the suction side of the blade, up to twice the incoming free-stream velocity. In figure 73, the normalized phase averaged velocity field for the cascade running at $Re = 450,000$, compared to the velocity field without the conveyor running. The phase location is so that the wake impinges on the blade at the phase locked position $\phi = 0$ (or $\phi = 1$). The absolute velocity field fluctuates very little throughout the conveyor cycle when compared to the field without the conveyor running. The velocity difference between the field at phase locked position ϕ and the field without the conveyor running ($\|U - U_0\| / U_\infty$) is provided in figure 74. The wake is clearly evidenced impacting the blade with a momentum deficit of approximately 10% with respect to the undisturbed field. The corresponding vorticity field is shown in figure 75 evidences the phase averaged vorticity field associated with the wake as it approaches the blade.

Finally, figure 76 shows Mie scattering visualizations of the blade with a film cooling jet located at the $x/C_x = 33\%$ location, operating at a blowing ratio of $BR_\infty = 0.5$, based on the free stream velocity such that $BR_\infty = U_j/U_\infty$. While the image at the top shows an undisturbed film cooling jet when the wake is away from the blade, the following images show the impact of the wake impinging on the blade and the disruptions of the film it creates.

DISTRIBUTION A: Distribution approved for public release.

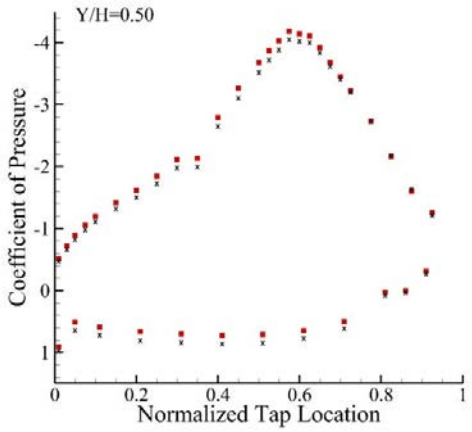

(a) $t/T = 0.0$

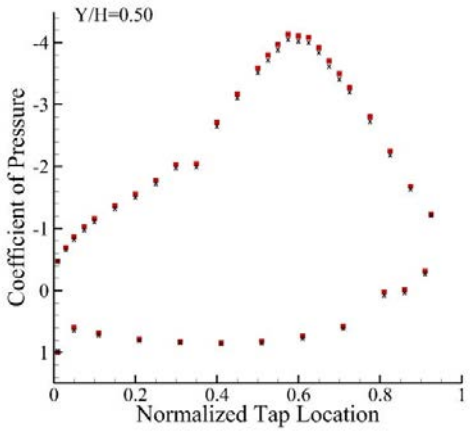

(b) $t/T = 0.2$

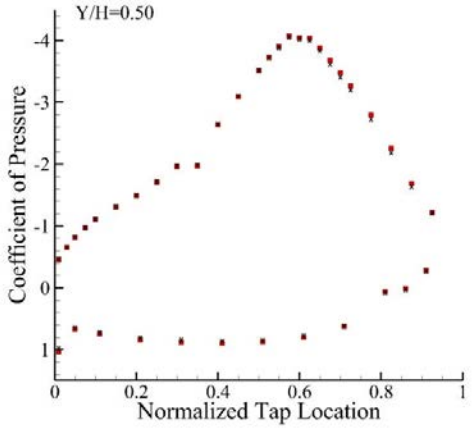

(c) $t/T = 0.4$

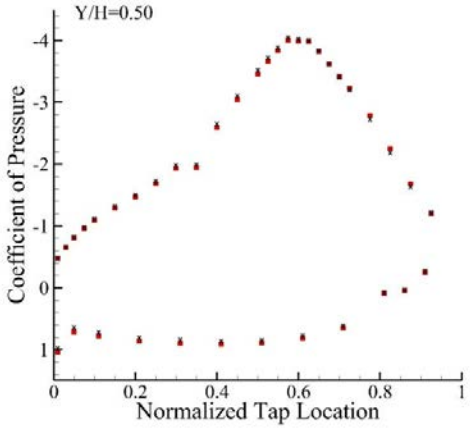

(d) $t/T = 0.6$

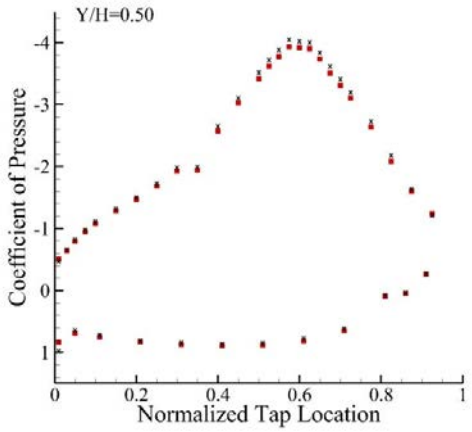

(e) $t/T = 0.8$

Figure 71: Phase Averaged Coefficient of Pressure Profile ($Y/H = 0.5$) at Different Times during a Cycle (*red symbols*) and time averaged coefficients of pressure profile (black symbols).

DISTRIBUTION A: Distribution approved for public release.

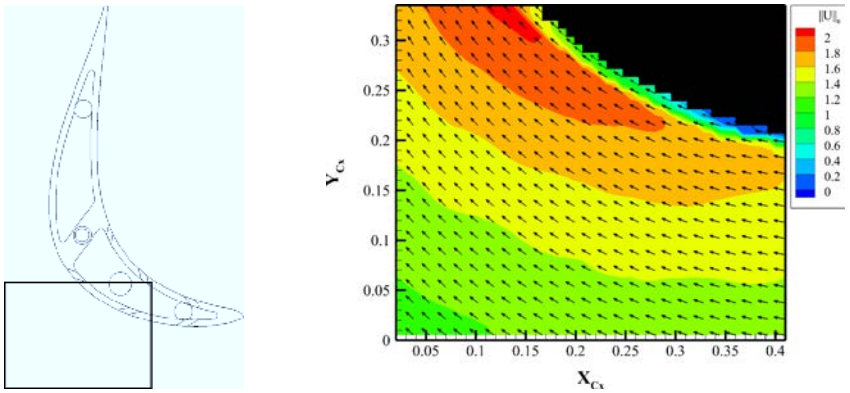

(a) (b)

Figure 72: a) Field of view; b) Normalized velocity magnitude with conveyor off - $\|U_0\|/U_\infty$, for $Re = 450,000$

DISTRIBUTION A: Distribution approved for public release.

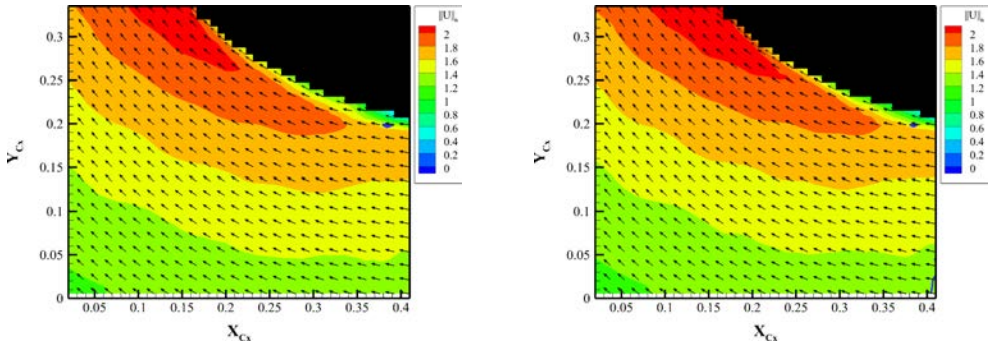

(a) $\phi = 0.13$

(b) $\phi = 0.26$

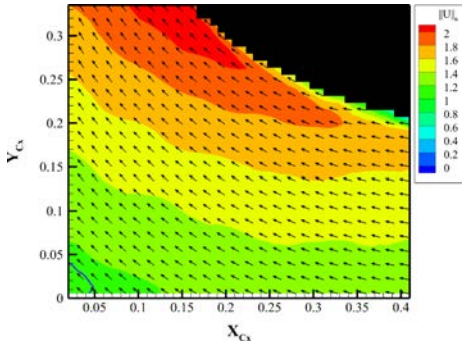

(c) $\phi = 0.40$

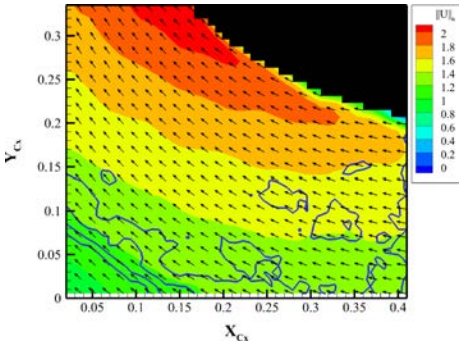

(d) $\phi = 0.53$

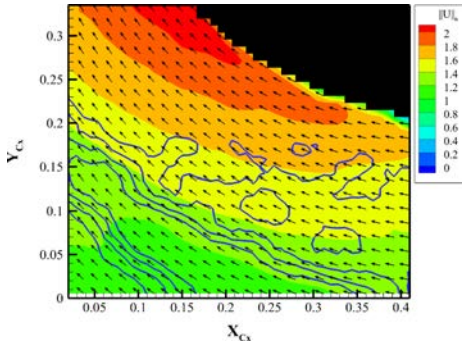

(e) $\phi = 0.66$

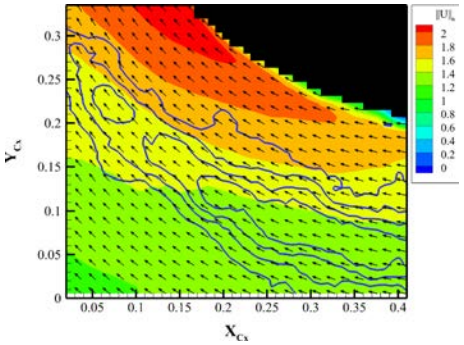

(f) $\phi = 0.80$

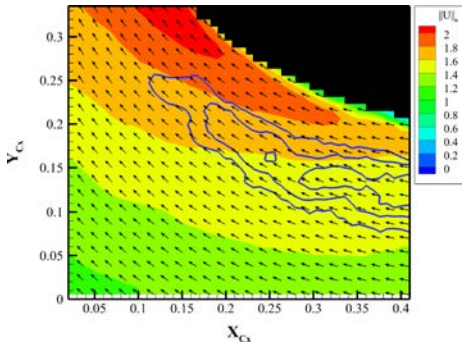

(g) $\phi = 0.93$

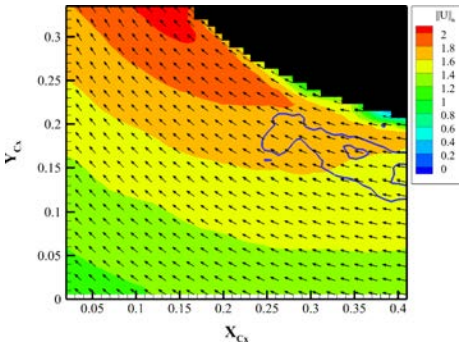

(h) $\phi = 1$

Figure 73: Phase Averaged Velocity magnitude $\|U\|/U_\infty$ with conveyor running, and $Re = 450,000$

DISTRIBUTION A: Distribution approved for public release.

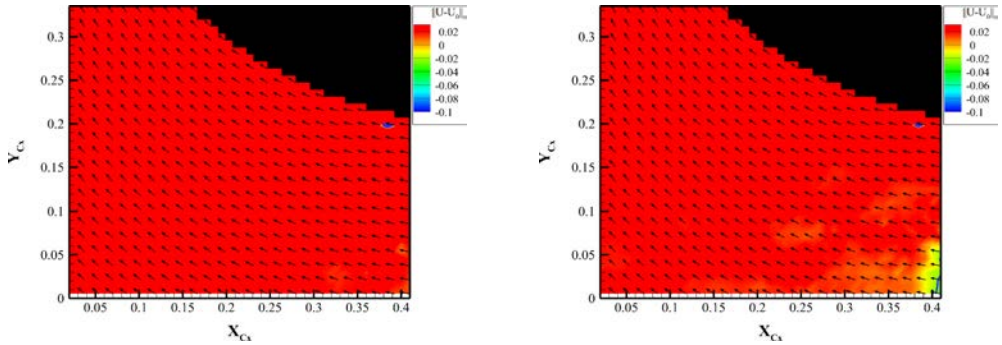

(a) $\phi = 0.13$

(b) $\phi = 0.26$

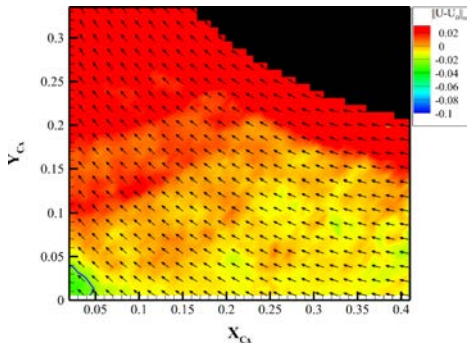

(c) $\phi = 0.40$

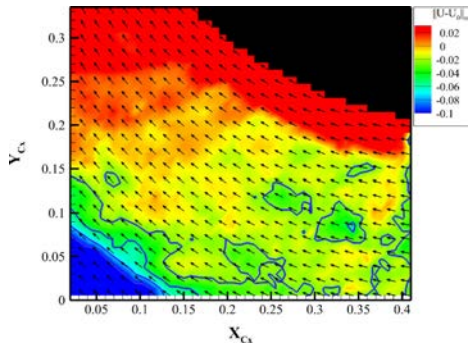

(d) $\phi = 0.53$

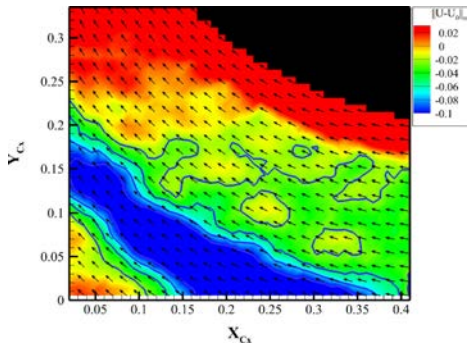

(e) $\phi = 0.66$

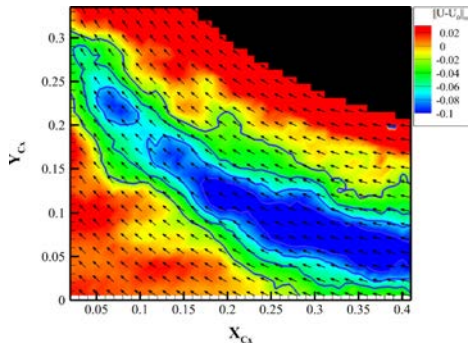

(f) $\phi = 0.80$

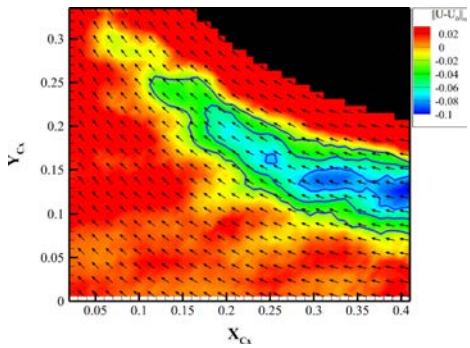

(g) $\phi = 0.93$

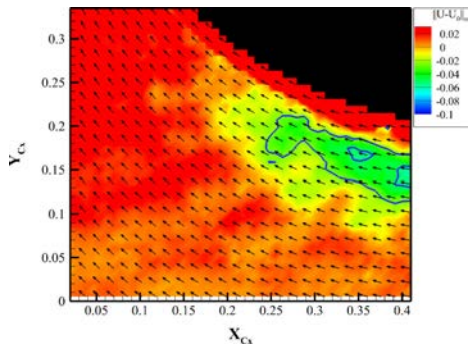

(h) $\phi = 1$

Figure 74: Phase Averaged Velocity magnitude difference $\|U - U_0\| / U_\infty$ with conveyor running, and $Re = 450,000$

DISTRIBUTION A: Distribution approved for public release.

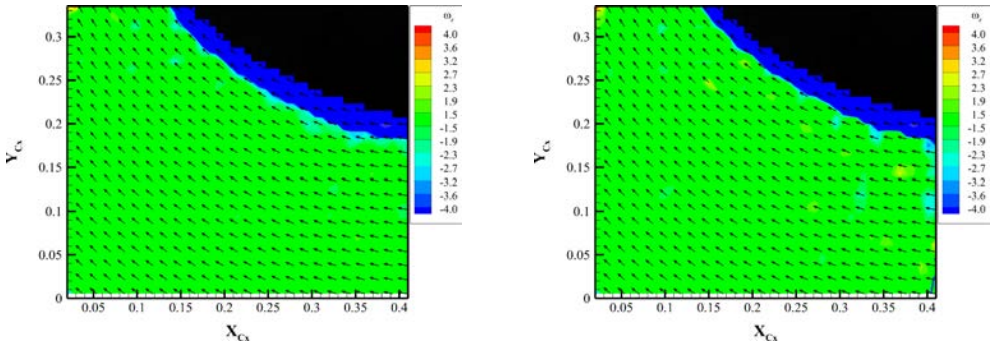

(a) $\phi = 0.13$

(b) $\phi = 0.26$

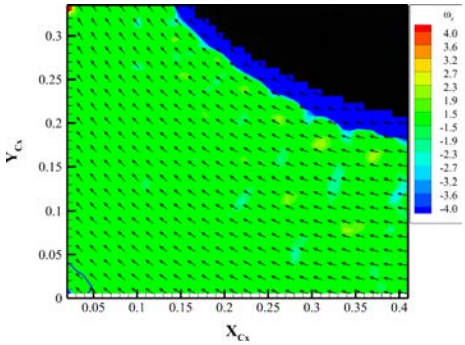

(c) $\phi = 0.40$

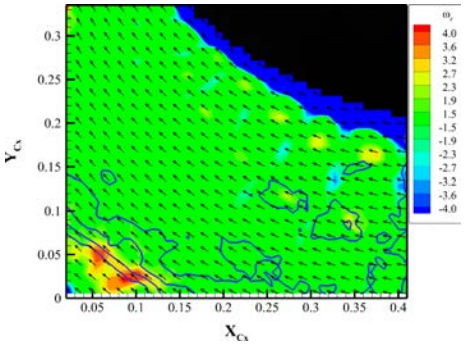

(d) $\phi = 0.53$

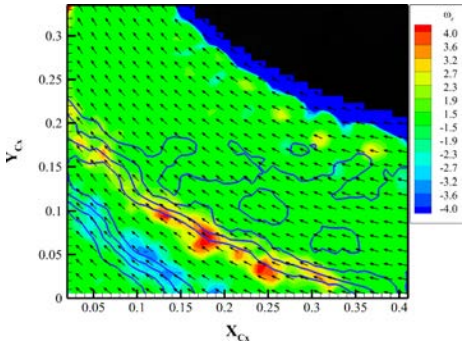

(e) $\phi = 0.66$

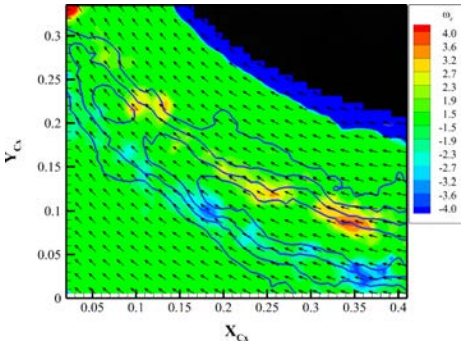

(f) $\phi = 0.80$

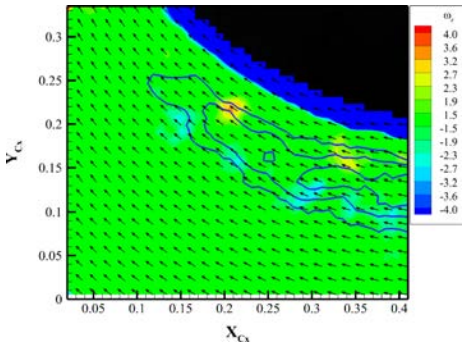

(g) $\phi = 0.93$

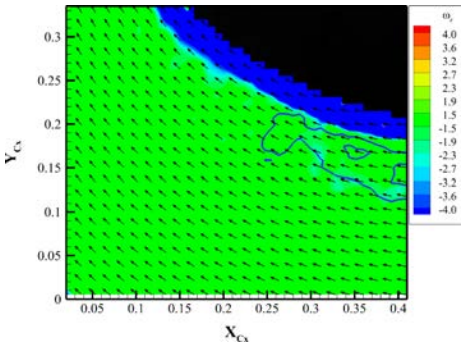

(h) $\phi = 1$

Figure 75: Phase Averaged Vorticity field of the normalized velocity field

DISTRIBUTION A: Distribution approved for public release.

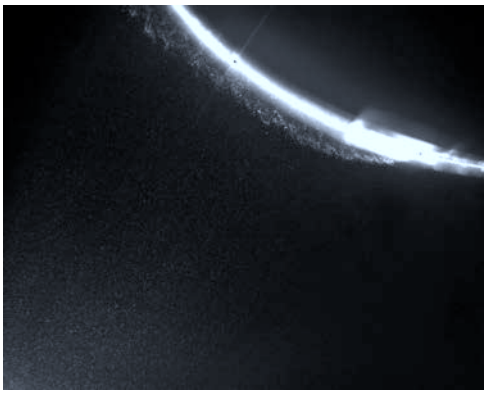

(a) Undisturbed film cooling jet

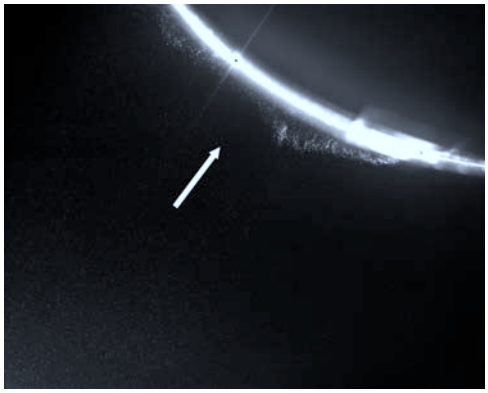

(b)

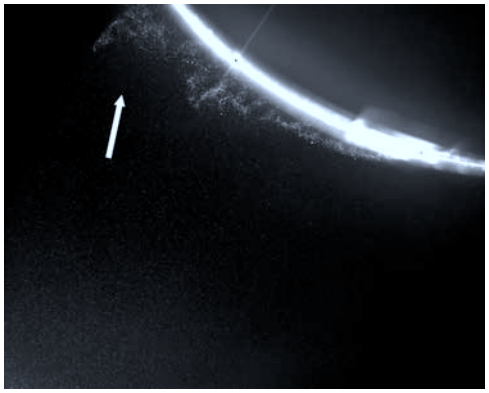

(c)

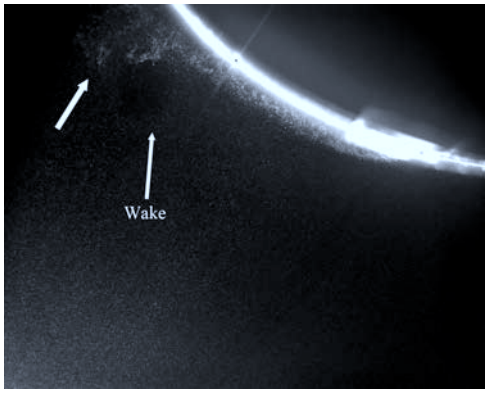

(d)

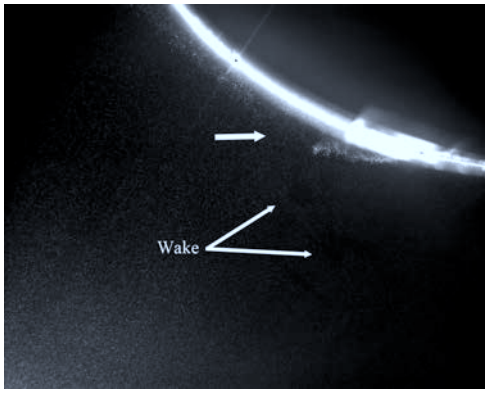

(e)

Figure 76: Undisturbed and disturbed ($\phi = 1$) film cooling jets at $BR = 0.5$, with conveyor running, and $Re = 450,000$.

DISTRIBUTION A: Distribution approved for public release.

Part III

Optimization, Reduced Order Modeling and Flow Control

DISTRIBUTION A: Distribution approved for public release.

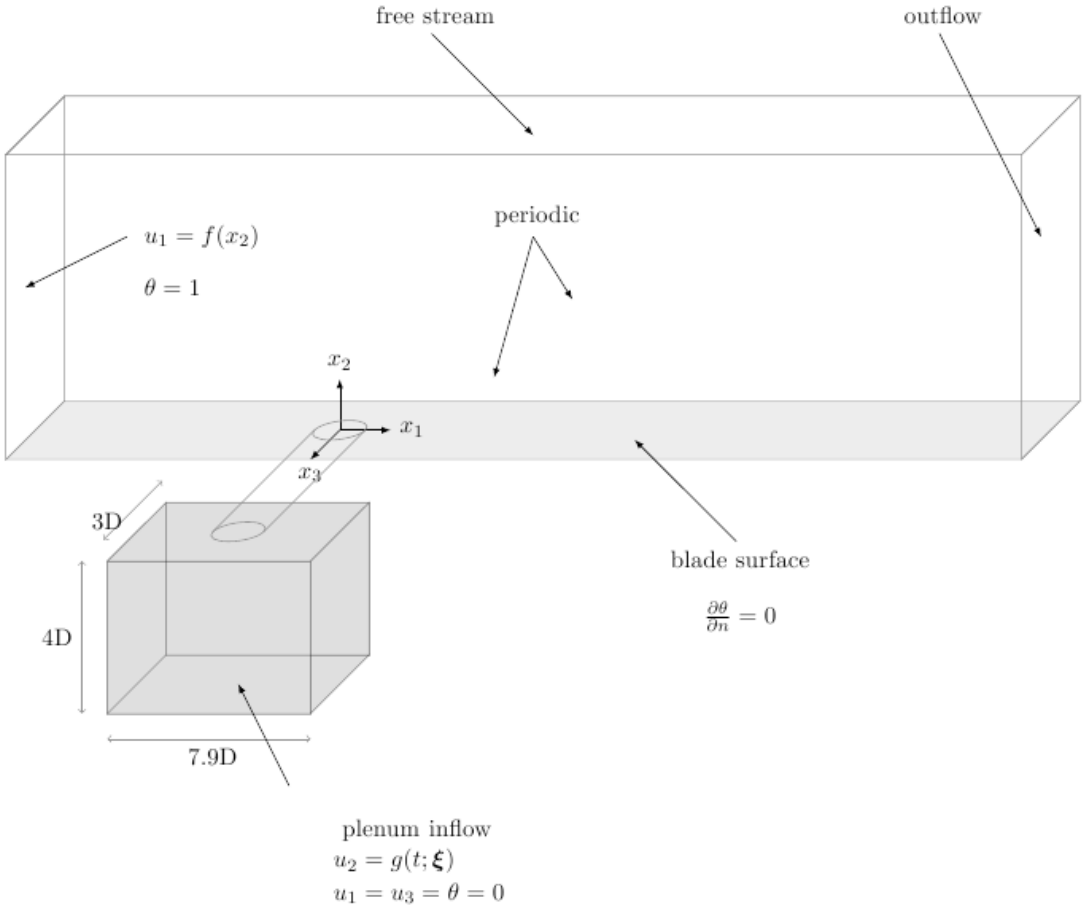

Figure 77: Schematic of the jet in cross-flow

1 Optimization of Forced Film Cooling Jets

1.1 Methodology

The incompressible Navier-Stokes/energy equations are solved without any use of a turbulence model by resolving all time and space scales. We consider $u = u(x,t;\xi)$, $p = p(x,t;\xi)$ and $\vartheta = \vartheta(x,t;\xi)$ where $\xi = (\xi_1, \xi_2)$ is a two- dimensional vector of design or control parameters. In the current study, design parameters are the duty cycle DC, and the non-dimensional pulsation period $Tp = U_\infty / Df$, where U_∞ is the cross-flow velocity, D is the jet diameter and f is the dimensional pulsation frequency.

As it will be explained later in this section DC and Tp are related to ξ_1 and ξ_2 through a linear mapping. The Reynolds number is defined as $Re = U_\infty D/\nu$, where ν is the kinematic viscosity. Figure 77 shows the schematic of the problem. The velocity signal at the bottom of the plenum, $g(t;\xi)$ is fixed by specifying the design parameters (DC, Tp) and the maximum and minimum plenum-inflow velocity. In figure 78, the generic form of the signal $g(t;\xi)$ is

DISTRIBUTION A: Distribution approved for public release.

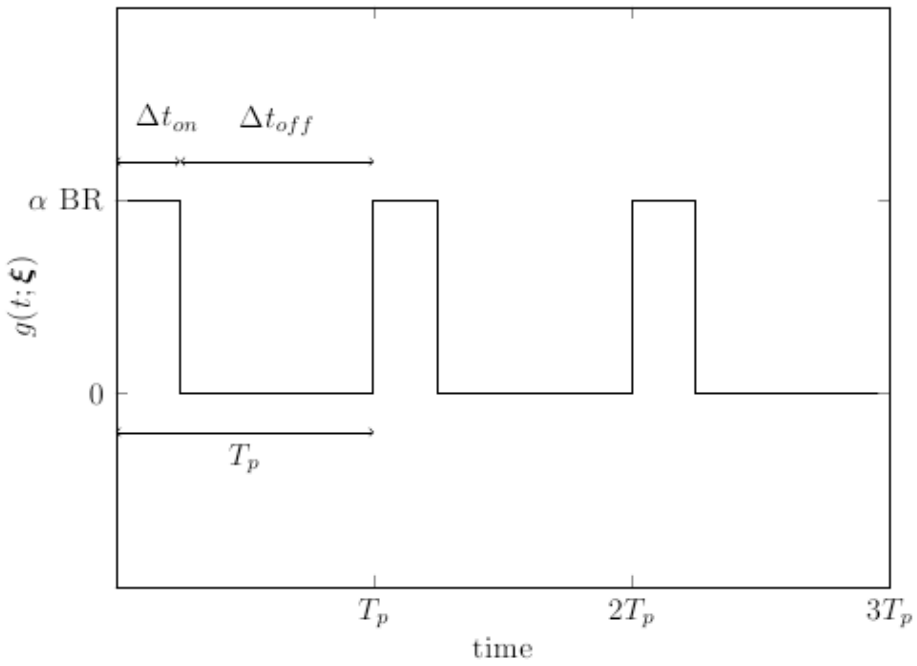

Figure 78: Blowing ration signal $g(t;\xi)$

shown. The amount of the time that the jet is on within each full period is denoted by Δt_{on} and therefore $DC = \Delta t_{on}/Tp$. We also introduce τ that shows the time percentage during a cycle. Therefore $\tau < DC$ represents the period that the jet is on and $\tau > DC$ when the jet is off. When the jet is on, the vertical velocity at the bottom of the plenum is equal to αBR. Here $\alpha = \pi D^2/4A_p$, with A_p being the area of the bottom of the plenum, accounts for the ratio of the area of the delivery tube to that of the plenum. When the jet is off, it is turned completely off and during this time the net mass flow rate through any x_2-section at the plenum or delivery tube is zero.

1.1.1 Optimization Problem

Our objective is to maximize the film cooling effectiveness as a function of duty cycle and pulsation period. To measure the effectiveness of film cooling we first define the spanwise-averaged film cooling effectiveness which is given by:

$$\eta(x_1,\xi) = \frac{1}{w\,(t_f - t_i)} \int_{t_i}^{t_f} \int_{-w/2}^{w/2} (1 - \theta\,(\mathbf{x}, t; \xi))\,|_{x_2=0} dx_3 dt$$

with w being the width of the cooled surface, t_i and t_f are the beginning and the end of the period over which the time-averaged quantities are calculated. In order to obtain an overall measure of the film cooling effectiveness, we further calculate the streamwise average of $\eta(x_1;\xi)$. This results:

$$\tilde{\eta}(\xi) = \frac{1}{x_{1_e} - x_{1_s}} \int_{x_{1_s}}^{x_{1_e}} \eta(x_1;\xi) dx_1$$

DISTRIBUTION A: Distribution approved for public release.

where x_{1_s} and x_{1_e} are the two ends of the interval in the streamwise direction within which the average film cooling effectiveness is calculated. The overall film cooling effectiveness, $\tilde{\eta}(\xi)$, is a function of two independent variables DC and Tp, with BR and geometry fixed. The goal is to find the DC and Tp at which the average film cooling effectiveness, $\tilde{\eta}(\xi)$, is globally maximum, and to understand the reasons that lead to this condition.

1.2 Simulation details

In all the cases in this study we perform direct numerical simulation on the jet in cross-flow with the schematic of the problem shown in figure 77. The origin of the coordinate system is at the center of the jet exit and x_1 is aligned with the streamwise direction, x_2 with the direction normal to the cooled surface and x_3 with the spanwise direction. The plenum has the length, height and width of $7.9D$, $4D$ and $3D$ respectively. The length of the delivery tube is $3.5D$ and the inclination angle is 35 degree. The mainstream domain, where the cross-flow and the coolant interact, spans the volume with the size of $22D \times 10D \times 3D$.

The center of the jet exit is located $7D$ downstream from the cross-flow inlet. The cross-flow boundary condition is assumed to be a laminar boundary layer flow with boundary layer thickness of $\delta_{99\%}/D = 0.5$ where $\delta_{99\%}$ is the thickness that the streamwise velocity in the boundary layer reaches 99% of the free-stream velocity. On the top boundary plane, free-stream flow is assumed with $u(x_1, 10, x_3) = (U_\infty, 0, 0)$ and $\vartheta(x_1, 10, x_3) = 1$, and on the spanwise direction periodic boundary condition is enforced. The periodic boundary condition mimics the situation where a row of holes are arranged in the spanwise direction. In the current case, the center-to-center distance between two consecutive holes is $3D$. A zero normal derivative boundary condition is assumed at the outflow. The uniform boundary condition $g(t;\xi)$ (see figure 78) is used for the vertical velocity component u_2 at the bottom of the plenum with $u_1 = u_3 = 0$ and $\vartheta = 0$. The area scaling factor is $\alpha = 0.0331$. As noted earlier, each pair of the design variables (DC, Tp), and the peak blowing ratio (the blowing ratio when the jet in on and is set to 1.5) specifies the signal $g(t;\xi)$. The Reynolds number, $Re_j = U_j D/\nu$, based on the jet space-averaged velocity (when the jet is on) is 1500 throughout and Prandtl number is $Pr = 1$. For all the wall boundaries, adiabatic condition is assumed for temperature. The computational time step was roughly 0.001. All simulations were advanced at least $40D/U_\infty$ before the statistics are collected. The statistics are then collected for approximately another $40D/U_\infty$. Care was taken to ensure that the calculation of the statistics starts at the beginning of a pulsation cycle and finishes at the end of another pulsation cycle. Additional sampling did not change the result.

1.2.1 Computational Mesh

We use hexahedral elements of spectral order of three and four in the current simulations. Figure 79(a) shows the three-dimensional view of the grid. To generate the grid, quadrilateral meshes were first generated in the x_1–x_3 planes in the main-stream domain, the delivery tube and the plenum. The quadrilateral elements exactly match across the common faces in between the volume parts. The two-dimensional mesh was then swept along the x_2 direction in the mainstream domain and plenum and along the axis of the cylinder in the delivery tube. The height of the first element in the cross-flow boundary layer is $0.06D$. The height of the elements increases (with 16 elements) using hyperbolic distribution to $0.3D$ at $x_2 = 4$. Two elements were used from $x_2 = 4$ to the top boundary at $x_2 = 10$. Note that flow in this region

DISTRIBUTION A: Distribution approved for public release.

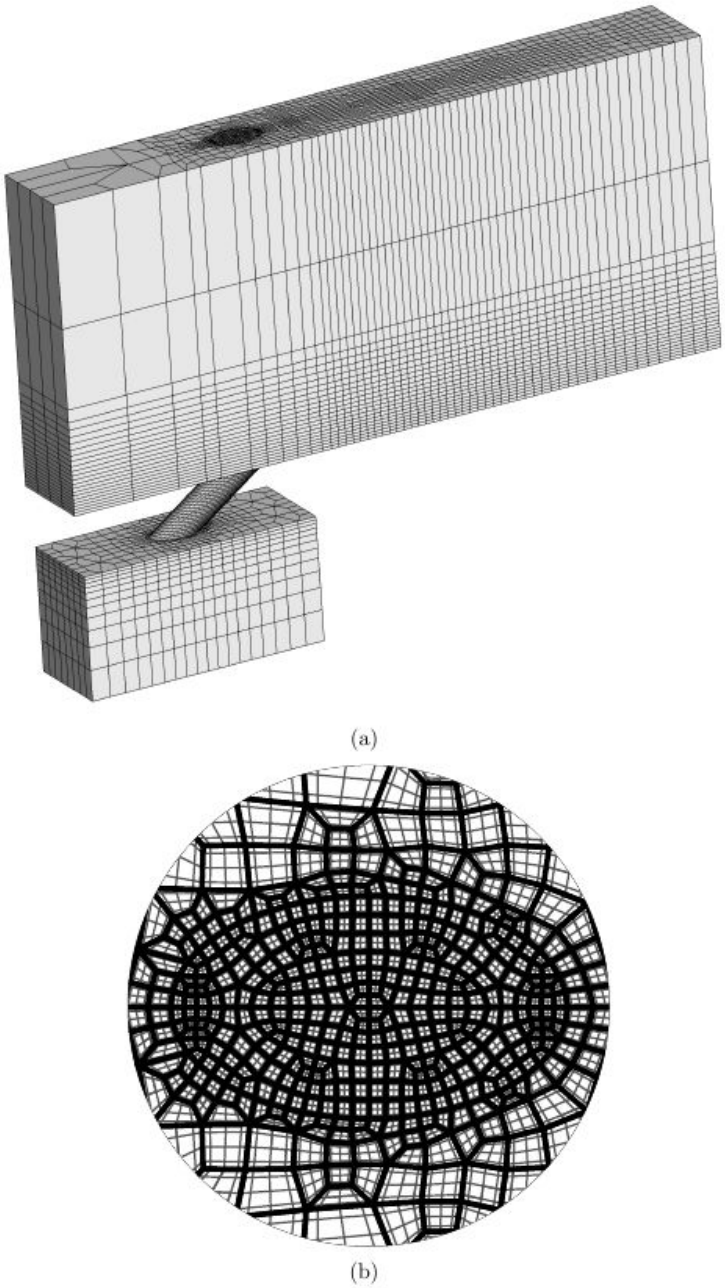

Figure 79: Unstructured hexahedral grid; (a) three-dimensional view; (b) x_1–x_3 view of the grid in the vicinity of the jet exit with spectral order $m = 4$.

DISTRIBUTION A: Distribution approved for public release.

remains steady with small gradients which justifies using large elements. Along the delivery tube, 16 elements with uniform distribution were used. The finest elements are found in the delivery tube, especially in the boundary layer region where flow is highly unsteady with steep gradients. A close x_1–x_3 view of the mesh in the vicinity of the jet exit is shown in figure 79(b). In the plenum, 11 elements were used in the x_2 direction with $\Delta x_2 = 0.06D$ for the topmost elements and $\Delta x_2 = 0.12D$ for the first element in the bottom. The elements in between were distributed using hyperbolic distribution. In total, 48162 hexahedral elements were created. In each element spectral polynomials with order three or four were used. This amounts to a total degree of freedom of 3.1 millions for spectral order three, and 6.0 millions for spectral order of four.

1.3 Results and Discussion

1.3.1 Effect of pulsation on film cooling performance

In examining these results, it is important to remember that the blowing ratio fluctuates between 1.5, when the valve is open, and 0, when the valve is closed, and any comparisons with the steady $BR = 1.5$ case is therefore not at a constant coolant mass injection rate when integrated over a time duration. For the pulsed cases, the integrated coolant injection rates are lower, and an equal or greater cooling effectiveness than the baseline steady jet of $BR = 1.5$ represents an improvement in the cooling strategy. We choose the pulsation period to be in the range of $Tp \in [0.5, 5]$, which corresponds to Strouhal number in the range of $St \in [0.2, 2]$, and duty cycle in the range of $DC \in [0.05, 1]$. All the sampling points with $DC = 1$ correspond to a steady jet and therefore only one simulation was performed for these points. Figure 80 shows the non-dimensional temperature at the x_2-plane which represents the cooling effectiveness on the surface and the flow temperature at the exit of the coolant hole. As noted earlier, the two control parameters being varied include the duty cycle (DC) and the time period of pulsation (Tp) which is inversely proportional to frequency or Strouhal number. The rightmost column represents the steady blowing condition at a BR of 1.5. The signature of the near-hole jet blow off and the downstream spread of the coolant jet on the surface can be seen. Both duty cycle and time period have important and significant influence on the cooling effectiveness. In figure 80, it is observed that the cooling effectiveness generally improves at a lower duty cycle (which represents a lower amount of integrated coolant injection) and higher frequencies, and that optimal conditions exist with global maxima in the lower left quadrant of the DC–Tp design space within the range of design parameters considered. However, the integrated values of the cooling effectiveness do not show any distinct linear or monotonic behavior in the design space, and local maxima or peaks are obtained at other points as shown later in figure 87. More discussions on the mechanisms leading to the global maxima are discussed in the next section for the case with $DC = 0.09$ and $Tp = 1.16$, which is a point close to the global-maxima condition. In figure 81 the temperature distributions at $Tp = 1.16$ for increasing DC from 0.09 to 1 (steady injection) are shown. One can see that in the baseline condition ($DC = 1$), the coolant jet is characterized by unsteady vortical structures that entrain and mix out the cross-flow. The cross-flow penetration to the surface is clearly evident in the longitudinal structures at elevated temperatures near the surface. As DC is reduced from 1, the turbulent structures and the near-wall thermal field are clearly influenced, with the lower duty cycles showing better organized structures and lower temperatures (presence of

DISTRIBUTION A: Distribution approved for public release.

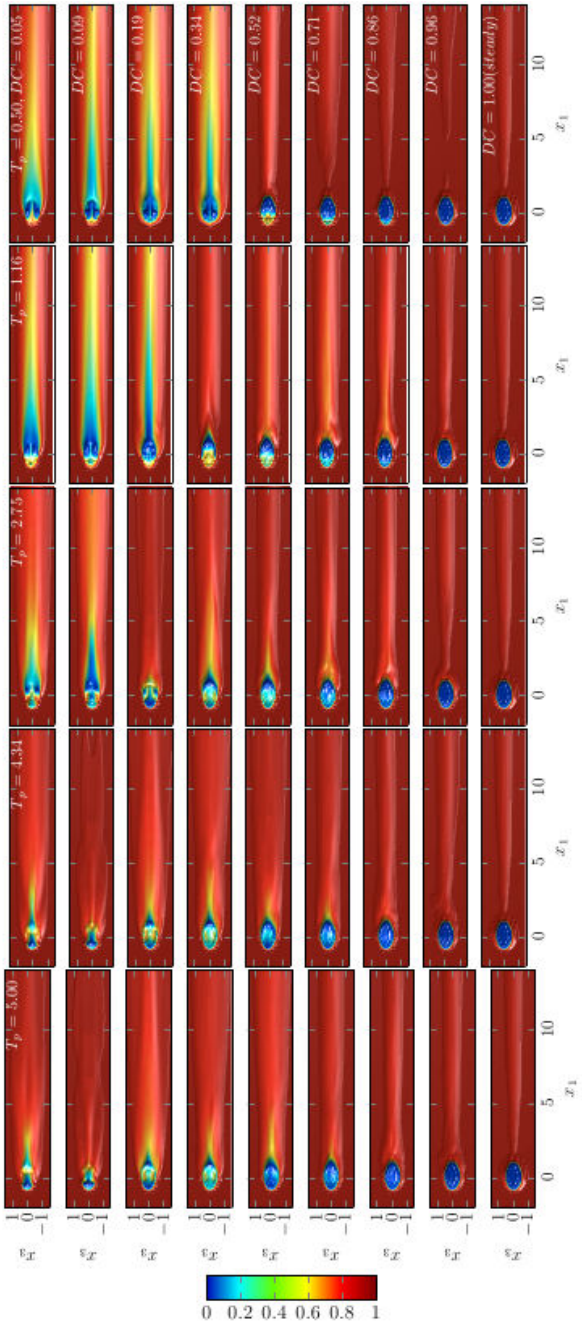

Figure 80: Time-averaged temperature contours for quadrature points on cooled surface ($x_2 = 0$). Each row: constant Tp; Each column: constant DC.

DISTRIBUTION A: Distribution approved for public release.

more coolant) near the wall. For DC larger than 0.34, the jet lift-off is observed immediately after entering the main domain resulting in poor coverage of the surface; this can also be seen in figure 80 where both the lateral and streamwise coverage of the coolant is poor. As DC is further decreased the coolant remains close to the surface and the cross-flow entrainment under the coolant jet and close to the surface is reduced, and therefore lower coolant temperatures near the surfaces are observed. Thus the film cooling provides an effective coverage. These observations translate to higher cooling effectiveness as it is also observed in figure 80. Further discussions on why the lower DC's (where the integrated coolant mass flowrate is lower) leads to improved cooling effectiveness is provided later, and is related to the interaction between the mainstream and the coolant flow leaving the delivery tube. Figure 82 shows the instantaneous temperature distribution in the vertical mid-plane ($x_3 = 0$) at $DC = 0.52$ with increasing time periods from 0.67 to 5. At higher time periods of $Tp \geq 1.89$, the coolant jet exhibits discrete vortex rings that are formed during the on-protion of the pulsation cycle. The same vortex structures were also recognized by (67) for a pulsed vertical jet. These vortex rings are responsible for carrying the coolant flow downstream of the jet hole. The distance between successive vortex rings increases as the pulsation frequency decreases or the time period increases. Note that the instantaneous blowing ratio during the on-portion of the cycle is $BR = 1.5$ which roughly becomes the velocity at which the vortex rings are convected along the axis of the delivery tube (35 degree with x_1). As a result, in figure 82, a distance of $d = 1.5Tp$ can be observed between two successive vortex rings. Since BR and DC remain unchanged for all the cases shown in figure 82, the higher pulsation period translates to more amount of the injected coolant, leading to the formation of larger and stronger vortex rings and greater instantaneous vertical-penetration. A visible trailing column can be seen for $Tp \geq 3.61$. For the case with $Tp = 4.34$ the upper shear layer shows strong oscillations, caused by the traveling vortices created when the flow leaves the plenum and enters the delivery tube and undergoes a sharp turn. As a result an unsteady separation bubble forms in the upstream side of the tube, generating vortical structures that for a large enough pulsation period, such as $Tp = 4.34$, can travel the pipe length of $3.5D$ and affect the upper shear layer; a phenomena that is absent in smaller pulsation periods.

1.3.2 Optimal and sub-optimal behavior

In this section we investigate three cases in more details. In the previous section it was clear that lower duty cycle and high pulsation frequency (lower Tp) leads to higher film cooling effectiveness. The first case that we consider has $DC = 0.09$ and $Tp = 1.16$ which lies in the high film-cooling-effectiveness region in the design space and shows near-optimal film cooling performance (see figure 87). Temperature contours at four time instants of one pulsation cycle for this case are shown in figure 83. Note that τ represents the percentage of time during each cycle with $\tau = 0\%$ being the beginning and $\tau = 100\%$ the end of the cycle, and thus for $\tau < DC$ the jet is on and for $\tau > DC$ the jet is completely off. At $\tau = 4\%$ the jet is on and the injected coolant initiates hairpin vortices (shown by arrows in figure 83) in the shear layer. The hairpin vortices are periodically generated and convected downstream. As the valve closes at $\tau = 9\%$, the cross-flow enters the delivery tube from the leading edge of the hole, pushing the coolant in the delivery tube towards the downstream side of the hole and the coolant leaves the tube from the downstream edge of the hole (this adjustment in the exit flow is driven by mass conservation since the plenum-inflow was abruptly shut off). The ingestion of the cross-flow into the delivery tube continues by forming a vortex ring that

DISTRIBUTION A: Distribution approved for public release.

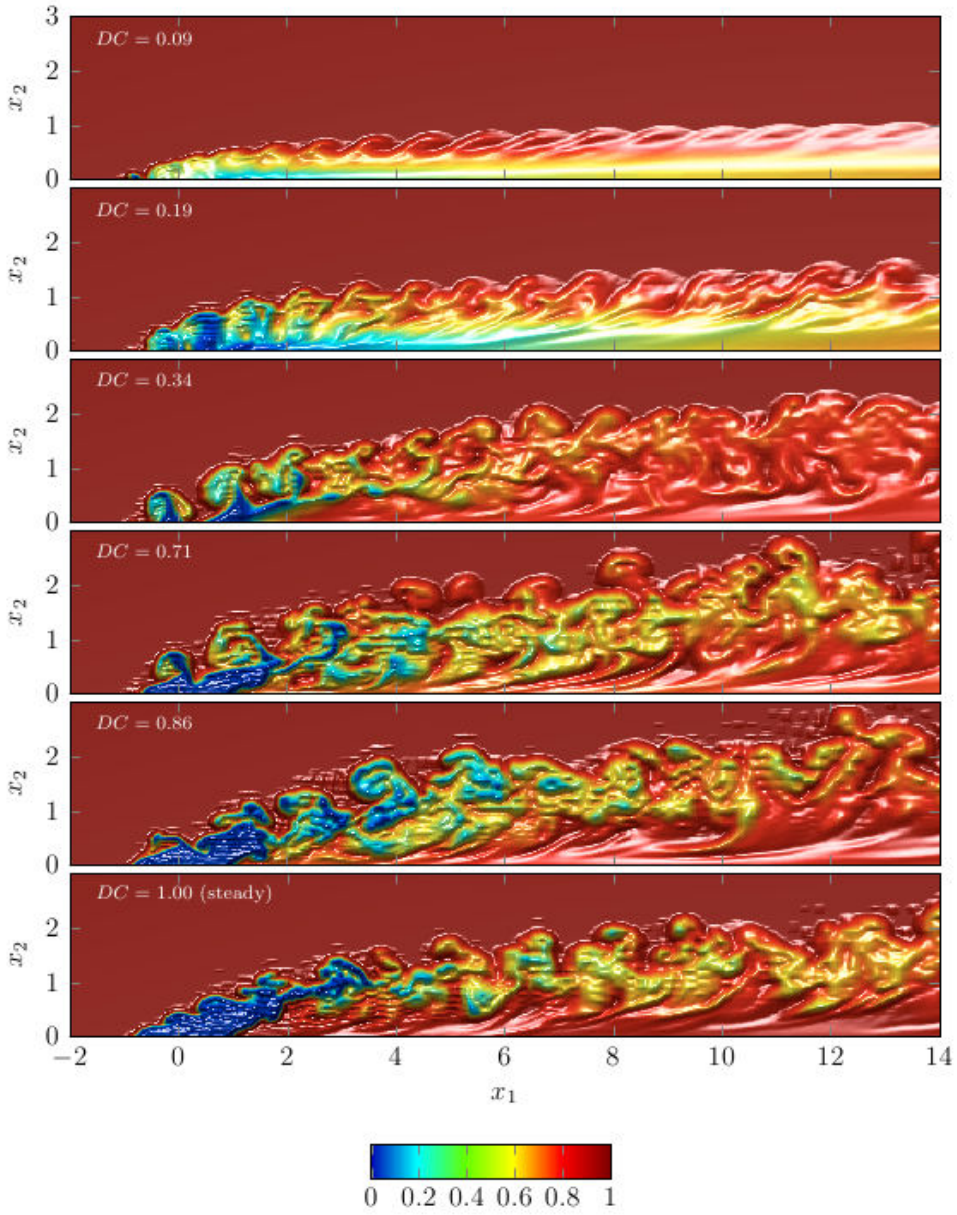

Figure 81: Instantaneous temperature surface in the mid-plane ($x_3 = 0$) with constant pulsation period of $Tp = 1.16$.

DISTRIBUTION A: Distribution approved for public release.

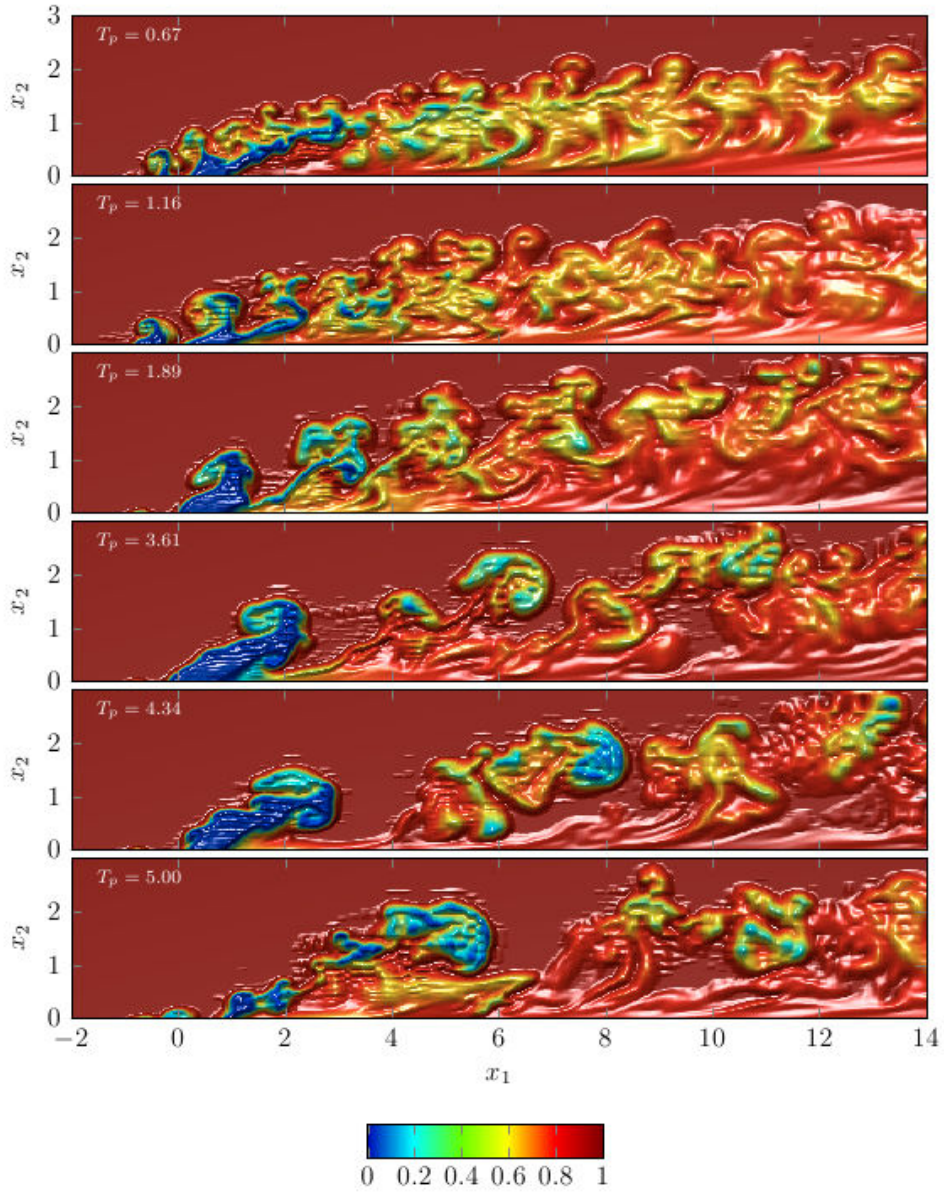

Figure 82: Instantaneous temperature surface in the mid-plane ($x_3 = 0$) with constant duty cycle of $DC = 0.52$.

DISTRIBUTION A: Distribution approved for public release.

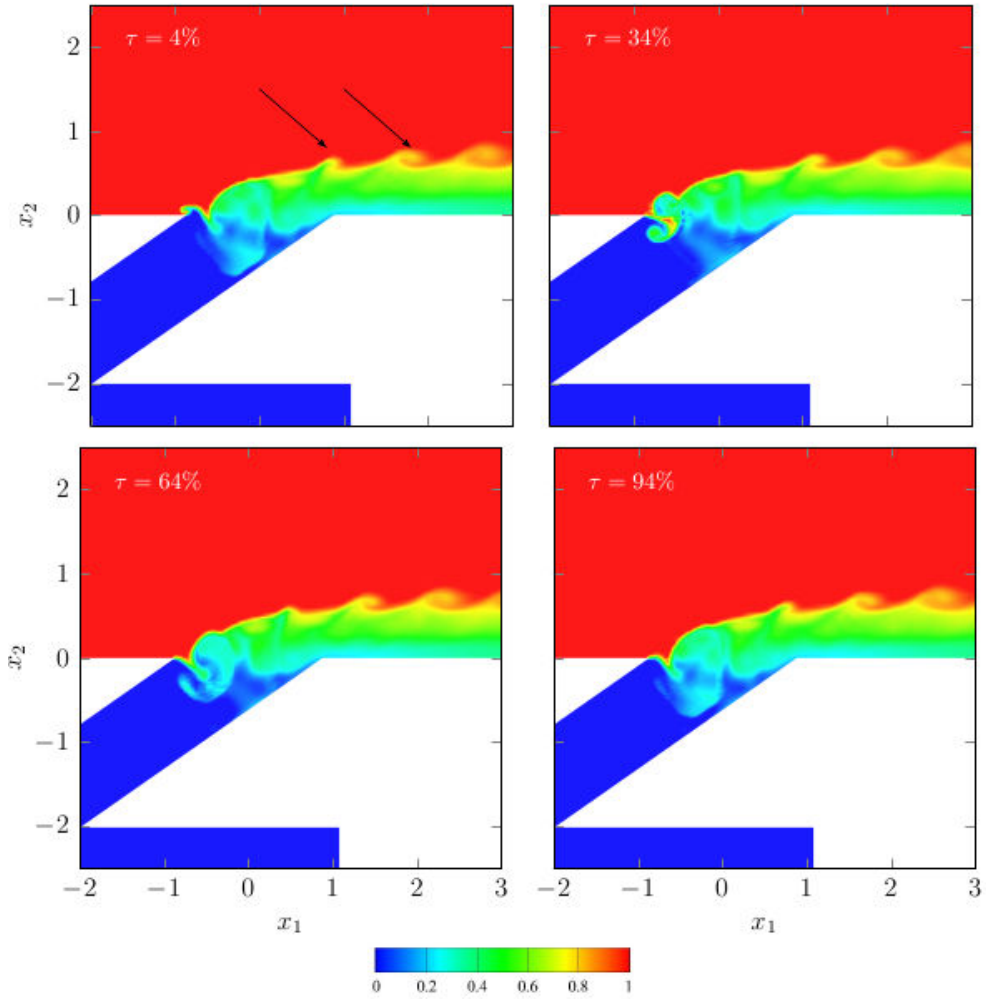

Figure 83: Snapshots of instantaneous temperature at $x_3 = 0$ during one pulsation cycle with $DC = 0.09$, $Tp = 1.16$, $\Delta t_{on} = 0.10$ and $\Delta t_{off} = 1.06$.

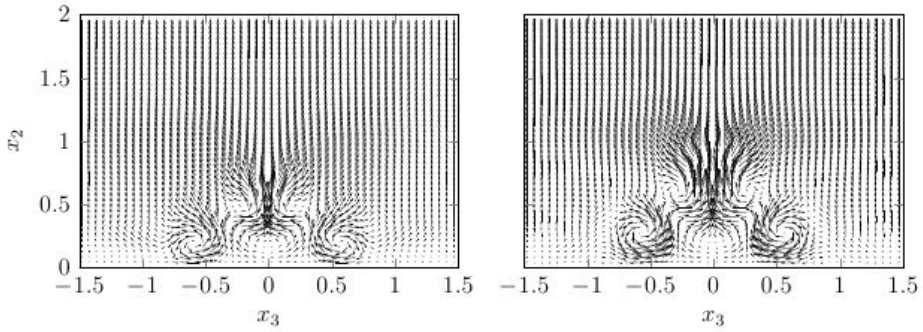

Figure 84: Instantaneousu_2−u_3 velocity vector field at: left $x_1 = 2$; right $x_1 = 4$, at $DC = 0.09$ and $Tp = 1.16$.

DISTRIBUTION A: Distribution approved for public release.

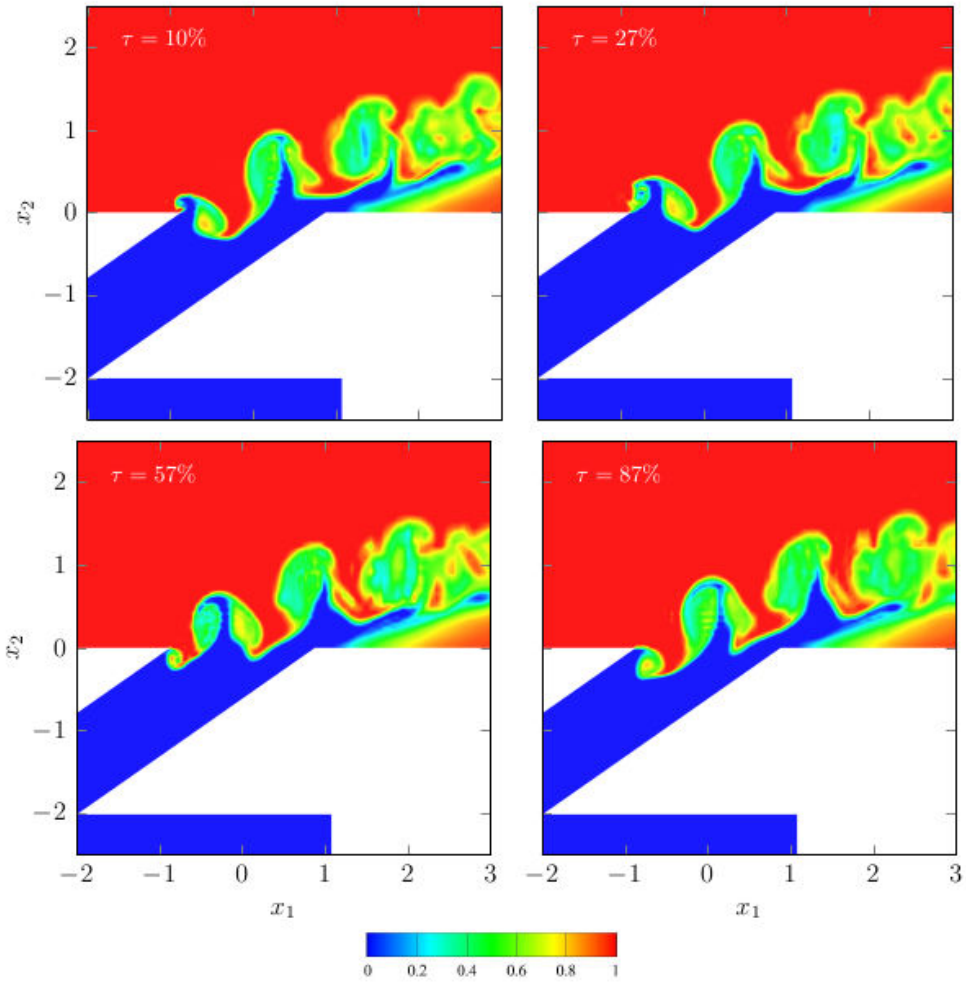

Figure 85: Snapshots of instantaneous temperature at $x_3 = 0$ during one pulsation cycle with $DC = 0.34$, $Tp = 1.16$, $\Delta t_{on} = 0.39$ and $\Delta t_{off} = 0.77$.

DISTRIBUTION A: Distribution approved for public release.

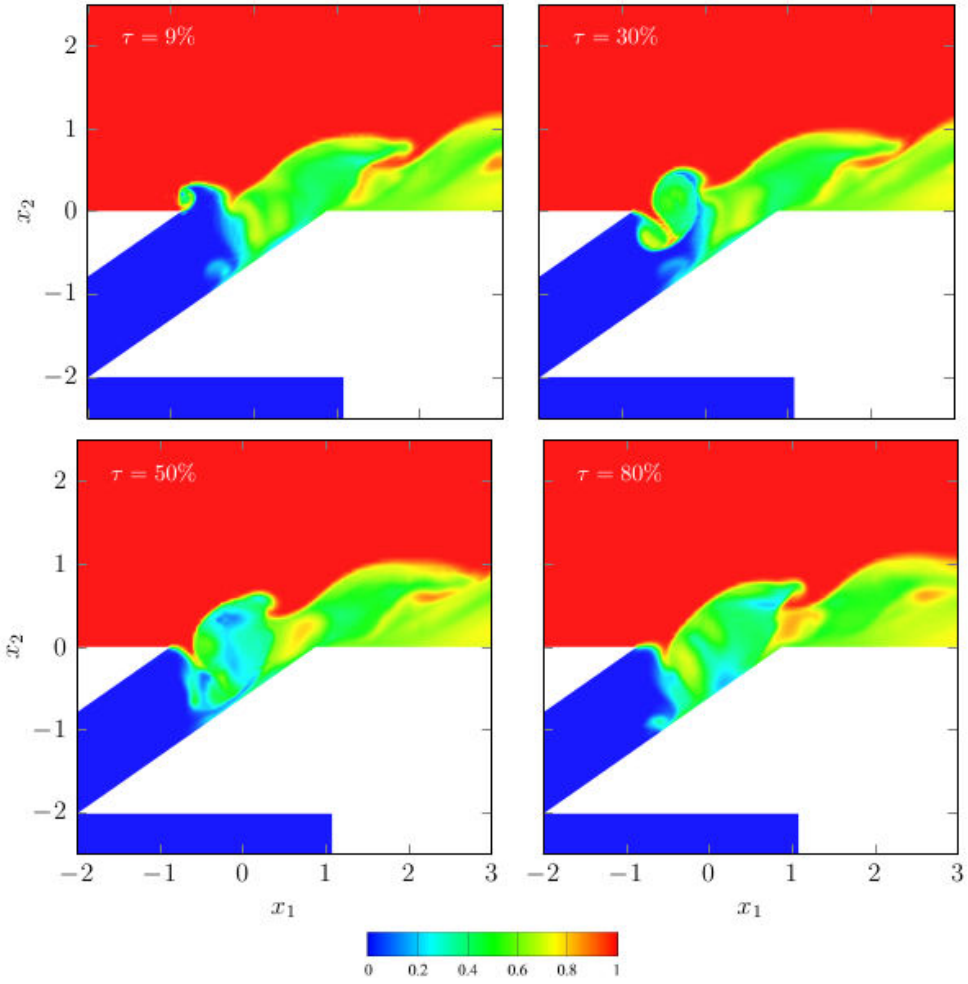

Figure 86: Snapshots of instantaneous temperature at $x_3 = 0$ during one pulsation cycle with $DC = 0.09$, $Tp = 2.75$, $\Delta t_{on} = 0.25$ and $\Delta t_{off} = 2.5$

DISTRIBUTION A: Distribution approved for public release.

is clearly visible in the tube and near the exit at $\tau = 34\%$ and $\tau = 64\%$. The ingested gas reaches very close to the opposite wall of the delivery tube at $\tau = 94\%$. Note that the speed of the propagation of the vortex ring inside the delivery tube is slightly less than the non-dimensional cross-flow velocity of one (due to entrainment), and during the off-portion of the cycle with non-dimensional $\Delta t_{off} = 1.06$ (corresponding to DC of 0.09), the vortex ring has long enough time to travel one non-dimensional unit of length (tube diameter) across the delivery tube and nearly reaches the opposite wall ($\tau = 94\%$). However, due to the short pulsation period, the plenum inflow is re-initiated before the ingested flow penetrates fully to the downstream-edge of the delivery tube, and before the ingested cross-flow gas can cause a significant temperature rise in the interior wall of the delivery tube; this can be seen at the beginning of the new cycle at time $\tau = 4\%$ in figure 83. Other than the hairpin vortices, the steady presence of a counter rotating vortex pair (CRVP) is observed. Figure 84 shows the lateral-vertical velocity vectors at two streamwise sections. A double-deck vortex pair is observed with the lower deck showing the CRVP and the upper deck is resulted by crossing the hairpin vortex legs. The velocity field that is induced by each pair of these vortex structures tend to lift the jet off the surface and unfavorably affects the cooling performance. The amount of the induced vertical velocity, however, is directly proportional to the strength of the vortex pair which is supplied by the amount of the coolant injection. Due to both short duty cycle ($DC = 0.09$) and pulsation period ($Tp = 1.16$), the induced vertical velocity for this case is small (0.01 of the cross-flow velocity) resulting in slow rise of the coolant from the surface (see the first image in figure 81) and thus providing an effective coverage of the surface. The second case we discuss here is the pulsed film cooling with higher duty cycle of $DC = 0.34$ compared to the first case and with the same pulsation period of $Tp = 1.16$. Four snapshots during one pulsation period are shown in figure 85. The top images show the injection of the coolant into the cross-flow. The coolant forms a vortex ring that gains more strength as the time progresses during the on-portion of the cycle and the size of the vortex ring increases from $\tau = 10\%$ to $\tau = 27\%$. In this case larger duty cycle injects more mass flow rate during the on-period and allows the complete formation of a vortex ring, an observation in contrast with the case at $DC = 0.09$ where the smaller duty cycle is not long enough to allow the formation of vortex rings during the injection time. The vortex rings, which carry significant amount of the coolant, penetrate the mainstream flow and are separated from the surface, thus allowing the entrainment of the cross-flow to the surface below the jet. This leads to poor coverage of the surface as it can be seen in figure 80. During the off-portion of the cycle the initial stages of the cross-flow ingestion into the delivery tube can be observed in figure 85 at $\tau = 57\%$ and $\tau = 87\%$ by the rolling up inside the hole. However, due to the low pulsation period ($Tp = 1.16$) and small non-dimensional time length in the off-portion of the cycle ($\Delta t_{off} = 0.77$), the hot gas cannot reach the tube walls before the next cycle begins. This shows that despite the ingestion of the hot gas into delivery tube, the wall temperature does not increase.

The third case investigated in this work is at $DC = 0.09$ and $Tp = 2.75$, which has the same duty cycle as that of the first case but higher pulsation time period. Four instants of temperature contours during one cycle are shown in figure 86. During the on-portion of the cycle ($\tau = 9\%$), a starting vortex forms which gains more strength compared to that of the first case (due to the longer Δt_{on} for this case) and grows larger in size, entraining more amount the hot mainstream flow, leading to increased mixing. During the off-portion of the cycle, a vortex ring similar to the first case forms, causing the ingestion of the cross-flow into the delivery tube. The longer amount of the pulsation period ($\Delta t_{off} = 2.50$) compared

DISTRIBUTION A: Distribution approved for public release.

to the first case ($\Delta t_{off} = 1.06$) gives the ingested gas enough time to impinge to the tube wall, causing significant increase in the wall temperature. Between two successive pulses, the cross-flow penetrates to the delivery tube surface due to larger lapses between the coolant pulses and thus adversely affecting the cooling coverage. The last two cases demonstrate the mechanisms that are responsible for the deterioration of the film cooling effectiveness when either duty cycle or pulsation period increases with respect to the near-optimal case ($DC = 0.09$ and $Tp = 1.16$). We also note that for pulsed cases with very small duty cycle ($DC < 0.05$), the film cooling coverage is severely affected by the overwhelming amount of the cross-flow compared to the coolant. Also for lower pulsation periods than $Tp = 1.16$ the overall film cooling effectiveness slightly decreases, but the physical mechanisms in the flow remain similar to the first case. Thus clearly, optimal conditions exists for the pulsation parameters, and the mechanisms controlling this are related to the dynamics near the jet-hole exit.

1.3.3 Film cooling response surface

In figure 87, the contour lines of the space- and time-averaged film cooling effectiveness vs. DC and Tp are shown. The global optimum is shown by point $P1$ and its design parameters are at $DC = 0.14$ and $Tp = 1.16$, which are close to those of the first case discussed in the previous section including the mechanisms responsible for such a behavior. Local optimums are denoted by points $P2$ to $P5$. The coordinate of points $P1 - P5$ are their respective values of averaged film cooling effectiveness are given in table 12. From the computational point of view an important observation is the presence of local optimums. This non-convex behavior of the objective function versus the design variables renders the gradient-based optimization strategies inappropriate for this problem, since the gradient-based algorithms will converge to a local optimum depending on the initial guess. This can be partially remedied by using different initial guesses. However for the current problem each initial guess leads to several expensive DNS simulations. Nevertheless certainty in obtaining the global optimum cannot be guaranteed in such approaches. Moreover the direct numerical simulations required in gradient-based approaches, have to be carried out in sequence due to the inherent dependence of the updated guess to previous iterations. In contrast, in the current approach all sample points are independent of each other and all simulations can be carried out concurrently, resulting in a significant scale up in the total computation performance. Another advantage of the current approach, although not exploited in the this study, lies in the fact that the obtained response surface can play the role of a surrogate model and can be utilized in different design scenarios, such as optimization cases where the objective function is the film cooling effectiveness with the amount of the coolant penalized with different factors, or the amount of ingestion penalized and so on. Note that once the response surface is obtained, investigating different optimization problems can be carried out very quickly without incurring the computational cost of the DNS.

1.4 Conclusions

In this chapter, we investigated the influence of duty cycle and pulsation frequency on film cooling effectiveness for a 35-degree inclined jet in cross-flow with a plenum attached to the delivery pipe. we have presented an efficient computational strategy that combines high-fidelity simulations and construction of a response surface in the design space to find

DISTRIBUTION A: Distribution approved for public release.

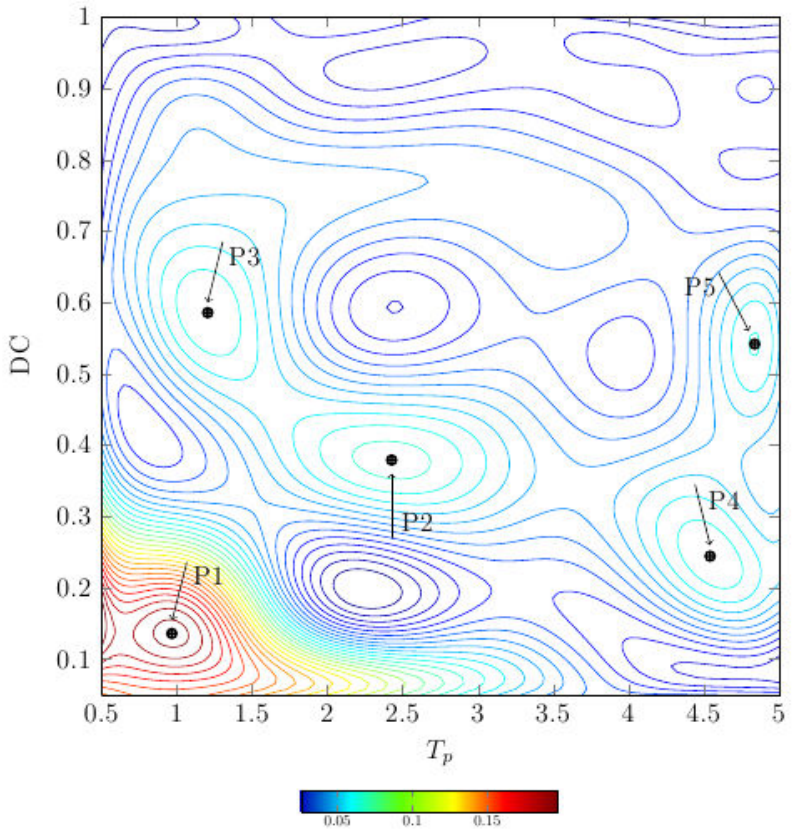

Figure 87: Contours of averaged film cooling effectiveness. Local and global maxima are shown with $P1$ being the global maximum and $P2$ to $P5$ are local maxima ordered with decreasing value. maxima ordered with decreasing value.

Table 12: Optimal design points

Point	DC	T_p	St	$\eta_N(\xi)$
$P1$	0.14	0.97	1.03	0.18
$P2$	0.38	2.43	0.41	0.08
$P3$	0.56	1.21	0.83	0.076
$P4$	0.24	4.54	0.22	0.075
$P5$	0.54	4.84	0.21	0.071

DISTRIBUTION A: Distribution approved for public release.

the optimal forcing parameters that maximizes the film cooling effectiveness. We carried out 73 direct numerical simulations and obtained the response surface of the averaged film cooling effectiveness as a function of the two design variables of duty cycle and pulsation period for a wide range of $DC \in [0.05, 1]$ and $Tp \in [0.5, 5]$. In summary the findings of this study are:

1. The optimal film cooling effectiveness occurs in the lower-left quadrant of the$DC-Tp$ design space, and at lower duty cycles ($DC = 0.14$) and higher frequencies ($St \sim 1$). During the off-period of coolant injection, flow adjustment near the delivery tube include ingestion of the mainstream flow into the tube and the propagation of this ingested front that pushes the coolant in the delivery tube to be squeezed out from the downstream edge of the hole. Thus coolant continues to spill out during the off-period, stays close to the surface, and provides improved coverage. For these cases a double-deck vortical structures were detected, with a hairpin vortex in the upper deck riding on top of a counter rotating vortex pair in the lower deck. The vertical velocity induced by each pair of vortices is small, leading to an attached coolant to the surface.

2. High duty cycles result in forming distinct vortex rings that are detached from the surface and lead to increased entrainment of the cross-flow and thus poor coverage.

3. High pulsation periods causes the penetration of the cross-flow to the delivery-tube trailing surface and causes a significant temperature rise in the delivery tube and an unfavorable effect on the film cooling effectiveness.

4. At lower pulsation periods, the ingested gas does not penetrate all the way to the trailing surface of the delivery tube, and does not cause an increase in the trailing wall temperature inside the tube.

5. Several local optimums were found, rendering the gradient-based optimization strategies inadequate for the current problem.

DISTRIBUTION A: Distribution approved for public release.

2 Canonical Systems Reduced Order Models

In this chapter, two-dimensional canonical flows, a two-sided lid driven cavity and a cylinder in cross-flow, are investigated. This is used to develop the necessary numerical tools and understanding of the POD-Galerkin model reduction method.

2.1 POD-Galerkin Method

The POD-Galerkin method is a combination of two operations providing a set of ordinary differential equations approximating the flow and temperature field empirical solutions. The resulting reduced order model equations for an unactuated flow are for the velocity field:

$$\dot{a_r}(t) = \sum_{i=1}^{N_V} \left(C_{i,0}^r + \frac{1}{Re} D_i^r \right) a_i(t) + \sum_{i=1}^{N_V} \sum_{j=1}^{i} C_{i,j}^r a_i(t) a_j(t) + \left(C_0^r + \frac{1}{Re} D_0^r \right) + P_r(t) \quad (1)$$

where

$$\vec{u} = \vec{\overline{u}} + \vec{u'} = \vec{\overline{u}} + \sum_{n=1}^{N_V} a_n(t) \vec{\varphi}_n(x)$$

$$C_0^r = -\left(\left(\vec{\overline{u}}.\nabla \right) \vec{\overline{u}}, \vec{\varphi}_r \right) = -\int_{\Omega_x} \overline{u}_l \frac{\partial}{\partial x_l} \left(\overline{u}_m \right) \varphi_{r,l} dx$$

$$D_0^r = \left(\triangle \vec{\overline{u}}, \vec{\varphi}_r \right) = \int_{\Omega_x} \frac{\partial}{\partial x_m \partial x_m} \left(\overline{u}_l \right) \varphi_{r.l} dx$$

$$C_{i,0}^r = -\left(\left(\vec{\overline{u}}.\nabla \right) \vec{\varphi}_i, \vec{\varphi}_r \right) - \left(\left(\vec{\varphi}_i.\nabla \right) \vec{\overline{u}}, \vec{\varphi}_r \right) = -\int_{\Omega_x} \left(\overline{u}_m \frac{\partial}{\partial x_m} \varphi_{i,l} + \varphi_{i,m} \frac{\partial}{\partial x_m} \overline{u}_l \right) \varphi_{r,l} dx$$

$$D_i^r = \left(\triangle \vec{\varphi}_i, \vec{\varphi}_r \right) = \int_{\Omega_x} \frac{\partial}{\partial x_m \partial x_m} \left(\varphi_{i,l} \right) \varphi_{r,l} dx$$

$$C_{i,j}^r = -\left(\left(\vec{\varphi}_i.\nabla \right) \vec{\varphi}_j, \vec{\varphi}_r \right) = -\int_{\Omega_x} \left(\varphi_{i,m} \frac{\partial}{\partial x_m} \varphi_{j,l} + \varphi_{j,m} \frac{\partial}{\partial x_m} \varphi_{i,l} \right) \varphi_{r,l} dx$$

$$P_r(t) = -\left(\nabla P(t), \vec{\varphi}_r \right)$$

and for the temperature field:

$$\dot{b}_s(t) = \sum_{i=1}^{N_V} E_{s,0}^i a_i(t) + \sum_{j=1}^{N_T} \left(E_{s,j}^0 + \frac{1}{Pr} \frac{1}{Re} F_{s,j} \right) b_j(t) + \sum_{i=1}^{N_V} \sum_{j=1}^{N_T} E_{s,j}^i a_i(t) b_j(t) + \left(E_{s,0}^0 + \frac{1}{Pr} \frac{1}{Re} F_{s,0} \right) \quad (2)$$

where

DISTRIBUTION A: Distribution approved for public release.

$$T = \overline{T} + T' = \overline{T} + \sum_{m=1}^{N_T} b_m(t)\psi_m(x)$$

$$E^0_{s,0} = -\left(\left(\vec{\overline{u}}.\nabla\right)\overline{T}, \psi_s\right) = -\int_{\Omega_x} \overline{u}_m \frac{\partial}{\partial x_m}\left(\overline{T}\right)\psi_s dx$$

$$F_{s,0} = \left(\triangle\overline{T}, \psi_s\right) = \int_{\Omega_x} \frac{\partial}{\partial x_m \partial x_m}\left(\overline{T}\right)\psi_s dx$$

$$E^i_{s,0} = -\left(\left(\vec{\varphi}_i.\nabla\right)\overline{T}, \psi_s\right) = -\int_{\Omega_x} \varphi_{i,m} \frac{\partial}{\partial x_m}\left(\overline{T}\right)\psi_s dx$$

$$E^0_{s,j} = -\left(\left(\vec{\overline{u}}.\nabla\right)\psi_j, \psi_s\right) = -\int_{\Omega_x} \overline{u}_m \frac{\partial}{\partial x_m}\left(\psi_j\right)\psi_s dx$$

$$F_{s,j} = \left(\triangle\psi_j, \psi_s\right) = \int_{\Omega_x} \frac{\partial}{\partial x_m \partial x_m}\left(\psi_j\right).\psi_s dx$$

$$E^j_{s,i} = -\left(\left(\vec{\varphi}_i.\nabla\right)\psi_j, \psi_s\right) = -\int_{\Omega_x} \varphi_{i,m} \frac{\partial}{\partial x_m}\left(\psi_j\right)\psi_s dx$$

In both equations, $\overline{u}_m$ corresponds to the m^{th} component of the vector $\vec{\overline{u}}$ and $\varphi_{r,l}$ corresponds to the l^{th} component of the vector $\vec{\varphi}_r$. Redundant indexes imply summation on those indexes according to Einstein notation.

Provided with initial values for $A(t_0) = [a_1(t_0), \ldots, a_{N_V}(t_0)]^\top$ and $B(t_0) = [b_1(t_0), \ldots, b_{N_T}(t_0)]^\top$ the set of ODEs can be integrated to obtain a prediction of the velocity and temperature field.

Both projected momentum and energy equations *RHS* are quadratic functions in terms of the coefficients a_i and b_j. Similarly to the full incompressible Navier Stokes and energy equations, the equations are only one-way coupled. The velocity equations are self-sufficient, while the temperature solution depends on the velocity field.

In the rest of this document, we will use indifferently a_i, a_i^{Vel} or a_i^V for the velocity POD temporal coefficients, and b_i, a_i^{Temp} or a_i^T for the temperature POD temporal coefficients.

In order to develop the methodology, the algorithms and the understanding of the POD-Galerkin reduced order modeling method, simple problems were first investigated.

2.2 Two-dimensional Two-sided Lid Driven Cavity

In order to develop the methodology, the algorithms and the understanding of the POD-Galerkin reduced order modeling method, simple problems were first investigated. The first investigated problem is a simple rectangular uniform cartesian grid, corresponding to a closed domain with homogeneous boundary conditions, low energy fluctuations and rather uniform length scales. In addition, to simplify and speed up the numerical simulations, the problem is chosen to be two-dimensional. These considerations lead the choice of a two-sided lid driven cavity flow (2D-2SLDC or 2SLDC).

DISTRIBUTION A: Distribution approved for public release.

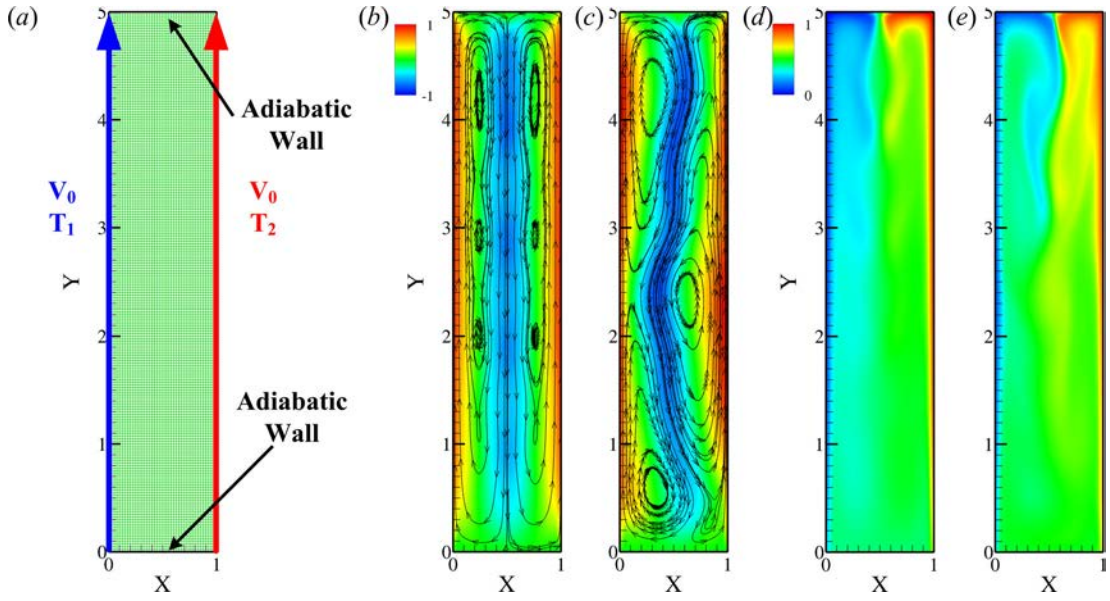

Figure 88: (a) Numerical domain and applied boundary conditions for the 2SLDC problem. (b) Time averaged flow field with V-velocity contours and U-V streamlines; (c) Instantaneous normalized flow field with V-velocity contours and U-V streamlines; (d) Time averaged normalized temperature field; (e) Instantaneous temperature field.

2.2.1 Numerical Setup

The numerical setup for this system is presented in figure 88. The domain is a rectangular domain of dimensions $1 \times 5m$ with a uniform mesh of 40×200 cells for a total of 8000 interior cells . The two "long" walls at $X = 0$ and $X = 1$ are driven at the same velocity of $V_0 = 0.05m.s^{-1}$ in the same direction but are maintained at two different temperatures of $T_1 = 300K$ and $T_2 = 350K$. The corresponding Reynolds number based on the cavity height $Re = V_0 h/\nu$, was approximately 1600. The two remaining "short" boundaries are adiabatic wall. This is a closed system without any mass going in or out the domain. The numerical model used was a two-dimensional approximation of Large Eddy Simulation model as implemented in Ansys Fluent^{TM}. The solver was second order in space and time. The time step used was of $\Delta t = 0.25s$ corresponding to a convective time step of $\Delta t_c = 2.5 \times 10^{-3}$ ($t_c = tV_0/h$) and resulting in maximum Courant's number ($u\Delta t/\Delta x$) of less than 0.5. In the rest of this section, the reported quantities will be normalized velocities $u = u^*/V_0$, $v = v^*/V_0$ and temperature $\theta = (T - T_1)/(T_2 - T_1)$.

2.2.2 Base Flow

Although not of particular interest in the current study, the base flow is rapidly described to put the results in the next sections in perspective. At low Reynolds numbers ($V_0 \approx 5 \times 10^{-3}$, $Re \approx 160$), the flow was found to be stable and stationary. In this regime, the flow field consisted of two large scale recirculation regions on each side of the problem symmetry line at $X = 0.5$. This configuration did not serve our purposes as some unsteadiness was required to obtain a meaningful reduced order model. As the value of the Reynolds number

DISTRIBUTION A: Distribution approved for public release.

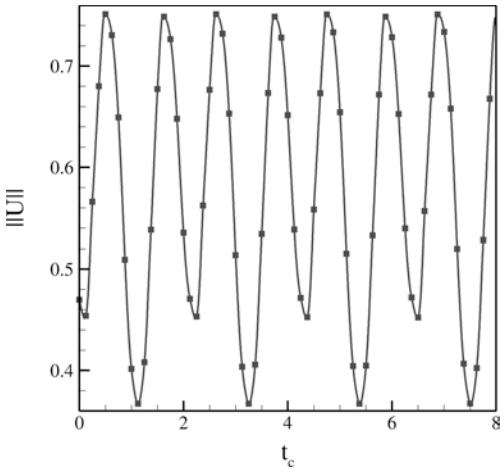

Figure 89: Velocity magnitude signal from probe located inside the cavity at $X = 0.5, Y = 2.5$ as a function of time.

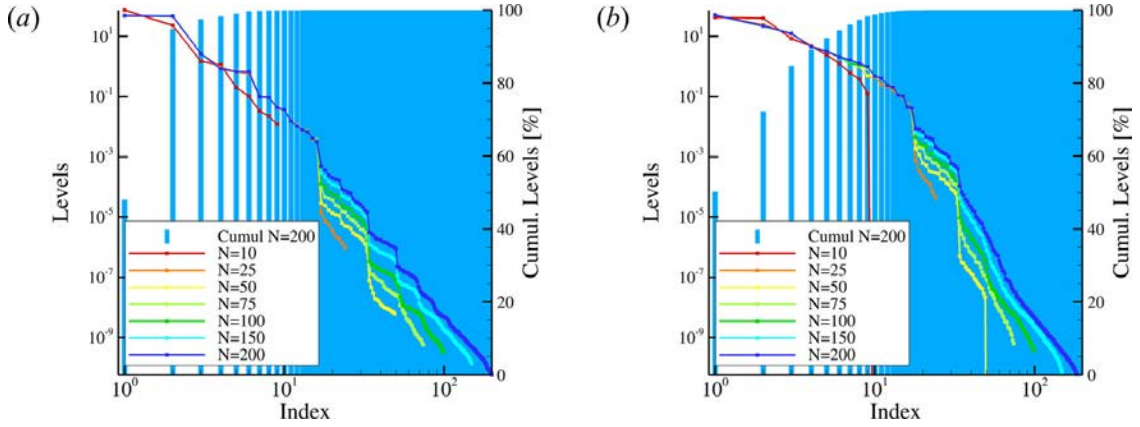

Figure 90: POD Energy distribution for different number N of snapshots included in the computation for (a) Velocity; (b) Temperature fields.

was increased to values of $V_0 = 0.05 m.s^{-1}$ instability started to develop and the recirculation cells started to be convected from the top domain to the bottom in a quasi-periodic manner. Figure 88(b) shows the time averaged velocity field with three distinct pairs of symmetric recirculation cells with respect to the center-line. An instantaneous snapshot in figure 88(c) shows three recirculation cells and highlights the fact that the instantaneous flow field is not symmetric. The associated time averaged and instantaneous temperature fields are also provided in figure 88$(d,\ e)$. This flow configuration was judged suitable for experimenting with reduced order modeling methods. A probe was placed inside the flow at the center of the domain $(X = 0.5, Y = 2.5)$ to record the velocity magnitude throughout the simulations. The signal is presented in figure 89. This signal shows that the flow is quasi-periodic with a dominant frequency of $9.25 \times 10^{-3} Hz$ corresponding to a scaled frequency of $St = St_0 = 0.925$ where St is the Strouhal number $St = fh/V_0$. This signal is also modulated at subharmonic frequency of $St_0/2 = 0.463$.

DISTRIBUTION A: Distribution approved for public release.

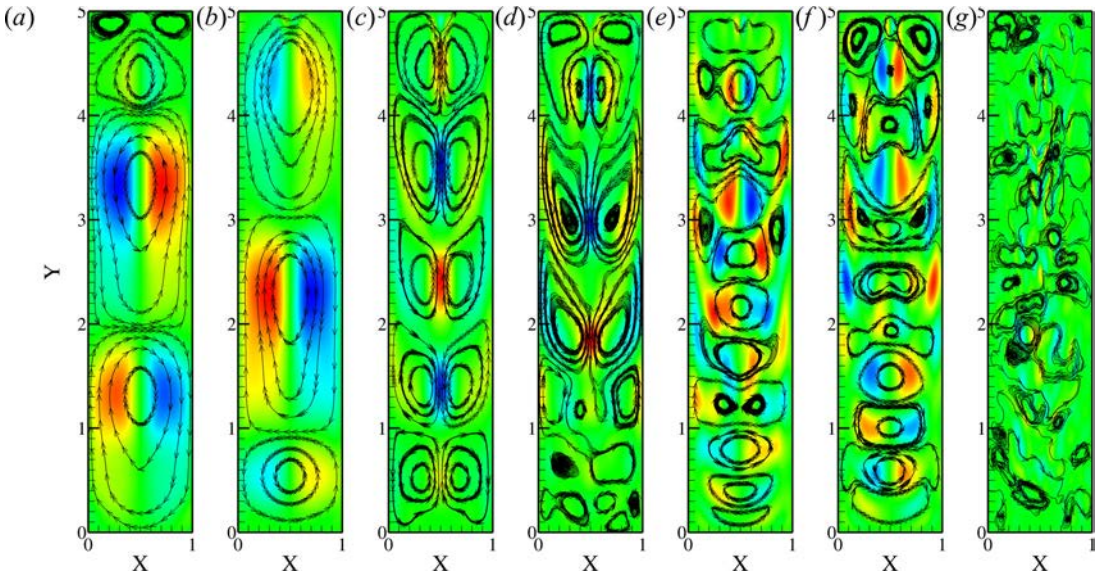

Figure 91: Velocity POD modes: (a) Mode1; (b) Mode2; (c) Mode3; (d) Mode4; (e) Mode5; (f) Mode6; (g) Mode20 for $N = 200$. U-V streamlines and V contours.

2.2.3 Proper Orthogonal Decomposition

Proper Orthogonal Decomposition is carried out using Sirovich Snapshot method on the fluctuation signal. Several decompositions including successively 10, 25, 50, 75, 100, 150 and 200 snapshots are investigated to observe the impact of the number of snapshots on the decomposition metrics. The snapshots are separated by 50 time steps for an equivalent convective time step of $\Delta t_c = 0.125$. This sampling is materialized by the symbols in figure 89 against the probe signal. Figure 90 shows the energy repartition for the different computations. The energy distribution converges rather rapidly to a unique distribution for the lower order modes (highest energy content) for $N > 50$ for the velocity field, but settles only for $N > 150$ for the temperature decomposition. This is a result of the non-optimality of the POD for the temperature signal since the thermal energy does not scale with the square of the temperature. In the rest of this section, the computations are carried out using the $N = 200$ POD modes for both temperature and velocity fields, in order to prevent any bias on the reduced order models introduced by an inaccurate temperature POD. For $N = 200$, the two first velocity POD modes carry as much as 94% of the total turbulent kinetic energy and a total of 5 and 9 modes are necessary to reconstruct respectively 99% and 99.9% of the total turbulent kinetic energy. On the other hand, the first two temperature modes carry "only" 73% of the total temperature signal fluctuation energy (pseudo-thermal energy) and a total of 11 and 15 POD modes are necessary to reconstruct respectively 99% and 99.9% of the total pseudo-thermal energy. These numbers are comparable to previous two-dimensional systems with simple flows.

The POD modes for the velocity and temperature are presented in figure 91 and figure 92 respectively. The first two modes are antisymmetric with respect to the flow center-line and exhibit three large recirculation regions. According to figure 90(a), they carry comparable amounts of energy, respectively 48% and 47% of the total energy. Peaks of identical sign

DISTRIBUTION A: Distribution approved for public release.

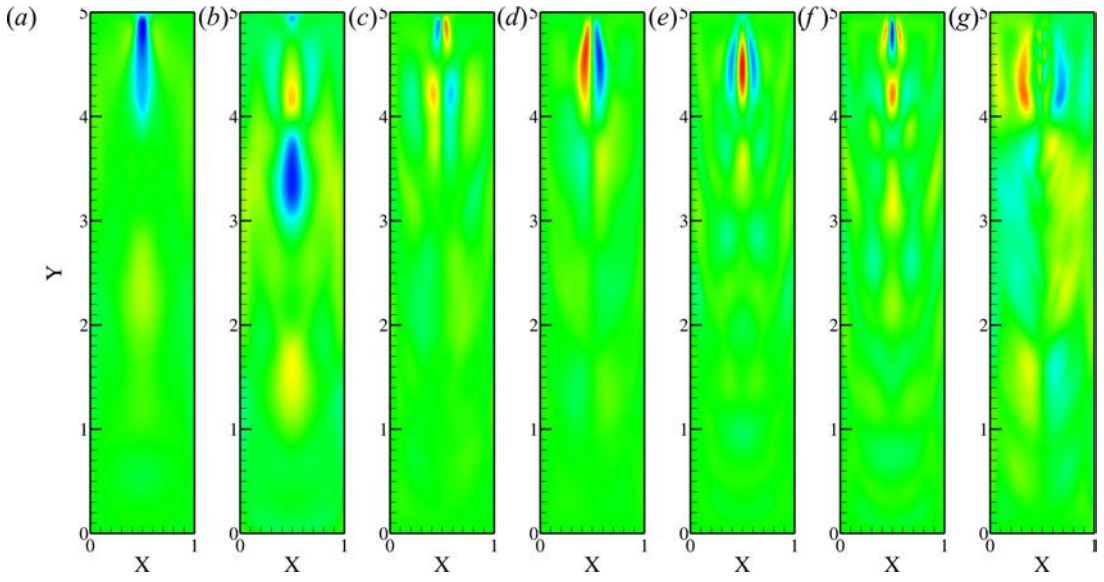

Figure 92: Temperature POD modes: (a) Mode1; (b) Mode2; (c) Mode3; (d) Mode4; (e) Mode5; (f) Mode6; (g) Mode20 for $N = 200$.

between modes 1 and 2 are however shifted in the Y-direction of approximately a quarter of a wavelength (mainly in the core of the flow). In addition, the temporal coefficients a_1 and a_2 in figure 93 appear identical with a phase shift of a quarter wavelength as well. These combined characteristics (identical energy levels, shape function and temporal coefficients shifted of a quarter of a wavelength) are typical of POD modes describing the convection of flow structures in a particular direction. Indeed, the sum of the two partial velocity fields $a_1\varphi_1$ and $a_2\varphi_2$ in the reconstructed signal results in the convection of the recirculation cells observed in the shape functions. Modes 3 and 4 on the other hand are symmetric and do not carry the same amount of energy. They describe the convection of smaller scale recirculation cells on each side of the symmetry line (2 cells per domain width). Modes 5 and 6 are again antisymmetric and of comparable energy content, and represent convection of again smaller scale recirculation cells (3 cells per domain width). As for modes 1 and 2, the temporal coefficients for modes 3 and 4 as well as for modes 5 and 6 have respectively similar frequencies but a quarter wavelength phase shift. Finally, mode 20 captures the dynamics of rather small scales and no real coherence can be found. The decrease in length scale captured by the successive modes is a classic and essential feature of the POD which by nature constructs a set of basis function with decreasing energy content, thus captures ever smaller fluctuations and length scales in higher order modes. This feature is in fact a key element in the process of reduced order modeling using truncated POD series to a finite number of POD modes therefore retaining only the lower order modes with the highest energy content susceptible to govern and represent the best the flow dynamics. Overall, the velocity shape functions appear to be organized in pairs of symmetric and antisymmetric modes with comparable energy content and temporal coefficient dominant frequency. The POD modes for the temperature decomposition show some similarities with the velocity decomposition. The first two POD modes capture rather large scale fluctuation areas, yet the decrease in length scale with increasing mode order is not as obvious as it is in the

DISTRIBUTION A: Distribution approved for public release.

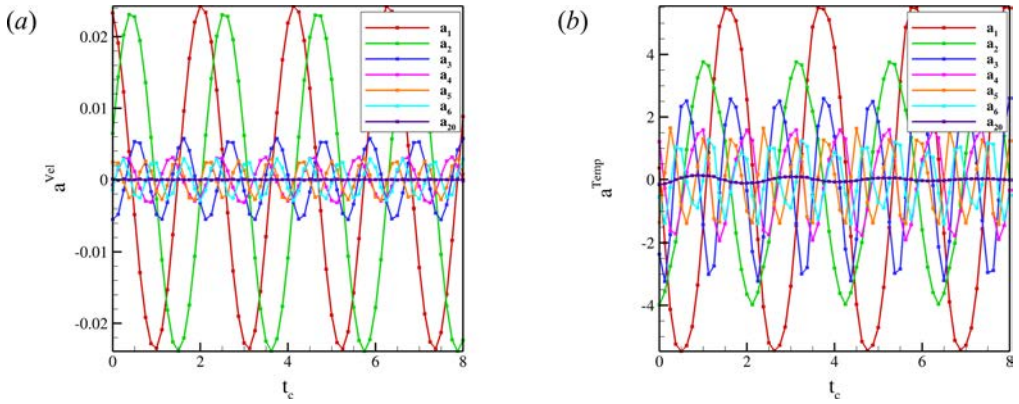

Figure 93: Temporal POD coefficients: (a) a_i^{Vel}; (b) a_i^{Temp} as a function of t_c for $N = 200$.

velocity decomposition. Similarly, the energy decay rate of energy distribution in figure $90(b)$ is not as significant as the velocity one. POD modes still appear to be associated in pairs of alternating symmetric and antisymmetric, yet the energy repartition between the individual modes of every pair is not as even as the one in the velocity decomposition. Once again, these results are attributed to the non-optimality of the POD to the decomposition of temperature signals.

The temporal coefficients a_i^{Vel} and a_i^{Temp} are presented in figure 93 and show that not only the temporal coefficients corresponding to a same pair of modes have similar amplitude (i.e. energy) and frequency, but that the frequency captured by the different pairs is increased with increasing modes orders. Modes 1 and 2 capture dynamics with a fundamental frequency of $St = 0.47 \approx St_0/2$, modes 3 and 4 with a frequency 1.5 times higher of $St = 0.705$, and modes 5 and 6 with a frequency twice as high $St = 0.94 \approx St_0$ where St_0 is the fundamental frequency directly evidenced in the probe signal of figure 89.

2.2.4 Reduced Order Model

Reduced order models are obtained for several combinations of the pair of values (N_V, N_T), respectively the number of velocity and temperature POD modes used in the reconstruction of the fields. The Galerkin projection is carried out on the POD results including 200 velocity fields and 200 temperature fields. The spatial derivatives of the respective POD modes are calculated using Tecplot$^{\text{TM}}$, utilizing a centered second order accurate scheme. Although the derivation scheme used by Tecplot to obtain the derivatives is most likely not identical to the one implemented in the Fluent solver, the error introduced by the change in scheme is deemed negligible with respect to the dropped POD terms in the velocity and temperature fields reconstructions. Moreover, the relatively refined mesh used in this simulation ensured local errors of the order, or inferior to, $\Delta x^2 \sim 6.10^{-4}$. The Galerkin coefficients of equations 1 and 2 are evaluated using the trapezoidal integration approximation. In this particular case, the velocity field and temperature fields are homogeneous at the boundary so that the pressure term $P_r(t)$ in equation 1 vanishes and does not require any additional calculations. The set of ODEs are integrated using both a 5^{th} order Runge-Kutta solver (Dormand-Prince pair 4/5 24 - DP45) and a variable order Adams-Bashforth-Moulton PECE solver (see 69) with a relative tolerance between 10^{-8} and 10^{-2}. The sensitivity of both solvers on

DISTRIBUTION A: Distribution approved for public release.

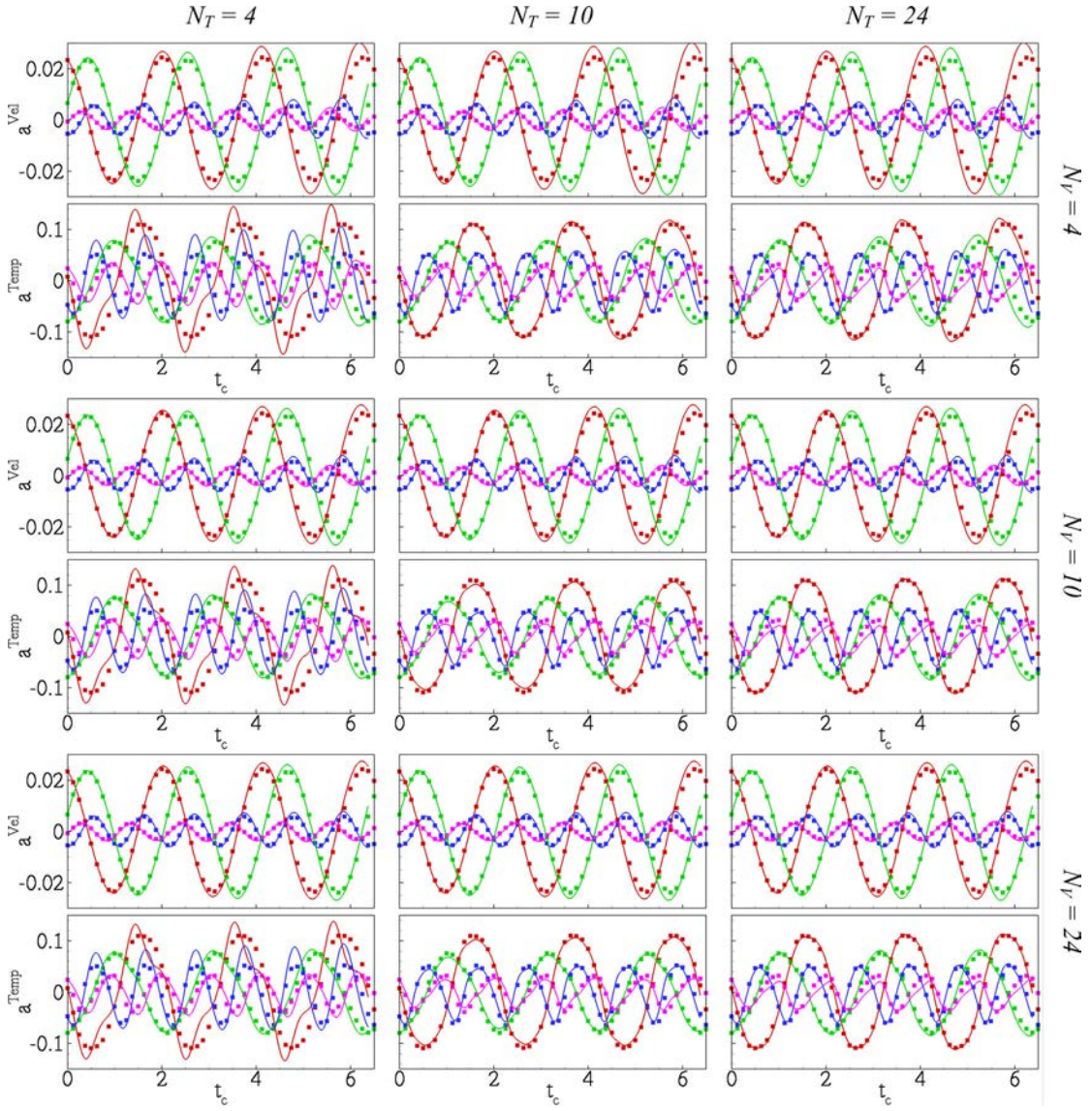

Figure 94: First four ROM temporal coefficients for the velocity and temperature fields obtained for several values of N_V and N_T (*solid lines*) along with corresponding POD temporal coefficients (*symbols*). a_1 (*red*), a_2 (*green*), a_3 (*blue*), a_4 (*magenta*).

DISTRIBUTION A: Distribution approved for public release.

the tolerance parameter was investigated and the solution did not evidence any significant differences beyond a tolerance of 10^{-4}. The presented following results are the one obtained using the DP45 algorithm with a relative tolerance of 10^{-4}. Both projected momentum and energy equations are solved simultaneously in a system of $N_V + N_T$ coupled ODEs.

The results from the integration of the reduced order model obtained from the Galerkin projection method are presented in figure 94 for several values of N_V and N_T, along with the corresponding POD coefficients corresponding to the projected LES data onto the POD basis. The results for the first four temporal coefficients show relatively good tracking for the velocity over the first periods corresponding to the dominant frequency as soon as $N_V = 4$. While the fidelity of the model appears to be improved by increasing the number of velocity POD modes to $N_V = 10$, no obvious improvement seems to occur between $N_V = 10$ and $N_V = 24$. This shows that the model is fully converged with 10 modes and that the remaining error is to be attributed to the numerous approximations made to obtain the set of ODEs including but not limited to, errors introduced by the solver numerical integration scheme, inaccuracy of the solution due to domain discretization, errors introduced by the mismatch in derivation scheme between the solver and the post-processing software, integrals approximations with the trapezoidal rule, etc. As expected from the fact that the velocity solution is decoupled from the temperature one, the changes in the value of N_T at fixed values of N_V do not visually affect the fidelity of the velocity ROM.

The impact of N_V and N_T on the temperature ROM fidelity is also evidenced in figure 94. With $N_T = 4$, the accuracy of the temperature ROM is poor and the tracking mediocre. However, the quality of the ROM is greatly improved for $N_T = 10$. When including 24 temperature modes, no significant improvement is observed on the first three coefficients and a certain degradation of the profile of the fourth coefficient occurs. Conversely to the velocity ROM, the changes in values of N_V at fixed N_T have a moderate yet visible influence on the temperature ROM tracking, in particular the "long term" accuracy of the model appears to be improved for increased number of velocity POD modes included.

Overall, very satisfying results are obtained using only 22 velocity modes and 6 temperature modes.

2.3 Two-dimensional Cylinder in a Cross-flow

While 2D-2SLDC problem constituted a good starting point, this flow was very well behaved and corresponded to a closed-flow configuration. To investigate open flow systems, a two-dimensional cylinder in a cross-flow is selected to assess the impact of neglecting the pressure terms in equation 1. In addition, the extensive documentation on this type of flow makes it an excellent candidate.

2.3.1 Numerical Setup

The numerical setup for the cylinder in cross-flow consists of a cylinder inside of diameter $D = 1m$ and a rectangular domain $16D$ wide (in the X direction) and $33D$ long (in the Y direction). A close-up view of the domain is provided in figure $95(a)$. The origin of the domain is located at the center of the cylinder and the inlet of the domain is at $Y = -8D$, therefore the outlet at $Y = 33D$. The grid is multi-block with an O-grid of $3D$ diameter surrounding the cylinder. The cell height at the cylinder wall is $2 \times 10^{-4}D$ for corresponding y^+ values of less than 0.25, well inside the boundary layer viscous sub-layer. The mesh

DISTRIBUTION A: Distribution approved for public release.

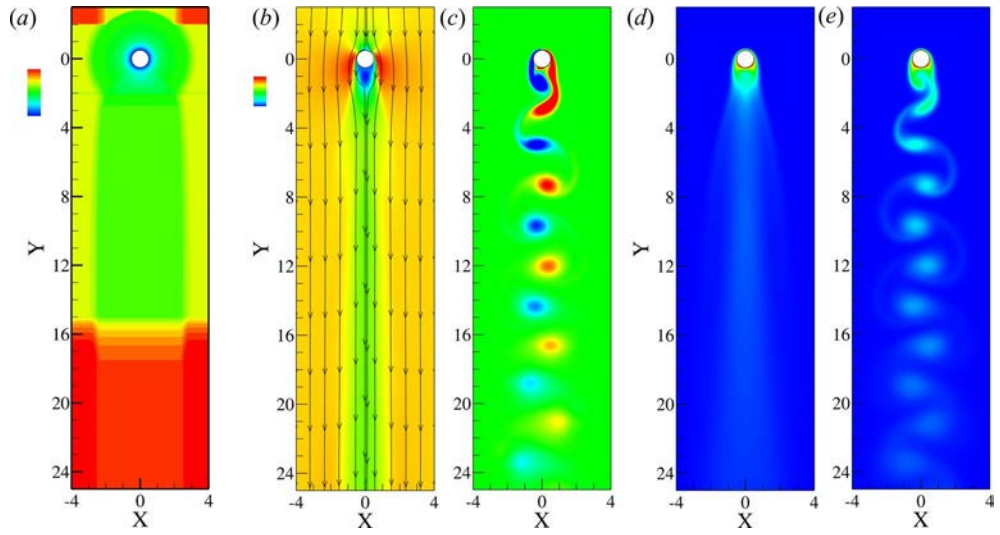

Figure 95: (a) Numerical domain and local cell surface area from $10^{-5}D^2$ $(blue)$ to $10^{-3}D^2$ (red). (b) Time averaged flow field with U-velocity contours and U-V streamlines; (c) Instantaneous normal vorticity; (d) Time averaged normalized temperature field; (e) Instantaneous temperature field.

counts a total of $250,000$ cells. Because of the high density of the mesh, the surface area of the individual cells is presented in figure $95(a)$, instead of the mesh itself, and still provides a good overview of the mesh distribution. At the inlet of the domain, normal velocity is imposed at $V_0 = 2.235 \times 10^{-3} m.s^{-1}$ for a corresponding Reynolds number ($Re_D = V_0 D/\nu$) of 150, within the unstable two-dimensional laminar regime. At the outlet of the domain, an outflow boundary condition is imposed. The sides of the domains are taken far away from the core of the flow and periodic boundary conditions are applied to them. A constant temperature of $T = T_1 = 300K$ is imposed at the domain inlet and a constant temperature of $T = T_2 = 350K$ is imposed at the cylinder wall. The numerical model used is a 2D approximation of the Large Eddy Simulation model as implemented in Ansys Fluent™ with a dynamic Smagorinsky-Lilly sub-grid scale model. The discretization scheme for the pressure, momentum and energy equation are respectively second order upwind, second order bounded central-differences and QUICK (Quadratic Upstream Interpolation for Convective Kinematics). The time discretization scheme is also second order. The integration time step used during the simulations is $\Delta t = 1s$ corresponding to a convective time step of $\Delta t_c = 2.2 \times 10^{-2}$ with $t_c = tV_0/D$. The maximum Courant's number ($u\Delta t/\Delta x$) is less than 0.9.

2.3.2 Base Flow

The base flow for this problem is well documented (see 75 for instance) and will only be described to put in perspective the following results. A recirculation region is located directly downstream of the cylinder (see figure $95b$) and contains a pair of vortical regions of opposite vorticity (see figure $95c$). At Reynolds numbers above the Hopf Bifurcation stability margin ($Re_D \approx 40$), the wake becomes unstable and the vortices composing the wake starts shedding

DISTRIBUTION A: Distribution approved for public release.

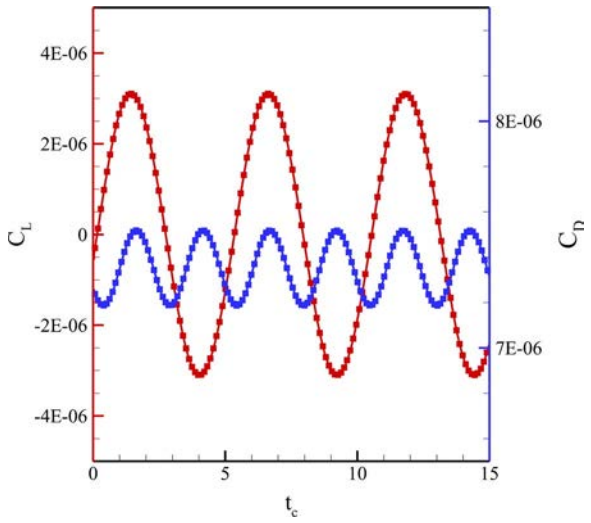

Figure 96: Integrated drag C_D and lift C_L coefficients as a function of convective time t_c. Symbols represent the sampling used for POD.

in an alternating periodic manner to form the well known Kármán vortex street observed in figure 95(c). The wake is characterized by the Strouhal number ($St = fD/V_0$) associated with the shedding frequency of the vortices, which is a function of the Reynolds number. In the current simulations at $Re_D = 150$, the fundamental shedding frequency is found to be $St_0 = 0.198$ in the lift coefficient C_L history of figure 96 while the drag coefficient C_D signature exhibits a fundamental twice as high. This is in agreement with previous findings from (71). For additional information on the velocity field of flows past circular cylinder, the reader is referred to (75). The temperature field is also presented in figure 95(d-e). Since the cylinder wall is the only surface at a prescribed temperature above cross-flow temperature, the average field shows that the only areas with elevated temperatures are the surroundings of the cylinder and the wake. The instantaneous temperature field in figure 95(e) is highly correlated to the vorticity field in figure 95(c) highlighting the thermal convection from the shedding wake vortices.

2.3.3 Proper Orthogonal Decomposition

As for the previous case, the proper orthogonal decomposition is carried out using the snapshot method. A sampling of $\Delta t_c = 5.5 \times 10^{-2}$, corresponding to 50 time steps, is used which is equivalent to 45 snapshots per period of the fundamental frequency and evidenced by the symbols in figure 96. Four decompositions including 45, 68, 90 and 135 snapshots are made for both the velocity and temperature fields in order to evaluate the influence of the number of snapshots on the convergence of the decomposition. Figure 97 presents the energy distribution from the decomposition of the velocity and temperature fields. For the velocity, the first 10 POD modes are identical for the decompositions including integer numbers of periods whereas the decomposition including a non-integer number of periods appears slightly different beyond the second mode. This is a well known result concerning POD decomposition of periodic flows, which in order to be accurate and optimum, requires an integer number of periods during the sampling (see 65). For the rest of this section, the

DISTRIBUTION A: Distribution approved for public release.

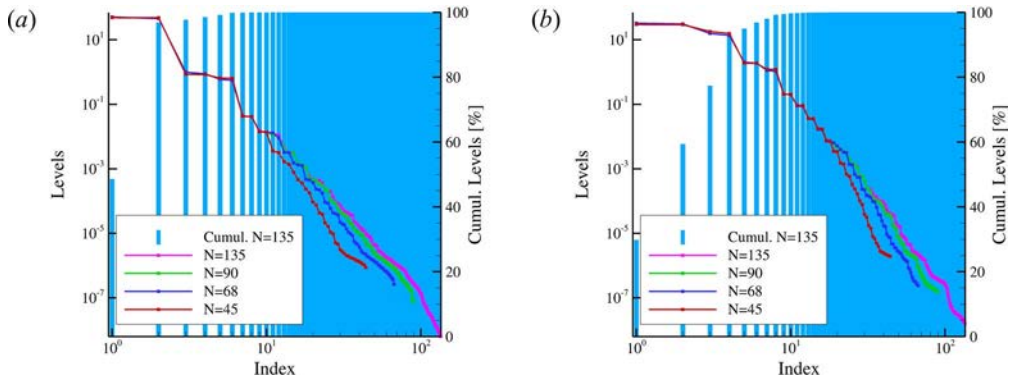

Figure 97: POD Energy distribution for different numbers of snapshots included in the computation for (a) Velocity; (b) Temperature fields.

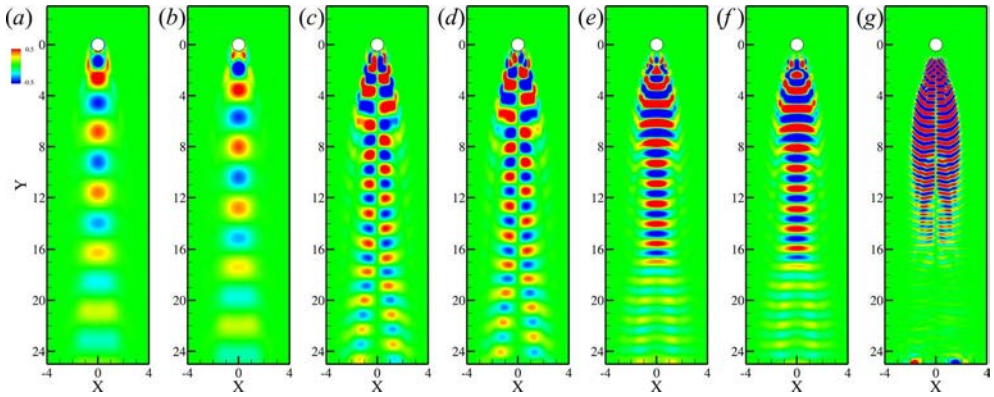

Figure 98: Vorticity from the velocity POD modes: (a) Mode1; (b) Mode2; (c) Mode3; (d) Mode4; (e) Mode5; (f) Mode6; (g) Mode20 for $N = 135$.

decomposition including 135 snapshots is used for reduced order modeling purposes, covering 3 shedding cycles, therefore allowing us to estimate the long term behavior of the ROMs. The first two velocity POD modes carry approximately 47% of the total turbulent kinetic energy each. A total of 5 and 8 velocity POD modes are required to respectively capture 99% and 99.9% of the total turbulent kinetic energy.

The difference between integer and non-integer sampling of the period is less obvious in the temperature decomposition yet remain visible. The first 18 modes for the temperature decomposition including an integer number of periods appear to be identical when including 1, 2 or 3 periods. Indeed, the energy distribution of the temperature decomposition is less optimal than the one in the velocity decomposition and the first two modes carry "only" 30% of the total pseudo-thermal energy. A total of 8 and 14 temperature POD modes are required to capture respectively 99% and 99.9% of the total pseudo-thermal energy which is significantly higher than for the velocity field decomposition. Once again, these observations evidence that while the POD is optimal in the sense of the kinetic energy, it is not in the sense of the thermal energy, therefore providing modes with lower energy content for the temperature decomposition.

DISTRIBUTION A: Distribution approved for public release.

The normal vorticity extracted from the shape functions of the velocity field decomposition is presented in figure 98. As for the 2SLDC results, the decomposition yields pairs of modes which are similar in terms of the size and shape of the vortical features they capture. The first mode in figure 98(a) is symmetric with respect to the flow symmetry line ($X = 0$) and captures vortical structures with scales of the order of the cylinder diameter, with alternating vorticity sign. The second mode is almost identical to the first one, with a shift in the pattern of a quarter wavelength towards the downstream direction. This shift, coupled with the $\pi/4$ shift in the phase of the temporal coefficient of mode 2 with respect to the one of mode 1 in figure 99, results in the downstream convection of vortical cells in the reconstructed signal $a_1(t)\varphi_1(x) + a_2(t)\varphi_2(x)$. This is comparable to the results obtained in the 2SLDC configuration. Modes 3 and 4 are the first antisymmetric modes and contain vortical cells of opposite sign on each side of the symmetry line with alternating sign in the downstream direction. The vorticity levels are rather high close to the recirculation region and decrease in intensity beyond $Y = 16$, with in addition, a bifurcation in the vortical structures trajectories beyond this point. It is rather unclear if this is to be related to the mesh density change beyond $Y = 16$ (visible in figure 95a) or to the natural decay of the vorticity due to diffusion. As for modes 1 and 2, the temporal coefficients for modes 3 and 4 are comparable in amplitude and frequency with a $\pi/4$ phase shift. Modes 5 and 6 exhibit a symmetric pattern similar to the one of modes 1 and 2, with yet twice as many changes in vorticity sign it the wake region. The vortical cells are rather elongated in the X-direction. The shape functions contain single cells with high vorticity up to $Y = 16$ and double cells on each side of the symmetry line with lower vorticity levels beyond that point. The temporal coefficients of modes 5 and 6 also exhibit a quarter period shift. Finally, mode 20 exhibits small scale fluctuations in the wake of the cylinder but, conversely to the 2SLDC results, conserves symmetry and coherence. It is worth noting that this latter mode also captures rather large scale structures (at least when compared to the ones directly downstream of the cylinder) near the domain outlet. This is a good example of the potential issues faced when using POD on flows involving various length and energy scales. Indeed, it is observed in figure 95(c) that the vorticity levels, and therefore the energy content, of the structures located directly downstream of the cylinder are significantly higher than the ones of the previously convected vortices on which diffusion has had an effect. Consequently, the POD will have a tendency to capture across the first POD modes the vortical structures in the near-field of the cylinder (as evidenced in figure 98a-f) and across the higher order modes the less energetic far-field structures. However, there is a certain overlap such that in mode 20, the far-field structures are captured along with smaller features of the near-field structures carrying less energy.

The POD modes for the temperature decomposition presented in figure 100 show strong similarities with the velocity ones. In particular modes 1 and 2 are symmetric with respect to the flow center-line, shifted in the downstream direction of a quarter wavelength with respect to each other and show strong similarities with the vorticity field of modes 5 and 6 from the velocity field decomposition. Modes 3 and 4 as well as 5 and 6 are antisymmetric. Once again, the higher order modes such as mode 20, capture simultaneously increasingly smaller scale features in the near-field but also larger, less energetic ones in the far-field.

The temporal coefficients for the velocity and temperature decompositions are presented in figure 99(a) and 99(b) respectively. While both decompositions result in series of pairs of coefficients with identical fundamental frequency and a $\pi/4$ phase shift, the fundamental frequency of the dominant velocity and temperature modes are different. While modes 1 and

DISTRIBUTION A: Distribution approved for public release.

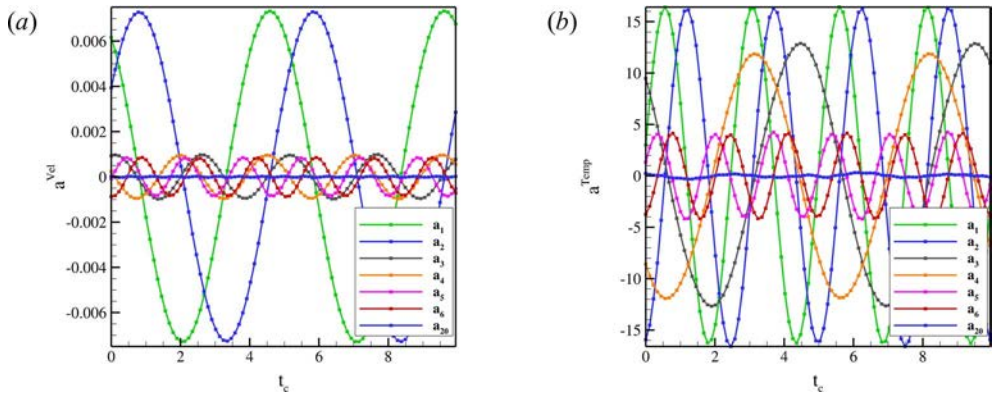

Figure 99: Temporal POD coefficients: (a) a_i^{Vel}; (b) a_i^{Temp} as a function of t_c for $N = 135$.

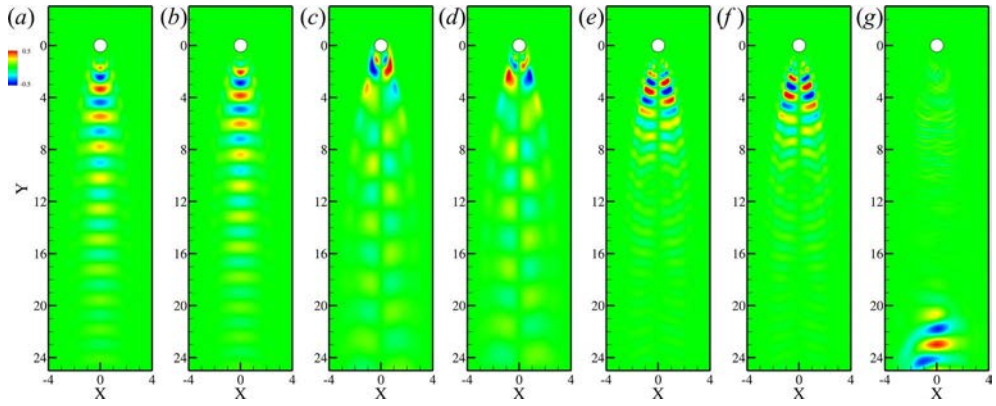

Figure 100: Temperature POD modes: (a) Mode1; (b) Mode2; (c) Mode3; (d) Mode4; (e) Mode5; (f) Mode6; (g) Mode20 for $N = 135$.

2 from the velocity field decomposition have a fundamental frequency equal to $St_0 = 0.198$ identical to the one found in figure 96 for the lift coefficient C_L, the first two temperature POD modes have a fundamental frequency of $2St_0$ corresponding to the one of the drag coefficient C_D in the same figure. Velocity modes 3 (and 4), modes 5 (and 6) and mode 20 have fundamental frequencies of respectively $2St_0$, $3St_0$ and $8St_0$ while temperature modes 3 (and 4), modes 5 (and 6) and mode 20 have respective fundamental frequencies St_0 and $4St_0$ and $5St_0$. Conversely to the 2SLDC decompositions, the fundamental frequencies captured by the "corresponding" velocity and temperature POD modes do not match. This is a reminder that although the velocity and temperature POD series are calculated based on the same data set of corresponding velocity and temperature fields, the obtained POD modes are decoupled from one another and there is no one-on-one equivalent between the velocity and temperature decompositions.

2.3.4 Reduced Order Model

Reduced order models are obtained for several combinations of the values N_V and N_T, respectively the number of POD modes used in the velocity and the temperature reconstruc-

DISTRIBUTION A: Distribution approved for public release.

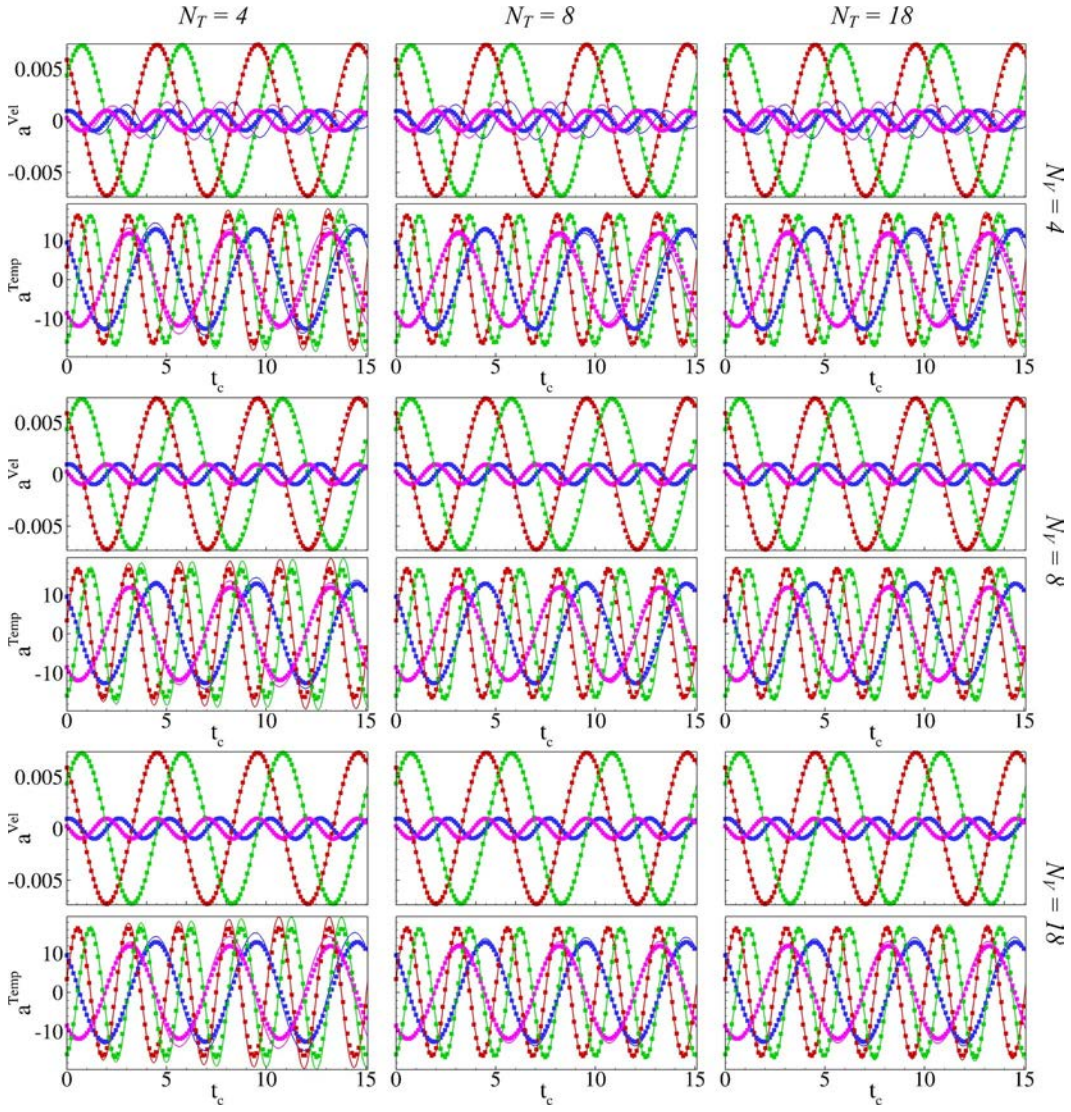

Figure 101: First four ROM temporal coefficients for the velocity and temperature fields obtained for several values of N_V and N_T (*solid lines*) along with corresponding POD temporal coefficients (*symbols*). a_1 (*red*), a_2 (*green*), a_3 (*blue*), a_4 (*magenta*).

tions, based on the decomposition including 135 snapshots described previously. As for the 2SLDC problem, the derivatives of the POD shape functions are obtained using Tecplot. A trapezoidal integration approximation is used to evaluate the Galerkin coefficients in equations 1 and 2 while the pressure term $P_r(t)$ in equation 1 is neglected. The ODEs are integrated using both the DP45 and ABM-PECE algorithms, with tolerance parameters of 10^{-8} to 10^{-2}. Once again, no significant differences are observed between both solvers and the integration results are sensibly identical beyond a relative tolerance of 10^{-4}. In the following, the equations for the velocity and the temperature are solved simultaneously using the DP45 algorithm with a tolerance of 10^{-4}.

DISTRIBUTION A: Distribution approved for public release.

The results from the integration of reduced order models are presented in figure 101 as a function of the parameters N_V and N_T for the first four temporal coefficients along with the corresponding POD coefficients (projected LES data). The results for the velocity ROM show excellent tracking over two periods for the first two temporal coefficients as early as $N_V = 4$. The accuracy of the ROM remains excellent for the following two modes with $N_V = 8$ and $N_V = 18$. As for the 2SLDC velocity ROM, no visible influence of N_T on the velocity solution is observed at fixed values of N_V. For $N_T = 4$, the temperature ROM is somewhat less accurate than its velocity counterpart on modes 1 and 2, but surprisingly good on mode 3 and 4. The ROM starts to diverge in the third period and the influence of N_V on the temperature ROM appears to be weak. For $N_T = 8$, the accuracy of the temperature ROM is greatly improved for the first two temporal coefficients over the $N_T = 4$ solution. The influence of N_V is however visible between $N_V = 4$ and $N_V = 8$, in particular for the third and fourth temporal coefficients. Finally, the results for $N_T = 18$ show reasonable accuracy at $N_V = 4$ and excellent qualitative tracking for $N_V = 8$ and $N_V = 18$. It is however worth noting that the accuracy in the third period appears to be slightly worse for the case with higher N_V, especially on the third and fourth modes. Overall good qualitative tracking of both velocity and temperature ROMs is obtained for $N_V = 8$ and $N_T = 8$.

Overall, good qualitative and quantitative agreement with the projected LES data is obtained using $N_V = 8, N_T = 18$, even though the pressure terms are being neglected.

DISTRIBUTION A: Distribution approved for public release.

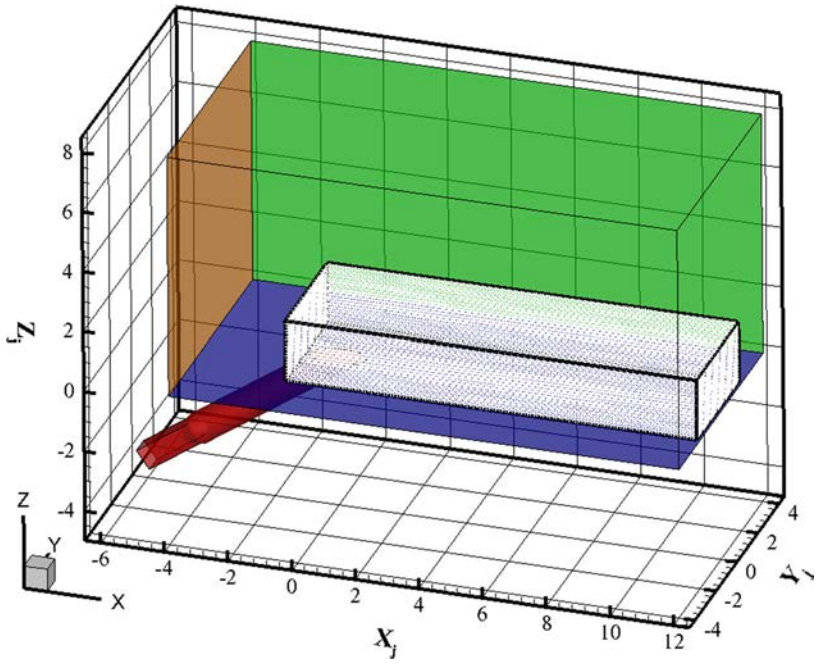

Figure 102: Proper Orthogonal Decomposition domain.

3 Film Cooling Jets Reduced Order Models

3.1 Preliminary Statistical POD Analysis of Film Cooling Jets

Before using the POD for reduced order modeling purposes, the decomposition is used for its flow analysis capabilities in order to isolate the dominant flow vortical structures in a quantitative way and identify any potential shortcomings of the method. POD is applied to both unforced and forced inclined jets described in the previous chapter. In this section, the Proper Orthogonal Decomposition is carried out on the complete velocity and temperature signals, without beforehand separating them into time averaged and fluctuation components.

3.1.1 Unforced Jets

The three-dimensional flow field and temperature field from LES at $BR = 0.15$ are analyzed using the snapshot method described in Chapter 4. A set of 200 statistically independent flow and temperature fields with a spatial density of 10 points per jet diameter is used. It is found that at the considered low turbulence levels, 300 snapshots and 20 vectors per jet diameters lead to sensibly identical results with yet considerably longer computation times. The analyzed sub-domain is presented in figure 102 and is such as $\{-1 \leq X_j \leq 12, -2 \leq Y_j \leq 2, 0 < Z_j \leq 2\}$ yielding 106,600 spatial points at the lowest resolution.

Figures 103(a-c), 104(a, b) present slices of the first four velocity POD modes (including the mean flow field) as well as the corresponding λ_2 (2^{nd} invariant of the velocity divergence tensor) iso-surfaces. The time averaged flow field exhibits the classical features of inclined jet in cross-flow and compares qualitatively well with previously reported results of (10). In particular the presence of a pair of counter-rotating vortices (CRVP) is visible in the $X_j = 6$

DISTRIBUTION A: Distribution approved for public release.

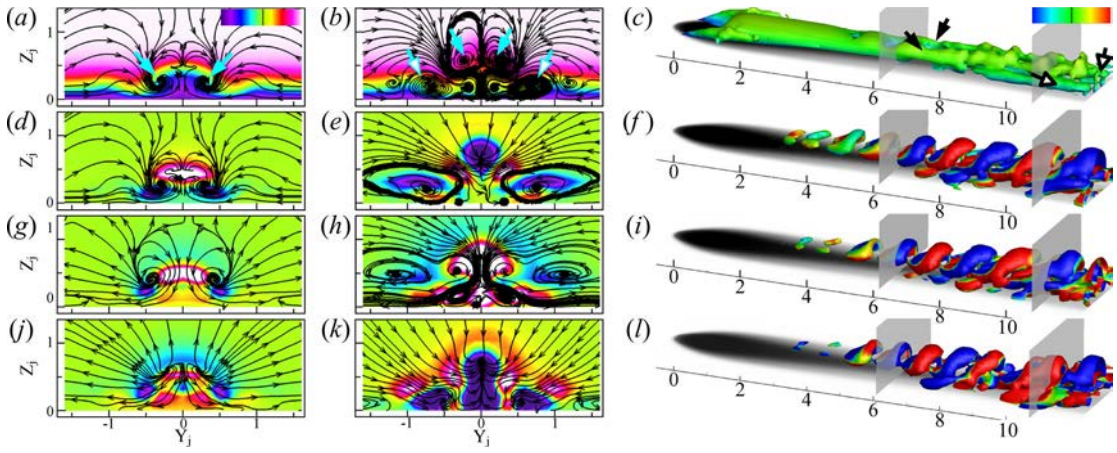

Figure 103: Mean flow (0^{th} POD Mode) and first 3 velocity POD modes at $BR = 0.15$ (a-c) Mode0; (d-f) Mode1; (g-i) Mode2; (j-l) Mode3. Slices at $X_j = 6$ (*left*), $X_j = 10.6$ (*center*) with U velocity contours and V-W streamlines. λ_2 iso-surfaces (*right*) computed from the corresponding POD modes colored by U velocity and mean wall temperature contours (*gray scale*).

and 10.6 slices (solid arrows) as well as in the $Z_j = 0.25$ slice with upward motion around the $Y_j = 0$ line surrounded by two lines of downward motion at $Y_j = \pm 0.5$. The CRVP is generated in the average field by the downstream convection of the shear layer hairpin vortices legs as for the vertical jet configuration. In addition at $X_j = 10.6$ a secondary pair of counter-rotating streamwise vortices (hollow arrows) of opposite vorticity is formed near the wall on each side of the jet, corresponding to the side vortices observed in figure 29. The side vortices are observed in figure 103(c) for $X_j > 9$ and materialized in the average flow field by vortex tubes along the jet core as well as in figure 104(b) through the formation of another 'stripe' of positive vertical motion at $Y_j = \pm 0.9$.

The remaining POD modes provide an orthogonal decomposition of the fluctuation part of the velocity. According to figure 105(a), the first two POD modes virtually capture the same amount of energy while being also very similar in shape when comparing figure 103(f) and 103(i), as well as figure 104 (c, d) and 104 (e, f) with a phase shift in the streamwise direction. Both modes exhibit alternating changes in the sign of the velocity components in the downstream direction. Hence, the cumulative effects of Mode1 and 2 alternating positive and negative velocity regions combined with the phase shifted variations in the signs of a_1^{Vel} and a_2^{Vel} in figure 105(b), generates a downstream motion. In the present case, this behavior is associated with the convection of the shear layer hairpin vortices which are the principal structures observed in the attached jet configuration, supported by λ_2 iso-surfaces in figures 104(f) and 104(i) exhibiting hairpin shapes similar to the one of hairpin vortices. The velocity vector field associated with the first two POD modes also exhibits in figures 104(c) and 104(e) focus points corresponding to the hairpins legs. It is also observed that the first modes are strong rather far away from the jet exit but not particularly significant near the jet exit. This is explained by the fact that proper orthogonal decomposition 'sorts' the modes with respect of the amount of kinetic energy they contain, thus sorting the scales of the structures as well, such that the most energetic modes (first modes) will usually represent

DISTRIBUTION A: Distribution approved for public release.

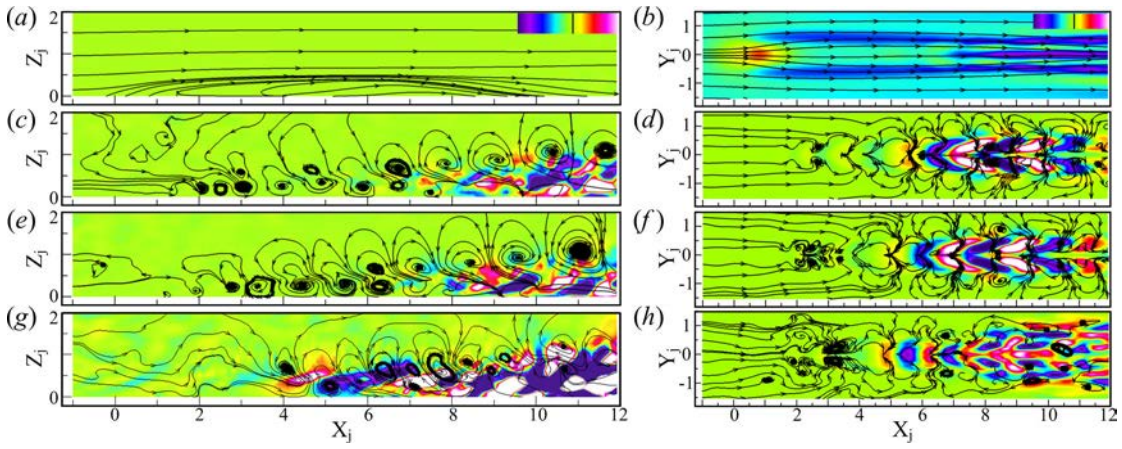

Figure 104: Mean flow and first 3 velocity POD modes at BR=0.15 (*a, b*) Mode0; (*c, d*) Mode1; (*e, f*) Mode2; (*g, h*) Mode3. Slices at $Y_j = 0$ with V velocity contours and U-W streamlines (*left*) and slices at $Z_j = 0.25$ with W velocity contours and U-V streamlines (*left*).

the largest structures. The third mode presented in figure 103(*k-m*) and 104(*g, h*) exhibits similarities with the first two modes with alternating positive and negative vertical velocity in the plane $Z_j = 0.25$, though the pattern appears less regular. In the plane $Y_j = 0$ of figure 104(*g*), the streamlines clearly show the formation of rollups in the jet upper shear layer. A strong negative streamwise velocity region is located near the symmetry plane ($Y_j = 0$) between the hairpin legs which is visible in the plane $X_j = 10.6$ as well. While streamwise vorticity from the fluctuations of the CRVP and side vortices is captured in the first two modes, no significant x-vorticity appears to be contained in the third mode at $X_j = 6$ or 10.6. Although according to figure 105(*a*) several other modes appear to carry a significant amount of energy, they will not be presented in the current document for the sake of brevity. However, it should be noted that the fourth mode resembles closely the third one yet with a 'phase shift' in the same way the first and second modes were related. The additional modes ($N \geq 5$) describe principally the dynamics of the near-wall region, particularly the side vortices and their interaction with the hairpin vortices.

The temperature field is analyzed as well using POD. Although the norm used in the standard proper orthogonal decomposition does not maximize the thermal energy, this method has been used in previous studies to provide a set of orthonormal functions that can be used to obtain a reduced order model of the temperature field (see previous sections). However, it can be argued that the decomposition may not be as 'optimal' as the one obtained for the velocity field in terms of energy. The 0^{th} mode (average temperature field) is presented in figure 106(*a-c*), and 107(*a, b*). The temperature field at the wall (figure 107*b*) is consistent with the one presented in figure 30(*a*). The contours in figure 106(*a, b*) show the averaged impact of the CRVP and the side-vortices on the temperature field. While the CRVP entrains hot cross-flow fluid near the wall, the side-vortices tend to increase the spread by varying jet fluid away from the jet core as the two lumps of cooler fluid at $Y_j = \pm 1$ suggest. In figure 105(*a*), the two first modes carry equivalent pseudo-thermal energy while figures 106(*f*) and 106(*i*) show that both modes, related to the hairpin shear

DISTRIBUTION A: Distribution approved for public release.

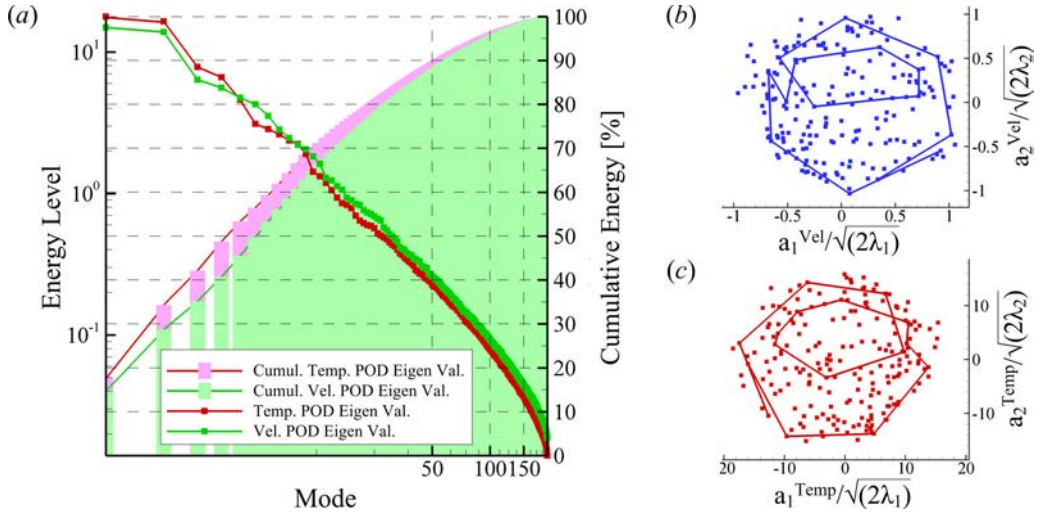

Figure 105: POD decomposition metrics for $BR = 0.15$ (a) POD modes eigenvalues and cumulative temperature and velocity energies; (b) First two velocity POD coefficients a_1^{Vel} and a_2^{Vel}; (c) First two temperature POD coefficients a_1^{Temp} and a_2^{Temp}.

layer vortices according to the shape of their iso-surfaces, are overall identical with a phase shift in the streamwise direction. Based on these considerations and given the distribution of the phase diagram in figure 105(c) showing alternating signs for a_1^{Temp} and a_2^{Temp}, it appears clearly that the first two modes describe the convective effect of the hairpin vortices on the temperature field. Near the wall at $Z_j \approx 0$ (figure 107d, f), the two modes exhibit similar shifted patterns yet a noticeable difference exists near $X_j = 10$ with the presence in the second mode of a pair of patches with a negative value (dark) on each side of the jet (around $Y_j = \pm 1$) which counterpart is not clearly found in the first mode. A comparable discrepancy between the two first modes is found in the same plane around $X_j = 8$, where in Mode1 a pair of patches of rather high positive values (white) near $Y_j = \pm 1$ are present yet no equivalent counter part is found in Mode2. These differences can be attributed to 'quasi-stationary' events occurring near the wall where the velocity is low and the convective effects are not as strong. Thus, while the positive patches in Mode1 appear to correspond to the effect of the hairpin vortices on the pinching of the jet coverage observed in the mean temperature field and attributed to cross-flow entrainment from the legs of the structures, the negative patches in Mode2 are likely to be associated to the spreading of the jet coverage due to the effects of the side vortices. For the sake of brevity, the 3^{rd} and 4^{th} modes are not presented here as they appeared very similar to the two first modes although at smaller length scales.

The 5^{th} mode, however associated with a lower eigenvalue (figure 105a), captures a different behavior as shown in figure 106(k-m) and figures 107(g, h). At $X_j = 6$ and $X_j = 10.6$, Mode5 exhibits two continuous zones in the streamwise direction with positive and negative values. This mode appears to capture a different type of mixing since conversely to Mode1 and 2 the spatial distribution of the mode is not alternating signs in the downstream direction and no other POD mode was found to assume a similar distribution. These observations suggest Mode5 is associated with the mixing behavior induced by the CRVP rather than the downstream convective effect of the hairpin vortices. Hence, the stacking

DISTRIBUTION A: Distribution approved for public release.

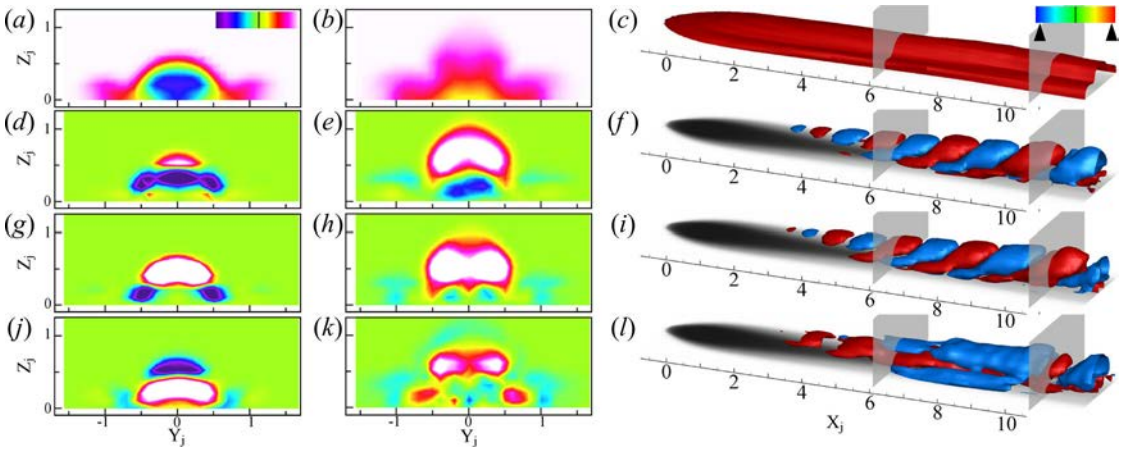

Figure 106: Mean temperature field (0^{th} POD mode) and first significant temperature POD modes at $BR = 0.15$ (*a-c*) Mode0; (*d-f*) Mode1; (*g-i*) Mode2; (*j-k*) Mode5. Slices $X_j = 6$ (*left*), $X_j = 10.6$ (*center*) with temperature contours. Iso-temperature surfaces (*right*) computed from corresponding POD modes (*red*: positive *blue*: negative) and mean wall temperature contours (*gray scale*).

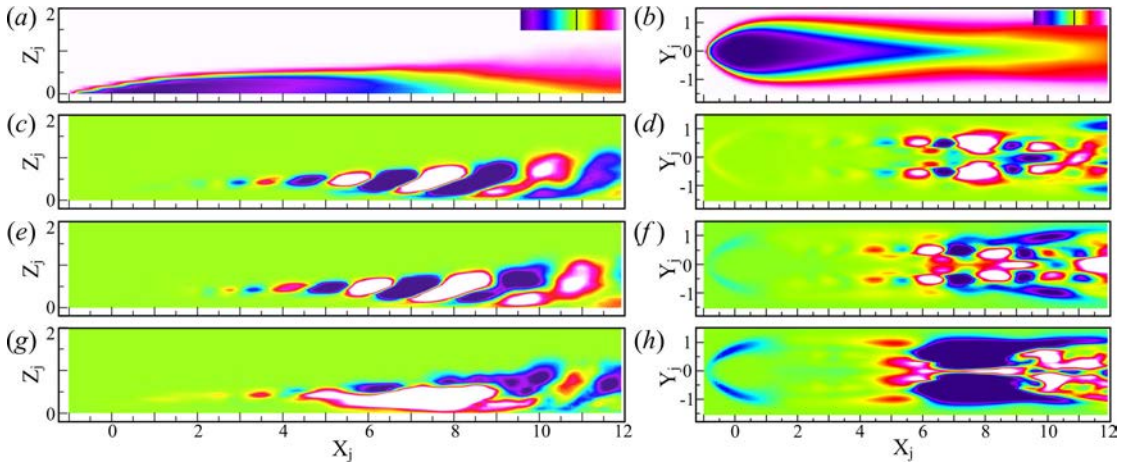

Figure 107: Mean temperature field and first significant temperature POD modes at $BR = 0.15$ (*a, b*) Mode0; (*c, d*) Mode1; (*e, f*) Mode2; (*g, h*) Mode5. Slices at $Y_j = 0$ with temperature contours (left) and slices at $Z_j = 0$ with temperature contours (*right*).

DISTRIBUTION A: Distribution approved for public release.

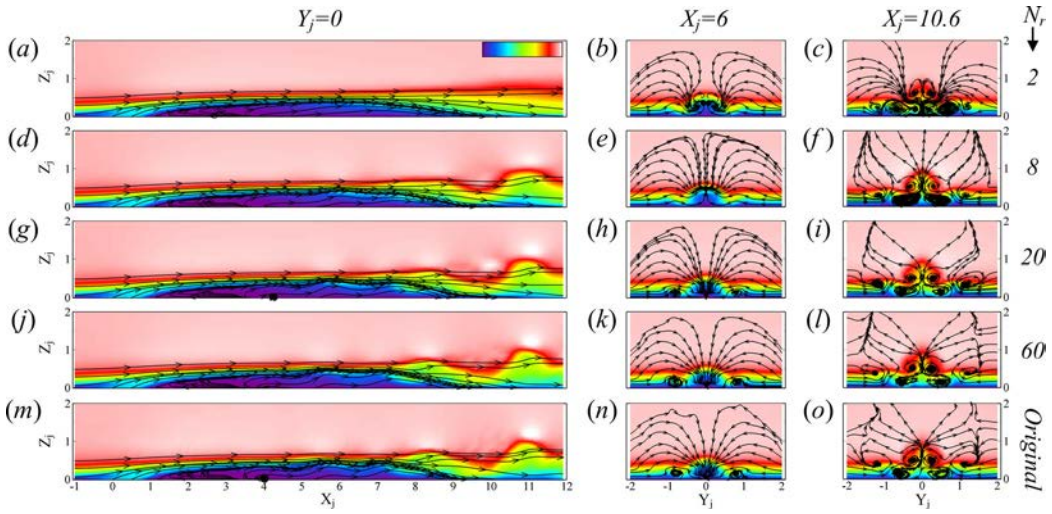

Figure 108: Reconstructed velocity field for multiple values of N_r. Stream traces correspond to in-plane velocity, contours to streamwise velocity.

of an area with negative values on top of one with positive values can be interpreted by the CRVP bringing cooler fluid to the upper part of the domain while entraining hotter fluid near the wall and toward the symmetry plane. Near the wall in figure 107(h), a large area of negative values is visible around $X_j = 8$, $Y_j = \pm 0.5$ where the jet coverage starts to degrade due to cross-flow entrainment. A similar distribution is found near the wall in Mode4 although the rest of the distribution is more consistent with the Mode3. From these observations, it can be argued that the temperature POD modes are more correlated than the velocity modes and part of the information associated with specific phenomena can be captured across several modes.

Figure 105(a) provides an estimation of the total amount of kinetic and pseudo-thermal energies captured by the POD modes as well as the cumulative energy captured by the N first modes. According to the latter, 61 velocity POD modes and 53 temperature POD modes are required to gather at least 90% of the total energy and respectively 156 and 163 modes to gather 99% while modes beyond respectively $N_V = 17$ and $N_T = 15$ carry less than 1% of the total energy.

In figure 108 an instantaneous velocity field is reconstructed from truncated POD series to assess the number of modes necessary to rebuild the dominant flow features. In the plane $Y_j = 0$, the first reconstruction using only 2 modes does not render the formation of the individual hairpin vortex present in the original snapshot at $X_j = 10.6$. This was to be expected due to the absence of information carried by higher order modes with respect to the hairpin vortices as seen in 103(l), thus justifying the lack of accuracy of the reconstructed field. The individual hairpin vortex is observed for $N_r \geq 8$. In the near field of the jet ($X_j < 6$) the reconstruction appears relatively close to the original field with as few modes as 8, due to the low fluctuation levels and limited length scales of the structures in this region. In the plane $X_j = 6$ however, the features of the original flow such as the two counter rotating vortices located at $Z_j = 0.3$, $Y_j = \pm 1$ are only consistently reconstructed for $N_r \geq 20$. Similarly in the plane $X_j = 10.6$, the location and scale of the multiple structures present in the original snapshot are only captured in reconstructions including

DISTRIBUTION A: Distribution approved for public release.

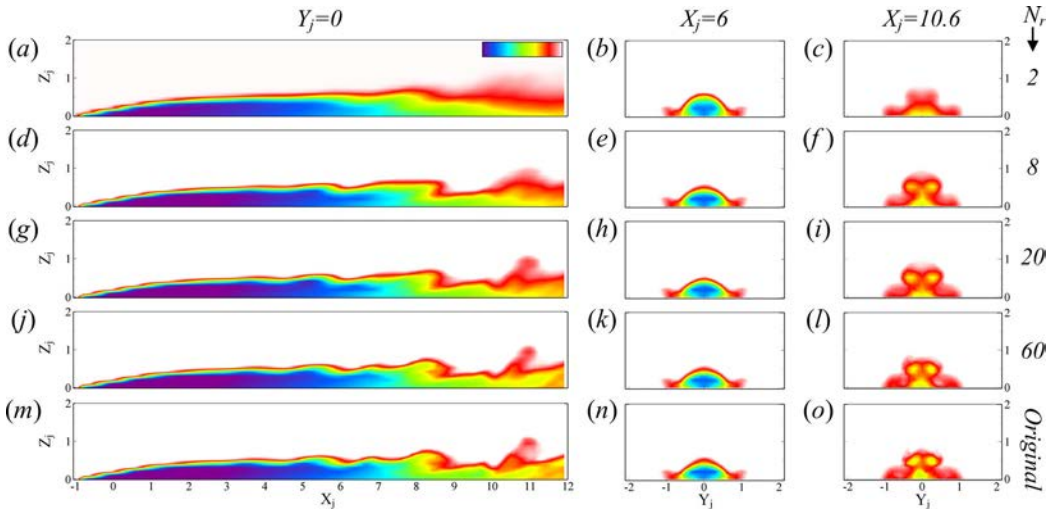

Figure 109: Reconstructed temperature field for multiple values of N_r.

20 modes or more. Overall, although closer from the actual snapshot, the reconstruction using 60 modes does not appear to constitute a significant improvement over the one with 20 modes in terms of the dominant features.

Figure 109 shows reconstructed and original temperature fields corresponding to figure 108. Overall in the plane $Y_j = 0$, the reconstructed temperature field appears to render individual structures beyond $N_r = 8$, with a relatively satisfying definition for $Nr \geq 20$. Similarly, in the planes $X_j = 6$ and $X_j = 10.6$, the reconstructed fields show very little differences. Beyond the qualitative examination of the reconstructed fields, time averaged error distributions with respect to the original field were also calculated to assess the quantitative accuracy obtained with a given number of POD modes. For the velocity field, the error in local kinetic energy. This choice has the advantage of combining all three velocity components into a single figure of merit in addition of being directly related to the norm used for the orthogonal decomposition. However, as the 0^{th} mode corresponds to the time averaged velocity field, not carrying any intrinsic error, it appears more adequate to monitor the error on the turbulent kinetic energy (TKE) rather than the total kinetic energy. The errors distributions on the turbulent kinetic energy are presented in figure 110. In the plane $Y_j = 0$, two zones can be identified. Beyond $X_j = 6$ the error on the decreases significantly to be almost zero for $N_r = 60$. However for $X_j < 6$, the error, although decreasing, stays significant in the jet shear layers even with as many as 100 POD modes. It should also be noted that the extent of this zone of relatively high error decreases with increasing number of POD modes included in the decomposition. This can be explained by the nature of the proper orthogonal decomposition and the norm associated with it, imposing a hierarchy of the modes based on the amount of kinetic energy they capture so that the first modes will capture the large scale structures of the domain. In jets in cross-flow, the principal instability responsible for the formation of the shear layer hairpin vortices is of the convective type and exhibits multiple length scales as it develops in the downstream direction to reach maximum intensity in the far-field. The POD modes thus capture first the downstream motion carrying the largest amount of energy and then progressively capture the lower shear layer fluctuations by going in a reverse direction to the development of the

DISTRIBUTION A: Distribution approved for public release.

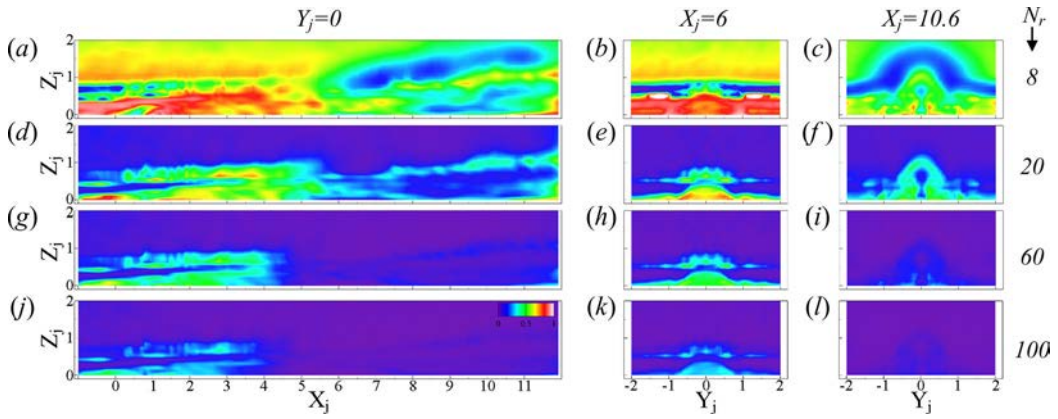

Figure 110: Average TKE error of the reconstructed fields for various values of N_r. Maximum contour value 1 (*white*).

instability thus justifying the relatively poor quality of the reconstruction in the near field of the jet. This constitutes one of the limitations of the standard POD which may lead to dynamical inaccuracy when trying to implement a reduced order model of the flow as pointed out by (36).

Since no perturbation on the temperature field is imposed at the inlets of the domain and by nature the energy equation is free of an explicit non-linear term in T capable of producing or sustaining fluctuations, in a large part of the domain the true temperature fluctuation is extremely low, even null, and thus induced extremely high errors on the fluctuation value when monitoring the reconstructed temperature field. Based on these considerations, it is decided to monitor the absolute relative error on the total temperature field rather than the fluctuation part, reported in figure 111. The error on the temperature field decreases consistently with increasing number of POD modes included in the reconstruction. Most of the error is concentrated beyond $X_j = 5$ where most of mixing and temperature fluctuations occur. It should be noted that similarly to the turbulent kinetic energy, the error in the shear layer of the near-field, appears to decrease at a slower rate than in the far-field. Overall with $N_r = 20$, the maximum error was found to be inferior to 2%, decreasing to less than 1% with $N_r = 60$.

3.1.2 Forced Jets

As for the steady state, LES flow fields and temperature fields for *Case X* at $St_\infty = 0.016$ are analyzed using 3D-POD. The domain and spatial sampling used for the forced cases are identical to the one described in the previous section. Based on the work of (73) on 2D-POD of a pulsed detached jet in cross-flow, an initial temporal sampling of 25 phase locked positions over 10 periods is considered. However, given that the forcing signal used in (73) was a sinusoidal, thus significantly different from the square wave used in the current study, a finer sampling of 50 phase locked positions over 10 cycles is preferred. The POD is computed on both the full time sequence and the phase averaged signal. As seen in figure 114, both methods provide sensibly similar results for the first 20 modes and starts to diverge for higher order modes. This result is expected and consistent with the findings of (73). Indeed, when considering the complete time sequence, the fluctuation part due to more fine-grained

DISTRIBUTION A: Distribution approved for public release.

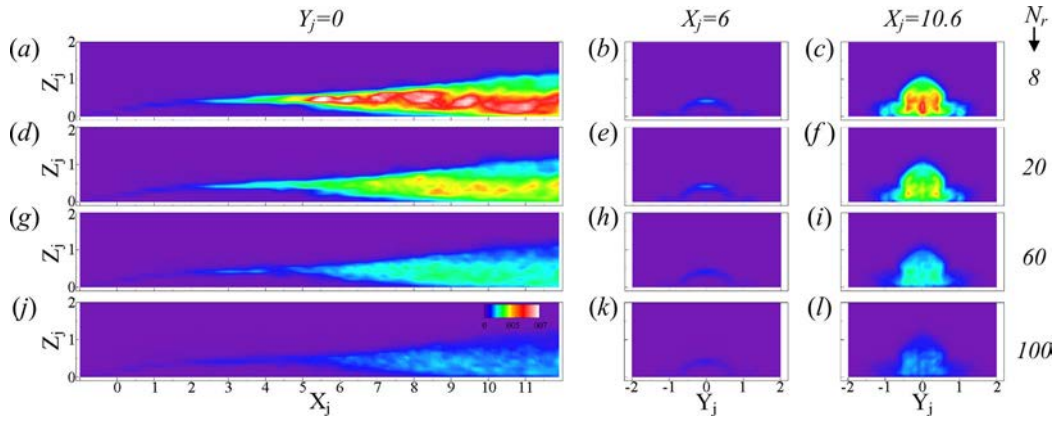

Figure 111: Average temperature error of the reconstructed field at various N_r values. Maximum contour value: 7.10^{-3} (*white*).

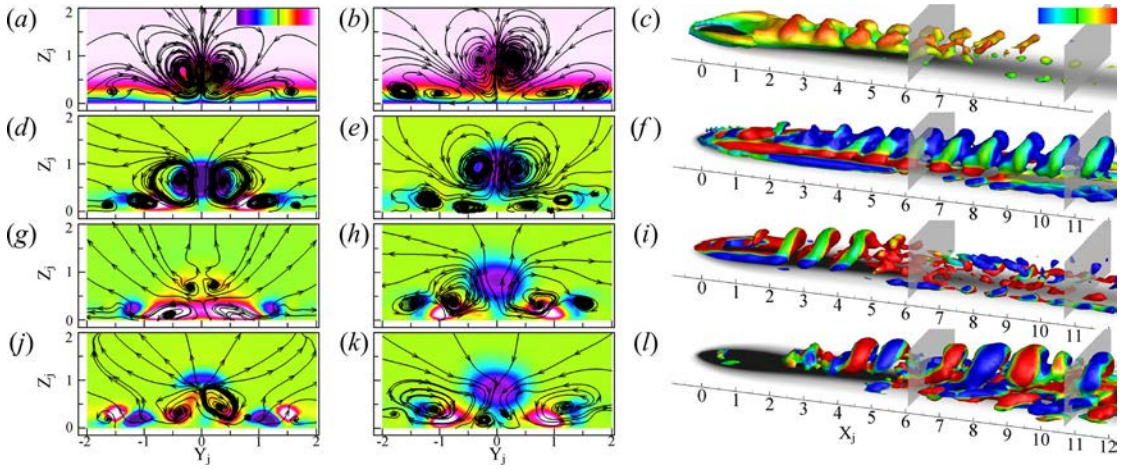

Figure 112: Mean flow (0^{th} POD Mode) and first significant velocity POD modes for *Case X* at $St_\infty = 0.016$ (*a-c*) Mode0; (*d-f*) Mode1; (*g-i*) Mode2; (*j-l*) Mode6. Slices at $X_j = 6$ (*left*), $X_j = 10.6$ (*right*) with U-velocity contours and V-W streamlines. λ_2 iso-surfaces (*right*) from corresponding POD modes colored by U-velocity and mean wall temperature contours (*gray scale*).

DISTRIBUTION A: Distribution approved for public release.

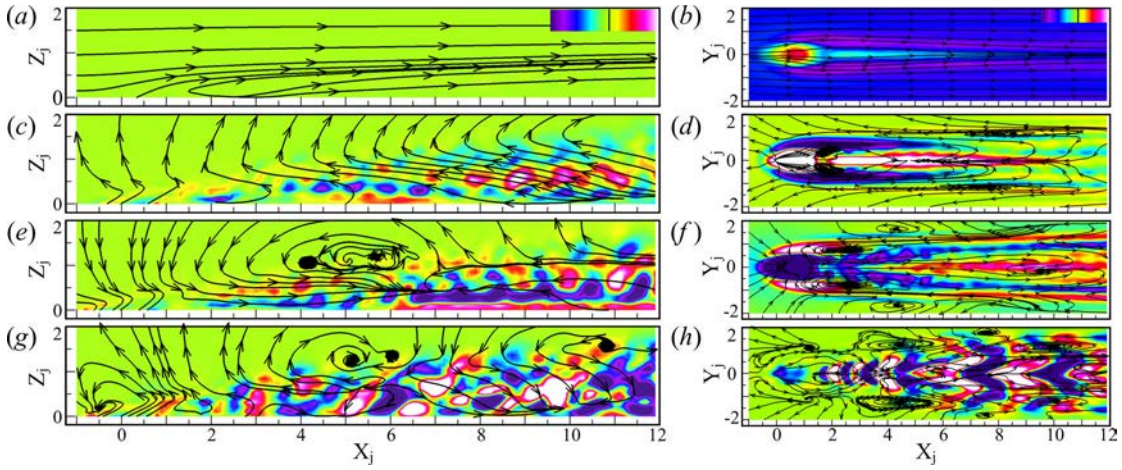

Figure 113: Mean flow and first significant velocity POD modes for *Case X* at $St_\infty = 0.016$; (*a, b*) Mode0; (*c, d*) Mode1; (*e, f*) Mode2; (*g, h*) Mode6. Slices at $Y_j = 0$ with V-velocity contours and U-W streamlines (*left*) and slices at $Z_j = 0.25$ with W-velocity contours and U-V streamlines (*right*).

turbulence is included in the signal and requires a large number of modes to be fully resolved. On the other hand, when analyzing the phase averaged signal, the turbulent fluctuation is removed from the signal thus requiring fewer modes to capture the bulk flow fluctuations (phase averaged). While in the steady state POD analysis, the turbulent fluctuations were considered important to model the flow behavior, in the pulsed system, the significant part was considered to be the phase averaged variation thus the results presented in this paper are based on the POD analysis of the phase averaged signal.

For the sake of brevity, figures 112 and 113 only present modes 0, 1, 2 and 6 issued from the decomposition of *Case X* at $St_\infty = 0.016$. As for the steady state, the 0^{th} mode corresponds to the average flow field. Based on the interpretations of the velocity shape functions it is possible to qualitatively identify which features of the forced jet are being captured by individual modes. The 1^{st} mode corresponds to the bulk flow fluctuation associated with the change in blowing ratio and captures the global jet expansion and shrinking occurring during a cycle. No evidence of a vortical structure is observed in the upper shear layer in figure 113(c), although a counter rotating vortex pair is visible in the constant X_j slices of figure 112(d) and 112(e). The 2^{nd} mode exhibits large scale structures in the jet upper shear layer in figure 113(e), converging velocity field toward the jet exit as well as strong vertical vorticity in the plane $Z_j = 0.25$ of figure 113(f), and is predominantly significant in the near field of the jet in figure 112(i). These considerations suggest that Mode2 is correlated to the large scale structures introduced at the transition from BR_l to BR_h and from BR_h to BR_l, being starting vortices and/or ingestion as described in the previous chapter. It should be noted that in this forced case, the cumulative captured kinetic energy of modes 1 and 2 is equivalent to 53% of the total kinetic energy which is to be put in perspective with the 30% in the steady state case at $BR = 0.15$. Modes 3 to 5 were very similar to the 2^{nd} mode with finer scales were considered as to capture smaller features associated with the introduction of the transient regimes and thus were not presented here for brevity. However, Mode6 in figure 113(g) evidences the presence of shear layer vortices consistent with the natural hairpin

DISTRIBUTION A: Distribution approved for public release.

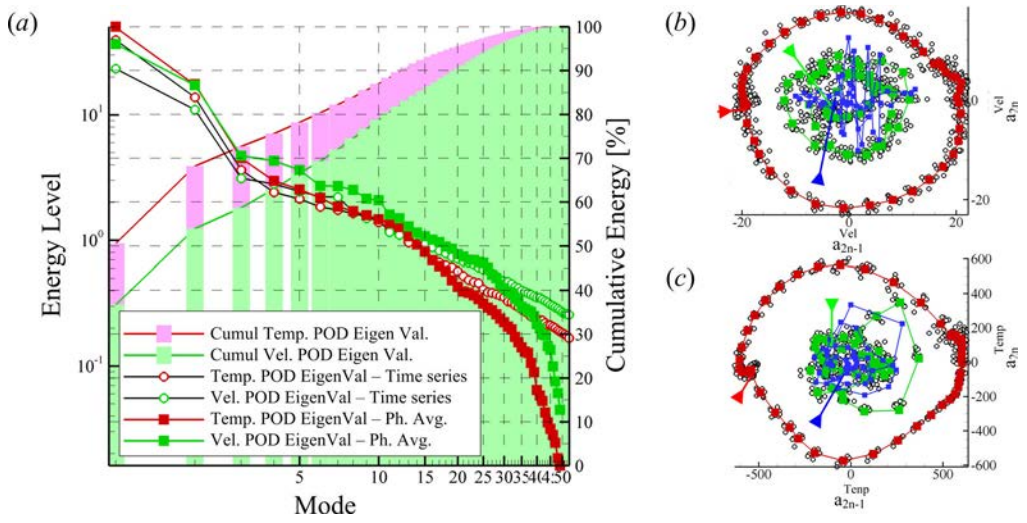

Figure 114: POD decomposition metrics for *Case X* at $St_\infty = 0.016$ (a) Temperature and velocity POD modes eigenvalues and cumulative energy; (b) Velocity POD coefficients; (c) Temperature POD coefficients. Open symbols correspond to full time sequence POD. Arrow points toward $t^* = 0$ in the time sequence.

vortices encountered in unforced conditions, and the λ_2 iso-surfaces of figure 112(m) are very comparable to the one found in dominants modes at $BR = 0.15$ (see previous section). This implies that the 6^{th} mode is likely related to the quasi-unforced behavior during either the low or high part of the cycle. This last point will be developed later and lead to the observation of the POD mode segregation. Conversely to the steady state, the circular shape of the phase diagram in figure 124(b) should not be interpreted as a sign of correlation between the 1^{st} and 2^{nd} modes since the signal is by nature periodic. However, the circular shape shows that both modes operate at the same frequency and with almost equal influence. Interestingly, clusters of points can be observed before the beginning (red arrow) of the cycle and before the transition from high to low blowing ratio (diametrically opposed to the red arrow) where both 1^{st} and 2^{nd} mode values stagnate, the former at a maximum (or minimum) and the latter at a zero value. This observation confirms the qualitative interpretation previously made where Mode1 would correspond to the bulk modulation of the jet envelope thus would be predominant away from the transition points, and Mode2 would correspond to the large scale structures of the transition and would have high values at the transitions.

The temperature field is analyzed as well using POD, the results of which are presented in figure 115 and 116. Similarly to the velocity field decomposition, the 0^{th} mode in figure 115(a-c), 116(a, b) corresponds to the average temperature field, while Modes 1 and higher correspond to the fluctuations around this time averaged field. As for the velocity decomposition, the 1^{st} mode, which is the most energetic, appears to describe the global temperature fluctuations due to the change in penetration associated with jet forcing. The 2^{nd} mode shows a more localized distribution with positive values in the vicinity of the jet exit and negative values in the far field. The phase diagram in figure 114(c) shows strong similarities with the one of the velocity field and suggests that while Modes1 and 2 have similar overall impact in terms of amplitude and frequency, the moments at which they

DISTRIBUTION A: Distribution approved for public release.

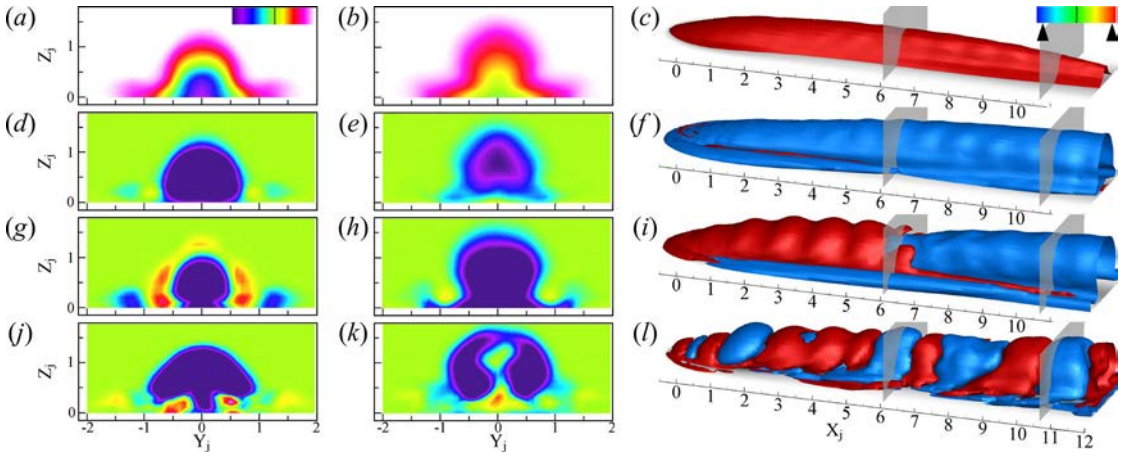

Figure 115: Mean temperature field (0^{th} POD mode) and first significant temperature POD modes for *Case X* at $St_\infty = 0.016$ (*a-c*) Mode0; (*d-f*) Mode1; (*g-i*) Mode2; (*j-l*) Mode10. Slices at $X_j = 6$ (*left*), $X_j = 10.6$ (*center*) with temperature contours. Iso-temperature surfaces (*right*) computed from the corresponding POD modes and mean wall temperature contours (*gray scale*).

are acting on the flow are different. Hence Mode1 has a stronger influence away from the transitions while Mode2 affects the flow mainly at the transitions moments. Modes 3 to 9 exhibited distributions similar to the one of Mode2 with yet smaller length scales and were considered to describe the smaller scale perturbations introduced by the transients thus not presented here. The 10^{th} mode though shows fluctuations in the jet shear layer further away from the jet exit which are consistent with the one observed in unforced conditions at $BR = 0.15$. This suggests that this mode captures the quasi-unforced nature of the jet away from the transitions. The energy distribution in figure 114(a) shows that a total of 41 velocity modes and 33 temperature modes are required to gather 99% of the total fluctuation energy.

To confirm the qualitative interpretations of the POD modes the coefficients a_1, a_2, a_6 for the velocity field and a_1, a_2, a_{10} for the temperature field were plotted in figure 117(a) versus t^* along with the phase averaged blowing ratio profile. In both decompositions, a_1 has broad periods of maxima in absolute value beyond $t^* = 0.20$ up to $t^* = 0.55$ and from $t^* = 0.80$ to $t^* = 1$, both corresponding to the respective established quasi-unforced regimes while a_2 exhibits more localized maxima, directly after the transitions, from one part of the cycle to the other. Modes 6 for velocity and 10 for temperature have significant values during the quasi-unforced regime in the high part of the cycle also confirming the qualitative analysis. The plots of intermediate coefficients (a_3 to a_5 for velocity and a_3 to a_9 for temperature) showed that their support of action was also localized within the transient regions of the cycle and the amplitude of their respective maxima was decreasing along with the width of the peak, exposing a more localized and finer scale influence. Although the transient and the high quasi-steady regimes are captured by modes 1 to 6, none of the first significant modes, except for the first one describing the bulk flow modulations, seem to have significant non-zero values during the low quasi-steady part of the cycle. Only modes beyond the 40^{th} one have their support of action localized during this part of the cycle as seen in figure 117(a) for

DISTRIBUTION A: Distribution approved for public release.

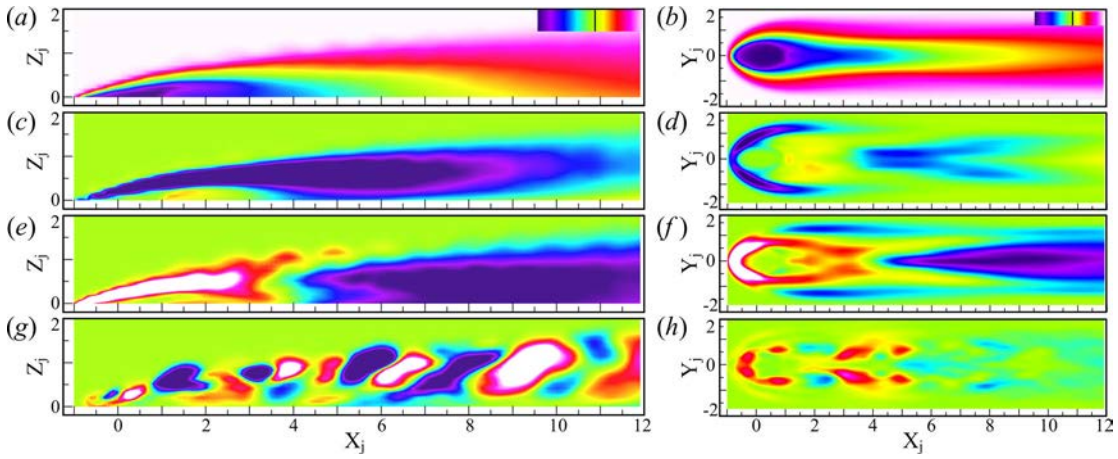

Figure 116: Mean temperature field and first significant temperature POD modes for *Case X* at $St_\infty = 0.016$ from LES; (*a, b*) Mode0; (*c, d*) Mode1; (*e, f*) Mode2; (*g, h*) Mode10. Slices at $Y_j = 0$ with temperature contours (*left*) and slices at $Z_j = 0$ with temperature contours.

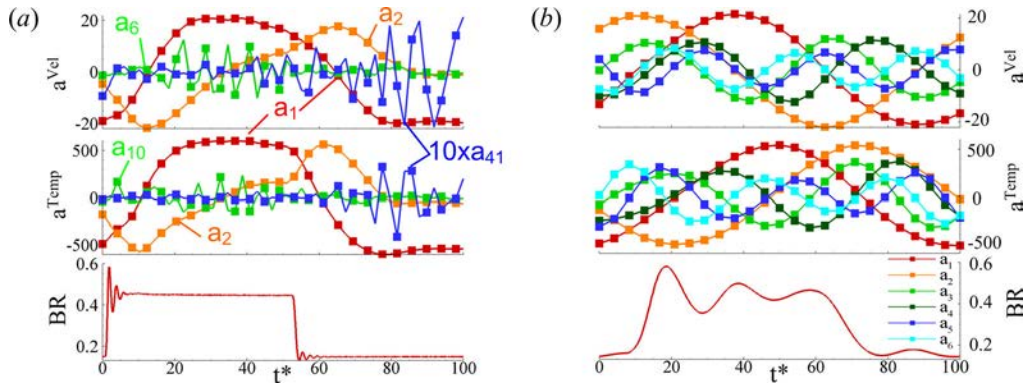

Figure 117: Temporal evolution of the POD modes coefficients a_i^{Vel} for the velocity (*top*) and a_i^{Temp} for temperature (*middle*) decompositions along with forcing blowing ratio profile (*bottom*) at (*a*) $St_\infty = 0.016$; (*b*) $St_\infty = 0159$. The values of a_{41} in (*a*) are multiplied by a factor 10 for increased visibility.

a_{41} (multiplied by 10 to increase visibility). This can be explained by the fact that vortical structures formed during the low quasi-unforced part of the cycle are relatively energetically weak, compared to the transient vortical structures or even the one formed during the quasi-steady high part of the cycle, thus are relegated to the end of the POD spectrum as weak perturbations.

Figure 118 shows the phase locations of the maximum and minimum values of the modal coefficients for each mode revealing the moment in the cycle where they have maximum influence. For both velocity and temperature, a clear pattern appears in the distribution of the maxima and minima. Indeed most of the 40 first modes have an influence on the high part of the cycle with some of them, similarly to Mode2 described previously, having effects at the transition from BR_h to BR_l as well. However, the support for modes 40 and above is

DISTRIBUTION A: Distribution approved for public release.

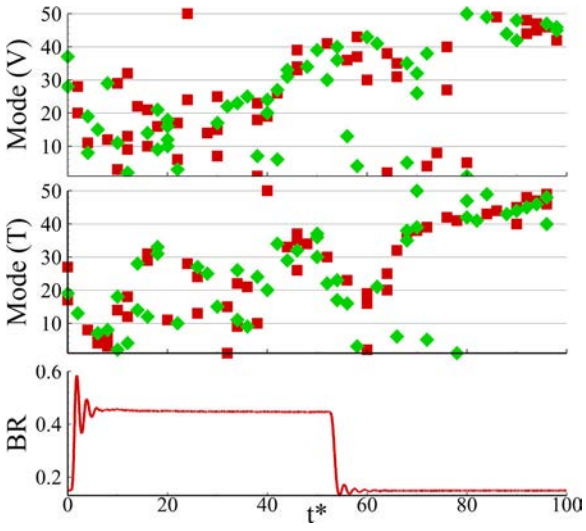

Figure 118: Phase distribution of the minima (*green diamond*) and maxima (*red squares*) associated with the POD modes coefficients a_i^{Vel} for the velocity (*top*) and a_i^{Temp} for the temperature (*middle*) along with phase averaged forcing signal (*bottom*).

almost exclusively located in the low quasi-unforced part of the cycle. Such segregation of the POD modes could have a negative impact on the reconstructed flow field as well as on a reduced order model resulting from truncation of the POD series as it would obliterate a significant part of the cycle.

Although Modes 1 and 2 are the most energetic, the complexity of the flow field generated at the transitions from one part of the cycle to the other prevents us from drawing definitive conclusions based only on the observation of these modes. They however provide a first order estimate of the impact of jet forcing on the temperature field, and particularly at the wall from a film cooling point of view. The first order effect of jet forcing on the wall temperature (corresponding to Mode1 in figure 115*d-f*, and 116*c, d*) appears to be located directly around the jet exit and corresponds to the increase in spread observed in figure 44(a) at the jet onset as well as directly downstream of the jet exit due to increase in coolant mass flow. Because a_1 changes sign throughout the cycle (positive over the high part and negative over the low part), the first order effect of jet forcing is a decrease in wall temperature during the high part and an increase during the low part. Overall, the highest values for Mode1 are located away from the wall suggesting a considerable waste of coolant in the free-stream. The second order effect represented by Mode2 shows that the transitional regime (during which Mode2 is dominant) affects more strongly the wall temperature than the bulk effect of forcing. The effect of the jet onset ($a_2 < 0$) over the average temperature field is to decrease the wall temperature locally around the jet exit due to local increase in spread, but increase it further downstream probably due to the increased entrainment associated with the starting structures lifting off of the wall. At the jet shutdown ($a_2 > 0$), the temperature around the jet increases due to the shrinking of the jet coverage associated with the decrease in coolant mass flow and the ingestion of cross-flow fluid. The downstream effect on the wall temperature is overall positive as the weaker vortical structures generated during the low part of the cycle do not entrain as much cross-flow and tend to remain attached to the wall.

DISTRIBUTION A: Distribution approved for public release.

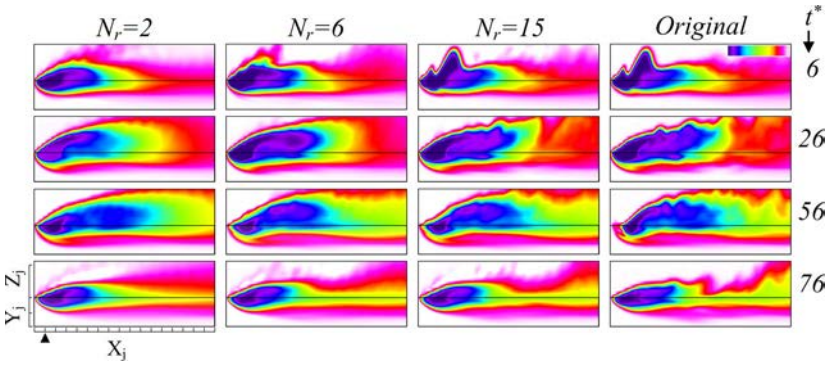

Figure 119: Reconstructed temperature field for multiple values of N_r at four different phase locations: $t^* = 0.06, 0.26, 0.56, 0.76$.

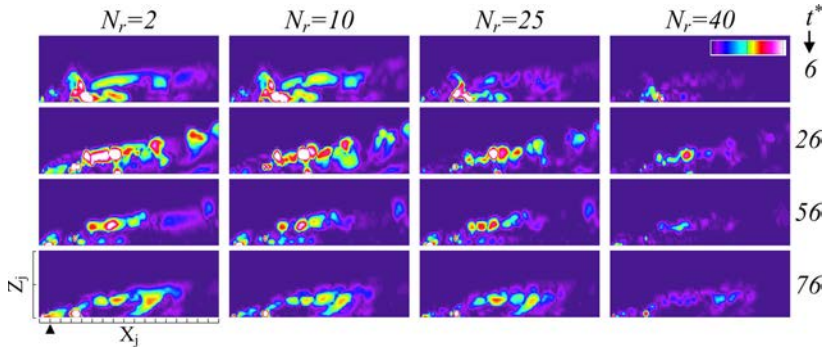

Figure 120: Error on the reconstructed velocity field for different N_r values estimated with phase averaged fluctuation of kinetic energy at $t^* = 0.06, 0.26, 0.56, 0.76$. Maximum value (*white*) is 9%.

Figure 119 presents the reconstructed temperature fields with $N_r = 2$, 6, and 15 modes along with the original temperature field at four phase locked positions. Overall the temperature field appears relatively well reconstructed with only 15 POD modes. However, while the increase from 2 to 15 modes brings significant improvement in the first 3 phase positions, the reconstruction at $t^* = 0.76$ does not show the same details as the one at $t^* = 0.06$ for $N_r = 15$. This is an illustration of the effect of the absence of the higher order modes capturing the behavior in the quasi-steady low part of the cycle. It should be noted that the reconstructed temperature field at the wall does exhibit the dominant features of the original field with only 6 modes.

Although the reconstructed velocity field is not presented, an estimate of the error on the reconstruction is shown in figure 120. Because the POD analysis was performed on the phase averaged signal, it is impossible to base the estimate of the error on the turbulent kinetic energy. Instead, the error (e_r) is estimated on the kinetic energy of the phase average fluctuation normalized by the total kinetic energy. Using $U_r = \bar{U} + \tilde{U}_r$ where U_r is the total reconstructed phase averaged field, $\bar{U}$ is the time averaged signal (equal to the true LES time averaged field) and $\tilde{U}_r$ the reconstructed phase averaged fluctuation using N_r POD modes.

DISTRIBUTION A: Distribution approved for public release.

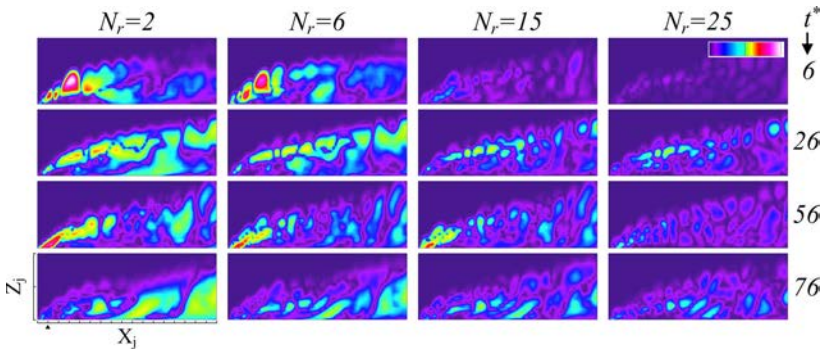

Figure 121: Error on the reconstructed temperature field for different values of N_r estimated using the total value of the temperature at $t^* = 0.06$, 0.26, 0.56, 0.76. Maximum value (*white*) is 9%.

Similarly, the true phase averaged velocity field can be decomposed into $U = \bar{U} + \tilde{U}$. The expression for the error on the phase averaged fluctuation is then:

$$e_r = \frac{\tilde{U_r}^2 + \tilde{V_r}^2 + \tilde{W_r}^2 - (\tilde{U}^2 + \tilde{V}^2 + \tilde{W}^2)}{U^2 + V^2 + W^2}$$

Figure 120 shows that the error decreases consistently with increasing numbers of modes although not equally across all phase positions. Indeed while the error decreases significantly from $N_r = 2$ to $N_r = 25$ at $t^* = 0.06$, it still stays relatively high for the other phase locations until $N_r = 40$. Even with $N_r = 40$, the reconstructions at $t^* = 0.26$ and 0.76 still show some error due to the truncation although in absolute value below 4% of the total instantaneous kinetic energy.

As for the steady state, the error on the reconstructed temperature field is estimated based on the relative error on total temperature (mean and fluctuation) and is presented in figure 121. Similarly to the velocity field, the error decreases consistently with increasing number of POD modes used in the reconstruction, although not homogeneously across all the phase positions. While the maximum error at $t^* = 0.06$ decreases from 9.2% at $N_r = 2$ to 0.2% at $N_r = 25$, corresponding to a factor of 46, it decreases at $t^* = 0.26$, 0.56 and 0.76 only by factors of respectively 2, 5, and 1.75. Nevertheless, the relative error does not exceed a maximum of 4% across the cycle with $N_r = 10$ and 2% with $N_r = 25$ and above. On both velocity and temperature fields, it is verified that the error asymptotically converges towards 0 when using all the modes for the reconstruction so that no loss of information is introduced by the proper orthogonal decomposition.

Simulation results from *Case X* at $St_\infty = 0.159$ are analyzed using 3D-POD as well. Identical domain and spatial samplings are used. The temporal sampling consists here of 25 phase locked positions over 10 cycles accounting for a total of 250 snapshots. As for the previous forced case, the decomposition is carried out on both the complete time sequence and the phase averaged signal. The complete energy distribution and the phase diagrams for the first 6 pairs of modes are presented in figure 124. Once again, decompositions of instantaneous and phase averaged flows are identical up to the 10^{th} POD mode and diverge for higher order modes due to the presence of the turbulent fluctuation in the full time sequence series. As for the previous case at $St_\infty = 0.016$, the decomposition on the phase averaged

DISTRIBUTION A: Distribution approved for public release.

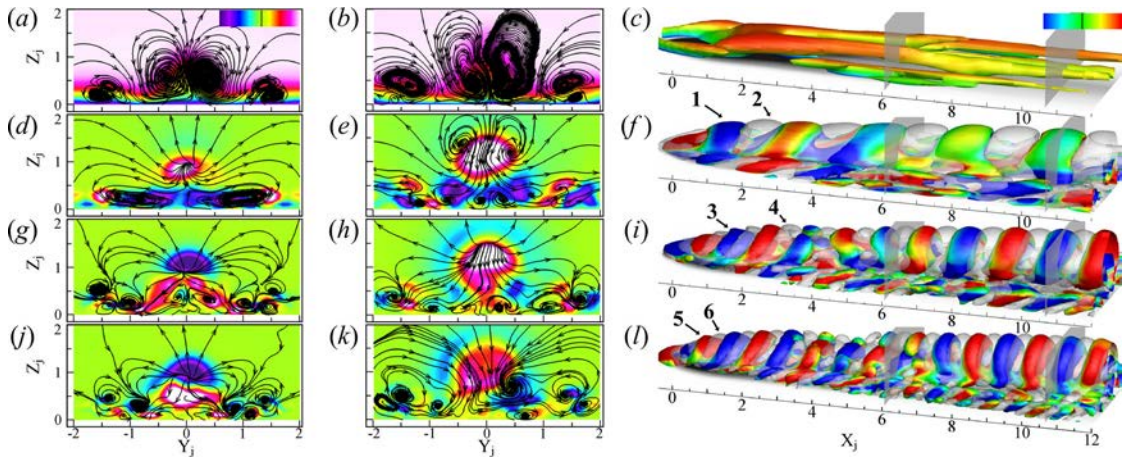

Figure 122: Mean flow (0^{th} POD Mode) and first significant velocity POD modes for *Case X* at $St_\infty = 0.159$ (*a-c*) Mode0; (*d-f*) Mode1; (*g-i*) Mode3; (*j-l*) Mode5. Slices at $X_j = 6$ (*left*), $X_j = 10.6$ (*center*) with U-velocity contours and V-W streamlines. λ_2 iso-surfaces (*right*) computed from corresponding POD modes and correlated mode (*white*) colored by the corresponding U-velocity and mean wall temperature contours (*gray scale*).

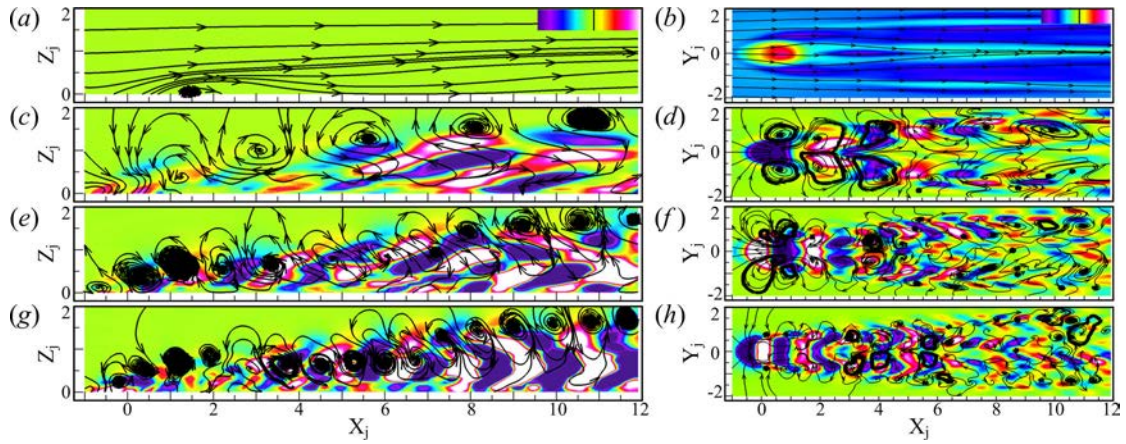

Figure 123: Mean flow and first significant velocity POD modes for *Case X* at $St_\infty = 0.159$ (*a, b*) Mode0; (*c, d*) Mode1; (*e, f*) Mode3; (*g, h*) Mode5. Slices at $Y_j = 0$ with V-velocity contours and U-W streamlines (*left*) and slices at $Z_j = 0.25$ with W-velocity contours and U-V streamlines (*right*).

DISTRIBUTION A: Distribution approved for public release.

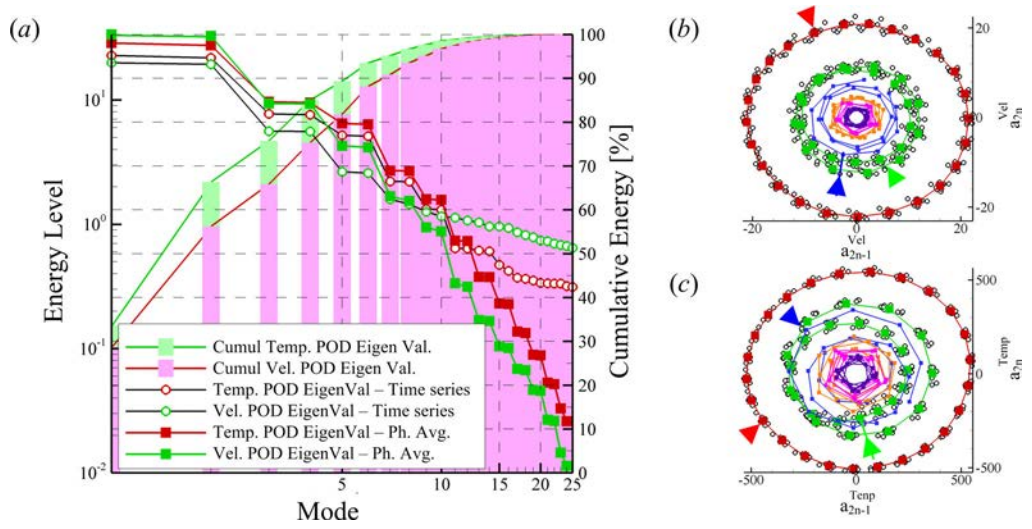

Figure 124: POD decomposition metrics for *Case X* at $St_\infty = 0.159$ from LES (a) POD modes eigenvalues and cumulative energy for temperature and velocity; (b) Velocity POD coefficients; (c) Temperature POD coefficients. Open symbols correspond to full time sequence POD. Arrow points toward $t^* = 0$ in the time sequence.

signal is preferred. The first noticeable difference between the two forced cases is found in the shape of the captured energy distribution. While in figure 114(a) at $St_\infty = 0.016$, the energy distribution does not exhibit a particular shape, the one at $St_\infty = 0.159$ assumes a clear stair-like shape. It should also be noted that the cumulative kinetic energy captured by the first two POD modes correspond to more than 65% of the total energy. Although in the presence of a forced case where the POD modes are automatically correlated to the forcing signal, the quasi-prefect circular distribution of the successive pairs of modes presented in the phase diagrams of figure 124(b) and 124(c) is a consequence of the stream-wise homogeneity of the flow making POD modes converge toward Fourier modes (see 34). This result is a consequence of the fact that at $St_\infty = 0.159$, multiple forcing cycles affect the flow field and that the dominant events are the generation and convection of the starting vortices. Hence the problem involves less length and time scales compared to the lower frequency case where the jet exhibited four distinct regimes each with distinct time and length scales.

POD modes issued from the decomposition of the velocity fields are presented in figures 122 and 123. While the 0^{th} POD mode corresponds to the average flow field, the 1^{st} and 2^{nd} are virtually identical with the exception of a phase shift in the downstream direction as seen in the superposition of λ_2 iso-surfaces in figure 122(f). Both modes assume the shape of multiple large scale hairpin vortices penetrating deeply in the free stream. A set of side vortices is visible in the λ_2 iso-surfaces as well as in the $X_j = 6$ slice of the flow field in figure 122(c). These correspond to the large scale side vortices formed near the wall close to the starting vortices and observed in instantaneous snapshots of figure 44. The third and fourth modes, also largely identical with a shift in phase, correspond to the first harmonic of the 1^{st} and 2^{nd} modes respectively. The phase diagram corresponding to these modes in 124(b) shows that while a_1^{Vel} and a_2^{Vel} complete a single revolution during a cycle, a_3^{Vel} and a_4^{Vel} complete two. Similarly, Modes 5 and 6 are the second harmonics of Modes 1 and 2

DISTRIBUTION A: Distribution approved for public release.

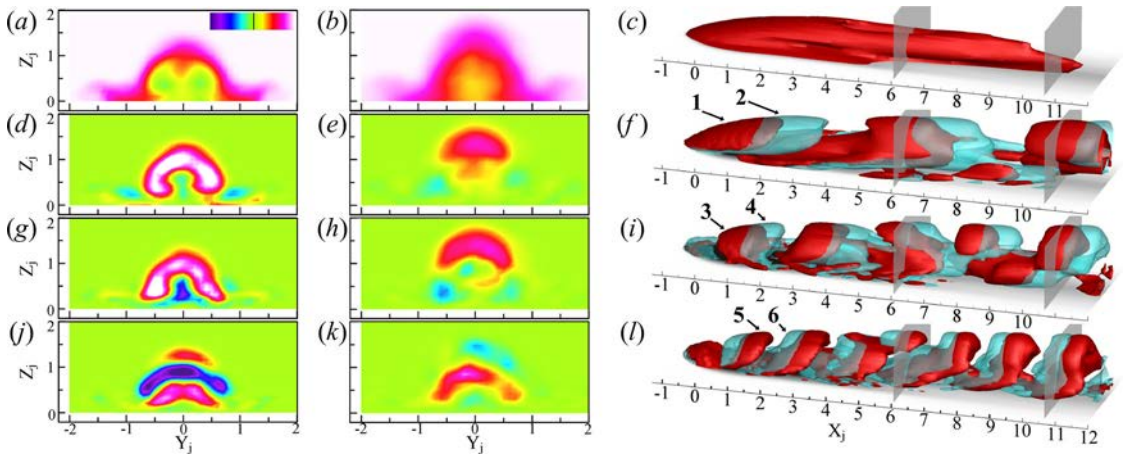

Figure 125: Mean temperature field (0^{th} POD mode) and first significant temperature POD modes for *Case X* at $St_\infty = 0.159$ (*a-c*) Mode0; (*d-f*) Mode1; (*g-i*) Mode3; (*j-l*) Mode5. Slices at $X_j = 6$ (*left*), $X_j = 10.6$ (*center*) with temperature contours. Iso-T surfaces (*right*) computed from corresponding pairs of POD modes (*transparent*) and mean wall temperature contours (*gray scale*).

respectively. The energy distribution in figure 124(a) shows that a total of 12 velocity modes and 15 temperature modes are required to reconstruct 99% of the total fluctuation energy.

As for the previous pulsed case, the modal coefficients a_1^{Vel} through a_6^{Vel} are plotted versus time along with the forcing signal in figure 117(b). The phase shift between the correlated pairs of modes is easily quantifiable and corresponds to a quarter of the period for the first two, an eighth for modes 3 and 4 and a sixteenth for modes 5 and 6. Conversely to the $St_\infty = 0.016$ case, none of the modes appears to dominate over one particular part of the forcing cycle and the coefficient converge towards cosine and/or sine functions.

The POD modes corresponding to the temperature field analysis are presented in figures 125 and 126. As in the velocity POD, the first two modes are quasi-identical with a shift in the stream-wise direction. The iso-surfaces in figure 125(f) have a hairpin-like shape, alternating positive and negative values in the stream-wise direction as in the unforced case at $BR = 0.15$. Higher order modes are paired similarly to the velocity field decomposition and correspond the successive harmonics of the first two modes. The evolution of the modal coefficients a_1^{Temp} through a_6^{Temp} with respect to time in figure 117(b) appears almost identical to the one obtained for the velocity field.

In opposition to the lower forcing frequency case, the impact of the different modes on the wall temperature decreases in scale and amplitude as mode order increases. Almost no impact on the wall temperature is observed beyond $X_j = 6$. In the vicinity of the jet exit, the 1^{st} temperature POD mode shows alternating positive and negative values due to the formation and convection of the starting structures. A band of high positive values covering part of the upstream edge of the jet exit is associated with the successive cross-flow ingestions and coverage increases occurring periodically at the jet shutdown and onset.

The reconstructed temperature field using 2, 4 and 6 POD modes is presented in figure 127. The reconstruction quality is homogeneous with time and although the finest details are not represented, the fields including 4 and more modes provide qualitatively a reasonably

DISTRIBUTION A: Distribution approved for public release.

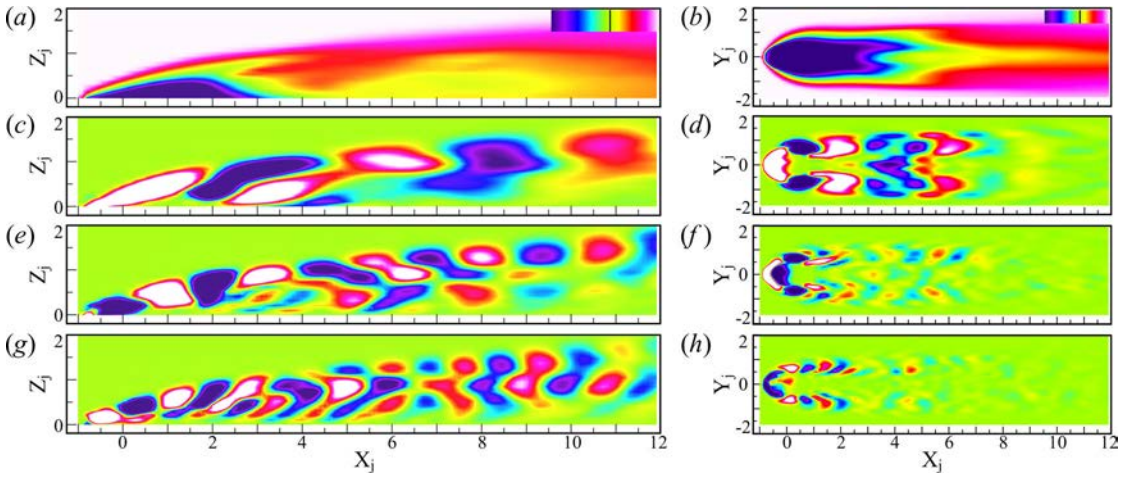

Figure 126: Mean temperature field and first significant temperature POD modes for *Case X* at $St_\infty = 0.159$ (*a, b*) Mode0; (*c, d*) Mode1; (*e, f*) Mode3; (*g, h*) Mode5. Slices at $Y_j = 0$ with temperature contours (*left*) and slices at $Z_j = 0$ with temperature contours (*right*).

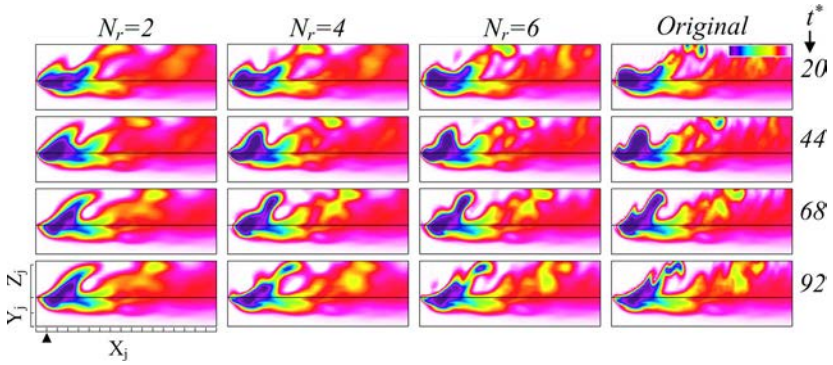

Figure 127: Reconstructed temperature field for multiple values of N_r at different phase location: $t^* = 0.2, 0.44, 0.68, 0.92$.

DISTRIBUTION A: Distribution approved for public release.

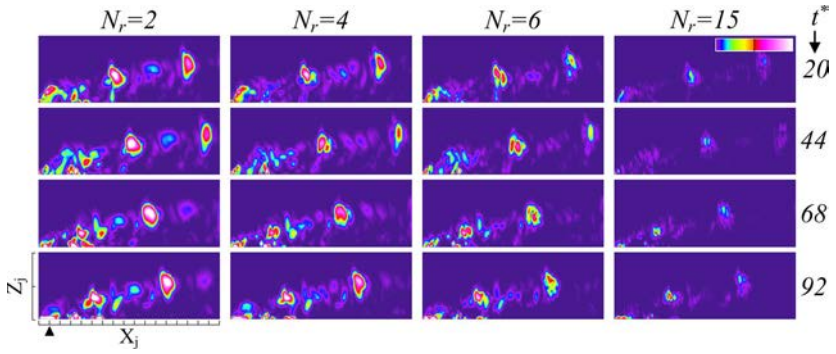

Figure 128: Error on the reconstructed velocity field for different N_r values estimated using the phase averaged fluctuation of kinetic energy at $t^* = 0.2, 0.44, 0.68, 0.92$. Maximum value (*white*) is 6%.

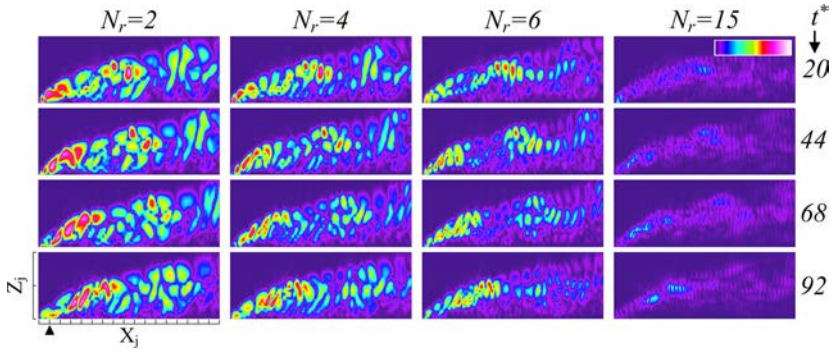

Figure 129: Error on the reconstructed temperature field for different values of N_r estimated using the total value of the temperature at $t^* = 0.2, 0.44, 0.68, 0.92$. Maximum value (*white*) is 6%.

good reconstruction. The error on the reconstructed velocity field and temperature fields are also investigated using different values of N_r. In figure 128 the error on the velocity field is estimated in the same way as for the lower forcing frequency case. The bulk of the error resides in the region where the core of the starting vortex is located which also corresponds to the regions of higher velocity fluctuations. In this higher forcing frequency case, the relative error decreases consistently with increasing number of included POD modes at all time steps. For $N_r = 15$, the overall maximum error does not exceed 4%. Finally, the error on the temperature field is also evaluated and presented in figure 129. As for the velocity reconstruction, the error decreases at all phase locations consistently with increasing number of POD modes included in the reconstruction. The effect of the individual modes is clearly visible on the reduction of the error as the scale of 'error patches' decreases with increasing values of N_r involving higher harmonics thus lower length scales. Six modes are required to obtain a maximum error inferior to 4% while 10 modes ensure a maximum error on the temperature field of the order of 2%.

These results evidence the sorting mechanism associated with proper orthogonal decomposition in both unforced and forced jets. In particular, in forced jet conditions, it is found

DISTRIBUTION A: Distribution approved for public release.

that the flows forced at low frequencies have decompositions which are much different from the ones at higher forcing frequencies when all other parameters are maintained fixed. In addition, due to the discrete length and energy scales introduced in forced jet conditions, the energy distribution of velocity and temperature decompositions are much more organized and exhibits a much more pronounced hierarchy compared to the unforced jet, even at the lowest blowing ratio.

3.2 Reduced Order Models

3.2.1 Stabilization Methods

The POD-Galerkin method was essentially applied to the film cooling jet simulations, although the three-dimensional, turbulent character of realistic film cooling flows can greatly affect the reduced order model accuracy and stability. Several stabilization methods were developped and applied to the unfoced and forced jets.

- *Local Linear Cazemier* stabilization - The first method implemented was developped by (15) and consist in a linear term added to the momentum equations. In the current study, similar considerations to the ones proposed by (15) were used in the heat equation to develop stabilizing parameters for the temperature ROM as well. The damped velocity model was then:

$$\begin{aligned} \dot{a_r}(t) = &\sum_{i=1}^{N_v} \left(C_{i0}^r + \frac{1}{Re_j} D_i^r \right) a_i(t) \\ &+ \sum_{i=1}^{N_v} \sum_{j=1}^{i} C_{ij}^r a_i(t) a_j(t) \\ &+ \left(C_0^r + \frac{1}{Re_j} D_0^r \right) + a_r(t) S_r^V \end{aligned} \tag{3}$$

with

$$S_r^V = -\frac{1}{\lambda_r} \sum_{i=1}^{N_V} \sum_{j=1}^{i} C_{ij}^r \left\langle a_i(t) a_j(t) a_r(t) \right\rangle - \left(C_{r0}^r + \frac{1}{Re_j} D_r^r \right) \tag{4}$$

DISTRIBUTION A: Distribution approved for public release.

The temperature model was then:

$$\begin{aligned}\dot{b}_s(t) = &\sum_{i=1}^{N_V} E^i_{s0} a_i(t) \\ &+ \sum_{j=1}^{N_T} \left(E^0_{sj} + \frac{1}{Pr}\frac{1}{Re_j} F_{sj} \right) b_j(t) \\ &+ \sum_{i=1}^{N_V}\sum_{j=1}^{N_T} E^i_{sj} a_i(t) b_j(t) \\ &+ \left(E^0_{s0} + \frac{1}{Pr}\frac{1}{Re_j} F_{s0} \right) + b_s S^T_s \end{aligned} \tag{5}$$

with

$$S^T_s = -\frac{1}{\sigma_s}\left(\sum_{i=1}^{N_V} E^i_{s0} \left\langle a_i(t) b_s(t) \right\rangle + \sum_{i=1}^{N_V}\sum_{j=1}^{N_T} E^i_{sj} \left\langle a_i(t) b_j(t) b_s(t) \right\rangle \right) - \left(E^0_{ss} + \frac{1}{Pr}\frac{1}{Re_j} F_{ss} \right) \tag{6}$$

- *Broad Linear Cazemier* stabilization - Another stabilization formulation was proposed, based on Bousinesq's eddy viscosity formulation and using Cazemier's energy conservation consideration. The damped model for the velocity was then:

$$\begin{aligned}\dot{a_r}(t) = &\sum_{i=1}^{N_v} \left(C^r_{i0} + \left(\frac{1}{Re_j} + \nu^r_T \right) D^r_i \right) a_i(t) \\ &+ \sum_{i=1}^{N_v}\sum_{j=1}^{i} C^r_{ij} a_i(t) a_j(t) \\ &+ \left(C^r_0 + \left(\frac{1}{Re_j} + \nu^r_T \right) D^r_0 \right) \end{aligned} \tag{7}$$

with

$$\nu^r_T = \frac{-1}{\lambda_r D^r_r}\left(\sum_{i=1}^{N_v}\sum_{j=1}^{i} C^r_{ij} \left\langle a_i(t) a_j(t) a_r(t) \right\rangle + \lambda_r \left(C^r_{r0} + \frac{1}{Re_j} D^r_r \right) \right) \tag{8}$$

DISTRIBUTION A: Distribution approved for public release.

The temperature model is then:

$$\begin{aligned}\dot{b}_s(t) = &\sum_{i=1}^{N_V} E^i_{s0} a_i(t) \\ &+ \sum_{j=1}^{N_T} \left(E^0_{sj} + \left(\frac{1}{Pr} + \alpha^s_T \right) \frac{1}{Re_j} F_{sj} \right) b_j(t) \\ &+ \sum_{i=1}^{N_V} \sum_{j=1}^{N_T} E^i_{sj} a_i(t) b_j(t) \\ &+ \left(E^0_{s0} + \left(\frac{1}{Pr} + \alpha^s_T \right) \frac{1}{Re_j} F_{s0} \right) \end{aligned} \tag{9}$$

with

$$\alpha^s_T = \frac{-1}{\frac{\sigma_s}{Re_j} F_{sj}} \left(\sum_{i=1}^{N_V} \sum_{j=1}^{N_T} E^i_{sj} \left\langle a_i(t) b_j(t) b_s(t) \right\rangle + \sum_{i=1}^{N_V} E^i_{s0} \left\langle a_i(t) b_s(t) \right\rangle + \left(E^0_{sj} + \frac{1}{Pr} \frac{1}{Re_j} F_{sj} \right) \sigma_s \right) \tag{10}$$

A relationship between the terms S^V_r, S^T_s, ν^r_T and α^s_T was established:

$$S^V_r = \frac{\nu^r_T}{D^r_r}, \qquad S^T_s = Re_j \frac{\alpha^s_T}{F_{ss}}$$

3.2.2 Unforced Jets

The first reduced order models obtained are based on unforced jets results. Two regimes, attached and transitional, are investigated. Due to the unlikelihood of the detached regime to benefit any film-cooling application, reduced order modeling of these flows is not pursued. In the perspective of obtaining a reduced order model for flow control, the complete domain has to be considered, in particular the jet pipe and its inlet plane which corresponds to the input plane for the control action.

3.2.2.1 Attached Regime The $BR = 0.15$ unforced jet is the first one investigated. The LES simulations are carried out using the parameters described in Chapter 3. A POD analysis is performed using a set of $1,000$ POD modes following Sirovich snapshot method. This represents a significant increase with respect to the preliminary study presented in the previous section which is justified by the extended domain in the downstream direction, the inclusion of the jet pipe in the decomposition, and the increased grid resolution. Snapshot sampling is done with an equivalent sampling frequency of $300Hz$ ($St_s = 4.8$). The POD metrics are presented in figure 130 for both the velocity and temperature fields decompositions. The first 6 to 8 POD velocity and temperature modes are organized in pairs carrying equivalent energy. The first two velocity modes carry each a little more than 5% of the total kinetic energy and the first two temperature modes carry each a little less than 10% of the total pseudo-thermal energy. To capture 99% of the kinetic energy, a total of 395 modes is

DISTRIBUTION A: Distribution approved for public release.

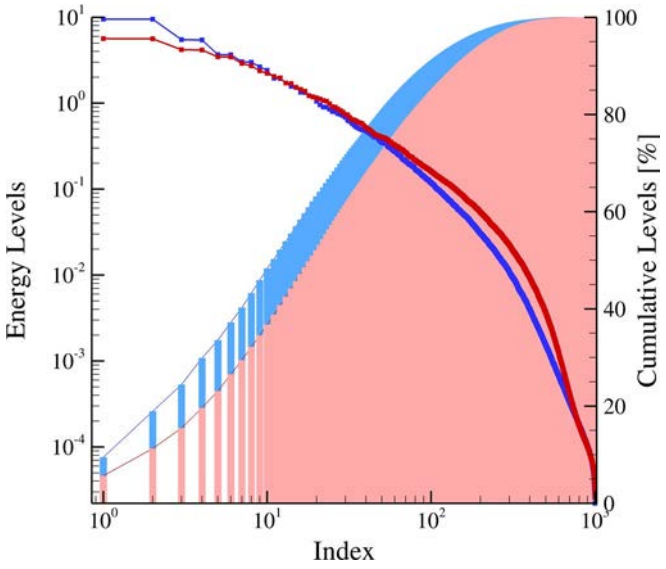

Figure 130: POD decomposition metrics for velocity (*red*) and temperature (*blue*) fields with $N = 1,000$ at $BR = 0.15$.

required, while 99% of the thermal energy is captured by the first 313 temperature modes. These constitute rather large numbers of modes and could pose an issue when integrating the reduced order models ordinary differential equations. The first 14 velocity POD modes λ_2 iso-surfaces are presented in figure 131 and confirm that the first POD modes are associated in pairs, shifted by a quarter of wave length in the downstream direction. Conversely to the preliminary decomposition, the first mode pair does not correspond to the hairpin vortices, but rather the near-wall side vortices. This is due to the ROM grid being extended in the downstream direction, therefore capturing more of the developing wall structures, which highlights the impact of the POD domain selection onto the hierarchy of the captured vortical structures. The first two modes also exhibit vortical structures in the jet tube developing due to the perturbations imposed at the jet inlet during the simulations. Hairpin vortices start appearing in the second pair of velocity modes, in particular in the mid-field. Higher order modes show structures similar to the ones of modes 1, 2 and 3, 4 or a combination of them at either higher spatial frequencies (modes 5, 6) or different locations (modes 13, 14). The first temperature modes in figure 132 are also associated in pairs of similar modes shifted in the downstream direction by a quarter wavelength, which is consistent with the preliminary statistical POD analysis. The first two modes capture the convective effect of the hairpin vortices on the temperature field, while modes 3 and 4 seem to capture temperature fluctuations closer to the wall and may be associated to the effects of the side vortices. Although the first pair of temperature modes captures fluctuations primarily in the mid-field, higher order modes capture features in both the near-field and far-field. Interestingly, modes 7 and 8 seem to represent fluctuations in the transverse planes, likely attributed to the darft of the hairpin vortices legs towards the symmetry plane.

Reduced order models are obtained using the Galerkin projection method described in the previous chapter. For all the following ROMs, the pressure terms arising in equation 1 at the boundaries have been neglected. Given the extent of the domain, not all Galerkin

DISTRIBUTION A: Distribution approved for public release.

coefficients corresponding to all $1,000$ POD modes are computed. In addition, the integration cost of more than $1,000$ non-linear coupled ODEs seem prohibitive and a maximum limit of 500 equations for the velocity and 500 temperature ROMs is set. Given the large domain and the important number of modes to be included, a parallel MPI code in Fortran 90 was developed to perform the projection across multiple platforms.

Evaluations of the error levels with respect to the true velocity and temperature fields showed that an optimum number of modes is found for all three time frames at approximately $N_V = 250$, 400 and 500 for respectively the short, medium and long term error estimates. The temperature error estimates also showed that a local minimum was found at $N_V = 250$, $N_T = 120$. The error levels of the medium and long term estimates decreased monotonously with increasing number of velocity POD modes, and increases monotonously with increasing number of temperature modes.

Figure 133 shows the integrated temporal coefficients a_i^V for the velocity ROM and a_i^T for the temperature ROM at $N_V = 250$ and $N_T = 120$, along with the corresponding projected LES results (POD temporal coefficients). Both velocity and temperature ROMs show reasonable agreement with the projected LES data up to $t_c = 1$ but start diverging from them beyond that point. The divergence occurs both in amplitude and phase and is particularly obvious in the first temperature coefficients. Several explanations can be thought of to justify the diverging behavior of the velocity and temperature modes. The first one comes from the truncation of the POD series and the presence of unresolved modes, potentially leading to less accurate models. Error estimates showed that increasing the number of POD modes does not necessarily lead to more accurate models. Another potential source of error could arise from neglecting the pressure term initially present in the equations. To verify the influence of the pressure term, an empirical pressure correction method as described in 58 is implemented and the complete ROM equations are integrated over identical time frames. The results are presented in figure 133 and show only very little difference with the non-corrected ROM. This provides an a posteriori confirmation of the original assumption of neglecting the pressure term. Another source of error can also come from the chaotic character of turbulent Navier Stokes equations which can lead two sets of infinitely close initial conditions towards two significantly different sets of solutions. Unfortunately, such chaotic behavior is intrinsic to turbulent fluid flows and can only be kept in mind when assessing the accuracy of reduced order models. Finally, a more fundamental source of error can originate from the initial set of snapshots considered to generate the POD basis. First, the sampling frequency used to collect the velocity and temperature fields snapshots acts as a temporal filter and cannot realistically provide a good representation of the vortical structures with a characteristic time-scale of the order of twice the sampling period according to Nyquist criterion. Moreover, the snapshots used in the current study being extracted from LES simulations, suffer from the inherent spatial and temporal filtering introduced by the LES model at the sub-grid scale level. Both temporal, and spatial filters introduced by the sampling but also the chosen turbulence model affect the representation of the smaller dissipative scales and can, combined with the POD series truncation, lead to significant underestimates of the effective momentum and thermal diffusivities.

To try to alleviate the underestimated diffusion, both local and broad linear stabilization methods are used to integrate the velocity and temperature ROMs at multiple values of N_V and N_T. Estimated error levels for the stabilized models on both the velocity and temperature fields drops significantly when using either one of the stabilization methods. The stabilized models evidence an optimum set of $(N_V, N_T) = (275, 100)$ at which minimum

DISTRIBUTION A: Distribution approved for public release.

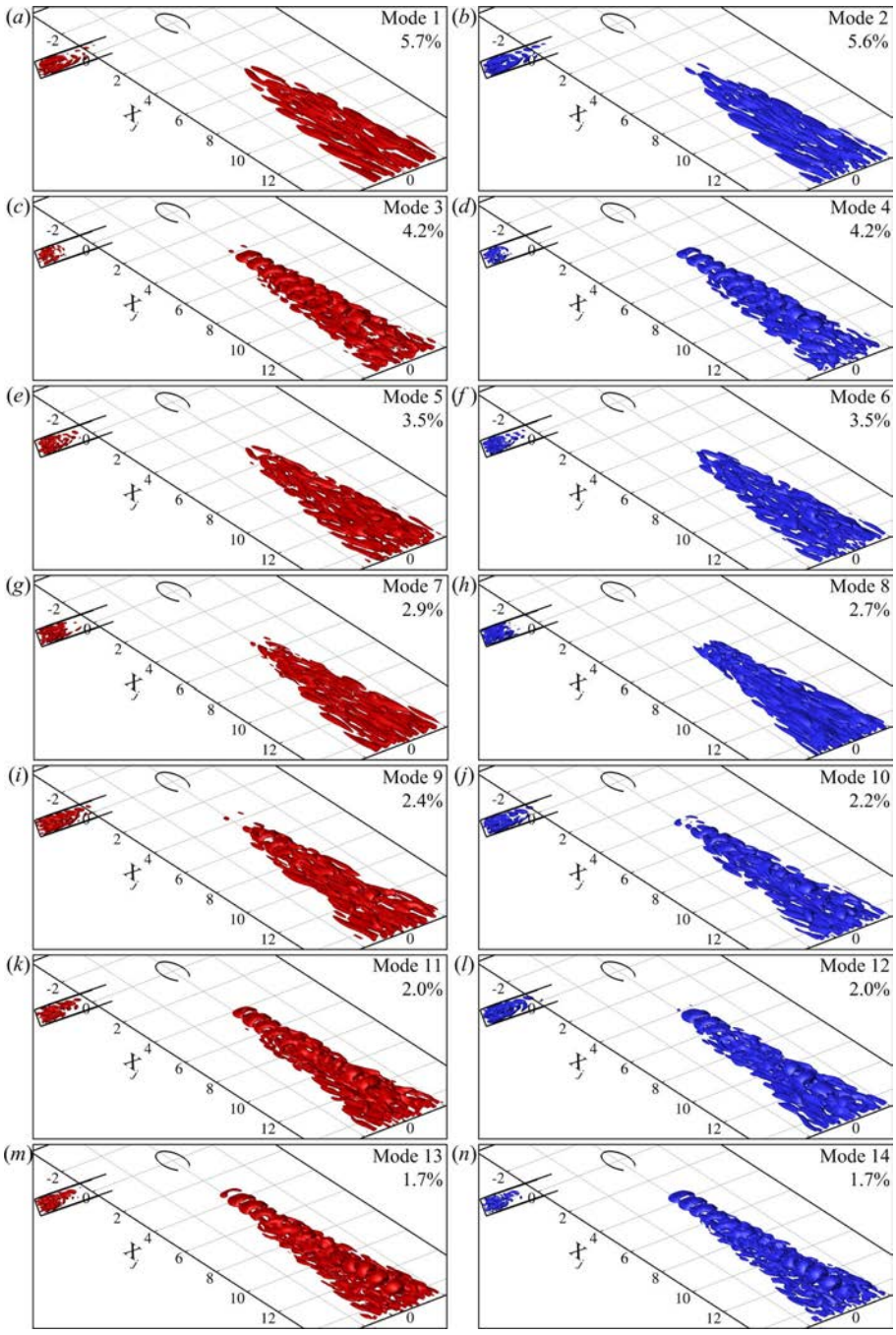

Figure 131: First 14 velocity POD modes λ_2 iso-surfaces for POD decomposition at $BR = 0.15$. Mode energy provided in percent of the total energy.

DISTRIBUTION A: Distribution approved for public release.

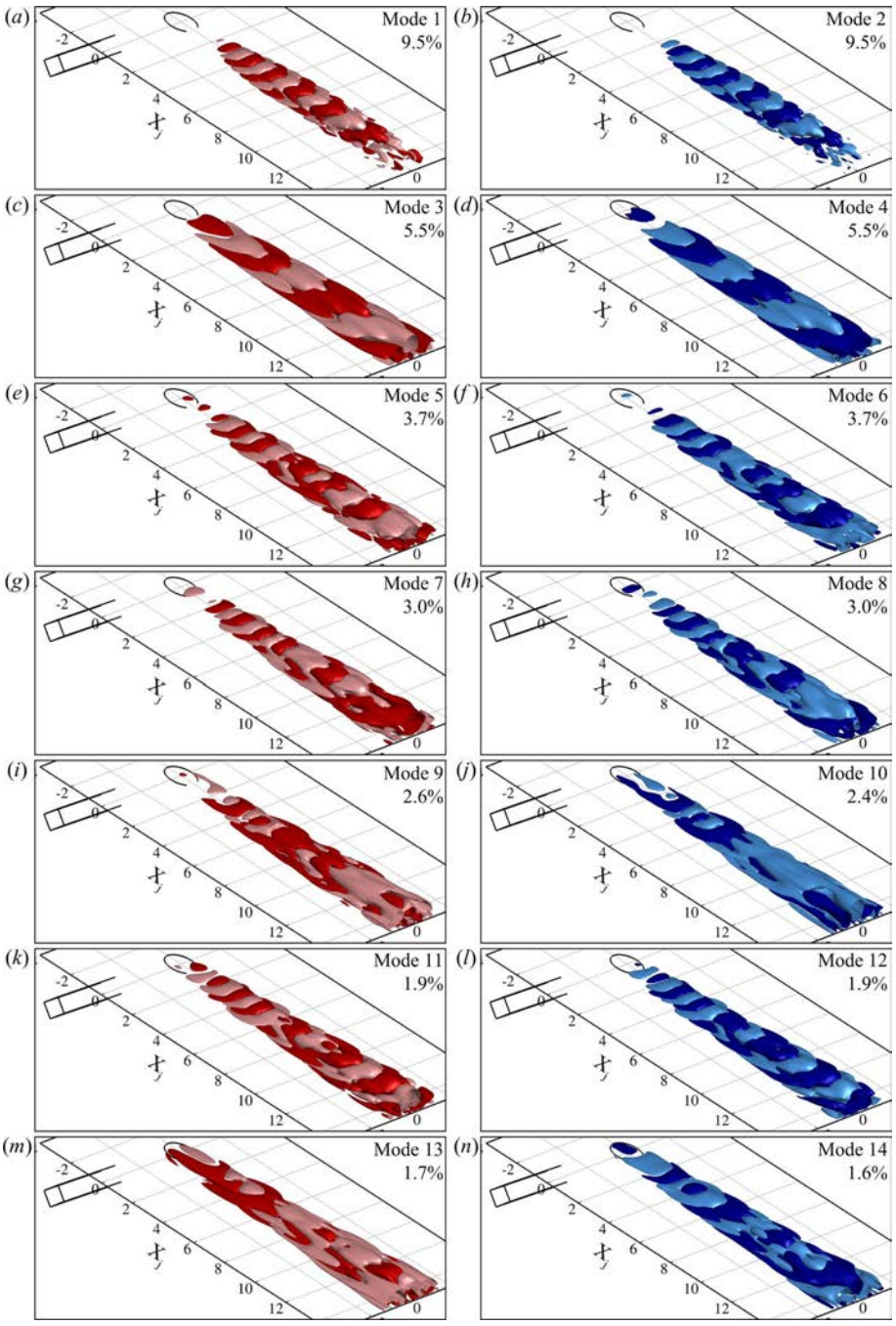

Figure 132: First 14 temperature POD modes iso-surfaces for POD decomposition at $BR = 0.15$. Pink and cyan contours are for negative values, red and blue for positive ones. Mode energy provided in percent of the total energy.

DISTRIBUTION A: Distribution approved for public release.

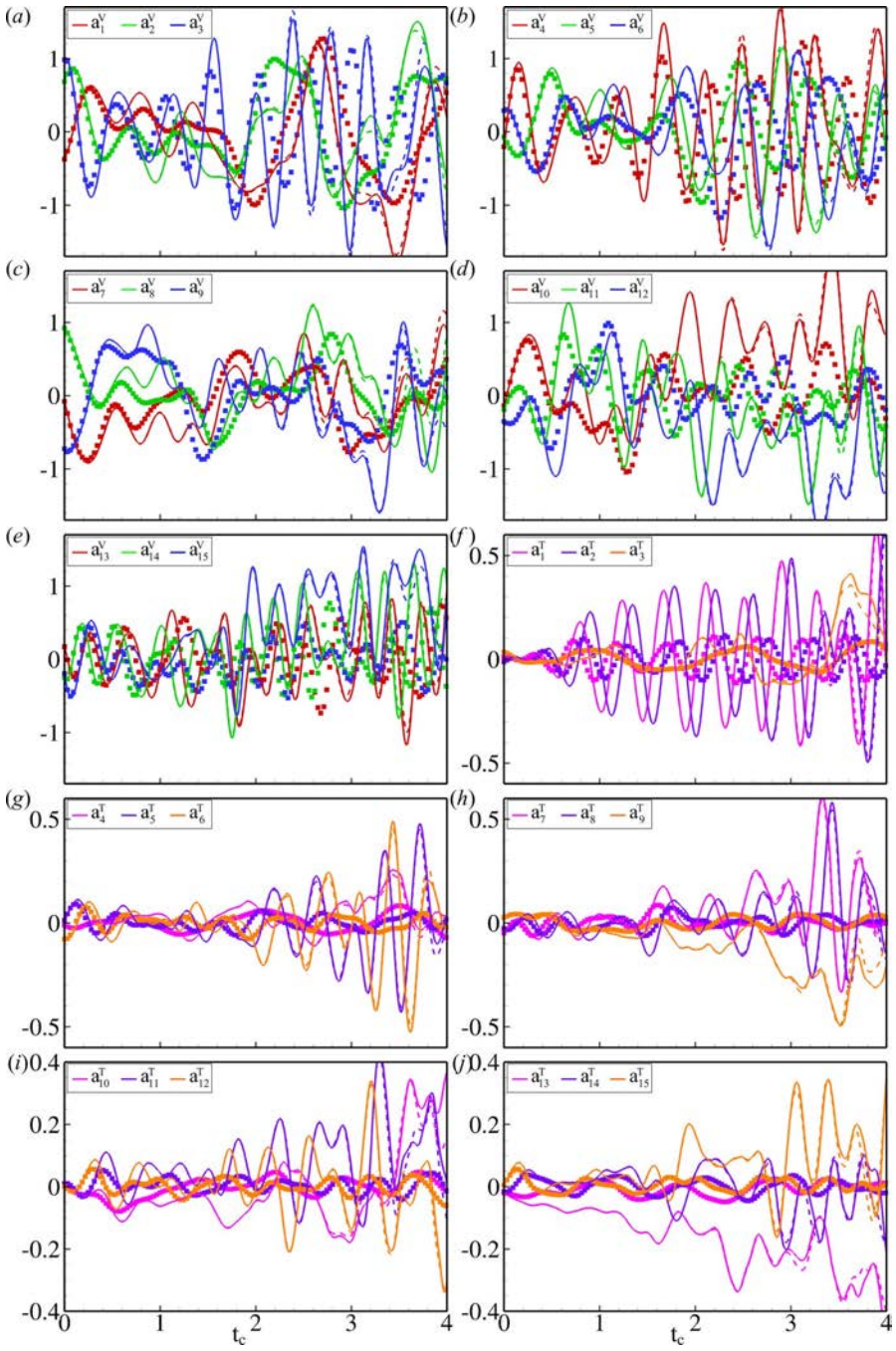

Figure 133: $BR = 0.15$ ROM temporal coefficients for the velocity and temperature fields obtained at $N_V = 250$, $N_T = 120$ without pressure correction (*solid lines*) and with pressure correction (*dashed lines*) along with corresponding POD temporal coefficients (*symbols*).

DISTRIBUTION A: Distribution approved for public release.

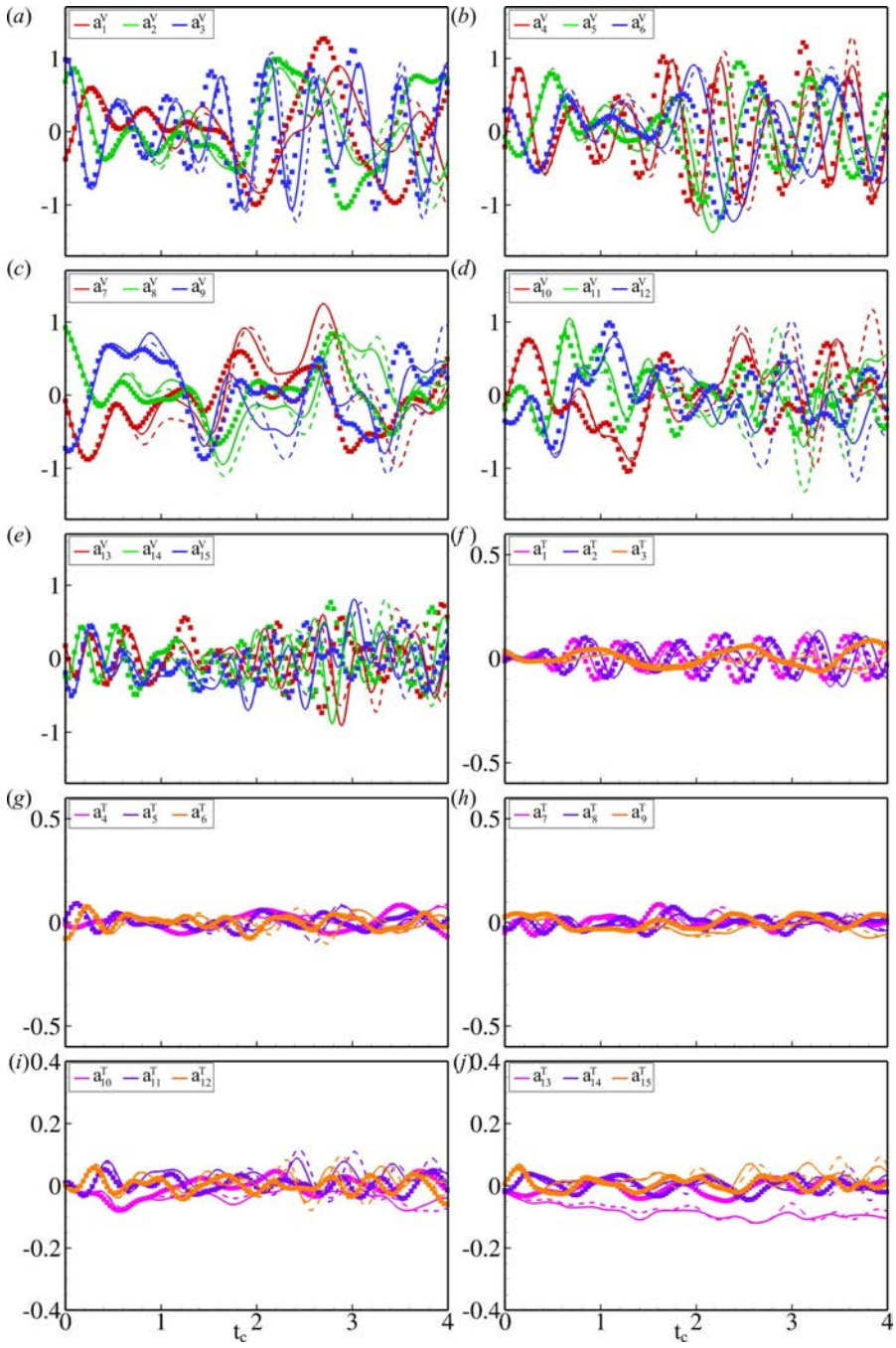

Figure 134: $BR = 0.15$ ROM temporal coefficients for the velocity and temperature fields obtained at $N_V = 275$, $N_T = 100$ with local linear stabilization (*solid lines*) and broad linear stabilization (*dashed lines*) along with corresponding POD temporal coefficients (*symbols*).

DISTRIBUTION A: Distribution approved for public release.

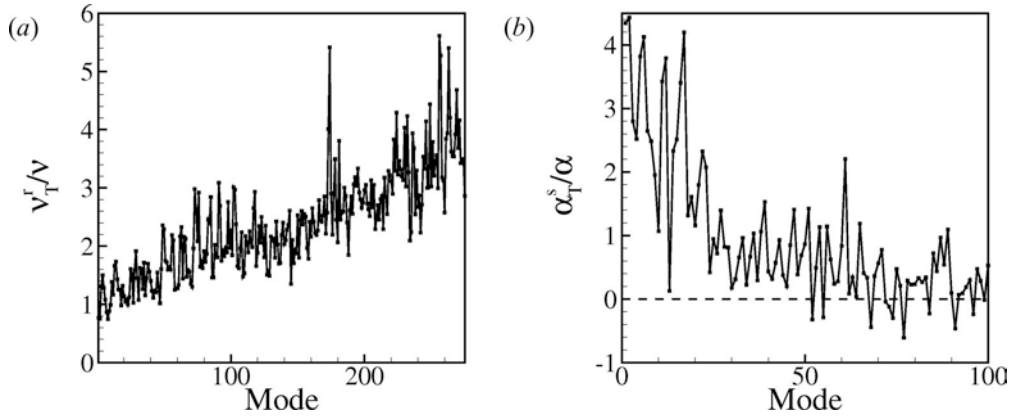

Figure 135: $BR = 0.15$ ROM (a) normalized turbulent momentum diffusivity ν_T^r/ν and (b) normalized turbulent thermal diffusivity α_T^s/α calculated for $N_V = 275$ and $N_T = 100$.

error levels are reached for both ROMs. Although they are comparable in magnitude, the error levels for the local stabilization are consistently slightly inferior to the corresponding ROMs integrated using the broad stabilization.

The best performing stabilized ROM, with $N_V = 275$, and $N_T = 100$, is presented in figure 134 for the velocity and temperature models integrated using both the local and broad damping methods. For the velocity, the agreement with the LES data is clearly improved over the non-stabilized ROM of figure 133 and reasonably good tracking is now obtained up to 3 convective time scale units. The temperature ROM accuracy is also enhanced, and in particular the amplitude divergence observed in the non-stabilized model is no longer visible. Once again, the local and broad stabilization methods provide very comparable ROMs although the former seems to outperform the latter by a small margin.

Finally, the normalized turbulent momentum (ν_T^r/ν) and thermal (α_T^s/α) diffusivities for the stabilized ROM calculated using equations 8 and 10 for $N_V = 275$ and $N_T = 100$ are presented in figure 135. The turbulent viscosity is always positive and increases consistently with the mode order. This confirms the fact that low order modes suffer from poorer modeling of the effective flow diffusivity and require more viscous damping. Indeed, while from the lower order mode point of view (larger scales), the energy cascade appears relatively accurately modeled, from the point of view of the higher order modes (smaller scales), closer to the truncation point, the energy cascade becomes less and less realistic and the absence of smaller dissipative scales or inaccuracies are more and more significant. The turbulent thermal diffusivity is for most of the modes positive but decreases in amplitude with increasing mode rank. Higher order modes even evidence negative turbulent thermal diffusivity values, effectively acting as a source term in the energy equation. This is to be expected since the truncated temperature POD series and the LES model prevent the modeling of heat generation through viscous dissipation.

3.2.2.2 Transitional Regime Simulations at $BR = 0.5$ are now used to obtain a reduced order model of the transitional jet. Simulations are obtained using the ROM grid and parameters described in Chapter 3. The POD analysis is performed using the same parameters as for the attached jet decomposition, including $1,000$ snapshots and an

DISTRIBUTION A: Distribution approved for public release.

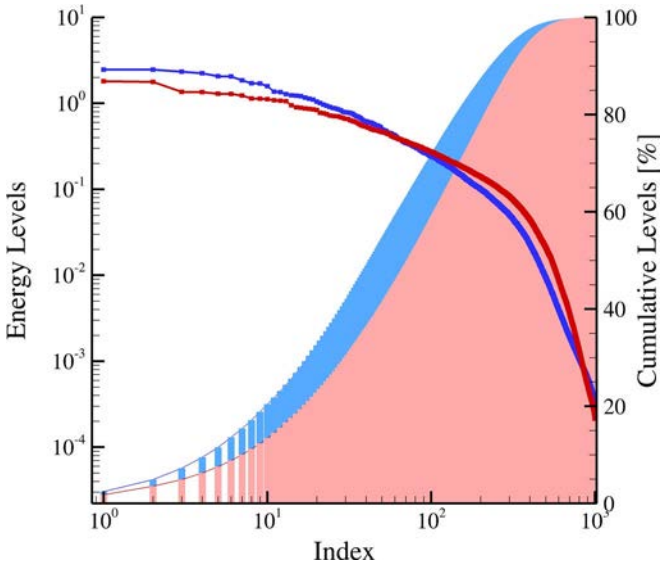

Figure 136: POD decomposition metrics for velocity (*red*) and temperature (*blue*) fields with $N = 1,000$ at $BR = 0.5$.

equivalent sampling frequency of $300Hz$ ($St_s = 4.8$) based on Sirovich snapshot method. The POD metrics are presented in figure 136 for both velocity and temperature decompositions. Compared to the previous case at $BR = 0.15$, both energy distributions are fuller which is a sign of a more turbulent flow involving a wider range of length scales. The first two POD modes have comparable energy content at approximately 1.75% each, while the first two temperature modes capture approximately 2.5% of the total pseudo-thermal energy. This is to be put in perspective with the respective 5% and 10% obtained at $BR = 0.15$. The 99% energy threshold is reached using 592 velocity modes and 521 temperature modes. This is beyond the limit which was set at 500 modes for each individual decomposition, though not by a large extent, so that effectively 97.8% of the total kinetic energy and 98.8% of the total pseudo-thermal energy can still be captured using 500 velocity and temperature modes. These numbers are assumed to be high enough to capture the significant dynamics of the flow. The velocity POD modes λ_2 iso-surfaces are presented in figure 137. As for the lower blowing ratio case, the first 12 modes are mostly associated in pairs of two modes with equivalent energy content, with features shifted in the downstream direction by a quarter of a wavelength from one mode to the other. The first pair captures large scale structures such as hairpin and wall vortices predominantly in the far-field. On the other hand, the second and third pairs represent comparable features but mostly in the mid-field. Higher order modes are grasping ever smaller structures throughout the domain, including the near-field. When comparing the POD modes obtained at $BR = 0.15$ and those obtained at $BR = 0.5$, it is interesting to notice how much "busier" the latter look and how all the modes at $BR = 0.5$ possess features across the complete flow domain. This is a result of the increased range of length and energy scales present in the higher blowing ratio case and is once more characteristic of more turbulent flows. The temperature POD modes are shown in figure 138 and present some interesting characteristics of their own. While in the $BR = 0.15$ case, the predominant modes were capturing fluctuations in the streamwise direction, the first two pairs of modes

DISTRIBUTION A: Distribution approved for public release.

at $BR = 0.5$ evidence simultaneously streamwise fluctuations in the far field and transverse ones in the near field close to the jet exit. This shows an evolution of the dominant convective mechanisms which at $BR = 0.15$ were primarily present in the far-field and associated to the hairpin vortices heads and side-vortices, but are now at $BR = 0.5$ also very strong in the near-field and associated with the counter-rotating vortex pair (through the hairpins legs). The temperature POD modes can also generally be matched in pairs of equivalent shape and energetic content, though some pairs having comparable energy levels can be mixed. For example, it appears rather clearly that modes 5 and 8 form a pair while modes 6 and 7 form another one which is "inserted" in between modes 5 and 8.

Reduced order models of the transitional unforced jet are obtained using the POD-Galerkin method. The ROM sensitivity to N_V and N_T was evaluated using estimates of the error surfaces for the velocity and temperature models for N_V and N_T values in the range $[30, 500] \times [30, 500]$. All surfaces exhibit missing areas corresponding to pairs of (N_V, N_T) values at which the ROM integration diverged within the time frame considered for the error evaluation. The primary reason for divergence resides in the velocity ROM instability, and only a few integrations with $N_V \leq 100$ were successful all the way to the $t_c = 6$ limit. The error levels on the velocity ROM, even in the short term, are considerable, conversely to the one on the temperature which are quite reasonable when compared to the non-stabilized results at $BR = 0.15$. Once again, considering the extent of the error levels, looking at medium and long term results would be rather hasty, and focus will be brought to the short term performance. The velocity ROM has a minimum error for $N_V = 350$, while the temperature ROM reaches minimum error on the modeled flow for $(N_V, N_T) = (350, 30)$ and minimum total error for $(N_V, N_T) = (30, 350)$. Figure 139 shows the integrated optimum ROMs. The model clearly diverges beyond $t_c = 2.5$ and the discrepancy appears to originate from the higher order velocity modes which amplitudes are growing significantly beyond $t_c = 1.5$. As the error propagates in the system, the lower order velocity and temperature modes are eventually diverging as well. It should be noted that since the integrated systems presented in figure 139 are not corresponding to each other, the diverging point do not clearly match. Nevertheless, both the velocity and temperature ROMs evidence rather good agreement with the projected LES data before the system starts to diverge ($t_c \leq 1$), which is an encouraging feature.

Following what was done in the attached jet model reduction, stabilizing terms are calculated and added to the velocity and temperature ROMs which are integrated using both local and broad stabilization formulations. Evaluated error surfaces for both methods showed that the ROM integrated with the local stabilization method to diverged more often than the ones integrated at the same values of (N_V, N_T) using the broad stabilization. This is especially the case for large values of N_V. In fact, none of the locally stabilized ROMs including more than 350 velocity modes can be integrated up to $t_c = 2$ (short term time frame) whereas it is possible to include all 500 velocity modes using the broad stabilization and integrate up to at least $t_c = 4$ (medium term time frame). Looking back at the $BR = 0.15$ stabilized ROMs, it appeared also impossible to obtain a converged solution for $N_V > 400$ when using the local stabilization, whereas $N_V = 500$ ROMs could be successfully integrated using the broad formulation stabilization. Overall, the minimum error levels attained for the velocity ROM are found to be on average one to two orders of magnitude lower when using broad stabilization compared to local stabilization. While the error on the modeled part of the velocity increases with increasing number of velocity modes before reaching a maximum around $N_V = 100$ and decreases again beyond that point, the total

DISTRIBUTION A: Distribution approved for public release.

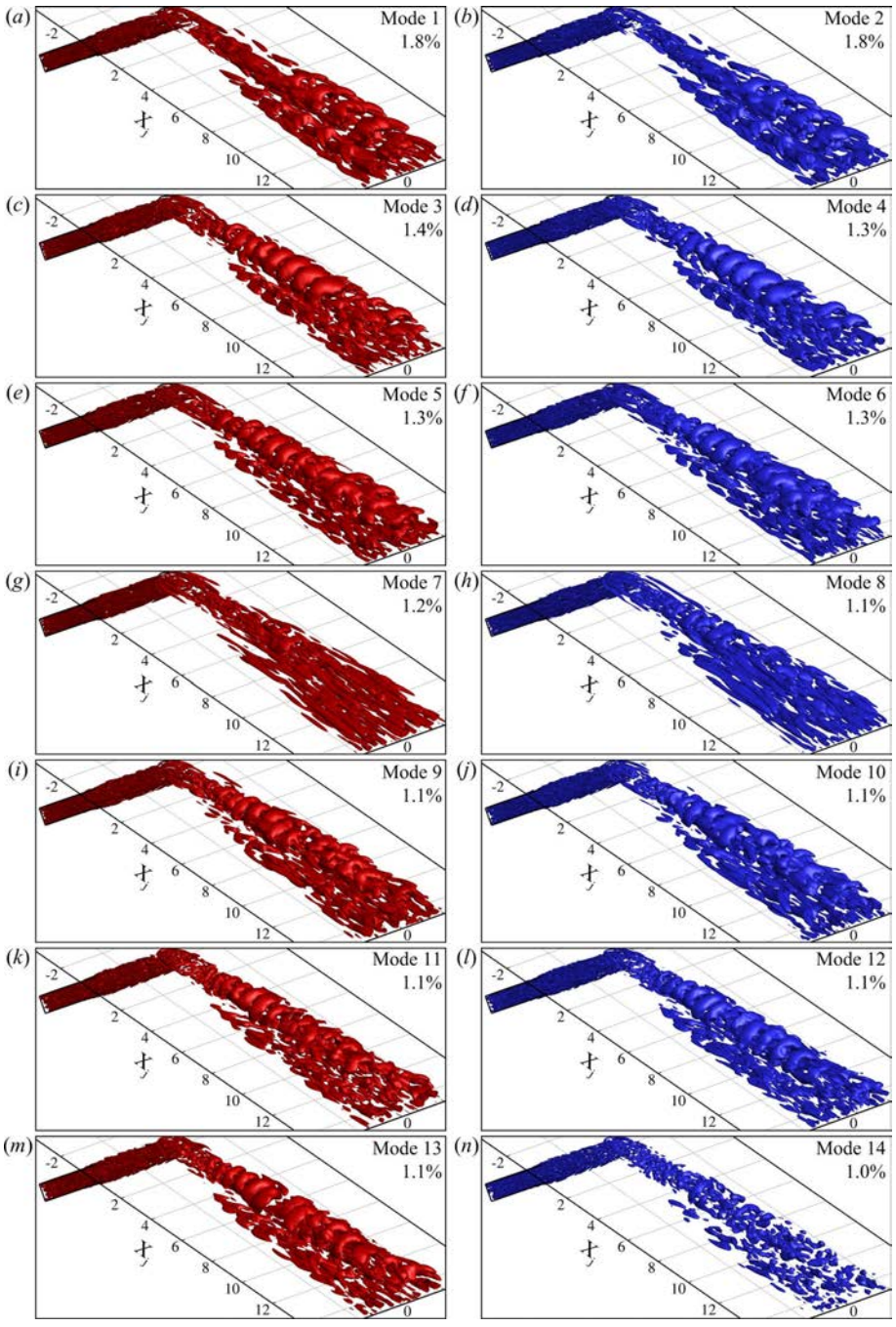

Figure 137: First 14 velocity POD modes λ_2 iso-surfaces for POD decomposition at $BR = 0.5$. Mode energy provided in percent of the total energy.

DISTRIBUTION A: Distribution approved for public release.

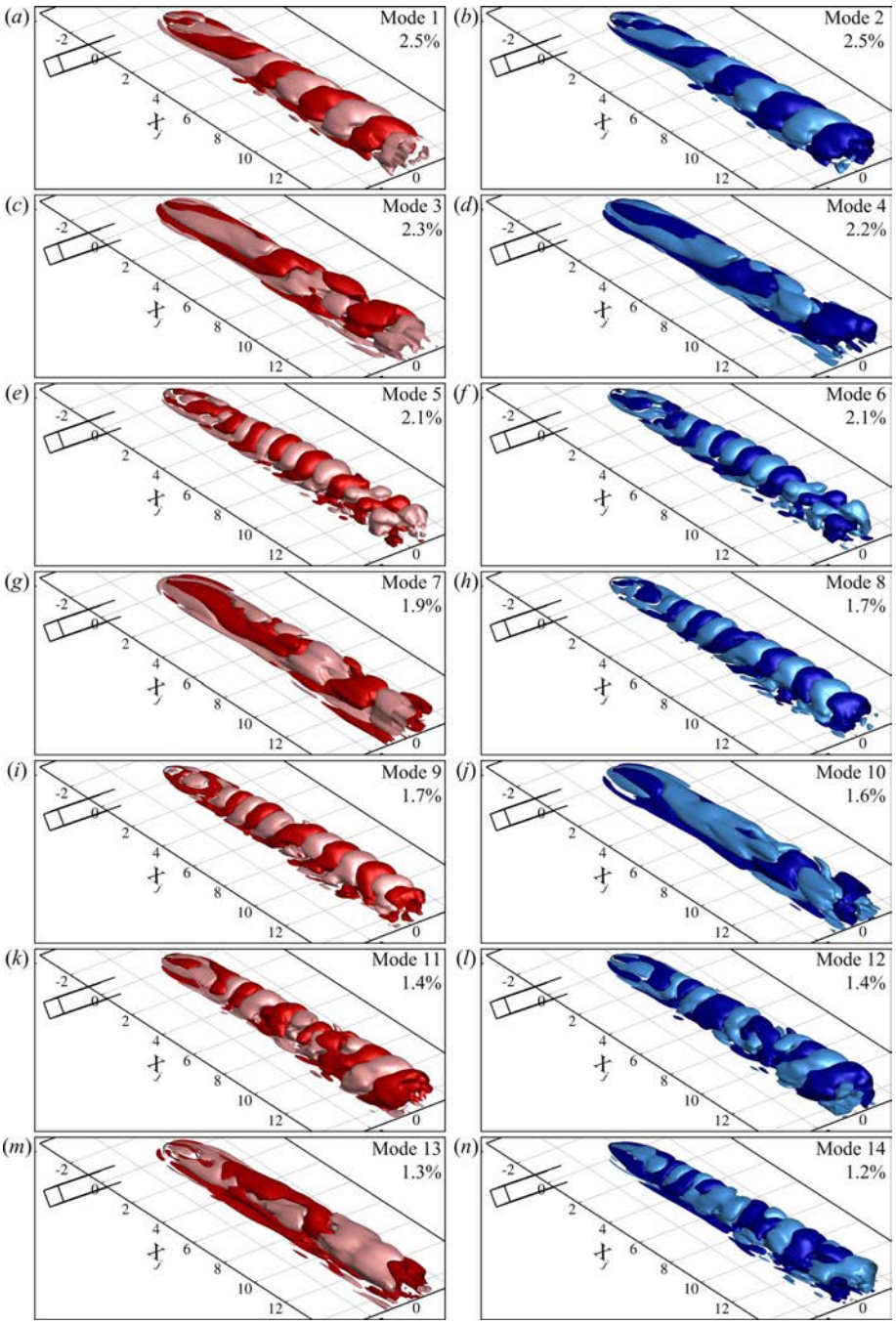

Figure 138: First 14 temperature POD modes iso-surfaces for POD decomposition at $BR = 0.5$. Pink and cyan contours are for negative values, red and blue for positive ones. Mode energy provided in percent of the total energy.

DISTRIBUTION A: Distribution approved for public release.

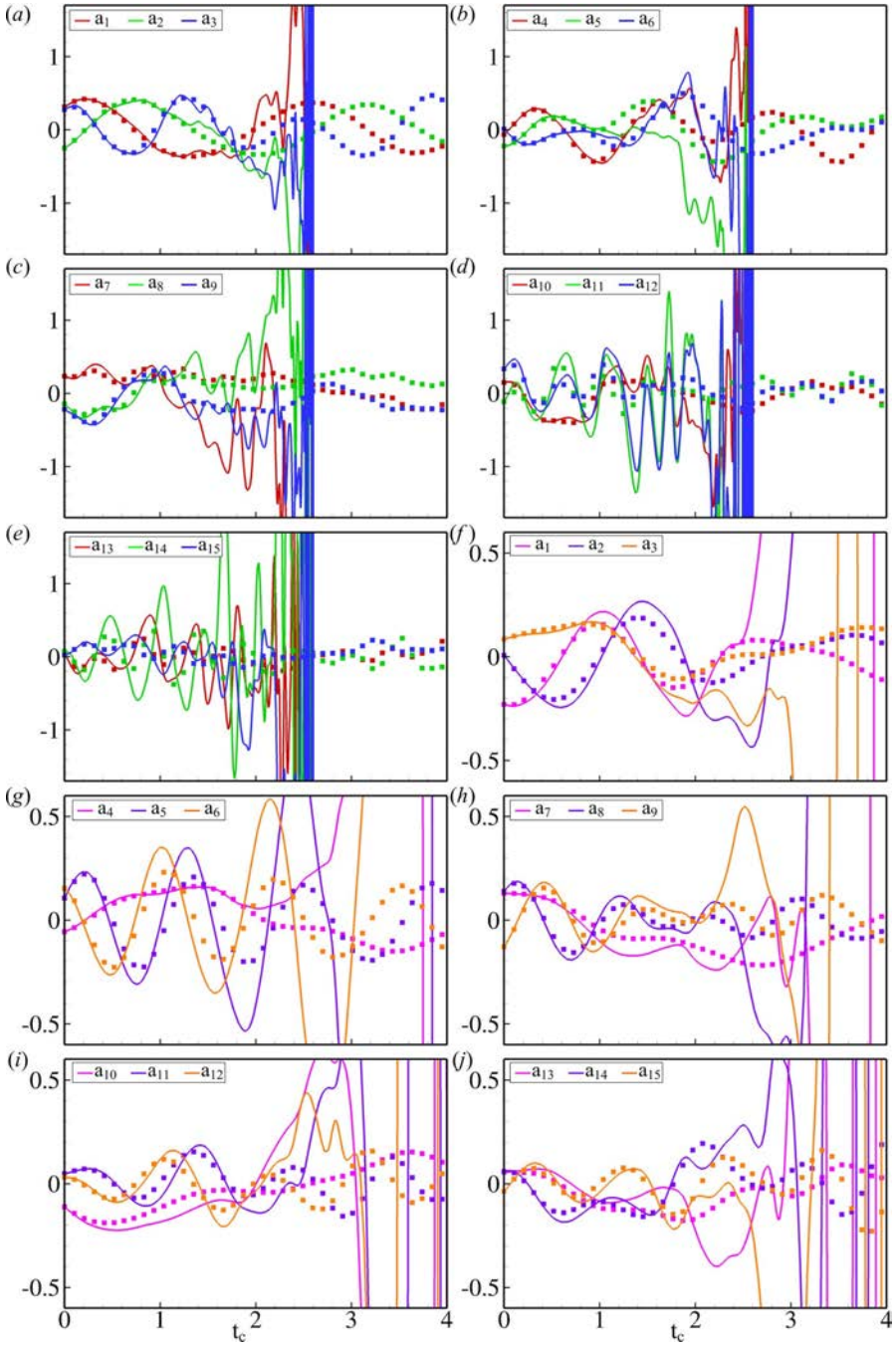

Figure 139: $BR = 0.5$ ROM temporal coefficients for the velocity at $N_V = 350$ and temperature fields obtained at $(N_V, N_T) = (30, 350)$ (*solid lines*) along with corresponding POD temporal coefficients (*symbols*).

DISTRIBUTION A: Distribution approved for public release.

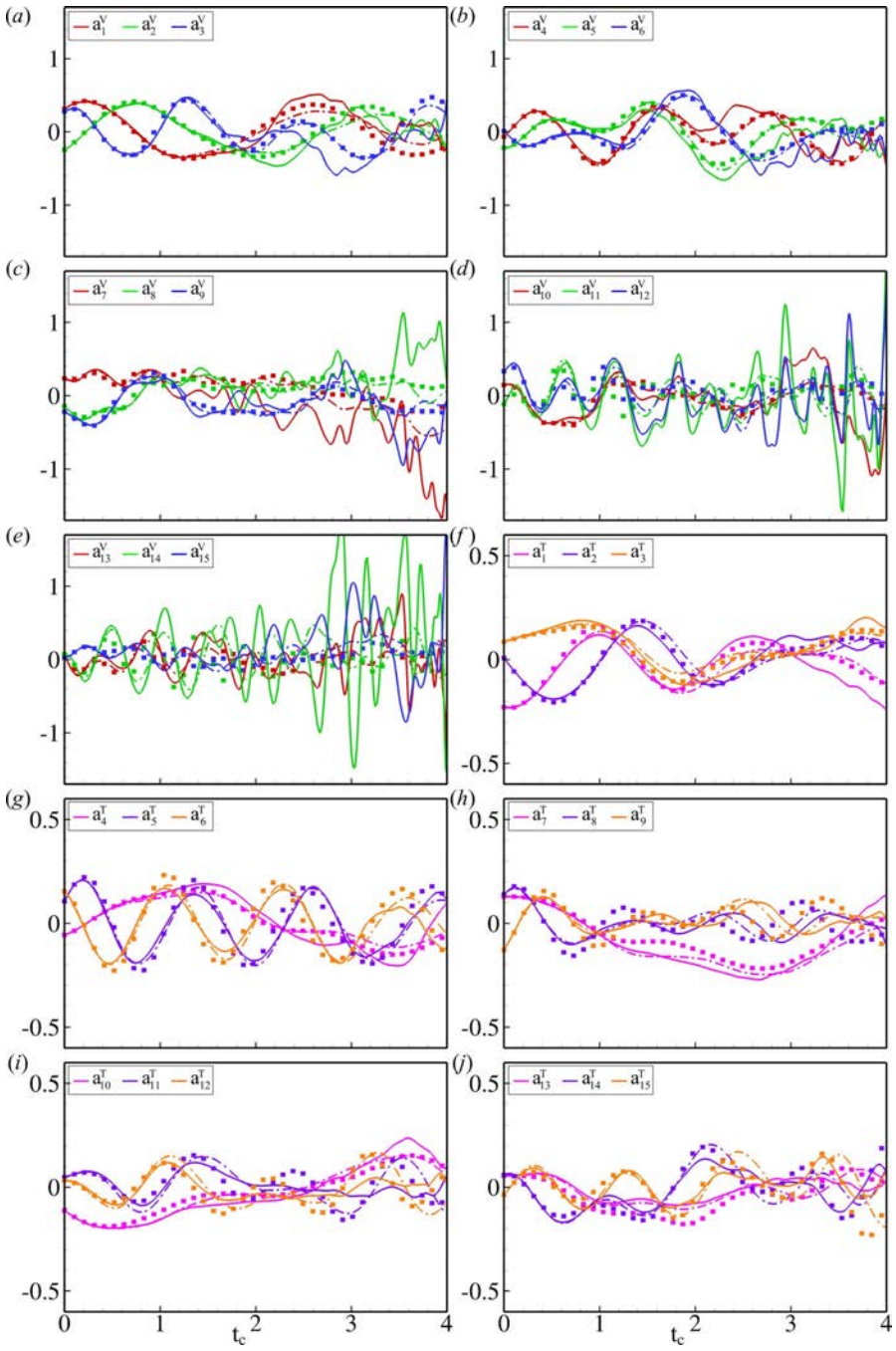

Figure 140: $BR = 0.5$ ROM temporal coefficients for the velocity and temperature fields obtained at $N_V = 350$, $N_T = 350$ with local linear stabilization (*solid lines*) and $N_V = 500$, $N_T = 300$ with broad linear stabilization (*dashed lines*) along with corresponding POD temporal coefficients (*symbols*).

DISTRIBUTION A: Distribution approved for public release.

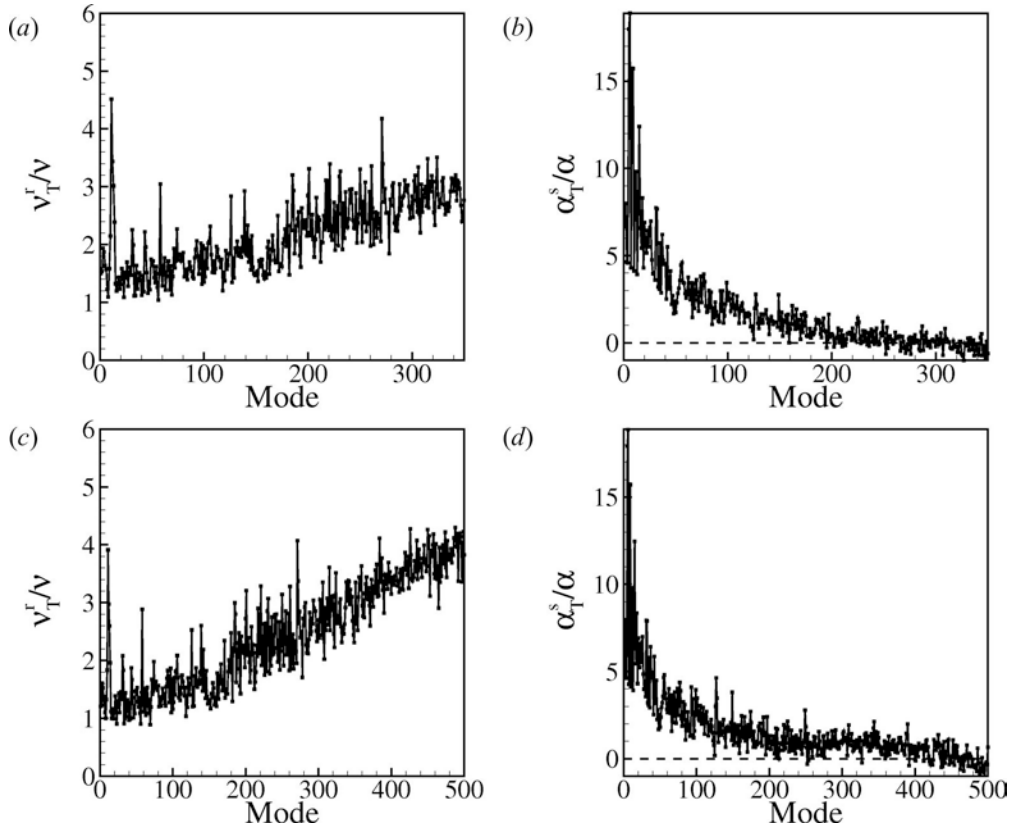

Figure 141: $BR = 0.5$ ROM $(a,\ c)$ normalized turbulent momentum diffusivity ν_T^r/ν and $(b,\ d)$ normalized turbulent thermal diffusivity α_T^s/α calculated for $(a,\ b)$ $N_V = 350$ and $N_T = 350$ and $(c,\ d)$ $N_V = 500$, $N_T = 300$.

error consistently decreases with increasing number of velocity modes. Thus, and because of the improved stability of the broadly stabilized ROMs, lower values of error can be reached for $N_V = 500$ which are unattainable by ROMs using the local stabilization method. The temperature ROM appears to be much less sensitive to the stabilization method used and the error levels using both methods are comparable in the short term, yet with a slight advantage to the broad stabilization method. This is due to the fact that the temperature ROMs for the transitional jet are almost insensitive to the value of N_V and can reach the lowest error levels with only a few velocity modes. In the medium and long term, the broad stabilization method also shows improved performance over the local one. Overall in the short term, the locally stabilized ROM reach minimum values value at $(N_V, N_T) = (350, 350)$ while the broadly stabilized ROM reach a minimum error values for $(N_V, N_T) = (500, 300)$. Similarly, the medium term error estimates show a minimum at $(N_V, N_T) = (350, 140)$ for the former and $(N_V, N_T) = (500, 200)$ for the latter.

Figure 140 presents the integrated ROMs using both local stabilization at $(N_V, N_T) = (350, 350)$ and broad stabilization for $(N_V, N_T) = (500, 300)$. The results show a clear improvement over the non-stabilized ROM in figure 139. No divergence of the extent of the one observed in the non-stabilized equations is found in the stabilized velocity ROMs though the amplitudes of the higher order modes of the locally stabilized equations start to increase

DISTRIBUTION A: Distribution approved for public release.

significantly beyond $t_c = 3$. This is clearly not the case for the broadly stabilized model which seems to follow the projected LES data all the way up to $t_c = 4$ (medium term). Less obvious differences are visible in the temperature ROMs which seem qualitatively very well behaved and follow the projected data nicely. A growing discrepancy is observed for the locally stabilized ROM towards the end of the considered time span $t_c \sim 4$, and is most likely a result of the growing amplitude of the corresponding high order velocity modes. Overall the broad stabilization method provides more stable and more accurate models of the transitional jet, in particular when including large numbers of POD modes compared to the locally stabilized method. The turbulent viscosity and thermal diffusivity for the optimum locally and broadly stabilized ROM are shown in figure 141. The trends for the turbulent viscosity ν_T are consistent with the one obtained for the attached jet, with increasing positive turbulent diffusivity for increasing mode order. The thermal diffusivity trends also follow the ones of the $BR = 0.15$ case, with positive values for lower order modes decreasing with mode rank. The higher order temperature modes evidence negative thermal diffusivity, accounting for heat generation due to viscous dissipation through the smaller scales.

3.2.3 Forced Jets

3.2.3.1 Instantaneous Flow Instantaneous velocity and temperature fields were the first one to be investigated in view to obtain a reduced order model of the forced flow.

Although reasonably good reduced order models were obtained for the unforced jet, it is unlikely those models will be able to capture and reproduce the dynamics of forced jets in cross-flow, and in particular the starting structures, which are generated in actuated conditions. To capture those dynamics, forced jet simulations were used to generate reduced order models by means of the POD-Galerkin method. The models for velocity and temperature fields were modified according to the decomposition proposed by (29). The velocity model was then:

$$\begin{aligned} \dot{a_r}(t) &= \sum_{i=1}^{N_V} \left(\tilde{C}^r_{i,0} + \frac{1}{Re_j} \tilde{D}^r_i \right) a_i(t) + \sum_{i=1}^{N_V} \sum_{j=1}^{i} \tilde{C}^r_{i,j} a_i(t) a_j(t) + \left(\tilde{C}^r_0 + \frac{1}{Re_j} \tilde{D}^r_0 \right) + P_r(t) \\ &+ \gamma(t) \left[\tilde{H}^r_0 + \frac{1}{Re_j} \tilde{L}^r_0 + \sum_{i=1}^{N_V} \tilde{H}^r_{i,0} a_i(t) \right] + \gamma^2(t) \tilde{K}^r_0 + \frac{d\gamma(t)}{dt} \tilde{G}^r_0 \end{aligned} \tag{11}$$

where

DISTRIBUTION A: Distribution approved for public release.

$$\vec{u} = \vec{\overline{u}} + \gamma(t)\vec{u}_{ref} + \vec{u'} = \vec{\overline{u}} + \gamma(t)\vec{u}_{ref} + \sum_{n=1}^{N_V} a_n(t)\vec{\varphi}_n(x)$$

$$\tilde{C}_0^r = -\left(\left(\vec{\overline{u}}.\nabla\right)\vec{\overline{u}}, \vec{\varphi}_r\right) = -\int_{\Omega_x} \overline{u}_l \frac{\partial}{\partial x_l}\left(\overline{u}_m\right)\varphi_{r,l}dx$$

$$\tilde{D}_0^r = \left(\triangle\vec{\overline{u}}, \vec{\varphi}_r\right) = \int_{\Omega_x} \frac{\partial}{\partial x_m \partial x_m}\left(\overline{u}_l\right)\varphi_{r.l}dx$$

$$\tilde{C}_{i,0}^r = -\left(\left(\vec{\overline{u}}.\nabla\right)\vec{\varphi}_i, \vec{\varphi_r}\right) - \left(\left(\vec{\varphi}_i.\nabla\right)\vec{\overline{u}}, \vec{\varphi}_r\right) = -\int_{\Omega_x}\left(\overline{u}_m \frac{\partial}{\partial x_m}\varphi_{i,l} + \varphi_{i,m}\frac{\partial}{\partial x_m}\overline{u}_l\right)\varphi_{r,l}dx$$

$$\tilde{D}_i^r = \left(\triangle\vec{\varphi}_i, \vec{\varphi}_r\right) = \int_{\Omega_x} \frac{\partial}{\partial x_m \partial x_m}\left(\varphi_{i,l}\right)\varphi_{r,l}dx$$

$$\tilde{C}_{i,j}^r = -\left(\left(\vec{\varphi}_i.\nabla\right)\vec{\varphi}_j, \vec{\varphi}_r\right) = -\int_{\Omega_x}\left(\varphi_{i,m}\frac{\partial}{\partial x_m}\varphi_{j,l} + \varphi_{j,m}\frac{\partial}{\partial x_m}\varphi_{i,l}\right)\varphi_{r,l}dx$$

$$P_r(t) = -\left(\nabla P(t), \vec{\varphi}_r\right)$$

$$\tilde{H}_0^r = -\left(\left(\vec{\overline{u}}.\nabla\right)\vec{u}_{ref}, \vec{\varphi}_r\right) - \left(\left(\vec{u}_{ref}.\nabla\right)\vec{\overline{u}}, \vec{\varphi}_r\right) = -\int_{\Omega_x}\left(\overline{u}_m \frac{\partial}{\partial x_m}u_{ref,l} + u_{ref,m}\frac{\partial}{\partial x_m}\overline{u}_l\right)\varphi_{r,l}dx$$

$$\tilde{L}_0^r = \left(\triangle\vec{u}_{ref}, \vec{\varphi}_r\right) = \int_{\Omega_x} \frac{\partial}{\partial x_m \partial x_m}\left(u_{ref,l}\right)\varphi_{r,l}dx$$

$$\tilde{H}_{i0}^r = -\left(\left(\vec{u}_{ref}.\nabla\right)\vec{\varphi}_i, \vec{\varphi}_r\right) - \left(\left(\vec{\varphi}_i.\nabla\right)\vec{u}_{ref}, \vec{\varphi}_r\right) = -\int_{\Omega_x}\left(u_{ref,m}\frac{\partial}{\partial x_m}\varphi_{i,l} + \varphi_{i,m}\frac{\partial}{\partial x_m}u_{ref,l}\right)\varphi_{r,l}dx$$

$$\tilde{K}_0^r = -\left(\left(\vec{u}_{ref}.\nabla\right)\vec{u}_{ref}, \vec{\varphi}_r\right) = -\int_{\Omega_x} u_{ref,l}\frac{\partial}{\partial x_l}\left(u_{ref,m}\right)\varphi_{r,l}dx$$

$$\tilde{G}_0^r = -\left(\vec{u}_{ref}, \vec{\varphi}_r\right) = -\int_{\Omega_x} u_{ref,l}\varphi_{r,l}dx$$

where $\gamma(t)$ is the control function, $\vec{u}_{ref}$ a reference velocity field, $\vec{\overline{u}}$ the average field and $\vec{u'}$ the fluctuation. In this study, $\gamma(t)$ is a square wave of amplitude 1. The reference velocity field is a time independent field chosen to represent the global impact of the control function on the flow. Effectively this term is used to homogenize the velocity at the control surface (jet inlet). For this particular study, the reference field $\vec{u}_{ref}$ is defined as:

$$\vec{u}_{ref} = \vec{\overline{u}}(BR = BR_h) - \vec{\overline{u}}(BR = BR_l) \tag{12}$$

The temperature model:

DISTRIBUTION A: Distribution approved for public release.

$$\dot{b}_s(t) = \sum_{i=1}^{N_V} \tilde{E}^i_{s,0} a_i(t) + \sum_{j=1}^{N_T} \left(\tilde{E}^0_{s,j} + \frac{1}{Pr}\frac{1}{Re_j}\tilde{F}_{s,j} \right) b_j(t) + \sum_{i=1}^{N_V}\sum_{j=1}^{N_T} \tilde{E}^i_{s,j} a_i(t) b_j(t) + \left(\tilde{E}^0_{s,0} + \frac{1}{Pr}\frac{1}{Re_j}\tilde{F}_{s,0} \right) + \gamma(t) \left[\tilde{N}^0_{s,0} + \sum_{j=1}^{N_T} b_j \tilde{N}^0_{s,j} \right] \quad (13)$$

where

$$T = \overline{T} + T' = \overline{T} + \sum_{m=1}^{N_T} b_m(t)\psi_m(x)$$

$$\tilde{E}^0_{s,0} = -\left(\left(\vec{\overline{u}}.\nabla\right)\overline{T}, \psi_s \right) = -\int_{\Omega_x} \overline{u}_m \frac{\partial}{\partial x_m}\left(\overline{T}\right)\psi_s dx$$

$$\tilde{F}_{s,0} = \left(\triangle\overline{T}, \psi_s \right) = \int_{\Omega_x} \frac{\partial}{\partial x_m \partial x_m}\left(\overline{T}\right)\psi_s dx$$

$$\tilde{E}^i_{s,0} = -\left(\left(\vec{\varphi}_i.\nabla\right)\overline{T}, \psi_s \right) = -\int_{\Omega_x} \varphi_{i,m} \frac{\partial}{\partial x_m}\left(\overline{T}\right)\psi_s dx$$

$$\tilde{E}^0_{s,j} = -\left(\left(\vec{\overline{u}}.\nabla\right)\psi_j, \psi_s \right) = -\int_{\Omega_x} \overline{u}_m \frac{\partial}{\partial x_m}\left(\psi_j\right)\psi_s dx$$

$$\tilde{F}_{s,j} = \left(\triangle\psi_j, \psi_s \right) = \int_{\Omega_x} \frac{\partial}{\partial x_m \partial x_m}\left(\psi_j\right).\psi_s dx$$

$$\tilde{E}^j_{s,i} = -\left(\left(\vec{\varphi}_i.\nabla\right)\psi_j, \psi_s \right) = -\int_{\Omega_x} \varphi_{i,m} \frac{\partial}{\partial x_m}\left(\psi_j\right)\psi_s dx$$

$$\tilde{N}^0_{s,0} = -\left(\left(\vec{u}_{ref}.\nabla\right)\overline{T}, \psi_s \right) = -\int_{\Omega_x} u_{ref,m} \frac{\partial}{\partial x_m}\left(\overline{T}\right)\psi_s dx$$

$$\tilde{N}^0_{s,j} = -\left(\left(\vec{u}_{ref}.\nabla\right)\psi_j, \psi_s \right) = -\int_{\Omega_x} u_{ref,m} \frac{\partial}{\partial x_m}\left(\psi_j\right)\psi_s dx$$

This decomposition carried out onto the temperature field evidenced the fact that the velocity control function $\gamma(t)$ appeared explicitely in the temperature model and therefore suggest that the temperature field could be (indirectly) controlled through the velocity field.

3.2.3.1.1 Reduced Order Models Based on the preliminary POD results, it was decided that forced cases at rather high forcing frequencies would constitute a good starting point to obtain a first reduced order model. In addition, it is believed that these flows could benefit more from controlled based tuning than lower forcing frequency ones, where the quasi-unforced parts of the cycle play too significant of a role and the error arising from the mode segregation evidenced previously could affect the stability and accuracy of the ROMs.

Forced jet simulations are carried out using the ROM grid described in Chapter 3 at forcing conditions corresponding to *Case IV* at $St_\infty = 0.159$. The jet inlet velocity is

DISTRIBUTION A: Distribution approved for public release.

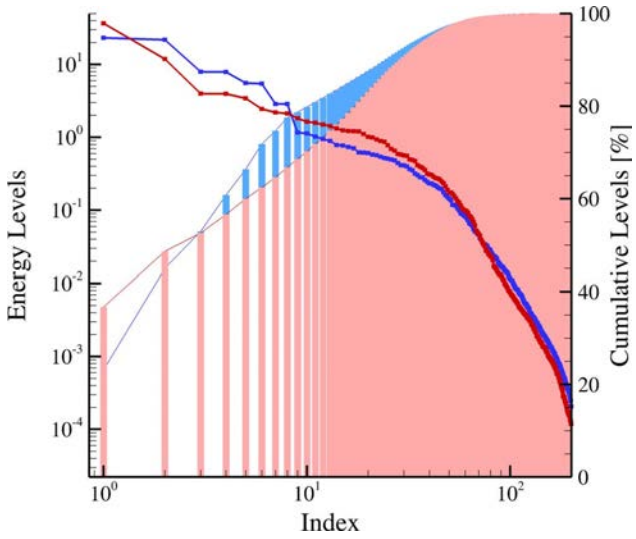

Figure 142: POD decomposition metrics for velocity (*red*) and temperature (*blue*) fields with $N = 200$ for *Case IV* at $St_\infty = 0.159$.

modulated using a square wave signal between $BR_h = 0.50$ and $BR_l = 0.150$. Snapshots are collected at 50 equally spaced phase-locked positions (equivalent sampling frequency $500Hz$ or $St_s = 7.9$) over four cycles for a total of 200 snapshots. In the following section, the transition from BR_l to BR_h occurs at $t_c = 0$.

The POD metrics are presented in figure 142 for both velocity and temperature decompositions. While the temperature metrics evidence the stair-like distribution of the energy levels mentioned in the POD preliminary study with the first two modes at 22% of the total pseudo-thermal energy each, the velocity distribution shows a clearly dominant first mode with 36% of the total kinetic energy while the second mode only carries 11%. This is due to the modified velocity decomposition including the control signal $\gamma(t)\vec{u}_{ref}$, which prevents from direct comparisons with the preliminary study. Overall, 65 velocity POD modes are required to reconstruct 99% of the total kinetic energy from $\vec{u}'$, and 70 temperature modes to reconstruct 99% of the total pseudo-thermal energy of T'.

The velocity POD modes λ_2 iso-surfaces are presented in figure 143, also including for reference the λ_2 iso-surfaces for the fields $\overline{\vec{u}}$ and $\vec{u}_{ref}$. The first two velocity POD modes capture predominantly large scale features at the jet exit likely corresponding to the starting structures, whereas higher order modes such as modes 3, 4, 5 and 6 also capture hairpin vortices in the mid and far-fields with increasing frequency. Interestingly, modes 7 to 12 appear to capture wall structures, predominantly in the far-field. The POD temporal coefficients in figure 145 show dynamics much different from the one of the preliminary POD at equivalent forcing conditions, which was again expected due to the different decomposition used in this section. The temperature POD modes in figure 144 are however much more similar to the ones observed in figure 125 in the preliminary study. The first modes exhibit large scale temperature fluctuation areas, associated with the convection of the starting vortex, while higher order modes correspond to higher harmonics of the first two modes, although the last temperature modes appear to capture anti-symmetric dynamics in the far-field region.

DISTRIBUTION A: Distribution approved for public release.

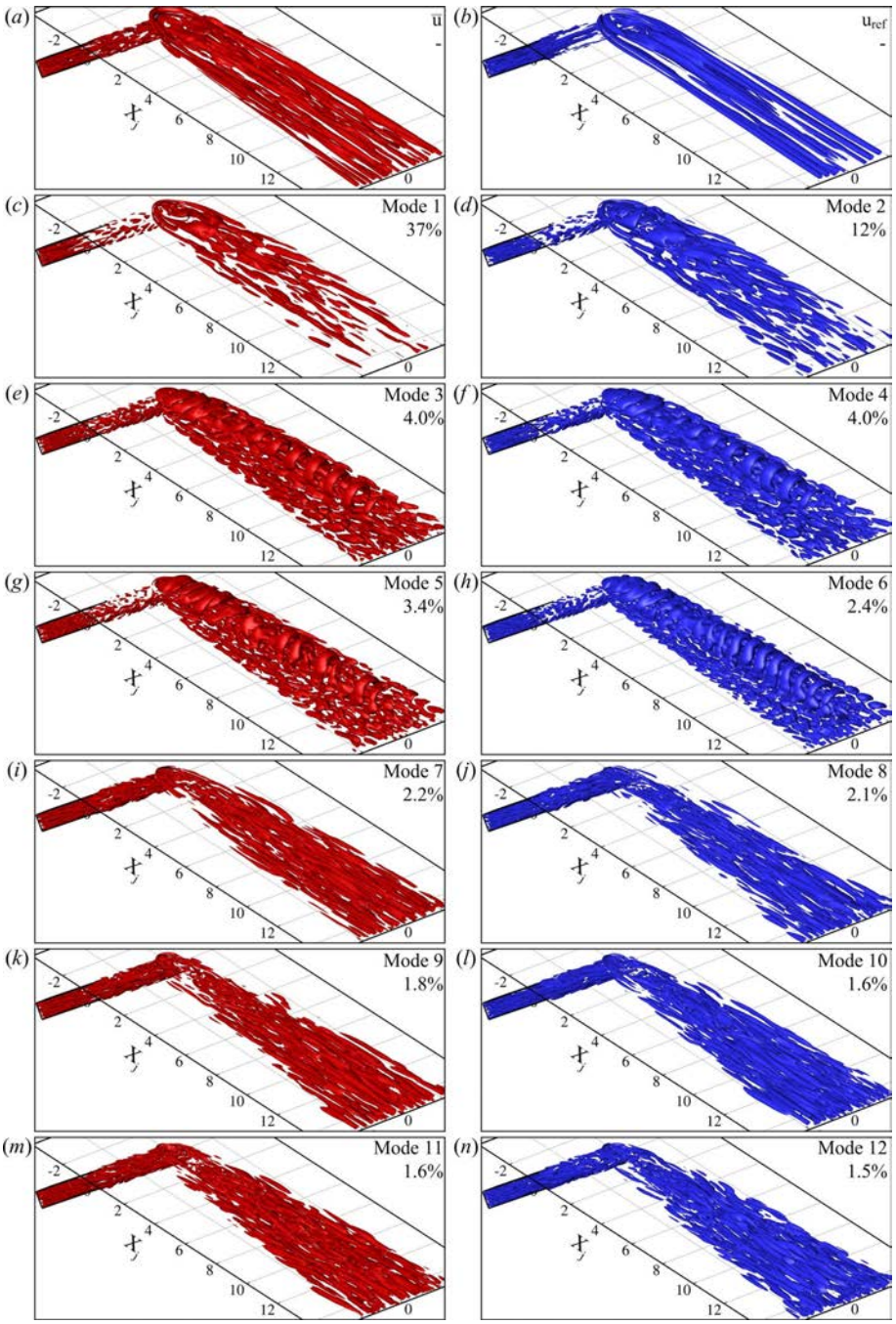

Figure 143: First 12 velocity POD modes along with $\vec{u}_m$ and $\vec{u}_{ref}$ λ_2 iso-surfaces for POD decomposition for *Case IV* at $St_\infty = 0.159$. Mode energy provided in percent of the total energy.

DISTRIBUTION A: Distribution approved for public release.

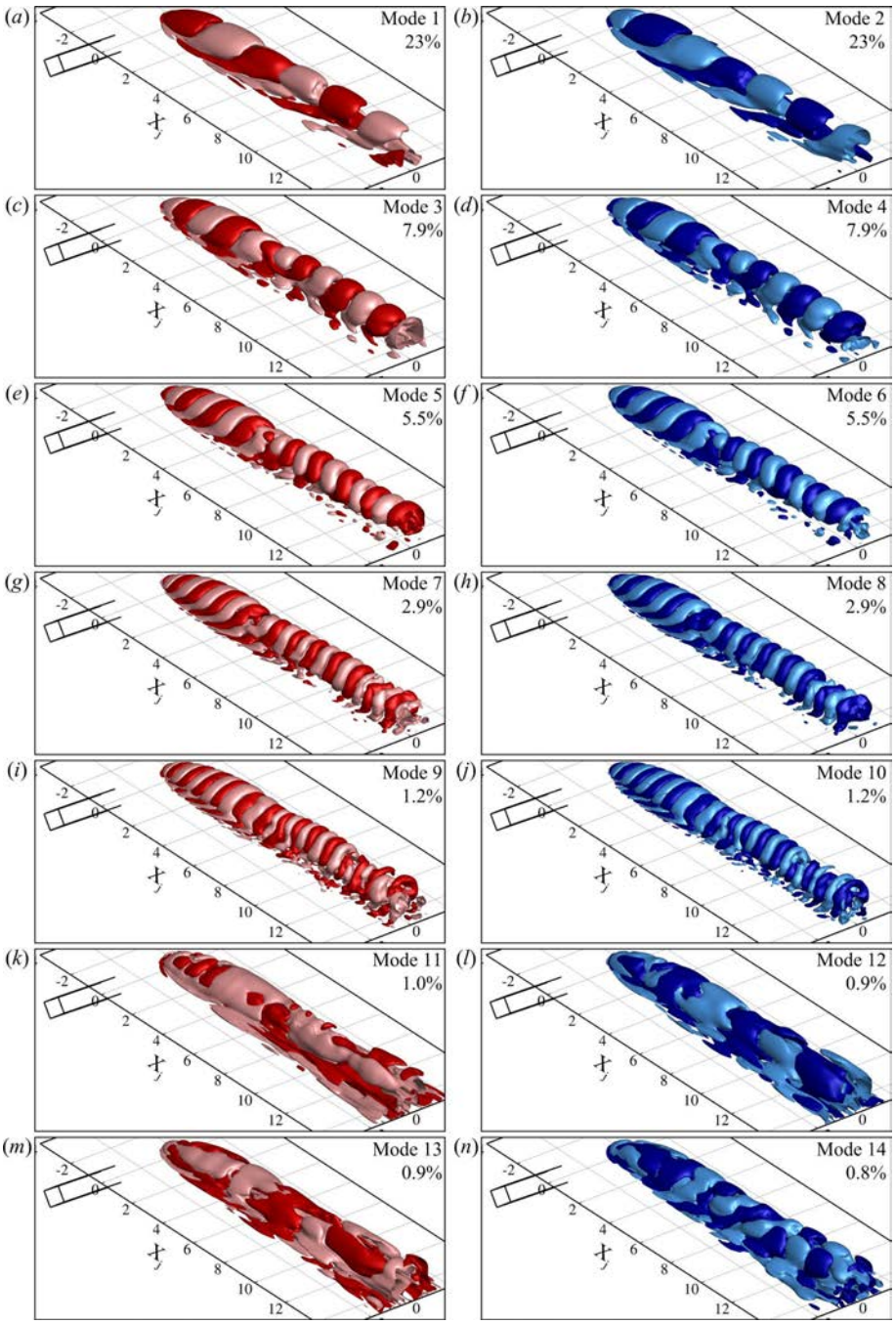

Figure 144: First 14 temperature POD modes iso-surfaces for POD decomposition for *Case IV* at $St_\infty = 0.159$. Pink and cyan contours are for negative values, red and blue for positive ones. Mode energy provided in percent of the total energy.

DISTRIBUTION A: Distribution approved for public release.

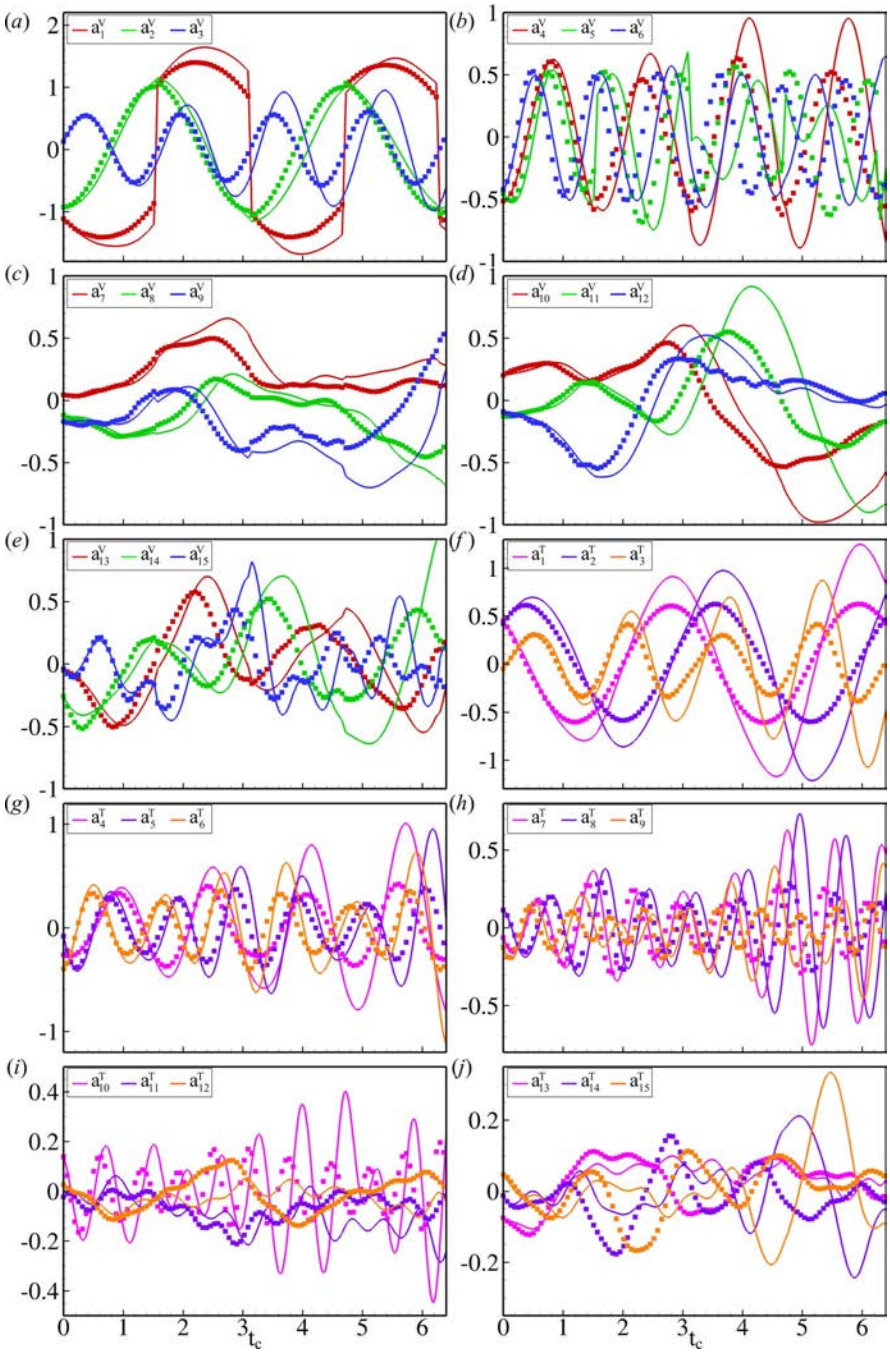

Figure 145: *Case IV* at $St_\infty = 0.159$ ROM temporal coefficients for the velocity ($N_V = 25$) and temperature ($(N_V, N_T) = (15, 45)$) fields (*solid lines*) along with corresponding POD temporal coefficients (*symbols*).

DISTRIBUTION A: Distribution approved for public release.

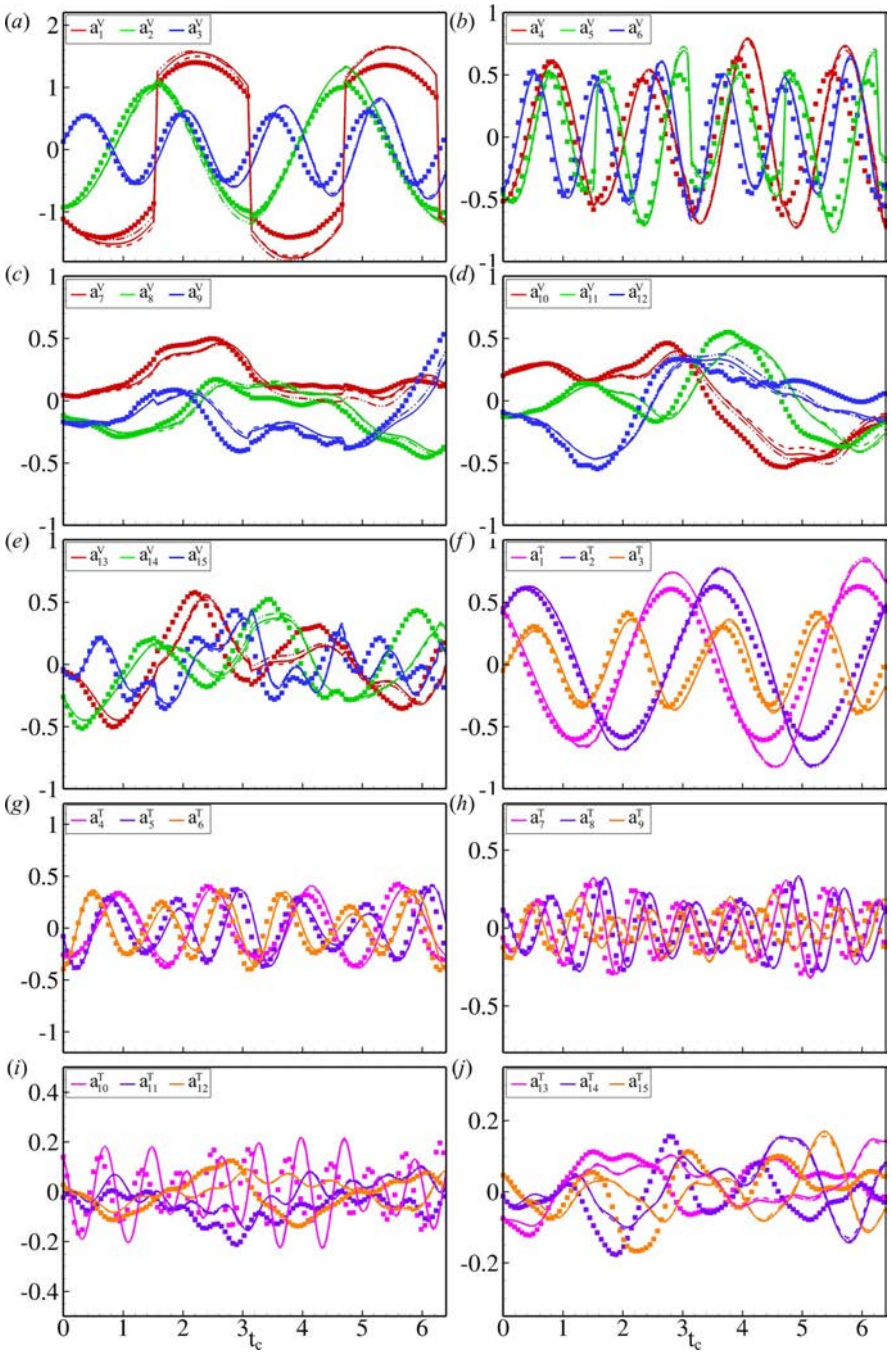

Figure 146: *Case IV* at $St_\infty = 0.159$ ROM temporal coefficients for the velocity ($N_V = 35$) and temperature ($(N_V, N_T) = (10, 30)$) fields using partial local (*solid*) partial broad (*dashed*) and asymptotic (*dash dot dot*) linear damping along with corresponding POD temporal coefficients (*symbols*).

DISTRIBUTION A: Distribution approved for public release.

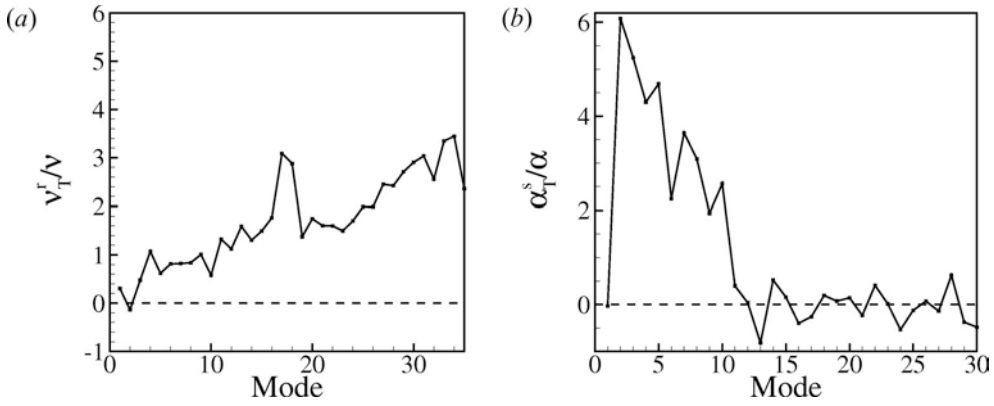

Figure 147: *Case IV* ROM (a) normalized turbulent momentum diffusivity ν_T^r/ν and (b) normalized turbulent thermal diffusivity α_T^s/α calculated for $N_V = 35$ and $N_T = 30$.

Reduced order models using the POD-Galerkin method are derived according to the method described in the previous section. Once again, the pressure term in equation 11 is neglected since ROMs integrated using empirical pressure correction term did not provide any noticeable improvement. In this case, it is possible to compute coefficients for all the velocity and temperature modes so that the complete set of ODEs representing 100% of the flow energy could be integrated. Error estimates are computed for (N_V, N_T) in $[10, 200] \times [10, 200]$ over one, two and three cycle periods and show that the error with respect to both the modeled flow and the total flow increases consistently with increasing number of velocity POD modes. However, the error levels for the best performing velocity and temperature ROMs are rather low, respectively around 8% and 16% over the first cycle period, especially when compared to non-stabilized unforced jets in the previous sections. It also seems that none of the ROMs including more than 125 velocity POD modes could be integrated over a full cycle, while ROMs including more than 90 velocity modes diverged before the end of the second cycle and those with more than 70 modes diverged before the end of the third one. Based on the total error $\overline{E_V^2}$, an optimum number of velocity modes of $N_V = 25$ for the velocity ROM is identified and based on $\overline{E_2^T}$ an optimum pair $(N_V, N_T) = (10, 45)$ for the temperature ROM corresponding to minimum total error is found. Both solutions are presented in figure 145. Overall, the agreement between both ROMs and the projected LES data is reasonably good. The most striking discrepancy resides in the first velocity equation, where the model diverges from the projected data systematically at the end of each part of the cycle, but is most of the time brought back into agreement at the next transition. The velocity model is performing reasonably well over two forcing cycles, although the agreement with the projected LES data clearly starts to be affected towards the end of the second cycle with significant discrepancy in amplitude and phase, even more so for the higher order modes. Similarly, rather good agreement between the temperature ROM and the projected data can be observed over at least the first cycle but phase and amplitude start diverging towards the end of the second cycle, in particular for higher order temperature modes.

Following the method used in the unforced jet configuration, the velocity and temperature reduced order models are integrated using partial local, broad and asymptotic stabilization methods. Corresponding error surfaces were computed and showed that all three methods had virtually identical minimum error level values, and stabilized ROMs integrations with

DISTRIBUTION A: Distribution approved for public release.

200 velocity modes over a full period (compared to a maximum of $N_V = 125$ for the non-stabilized ROMs). While the local and broad methods only permits to integrate ROMs with $N_V \leq 150$ over more than two periods (compared to $N_V \leq 75$ for the non-stabilized ROMs), the asymptotic method permits to integrate ROMs with $N_V \leq 190$ over two periods, and $N_V \leq 180$ over three periods, therefore showing the latter stabilizes systems with large number of velocity modes better. Minimum error levels for all methods are consistently lower than the non-stabilized ROMs by approximately a factor 4 for the velocity ROMs and by a factor 3 in the short term and a factor 60 in the long term for the temperature ROMs. Optimum values for the number of velocity and temperature POD modes correspond to $N_V = 35$ for the velocity ROM and$(N_V, N_T) = (10, 30)$ for the temperature ROM. The temporal coefficients for those integrated reduced order models are presented in figure 146. While the behavior of the first velocity mode is only marginally improved, most of the amplitude and phase discrepancies growing during the second forcing cycle are significantly reduced when using any of the stabilization methods. Overall, the dynamics of the stabilized ROMs using any of the damping methods are quite satisfying over at least 2 cycles.

Finally, the values for the turbulent viscosity and turbulent thermal diffusivity for the stabilized ROMs are presented in figure 147. Interestingly, while most of the velocity modes have a positive turbulent viscosity, the second one actually requires a negative value. Similarly, the first temperature mode requires a negative turbulent thermal diffusivity which is quite different from the unforced jets results. At this point, it should be kept in mind that first, the decomposed (and therefore integrated) signal does not correspond to the overall velocity fluctuation, but rather to the deviation from the reference signal $\gamma(t)\vec{u}_{ref}$ and therefore cannot be directly interpreted as a physical field. Then, it is reminded that the stabilization method adopted here is only an asymptotic (partial) method and only takes care of the under-diffusive character of the uncontrolled flow. Because of this, it is believed that a more complete formulation of the energy conservation constraints (including conservation for $\frac{d\gamma}{dt} \neq 0$) would greatly improve the ROM dynamics and in particular the deviations of the first mode.

3.2.3.2 Phase Averaged Flow Based on the results from the preliminary POD, study showing only little difference between instantaneous and phase averaged flow POD decompositions, the question of whether or not it is possible to obtain a reduced order model for the phase averaged flow is posed. In other terms, if most of the turbulent fluctuation part of the instantaneous velocity field is removed in the process of truncating the POD series, why not only model the dominant phase averaged features in the first place ? A similar approach to the one described in the instantaneous forced flow was applied to the phase averaged signal.

3.2.3.2.1 Reduced Order Models A phase averaged flow is obtained using the same parameters as for the instantaneous flow, for a solution integrated over 10 forcing cycles. The flow is then phase averaged at the same 50 discrete phase locations as for the previous decomposition, thus providing a set of 50 POD snapshots. The transition from BR_l to BR_h occurs at $t_c = 0$. The POD metrics are presented in figure 148. Overall, the energy distributions for both velocity and temperature POD modes are very comparable to the one in figure 142 for the instantaneous flow, in particular for the dominant mode. This is in agreement with the results from the preliminary POD analysis. The first velocity mode is dominant with 37% of the energy which is equivalent to the energy content of the first mode in the instantaneous decomposition. The second mode is significantly weaker with 17% of the

DISTRIBUTION A: Distribution approved for public release.

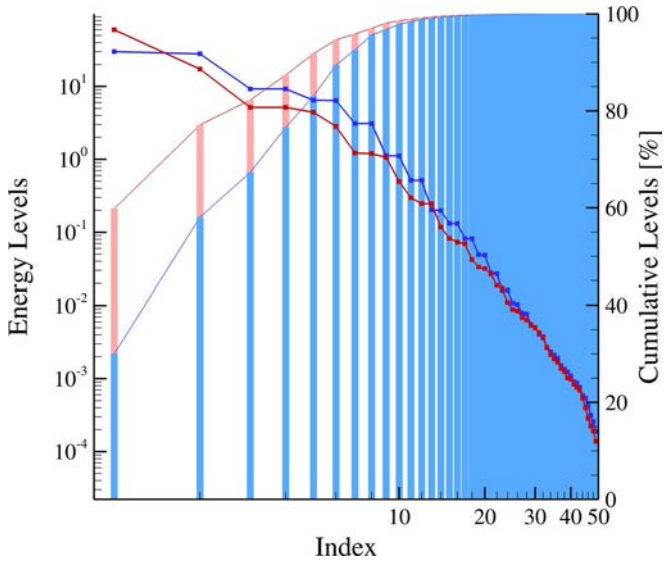

Figure 148: POD decomposition metrics for velocity (*red*) and temperature (*blue*) fields with $N = 200$ for *phase average Case IV* at $St_\infty = 0.159$.

total kinetic energy, against 11% for the second mode of the instantaneous decomposition. The temperature energy levels also exhibit a stair-like distribution, characteristic of flows dominated by strong convective mechanisms. The energy content from the phase averaged temperature field decomposition is globally higher than corresponding modes from the instantaneous one. The 99% total kinetic energy and pseudo-thermal cumulative energy thresholds are reached when including 12 velocity modes and 12 temperature modes respectively. In comparison, thresholds for their instantaneous fields counterparts were corresponding to 65 modes for the velocity field and 70 modes for the temperature field. The phase average values agree also quite well with the ones obtained in the preliminary study (respectively 12 and 15). The POD shape functions for the velocity and temperature are presented in figure 149 and 150. The first 6 velocity modes and 10 temperature modes bear strong resemblance with the instantaneous decompositions in the previous section. However, higher order modes, which here correspond to higher harmonics of the lower order ones, differ quite significantly from their counterparts in the instantaneous decomposition which are capturing either wall structures or anti-symmetric behavior.

Reduced order models corresponding to the non-stabilized equations are integrated for multiple values of (N_V, N_T) in the range $[5, 50] \times [5, 50]$ and corresponding error surfaces were generated. All the ROMs are successfully integrated up to three forcing cycles including all 50 velocity and temperature modes. In general, increasing the number of velocity modes has a negative impact on velocity and temperature error levels, and increasing the number of temperature modes also has a rather negative impact on the temperature error levels. However, the overall error levels are quite low when compared to the instantaneous ROMs with as much as an order of magnitude difference on the total velocity error in the short term. Because the error levels are overall low, it was decided to present in figure 151 the best performing integrated ROMs, such that $N_V > 12$ and $N_T > 12$, corresponding to the 99% energy threshold values from the POD. For the velocity model, this corresponds to $N_V = 14$

DISTRIBUTION A: Distribution approved for public release.

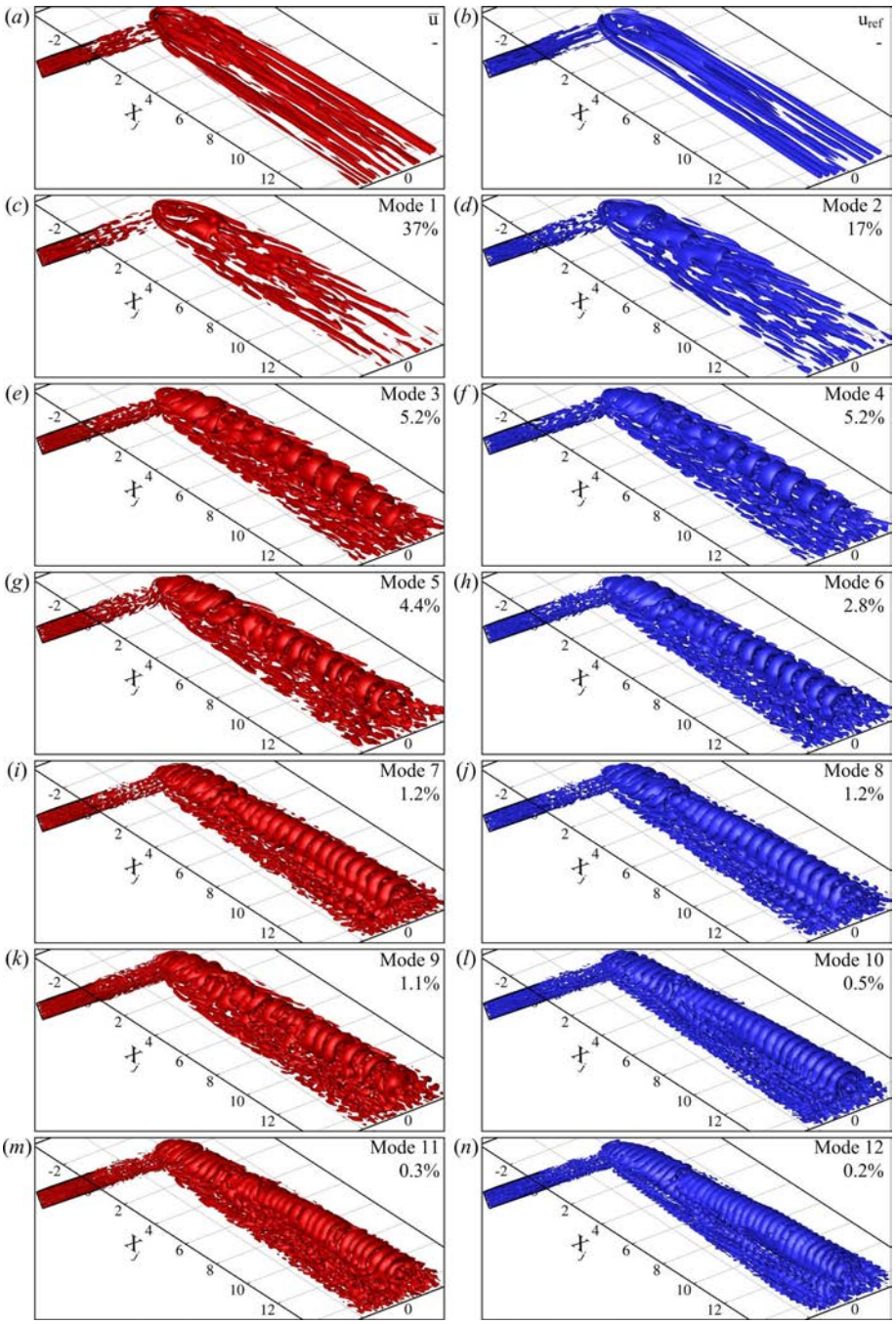

Figure 149: First 12 velocity POD modes along with $\vec{u}_m$ and $\vec{u}_{ref}$ λ_2 iso-surfaces for POD decomposition for *phase averaged Case IV* at $St_\infty = 0.159$. Mode energy provided in percent of the total energy.

DISTRIBUTION A: Distribution approved for public release.

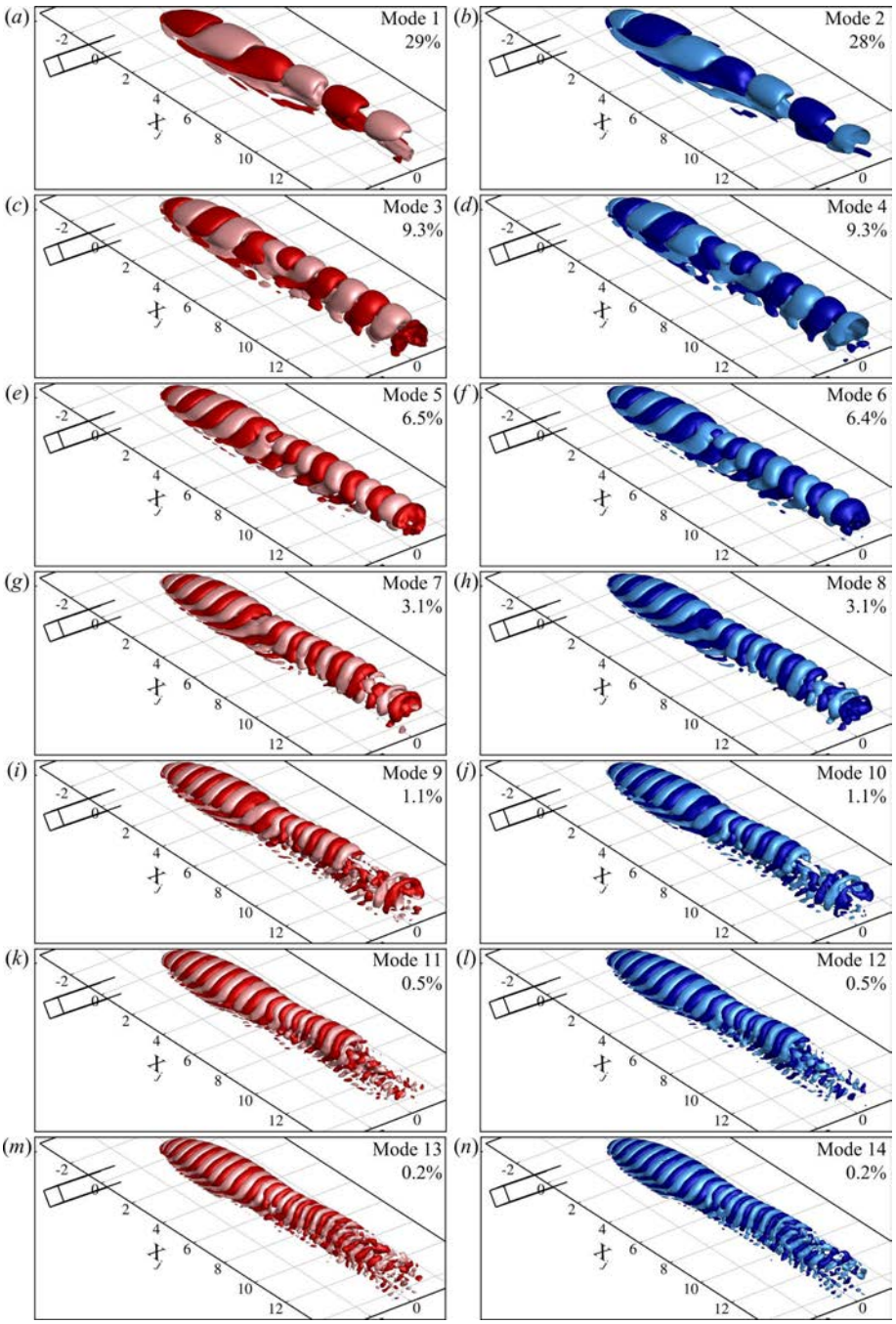

Figure 150: First 14 temperature POD modes iso-surfaces for POD decomposition for *phase averaged Case IV* at $St_\infty = 0.159$. Pink and cyan contours are for negative values, red and blue for positive ones. Mode energy provided in percent of the total energy.

DISTRIBUTION A: Distribution approved for public release.

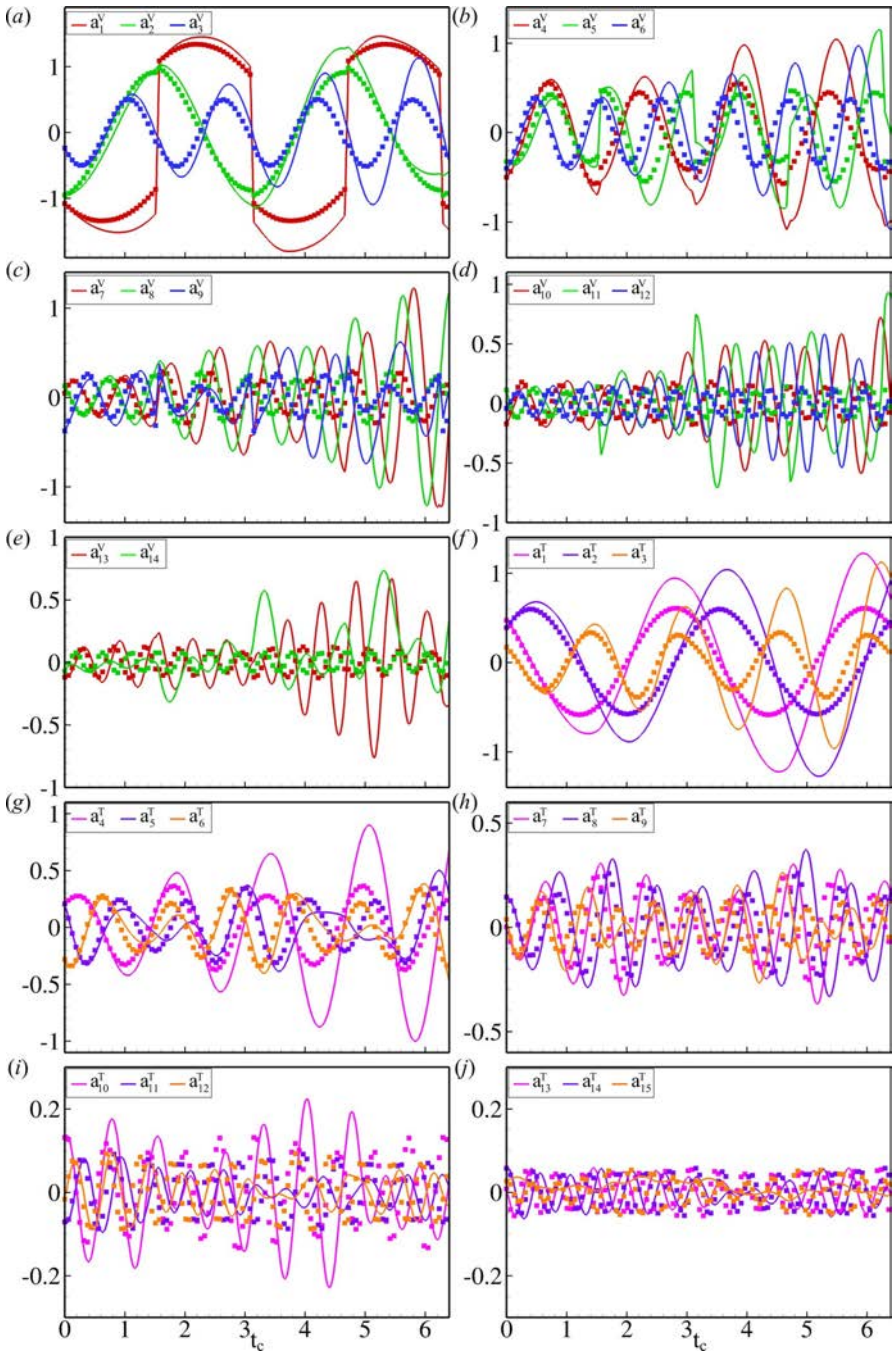

Figure 151: *phase averaged Case IV* at $St_\infty = 0.159$ ROM temporal coefficients for the velocity ($N_V = 14$) and temperature ($(N_V, N_T) = (25, 15)$) fields (*solid lines*) along with corresponding POD temporal coefficients (*symbols*).

DISTRIBUTION A: Distribution approved for public release.

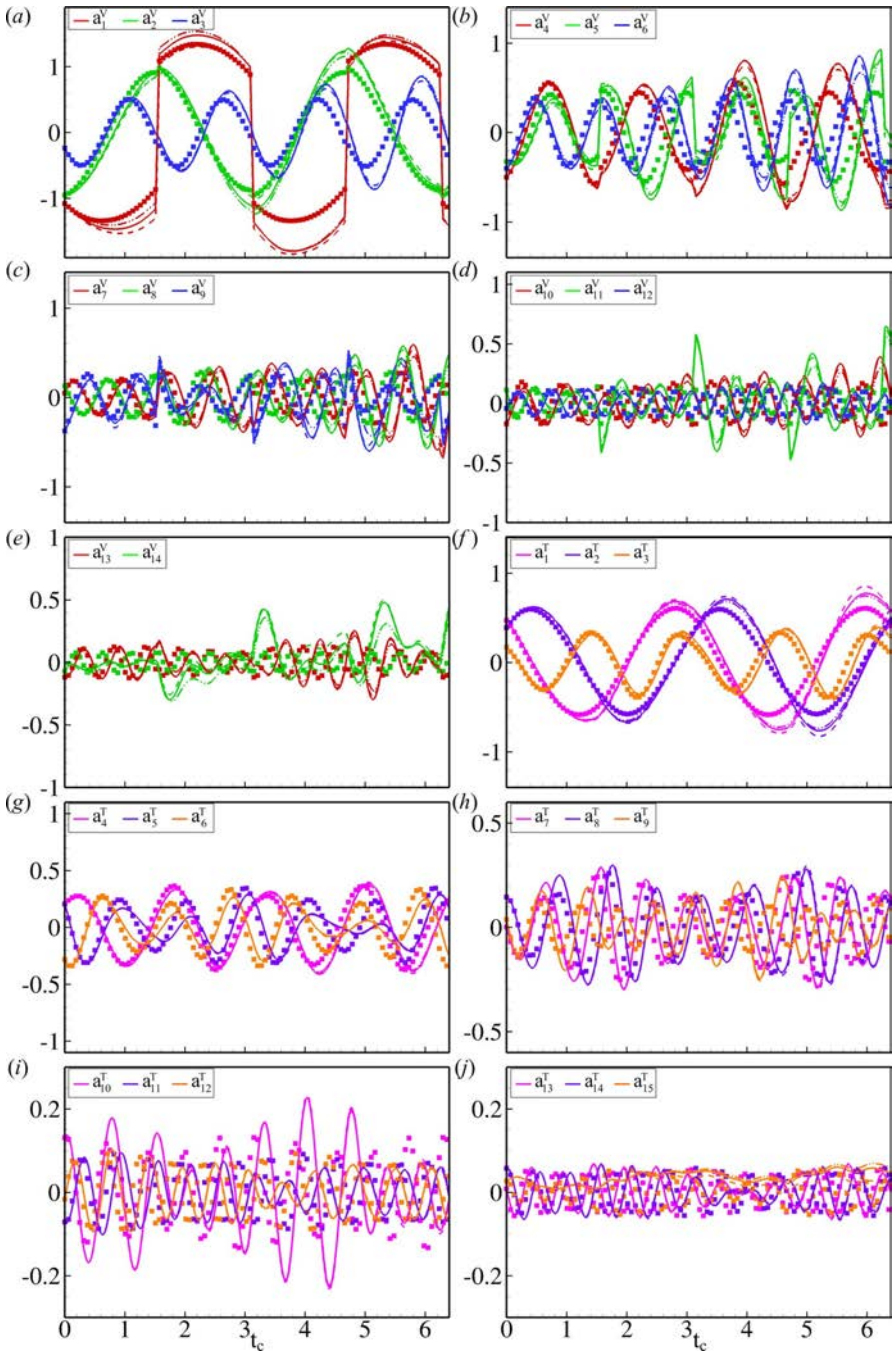

Figure 152: *phase averaged Case IV* at $St_\infty = 0.159$ ROM temporal coefficients for the velocity ($N_V = 14$) and temperature ($(N_V, N_T) = (25, 15)$) fields using partial local (*solid*), partial broad (*dashed*) and asymptotic (*dashed dot dot*) linear damping along with corresponding POD temporal coefficients (*symbols*).

DISTRIBUTION A: Distribution approved for public release.

and for the temperature model to $(N_V, N_T) = (25, 15)$.The agreement between projected LES data and ROM integrated results is qualitatively comparable to the one obtained for the instantaneous flow field, with however only half the number of modes. Once again, a clear discrepancy in the first velocity mode is observed. Amplitude and phase are starting to diverge during the second cycle, although the amplitudes appear to grow less for the higher orders in the phase averaged field than the instantaneous one. While slowly deteriorating, the agreement between the reduced order model the projected LES data over two forcing cycles is found to be reasonably good.

The reduced order models are then integrated using local, broad and asymptotic stabilization methods and the corresponding error surfaces are computed. All three stabilization methods exhibit comparable error levels, although in the long term, ROMs with $N_T = 50$ stabilized using the local and asymptotic methods start diverging in the second cycle. The asymptotic formulation provides more stability to the systems integrated using large numbers of velocity modes and slightly better performance in the long term when compared to the other two. Minimum total error levels on the velocity fields for the stabilized ROMs are on average two time lower in the short term, and almost ten times lower in the long term than comparable non-stabilized ROMs. The effect of the stabilization is even greater on the temperature field with total error levels decreased by a factor 10 in the short term and a factor 100 in the long term. The stabilized reduced order models corresponding to the ones presented previously are shown in figure 152. Overall, the agreement between LES projected data and integrated ROMs is clearly improved over the non-stabilized models with exception of the first velocity POD mode which is left quasi-unchanged. The asymptotically stabilized velocity ROM seems to have slightly better performance towards the end of the second cycle, in particular when considering higher order modes, though the difference is not significant enough to draw any definitive conclusion. The temperature ROM is almost completely insensitive to the type of stabilization method used, yet shows clearly improved agreement with the projected data. Finally, the computed turbulent viscosity and thermal diffusivity are presented in figure 153. Although not many points are shown here because of the low values of N_V and N_T, the trends appear to be similar to the ones obtained for the instantaneous fields, with globally increasing values of the turbulent viscosity and decreasing values of the turbulent thermal diffusivity for increasing mode ranks.

3.3 Conclusion

The preliminary POD analysis of the inclined film cooling jet at $BR = 0.15$ described in this section showed that when considering only part of the physical domain and at such low blowing ratios, POD converged when using 200 snapshots. A total of 78 velocity modes and 76 temperature modes were necessary to gather 99% of the total fluctuation energy. The most energetic velocity POD modes were found to be associated with the convection of the shear layer vortices encountered at this blowing ratio while higher order modes accounted for their interaction with side vortices located near the wall. The temperature analysis led to a more convoluted decomposition, due to the non-optimality of the norm associated to standard POD. The reconstruction of both fields has shown that satisfactory results can be obtained by including a total of 20 POD modes. However, due to the nature of the proper orthogonal decomposition, the relative error in the vicinity of the jet exit remains high and could potentially affect the behavior of a reduced order model based on a truncated series. Preliminary proper orthogonal decomposition analysis was also carried on the pulsed

DISTRIBUTION A: Distribution approved for public release.

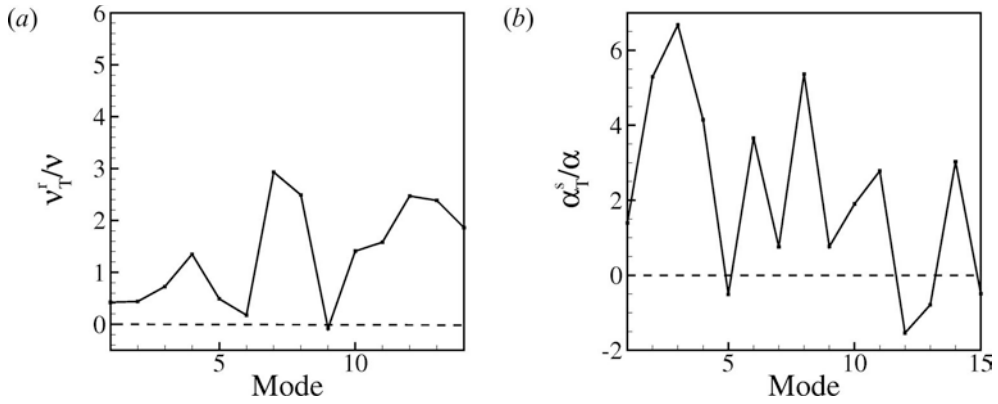

Figure 153: *phase averaged Case IV* ROM (a) normalized turbulent momentum diffusivity ν_T^r/ν and (b) normalized turbulent thermal diffusivity α_T^s/α calculated for $N_V = 14$ and $N_T = 15$.

jet at two distinct forcing frequencies. The analysis of the lowest frequency case ($St_\infty = 0.016$) included 50 phase averaged snapshots and showed that a total of 41 velocity and 33 temperature modes were required to gather more than 99% of the fluctuation energy. The different POD modes had a distinct support of action due to the presence of multiple flow regime within a single forcing cycle. Because of the segregation of the POD modes to specific cycle parts, the POD series truncation for the forced flow could lead to the suppression of the dynamics of part of the cycle. The higher forcing frequency ($St_\infty = 0.159$) analysis included 25 phase averaged modes and required 12 velocity and 15 temperature modes to capture more than 99% of the total fluctuation energy. The POD revealed the homogeneity of the flow in the streamwise direction due to the limited range of length and time scales present in the domain. Because of the significantly greater complexity of the problem at low forcing frequency, 40 POD modes were required to obtain less than 4% relative error on the velocity field, while the same error levels were reached with only 15 modes in the higher frequency case. The temperature field required fewer modes and respectively 10 and 6 modes were necessary at $St_\infty = 0.016$ and $St_\infty = 0.159$ to reach identical accuracy levels.

Reduced order modeling efforts were carried out using a refined grid and over the complete simulation domain, following the POD-Galerkin method described in the previous chapter. Stabilization methods, necessary in realistic three dimensional flows, were discussed and an extension of the model introduced by 15 was proposed. Unforced jets were first considered in both attached and transitional regimes. In the attached jet regime, the effects of the POD domain selection were evidenced by the change of the dominant structures from hairpin vortices to wall vortices between the preliminary analysis and the full domain decomposition. Although decreasing with increasing number of modes, the error levels on the total velocity field of the non-stabilized reduced order models were found to be quite significant. In the short term ($\Delta t_c < 2$), minimum error levels were reached for $(N_V, N_T) = (250, 120)$ but tracking was found to be qualitatively poor beyond $t_c = 1$. A growing divergence in the amplitude and phase of the ROMs was attributed to the interruption of the energy cascade introduced by the POD series truncation, the turbulence model used in the simulations, and the sampling frequency used in the snapshot collection. Stabilized ROMs using either local or broad linear stabilization methods evidenced greatly improved performance over

DISTRIBUTION A: Distribution approved for public release.

non stabilized ones, with error levels over 30 times lower for the velocity field and 200 times lower in the long term for the temperature ROM. Minimum error levels were reached for the stabilized ROMs using $(N_V, N_T) = (275, 100)$. Stabilized ROMs showed reasonable agreement with the projected LES data up to three convective time scale units. In the transitional jet regime, the POD reflected well the increased turbulent character of the flow, with fuller energy distributions and busier POD modes. Non stabilized reduced order models were derived and integrated for values of (N_V, N_T) in the range $[30, 500] \times [30, 500]$. The equations corresponding to the higher order modes were found to diverge rather rapidly beyond $t_c = 1$ and cause the entire system, including the temperature ROM, to diverge around $t_c = 2.5$, preventing any integration past this point. Consequently, error levels for the velocity ROMs in the short term were found to be extremely high, while corresponding temperature error levels were found to be surprisingly lower than comparable results in the attached configuration. Reduced order models including local and broad stabilization terms exhibited much improved error levels. It was found that the broad stabilization method was much more effective when integrating systems including large number of velocity POD modes and therefore permitted to further reduce error levels on the velocity field, even more so in the long term. The temperature ROMs were however much less sensitive to the type of stabilization method used than the velocity models. Qualitatively, both stabilization methods provided much improved ROMs dynamics with an advantage to the broadly stabilized reduced order models which showed very good agreement with the projected LES data at least up to $t_c = 4$.

Reduced order models for instantaneous and phase averaged forced flows at $BR_h = 0.5$, $BR_l = 0.15$, $DC = 50\%$ and $St_\infty = 0.159$ were obtained and integrated. Instantaneous flows were decomposed using (29) formulation. While the POD metrics and shape function of the temperature field were quite similar to the ones of the preliminary study, the POD for the velocity was found to be different due to the use of a different velocity field decomposition. Non-stabilized ROMs showed reasonable agreement with the projected LES data, although divergence started to grow during the second forcing cycle. Three stabilization methods were proposed (two partial and one complete asymptotic) and applied to the velocity and temperature models. All three methods provided significant improvement over the non-stabilized equations with yet a small advantage to the asymptotic stabilization when dealing with systems including larger numbers of velocity modes. Overall any of the stabilized model provided satisfying representation of the flow over at least two cycle periods. Reduced order model equations for the phase averaged flow were derived by neglecting a priori the Reynolds stresses and correcting for those a posteriori when using stabilization methods. Overall, reduced order models of the phase averaged flow were found to perform at least as well as the ones for the instantaneous flow using only half as many modes, thus reducing the computational cost associated with the integration of reduced order models. The stabilized equations provided significant improvement over the non stabilized ones, in particular for the temperature model. It appears clear that the introduction of discrete, strong vortical structures through jet actuation, provided a much better defined and more distinct POD basis responsible for the better accuracy of the forced ROMs over the unforced ones.

These results show that reasonably accurate reduced order models could be obtained for the attached and transient unforced regimes and quite accurate models could be obtained for both the instantaneous and phase averaged flows. Phase averaged models provided comparable error levels to those of instantaneous ones using only half the number of velocity and temperature modes. In all the investigated cases, stabilization methods were found to

DISTRIBUTION A: Distribution approved for public release.

be beneficial, if not necessary. In unforced conditions, the local linear stabilization of (15) and the proposed broad linear stabilization methods exhibited comparable performances, yet the broad formulation usually resulted in more stable equations allowing the integration of larger system and leading to lower error levels. This was particularly true for the more turbulent transient jet regime. In forced conditions, all three proposed methods, damping either only the base flow or both the base and controlled flows in an asymptotic way, provided comparable results in terms of the global error estimates and the agreement of the ROMs dynamics with the projected LES data. The asymptotic formulation seemed to provide some improved stabilization for models including large numbers of modes, compared to the other two. Further improvement of the reduced order models in both unforced and forced conditions will require more sophisticated stabilization methods, in particular with time-dependent capabilities. This is especially true for the forced jet. However, as it stands, it is believed the presented methods provide acceptable models in unforced conditions and relatively good ones in forced conditions, so that they can serve as an initial set of governing equations for the development of a flow controller.

DISTRIBUTION A: Distribution approved for public release.

4 Flow Control

4.1 Jet in Cross-flow Modeling

We consider the 3D Navier-Stokes (N-S) and continuity equations for an incompressible Newtonian fluid as the fluid flow model

$$\frac{\partial \mathbf{u}}{\partial t} + (\mathbf{u} \cdot \nabla)\,\mathbf{u} = -\nabla P + \frac{1}{Re}\nabla^2 \mathbf{u} \tag{14}$$

$$\nabla \cdot \mathbf{u} = 0 \tag{15}$$

where $\mathbf{u} = [u(x,y,z,t) \quad v(x,y,z,t) \quad w(x,y,z,t)]^T$. The problem setup consists of a computational box of dimensions $17D \times 10D \times 3D$ with a cross section in the xy plane along $z = 1.5D$ shown in Figure 154.

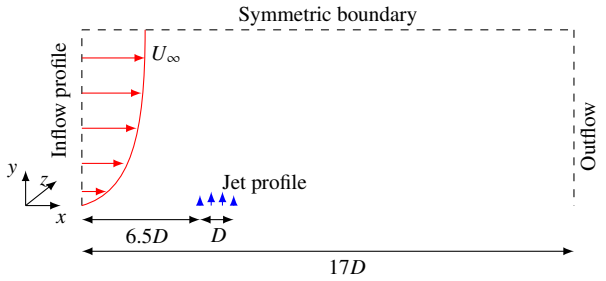

Figure 154: Jet in cross-flow setup

The following physical Dirichlet boundary conditions are prescribed

$$\mathbf{u}(\mathbf{x},t) = \begin{cases} \tilde{c}(t)\tilde{\mathbf{h}}_1(\mathbf{x}), & \text{jet inflow} \\ \tilde{a}_0(t)\tilde{\mathbf{h}}_0(\mathbf{x}), & \text{inflow} \\ 0, & \text{wall} \end{cases} \tag{16}$$

with the inflow boundary condition given by the Blasius solution. The jet inlflow boundary condition is implemented as

$$\tilde{\mathbf{h}}_1(\mathbf{x}) = \begin{bmatrix} 0 & (1-r^2)\,e^{-\left(\frac{r}{0.7}\right)^4} & 0 \end{bmatrix}^T,$$

where r is the distance from the jet center in the xz plane. Notice that this model corresponds to a vertical jet. This expression is intended to model the parabolic velocity profile of pipe Poiseuille flow and is used in several studies, including (5) and (37). At the outflow, a non-reflective boundary condition is used where the gradient of the velocity normal to the boundary is assumed to be zero. On the top of the domain, the boundary condition is given by $\frac{\partial u}{\partial y} = 0, v = 0$.

In this setup the following variables are used to non-dimensionalize the problem: U_∞, the free stream cross-flow velocity, V, the peak inflow velocity of the jet, D, the jet diameter, and ν, the kinematic viscosity. We characterize the jet in cross-flow with the 2 independent

DISTRIBUTION A: Distribution approved for public release.

dimensionless parameters: $Re = \frac{U_\infty D}{\nu}$, the free stream Reynolds number, and $R = \frac{V}{U_\infty}$, the velocity ratio.

4.1.1 Numerical Method

We use the hybrid staggered/semi-staggered finite difference algorithm described in (4) to numerically solve the N-S equation in a parallel computing environment. This direct numerical simulation (DNS) algorithm uses the fractional step method to advance the solution in time in two steps: 1) A semi-staggered grid structure is used to discretize the momentum equations and solve for an intermediate velocity with the pressure gradient term absent, and 2) A staggered grid is used to discretize the Poisson-Neumann equation that adds the pressure gradient to the projection step. All the components of velocity are stored at the cell vertices and pressure is stored at the cell centers. The momentum equations are discretized at cell vertices thus providing a consistent discretization of the diffusive and convective terms as the boundaries are approached. The discrete divergence and gradient operators of the projection step are constructed on a staggered gird layout leading to the exact satisfaction of the discrete continuity equation. It is important to note that the solution of the Poisson-Neumann equation in the projection step is free of any spurious eigenmodes.

A grid with 1,479,072 vertices as shown in Figure 155 was used for the simulations. Using 8 Intel XeonE5620 2.4Ghz, 12M cache processors, it took about 8s to advance the solution one time-step.

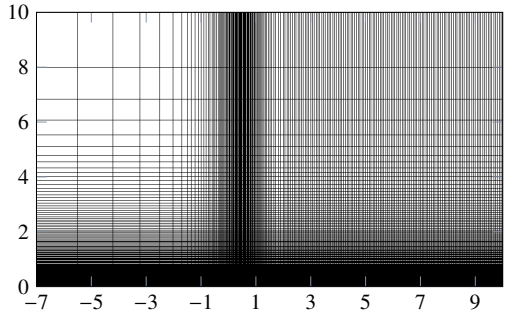

Figure 155: Grid used for simulations

4.1.2 Reduced Order Model Based on POD/Galerkin Projection

We now give a brief overview of the the well-known POD/Galerkin projection method for obtaining reduced order models of the N-S equation. For a detailed treatment of the POD and Galerkin projection, see (35, 43, 70) and the references therein.

We start out with a given solution flow field ensemble $\mathcal{U} = \{\mathbf{u}_1, \ldots, \mathbf{u}_N\}$, where $\mathbf{u}_i = \mathbf{u}(\mathbf{x}, t_i)$, and N is the number of solutions that has been generated by DNS. Given $\mathcal{U}$, the POD problem consists in finding orthonormal basis functions $\{\boldsymbol{\phi}_i\}_{i=1}^n$ that solve

$$\min_{\{\boldsymbol{\phi}_k\}_{k=1}^n} \sum_{i=1}^{N} \left\| \mathbf{u}_i - \sum_{j=1}^{n} (\mathbf{u}_i, \boldsymbol{\phi}_j)_J \boldsymbol{\phi}_j(\mathbf{x}) \right\|^2 \quad s.t. \quad (\boldsymbol{\phi}_i, \boldsymbol{\phi}_j) = \delta_{ij}, \tag{17}$$

DISTRIBUTION A: Distribution approved for public release.

where δ_{ij} is the Kronecker delta and $(\cdot,\cdot)$ is an inner product. The solution to the discretized version of (17) is given by a singular value decomposition (SVD) of the snapshot data matrix, $\mathcal{X} = [\mathbf{u}_1 \quad \mathbf{u}_2 \quad \cdots \quad \mathbf{u}_N]$, and the basis functions $\{\boldsymbol{\phi}_i\}_{i=1}^n$ are called *POD basis functions*.

The next step is to assume that $\mathbf{u}(\mathbf{x},t)$ admits a modal expansion of the form

$$\mathbf{u}(\mathbf{x},t) = \sum_{i=1}^{n} a_i(t)\boldsymbol{\phi}_i(\mathbf{x}) + \tilde{a}_0(t)\tilde{\mathbf{h}}_0(\mathbf{x}) + \tilde{c}(t)\tilde{\mathbf{h}}_1(\mathbf{x}) \tag{18}$$

where $\boldsymbol{\phi}_i, i = 1,\ldots,n$ are homogeneous on the boundary POD basis functions and $\tilde{\mathbf{h}}_0$ and $\tilde{\mathbf{h}}_1$ are control basis functions. The control basis functions are divergence-free extensions of the boundary conditions in (16) (i.e., they match boundary conditions and are divergence-free in the domain). Since there is no danger of confusion, we refer to the spatial component of the boundary conditions and the control basis functions by the same symbol. The following procedure is a simple and straightforward way to construct the control basis functions: Denote $\mathbf{u}_{unact}(\mathbf{x},t)$ an *unactuated solution* when it is a solution obtained with boundary conditions $\tilde{c}(t) = 0$ and $\tilde{a}_0(t) = a_0$. Denote $\mathbf{u}_{act}(\mathbf{x},t)$ an *actuated solution* when it is a solution obtained with boundary conditions $\tilde{c}(t) \neq 0$ and $\tilde{a}_0(t) = a_0$. The term $\tilde{\mathbf{h}}_0(\mathbf{x})$ is taken as the time average of an unactuated solution and $\tilde{\mathbf{h}}_1(\mathbf{x})$ is taken as the time average of $\mathbf{u}_{act}(\mathbf{x},t) - \mathbf{u}_{unact}(\mathbf{x},t)$.

In the literature there are several other methods on how to compute the control basis functions, for example (59), (40), (60), (14), and (64). We could use any of these methods to obtain a ROM but we take a slightly different route. The reason is that we prefer to construct control basis functions that are orthonormal to the POD basis functions in order to simplify the ROM for controller design purposes. Inspired by the Gram-Schmidt algorithm, we use the following procedure to compute these orthonormal POD and control basis functions:

1. Let $\mathcal{X}_h$ denote a snapshot matrix corresponding to

$$\mathbf{u}(\mathbf{x},t) - \tilde{a}_0(t)\tilde{\mathbf{h}}_0(\mathbf{x}) - \tilde{c}(t)\tilde{\mathbf{h}}_1(\mathbf{x}). \tag{19}$$

   Note that $\mathcal{X}_h$ is homogeneous on the boundary.

2. Obtain the POD basis functions corresponding to $\mathcal{X}_h$, i.e., SVD factorization of $\mathcal{X}$. The POD basis will be zero on the boundary by construction.

3. Compute $\mathbf{h}_0 = \frac{\tilde{\mathbf{h}}_0 - \sum_{i=1}^n \left(\tilde{\mathbf{h}}_0, \boldsymbol{\phi}_i\right)\boldsymbol{\phi}_i}{\|\tilde{\mathbf{h}}_0 - \sum_{j=1}^n \left(\tilde{\mathbf{h}}_0, \boldsymbol{\phi}_j\right)\boldsymbol{\phi}_j\|}$.
   Compute $\mathbf{h}_1 = \frac{\tilde{\mathbf{h}}_1 - \sum_{j=1}^n \left(\tilde{\mathbf{h}}_1, \boldsymbol{\phi}_j\right)\boldsymbol{\phi}_j - \left(\tilde{\mathbf{h}}_1, \mathbf{h}_0\right)\mathbf{h}_0}{\|\tilde{\mathbf{h}}_1 - \sum_{j=1}^n \left(\tilde{\mathbf{h}}_1, \boldsymbol{\phi}_j\right)\boldsymbol{\phi}_j - \left(\tilde{\mathbf{h}}_1, \mathbf{h}_0\right)\mathbf{h}_0\|}$.

Note that $\mathbf{h}_0$ and $\mathbf{h}_1$ are orthogonal to the POD basis by the construction in step 3. We denote the final orthonormal modal expansion as

$$\mathbf{u}_{ROM}(\mathbf{x},t) = \sum_{i=1}^{n} a_i(t)\boldsymbol{\phi}_i(\mathbf{x}) + a_0(t)\mathbf{h}_0(\mathbf{x}) + c(t)\mathbf{h}_1(\mathbf{x}) \tag{20}$$

where $\mathbf{h}_0(\mathbf{x})$ is called the *inflow basis* and $\mathbf{h}_1(\mathbf{x})$ is called the *control basis*.

DISTRIBUTION A: Distribution approved for public release.

Finally, a standard Galerkin projection with POD, inflow, and control basis functions can be carried out to derive the ROM. This is done by projecting (14), the N-S equation, to the i^{th} POD basis function as follows

$$\int_\Omega \frac{\partial \mathbf{u}}{\partial t} \cdot \boldsymbol{\phi}_i d\mathbf{x} + \int_\Omega \mathbf{u} \cdot \nabla \mathbf{u} \cdot \boldsymbol{\phi}_i d\mathbf{x} = -\int_\Omega \nabla P \cdot \boldsymbol{\phi}_i d\mathbf{x} + \int_\Omega \frac{1}{Re} \nabla^2 \mathbf{u} \cdot \boldsymbol{\phi}_i d\mathbf{x}, \tag{21}$$

where the integration is done over the whole spatial domain, Ω. Using integration by parts on the term $\int_\Omega \frac{1}{Re} \nabla^2 \mathbf{u} \cdot \boldsymbol{\phi}_i d\mathbf{x}$ and noting that the POD basis functions are divergence-free and homogeneous on the boundary, we obtain

$$\int_\Omega \frac{\partial \mathbf{u}}{\partial t} \cdot \boldsymbol{\phi}_i d\mathbf{x} + \int_\Omega \mathbf{u} \cdot \nabla \mathbf{u} \cdot \boldsymbol{\phi}_i d\mathbf{x} + \frac{1}{Re} \int_\Omega \nabla \mathbf{u} \cdot \nabla \boldsymbol{\phi}_i d\mathbf{x} = 0. \tag{22}$$

Recall that the POD basis functions are divergence-free, therefore (15), the continuity equation, is automatically satisfied. Finally, we substitute $\mathbf{u}$ with its truncated orthonormal modal expansion (20) and insert it into (22) to obtain the nonlinear system of differential equations:

$$\begin{aligned} \dot{\bar{\chi}} = \bar{A}\bar{\chi} + \bar{B}\bar{u} + \begin{bmatrix} \bar{\chi}^T \bar{N}_1 \bar{\chi} \\ \vdots \\ \bar{\chi}^T \bar{N}_n \bar{\chi} \end{bmatrix} + \begin{bmatrix} \bar{\chi}^T \bar{M}_1 \bar{u} \\ \vdots \\ \bar{\chi}^T \bar{M}_n \bar{u} \end{bmatrix} + \begin{bmatrix} \bar{u}^T \bar{K}_1 \bar{u} \\ \vdots \\ \bar{u}^T \bar{K}_n \bar{u} \end{bmatrix} + a_0 \bar{D}_1 \bar{\chi} \\ + a_0 \bar{D}_2 \bar{u} + \bar{D}_3 a_0 + \bar{D}_4 a_0^2 \end{aligned} \tag{23}$$

with matrices

$$\begin{aligned} \bar{A}_{ij} &= -\frac{1}{Re} \left(\nabla \boldsymbol{\phi}_j, \nabla \boldsymbol{\phi}_i \right), \bar{B}_{i1} = -\frac{1}{Re} \left(\nabla \mathbf{h}_1, \nabla \boldsymbol{\phi}_i \right), \\ \bar{N}_{i_{jk}} &= -\left(\boldsymbol{\phi}_j \cdot \nabla \boldsymbol{\phi}_k, \boldsymbol{\phi}_i \right), \bar{M}_{i_{j1}} = -\left(\boldsymbol{\phi}_j \cdot \nabla \mathbf{h}_1, \boldsymbol{\phi}_i \right) - \left(\mathbf{h}_1 \cdot \nabla \boldsymbol{\phi}_j, \boldsymbol{\phi}_i \right), \\ \bar{K}_i &= -\left(\mathbf{h}_1 \cdot \nabla \mathbf{h}_1, \boldsymbol{\phi}_i \right), \bar{D}_{1_{ij}} = -\left(\mathbf{h}_0 \cdot \nabla \boldsymbol{\phi}_j, \boldsymbol{\phi}_i \right) - \left(\boldsymbol{\phi}_j \cdot \nabla \mathbf{h}_0, \boldsymbol{\phi}_i \right), \\ \bar{D}_{2_{i1}} &= -\left(\mathbf{h}_0 \cdot \nabla \mathbf{h}_1, \boldsymbol{\phi}_i \right) - \left(\mathbf{h}_1 \cdot \nabla \mathbf{h}_0, \boldsymbol{\phi}_i \right), \tilde{D}_{3_i} = -\frac{1}{Re} \left(\nabla \mathbf{h}_0, \nabla \boldsymbol{\phi}_i \right), \\ \tilde{D}_{4_i} &= -\left(\mathbf{h}_0 \cdot \nabla \mathbf{h}_0, \boldsymbol{\phi}_i \right). \end{aligned}$$

It is clear that $\bar{\chi}(t)$ is the n-dimensional state vector consisting of $\{a_i(t)\}_{i=1}^n$ as its elements, and $\bar{u}(t)$ is the scalar input signal $c(t)$. We highlight that since the inflow and control basis are orthogonal to the POD basis, the terms $\dot{a}_0$ and $\dot{c}$ are zeroed out.

There will be an error associated with the ROM solution and the DNS solution. The relative error difference between the DNS and ROM solution that we focus on is the same

DISTRIBUTION A: Distribution approved for public release.

one that we consider for the POD problem, i.e.,

$$E_{\mathbf{u}} = \left(\frac{\sum_{i=1}^{N} \|\mathbf{u}_{DNS}(t_i) - \mathbf{u}_{ROM}(t_i)\|^2}{\sum_{i=1}^{N} \|\mathbf{u}_{DNS}(t_i)\|^2} \right). \tag{24}$$

It is important to note that due to the inclusion of the inflow and control basis, the modal expansion in (20) is not optimal in the POD sense anymore, although we will see in Section 4.3 that the error is not significant.

4.2 Feedback Control

4.2.1 Problem Statement

The problem we consider is a ROM-based velocity tracking problem. Specifically, we wish for the flow field in the domain to asymptotically track a time-invariant solution of the N-S equation, i.e,

$$\lim_{t\to\infty} (\mathbf{u}(\mathbf{x}, t) - \mathbf{u}_d(\mathbf{x})) = 0$$

or equivalently in the ROM state-space

$$\lim_{t\to\infty} (\bar{\chi}(t) - \bar{\chi}_d) = 0.$$

A straightforward approach would be to select a small enough Re and constant R and let the dynamics evolve so that a time-invariant solution is obtained. A time-invariant solution obtained with a constant inflow boundary condition and velocity ratio is called an *operating point* and denoted by $(\bar{\chi}_d, \bar{u}_d)$. It is crucial to note that this approach would yield a stable operating point since even in the presence of perturbations, this is the solution that the flow converges to. Our objective is to stabilize the flow to an unstable operating point, i.e., one that cannot by reached by simply evolving the fluid dynamics. The problem of designing a stabilizing feedback controller is compounded by the fact that the ROM is a nonlinear system. In this case a popular approach is to linearize the dynamics around an operating point and design a linear controller that will locally stabilize the ROM. While this is a simple and effective solution, the shortcoming of this method is that the designer does not have a verifiable check to guarantee that the linear controller will stabilize the operating point of the nonlinear system. In the control literature this is formally known as providing an estimate of the RoA. Roughly speaking, the region of attraction is the set of initial conditions of the ROM that are guaranteed to converge to an operating point. Therefore the problem we consider is to design a controller that achieves velocity-tracking with a guaranteed estimate of the RoA.

4.2.2 Controller Design

The first step in the design process is to define a new system, called the perturbation ROM, with the operating point that we want to stabilize, $(\bar{\chi}_d, \bar{u}_d)$, as its origin. Let $\chi = \bar{\chi} - \bar{\chi}_d$

DISTRIBUTION A: Distribution approved for public release.

and $u = \bar{u} - \bar{u}_d$. Then the perturbation ROM is given by

$$\dot{\chi}(t) = f(\chi, u) = A(\bar{\chi}_d, \bar{u}_d)\chi(t) + B(\bar{\chi}_d, \bar{u}_d)u(t) + Q[\chi(t), u(t)] \tag{25}$$

where

$$A = \bar{A} + a_0\bar{D}_1 + \begin{bmatrix} \bar{\chi}_d^T N_1 \\ \vdots \\ \bar{\chi}_d^T N_n \end{bmatrix} + \begin{bmatrix} \bar{u}_d^T \bar{M}_1^T \\ \vdots \\ \bar{u}_d^T \bar{M}_n^T \end{bmatrix},$$

$$B = \bar{B} + a_0\bar{D}_2 + \begin{bmatrix} \bar{\chi}_d^T \bar{M}_1 \\ \vdots \\ \bar{\chi}_d^T \bar{M}_n \end{bmatrix} + \begin{bmatrix} \bar{u}_d^T K_1 \\ \vdots \\ \bar{u}_d^T K_n \end{bmatrix},$$

and $Q[\cdot, \cdot]$ is a quadratic term given by

$$Q[\chi, u] = \begin{bmatrix} \chi^T \bar{N}_1 \chi \\ \vdots \\ \chi^T \bar{N}_n \chi \end{bmatrix} + \begin{bmatrix} \chi^T \bar{M}_1 u \\ \vdots \\ \chi^T \bar{M}_n u \end{bmatrix} + \begin{bmatrix} u^T \bar{K}_1 u \\ \vdots \\ u^T \bar{K}_n u \end{bmatrix},$$

with matrices $N_i = \bar{N}_i^T + \bar{N}_i$ and $K_i = \bar{K}_i^T + \bar{K}_i$. Note that in this case $\bar{\chi}_d$ and $\bar{u}_d$ are constant, hence A and B are time-invariant. We could also consider stabilization to a trajectory, $\bar{\chi}_d(t)$ and $\bar{u}_d(t)$, in which case $A(\cdot)$ and $B(\cdot)$ will be time varying.

The perturbation ROM (25) with linear state feedback $u(t) = Fx(t)$ is given by

$$\dot{\chi}(t) = f_F(\chi, F\chi) = A_F\chi(t) + Q[\chi(t), F\chi(t)], \;\; \chi(0) = \chi_0 \tag{26}$$

where $A_F = A + BF$. We model the quadratic nonlinearity as a lumped uncertain term, $\Delta(t)$, which allows us to rewrite (26) as

$$\dot{\chi}(t) = f_\Delta(\chi, F\chi, \Delta), \;\; \chi(0) = \chi_0 \tag{27}$$

Specifically, the time-varying uncertainty is of the following form

$$\Delta(t) = \begin{bmatrix} \chi^T & \chi^T F^T \end{bmatrix} \tag{28}$$

which allows us to write (27) as

$$\dot{\chi} = A_F\chi(t) + \begin{bmatrix} \Delta(t) \begin{bmatrix} N_1 & M_1 \\ 0 & K_1 \end{bmatrix} \\ \vdots \\ \Delta(t) \begin{bmatrix} N_n & M_n \\ 0 & K_n \end{bmatrix} \end{bmatrix} \begin{bmatrix} \chi \\ F\chi \end{bmatrix}. \tag{29}$$

A critical point is that we assume that $\Delta(t)$ belongs to the bounding set $\mathbf{\Delta} = \left\{\chi : \Delta^T(t)\Delta(t) \leq \delta^2 I\right\}$ and $\delta > 0$. As we will see later, this assumption is intimately related to the RoA. At this point we define the notion of quadratic stability which was originally introduced in the

DISTRIBUTION A: Distribution approved for public release.

robust control literature to deal with time-varying uncertainties (7). The definition we use is adapted from (19).

Definition 1. *[Quadratic Stability] Let $V(\chi) = \chi^T P \chi$ and $\mathbf{\Delta}$ be a bounding set. System (27) is quadratically stable at $\chi = 0$ if there exists a symmetric matrix $P > 0$ and a scalar $\alpha > 0$ such that the Lyapunov derivative $\dot{V}(\chi, \Delta)$ satisfies*

$$\dot{V}(\chi, \Delta) \leq -\alpha \left\|\chi\right\|^2 \text{ for all } \Delta \in \mathbf{\Delta}. \tag{30}$$

Note that quadratic stability implies the well-known asymptotic stability by Lyapunov's direct method. We now define the RoQA which will give us a verifiable check on the region of the ROM state-space in which our controller design method stabilizes the nonlinear ROM.

Definition 2. *[RoQA] If there exists an $\epsilon > 0$ such that $\mathcal{B}_P(\epsilon) \subseteq \mathbf{\Delta}$ then the RoQA is defined as $\left\{\chi_0 : \chi_0^T P \chi_0 < \epsilon\right\}$.*

The RoQA is therefore basically the largest ellipsoid that fits inside the region of the state-space of the ROM where the Lyapunov derivative is negative. The concept of a bounding set allows us to establish quadratic stability results since $\Delta(t)$ is used to model the terms related to $Q[\chi, F\chi]$ when these appear in the expression of the Lyapunov derivative of V. The driving design principle is to simultaneously determine a feedback gain F that enlarges the region of the state-space of the ROM where (30) holds, i.e., ϵ, and to determine the largest invariant ellipsoid that is contained in that region, i.e., the matrix P. In the context of the nonlinear control literature, the principle we follow is formally known as determining a regional *control Lyapunov function (clf)*, for more details see (45).

The design method can now be stated as follows.

Design method: Let $\Delta(t)$ be as in (28) with bounding set $\mathbf{\Delta} = \left\{\chi : \Delta^T(t)\Delta(t) \leq \delta^2 I\right\}$ and $\delta > 0$. The system (26) is quadratically stable if there exist solutions $Y = Y^T$ and Z to the linear matrix inequalities (LMIs)

$$Y > 0 \tag{31}$$

$$\begin{bmatrix} YA^T + AY + Z^T B^T + BZ + I & Y^T C^T + Z^T D^T \\ CY + DZ & -\frac{1}{\delta^2} I \end{bmatrix} < 0 \tag{32}$$

with RoQA $\mathcal{B}_P(\epsilon)$, where $\epsilon = \dfrac{\delta^2}{\lambda_{\max}\left(\begin{bmatrix} I \\ F \end{bmatrix} Y \begin{bmatrix} I & F^T \end{bmatrix}\right)}$ and $P = Y^{-1}$. The state feedback gain is given by $F = ZY^{-1}$.

Note: Several convex optimization packages are available which may be used to obtain the controller matrices Y and Z. Some of these are the Robust control toolbox in Matlab, `cvx` package for Matlab and `cvxopt` for Python.

Since the estimated RoQA of the perturbation ROM may be small, we propose a switching strategy combined with our design method to effectively enlarge the RoQA of the ROM if the operating points are 'close enough to each other'. This larger region is defined as follows.

Definition 3. *[Centered-ϵ-Cover] The state-space of the ROM is said to have a centered-ϵ-cover, if the center of each perturbation RoQA is contained inside a neighboring perturbation RoQA.*

DISTRIBUTION A: Distribution approved for public release.

Therefore, if the ROM has a centered-ϵ-cover, then each initial state $\bar{\chi}_0$ can be attracted to the center of the next perturbation RoQA by an appropriate state feedback control law. If we design a feedback gain F_i for each of these perturbation RoQAs we can switch the controller gain between the different F_is to semi-globally stabilize the ROM. This is illustrated in Figure 156 for a system with two operating points, one corresponding to ϵ_1 and another to ϵ_2.

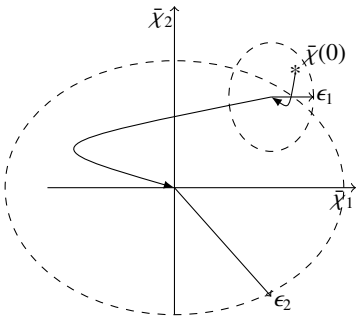

Figure 156: Equilibria path program example

For more details and formal proofs regarding this controller design method see (2).

4.3 Results

4.3.1 Open Loop Dynamics

We now present DNS and ROM simulation results for the system in open loop. The simulation results correspond to $Re = 650$ and $R = 1$ ($\bar{u} = 1, \bar{a}_0 = 1$). After about 7 flow-throughs, snapshots were collected and the POD and control basis functions were computed using the method described in Section 4.1.2. A total of 180 snapshots with a sampling period of $\Delta t = 0.0665$ were collected to compute the POD basis; this spans about 3.5 shedding cycles. The energy distribution in the POD modes is shown in Figure 157. We note that the singular values appear in pairs, a characteristic of flow systems with traveling structures (23).

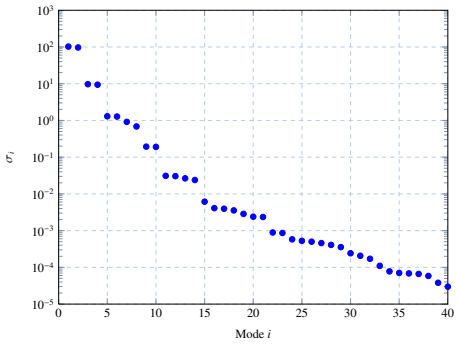

Figure 157: Energy in σ_i

Most of the energy is contained in the first 8 modes as shown in Table 13.

DISTRIBUTION A: Distribution approved for public release.

n	% Energy
8	92.9
16	98.1
32	99.7

Table 13: Energy captured by POD expansion

In Figures 158 and 159 we plot the λ_2-criterion, as defined in (38) and (16), of a selected number of POD basis functions and the control basis.

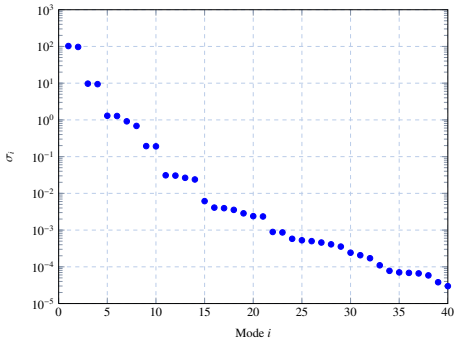

Figure 158: λ_2-criterion of POD basis functions ($\lambda_2 = -0.06$)

DISTRIBUTION A: Distribution approved for public release.

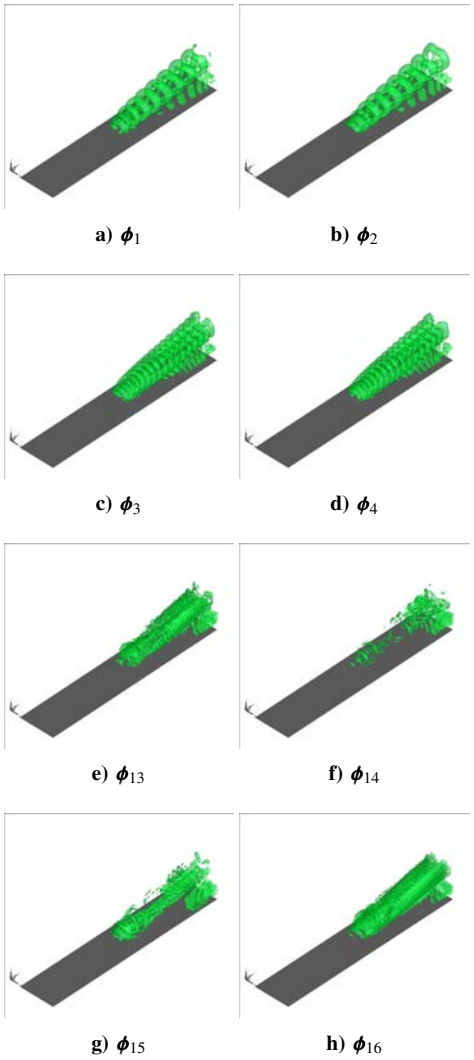

Figure 159: λ_2-criterion of control basis function ($\lambda_2 = -0.06$)

From the figures we can see the features of the coherent structures of the jet in cross-flow such as the horseshoe vortex, jet shear-layer vortices, and wake vortices. Figure 160 shows the x component of velocity at different time instants.

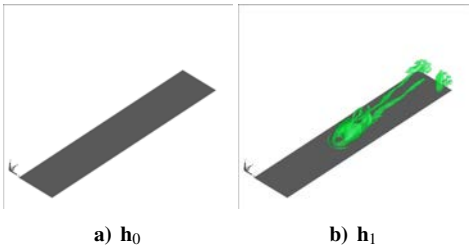

Figure 160: x-component of velocity. Top: DNS. Bottom: ROM, $n = 32$.

DISTRIBUTION A: Distribution approved for public release.

It is important to note that the fidelity of the ROM solution tends to decay as time advances. This becomes evident when the time history of $\bar{\chi}(t)$, or POD coefficients are visualized. Figure 161 shows the time history of the first and last 8 elements of $\bar{\chi}(t)$ as well as the projection of the DNS data to the POD coefficients $\{a_i(t)\}_{i=1}^{32}$. First, we notice that the ROM and DNS solutions match well at the beginning, and the time at which the DNS and ROM solutions start to diverge depends on the mode number. For example, the 7^{th} mode matches well up until $t = 5$, while the 1^{st} mode starts to diverge around $t = 1$. The figures also show that the amplitude of the higher modes grows in the ROM solution, while they stay 'small' in the projected DNS data. This behavior helps to explain the appearance of high frequency features in the flow in Figure 160. The solutions of the $n = 16$ ROM exhibit the same behavior but due to space limitations we do not present them. It is well known that ROMs usually diverge to a limit cycle not present in the original data as time advances, this has been reported in (17), (51), and chapter 5 in (66), among many others.

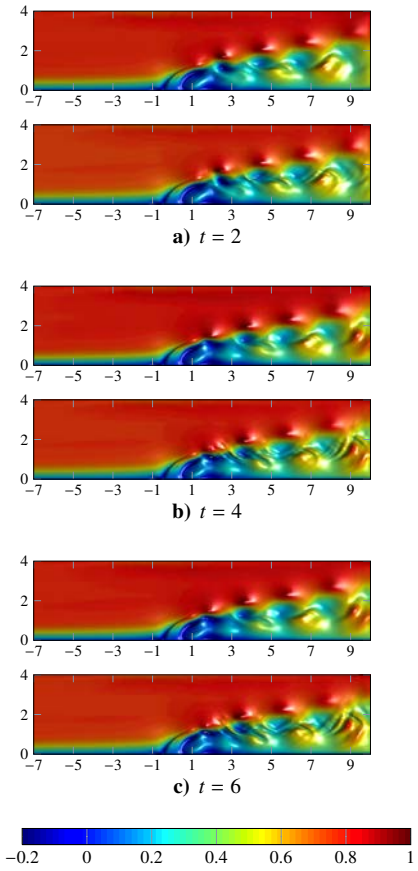

Figure 161: ROM (solid) and DNS (dotted) solution, $n = 32$

The error for the $n = 16$ model, as calculated in (24), is $E_{\mathbf{u}} = 1.99 \times 10^{-4}$ and the error for the $n = 32$ model is $E_{\mathbf{u}} = 1.95 \times 10^{-4}$. In addition, we plot the error in (24) as a function of time (i.e., the sequence) in Figure 162. Two observations that we obtain from that plot are that the difference in energy captured between a 16 and 32 order model is not significant

DISTRIBUTION A: Distribution approved for public release.

and that the difference is larger for low values of t. As time increases the error seems to converge to the same values for both $n = 16$ and $n = 32$.

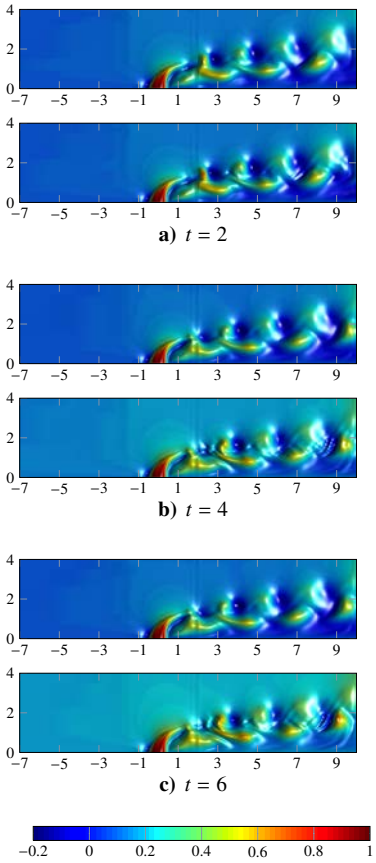

Figure 162: Error between DNS and ROM solution

4.3.2 Closed Loop Dynamics

Since the error dynamics for the $n = 16$ and $n = 32$ ROM are very similar, we focus on the $n = 16$ model for the controller design. The first issue we deal with is which operating point to pick. Using the MATLAB function `fsolve` we numerically solve

$$f(\bar{\chi}, \bar{u}, a_0) = 0$$

in (23) with $\bar{u} = 1$ and $a_0 = 1$ to obtain the desired operating point $\bar{\chi}_d^{(1)}$. To obtain the second operating point, $\bar{\chi}_d^{(2)}$, we set $\bar{u} = 1.0010$ and $a_0 = 1$. The values of the states for the first operating points is shown in Table 14. The second operating point is not reported due to space considerations.

DISTRIBUTION A: Distribution approved for public release.

State	Value		State	Value
$\bar{\chi}_{d_1}^{(1)}$	0.1804		$\bar{\chi}_{d_9}^{(1)}$	0.0112
$\bar{\chi}_{d_2}^{(1)}$	-0.2973		$\bar{\chi}_{d_{10}}^{(1)}$	0.0201
$\bar{\chi}_{d_3}^{(1)}$	-0.0015		$\bar{\chi}_{d_{11}}^{(1)}$	-0.0013
$\bar{\chi}_{d_4}^{(1)}$	0.0420		$\bar{\chi}_{d_{12}}^{(1)}$	0.0289
$\bar{\chi}_{d_5}^{(1)}$	0.0219		$\bar{\chi}_{d_{13}}^{(1)}$	0.0177
$\bar{\chi}_{d_6}^{(1)}$	-0.0690		$\bar{\chi}_{d_{14}}^{(1)}$	0.2212
$\bar{\chi}_{d_7}^{(1)}$	0.2815		$\bar{\chi}_{d_{15}}^{(1)}$	-0.4283
$\bar{\chi}_{d_8}^{(1)}$	0.3764		$\bar{\chi}_{d_{16}}^{(1)}$	-0.1707

Table 14: Operating point $\bar{\chi}_d^{(1)}$

With an operating point identified, we now study the stability of the operating point. Figure 163 clearly shows that if the ROM is solved with a small perturbation to $\bar{\chi}(0) = \bar{\chi}_d^{(1)}$, then the resulting solution eventually leaves the operating point.

To verify our intuition, Figure 164 shows the eigenvalues of the matrix A of the perturbation system at $\bar{\chi}_d^{(1)}$. The two pairs of eigenvalues on the right hand side of the imaginary axis reveal that the selected operating point is indeed unstable. The role of the feedback controller then is to shift the unstable eigenvalues to the left hand side of the imaginary axis and to enlarge the RoQA of the perturbation system.

Figure 165 shows the location of the eigenvalues of the matrix $A+BF$ of the perturbation ROM at $\bar{\chi}_d^{(1)}$ with the feedback gain F designed using the method in Section 4.2.

A similar argument holds for the perturbation system at $\bar{\chi}_d^{(2)}$, although we don't include the plots due to space constraints. The ROM solution of the perturbation system clearly depicts the stabilizing effect of the controller as shown in Figure 166.

We can see from Figure 166 that the RoQA is fairly small. This means that to stabilize the ROM, a fairly large number of switches will be required if the initial condition is far away from $\bar{\chi}_d^{(1)}$. However, this method provides us with an estimate of the RoQA while a simpler linearization study only provides local results, i.e., the RoQA may be vanishingly small. Figure 167 shows a two stage equilibria path simulation, from $\bar{\chi}_0$ to $\bar{\chi}_d^{(1)}$ and settling at $\bar{\chi}_d^{(2)}$.

The initial condition for the simulation is shown in Table 15. It is computed via our controller design method and lies in the maximized RoQA. The location of $\bar{\chi}_d^{(2)}$ is chosen such that $\bar{\chi}_d^{(1)}$ lies in the RoQA of $\bar{\chi}_d^{(2)}$. The switch occurs at $t = 12$ and clearly shows up in the plot of the control signal.

The result presented in Figure 167 corresponds to the setup shown in Figure 168 (a), i.e, the ROM. Once a state feedback F has been designed, it is inserted into a DNS simulation as shown in Figure 168 (b) and (c) to evaluate the performance of the controller in the full order model.

DISTRIBUTION A: Distribution approved for public release.

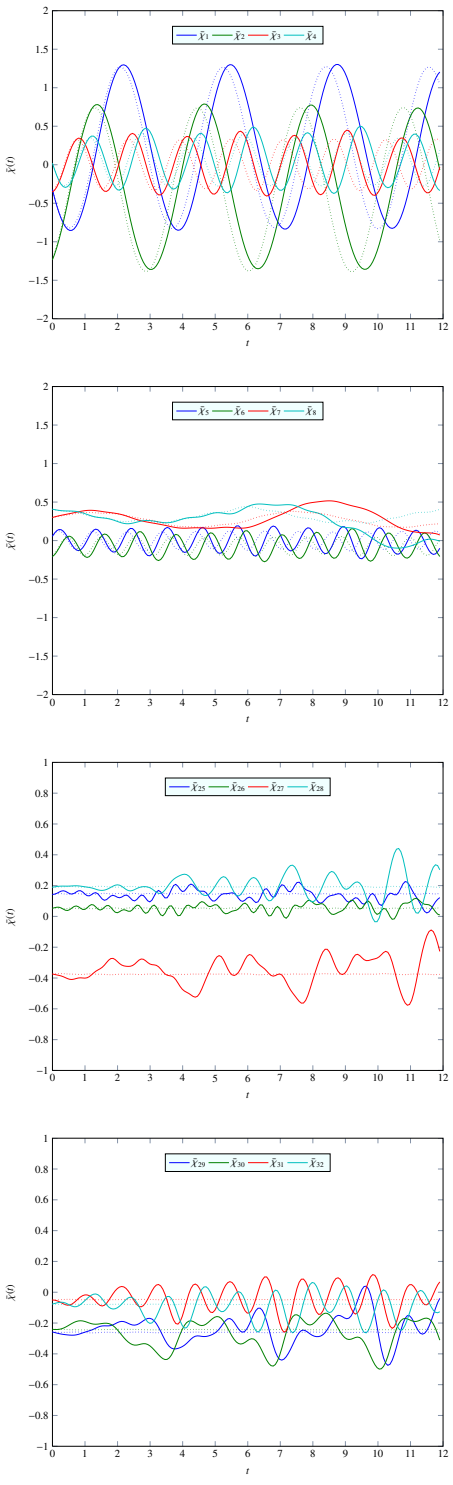

Figure 163: ROM solution with $\bar{\chi}_0 = \bar{\chi}_d^{(1)}$

DISTRIBUTION A: Distribution approved for public release.

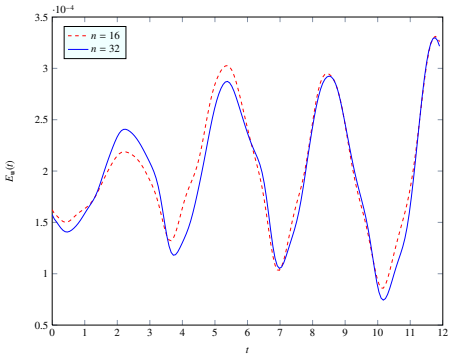

Figure 164: Eigenvalues of A (perturbation at $\bar{\chi}_d^{(1)}$)

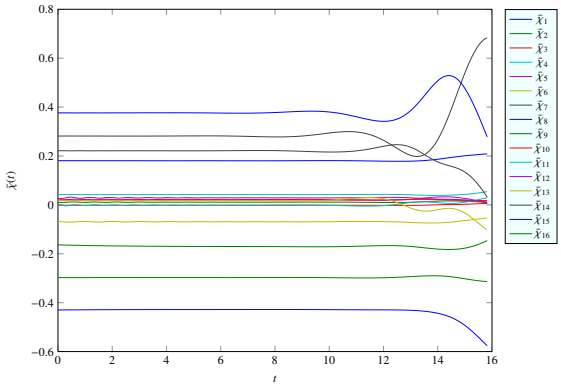

Figure 165: Eigenvalues of A+BF (perturbation at $\bar{\chi}_d^{(1)}$)

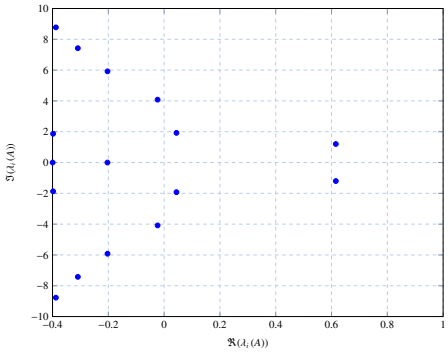

Figure 166: ROM solution in closed loop (perturbation at $\bar{\chi}_d^{(1)}$)

The results of the ROM and DNS in closed loop (implementation 1) are shown in Figure 169. There is a noticeable difference between the ROM and DNS solution starting at around $t = 2$ and from then onwards the DNS solution leaves the operating condition. In this sense, the behavior between the ROM and DNS solution is the same as in open loop, eventually the ROM solution loses fidelity. The solution using DNS implementation 2 behaves similarly

DISTRIBUTION A: Distribution approved for public release.

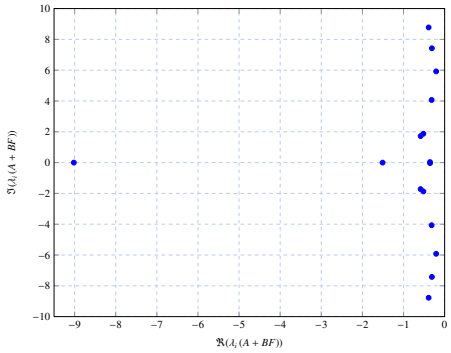

Figure 167: ROM solution in closed loop and input signal

State	Value		State	Value
$\bar{\chi}_1$	0.1807		$\bar{\chi}_9$	0.0108
$\bar{\chi}_2$	-0.2974		$\bar{\chi}_{10}$	0.0197
$\bar{\chi}_3$	-0.0015		$\bar{\chi}_{11}$	-0.0003
$\bar{\chi}_4$	0.0419		$\bar{\chi}_{12}$	0.0286
$\bar{\chi}_5$	0.0215		$\bar{\chi}_{13}$	0.0183
$\bar{\chi}_6$	-0.0688		$\bar{\chi}_{14}$	0.2212
$\bar{\chi}_7$	0.2815		$\bar{\chi}_{15}$	-0.4296
$\bar{\chi}_8$	0.3763		$\bar{\chi}_{16}$	-0.1657

Table 15: Initial condition for switched system simulation, $\bar{\chi}_0$

in the first few units of time, but the control signal calculated in this setup diverges from the signal $c_1(t)$ of Figure 168 (a) . After about $t = 2$ the control signal behaves erratically which illustrates the difficulty in implementing the control signal from the ROM to the DNS simulation.

4.4 Conclusion

We have presented a design method for feedback stabilization of a ROM of a jet in cross-flow. The proposed controller is linear and in addition to regionally stabilizing the nonlinear ROM, also enlarges the estimate of the RoQA. Stability is therefore guaranteed around a region of the operating point. The RoQA is computed by a simple formula based on the solution to a set of LMIs. The overall design consists of a sequence of linear controllers implemented in a switching strategy that regionally stabilize the desired equilibrium under the assumption that the system admits a centered-ϵ-cover. If this assumption is satisfied, then the switching controller will achieve semi-global stabilization of the nonlinear system. The controller that was designed based on the ROM was able to stabilize the flow to the selected operating point in DNS for a short time period until the DNS solution diverged to

DISTRIBUTION A: Distribution approved for public release.

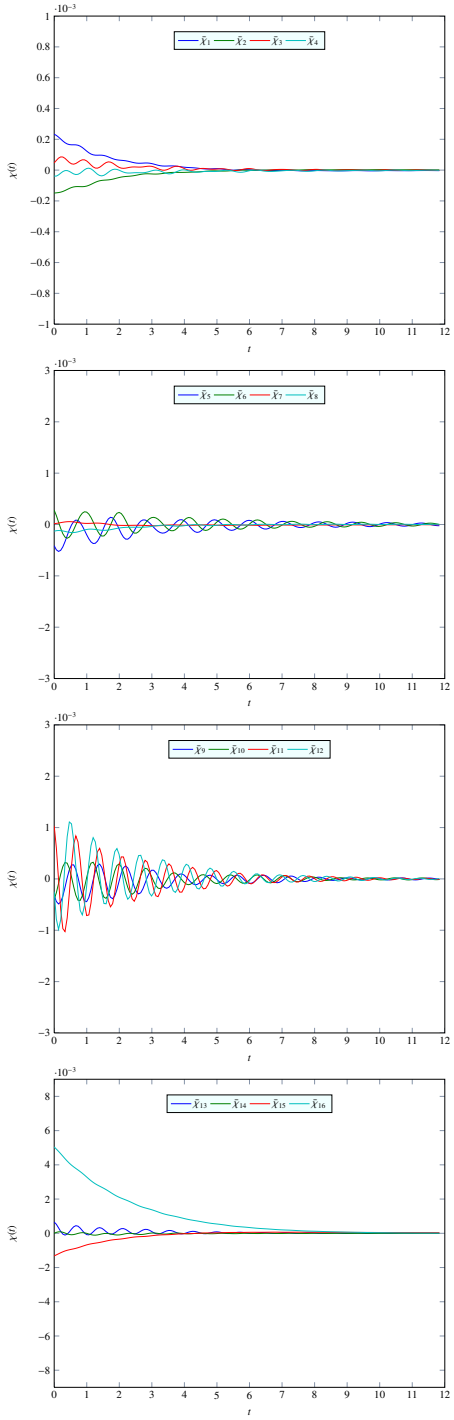

Figure 168: DNS closed loop implementations

another operating condition. This highlights the difficulties encountered when a controller is designed for a ROM and then implemented on the full system.

DISTRIBUTION A: Distribution approved for public release.

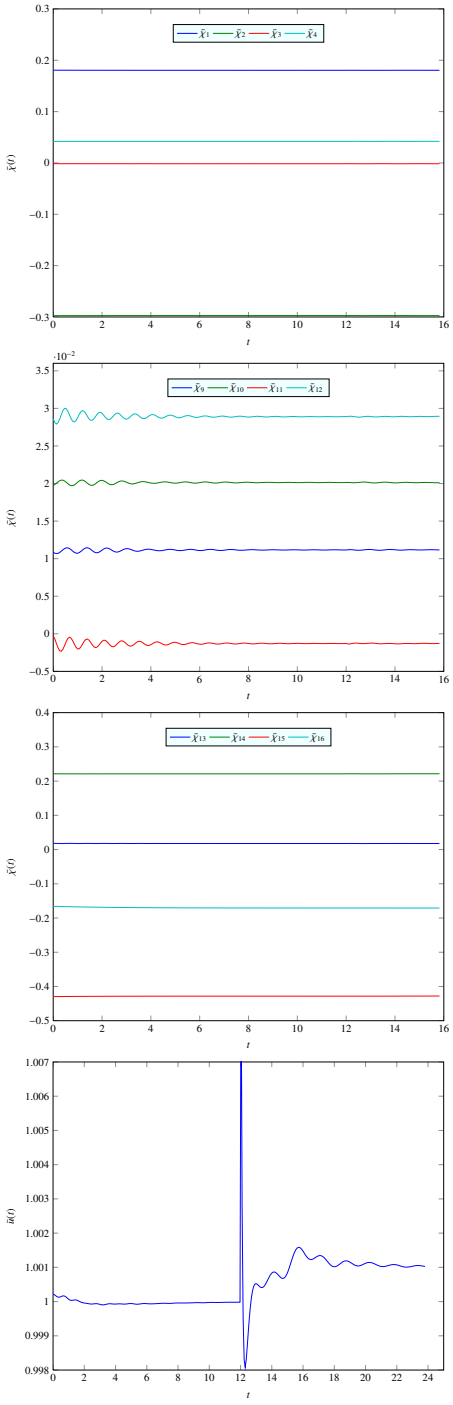

Figure 169: x-component of velocity in closed loop. Top: DNS. Bottom: ROM.

DISTRIBUTION A: Distribution approved for public release.

References

[1] S. Ahuja and C.W. Rowley. Feedback control of unstable steady states of flow past a flat plate using reduced-order estimators. *Journal of Fluid Mechanics*, 645:447–478, 2010.

[2] Luis Alvergue, Guoxiang Gu, and Sumanta Acharya. A generalized sector bound approach to feedback stabilization of nonlinear control systems. *International Journal of Robust and Nonlinear Control*, 23(14):1563–1580, 2013.

[3] M. Amitay, V. Kibens, D. Parekh, and A. Glezer. *The dynamics of flow reattachment over a thick airfoil controlled by synthetic jet actuators*. Aerospace Sciences Meetings. American Institute of Aeronautics and Astronautics, 1999. doi:10.2514/6.1999-1001.

[4] Hessam Babaee and Sumanta Acharya. A semi-staggered numerical procedure for the incompressible Navier-Stokes equations on curvilinear grids. In *ASME 2011 International Mechanical Engineering Congress and Exposition (IMECE2011)*, pages 927–936, 2011.

[5] Shervin Bagheri, Philipp Schlatter, Peter J. Schmid, and Dan S. Henningson. Global stability of a jet in crossflow. *Journal of Fluid Mechanics*, 624:33–44, 2009.

[6] Alexandre Barbagallo, Denis Sipp, and Peter J. Schmid. Closed-loop control of an open cavity flow using reduced-order models. *Journal of Fluid Mechanics*, 641:1–50, 2009.

[7] B. R. Barmish. Stabilization of uncertain systems via linear control. *IEEE Transactions on Automatic Control*, 28(8):848–850, 1983.

[8] C. M. Bell, P. M. Ligrani, W. A. Hull, and C. M. Norton. Film cooling subject to bulk flow pulsations: effects of blowing ratio, freestream velocity, and pulsation frequency. *International Journal of Heat and Mass Transfer*, 42(23):4333 – 4344, 1999.

[9] M. Bergmann, L. Cordier, and J-P. Brancher. Drag minimization of the cylinder wake by trust-region proper orthogonal decomposition. In Rudibert King, editor, *Active Flow Control*, volume 95 of *Notes on Numerical Fluid Mechanics and Multidisciplinary Design*, pages 309–324. Springer Berlin / Heidelberg, 2007.

[10] S. Bernsdorf, M. G. Rose, and R. S. Abhari. Modeling of film cooling—part i: Experimental study of flow structure. *Journal of Turbomachinery*, 128(1):141–149, 2006.

[11] Franco Blanchini. Set invariance in control. *Automatica*, 35(11):1747–1768, 1999.

[12] J. P. Bons, R. Sondergaard, and R. B. Rivir. Turbine separation control using pulsed vortex generator jets. *Journal of Turbomachinery*, 123(2):198–206, 2001.

[13] R. S. Bunker. A review of shaped hole turbine film-cooling technology. *Journal of Heat Transfer*, 127(4):441–453, 2005.

[14] John Burkardt, Max Gunzburger, and Hyung-Chun Lee. POD and CVT-based reduced-order modeling of Navier–Stokes flows. *Computer Methods Appl. Mech. Engrg.*, 196:337–355, 2006.

DISTRIBUTION A: Distribution approved for public release.

[15] W. Cazemier, R. W. C. P. Verstappen, and A. E. P. Veldman. Proper orthogonal decomposition and low-dimensional models for driven cavity flows. *Physics of Fluids*, 10(7):1685–1699, 1998.

[16] Pinaki Chakraborty, S. Balachandar, and Ronald J. Adrian. On the relationships between local vortex identification schemes. *Journal of Fluid Mechanics*, 535:189–214, 2005.

[17] Tim Colonius Clarence W. Rowley and Richard M. Murray. Model reduction for compressible flows using POD and Galerkin projection. *Physica D*, 189:115–129, 2004.

[18] Debora A Compton and James P Johnston. Streamwise vortex production by pitched and skewed jets in a turbulent boundary layer. *AIAA journal*, 30(3):640–647, 1992.

[19] Martin Corless. Robust stability analysis and controller design with quadratic Lyapunov functions. In Alan Zinober, editor, *Variable Structure and Lyapunov Control*, volume 193 of *Lecture Notes in Control and Information Sciences*, pages 181–203. Springer Berlin / Heidelberg, 1994.

[20] L. Cortelezzi and A. R. Karagozian. On the formation of the counter-rotating vortex pair in transverse jets. *Journal of Fluid Mechanics*, 446:347–373, 2001.

[21] S. M. Coulthard, R. J. Volino, and K. A. Flack. Effect of jet pulsing on film cooling-part i: Effectiveness and flow-field temperature results. *Journal of Turbomachinery*, 129(2):232–246, 2007.

[22] M. Couplet, C. Basdevant, and P. Sagaut. Calibrated reduced-order pod-galerkin system for fluid flow modelling. *Journal of Computational Physics*, 207(1):192–220, 2005.

[23] A. E. Deane, I. G. Kevrekidis, G. E. Karniadakis, and S. A. Orszag. Low dimensional models for complex geometry flows: Application to grooved channels and circular cylinders. *Physics of Fluids A*, 3(10):2337–2354, 1991.

[24] J. R. Dormand and P. J. Prince. A family of embedded runge-kutta formulae. *Journal of Computational and Applied Mathematics*, 6(1):19 – 26, 1980.

[25] S. V. Ekkad, S. Ou, and R. B. Rivir. Effect of jet pulsation and duty cycle on film cooling from a single jet on a leading edge model. *Journal of Turbomachinery*, 128(July 2006):564–571, 2006.

[26] T. F. Fric and A. Roshko. Vortical structure in the wake of a transverse jet. *Journal of Fluid Mechanics*, 279:1–47, 1994.

[27] Roberto Genesio, Michele Tartaglia, and Antonio Vicino. On the estimation of asymptotic stability regions: State of the art and new proposals. *IEEE Transactions on Automatic Control*, 30(8):747–755, 1985.

[28] S. Gopalan, B. M. Abraham, and J. Katz. The structure of a jet in cross flow at low velocity ratios. *Physics of Fluids*, 16(6):2067–2087, 2004.

DISTRIBUTION A: Distribution approved for public release.

[29] W. R. Graham, J. Peraire, and K. Y. Tang. Optimal control of vortex shedding using low-order models. part i - open-loop model development. *International Journal for Numerical Methods in Engineering*, 44(7):945–972, 1999.

[30] W. R. Graham, J. Peraire, and K. Y. Tang. Optimal control of vortex shedding using low-order models. part ii - model-based control. *International Journal for Numerical Methods in Engineering*, 44(7):973–990, 1999.

[31] X. Guo, W. Schroder, and M. Meinke. Large-eddy simulations of film cooling flows. *Computers & Fluids*, 35(6):587–606, 2006.

[32] L Hansen and J Bons. Flow measurements of vortex generator jets in separating boundary layer. *Journal of propulsion and power*, 22(3):558–566, 2006.

[33] FS Henry and H Pearcey. Numerical model of boundary-layer control using air-jet generated vortices. *AIAA journal*, 32(12):2415–2425, 1994.

[34] P. Holmes, J. L. Lumley, and G. Berkooz. *Turbulence, coherent structures, dynamical systems and symmetry*. Cambridge Univ Pr, 1998.

[35] Philip Holmes, John L. Lumley, and Gal Berkooz. *Turbulence, Coherent Structures, Dynamical Systems and Symmetry*. Cambridge University Press, 1996.

[36] M. Ilak and C. W. Rowley. Modeling of transitional channel flow using balanced proper orthogonal decomposition. *Physics of Fluids*, 20(3):034103–17, 2008.

[37] Miloš Ilak, Philipp Schlatter, Shervin Bagheri, and Dan S. Henningson. Bifurcation and stability analysis of a jet in crossflow: onset of global instability at a low velocity ratio. *Journal of Fluid Mechanics*, 696:94–121, 2012.

[38] J. Jeong and F. Hussain. On the identification of a vortex. *Journal of Fluid Mechanics*, 285:69–94, 1995.

[39] Sanjay S. Joshi, Jason L. Speyer, and John Kim. A systems theory approach to the feedback stabilization of infinitesimal and finite-amplitude disturbances in plane poiseuille flow. *Journal of Fluid Mechanics*, 332:157–184, 1997.

[40] Coşku Kasnakoğlu, Andrea Serrani, and Mehmet Önder Efe. Control input separation by actuation mode expansion for flow control problems. *International Journal of Control*, 81:1475–1492, 2008.

[41] R. M. Kelso, T. T. Lim, and A. E. Perry. An experimental study of round jets in cross-flow. *Journal of Fluid Mechanics*, 306:111–144, 1996.

[42] R. M. Kelso and A. J. Smits. Horseshoe vortex systems resulting from the interaction between a laminar boundary layer and a transverse jet. *Physics of Fluids*, 7(1):153–8, 1995.

[43] Michael Kirby. *Geometric Data Analysis: An Empirical Approach to Dimensionality Reduction and the Study of Patterns*. Wiley-Interscience, 2000.

DISTRIBUTION A: Distribution approved for public release.

[44] A. Krothapalli and L. Lourenco. Separated flow upstream of a jet in crossflow. *AIAA Journal*, 28(3):414–420, 1990.

[45] Miroslav Krstić, Ioannis Kanellakopoulos, and Petar V. Kokotović. *Nonlinear and Adaptive Control Design*. John Wiley & Sons, USA, 1995.

[46] P. S. Krueger, J. O. Dabiri, and M. Gharib. The formation number of vortex rings formed in uniform background co-flow. *Journal of Fluid Mechanics*, 556:147–166, 2006.

[47] Sang Woo Lee, Joon Sik Lee, and Sung Tack Ro. Experimental study on the flow characteristics of streamwise inclined jets in crossflow on flat plate. *Journal of turbomachinery*, 116(1):97–105, 1994.

[48] P. M. Ligrani, R. Gong, J. M. Cuthrell, and J. S. Lee. Bulk flow pulsations and film cooling - i. injectant behavior. *International Journal of Heat and Mass Transfer*, 39(11):2271–2282, 1996.

[49] P. M. Ligrani, R. Gong, J. M. Cuthrell, and J. S. Lee. Bulk flow pulsations and film cooling - ii. flow structure and film effectiveness. *International Journal of Heat and Mass Transfer*, 39(11):2283 – 2292, 1996.

[50] JC Lin, FG Howard, DM Bushnell, and GV Selby. Investigation of several passive and active methods for turbulent flow separation control. In *AIAA, Fluid Dynamics, 21st Plasma Dynamics and Lasers Conference, 21st, Seattle, WA, June 18-20, 1990. 17 p.*, volume 1, 1990.

[51] Xia Ma and George M. Karniadakis. A low-dimensional model for simulating three-dimensional cylinder flow. *Journal of Fluid Mechanics*, 458:181–190, 2002.

[52] Y. M. Marzouk and A. F. Ghoniem. Vorticity structure and evolution in a transverse jet. *Journal of Fluid Mechanics*, 575:267–305, 2007.

[53] K. T. McGovern and J. H. Leylek. A detailed analysis of film cooling physics: Part ii—compound-angle injection with cylindrical holes. *Journal of Turbomachinery*, 122(1):113–121, 2000.

[54] Keith R McManus, Hartmut H Legner, and Steven J Davis. Pulsed vortex generator jets for active control of flow separation. *AIAA paper*, (94-2218):5, 1994.

[55] D. E. Nikitopoulos, S. Acharya, J. Oertling, and F. H. Muldoon. On active control of film-cooling flows. In *ASME Turbo Expo*, 2006.

[56] D. E. Nikitopoulos and J. T. C. Liu. Nonlinear binary-mode interactions in a developing mixing layer. *Journal of Fluid Mechanics*, 179(1):345–370, 1987.

[57] D. E. Nikitopoulos and J. T. C. Liu. Nonlinear three-mode interactions in a developing mixing layer. *Physics of Fluids*, 13:966, 2001.

[58] B. R. Noack, P. Papas, and P. A. Monkewitz. The need for a pressure-term representation in empirical galerkin models of incompressible shear flows. *Journal of Fluid Mechanics*, 523:339–365, 2005.

DISTRIBUTION A: Distribution approved for public release.

[59] Bernd R. Noack, Gilead Tadmor, and Marek Morzyński. Actuation models and dissipative control in empirical galerkin models of fluid flows. In *2004 American Control Conference*, pages 5722–5727, 2004.

[60] Bernd R. Noack, Gilead Tadmor, and Marek Morzyński. Low-dimensional models for feedback flow control. part I: Empirical galerkin models. In *2nd AIAA Flow Control Conference*, 2004.

[61] M. Raffel, C. E. Willert, and J. Kompenhans. *Particle image velocimetry: a practical guide*. Springer Verlag, 1998.

[62] S. Raghunathan, J. Watterson, R. Cooper, and S. Lee. *Short wide angle diffuser with pulse jet control*. Aerospace Sciences Meetings. American Institute of Aeronautics and Astronautics, 1999. doi:10.2514/6.1999-280.

[63] S. S. Ravindran. Reduced-order adaptive controllers for fluid flows using pod. *Journal of Scientific Computing*, 15(4):457–478, 2000.

[64] S.S. Ravindran. Optimal boundary feedback flow stabilization by model reduction. *Computer Methods Appl. Mech. Engrg.*, 196:2555–2569, 2007.

[65] C. W. Rowley. Model reduction for fluids, using balanced proper orthogonal decomposition. *International Journal of Bifurcation Chaos in Applied Sciences and Engineering*, 15(3):997–1014, 2005.

[66] Clarence Rowley. *Modeling, Simulation, and Control of Cavity Flow Oscillations*. PhD thesis, California Institute of Technology, 2002.

[67] R. Sau and K. Mahesh. Dynamics and mixing of vortex rings in crossflow. *Journal of Fluid Mechanics*, 604:389–409, 2008.

[68] Onofrio Semeraro, Servin Bagheri, Luca Brandt, and Dan S. Henningson. Feedback control of three-dimensional optimal disturbances using reduced-order models. *Journal of Fluid Mechanics*, 677:63–102, 2011.

[69] L. F. Shampine and M. K. Gordon. *Computer solution of ordinary differential equations : the initial value problem*. San Francisco : W. H. Freeman, 1975. Includes index.

[70] Lawrence Sirovich. Turbulence and the dynamics of coherent structures part i: Coherent structures. *Quarterly of Applied Mathematics*, 45(3):561–571, 1987.

[71] M. Thompson, K. Hourigan, and J. Sheridan. Three-dimensional instabilities in the wake of a circular cylinder. *Experimental Thermal and Fluid Science*, 12(2):190–196, 1996.

[72] M. Tyagi and S. Acharya. Large eddy simulation of film cooling flow from an inclined cylindrical jet. *Journal of Turbomachinery*, 125(4):734–742, 2003.

[73] R. Vernet, L. Thomas, and L. David. Analysis and reconstruction of a pulsed jet in crossflow by multi-plane snapshot pod. *Experiments in Fluids*, 47:707–720, 2009. 10.1007/s00348-009-0730-6.

DISTRIBUTION A: Distribution approved for public release.

[74] C. Vezier. Dynamics of vortical structures in a low-blowing-ratio pulsed transverse jet. Master's thesis, Louisiana State University, 2009.

[75] C. H. K. Williamson. Vortex dynamics in the cylinder wake. *Annual Review of Fluid Mechanics*, 28(1):477–539, 1996.

[76] K. M. Womack, R. J. Volino, and M. P. Schultz. Combined effects of wakes and jet pulsing on film cooling. *Journal of Turbomachinery*, 130(4):041010–12, 2008.

[77] K. M. Womack, R. J. Volino, and M. P. Schultz. Measurements in film cooling flows with periodic wakes. *Journal of Turbomachinery*, 130(4):041008, 2008.

[78] Jie-Zhi Wu, Xi-Yun Lu, Andrew G Denny, Meng Fan, and Jain-Ming Wu. Post-stall flow control on an airfoil by local unsteady forcing. *Journal of Fluid Mechanics*, 371(1):21–58, 1998.

[79] C. H. N. Yuen and R. F. Martinez-Botas. Film cooling characteristics of a single round hole at various streamwise angles in a crossflow: Part i effectiveness. *International Journal of Heat and Mass Transfer*, 46(2):221 – 235, 2003.

DISTRIBUTION A: Distribution approved for public release.

AFOSR Deliverables Submission Survey

Response ID:3056 Data

1.

If you have any questions, please contact your Program Manager or Assistant Program Manager.

Air Force Office of Science and Research
875 Randolph Street
Suite 325 Room 3112
Arlington, VA 22203

1. Report Type

Final Report

Primary Contact E-mail
Contact email if there is a problem with the report.

medimi@lsu.edu

Primary Contact Phone Number
Contact phone number if there is a problem with the report

225-663-0583

Organization / Institution name

Louisiana State University

Award Information

Grant/Contract Title
The full title of the funded effort.

Towards Combined Active Control of Film Cooling and Turbine Blade Aerodynamics.Towards Combined Active Control of Film Cooling and Turbine Blade Aerodynamics

Grant/Contract Number
AFOSR assigned control number. It must begin with "FA9550" or "F49620" or "FA2386".

FA9550-08-1-0440

Principal Investigator Name
The full name of the principal investigator on the grant or contract.

Dimitris E. Nikitopoulos

Program Manager
The AFOSR Program Manager currently assigned to the award

Dr. Douglas Smith

Report Information - Annual Report

Report Information - Final Report

DISTRIBUTION A: Distribution approved for public release.

Report Information - Conference/Workshop Report

Report Information - Equipment Report

Report Information - Patent/Invention Report, DD882

Report Information - Financial Report, SF425

Report Information - STTR Status Report

Report Information - STTR Annual Progress Report

For an annual report, the reporting period start date is either start date of the grant, if this is the first report, or 1 day after the due date of the previous report. The end date is due date of this report.

The reporting period start and end dates are the start and end dates of the award.

Reporting Period Start Date

8/15/2008

Reporting Period End Date

8/14/2013

Report Abstract:

In the Abstract section, please list any accomplishments that have been made since the last report submission (or since the beginning of the award if this is the first report).
Please do not type "see report" here, include at least an abstract, 250 words or more, of the accomplishments mentioned in your report.

Report Abstract:

In the Abstract section, enter the Final Conference Report. This is a summary of all scientific papers presented and a list of all attendees.

Report Abstract:

In the Abstract section, enter the Final Performance Report.

The Final Performance Report will identify the acquired equipment (although it may vary from that described in your proposal) by name and associated costs. The Final Performance Report shall summarize the research or educational project for which the equipment will be used.

The patent and inventions coverage contained in Article 36, Intangible Property, of the Research Terms and Conditions does not apply to this award.

DISTRIBUTION A: Distribution approved for public release.

Article 15, Intangible Property, in the AFOSR Agency Specific Requirements does not apply to this award.

Abstract

In this study, actively controlled film cooling flows were investigated in view of improved film cooling metrics and increased adaptability using experimental and numerical methods. In the first place a mechanistic analysis was carried out on unforced and forced film cooling geometries of a vertical and an inclined jet in cross-flow. Using experimental measurements and visualizations, as well as Large Eddy simulations, characteristic vortical system regimes for forced film cooling jets were evidenced and scaling parameters governing those regimes were identified. A cutting edge linear cascade facility including a realistic wake generator was designed, fabricated and validated and characterization of the L1-A blade profile wake under periodic unsteady free-stream conditions were conducted. PIV measurements and Mie scattering visualizations evidenced the effect of the wake on film cooling jets as it impinged the blade. An optimization method using Direct Numerical Simulations was developed to identify optimum forcing parameters for improved film cooling metrics. The first Reduced Order Models (ROMs) of unforced and forced film cooling jets velocity and temperature fields were derived using the POD-Galerkin projection method. ROM stabilization techniques were developed and implemented to improve the models stability and accuracy. The impact of forcing parameters on film cooling ROMs, in particular blowing ratio and forcing frequency, were investigated and evidenced the necessity to implement efficient stabilization methods at high jet blowing ratios. Finally, a linear state feedback controller for stabilization of a POD-based ROM of film cooling system was developed and implemented. The sequence of linear controllers regionally stabilizing the desired equilibrium was used to successfully stabilize a film cooling jet ROM to a steady low kinetic energy flow. The designed controller was able to stabilize the flow to the selected operating point in DNS for a short time period until the DNS solution diverged to another operating condition.

Distribution Statement
This is block 12 on the SF298 form.

Distribution A - Approved for Public Release

Explanation for Distribution Statement
If this is not approved for public release, please provide a short explanation. E.g., contains proprietary information.

NOTE: Extra documentation is NOT required for this report. If you would like to send additional documentation, send it directly to your Program Manager or Assistant Program Manager.

SF298 Form
Please attach your SF298 form. A blank SF298 can be found here. Please do not spend extra effort to password protect or secure the PDF, we want to read your SF298. The maximum file size for SF298's is 50MB.

AFD-070820-035_v4_print.pdf

Upload the Report Document. The maximum file size for the Report Document is 50MB.

FA9550-08-1-0440_Final_Report.pdf

Upload a Report Document, if any. The maximum file size for the Report Document is 50MB.

Additional Information

Archival Publications (published) during reporting period:

Guillaume Bidan and Dimitris E. Nikitopoulos, “Fundamental Study of Modulated Transverse Jets from a Film-Cooling Perspective”, AIAA Journal, Vol. 49, No. 7 (2011), pp. 1498-1510, doi: 10.2514/1.J050903.

Alvergue, Luis, Guoxiang Gu, and Sumanta Acharya, “A generalized sector-bound approach to feedback stabilization of nonlinear control systems”, International Journal of Robust and Nonlinear Control (2012), Vol. 23, No. 14, pp.1563-1580, doi: 10.1002/rnc.2843.

Guillaume Bidan, Clémentine Vézier and Dimitris E. Nikitopoulos, “Study of unforced and modulated film-cooling jets using proper orthogonal decomposition–part I: unforced jets”, Journal of Turbomachinery, Vol. 135, No. 2 (2013), pp. 021037, doi: 10.1115/1.4006599.

Guillaume Bidan, Clémentine Vézier and Dimitris E. Nikitopoulos, “Study of unforced and modulated film-cooling jets using proper orthogonal decomposition–part II: forced jets”, Journal of Turbomachinery, Vol. 135, No. 2 (2013), pp. 021038, doi: 10.1115/1.4006600.

Guillaume Bidan and Dimitris E. Nikitopoulos, “On steady and pulsed low-blowing ratio transverse jets”, Journal of Fluid Mechanics, Vol. 714 (2013), pp. 393-433, doi: i:10.1017/jfm.2012.482.

Luis Alvergue, Guoxiang Gu, and Sumanta Acharya, “A Generalized Sector Bound Approach to Feedback Stabilization of Nonlinear Control Systems”, International Journal of Robust and Nonlinear Control, Vol. 23, No. 14 (2013), pp. 1563-1580.

Changes in research objectives (if any):

The experimental work has been delayed by a period of approximately 20 months starting shortly after the beginning of the grant. There are two major reasons for the delay. First, a leak on the roof of the wind-tunnel laboratory building caused by a tree fall during hurricane Gustav (9/2008) destroyed the pulsed laser used for visualizations and PIV and caused the warping of the wind-tunnel screen and contraction sections, which resulted in unacceptably poor flow quality for experiments. The second cause for this delay was the subsequent renovation of the building in which the Wind-Tunnel is located, and in which the cascade facility for this project would be located. The construction shut down operations from 1/2009-7/2010. These problems and delays were documented in the annual reports for the project as they occurred. During this period no experiments could be conducted, and indeed they did not start in earnest until 9/2010 after the laboratory was cleaned and the equipment reconnected and tested.

Heat transfer measurements on the cascade facility were not possible and were not carried out;

A new cascade facility was designed and built in view of an existing one not being adequate for the purpose and not being serviceable. The latter was dismantled and rendered not operational because of it being transferred to another building. Furthermore, the wake generator of this facility did not meet the desired requirements. This in addition to the aforementioned delays resulting from the damages caused by hurricane Gustav and construction work, significantly affected the progress of experimental measurements on realistic film cooling systems. For these reasons, investigations on interactions between film cooling jets and flow separation region were not possible, and focus was kept on investigation of forced film cooling physics, their optimization and reduced order modeling.

The fundamental scope of work was substantially expanded in order to meet the challenges of developing 3D reduced order models for the complex film-cooling flows addressed by the project. This was deemed necessary in order to lay the groundwork towards the combined active control of film cooling flows and turbine blade aerodynamics.

Based on these considerations, the initial objectives were changed to:

Experimental investigations:

To perform a fundamental mechanistic analysis of unforced and forced low blowing ratio jets in cross-flow. To this end, both vertical and inclined low blowing ratios forced and unforced jets in cross-flow will be investigated in an effort to extend the otherwise extensive literature concerning those flows at high blowing ratios.

To develop, build and characterize a realistic film cooling linear cascade type capable of producing engine like Reynolds numbers (Re\simeq500,000
) with realistic incoming wake signatures. This facility would be capable of reproducing engine conditions in the turbine stages beyond the first nozzle guide vanes. This facility will be designed around an AFRL L1-A profile, equipped with film cooling holes.

To provide support in developing a reduced order model of unforced and forced film cooling velocity and temperature fields.

Numerical effort:

To identify optimum forcing conditions for forced film cooling systems. To this end, Direct Numerical Simulations of film cooling systems will be carried out and a methodology for the identification of optimum forcing parameters will be developed.

Investigate in detail the influence of control actions on the ROMs and contribute to their development from simulation data.

Implement and assess the feedback control scheme/algorithm through numerical simulation experiments.

To develop a reduced order model of unforced and forced film cooling velocity and temperature fields. .

Theoretical control:

Develop a feedback flow-control algorithm utilizing ROMs emanating from corresponding tasks of the

experimental and numerical efforts. Part of this task was also to be directed to the development of the ROMs themselves.

Support the implementation of this algorithm on the physical as well as on the numerical experiments and assess its performance.

Change in AFOSR Program Manager, if any:

Grant was initially set up under Dr. John Schmisseur

Extensions granted or milestones slipped, if any:

A no-cost extension was granted in 2011 for two years.

For an STTR Status or STTR Annual Progress Report, please e-mail your program manager directly.

AFOSR LRIR Number

LRIR Title

Reporting Period

Laboratory Task Manager

Program Officer

Report Information - LRIR Report

Research Objectives

Technical Summary

Funding Summary by Cost Category (by FY, $K)

	Starting FY	FY+1	FY+2
Non-Military Government Personnel Costs			
In-house Contractor Costs			
Travel (Be Specific)			
Training (Be Specific)			
Supplies			
Other Expenses (Be Specific)			
Total Resource Requirements			

Report Document

Appendix Documents

2. Thank You

E-mail user

Nov 14, 2013 17:26:53 Success: Email Sent to: medimi@lsu.edu

Your report has been submitted. You should receive an email confirmation soon that it is being processed by AFOSR. Please print this page as proof of submission. Thank you.

Principal Investigator Name: Dimitris E. Nikitopoulos

Primary medimi@lsu.edu

DISTRIBUTION A: Distribution approved for public release.

Contact E-mail:	
Primary Contat Phone Number:	225-663-0583
Grant/Contract Title:	Towards Combined Active Control of Film Cooling and Turbine Blade Aerodynamics.Towards Combined Active Control of Film Cooling and Turbine Blade Aerodynamics
Grant/Contract Number:	FA9550-08-1-0440
Program Manager:	Dr. Douglas Smith
Report Type:	Final Technical
Reporting Period Start Date:	8/15/2008
Reporting Period End Date:	8/14/2013
Abstract:	In this study, actively controlled film cooling flows were investigated in view of improved film cooling metrics and increased adaptability using experimental and numerical methods. In the first place a mechanistic analysis was carried out on unforced and forced film cooling geometries of a vertical and an inclined jet in cross-flow. Using experimental measurements and visualizations, as well as Large Eddy simulations, characteristic vortical system regimes for forced film cooling jets were evidenced and scaling parameters governing those regimes were identified. A cutting edge linear cascade facility including a realistic wake generator was designed, fabricated and validated and characterization of the L1-A blade profile wake under periodic unsteady free-stream conditions were conducted. PIV measurements and Mie scattering visualizations evidenced the effect of the wake on film cooling jets as it impinged the blade. An optimization method using Direct Numerical Simulations was developed to identify optimum forcing parameters for improved film cooling metrics. The first Reduced Order Models (ROMs) of unforced and forced film cooling jets velocity and temperature fields were derived using the POD-Galerkin projection method. ROM stabilization techniques were developed and implemented to improve the models stability and accuracy. The impact of forcing parameters on film cooling ROMs, in particular blowing ratio and forcing frequency, were investigated and evidenced the necessity to implement efficient stabilization methods at high jet blowing ratios. Finally, a linear state feedback controller for stabilization of a POD-based ROM of film cooling system was developed and implemented. The sequence of linear controllers regionally stabilizing the desired equilibrium was used to successfully stabilize a film cooling jet ROM to a steady low kinetic energy flow. The designed controller was able to stabilize the flow to the selected operating point in DNS for a short time period until the DNS solution diverged to another operating condition.
Distribution Statement:	Distribution A - Approved for Public Release
SF298 Form:	11-f62241dd063486fd521bcee8b78e649a_AFD-070820-035_v4_print.pdf
Report Document	55-fb6ff20f97e3a8ecfb82aafbad4fafb3_FA9550-08-1-0440_Final_Report.pdf
Archival Publications:	Guillaume Bidan and Dimitris E. Nikitopoulos, “Fundamental Study of Modulated Transverse Jets from a Film-Cooling Perspective”, AIAA Journal, Vol. 49, No. 7 (2011), pp. 1498-1510, doi: 10.2514/1.J050903. Alvergue, Luis, Guoxiang Gu, and Sumanta Acharya, “A generalized sector-bound approach to feedback stabilization of nonlinear control systems”, International Journal of Robust and Nonlinear Control (2012), Vol. 23, No. 14, pp.1563-1580, doi: 10.1002/rnc.2843. Guillaume Bidan, Clémentine Vézier and Dimitris E. Nikitopoulos, “Study of unforced and modulated film-cooling jets using proper orthogonal decomposition–part I: unforced jets”, Journal of Turbomachinery, Vol. 135, No. 2 (2013), pp. 021037, doi: 10.1115/1.4006599. Guillaume Bidan, Clémentine Vézier and Dimitris E. Nikitopoulos, “Study of unforced and modulated film-cooling jets using proper orthogonal decomposition–part II: forced jets”, Journal of Turbomachinery, Vol. 135, No. 2 (2013), pp. 021038, doi: 10.1115/1.4006600. Guillaume Bidan and Dimitris E. Nikitopoulos, “On steady and pulsed low-blowing ratio transverse jets”, Journal of Fluid Mechanics, Vol. 714 (2013), pp. 393-433, doi: i:10.1017/jfm.2012.482. Luis Alvergue, Guoxiang Gu, and Sumanta Acharya, “A Generalized Sector Bound Approach to Feedback Stabilization of Nonlinear Control Systems”, International Journal of Robust and Nonlinear Control, Vol. 23, No. 14 (2013), pp. 1563-1580.
Changes in Research objectives:	The experimental work has been delayed by a period of approximately 20 months starting shortly after the beginning of the grant. There are two major reasons for the delay. First, a leak on the roof of the wind-tunnel laboratory building caused by a tree fall during hurricane Gustav (9/2008) destroyed the pulsed laser used for visualizations and PIV and caused the warping of the wind-tunnel screen and contraction sections, which resulted in unacceptably poor flow quality for experiments. The second cause for this delay was the subsequent renovation of the building in which the Wind-Tunnel is located, and in which the cascade facility for this project would be located. The construction shut down operations from 1/2009-7/2010. These problems and delays were documented in the annual reports for the project as they occurred. During this period no experiments could be conducted, and indeed they did not start in earnest until 9/2010 after the laboratory was cleaned and the equipment reconnected and tested. Heat transfer measurements on the cascade facility were not possible and were not carried out; A new cascade facility was designed and built in view of an existing one not being adequate for the purpose and not being serviceable. The latter was dismantled and rendered not operational because of it being transferred to another building. Furthermore, the wake generator of this facility did not meet the desired requirements. This in addition to the aforementioned delays resulting from the damages caused by hurricane Gustav and construction work significantly affected the

DISTRIBUTION A: Distribution approved for public release.

progress of experimental measurements on realistic film cooling systems. For these reasons, investigations on interactions between film cooling jets and flow separation region were not possible, and focus was kept on investigation of forced film cooling physics, their optimization and reduced order modeling.

The fundamental scope of work was substantially expanded in order to meet the challenges of developing 3D reduced order models for the complex film-cooling flows addressed by the project. This was deemed necessary in order to lay the groundwork towards the combined active control of film cooling flows and turbine blade aerodynamics.

Based on these considerations, the initial objectives were changed to:

Experimental investigations:

To perform a fundamental mechanistic analysis of unforced and forced low blowing ratio jets in cross-flow. To this end, both vertical and inclined low blowing ratios forced and unforced jets in cross-flow will be investigated in an effort to extend the otherwise extensive literature concerning those flows at high blowing ratios.

To develop, build and characterize a realistic film cooling linear cascade type capable of producing engine like Reynolds numbers (Resimeq500,000
) with realistic incoming wake signatures. This facility would be capable of reproducing engine conditions in the turbine stages beyond the first nozzle guide vanes. This facility will be designed around an AFRL L1-A profile, equipped with film cooling holes.

To provide support in developing a reduced order model of unforced and forced film cooling velocity and temperature fields.

Numerical effort:

To identify optimum forcing conditions for forced film cooling systems. To this end, Direct Numerical Simulations of film cooling systems will be carried out and a methodology for the identification of optimum forcing parameters will be developed.

Investigate in detail the influence of control actions on the ROMs and contribute to their development from simulation data.

Implement and assess the feedback control scheme/algorithm through numerical simulation experiments.

To develop a reduced order model of unforced and forced film cooling velocity and temperature fields. .

Theoretical control:

Develop a feedback flow-control algorithm utilizing ROMs emanating from corresponding tasks of the experimental and numerical efforts. Part of this task was also to be directed to the development of the ROMs themselves.

Support the implementation of this algorithm on the physical as well as on the numerical experiments and assess its performance.

Change in AFOSR Program Manager, if any: Grant was initially set up under Dr. John Schmisseur

Extensions granted or milestones slipped, if any: A no-cost extension was granted in 2011 for two years.

Response ID: 3056

Survey Submitted:	Nov 14, 2013 (5:26 PM)
IP Address:	130.39.97.186
Language:	English (en-US,en;q=0.8,de;q=0.6,fr;q=0.4)
User Agent:	Mozilla/5.0 (X11; Linux x86_64) AppleWebKit/537.36 (KHTML, like Gecko) Chrome/28.0.1500.71 Safari/537.36
Http Referrer:	http://www.wpafb.af.mil/library/factsheets/factsheet.asp?id=9389
Page Path:	1 : (SKU: 1) 2 : Thank You (SKU: 2)
SessionID:	1384467766_52854d36a9d4e0.20613503

DISTRIBUTION A: Distribution approved for public release.

Response Location

Country:	United States
Region:	LA
City:	Baton Rouge
Postal Code:	70803
Long & Lat:	Lat: 30.405001, Long:-91.186798

DISTRIBUTION A: Distribution approved for public release.